THE PETROLOGY AND GEOCHEMISTRY OF THE IMPACTITE SEQUENCE AND SELECTED TARGET ROCKS FROM THE YAXCOPOIL-1 BOREHOLE, CHICXULUB IMPACT STRUCTURE, YUCATÁN PENINSULA, MEXICO

By

Martin Guillaume Tuchscherer

A dissertation submitted to the Faculty of Science,
University of the Witwatersrand,
in fulfilment of the requirements for the degree of:

Doctor of Philosophy

Johannesburg, South Africa, 2008

Statement of original contribution

I declare that this dissertation is my own, unaided work. It is being submitted for the Degree of Doctor of Philosophy in the University of the Witwatersrand, Johannesburg, South Africa. It has not been submitted before any degree or examination in any other University.

_____

(Signature of candidate)

Abstract

Geological and geophysical investigations of the Chicxulub meteorite impact structure have been ongoing since its scientific recognition in 1991 (Hildebrand et al. 1991). The structure is of important significance because it is currently the only known impact crater that is linked to a global catastrophe, the Cretaceous/Tertiary boundary that occurred 65 Ma years ago. Major climatic and biological changes occurred at this interval that include the disappearance of ~70% of all living species, in particular the dinosaurs. A global iridium anomaly along with the occurrence of shocked quartz grains characterize a thin clay layer at this interval that led to the search for a large meteorite impact crater on continental crust. A large "volcanic" igneous province identified by oil exploration boreholes on the NW region of the Yucatán Peninsula was eventually recognized as a vast impactite deposit associated with a 180 km wide crater. Until 2002, only small grab and chip samples had been described from Chicxulub. This lack of sampling and, thus, poor understanding of the cratering conditions at Chicxulub led the International Continental Drilling Program (ICDP) to fund and drill the Yaxcopoil-1 borehole.

The Yaxcopoil-1 (Yax-1) borehole was drilled 60 km south-southwest from the center of the Chicxulub meteoritic impact. It intersected 794.63 m of post-impact cover rocks, 100.31 m of impactites, and 616.03 m of Cretaceous target rocks, terminating at a final depth of 1510.97 m. The impactite interval, as well as several selected samples from the Cretaceous target rocks, is the focus of this scientific investigation. In conjunction with this work, the Yax-1 core was studied by numerous international research groups and is, thus, currently one of the best studied continuous diamond drill core from an impact crater. This petrographic and geochemical investigation provides further understanding on the primary and secondary conditions that influenced the formation of the Yax-1 impactites and selected target rocks.

Five units have been recognized in the impactite interval. These subdivisions are based on macro- and microscopic observations and are complemented by geochemical characteristics. Unit 1 (795-822 m) comprises subrounded melt rock particles that are poorly sorted, yet show a progressive

gradation with height, are self supported, show perlitic devitrification texture, and are generally fine-grained. Unit 2 (823-846 m) and Unit 3 (846-861 m) are relatively similar, as they both consist of a groundmass-supported breccia with melt rock particles that are angular, fluidal, and vesiculated in texture. The groundmass in both units is pervaded by numerous carbonate-veinlets and decreases in volume towards Unit 3 because of compaction. Unit 2 and Unit 1 are both altered to a predominantly green colour by the pervasive conversion of silicate phases from clay minerals. Unit 3 is of a variegated character and is suggested to be the less altered unit bove Unit 4. Unit 4 (861-885 m) comprises a massive yet brecciated microcrystalline impact melt rock. It is primarily of a silicate composition and contains only minor secondary carbonate crystals. All lithic fragments are of silicate compositions. Unit 5 (885-895 m) shows the greatest variation in the proportion of melt rock particles and lithic fragments. The melt rock particles contain numerous microlites that crystallized below the glass-transition temperature. These are suspended in a carbonate groundmass that is either of a primary impact melt origin or of a secondary nature. Units 1 and 5 both contain foraminifera fossils and greater proportions of carbonate clasts than any other units. All unit show shock metamorphic characteristics, i.e., planar deformation features, ballenquartz, and checkerboard feldspar.

Geochemical results have been obtained by various analytical techniques in order to constrain cratering and alteration processes at various sampling scales. Main results reveal that samples from units 1 and 2 have been leached of their alkali elements, show negative Ce anomalies on a microscopic scale, and show less major element variation on a bulk sample scale than lower units. The groundmass in units 1 to 3 comprises a microcrystalline calcite and altered alkali element-, Ca- and Si- rich cement. In units 2, 3, and 5 melt rock particles are of a heterogeneous composition. In Unit 1, melt rock particles are highly altered, therefore volatile rich, and are of a more homogeneous composition than those of other units. On a bulk sampling scale, the silicate component for the whole impactite sequence shows remarkable homogeneity. Major and trace element compositions show that this component and Unit 4 are typical of the upper continental crust. The carbonate component is more calcite rich than dolomitic

and most likely represents strong secondary alteration. No significant sulfur content was measured compared to published known target rock values. The contents of the siderophile elements, including Ni, Co, Ir, and Cr, do not indicate the presence of a significant extraterrestrial component in the Yax-1 impactites.

Cretaceous rocks were also sampled in order to provide compositional constraints with the impactites and observe any shock related metamorphic features. Petrographic observations indicate that the Cretaceous rocks in the Yaxcopoil-1 drill core likely register a multistage deformation history that spans the period from pre- to post-impact. Contrary to previous studies that claimed evidence for the presence of impact melt breccia injection veins, no evidence was found from samples located between 1347–1348 m depth for the presence of melt breccia.

An emplacement mechanism for the impactite sequence is proposed with regards to cratering. Unit 5 is interpreted as an early ejecta deposit that was emplaced following the passage of the initial ejecta curtain during the excavation stage of cratering. Unit 4 is an allogenic siliceous melt rock body that originated primarily from the fusion of the silicate crystalline basement. The origin of Unit 4 is based on geochemical and petrographic arguments, i.e., no carbonate component to the melt could be detected and only igneous/metamorphic mineral/rock fragments were observed in it. It is suggested Unit 4 was emplaced as an outward flow of fused crystalline basement rocks from the collapsing central uplift or it may have also been deposited from the fallback of a large melt bomb. Brecciation occurred post-deposition as fragments fit together like pieces of a jig-saw puzzle. Units 2 and 3 represent unreworked fallback suevite deposits. Vesiculated melt rock particles are a testimony of the volatile rich nature of the collapsing impact plume. Volatiles are believed to have helped disperse the suevite and inhibited the melt rock particles from undergoing compositional homogenization. Unit 1 represents a reworked fallback deposit that formed from the resurge of seawater into the impact basin. Unit 2 is the altered equivalent of Unit 3 and along with Unit 1 underwent significant post-depositional phyllosilicate alteration from circulating fluids at the top of the suevite pile.

Dedication

To *Elizabeth Ruth Sharman*, who stood by me throughout this work.

Ackowledgements

I would like to first thank my supervisors, Profs Uwe Reimold and Roger Gibson, for allowing me to come to the University of the Witwatersrand in South Africa to work on the fascinating rocks of the Chicxulub Yaxcopoil-1 impactites. Without their continuous support, drive, and supervision, this work would not have been possible and as extensive. Great thanks are also given to Prof. Christian Koeberl at the Department of Geological Sciences at the University of Vienna for providing all of the INAA trace element data, iridium γ-γ coincidence spectrometry results, and insightful discussions while interpreting these results.

The following people at the Universtiy of the Witwatersrand are also acknowledged for their help during this work. The staff at the electron microscopy unit, in particular Prof. Michael J Witcomb, is thanked for their help during thin section imaging and analysis. Thanks are also given to Prof. Lew Ashwal for providing additional thoughtful discussion and insight while manipulating the large amount of geochemical data. Sharon Turner is thanked for her help while operating the X-ray diffractometer. Numerous thanks are given to the support staff of the School of Geosciences: Safia Cannell, Dalena Blithental, Matt Kitching, Mitch Miles, and Alex Mathebula.

At the Council for Geoscience in Tshwane (ex-Pretoria), the following people are thanked for their help during image analysis and electron microprobe work: Dr. Deon de Bruin, Annabe Walliser, and Maria Anastova.

Andreas Späth at the University of Cape Town is thanked for his help during the acquisition of trace element data by LA-ICP-MS.

All of my close fellow graduate students at the School of Geosciences are thanked: Dr. Frank Wieland, Dr. Christiano Lana, Louise Coney, Dr. Robert Kieffer, Dr. Fred Mpethu, Dr. Lynnette Greyling, Fiona Stevens, Dr. Shawn Letts, Denise Pone, and Dr. James Roberts. Without your friendship and comraderie, this whole academic endeavour would have been a lot less enjoyable!

Trevor Richardson, Dr. John Hancox, and Ian McCutcheon are thanked for their support while at Caracle Creek International Consulting.

Acknowlegements are given to the official reviewers of this thesis, Dr. Burkhard O. Dressler, Prof. David A. Kring, and Prof. Allan H. Wilson. Thank you for taking the time to read this thesis and providing me with your scientific and editorial oversight.

Last but not least, gratitude and appreciation are given to my wife, Libby Sharman, for being supportive and understanding during this work.

Table of contents

List of figures

List of tables

Abreviations

BSE:	Backscatter electron
Cc:	Calcite
CEMY:	Cretaceous end-member for the Yax-1 borehole
CL:	Cathodoluminescence
CTIY:	Cretaceous target rock interval of the Yax-1 borehole
DSDP:	Deep Sea Drilling Project
EMPA:	Electron microprobe analysis
Gdm:	Groundmass
ICDP:	International Continental Drilling Program
INAA:	Instrumental neutron activation analysis
K-Felds:	Potassium feldspar
K/T:	Cretaceous/Tertiary
LA-ICP-MS:	Laser ablation-iductively coupled-mass spectrometry
LOI:	Loss on ignition
MAPS:	Meteoritics and Planetary Science
Meso:	Mesostasis
Mic:	Microlite
MRP:	Melt rock particle
ODP:	Ocean Drilling Program
PEMEX:	Petróleos Mexicanos
Pl:	Plagioclase
Qtz:	Quartz
REE:	Rare earth element
SEM:	Scanning electron microscope
SEMY:	Siliceous end-member for the Yax-1 borehole
UNAM:	Universidad Nacional Autonoma de Mexico
XRD:	X-ray diffraction
XRF:	X-ray fluorescence
Yax-1:	Yaxcopoil-1

1. Introduction

The study of impact cratering has only recently come of age in the geoscience community (e.g., Reimold 2003; French 2004). Currently 174 impact craters have been positively identified on Earth (UNB Earth Impact Database, February, 2008). This is primarily because the recognition of macro- and microscopic shock metamorphic features are well known today and satellite imagery is more readily available. It is also presently widely accepted that impact cratering is a ubiquitous process that occurs throughout the solar system (e.g., Taylor 1982, 1992). All space probes that have ventured to the inner planets, moons, comets, and asteroids of our solar system have photographed various types of impact craters. However, because Earth is an active planetary body consisting of tectonic plates, oceans, and an atmosphere, its surface is constantly being renewed by erosion, the redeposition of sediments, and the subduction of tectonic plates. Because of this activity, Earth does not possess an extensive impact cratering record. The currently oldest and coincidently biggest crater on Earth is the Vredefort Structure, which is 2.02 Ga years old (Kamo et al. 1996). In comparison to the age of the Earth, which is 4.5 Ga old (Patterson 1956), this indicates a thorough loss of the terrestrial cratering record. This preferential obliteration therefore makes it difficult to obtain samples, study and, thus, understand impact cratering processes by first order observations. This is why in 2002 the International Continental Drilling Program (ICDP) drilled the Yaxcopoil-1 (Yax-1) borehole 60 km south-southwest of the center of the Chicxulub impact crater (Dressler et al. 2003a, Fig. 1.1.). The detailed description of impact melt rocks and breccias from this borehole are the focus of this thesis.

Chicxulub became a scientific drilling target because it is the world's third largest known impact structure and the only one linked to a global mass exctinction event. The reason why drilling Yax-1 was of great importance is that no continuous impactite diamond drill core had been previously recovered from the buried crater, rock density data were required to calibrate geophysical seismic surveys, and no extensive detailed petrographic and geochemical studies had ever been performed on a continuous intersection of Chicxulub impact melt rocks and breccias. Before this ICDP program, several small and discontinuous impact melt

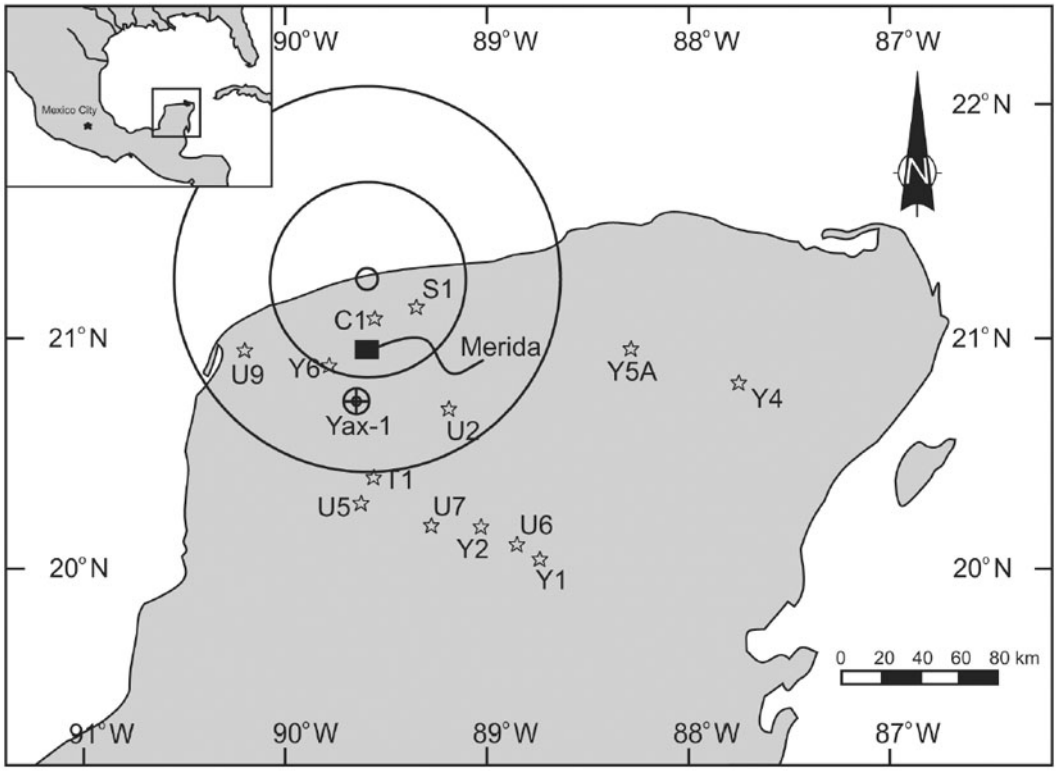

Fig. 1.1. The Chicxulub impact structure is located at the northwestern edge of the Yucatán Peninsula. The ICDP Yaxcopoil-1 borehole is located 60 km south-southwest from the center of the structure. The outer circle represents the postulated position of the crater diameter at ~195 km, based on seismic imaging of the most significant inward-facing scarp (Morgan et al., 2002). The inner circle represents the extent of the postulated transient cavity at ~100 km, based on seismic imaging of the disturbed Cretaceous sedimentary sequence (Morgan et al., 2002). All nearby diamond drill hole locations are plotted after Lopez-Ramos (1975) and Persaud and Sharpton (1998).

and breccia core samples from the buried Chicxulub crater had already been characterized petrologically and geochemically (e.g., Hildebrand et al. 1991; Kring and Boynton 1992; Sharpton et al. 1992; Swisher et al.1992; Blum et al. 1993; Koeberl 1993a; Meyerhoff et al. 1994; Schuraytz et al. 1994; Ward et al. 1995; Urrutia-Fucugauchi et al. 1996; Warren et al. 1996; Kettrup et al. 2000; Lounejeva et al. 2003; Claeys 2003). These were provided by the Mexican national petroleum company (PEMEX) through oil exploration boreholes and the Universidad Nacional de Mexico (UNAM) short surface drilling program (Lopez Ramos 1975; Urrutia-Fucugauchi et al. 1996). However, these only provided a glimpse of the complex impact-related processes involved at Chicxulub. Yax-1 was therefore positioned in a region that was believed to intersect a thick succession of impactites, in the outer, down-faulted, ring of the Chicxulub structure (Sharpton et al. 1996; Sharpton 2000). Contrary to the expected large

volume of impactites to be intersected by Yax-1, only 100 m were retrieved. This was attributed to poorly calibrated seismic geophysical profiles. Despite this shortfall, extensive scientific work was achieved on the Yax-1 core.

The scientific investigation of the Yax-1 impactites was expected to provide various types of information ranging from the way the impactites were deposited, the shock pressures and temperatures they were subjected to, the extent of melting, excavation, mixing, hydrothermal alteration, magnetic properties, geochemical characteristics (i.e., major, trace, and isotopic signature), meteorite contamination (the highly siderophile element signature), and potential kill mechanism for the associated mass extinction event. Much of this information has now been published in a Yaxcopoil-1 special issue of the journal Meteoritics and Planetary Sciences (MAPS, vol. 39, issues # 6, 7). This thesis is an additional contribution to the wealth of scientific data that was produced from the Yaxcopoil-1 borehole. The objectives of this scientific research on the Chicxulub Yax-1 rocks are presented in the following section.

1.1. Objectives

Numerous reasons have motivated the scientific drilling of the Chicxulub crater. The crater is fairly young (64.98 ± 0.05 Ma, Swisher et al. 1992) and it has, not undergone substantial regional metamorphism and/or structural deformation on the Yucatán Peninsula. As mentioned previously, the only samples that were available prior to Yax-1 were in the form of core, chips and grab samples obtained from PEMEX oil exploration boreholes and the shallow UNAM scientific drilling program. These samples, although extensively studied (see section 1.3.4.), only provided limited insight. The International Continental Drilling Project (ICDP) Yax-1 core was therefore extracted in order to provide additional detailed information regarding the processes involved during impact cratering.

The prime objective of this thesis was to understand the genetic history of the Yax-1 impactites as it relates to impact cratering. This was achieved by detailed petrographic and geochemical characterization at a macro- and microscale with the help of various analytical techniques (see section 1.7. for details on these techniques). Primary and secondary features were identified in

order to understand various processes, i.e., constrain the extent of melting and mixing of the various target rocks, search for the meteoritic component, interpret the emplacement mechanism for the various impactite units, and evaluate subsequent hydrothermal and diagenetic alteration. This provided key characteristics that also enabled to define and classify the impactites. The identification of shock-related metamorphic features, i.e., planar deformation features, ballenquartz, isotropic quartz, and melt particles, also enabled constraints to be placed on shock pressures and temperatures and, thus, provide an insight into the amount of energy released by the Chicxulub impact event. The identification of alteration minerals (phyllosilicates, zeolites, secondary minerals) was also undertaken in order to constrain post-impact hydrothermal activity. Several samples were also selected from the Cretaceous carbonate target rocks in order to provide geochemical constraints on the impactites and also to discern any shock-related metamorphic overprints that they may have registered, further constraining the magnitude of the Chicxulub impact event. These objectives were selected in order to allow a comprehensive investigation and interpretation of the Yax-1 impactites.

The main research questions sought by this scientific investigation are:

1. To understand the degree of shock melting undergone by various inclusion types (e.g. carbonate, sulfate, and silicate inclusions).
2. Constrain the pressures and temperatures associated with the impact-induced shock metamorphism.
3. Understand how the glasses and melted inclusions evolved under the extreme conditions of cratering.
4. Characterize and describe textural features that provide insight into the thermodynamics of the various melts.
5. Establish the crystallization history of the various impact melt rocks.
6. Determine the degree of mixing (heterogeneity/homogeneity) within the breccia and glasses.
7. Determine vertical variations within the retrieved Yax-1 core.
8. Interpret the cratering dynamics responsible for the inclusion population (excavation stage).

9. Determine the bulk geochemical composition of the Yax-1 borehole.
10. Extrapolate the possible depth of cratering.
11. Determine the mineralogy and composition of any extraterrestrial phase.
12. Describe in detail footwall breccia zones (cataclasites, oil shales, or possibly friction or shock melt) and invetigate how their presence relates to the cratering process.

1.2. The K/T boundary

An impressive list of crucial evidence has emerged in support of a cosmic collision at the K/T boundary 65 Ma years ago (e.g., Smit 1999). This includes the following:

- The widespread deposition of glass spherules around the Caribbean and worldwide (e.g., Sigurdsson et al. 1991; Smit et al. 1992; Premo and Izett 1992; Koeberl and Sigurdsson 1992; Koeberl 1993a; Oskarsson et al. 1996; Chaussidon et al. 1996; Hough et al. 1998, Fig. 1.2a, b).
- The fallout of shocked zircon grains with Pan-African ages (Kamo and Krogh 1995, Fig. 1.2c) similar to the age of the crystalline basement at Chicxulub (Krogh et al. 1993; Wittman et al. 2006).
- Ni-rich spinels (Cisowski 1990; Kyte and Bostwick 1995; Gayraud et al. 1996; Ebel and Grossman 2005).
- Ca-rich clinopyroxene in glass (Smit 1999, Fig. 1.2d).
- The global distribution of shock metamorphic quartz (Bohor 1990; Owen et al. 1990; Izett 1990; Alvarez et al. 1995; Bostwick and Kyte 1996; Goto et al. 2002, Morgan et al. 2006; Fig. 1.2e).
- The identification of fullerenes (Heymann et al. 1994; Heymann et al. 1996; Buseck 2002, Fig. 1.2f).
- Anomalous extraterrestrial siderophile element concentrations in spherules and the K/T boundary red clay layer, specifically, the famous iridium anomaly (Orth et al. 1981; Alvarez et al. 1982; Schmitz et al. 1988; Evans et al. 1995; Schuraytz et al. 1996, Fig. 1.2g).
- A meteorite fragment (Kyte 1998, Fig. 1.2h).
- Carbon/ash deposits consistent with global wildfires (Argyle et al. 1986; Wolbach et al. 1990; Kring and Durda 2002).
- The fallout occurrence of the high-pressure silica polymorph stishovite (McHone et al. 1989).
- Fallout micro-diamonds (Gilmour et al. 1992; Hough et al. 1997).

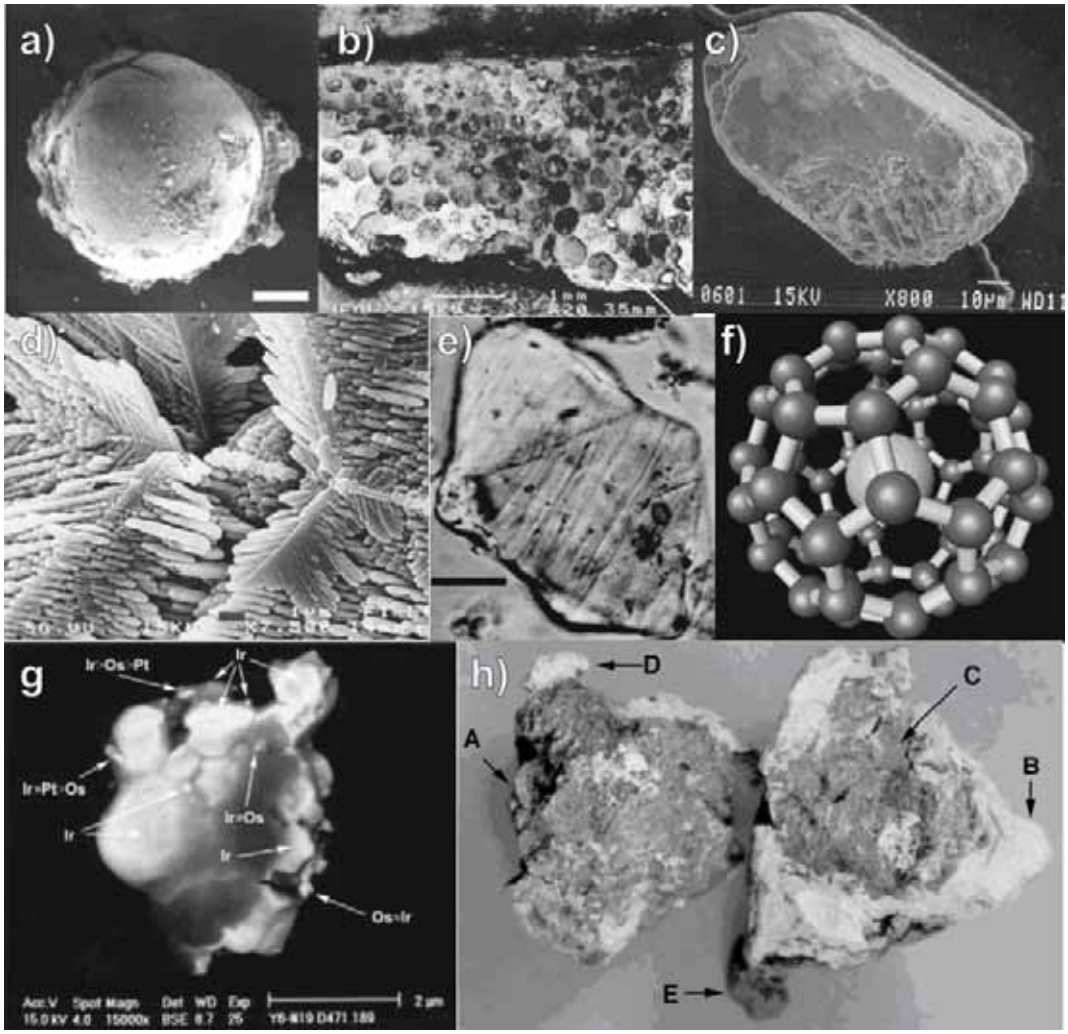

Fig. 1.2. Photographs of key geological evidence that links the K/T boundary with a meteorite impact event: a) SEM image of smectite spherule from Blake Nose, scale bar = 200 µm (ODP Leg 171B, from Martinez-Ruiz et al. 2000); b) SEM image of graded spherule layer, rich in Ir (86 ng/g), from Tetri-Tskaro, near Tbilisi, Republic of Georgia, scale bar = 1mm (from Smit 1999); c) SEM image of shocked zircon grain from the Rock Creek site, south-central Saskatchewan, scale bar = 10 µm (from Kamo and Krogh 1995); d) SEM image of clinopyroxene dendrites etched out of glass by seawater; from DSDP site 577b, scale bar = 1 µm (from Smit 1999); e) Cross-polarized light image of rare shocked quartz grain from Albion Formation diamictite bed, Albion Island, Belize, scale bar = 20 µm (from Pope et al. 1999); f) C60 (fullerenes) molecule with caged atom in its center (from Buseck 2002); g) Backscattered electron image of Ir-bearing particle extracted from the Y6 borehole, sample N19-R(b), scale bar = 2 µm (from Schurayz et al. 1998); and h) small meteorite fragment (A, width = 2.5 mm) retrieved from DSDP Site 576, (B) light-brown clay, (C) cavity from which meteorite was encased, (D) light-brown clay on meteorite, (E) dark-brown clay (from Kyte 1998).

The associated mass extinction (e.g., Alvarez et al. 1980; Raup 1991; Ryder et al. 1996; Hallam and Wignall 1997; Koeberl and MacLeod 2002) is, thus, believed to be the product of a meteorite impact and is currently the only such coincidence in the Earth's biological and geological history.

Prior to the impact hypothesis, various extinction mechanisms had been proposed for this great dying: lethal radiation from a nearby supernova (Terry and Tucker 1968), the progressive increase of CO_2 owing to a global greenhouse effect elevating mean global temperatures (McLean 1982), anoxia in the oceans via a shallowing of the oxygen minimum zone (e.g., Kajiwara and Kaiho 1992), an arctic spillover of fresh cold water into the world oceans killing most tropical planktonic life (Gartner and Keany 1978), major volcanism at the Deccan Traps spewing lethal doses of aerosol and toxic gases into the atmosphere (Courtillot et al. 1996; Glasby and Kunzendorf 1996), a Verneshot event, i.e., the massive and violent eruption of trapped gases through thick crust (Morgan et al. 2004), and a major marine regression affecting organism on shallow continental shelves (Keller et al. 1993, 1996; see the books by Hallam and Wignall 1997 and Alvarez 1997 for greater details). Despite these various hypotheses, the accumulated evidence at the K/T boundary strongly favoured a global catastrophe by the impact of an asteroid or comet (e.g., Alvarez et al. 1984; Ryder 1996; Hildebrand et al. 1991; Claeys et al., 2002). However, researchers still argue for a combination of catastrophic events at/or just prior to the boundary, i.e., through multiple impacts, volcanism combined with impact, regression, and oceanic anoxia (Gartner and McGuirk 1979; Officer and Drake 1983; Courtillot et al. 1996, 2000; Keller 2003, 2004).

The Cretaceous/Tertiary boundary can be correlated throughout the world at approximately 65 Ma and is the most recent of the 5 major Phanerozoic mass extinctions. Various forms of life disappeared simultaneously at the K/T boundary such as the dinosaurs, marine and flying reptiles, belemnites, ammonites, numerous bilvalves, and extensive groups of phyto- and zooplankton (e.g., Hallam and Perch-Nielsen 1990; Steuber et al. 2003; Fastovky et al. 2005). It is estimated that about 76% of all living species and 47% of all genera became extinct (Jablonski 1994). The boundary is also well known owing to an unusual iridium anomaly that is found throughout the world (e.g., Alvarez et al. 1980; Smit and Hertogen 1980). Iridium is a highly siderophile element that is usually extremely rare in upper crustal rocks, especially sedimentary rocks. This is because mostly all siderophile elements segregated into the core during the early

core-mantle differentiation of the Earth (e.g., McDonough 2003). It was therefore postulated by Alvarez et al. (1980) that this anomalous iridium in upper crustal rocks should reflect some kind of extraterrestrial contamination, either through the constant influx of meteorite and interplanetary dust particles to Earth or a major meteoritic impact.

The International Commission on Stratigraphy (ICS) defined the global K/T boundary stratotype section and point (GSSP) at El Kef, Tunisia, owing to the well preserved and continuous record of sedimentary rocks across the interval (e.g., Keller et al. 1995). The boundary is typically marked by a thin red clay layer believed to be the altered remnant of an ejecta layer that is rich in iridium, shocked quartz grains, Ni-rich spinels, and altered microkrystites (Smit 1999). The official boundary has, thus, been placed below this red clay layer, which can be correlated worldwide, except in the Gulf of Mexico where mass wasting from the Chicxulub impact by continental margin collapse and tsunami deposits (Smit and Romein 1985; Bourgeois et al. 1988; Bralower et al. 1998; Tada et al. 2002; Arenillas et al. 2006; Schulte et al. 2006) disturbed normal sedimentation processes. However, K/T boundary DSDP 536 and 540 do not show evidence of tsunami activity but mass wasting due to the collapse of the Campeche platform margin (Smit 1999). Approximately 345 K/T boundary sites have been recorded throughout the world, with 101 containing ejecta debris and 85 showing a positive Ir anomaly (Claeys et al. 2002). The boundary occurs in the magnetozone 29R and can be correlated on land and in the marine realm by a “fern spike” (Tschudy et al. 1984; Fleming and Nichols 1990) and the mass disappearance of numerous planktonic foraminifera species, respectively (Hallam and Wignall 1997). Numerous organisms were affected, including calcareous nanoplankton (85 % of the Cretaceous species became extinct), ammonites, brachiopods, and bryozoans. Out of the marine reptiles, it is believed that the ichthyosaurs and plesiosaurs were in slow decline already towards the end of the Cretaceous. However, mosasaurs, which underwent a major late Cretaceous radiation, became completely extinct. Conversely, there is disagreement whether terrestrial reptiles disappeared gradually or suddenly at the K/T boundary, as vertebrate fossils generally occur only sporadically in the stratigraphic record and well preserved continental K/T

boundary sites are rare (e.g., Buffetaut 1990; Galbrun 1997; Fastovky and Sheehan 2005). With regards to plant life, known sites in North America (e.g., Braman and Sweet 1999) and north-eastern Asia (Vajda et al. 2001) were considerably affected by the extinction event. Other geochemical indicators that can be found or straddle the boundary include a negative $\delta^{13}C$ isotopic excursion in marine sedimentary rocks due to the collapse of planktonic micro-life (Keller and Lindinger 1989) and a characteristic $^{87}Sr/^{86}Sr$ peak (Macdougall 1988). The latter is believed to result from an increased terrigenous input into the global oceans because of increased weathering and runoff during a regression and/or due to acid rain following impact (Hallam and Wignall 1997).

1.3. The Chicxulub impact structure

The Chicxulub structure is the third largest known impact structure on Earth (180 km, Hildebrand et al. 1991; Grieve and Therriault 2000). It has also become the widely accepted "smoking gun" for the catastrophic events associated with the Cretaceous/Tertiary (K/T) boundary mass extinction. Extensive scientific evidence supported the hypothesis that a meteoritic impact was responsible for the K/T boundary (e.g., Bohor 1990). The worldwide preferential size distribution of shocked quartz grains and higher iridium concentrations indicated a potential crater site in North America rather than Europe, Asia or the Southern Hemisphere (e.g., Bohor et al. 1987; Izett 1990; Alvarez et al. 1995; Claeys et al. 2002). Early in this search only one small crater, the 35 km wide Manson impact structure of Iowa had been identified in North America as a potential candidate. Because of its small size, however, the crater was never recognized as the K/T boundary smoking gun. The Manson impact crater had a similar age to the K/T boundary (65.7 ± 1.0 Ma; Kunk et al. 1989) but this was subsequently corrected to 73.8 ± 0.3 Ma by Izett et al. (1993). Eventually a much larger impact structure was discovered at Chicxulub (Hildebrand et al. 1991). The structure was found straddling the north-western coastline of the Yucatán Peninsula of Mexico (Fig. 1.1). Initial attempts poorly constrained the crater's size between 180 and 300 km wide (Hildebrand et al. 1991; Sharpton et al. 1996; Pope et al. 1996). Ironically, knowledge of a circular feature in the Yucatán

subsurface had already been reported ten years before by Penfield and Camargo (1981) and had even been drilled by PEMEX (Lopez Ramos 1975). These authors suggested this area represented a major igneous province but also postulated an impact origin for the unusual andesitic rocks and the structure. The improper recognition of characteristic shock metamorphic features precluded the proper identification of the structure, whose melt rocks had been misidentified as pyroclastic rocks, bentonite, and andesite. Even after the recognition that these rocks were clearly of impact origin through the recognition of shock metamorphic features, some geologists still advocated a volcanic source for the Chicxulub impact melt rocks and suevites (Meyerhoff et al. 1994). Nevertheless, additional evidence gathered from nearby K/T boundary sites and tsunami deposits with shocked quartz in the Caribbean (Bourgeois et al. 1988; Hildebrand and Boynton 1990) confirmed the recognition of Chicxulub as the K/T boundary crater.

Despite the fact that Chicxulub is generally agreed to be associated with the K/T boundary (e.g., Smit 1999), it must be mentioned that the age of the impact and its associated ejecta deposits in the vicinity of the Caribbean Sea are still highly debated (e.g., Keller et al. 2004a). It has been argued by several researchers that the Chicxulub impact event predated the K/T boundary by ~ 300 Ka (e.g., Ward et al. 1995; Stinnesbeck et al. 2001; Keller et al. 2004; and Stüben et al. 2005). These claims are primarily based on: 1- the inconsistent co-occurrence of breccia deposits with the Ir anomaly, 2- the occurrence of an impact ejecta layer interbedded in Late Maastrichtian marls, 3- the occurrence of early Danian foraminifera in breccia deposits, and 4- the suspected occurrence of Maastrichtian foraminifera fossils in laminated limestone overlying the impactites of the Yax-1 borehole. However, several independent research groups have interpreted these observations (by the Keller group) as the results of mass wasting processes typical of tsunami-type activity associated with the Chicxulub impact (e.g., Matsui et al. 2002; Norris and Firth 2002; Tada et al. 2002; Goto et al. 2004; Alegret et al. 2005; Lawton et al. 2005; Scassso et al. 2005; Arenillas et al. 2006; Schulte et al. 2006).

This debate, although interesting and highly controversial, has no direct bearing on this thesis, as the primary objectives of this work are to characterize

and understand impact-related processes in impactites of the Yax-1 borehole. The Chicxulub structure is uncontested as being of impact origin. Controversy did exist in the past, as it had once been postulated by Lopez Ramos (1975) and Meyerhoff et al. (1994) that the Chicxulub melt rocks were part of a large magmatic province. However, the abundance of impact-related shock metamorphic evidence characterized in samples from various boreholes, e.g., Y2, Y6, C1, Yax-1 (Hildebrand et al 1991; Sharpton et al. 1992; Tuchscherer et al. 2004a and references therein) have provided the uncontested proof for its impact origin.

1.3.1. Geophysics

Since the discovery of the Chicxulub impact structure, extensive geophysical investigations have been made to properly constrain its size and subsurface features. In their discovery paper, Hildebrand et al. (1991) described a circular, negative (-30 mgal) Bouger gravity anomaly of 180 km diameter (Fig. 1.3). Total magnetic field data presented by Lopez Ramos (1975) and Penfield and Camargo (1980) delineated a 210 km diameter structure, characterized by large-amplitude, short wavelength anomalies. This was substantiated by Pilkington et al. (1994), Espindola et al. (1995), and Hildebrand et al. (1995). However, subsequent papers suggested the structure could measure between 250 and 300 km in diameter, according to reprocessed gravity data (Sharpton et al. 1993, 1996; Urrutia-Fucugauchi et al. 1996, Fig. 1.4) and topographic expression features (Pope et al. 1996, Fig. 1.5). Based on scaling estimates from gravity and core logs, Sharpton et al. (1996) suggested that the Chicxulub crater was actually about 300 km wide and had an initial minimum transient cavity diameter of 110 km. A diameter of 200 km was eventually confirmed through offshore 2D seismic surveying, which also indicated a multi-ring morphology (Morgan et al. 1997, 1999; Morgan and Warner 1999, Fig. 1.6). These data delineated three rings: a peak ring, a crater rim, and an outer ring. Normal faulting was observed as inward downfaulting of the middle and lower crust, and of the Moho down to 35 km depth. Intense faulting was imaged between 35 and 55 km radial distance from the center of the crater. It is believed this region coincides with the

postulated outer collapse of the transient cavity, which is interpreted to have been ~100 km in diameter (Morgan et al. 1997; Morgan et al. 2002). New seismic data obtained in 2005 from the research vessel Maurice Ewing also suggest this region is part of a collapsed terrace (McDonald et al. 2005; Morgan et al. 2005). The latest remote sensing data from the Shuttle radar topographic mission (SRTM) indicate a topographic rim-to-center radius of 129 km (Kinsland et al. 2005, Fig. 1.7).

1.3.2. Geological setting and surface morphology

Because of the poor exposure, dense vegetation, the lack of adequate road access, non-existent surface drainage, caliche cover and low relief, the geology of the Yucatán Peninsula is poorly understood. The best geological description is by Lopez Ramos (1975, Fig. 1.8). Most of what is known about the Yucatán Peninsula subsurface geology has been inferred from diamond drilling by oil-

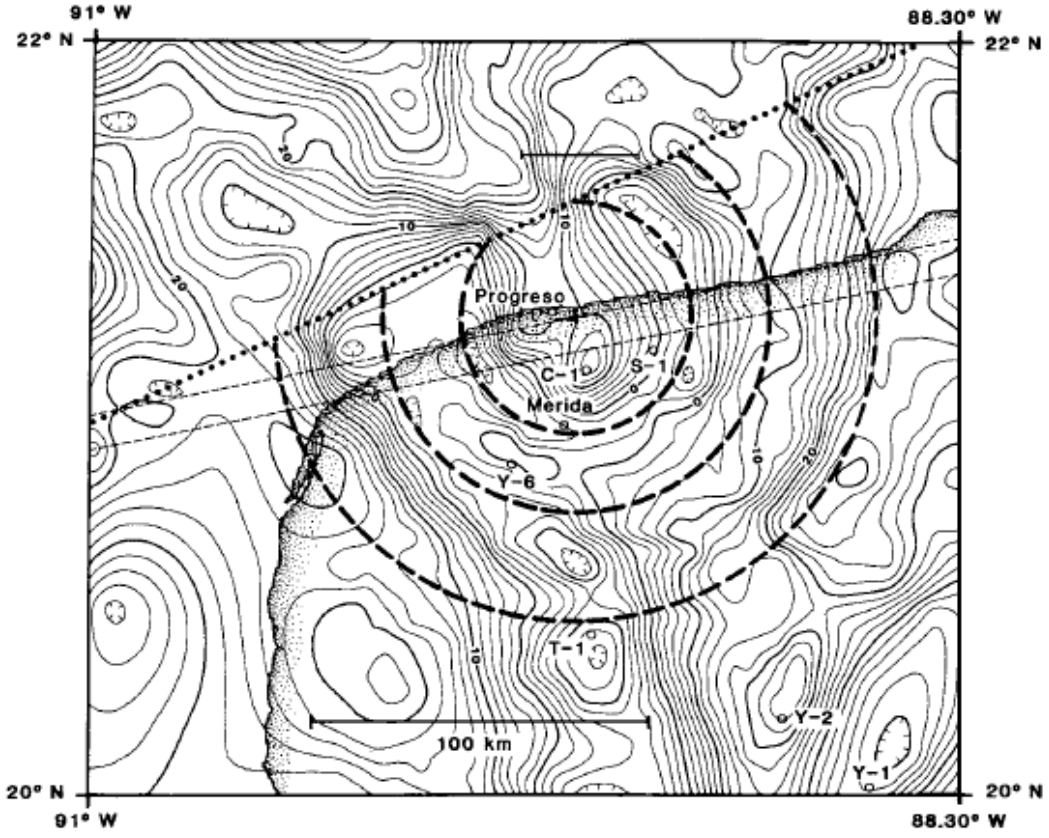

Fig. 1.3. Contoured Bouger gravity data, contours = 2 mgal (from Hildebrand et al. 1991).

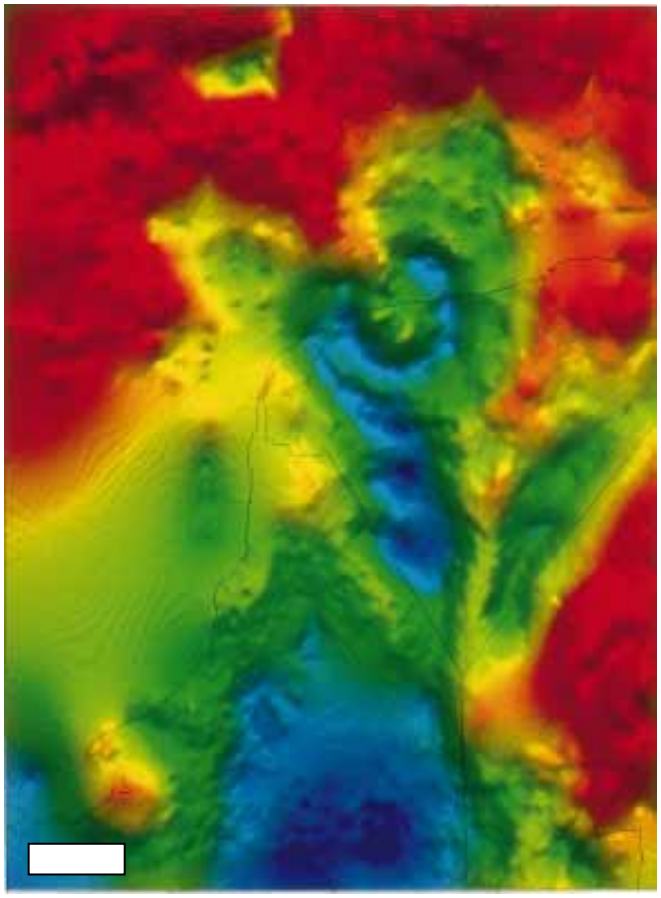

Fig. 1.4. Shaded relief gravity data, red = high gravity, red and violet = gravity low, scale bar = 100 km (from Sharpton et al. 1996).

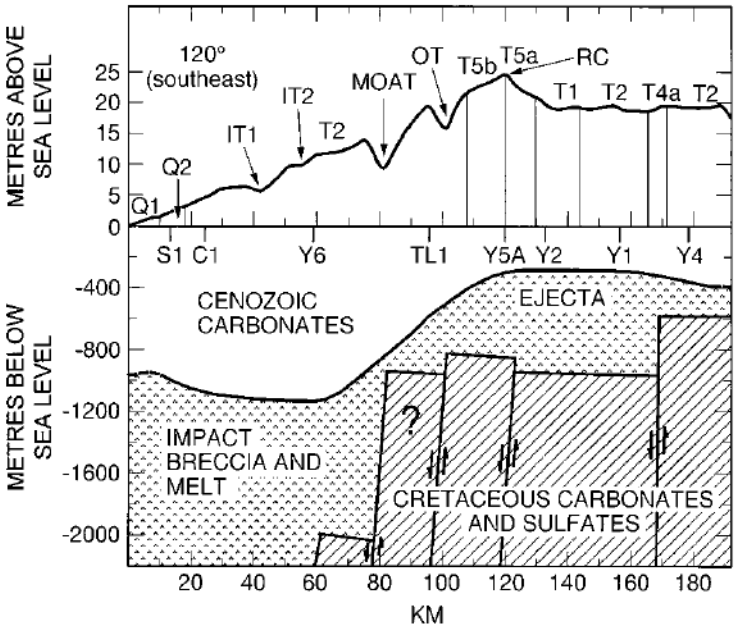

Fig. 1.5. Topographic features from digital elevation measurements along 120^{o} radial traverses from the center of the Chicxulub structure, IT = inner trough, OT=outer trough, RC=ridge crest (from Pope et al. 1996).

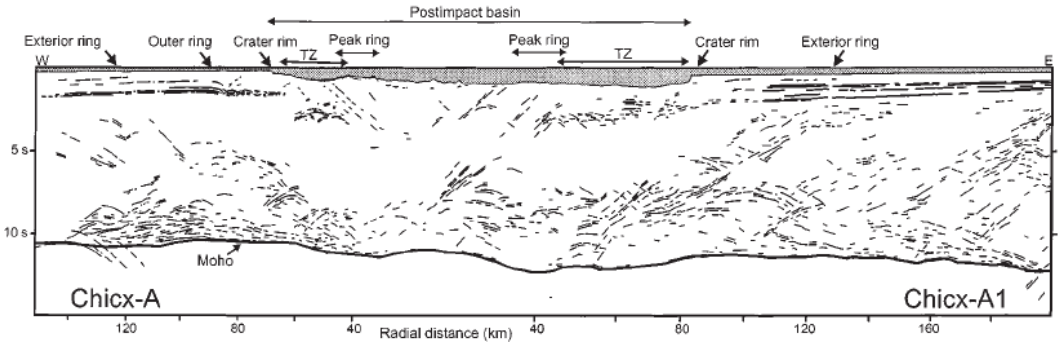

Fig. 1.6. Line drawing of a deep reflection seismic profile delineating zones of major disturbance (gray pattern = Tertiary rock cover, Moho is at 11-12 seconds TWTT, two way travel time, or about 35 km depth, TZ = terraced zone, 20-35 km wide, image from Morgan and Warner 1999).

Fig. 1.7. Shuttle radar topography mission (SRTM) digital elevation map of the northwestern region of the Yucatán Peninsula, North is up (the image is ~311 km in the east-west direction, from Kinsland et al. 2005).

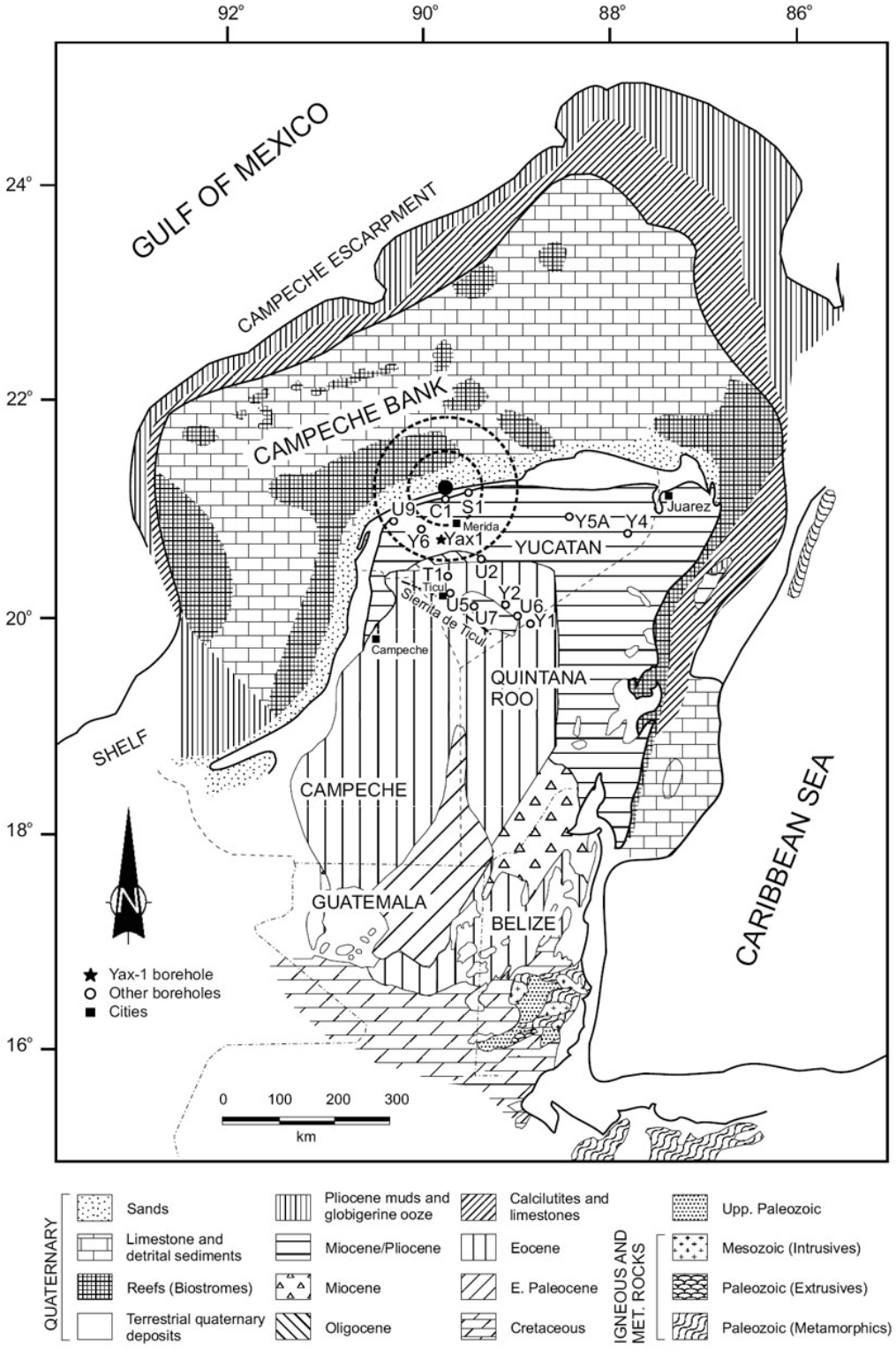

Fig. 1.8. Surface and offshore geology of the Yucatán Peninsula of Mexico with location of the Chicxulub impact structure, as well as the Yaxcopoil-1 (Yax-1) and other boreholes (geology modified after Lopez Ramos 1975). Note that the nearest exposures of Cretaceous target rocks occur in Belize and Guatemala, several hundred kilometers from the impact structure.

exploration and the Universidad Nacional Autonoma de Mexico (UNAM, see next section). Quaternary and Tertiary rocks (primarily loose sands, limestone, shale, and marls) currently overlie the Chicxulub structure (Fig. 1.8). Offshore rocks comprise Quaternary limestone with extensive biostromes. The nearest exposed target Cretaceous and Upper Paleozoic sedimentary and crystalline basement rocks can be found to the south of the Yucatán Peninsula, in Belize and Guatemala, where also good K/T boundary sites with known Chicxulub ejecta occur (e.g., Keller and Stinnesbeck 2000; Pope et al. 2005). Sedimentary Cretaceous rocks are mostly evaporites and comprise dolomite, anhydrite, argillaceous limestone, and limestone. The crystalline rocks belong to a deeply eroded orogenic belt that consists of schists and granitic intrusions that are overlain by carbonaceous shales and sandstone (de Cserna 1989).

The surface morphology of the Yucatán Peninsula can be divided into three physiographic regions. The northern region is characterized by very low and flat topography all the way from the Gulf of Mexico towards the Sierrita de Ticul. The second region, the Sierrita, is about 50 to 100 m in elevation and trends for 110 km northwest – southeast with a prominent scarp towards the northeast. To the south, the third region of the Yucatán is defined by a central plain that extends between the Gulf of Mexico and the Caribbean Sea. Greater topography is encountered farther towards the southeast, beyond the Arco de la Libertad and the Maya mountains, where the closest exposures of basement crystalline rocks occur (Lopez Ramos 1975).

1.3.3. Target stratigraphy

The study of Lopez-Ramos (1975) provides the best stratigraphic compilation of core logs for the Yucatán Peninsula. Rhyolites were encountered in the Y1 borehole at a depth of 3,200 m. These were dated at ~ 410 Ma (Rb/Sr) with a metamorphic episode at 300 Ma (Lopez-Ramos 1975). The metamorphic ages coincide with dates obtained from volcanic rocks in the Maya Mountains. The Y4 borehole was also reported to have encountered basement rocks, namely light-gray, yellow-brown, weathered, and slightly metamorphosed quartzite.

Lopez Ramos (1975) indicated that towards the south of the Yucatán Peninsula, in British Honduras, schists and gneissic rocks were encountered in numerous wells at a depth of ~2165 m. Overlying the basement rocks, the widespread and uncomformable occurrence of red beds of the Todos Santos Formation can be found. These are believed to be of Cretaceous-Jurassic or Triassic-Jurassic age and comprise siltstones and sandstones with some quartz gravel intercalations (Lopez Ramos 1975). Overlying the red beds is a thick and extensive sequence of evaporites, named "Yucatán Evaporites". These have been subdivided into 3 units, Y-I, Y-M, Y-S, by Lopez Ramos (1975) based on the Y1 borehole. The lowermost unit (Y-I, 3089 – 2265 m) comprises anhydrite, bentonite, pelitic tuff, and limestone. Unit Y-M (2265 – 1487 m) contains limestone interlayered with anhydrite, massive anhydrite, anhydrite with gypsum, and dolomite. The uppermost unit Y-S (1487 – 265 m) comprises mostly anhydrite with some sporadic limestone, calcarenite, and limestone with oolites. Tertiary rocks from the C1, Y6, and S1 boreholes have also been described by Lopez Ramos (1975) and subdivided according to age: Paleocene, Eocene, Oligocene, Miocene-Pliocene, and Pliocene-Pleistocene. In general, the rocks comprise light-gray and fine-grained limestones, marl, green-gray lutite, and minor clay horizons. In the C1, Y6 and S1 wells, Tertiary rocks can be found at a depth of ~1000 m. However, further away from the Chicxulub impact structure, these are found at a depth of <500 m (see Figs 1.6 and 2.2 for a cross-section).

A more recent study of the subsurface stratigraphy of the Yucatán platform was published by Ward et al. (1995). These authors presented core logs from boreholes T1, Y2, Y1, Y6, C1, Y5 and Y4 in order to show the dominant lithological composition of Cretaceous and Tertiary rocks and also to constrain the extent of the andesitic melt rocks and polymict breccias associated with the Chicxulub impact structure. Ward et al. (1995) indicated that the basement was intersected at 2418 m and 3203 m depths in wells Y4 and Y1, respectively, and that it comprised a Paleozoic metamorphic terrain. They subdivided the Mesozoic rocks above the basement into seven subunits (A to G), with the last unit representing an extensive end-Cretaceous breccia deposit. The lowermost unit A comprised Jurassic to Early-Cretaceous red and gray sandstones, shale and silty

dolomite that overlie the basement. Units B to G (bottom to top) generally comprise interlayered dolomite with anhydrite and limestone, and represent shallow-water, subtidal, shallow-platform, and restricted evaporitic depositional environments. Ward et al. (1995) postulated that the pre-impact stratigraphy comprised – volumetrically – 35 to 40 vol% dolomite, 25 to 30 vol% limestone, 25 to 30 vol% anhydrite, and 3 to 4 vol% sandstone and shale. They reported that an impact origin for the extensive breccia deposits was the most likely interpretation but warned that these may have pre-dated the K/T boundary, as biostratigraphy alone could not constrain the exact age of the crater structure. This problem arose because a stratum overlying the breccia deposit contained characteristic upper Maastrichtian planktic foraminifera and was interpreted to have been deposited under normal marine conditions.

1.3.4. Previous results on Chicxulub impactites

Before 2002, thirteen boreholes had been drilled in and around the Chicxulub impact structure. Most cores (C1, S1, Y1, Y2, Y4, Y5A, Y6, T1, Fig. 1.1) were recovered by the Mexican national oil company (PEMEX) in the search for hydrocarbons during the late 1960's and 1970's. After Chicxulub had been established as an impact structure, subsequent drilling was undertaken by the Universidad Autonoma de Mexico (UNAM boreholes 1-7, Figs 1.1 and 1.8). Although drilling appears extensive, only a few scientific publications were produced that focused on the petrology and the chemistry of retrieved impactite samples. Prior to the recognition of the impact origin of these rocks, the impactites were considered volcanic andesites. It was eventually recognized that these impact melt and breccia samples provided the proof for the impact origin of the Chicxulub structure through the recognition of shock metamorphic micro-features (Hildebrand et al. 1991). Some of the previous findings obtained from the impactites placed constraints on their crystallization age and, thus, the age of the impact, as well as their geochemical characteristics and isotopic signature (Hildebrand et al. 1991; Kring and Boynton 1992; Swisher et al. 1992; Sharpton et al. 1992; Koeberl 1993a; Blum et al. 1993, Schuraytz et al. 1994; Kettrup et al. 2000). These observations have been important in revealing some of the extent of

melting and target rock mixing. These have also been important at correlating the crater with known worldwide fallout and ejecta deposits. Because there is no compilation of this scientific work thus far, it is deemed appropriate to include the relevant findings here.

Hildebrand et al. (1991) published the discovery of the Chicxulub Structure and provided petrographic and geochemical characteristics of core samples recovered from the Y6 (Yucatán 6) and Y2 (Yucatán 2) wells. Their report provided conclusive evidence of the impact origin of this large (260 – 180 km) circular structure. They also revealed that numerous other wells, e.g., C1 (Chicxulub 1) and S1 (Sacapuc 1), intersected coarse clastic breccias and impact melt. They described retrieved impactite samples as similar to igneous rocks and glass having an andesitic composition. Glass was reported to underlie polymict breccias in wells C1 and S1, whereas andesitic rocks, or impact melt, were observed in well Y6 and below the andesitic glass in C1. The Y6-N14 breccia sample comprised a fine-grained calcite matrix (25 vol%) and sedimentary (limestone and anhydrite at 5 vol%) and igneous clasts (65 vol%). Hildebrand et al. (1991) reported igneous clasts, or melt fragments, that were composed primarily of a microcrystalline groundmass that contained K-feldspar ($Ab_{14-39}Or_{85-2}An_{1-5}$), plagioclase ($An_{13}Ab_{84}Or_3$) and augite ($Wo_{50}En_{39}Fs_{11}$). Half the igneous clasts contained lithic inclusions and "ropy" textured sheet silicates. Quartz grains revealed multiple sets of planar deformation features (PDFs) and augite reaction rims. The Y6-N17 sample represented a microcrystalline (5 – 10 μm) andesitic rock with K-feldspar ($Ab_{17-99}Or_{0-82}An_1$), plagioclase ($An_{30-49}Ab_{48-64}Or_{3-6}$), augite ($Wo_{45-49}En_{17-44}Fs_{11-34}$), magnetite, ulvöspinel, and apatite crystals. A sample from Y2 (Y2-N6) contained disaggregated core fragments that originally were part of a poorly sorted polymict breccia deposit. Clasts were rounded to angular and comprised calcareous, dolomitic, fossiliferous limestones, anhydrite (of unspecified modal %), and marl. Shocked feldspar, checkerboard plagioclase, and quartz grains with single to multiple sets of PDFs were also observed within this sample. The Y6-N17 sample gave a ϵ_{Nd} value of –5.0 and ϵ_{Sr} value of +55, close to the isotopic composition of impact glasses found in Haiti (Premo and Izett 1991).

Kring and Boynton (1992) re-examined sample Y6-N17 first described by Hildebrand et al. (1991). The sample rested above 8 m of anhydrite and was found below a polymict breccia deposit. However, it was difficult to confirm an impact origin, as no shocked quartz and plagioclase could be identified in this andesitic rock. In order to constrain its provenance, Kring and Boynton (1992) demonstrated that compositionally the rock did not follow traditional calc-alkaline and tholeiitic igneous trends, when plotted on an olivine – clinopyroxene – quartz – plagioclase pseudoternary projection. In support of an impact origin, they indicated that Haitian impact melt spherules lay on a mixing line with the Chicxulub andesitic melt rock. They also showed that the melt rock's andesitic composition could be modelled as a mixture of known Yucatán upper sedimentary and basement crystalline rocks, i.e. 12% Y6-N17 groundmass, 72% mica schist, 4% sandstone, 2% dolomite, and 10% limestone/anhydrite. They also suggested that a small contribution from mafic rocks was required to account for the gabbroic mineralogical assemblage of the melt rocks.

Swisher et al. (1992) produced the first $^{40}Ar/^{39}Ar$ radiometric age for the Chicxulub andesitic melt rocks firmly linking the Chicxulub structure chronologically with the K/T boundary. A sample from the C1 well produced an apparent age of 64.98 ± 0.05 Ma that is indistinguishable from ages of impact glass samples from Beloc (Haiti) and Arroyo el Mimbral (northeastern Mexico) (Sigurdsson et al. 1991; Smit et al. 1992). They also indicated that the glassy feldspathic groundmass of this sample had an andesitic composition, in agreement with the known spherule compositions from Beloc and Arroyo el Mimbral. The andesitic melt sample was composed of a fine-grained mixture of plagioclase and K-feldspar of various compositions that are unlike those of any known volcanic andesitic rock. Swisher et al. (1992) suggested that this unusual rock was most likely the product of fused target rocks as produced by an impact.

A study by Sharpton et al. (1992) confirmed the findings of Kring and Boynton (1992) and Swisher et al. (1992). Sharpton et al. (1992) observed samples from the C1 and Y6 wells (samples Y6-N14, N17, N19 and C1-N10 where samples N14 and N17 had already been described by Hildebrand et al. 1991 and Kring and Boynton 1992). The new sample Y6-N19 comprised 4 – 8

cm sized fragments of a fine-grained and glassy melt rock suspended in a melt matrix composed primarily of pyroxene and feldspar. Sharpton et al. (1992) indicated that this sample did not show much alteration. Clasts derived from the basement were 0.2 – 1.0 cm in width, appeared suspended in the melt matrix, and revealed various "degrees of digestion". Sample C1-N10 was described as a fine- to medium-grained crystalline melt rock that comprised subhedral to euhedral pyroxene, feldspar, and interstitial cryptocrystalline and microcrystalline mineralogical phases. No alteration or semi-digested inclusions were observed in this sample. As previously described by Hildebrand et al. (1991) and Swisher et al. (1992), Sharpton et al. (1992) showed that these rocks had an andesitic to dacitic composition, consistent with heterogeneous assimilation of target rocks. They also revealed that samples Y6-N14 and N19 contained numerous, cm-sized silicate inclusions from granitic gneiss, quartz-mica schist, metaquartzite, and rare mylonite. These fragments implied that the Yucatán crystalline basement comprised a medium- to high-grade metamorphic terrain. Microprobe analyses of feldspar in the granitic gneiss inclusions gave compositions of $An_{1-16}Ab_{13-96}Or_{1-85}$. Accessory minerals included biotite, pyroxene, and hornblende, whereas trace minerals comprised sphene, apatite, and zircon. Sharpton et al. (1992) also observed numerous shock features: planar deformation features (PDFs), shock mosaicism, feldspathic diaplectic glass, and maskelynite. They observed that phyllosilicate clasts contained ≤ 1 mm wide irregular glass domains similar in composition to feldspars in the granitic gneiss. Sharpton et al. (1992) also analyzed unusual abundances of iridium within the C1-N10 and Y6-N19 samples. The results indicated variable concentrations, the highest values being 2.5 ± 0.5 ppb and 13.5 ± 0.9 ppb; much higher than typical crustal values. This was proof for an extraterrestrial component. Radiometric age dating with the $^{40}Ar/^{39}Ar$ technique of the C1-N10-1A sample by Sharpton et al. (1992) revealed results similar to those by Swisher et al. (1992), yielding a crystallization age of 65.2 ± 0.4 Ma. Sharpton et al. (1992) also investigated the magnetic properties of two split samples from Y6-N17. They determined that the melt rocks crystallized in a period of reversed geomagnetic polarity such as chron 29R, which occurred between 64.68 and 65.37 Ma. Sharpton et al. (1996) indicated that the Chicxulub

melt breccias were typical of the impact melts of large impact structures such as the Ries, Wanapitei, Haughton, Popigai, and Sudbury. The observed sequence within the retrieved cores (Y6 and C1) comprised suevitic breccias (polymict clastic-matrix breccia with impact generated melt-particles), weakly shocked crater fill, and ejecta deposits similar to the Bunte Breccia described from the Ries crater (Hörz and Banholzer 1980; Hörz et al. 1983). Sharpton et al. (1996) also observed a lithological grading in the Y6 and S1 cores and interpreted this as the product of fallback sorting or secondary sedimentary reworking.

Petrographic and geochemical studies on Chicxulub melt rocks were necessary to constrain the origin of known impact glass deposits found throughout the Caribbean. Because the Manson impact crater of Iowa revealed a similar age as the Chicxulub crater (65.7 ± 1.0 Ma; Kunk et al. 1989, subsequently corrected to 73.8 ± 0.3 Ma by Izett et al. 1993), several research groups tried to constrain the source of Haitian impact glasses. Koeberl (1993) used major and trace element geochemistry combined with $\delta^{34}S$ and $\delta^{11}B$ isotopes to build a link between Haitian impact glasses and the Chicxulub structure. Several breccia and sedimentary evaporitic, sandstone, and meta-quartzitic samples were selected from Yucatán boreholes, the Y1, Y2, Y4, and Y5A boreholes (Y1-N42, -N43, Y2-N6, Y2-N9, Y4-N31, Y4-N36, and Y5A-N11). Major element mixing estimates between these known sedimentary target rock compositions and an andesite composition did not reproduce the Haitian yellow impact glass composition. Koeberl (1993) indicated that the sampled Yucatán sedimentary rocks had low REE concentrations and negative Eu anomalies. When this phase was mixed with an andesitic component, they produced results much too low compared to the Haitian glass compositions. Although the $\delta^{34}S$ isotope compositions of several silica-poor evaporitic breccia samples were close to those of the Haiti yellow impact glass, $\delta^{11}B$ isotope values, which were found to be high in evaporitic rocks, were far too low to account for this component. Koeberl (1993), therefore, concluded that evaporites did not contribute to the Haitian glasses, but that siliceous rocks might have been present at Chicxulub ground zero, or that breccias sampled by the Y2 borehole may not be of impact origin.

Another study aimed at correlating Haitian glasses with the Chicxulub structure was published by Blum et al. (1992, 1993). These authors determined strontium, neodymium, and oxygen isotopes on Chicxulub melt rocks. Blum et al. (1993) analyzed two samples, fine- to medium-grained melt rocks containing pyroxene, feldspar, quartz, and opaques, from the C1 borehole (C1-N10-1A and C1-N10-2). They indicated that these samples were pristine and revealed no signs of obvious chemical and isotopic alteration. Their results enabled them to determine, without doubt, that the Haitian Beloc Formation impact glasses are indeed products of the Chicxulub impact, as they revealed ϵ_{Nd} and ϵ_{Sr} values (-2.9 and +58.5, respectively) identical to Chicxulub samples and lay on the same black and yellow impact glass $^{87}Sr/^{86}Sr$ – $\delta^{18}O$ mixing line (see Fig. 1 of Blum et al. 1993). Based on low $\delta^{18}O$ values, these authors suggested that the melt rocks (8.2 – 8.4‰ SMOW) and glasses (6.0 – 9.0‰ SMOW) were the product of mixing between a carbonate platform and an igneous or meta-sedimentary lithic component, and, thus, were of impact origin.

A detailed petrographic study of impact melt breccia samples from the Y6 and C1 cores was undertaken by Schuraytz et al. (1994). These authors indicated that the breccia samples Y6-N17 and -N19 were extremely variable with respect to clast size, lithic abundances, color, grain size, matrix porosity, and secondary hydrothermal alteration. The matrix comprised 5 – 15 μm long, subhedral to euhedral pyroxene and plagioclase crystals in a cryptocrystalline quartzofeldspathic mesostasis with variable porosity. Micrographic intergrowths between pyroxene, magnetite, and vermicular feldspar in this matrix formed clot-like domains. Electron microprobe analysis of feldspar indicated nonstoichiometric compositions of $An_{26-48}Ab_{46-49}Or_{3-28}$ rimmed by K-feldspar, $An_2Ab_{10}Or_{88}$. Pyroxene analyses indicated exclusively clinopyroxene compositions of $En_{40-55}Wo_{38-50}Fs_{7-20}$. Alteration of the mesostasis is characterized by the growth of anhedral albite (Ab_{99}) with quartz, K-feldspar, epidote, chlorite, and oscillatory-zoned pyrite. Anhydrite comprises up to 8 vol % of the rock; the inclusion content averaged 35 vol %. Schuraytz et al. (1994) indicated that the Y6 rocks were richer in platform-sedimentary target rocks and, thus, CaO, whereas the C1 melt rocks originated from a more siliceous basement source of dacite to

andesite composition. Based on grain size and the low clastic lithic content, these authors suggested that the melt rocks had undergone slower cooling than lithic clast-rich samples and were worth investigating for potential Sudbury-style mineralization.

In a subsequent study, Schuraytz et al. (1996) attempted to isolate the Ir-bearing phase, as 13.8 ± 0.7 ppb iridium had been found in sample C1-N10-1 (Sharpton et al. 1992). By scanning electron microscopy, they were able to locate a 4 μm x 2.5 μm x 0.5 μm Iridium particle (similar to Fig. 1.2g). This grain was believed to account for half the iridium in the original 65 mg of sample C1-N10-1. Schuraytz et al. (1996) indicated that C1 and C3 carbonaceous chondrite meteorites are the only ones known to contain similar Ir particles and, thus, could be the type of projectile responsible for the formation of the Chicxulub crater. This interpretation has since been confirmed by $^{53}Cr/^{52}Cr$ isotope analyses of K/T boundary samples from Stevns Klint (Denmark) and Caravaca (Spain) (Shukolyukov and Lugmair 1998).

Meyerhoff et al. (1994) published a controversial log for the Y6 borehole that was produced while the authors were consulting for PEMEX. They interpreted the igneous-textured impactite interval (between 1200 to 1640 m depth) as a succession of six volcanic flows, each separated by bentonite intervals. The multiple bentonite horizons were interpreted to represent periods of volcanic quiescence and, thus, surficial weathering. The authors indicated that there were no similarities between these igneous rocks and previously described impact melt sheets and that the latter were usually homogeneous in composition (Grieve and Floran 1978; Engelhardt 1984). Meyerhoff et al. (1994), thus, criticized Sharpton et al. (1992) for misinterpreting volcanic rocks. Sharpton et al. (1992) had presented geochemical evidence that showed the impactites had highly variable and unusual compositions. Meyerhoff et al. (1994) added that planar deformation features (PDFs) described by Sharpton et al. (1992) were actually tectonic and volcanic in origin, as they represented "modest" ω and π lamellae, as well as multiple angles between 40^{o} to 90^{o} and, thus, were not true impact-derived PDFs. Tectonically deformed quartz grains from sample Y6-N14, described by Quezada Muneton et al. (1992), revealed "slight curvature with bifurcations and variable

lamellae widths". Based on these observations, Meyerhoff et al. (1994) suggested that the Chicxulub structure was actually of volcanic origin and the igneous rocks represented a volcanic sequence of Late Cretaceous age. These allegations, along with the assumed documentation of shock-related PDFs at other volcanic centers (e.g., Carter et al. 1986), set the stage for more in-depth studies of shock-related quartz (e.g., Stöffler and Langenhorst 1994; Grieve et al. 1996; Huffman and Reimold 1996).

Warren et al. (1996) described several impactite samples (C1-N9, Y6-N17 and -N19). The matrix of the Y6 core rocks was described as aphanitic and fine-grained (<10 μm). The matrix also contained coarser lithic clasts (~20 vol %) of diverse compositions. The rocks from the C1 core were described as the coarsest impactite samples, with grain sizes of ~0.3 mm. Warren et al. (1996) suggested that the inclusion content was anti-correlated with the matrix grain size, i.e., the more inclusions present, the finer the groundmass. They proposed that the incorporation of cold inclusions into the impact melt acted as a heat sink and, thus, provided a quenching effect. Warren et al. (1996) also demonstrated that the impactite rocks recovered from the center of the Chicxulub crater had a whole-rock geochemical composition similar to average upper crust and, thus, were of impact origin.

Petrographic and magnetic susceptibility characteristics of the UNAM-6 and UNAM-7 boreholes were discussed by Urrutia-Fucugauchi et al. (1996). These authors indicated that the ~255 m thick UNAM-6 evaporite breccia interval did not reveal a characteristic magnetic susceptibility signature. The carbonate sediments and the breccia had similar susceptibility values throughout the borehole. The breccia were composed of variegated (white to gray) evaporites, limestone, dolomitized limestone, gypsum, and anhydrite fragments, up to 4 cm in size. Approximately 5 vol% of the clasts were converted to clay minerals, whereas 60 % of the matrix did not have a carbonate composition and was composed of clay or "sand-sized particles". In contrast, the UNAM-7 borehole revealed an upper breccia interval that contained two zones of high magnetic susceptibility, between 210 – 280 m and 330 – 360 m. The lower breccia interval did not reveal a high magnetic susceptibility signature. The upper breccia

contained abundant allogenic basement clasts, whereas the lower breccia contained abundant anhydrite and gypsum clasts. The authors suggested that the high susceptibility values in the upper breccia sequence were derived from the high silicate basement clast proportions and, thus, proposed that this type of inverted stratigraphy could be analogous to the Bunte Breccia of the Ries impact crater. Because allogenic breccias were present up to 126 km from the Chicxulub crater center and evaporite breccias up to 150 km, Urrutia-Fucugauchi et al. (1996) suggested that the Chicxulub structure could be 300 km in diameter, as proposed by Sharpton et al. (1996).

Petrographic and geochemical results from Chicxulub melt rocks were reported by Kettrup et al. (2000). These authors used whole-rock major element, stable and radiogenic isotope data to determine the nature of the Yucatán basement and the degree of mixing present in impact melt rocks and Haitian impact glass. Their samples included C1 and Y6 samples C1-N9 and -N10, Y6-N14, -N17, -N19, and two additional samples (Y6-N15 and N16) that had not been previously described. A somewhat more detailed description of these samples was given, i.e., the carbonate groundmass of sample Y6-N14 was described to contain Cretaceous foraminifera. The lithic clast contents of all the Y6 samples were described to be similar; however, the uppermost Y6-N14 sample was observed to contain fewer granitic gneiss clasts. Kettrup et al. (2000) indicated that, compositionally, the Chicxulub melt rocks were more heterogeneous than previously indicated. This was attributed to the ubiquitous presence of small clasts within the samples, to the small, non-representative size of the samples, and to the varied feldspar component within basement rocks. Melts with a high CaO content were interpreted to be influenced by the platform carbonate sediments. Stable isotopes indicated that the siliceous melt groundmass of the Y6 samples had a $\delta^{13}C$ composition of -3‰, similar to marine carbonates. The $\delta^{18}O$ compositions were similar to the values reported by Blum et al. (1993) and those of Haitian impact glass, between 9.9 and 12.4‰. The $^{87}Sr/^{86}Sr$ ratios ranged between 0.7079 and 0.7094 and $^{143}Nd/^{144}Nd$ ratios clustered near ~0.51235. Negative T^{Sr}_{UR} values and unrealistic model ages indicated Rb loss owing to secondary hydrothermal alteration; calculated ages ranged from 830 to

1833 Ma. A mean T^{Nd}_{DM} model age was also calculated at 1.12 ± 0.03 Ga, in agreement with previously published values for the black Haitian impact glass (Premo and Izett 1992). Kettrup et al. (2000) published ε_{Nd} and ε_{Sr} data ranging between –2 and –6, and +55 and +69, respectively, in agreement with results from Hildebrand et al. (1991) and Blum et al. (1993). They indicated that to account for the ε_{Nd}-ε_{Sr} values, a mafic component was required in order to model the less negative values produced from the C1 samples and Haiti impact glasses.

The most recent study on Chicxulub impactites, prior to the Yax-1 consortium results of 2004, was undertaken by Claeys et al. (2003). These authors recognized three subdivisions in the impactites of the Y6 borehole: i) an upper, fine-grained, carbonate-rich, fossil-bearing suevite; ii) a middle, relatively coarser-grained, suevite rich in altered silicate melt particles and silicate basement clasts; and iii) a lower, so-called "thermometamorphic" suevite rich in melt fragments, large evaporite clasts, and shocked basement clasts. Thermal metamorphism of this latter unit, i.e., recrystallization of its groundmass, was thought by these authors to have been induced by an underlying, now crystalline, impact melt layer. Claeys et al. (2003) proposed that the upper suevite represented either a late fall-back deposit or an interval that was reworked by seawater resurging into the impact basin; the middle suevite represented a typical suevite deposit that originated as fall-back out of a collapsing ejecta plume; and that the lower unit represented either an early ejecta/fall-back deposit or material that was deposited on the outermost flank of the collapsed transient cavity by inward movement of material during the modification stage of cratering.

1.4. Impact cratering

Prior to the 1960's, impact cratering was not widely regarded as a significant geological process on Earth. This resulted from the then-poor recognition of impact craters and also from the lack of understanding of planetary processes in general. Space exploration and several decades of work by dedicated cratering specialists have changed this perception. The study of shock metamorphic effects on rocks has allowed the recognition of 174 impact craters on Earth (UNB Earth Impact Database, February, 2008). Impact structures have

been observed on every rocky or icy planetary body by space probes. Numerical modeling and shock-wave experiments, in conjunction with detailed field work, have allowed for a greater understanding of the overall cratering process (e.g., Roddy et al. 1977; Melosh 1989; French 1998).

Fortunately impacts do not occur very often. A 1 km wide impact crater, e.g., the Barringer (Meteor) Crater of Arizona, occurs every 1,600 years. Global killers, like Chicxulub, occur on a much greater time scale, i.e., once every 150 Ma (French 1998). Because impacts are so rare, it is fitting to describe the circumstances and consequences of the only observed impact event in human history, i.e., the collision of the comet Shoemaker-Levy 9 on the surface of Jupiter. This event was observed in July 1994 by land-based telescopes, the Hubble Space Telescope, and several space-probes. It provided an opportunity to constrain various scientific aspects of impact cratering, e.g., size and velocity of the comet and energy released. Jupiter has a phenomenal gravitational pull and, therefore, is subjected to a much greater impact flux. This pull split the originally 9 km wide comet Shoemaker-Levy 9 into 21 pieces on July 8, 1992 when the comet passed the giant planet at a distance of 1.6 Jupiter radii (Chodas and Yeomans 1993). Observations from the Hubble Space Telescope indicated for the largest 11 nuclei sizes were estimated to range in scale from 2.5 to 4.3 km in diameter (Weaver et al. 1994). The energy unleashed by the subsequent impact event with the planet was estimated to be close to 10^8 megatons of TNT, greater than any energy unleashed from any currently known impact structure on Earth. The impact left huge black scars on Jupiter's surface that triggered the ascent of impact plumes that were still visible by telescope beyond the planet's terminator. The diameters of these scars were estimated to be of the same magnitude as that of the Earth. The impact of comet Shoemaker-Levy 9 on Jupiter is the only confirmed and observed impact event on a planetary body and was, thus, of great scientific importance for the field of impact cratering.

1.4.1. Crater formation

Most meteorites travel at phenomenal speeds of tens of kilometers per second (e.g., Melosh 1989). Small projectiles that are usually a few meters across

disintegrate in the atmosphere and lose their original kinetic energy. Most meteorites enter our atmosphere in this way and are, thus, called falls. If fragments do survive, they will travel at speeds no greater than a few hundred meters per second and will excavate a pit that is not much wider than the meteorite itself. The ablation process during entry produces a characteristic fusion crust, which allows for the identification of meteorites. Slightly larger and especially poorly lithified meteorites or comets explode in the atmosphere. Such an event occurred over Siberia, Russia, in 1908 that is referred as the Tunguska event (French 1998). Meteorites that are large and solid enough are able to punch through the Earth's atmosphere and strike the surface. Meteorites that remain at hyper-velocities upon striking the ground produce much larger craters and affect target rocks in ways that are totally different from normal endogenic geological processes. The cratering process has been subdivided into three distinct stages, each with its own specific characteristics: 1- contact and compression, 2- excavation, and 3- modification (e.g., Melosh 1989). The most important details of these stages are described in the sections below.

1.4.1.1. Contact and compression stage

This stage begins when the leading edge of the bolide makes first contact with the target surface. At this instant, the projectile begins to rapidly decelerate and its tremendous kinetic energy is transferred to the target rocks by shock waves. Simultaneously, a complementary shock wave is also transferred back into the projectile and upon reaching its trailing edge, allows for its decompression and instantaneous conversion to melt and vapor phases. Intense shock waves with pressures in excess of 100 to several 10s GPa drive this process, which spans several milliseconds to one second. As the shock waves expand from the point of impact, they cover an ever-expanding surface area and, thus, decrease in energy density. Energy transfer to the target rocks is recorded as heat, mechanical deformation, and particle acceleration. It has been determined experimentally that the peak shock pressure ($\mathbf{P_s}$) decreases exponentially with radial distance from the impact point **R** according to the following equation: $\mathbf{P_s} \propto \mathbf{1/R^n}$ (eq. 1, Melosh, 1998). This expanding hemispherical shock wave allows for

the characterization of unique shock metamorphic zones in rocks at specific pressures and temperatures and, thus, distance from the point of impact (Fig. 1.9). Large hypervelocity impacts will produce shock pressures in excess of 100 GPa, allowing for total melting and even vaporization of the projectile along with a large proportion of the target rock. As postulated by equation 1, shock pressures attenuate with distance and can still reach values of 10-50 GPa for several kilometers. With greater distance from the point of impact, the shock waves eventually become subsonic (5-8 km/s) and grade into typical elastic or seismic waves. These waves do not produce any shock-related characteristics but are similar to typical endogenic seismic waves that cause brecciation, faulting, and landslides (French, 1998). This attenuation explains why shock-related features are usually only found within a fraction of the crater radius.

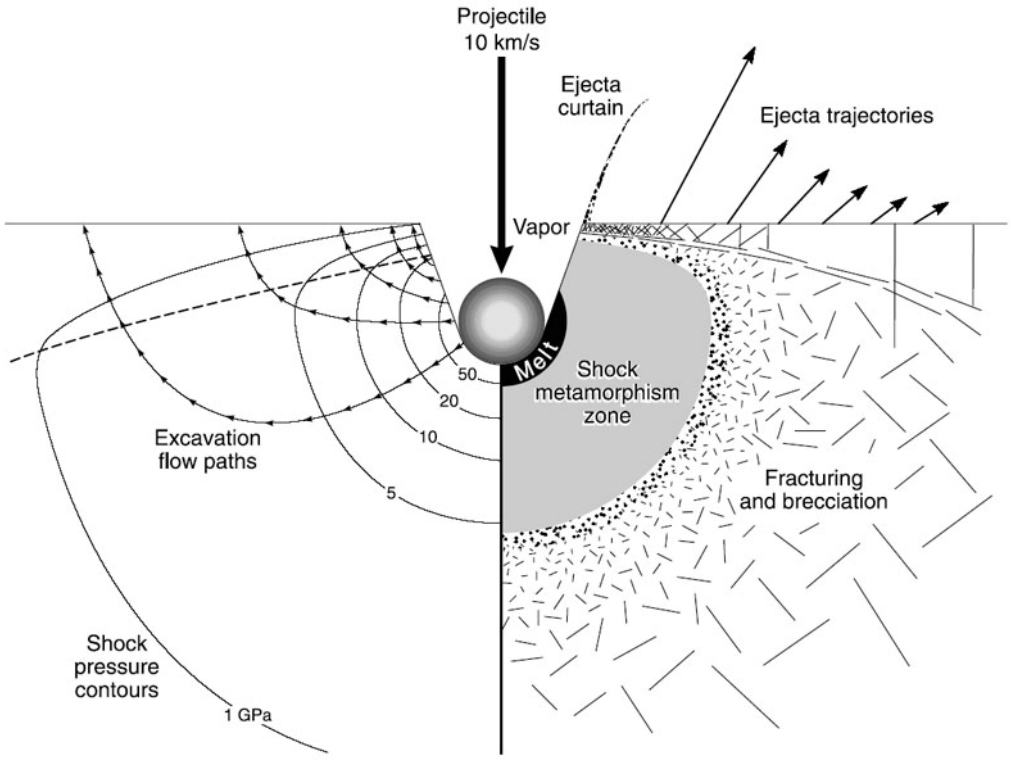

Fig. 1.9. Schematic of the contact/compression stage of cratering (from French 1998). Notice that peak shock pressures (in GPa) decrease exponentially away from the point of impact and the shock metamorphic zone is limited to the 5 – 50 GPa interval. Melting occurs at pressures > 50 GPa whereas fracturing and brecciation at < 5 GPa.

1.4.1.2. Excavation Stage

The process of excavation begins immediately after the bolide has struck the target rocks and shock waves begin to propagate. Shock waves that encounter the near-surface close to the point of impact are reflected downwards as release waves or rarefaction waves and allow for target rocks to be spalled. Spalling can be energetic enough for target rocks to be sent into space. Excavation is initiated when the tensional stress imparted by these waves exceeds the mechanical strength of the rocks. These rocks then begin to fracture, shatter, and are set in motion as individual fragments along excavation flow lines (Fig. 1.10). At diverse places in the developing cavity, the rock particles begin to move in various directions. Fragments in the upper target rocks travel upwards and outwards, whereas those below the point of impact move downwards and outwards. The rock fragments, along with shock-produced melt, flow along a contour path that eventually produces a bowl-shaped transient cavity (TC, Fig. 1.10). Because the released energy is so great, rock fragments can travel at phenomenal speeds (10 – 0.1 km/s), which explains why the TC is typically 20 to 30 times greater than the diameter of the projectile (French 1998). Excavation continues until the energy of the tensional release waves cannot exceed the mechanical strength of the rocks. At this point the excavated cavity reaches its maximum dimension, which initiates the onset of the modification stage. It has been determined that the TC adopts an ~ 1:3 depth-to-width ratio (Melosh 1989;

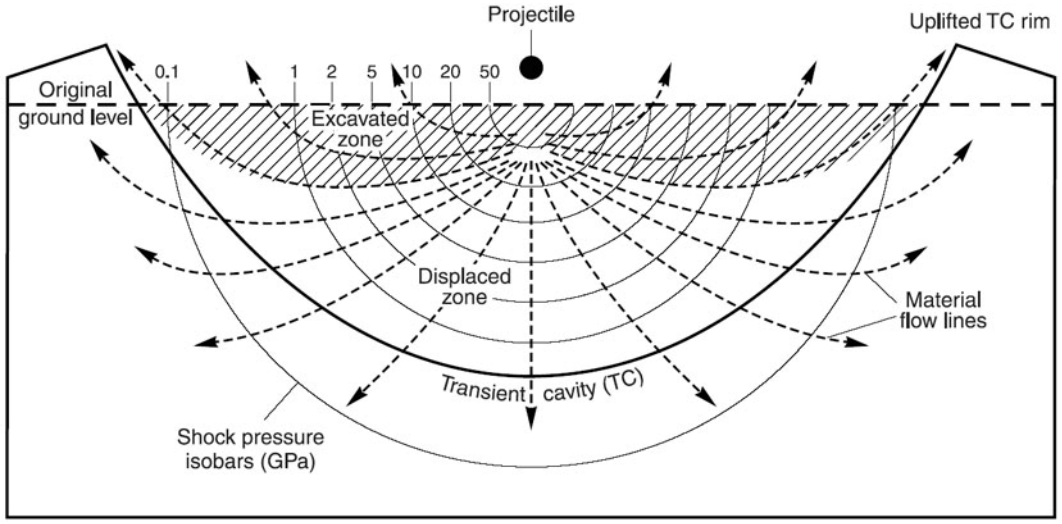

Fig. 1.10. Depiction of excavation flow lines (dashed arrows) with respect to original shock pressure isobars (thin solid hemispherical lines, in GPa) and the displaced versus excavated (oblique line pattern) transient crater zones (from French 1998).

French 1998). The crater is also characterized by an uplifted rim, a region of uplift where excavation forces ceased to propel rock fragments upwards but froze *in situ*. This whole process is much longer than the contact and compression stage. A crater the size of the Barringer (Meteor) Crater in Arizona (~1.2 km diameter, Fig. 1.11), is believed to be excavated in 6 seconds. If the excavation flow propagates at 1 km/s, a 200 km wide transient crater can be excavated in 90 to 120 seconds (Melosh 1989).

Fig. 1.11. The Barringer (Meteor) Crater located in Arizona is a classic example of a simple-bowled shaped crater (from French 1998).

1.4.1.3. Modification Stage

As soon as the excavation stage is complete, modification of the transient cavity begins. This usually occurs by downward gravitational collapse of the inner rim, which forms characteristic terraces, by the rapid infill of the transient cavity from fallback material, and by rebound, i.e., rapid isostatic readjustment of the central region of the crater. This latter is known to form a central inner peak and/or a central peak ring. Large volumes of rocks are involved and move inward from the outside, upwards at the center, and outwards during central peak collapse in large impact craters. The major modification processes can last up to several minutes, whereas prolonged processes such as crater infill by sedimentation, erosion, and seismic readjustments can take many years to millions of years. A major factor that determines the degree of modification of a crater is its size. On Earth, craters that are less than 2-4 km in diameter will not be subject to major readjustment of the initial transient cavity. Such craters are called simple bowl-

shaped craters (Fig. 1.11). The limit above which a crater undergoes major readjustments, the transition from simple to complex crater forms, is dictated by a planetary body's gravity. This is a function that is inversely related to the gravitational acceleration (Melosh 1989). Complex craters with increasing diameter are characterized by an inner peak, an inner peak ring (Fig. 1.12a) and, for the largest craters, multi-ring structures (Fig. 1.12b). The process by which modification occurs is still hotly debated. Various theories have been proposed that try to explain the Bingham fluid-like properties (a material that, above a particular stress yield point, adopts fluid-like behaviour) of rocks during collapse, such as frictional sliding of individual blocks (Spray 1995) and acoustic fluidization (Melosh 1989). It has been suggested that the Chicxulub structure may represent a multi-ring basin (Melosh 1997).

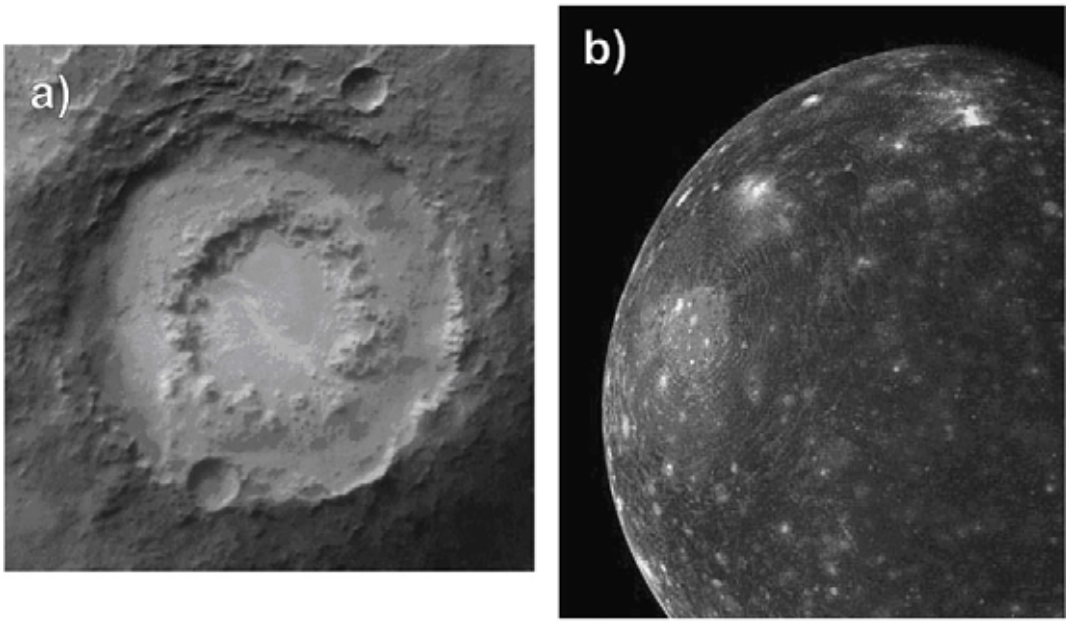

Fig. 1.12. a) Mars orbiting camera (MOC) photograph of the Lowell crater on Mars, diameter = 180 km, showing a classic inner peak ring (NASA photograph); b) Galileo spacecraft photograph of the Valhala basin on Callisto, diameter = 2000 km, the solar system's largest multiring basin (NASA photograph).

1.5. The Yaxcopoil-1 borehole

The Yax-1 core was drilled between December 2001 and February 2002 60 km south-southwest from the center of the Chicxulub impact structure (Fig. 1.1 and 1.8). This drill site was chosen because the Yax-1 hole would fill a gap in a string of previous boreholes, i.e., between the Y6 and T1 boreholes (Sharpton 2000). Prior to drilling, detailed geophysical analysis was performed to constrain

the crater subsurface geology. As shown in Sharpton et al. (their Fig. 5, 1996), extensive breccia deposits and melt rocks were expected to be intersected in the Yax-1 hole, given that the Y6 and T1 boreholes intersected 490 m of suevite and impact melt rock, and 930 m of Bunte Breccia-like deposits, respectively. A potentially similar large breccia deposit was interpreted to occur at the Yax-1 site within the down-faulted annular trough. This trough is defined by a ~10 mgal gravity low (Sharpton et al. 1993). Seismic reflection imaging (Morgan et al. 1997) suggested a similar stratigraphic profile to that of the Y6 borehole and, thus, a similar intersection of melt breccias was expected. From these seismic data, it was also determined that the Cretaceous rocks at the Yax-1 site belonged to a series of disturbed slumped blocks that extended 40 – 85 km from the crater center (Morgan et al. 1997).

The borehole reached a depth of 1511 m and intersected 795 m of Tertiary rocks, 100 m of impactites, and 616 m of Cretaceous target rocks (Fig. 1.13). Rotary drilling was first used down to 404 m, which did not provide any core recovery. Below 404 m depth, the wireline technique was employed with ~98.5 % core recovery. For greater details on the drilling techniques, down-hole geophysical logs, and other technical specifics, refer to Wohlgemuth et al. (2004). The core was first logged by Dressler (2002), which provided the basis for all future investigations. Tertiary rocks were logged as interlayered carbonaceous silstones, calcarenite, and rare conglomerates and turbidites. Dressler (2003a) subdivided the subsequent impactites into 6 units. Unit 1 (794.63 – 808.02 m) was described as a reworked suevite that contained small sedimentary clasts (<0.5 cm), showed horizontal alignment of elongate clasts, rough sorting, and predominant green coloration of altered melt particles. Clasts were observed to consist of gneiss, granodiorite, granite, limestone with foraminifera fossils, and dolomite. The contact with Unit 2 was observed to be gradational over an interval of 20 cm. Unit 2 (808 – 822 m), contrary to Unit 1, was characterized by a lack of lamination and clast size sorting. All melt particles were also altered green and clasts were similar to those found in Unit 1. Unit 3 (822 – 845 m) was defined by a distinctive fine-grained, brown matrix – thought to be a melt matrix – that supported relatively fewer large clasts. Thus, it was named a “chocolate-brown

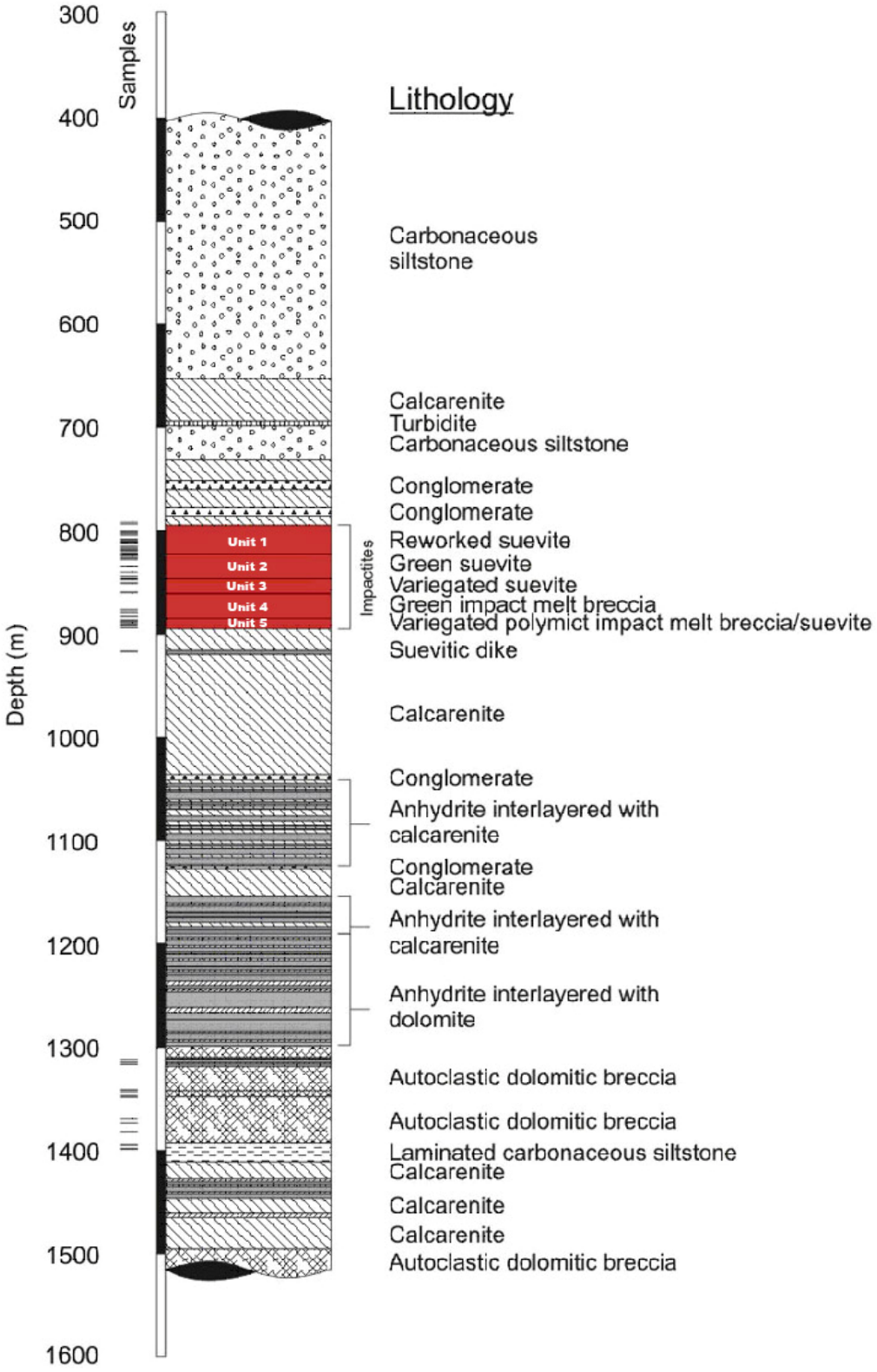

Fig. 1.13. Stratigraphy of the Yax-1 borehole as logged by Dressler (2002). Impactite subdivisions and terminology originate from this work. A total of 75 samples were obtained for this study and are indicated as thin black lines on the left side of the diagram.

melt breccia" (Dressler et al. 2003a). Contrary to units 1 and 2, Unit 3 green melt particles are all groundmass-supported, show internal schlieric texture, and are subrounded and schlieric in shape, indicative of an un-reworked primary suevitic deposit. Unit 4 (845 – 861 m) displayed a coarse and heterogeneous character that involved contorted, flow-laminated, and welded melt rock fragments of various colours, from which this unit gained its original name "suevitic breccia, variegated, glass rich". This unit has a gradational contact with Unit 3. Unit 5 (861 – 884 m) has an abrupt upper contact. This unit is characterized by flow-laminated green melt rock fragments that locally fit together like the pieces of a jigsaw puzzle. It was, thus, named "green, monomict, autogene melt breccia". The green fragments are locally held together by a fine-grained carbonate matrix that contains generally molten basement rock clasts. The lowermost impactite unit (Unit 6, 884 – 894 m) has a gradational upper contact and displays an increase in size, abundance, and diversity of target rock fragments. Melt fragments display green to tan, and light gray colours, whereas the carbonate groundmass is light tan to light brown. This groundmass is locally flow-textured and contains target rock fragments as well as melt-rock shards. This unit is named "variegated, polymict, allogenic, clast rich melt breccia". This thesis only recognizes five subdivisions, where the upper two units have been combined into one. This is because the petrographic characteristics that define these units are similar. The poorly lithified state of Unit 1 is the only distinguishing feature from the Unit 2 of Dressler et al. (2003a). This is discussed in greater detail in the petrography section of Chapter 2.

The Cretaceous rocks were described by Dressler et al. (2003a) to have the following composition: 63 vol% dolomite, 27 vol% anhydrite, 10 vol% argillaceous limestone. Several breccia zones were intersected in these Cretaceous rocks: melt-bearing breccias at 910, 916, and 1348 m; lithic breccias at 1314-1316, 1341, and 1398-1399 m; black oil-bearing rocks at 1350, 1369, 1372, 1382, 1394, 1397, 1399, and 1420 m; and wide deformation zones between 1310-1400 m, and 1496-1510 m (Kenkmann et al. 2003). For a discussion on the origin of these deformation zones, see section 4.8.5. of this thesis.

1.6. Samples

A total of 75 samples were collected during the April ICDP 2002 sampling party at the UNAM in Mexico City. These comprised either ¼ core samples or measured 1 cm^3 in volume (see Appendix A.3). One sample was obtained from the upper Tertiary rocks, 54 samples originate from the impactites, and 21 from the Cretaceous sequence. For pictures of the Yax-1 core, see Appendix A.1. For a list of the selected samples with petrographic descriptions, refer to Appendix A.2. Additional petrographic descriptions for the same samples described in Appendix A.2 can be found in Chapters 2 – 5, sections 2.5, 3.3, 4.4, and 5.5.

1.7. Methodology

Several techniques have been applied to obtain petrographic and geochemical data. First, macro-petrographic observations were made and basic characteristics, e.g., melt particle and clast color and size, groundmass color and grain size, as well as secondary alteration features were noted. Microscopic observations were then undertaken on polished thin sections using a standard petrographic polarizing microscope. Thin sections of interest were selected for cathodoluminescence (CL) observations at the University of the Witwatersrand School of Geosciences (see section 2.5.2 for details on this technique). These were subsequently carbon-coated for scanning electron microscope (SEM) backscattered electron imaging at the University of the Witwatersrand Electron Microscopy Unit and at the Council for Geoscience in Pretoria. Phase compositions were obtained using quantitative wavelength dispersive and energy dispersive X-ray analysis systems equipped on the SEM at the Council for Geoscience. The operating conditions for the SEM and EMPA are both described in sections 2.5.2 and 5.4. Mineralogical identification was also established with the use of X-ray diffraction (XRD) analysis at the University of the Witwatersrand X-ray analytical facility. Major element geochemical analysis was obtained by standard X-ray fluorescence spectrometry (XRF) at Setpoint Laboratories in Johannesburg, and trace element analyses were determined by INAA at the Department of Geological Sciences in Vienna, Austria. For details on the methodology of these two techniques refer to sections 3.3 and 4.5. Additional

trace element results were obtained at the micro-scale using a laser-ablation inductively-coupled-plasma mass-spectrometer (LA-ICP-MS) at the University of Cape Town. Details on the operating conditions used on the LA-ICP-MS are described in section 5.4.

1.8. Thesis Layout

The thesis is divided into 8 chapters; the 4 central chapters (Chapters 2-5) each represent a published article in the journal Meteoritics and Planetary Science (MAPS). Chapter 1 introduces the objectives of this research; the methodology used, sample depth, and provides background about the impact cratering process, the K/T boundary, and the Yax-1 borehole. A summary of all the previous work that has been done on Chicxulub impactite samples is also presented. Chapters 2 and 3 are both articles that were been published in the MAPS ICDP Yax-1 special issue (MAPS vol. 39, issues # 6, 7). These chapters introduce some of the first detailed petrographic and geochemical characteristics of the retrieved Yax-1 impactites. These were published along with other similar papers, written by several international research groups. Chapter 4 is a paper that was published in the MAPS special issue in honour of Prof. Dieter Stöffler's retirement (MAPS vol. 40, issues # 9-10). This article describes additional petrographic and geochemical findings in an attempt to characterize the various phases that make up the impactites (groundmass, melt particles, impact melt, and retrieved lithic clasts). These are then compared with respect to the upper crust, calculated end-members, and known lithic clast compositions using trace element data. Several samples from the Cretaceous target rock interval are also described petrographically with respect to possible shock and endogenic deformation. An estimated geochemical composition for the Cretaceous target rock interval of the Yax-1 borehole is also presented. A detailed EMPA and LA-ICP-MS study of selected melt particles from the Yax-1 borehole constitutes Chapter 5. It describes the first trace element data obtained from Yax-1 melt particles by micro-analytical technique. This study was undertaken in order to provide additional insight into the formation, mixing, cooling, and alteration history of the melt particles. Chapter 6 amalgamates the main research results from chapters 2-5 into

a coherent concluding chapter. Final conclusions are presented in Chapter 7 and recommendations in Chapter 8.

Because Chapters 2-5 are published articles in the American journal Meteoritics and Planetary Sciences, this thesis is written in American English and all referencing is formatted according to this journal's style. It should be noted that the figure and table numbering in these chapters have been modified from the original published article in order to accommodate the formatting of this thesis. All references have been compiled into one comprehensive bibliography, which is located at the end of the thesis. Tables that contain extensive geochemical data or that are found in the online MAPS data repository have been included in this work as appendices. Executive summaries detailing the co-author's responsibilities, objectives, and main research results for the four main chapters (Chapters 2 – 5) are presented in the following section.

1.8.1. Chapter 2

The objective of this chapter, which appeared as a published article in MAPS (Tuchscherer et al. 2004a), was to provide a thorough petrographic description and classification of the Yax-1 impactites. This work was aimed at the identification of key macro- and microscopic petrographic characteristics in order to better define the observed units, define alteration features, determine the extent of shock metamorphism, melting, mixing of lithological components, and to understand the emplacement mechanism for these impactites. Point counting with the use of a standard petrographic microscope and several other analytical techniques such as cathodoluminescence (CL), scanning electron microscopy (SEM), electron microprobe analysis (EMPA), and X-ray diffraction (XRD) contributed to this work.

All of the sampling, research, observations, interpretations, drafting of figures, and the writing of this manuscript (Chapter 2, Tuchscherer et al. 2004a) are the product of M.G. Tuchscherer. Initial sampling of the Yaxcopoil-1 borehole was undertaken by M.G. Tuchscherer at the Universidad Autonoma de Mexico in April 2002. The XRD, CL and some of the SEM observations were all done at the School of Geosciences and Electron Micoscopy Unit at the University

of the Witwatersrand. All of the EMPA and digital SEM image analysis were performed at the Council for Geoscience in Pretoria, South Africa. Co-authors for this work, Profs W.U. Reimold and R.L. Gibson, provided academic supervision and suggestions with the discussion of the results. Prof. C. Koeberl provided useful discussion when interpreting the geochemical results and Dr. D. de Bruin collaborated with the acquisition of EMPA results at the Council for Geosciences in Pretoria, South Africa.

1.8.2. Chapter 3

This chapter was published in the Yax-1 special issue of MAPS (Tuchscherer et al. 2004b). Major and trace element analyses were obtained on bulk impactite samples (i.e., 8 – 16 cm^3) in order to determine overall geochemical compositions. This information allowed quantitative estimates on how much crystalline basement material was mixed with supracrustal carbonate rocks and the meteorite itself (mixing between carbonate, mafic, and felsic fractions). These data also helped to determine the efficiency of mixing within respective units and any secondary alteration effects. The search for Iridium, which provides a good proxy for an extra-terrestrial component, benefited from the γ-γ iridium coincidence spectrometry technique, which allows detection limits at the parts per trillion (ppt) level. Major elements were obtained by X-ray fluorescence at Setpoint Laboratories in Johnnesburg, South Africa. All trace elements were acquired at the Department of Geological Sciences in Austria, Vienna.

All of the sampling, research, observations, interpretations, drafting of figures, and the writing of this manuscript are the product of M.G. Tuchscherer. Co-authors for this work, Profs W.U. Reimold and R.L. Gibson, provided academic supervision and helpful suggestions while interpreting the results. Selected samples were sent by M.G. Tuchscherer to Prof. C. Koeberl at the Department of Geological Sciences in Vienna, Austria for INAA. This technique provided all of the trace element data. Prof. C. Koeberl also provided helpful suggestions while interpreting the trace element results, especially with the γ-γ iridium data.

1.8.3. Chapter 4

In this contribution, additional trace element data for Yax-1 impactite subsamples and major and trace element data for selected Cretaceous target rocks are discussed, together with petrographic observations. The compositions of melt particles, bulk suevite, suevitic groundmass, and several target lithologies including anhydrite, dolomite, argillaceous limestone, and oil shale are compared. The aim was to provide greater insight into the various chemical components that make up the impactites, which also provide constraints on mixing. Carbonate and silicate compositional end-members were calculated from the bulk geochemical data presented in Chapter 3 to compare with the calculated composition of the Cretaceous target rock interval of the Yax-1 borehole, the composition of the upper continental crust, sampled bulk suevite, suevitic groundmass, melt particles, and retrieved basement and supracrustal clasts.

All of the sampling, research, observations, interpretations, drafting of figures, and the writing of this manuscript are the product of M.G. Tuchscherer. Profs W.U. Reimold and R.L. Gibson provided academic supervision as well as helpful discussion when interpreting the data. As in Chapter 3, Prof. C. Koeberl, at the Department of Geological Sciences at the University of Vienna, provided all of the INAA trace element analysis results. Prof. C. Koeberl also provided valuable discussion when interpreting these results. All of the major element results obtained from selected Cretaceous target rock samples were obtained by Setpoint Laboraties in Johannesburg, South Africa.

1.8.4. Chapter 5

This study was aimed at further describing, analyzing and interpreting petrographic, major and trace element compositions of melt particles at the microscopic scale. This was done in order to further understand the mixing of melts, constrain the precursor rock composition(s), characterize alteration effects, and determine the formation of various melt particle types. This is the first study of its kind that investigates the trace element compositions of melt particles obtained with the LA-ICP-MS analytical technique. Compared with previous INAA results that require samples at the millimeter to centimeter scale, this

technique allows the determination of various trace element compositions at the micro-scale. This enhanced resolution provides greater insight into the formation, mixing, and alteration history of melt rock particles.

This work, the sampling, EMPA + LA-ICP-MS analysis, research, drafting figures, writing, and interpretations are the product of M.G. Tuchscherer. Co-authors, Profs W. U. Reimold and R.L. Gibson, provided academic supervision and discussion while interpreting the data. Dr. D. de Bruin, at the Council for Geosciences in Pretoria, South Africa, collaborated with this research by providing access to the electron microprobe. Dr. de Bruin also provided helpful suggestions during the processing of the data. Dr. A. Späth at the Department of Geological Sciences at the University of Cape Town, South Africa, provided invaluable help while acquiring trace element data by LA-ICP-MS.

2. First petrographic results on impactites from the Yaxcopoil-1 borehole, Chicxulub Structure, Mexico[1]

2.1. Abstract

The ICDP Yaxcopoil-1 borehole located 60 km SSW into the Chicxulub impact structure intercepted an interval of allogenic impactites (795-895 m depth). Petrographic analysis of these impactites allows them to be differentiated into five units based on their textural and modal variations. Unit 1 (795–922 m) comprises an apparently reworked, poorly sorted and graded, fine-grained, clast-supported, melt fragment-bearing suevitic breccia. The interstitial material, similar to Units 2 and 3, is permeated by numerous carbonate veinlets. Units 2 (823–846 m) and 3 (846-861 m) are groundmass-supported breccias that comprise green to variegated angular and fluidal melt particles. The groundmass of units 2 and 3 comprises predominantly fine-grained calcite, altered alkali element-, Ca- and Si-rich cement, as well as occasional lithic fragments. Unit 4 (861–885 m) represents a massive, variably devitrified and brecciated impact melt rock. The lowermost unit, Unit 5 (885–895 m), comprises highly variable proportions of melt rock particles (MRP) and lithic fragments in a fine-grained, carbonate-dominated groundmass. This groundmass could represent either a secondary hydrothermal phase or a carbonate melt phase, or both. Units 1 and 5 contain well-preserved foraminifera fossils and a significantly higher proportion of carbonate clasts than the other units. All units show diagnostic shock deformation features in quartz and feldspar clasts.

Our observations reveal that most felsic and all mafic MRP are altered. They register extensive K-metasomatism. In terms of emplacement, we suggest units 1 to 3 represent fallout suevite from a collapsing impact plume, whereby Unit 1 was subsequently reworked by resurging water. Unit 4 represents a coherent impact melt body, formation of which involved a significant proportion

[1] Tuchscherer M. G., Reimold W. U., Koeberl C., Gibson R. L. and de Bruin, D. 2004. First petrographic results on impactites from the Yaxcopoil-1 borehole, Chicxulub Structure, Mexico. Meteoritics & Planetary Science 39:899-930.

of crystalline basement. Unit 5 is believed to represent an initial ejecta/ground-surge deposit.

2.2. Introduction

Since its discovery (Penfield and Camargo, 1981; Hildebrand et al., 1991), the Chicxulub impact structure has been widely accepted as the "smoking gun" for the catastrophic impact event associated with the 65 Ma Cretaceous-Tertiary (K/T) boundary. Recent publications that question this association (Keller et al., 2003a, 2004) are based on very limited data that are quite doubtful. Crucial evidence in support of a collision with an extraterrestrial projectile at that time includes the widespread deposition of glass spherules around the Caribbean and beyond (e.g., Sigurdsson et al., 1991; Smit et al., 1992; Premo and Izett, 1992; Koeberl and Sigurdsson, 1992; Koeberl, 1993; Oskarsson et al., 1996; Chaussidon et al., 1996; Hough et al., 1998; Smit, 1999), the global distribution of shock metamorphic quartz (Bohor, 1990; Owen et al., 1990; Alvarez et al., 1995; Bostwick and Kyte, 1996; Goto et al., 2002), anomalous PGE concentrations with chondritic character (Alvarez et al., 1980, Kyte et al. 1980, Smit and Hertogen, 1980; Orth et al., 1981; Schmitz, 1988; Evans et al., 1995), Ni-rich spinels (Cisowski, 1990; Kyte and Bostwick, 1995; Gayraud et al., 1996), the presence of fullerenes (Heymann et al., 1994; Heymann et al., 1996; Buseck, 2002), evidence for a global occurrence of wildfires (Argyle et al., 1986; Wolbach et al., 1985, 1990; Kring and Durda, 2001), and nano- to micro-diamonds found worldwide in the K/T boundary clay layer (Gilmour et al., 1992; Hough et al., 1997). The major mass extinction event at the K/T boundary has been widely linked to this cosmic catastrophe (e.g., Alvarez et al., 1980; Wolbach et al., 1985; Pope et al., 1994; and papers in Sharpton and Ward, 1990; Ryder et al., 1996; and Koeberl and MacLeod, 2003).

Impact melt rock and breccia samples provided the confirmation of the impact origin of the Chicxulub structure (Hildebrand et al., 1991; Kring and Boynton, 1992; Swisher et al., 1992; Sharpton et al., 1992; Koeberl, 1993; Blum et al., 1993, Schuraytz et al., 1994; Kettrup et al., 2000; Claeys et al., 2003). Some of the earlier findings placed constraints on the impact melt crystallization

age and, thus, the age of the impact, its link to the K/T boundary mass extinction, as well as the geochemical characteristics and isotopic signature of the melt. These observations have neither resolved the extent of melting by the Chicxulub impact event nor the extent of target rock mixing in formation of the melt.

Because no other well-preserved impact structure of Chicxulub size (ca. 195 km diameter; Morgan et al., 2002) is accessible for detailed analysis, the crater was re-drilled between December 2001 and February 2002 by the International Continental Scientific Drilling Program (ICDP; Dressler et al., 2003a,b). Chicxulub is the third largest impact structure currently identified on Earth (Grieve and Therriault, 2001; Whitehead, 2004) and the only such large one that is almost preserved (but unfortunately not well accessible). For this reason, scientific drilling of the crater is the prime tool to obtain the scientific objectives aimed at elucidating the internal structure and fill of such a large impact structure. The Yaxcopoil-1 borehole was drilled circa 60 km from the center of the impact structure (Fig. 2.1), in anticipation of intersecting a thick and complete impactite sequence, as interpreted from nearby geophysical data (e.g., Sharpton et al., 1996, their Fig. 5; Morgan et al., 2000, their Figs 3 and 4) and suggested by the stratigraphy of neighbouring earlier drill cores (Fig. 2.2). A complete section of impactite was desirable for its potential to contribute to solving important issues such as the total melt volume, mixing of target rocks, distribution and origin of shocked material, lateral distribution of ejecta and fate of the meteoritic projectile. However, the Yaxcopoil-1 borehole intercepted only 100 m of impactites, probably because no seismic data existed for the borehole location. Here, we report our first results of a detailed petrographic investigation of this interval, including detailed description of the various units, modal analyses, cathodoluminescence, scanning electron microscopic (SEM), electron microprobe (EMP), and X-ray diffraction (XRD) results. The objectives of this work are to provide petrographic constraints for the stratigraphic subdivision of various impactite units and their formation, constrain melt compositions, investigate primary versus secondary mineralogical features, characterize the lithic and mineral clast content in the impactites with a view to contributing to the understanding of the Chicxulub target composition, determine the nature of shock

metamorphic effects in the clasts and their distribution over the stratigraphic section, and to integrate these results in an attempt to contribute to an emplacement model for this sequence.

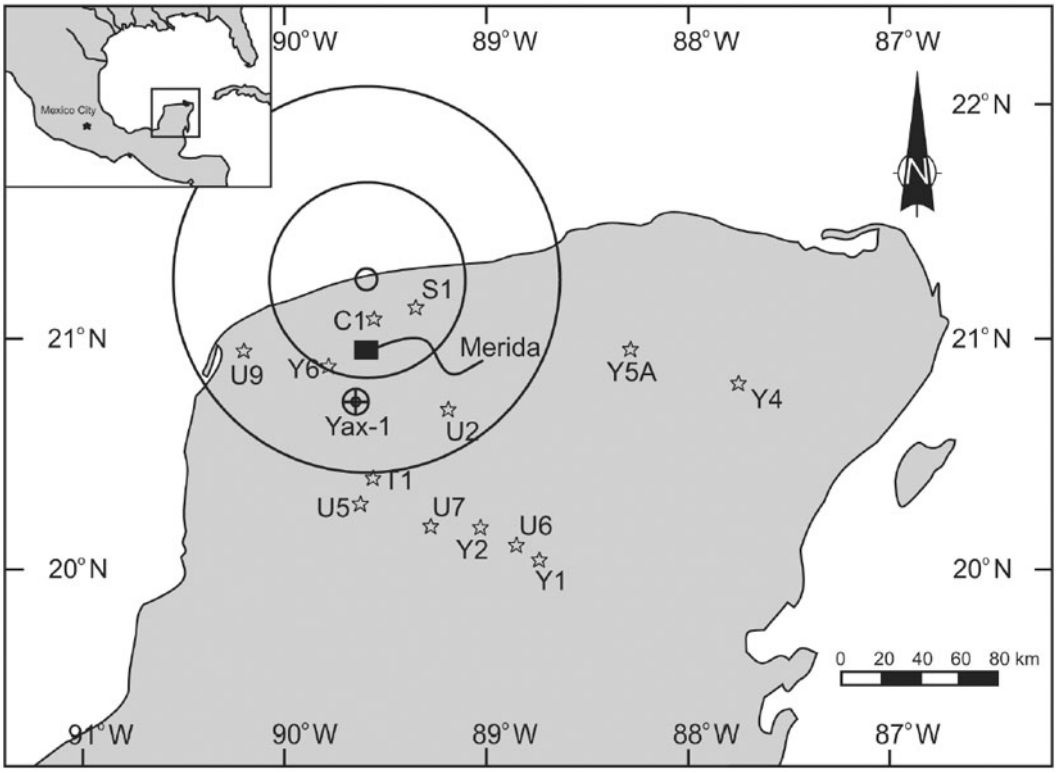

Fig. 2.1. The Chixculub meteorite impact site is located on the northwestern part of the Yucatán Peninsula of Mexico. The ICDP borehole is located ~60 km towards the south of the center of the structure. The circles shown here represent the extent of the postulated transient cavity at ~100 km (Morgan et al. 2002) and the postulated crater diameter at ~195 km from the outermost most significant inward-facing scarp (Morgan et al. 2002). Also shown are all nearby diamond drill hole localities (borehole localities from Persaud and Sharpton, 1998; Sharpton et al., 1999).

2.3. Previous drilling of Chicxulub

As seen in Fig. 2.1, fourteen boreholes have been drilled to date in the area of the Chicxulub structure and its immediate vicinity. Most cores (C1, S1, Y1, Y2, Y4, Y5A, Y6, T1 – Fig. 2.1) were recovered by the Mexican national oil company PEMEX during hydrocarbon exploration in the late 1960s and 1970s (Hildebrand et al., 1991). The stratigraphies of these boreholes are compared in Fig. 2.2. After Chicxulub had been established as an impact structure (Hildebrand et al., 1991), additional drilling was undertaken by the *Universidad Nacional Autonoma de Mexico* (UNAM; boreholes 2, 5-7, 9). Although drilling was extensive, only few scientific publications on the petrology and the chemistry of impactites have been published to date (Hildebrand et al., 1991; Kring and

Boynton, 1992; Swisher et al., 1992; Sharpton et al., 1992; Koeberl, 1993; Blum et al., 1993, Schuraytz et al., 1994; Meyerhoff et al., 1994; Ward et al., 1995; Warren et al., 1996; Urrutia-Fucugauchi et al., 1996; Kettrup et al., 2000; Claeys et al., 2003). Impact melt samples from the C1 and Y6 boreholes were described having an andesitic to dacitic composition (Hildebrand et al., 1991; Kring and Boynton, 1992; Sharpton et al., 1992; Warren et al., 1996). The Y6 samples were observed to be richer in platform-sedimentary clasts than the C1 samples (e.g., Schuraytz et al., 1994; Claeys et al., 2003). Borehole Y6 is located in the impact basin (the so-called moat) around the central peak ring. The T1 borehole is located just outside the crater rim (assuming a 195 km wide crater, Morgan et al., 1997). Farther out from the center of the crater, samples from the UNAM 5, 7, and 6 boreholes were observed to contain progressively lower proportions of siliceous basement inclusions and an increasing sedimentary component (Urrutia-Fucugauchi et al., 1996; Sharpton et al., 1999).

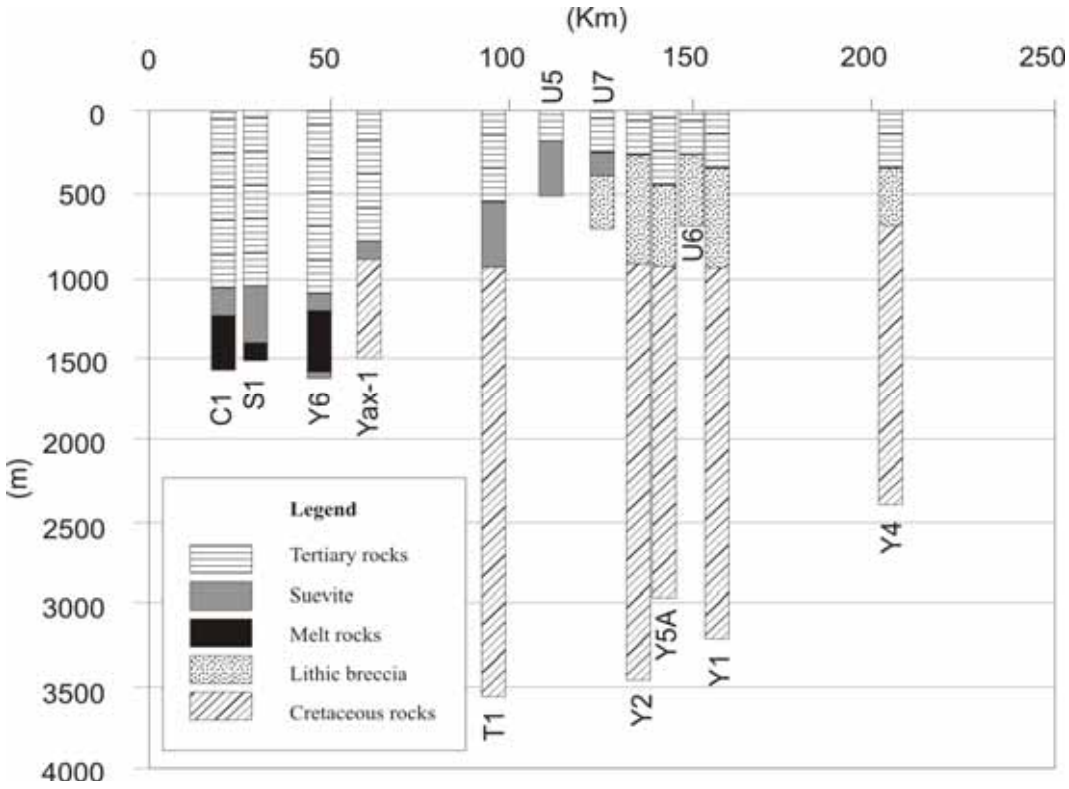

Fig. 2.2. Projected vertical cross-section through the Chicxulub impact structure (0 km = crater center) with all published exploratory and scientific boreholes, as compiled by Stöffler et al. (2003b). Note that the Yaxcopoil-1 borehole overlies a region of faulted and displaced Cretaceous rocks similar to the T1 borehole between 900 and 1500 m (Ward et al. 1995). It can be seen that the C1, S1, and Y6 boreholes were all drilled into a comparatively thicker sequence of Tertiary rocks, covering the infilled impact basin.

Kring and Boynton (1992) showed that, compositionally, these melt rocks do not follow traditional calc-alkaline and tholeiitic igneous trends and demonstrated – in support of an impact origin – that Haitian impact melt lay on a similar mixing-line as that established for Chicxulub impactites. Kring and Boynton (1992) indicated that the andesitic melt composition could be modeled as a mixture of upper sedimentary and crystalline basement rocks known to occur in the Yucatán crust, i.e., 12% (by volume) Y6-N17 groundmass, 72% mica schist, 4% sandstone, 2% dolomite, and 10% limestone/anhydrite. Sharpton et al. (1992) also showed that some of the the Y6 and C1 melt rocks contained unusually high abundances of iridium, the highest values being 2.5 ± 0.5 and 13.5 ± 0.9 ppb, indicating the presence of an extraterrestrial component, as also established for the K/T boundary layer at numerous locations (e.g., Alvarez et al., 1980). This was confirmed for C1 melt rocks by Koeberl et al. (1994) from osmium isotopic studies. Radiometric dating by Sharpton et al. (1992) of the Y6 and C1 melt rocks with the ^{40}Ar-^{39}Ar technique produced a crystallization age of 65.2 ± 0.4 Ma, similar to the results of Swisher et al. (1992). Schuraytz et al. (1994) suggested that Y6 and C1 crystalline impact melt rocks had undergone slow cooling and, thus, might be worth investigating for potential Sudbury-style mineralization. They also proposed that C1 or C3 carbonaceous chondrite meteorites could represent the type of projectile responsible for the formation of the Chicxulub crater, as the impactites contained rare but characteristic high-iridium particles only found in such meteorites. Warren et al. (1996) concluded that the clast content of impact melt rock from the C1 and Y6 drill cores was negatively-correlated with matrix grain size, as also known from other impact structures. They proposed that the incorporation of cold inclusions into the impact melt acted as a heat sink, providing a quenching effect. Further insight into the subsurface stratigraphy of the Yucatán platform was given by Ward et al. (1995) through a compilation of logs from boreholes T1, Y2, Y1, Y6, C1, Y5, and Y4 (compare with Fig. 2.2). They emphasized that the basement was intersected at 2418 m and 3203 m in wells Y4 and Y1, respectively, and that it comprised a Paleozoic metamorphic terrain of Pan-African age (~545 Ma, Krogh et al., 1993; Kamo et al., 1995). Ward et al. (1995) postulated that the pre-impact sedimentary rock

stratigraphy comprised 35 to 40 vol% dolomite, 25 to 30 vol% limestone, 25 to 30 vol% anhydrite, and 3 to 4 vol% sandstone and shale.

Petrographic and geochemical results from Chicxulub melt rocks (drill cores Y6 and C1) were recently reported by Kettrup et al. (2000, 2003) and Claeys et al. (2003). They indicated that the Chicxulub melt rocks are more heterogeneous than previously thought. Kettrup et al. (2000) concluded that a mafic component was required in order to model the variation between C1 melt rock and Haitian impact glasses. These authors also determined that the melt rocks and ejecta deposits had different isotopic and major element characteristics and, thus, indirectly revealed the complex geological character of the Yucatán crust. Kettrup et al. (2003) suggested the Chicxulub impact may have sampled Gondwanan and Laurentian crust.

Claeys et al. (2003) recognized three subdivisions in the impactites of the Y6 borehole: i) an upper, fine-grained, carbonate-rich, fossil-bearing suevite; ii) a middle, relatively coarser-grained, suevite rich in altered silicate melt particles and silicate basement clasts; and iii) a lower, so-called "thermometamorphic" suevite rich in melt fragments, large evaporite clasts, and shocked basement clasts. Thermal metamorphism of this latter unit, i.e., recrystallization of its groundmass, was thought by these authors to have been induced by an underlying, now crystalline, impact melt layer. Claeys et al. (2003) proposed that the upper suevite represented either a late fall-back deposit or an interval that was reworked by seawater resurging into the impact basin; the middle suevite represented a typical suevite deposit that originated as fall-back out of a collapsing ejecta plume; and that the lower unit represented either an early ejecta/fall-back deposit or material that was deposited on the outermost flank of the collapsed transient cavity by inward-movement of material, during the modification stage of cratering.

The currently available data indicate that the Yucatán crust represents a much more varied geological terrain than previously thought. Inclusions observed within retrieved cores mostly originate from the crystalline basement and include granite, schist, gneiss, and amphibolite, besides a sedimentary carbonate- and anhydrite- dominated component. The crystalline lithologies represent a

metamorphic terrane that is related to the Grenvillian orogeny (Kettrup et al., 2003) and also involves crust that was recycled during Pan-African times.

2.4. The Yaxcopoil-1 drill core

Yaxcopoil-1 is located ~60 km from the center of the Chicxulub structure (Fig.2.1). It extends to a final depth of 1511 m (Fig. 2.2). The drill site was chosen in order to better elucidate the composition of the structure in a gap between a string of earlier boreholes (Sharpton, 2000; our Fig. 2.2) and as a thick impactite intersection was expected. Prior to drilling, detailed geophysical analysis was carried out to constrain the sub-surface structure and geology. As shown by Sharpton et al. (their Fig. 5, 1996), extensive breccia deposits and melt rocks were expected to be intersected at the Yax-1 site, at least comparable to those in the Y6 and T1 boreholes, where 490 m of suevite and melt rocks and 930 m of "Bunte Breccia"-like deposits had been intersected, respectively. Geophysical data (gravity, Sharpton et al., 1993; seismics Morgan et al., 1997; 2000; 2002) predicted that the site, located in an annular trough around the peak ring structure, was favourable for preservation of a thick breccia deposit. From the seismic data, it was also determined that the Cretaceous rocks at the Yax-1 site seemingly were part of disturbed, slumped blocks that occurred between 40 and 75 km from the crater center. Based on the interpretation of geophysical information (Morgan et al., 2002), the drilling site corresponded to a point ~37.5 km inward from the crater rim.

The Yax-1 borehole intersected 795 m of Tertiary rocks (mostly interlayered carbonaceous siltstones and calcarenites), 100 m of suevitic breccia and melt rock, and 615 m of presumably displaced Cretaceous rocks (comprising interlayered calcarenite, dolomite, and anhydrite, with minor siltstones and conglomerates) (Dressler et al., 2003a,b). The field log for the drill-core and the terminology developed by Dressler (2003a,b) provide a stratigraphic basis for all ongoing investigations (Table 2.1). The focus of our work, the impactite sequence, was initially differentiated into *six* stratigraphic units based on macroscopic core logging observations (color, grain size, fabric, and texture);

Table 2.1. Comparison of Yaxcopoil-1 impactite lithological units, as proposed by various research groups.

Units	Depth (m)	Dressler et al. 2003a,b	Stöffler et al. 2003a	Kring et al. 2003a	Tuchscherer et al. 2003 and this work
1	795 – 808	Redeposited suevite	Upper sorted suevite (USS)	Fine-grained reworked suevite (13 m)	Fining upwards, sorted, and reworked suevite
2	808 – 823	Suevite	Lower sorted suevite (LSS)	Matrix /clast supported suevite (15 m)	
3	823 – 846	Chocolate-brown melt breccia	Upper suevite (US)	Melt-rich breccia (23 m)	Suevite
4	846 – 861	Suevitic breccia, variegated, glass rich	Middle suevite (MS)	Melt-rich breccia agglomerate (15 m)	Variegated melt rock fragment rich suevite
5	861 – 885	Green, monomict, autogene melt breccia	Suevitic breccia with cataclastic melt rock (SB)	Coherent , massive, green impact melt unit (24 m)	Green impact melt rock breccia
6	885 – 895	Variegated, polymict, allogenic, clast melt breccia	Lower suevite (LS)	Brecciated, carbonate-charged, green melt unit (10 m)	Variegated, polymict, impact melt breccia or suevite

most groups working on this drill core have accepted this general stratigraphy, but as we will discuss in detail below, we favour a *five-fold* division.

2.4.1. Borehole stratigraphy

The borehole stratigraphy can be summarized as follows, after Dressler et al. (2003a): upper Tertiary rocks were intersected from 404 m (beginning of continuous coring) to 795 m depth. This interval comprises a foraminifera-rich, rhythmic laminated, hemipelagic sequence of anoxic limestones that alternate with bioturbated marls (Dressler et al., 2003a). Below 600 m depth, several conglomeratic mass flows are intercalated with hemipelagic sediments (calcarenite, calcareous siltstone, and minor chert). Between 795 and 895 m, a 100 m thick impactite sequence was drilled (see our detailed descriptions for units 1 to 5 below). Below this depth, sedimentary platform rocks comprise poorly fossiliferous limestone, dolomite, and anhydrite, of which the latter makes up 27.4 % (Dressler et al., 2003a). Several breccia zones were intersected in these Cretaceous rocks: melt-bearing breccias at ca. 909-910, 916, 1348 m; lithic breccias at 1314-1316, 1341, 1398-1399 m; black oil-bearing shear zones at 1350,

1369, 1372, 1382, 1394, 1397, 1399, 1420 m; and several wide, brittle deformation zones between 1310-1400 m, and 1496-1510 m (Kenkmann et al., 2003).

Dressler (2003a,b) identified a number of key lithological criteria for each impactite unit (Table 2.1). Laminations, at the top, and clast size sorting are observed within his Unit 1 (795–808 m). Unit 2 (808–823 m), in contrast, contains no lamination or clast-size sorting. Unit 3 (823–846 m) was defined by a distinct fine-grained, brown matrix – thought to be a melt matrix – that supports relatively fewer large melt and lithic fragments than observed in the upper units. Thus, Unit 3 was termed a "chocolate-brown melt breccia" (Dressler et al., 2003a). Unit 4 (846–861 m) displays a very coarse and heterogeneous character that involves contorted, flow-structured and welded melt fragments of various colors, from which this unit gained its working name "suevitic breccia, variegated, melt rich". This unit has a gradational contact with Unit 3. Unit 5 (861–885 m) displays an abrupt upper contact. It is characterized by flow-structured green melt fragments that locally fit together like the pieces of a jigsaw puzzle and was, thus, named "green, monomict, autogene melt breccia" by Dressler et al. (2003a). The green melt fragments are, in places, supported by a fine-grained carbonate matrix that contains a high proportion of originally mostly molten basement rock clasts. The lowermost impactite unit (Unit 6, 885–895 m) follows with a gradational upper contact and displays an increase in size, abundance, and diversity of target rock fragments. Melt fragments display green to tan, and light gray colors. The carbonate groundmass is light tan to light brown. The groundmass is locally flow-textured and contains very small target rock fragments as well as melt rock particles. This unit was, thus, named "variegated, polymict, allogenic, clast-rich melt breccia" (Dressler et al., 2003a).

2.5. Petrographic results

2.5.1. Macroscopic observations

Macroscopic observations were made on the Yax-1 core samples at the first ICDP sampling party at UNAM, Mexico City, in April 2002. In the

following section, a description of the impactites and some of the overlying reworked suevitic/carbonate material is presented. From top to bottom of the impactite interval five units (Tables 2.1 and 2.2) are distinguished on the basis of melt rock content, melt fragment size, morphology, color, groundmass type, and lithic mineral clast content.

Table 2.2. Yaxcopoil-1 impactite-lithological characteristics (this work)

Units	Depth (m)	Lithological characteristics
1	795 – 823	Fining upward, sorted, reworked, and clast supported breccia deposit. Contains limestone and fossil fragments. Altered melt typically has greenish color.
2	823 – 846	A fine-grained, groundmass-supported breccia that contains green fluidal textured, angular, and rounded melt rock fragments.
3	846 – 861	A fine-grained, groundmass-supported breccia that contains variegated, angular, and rounded melt rock fragments. Abundance of large brown melt rock masses increase with depth.
4	861 – 885	A massive but strongly brecciated green melt rock unit. Melt fragments display flow-textures.
5	885 – 895	A melt breccia comprising variegated altered melt rock fragments and polymict lithic/mineral clasts and foraminifera suspended in a fine-grained carbonate groundmass.

2.5.1.1. Top reworked suevitic and sedimentary rocks

The 50 cm interval above the upper impactite contact, between 794.1 and 794.6 m depth, comprises a very fine-grained, medium-brown to light beige carbonate interval. Fine-scale cross bedding characterizes the overlying material. Also observed are 1 cm thick, green, sedimentary lenses of reworked, altered, green melt particles. Rare, small, variegated and spotted drop-stones ~1 cm in size - possibly representing fragments of the underlying reworked suevite - were also noted. This interval grades over 5 cm into the underlying, massive suevitic rocks.

2.5.1.2. Unit 1

The uppermost impactite between 795 and 808 m depth comprises a heavily altered and reworked, suevitic rock containing a large proportion of altered, green melt rock particles. The rock is largely particle-supported. Melt particles are sub-rounded, microcrystalline, and relatively well sorted, compared to the underlying units. The average fragment size is ~2 mm. This unit is

extremely friable (poorly consolidated) and was, therefore, not diamond-sawed for sampling. According to Dressler et al. (2003a), there is a sharp contact with the underlying package at *circa* 808 m. The material between 808 and 823 m is distinctly more consolidated than the upper part of Unit 1. Compared to the overlying segment, angular (shard-like) melt and lithic particles become progressively more inequigranular (less sorted), coarser (average ~8 mm, generally 2 cm), and angular with depth (Fig. 2.3a). Most melt particles are green, others are brown or dark gray. Recognizable lithic inclusions comprise primarily sedimentary clasts including limestone, dolomite, and siltstone, but also a few small (<0.5 cm), mottled, pinkish-white granitic clasts.

2.5.1.3. Unit 2

The upper and lower contacts of this unit, at 823 and 846 m, respectively, are gradational but, relative to Unit 3, Unit 2 has a distinctive color, lithic fragment population and size, and melt particle size. Relative to the predominantly light olive-green Unit 1, the groundmass in Unit 2 is medium-gray. This color only became apparent upon drying out of the core - immediately after extraction of the core, the groundmass was medium-brown. Clasts in this unit are highly inequigranular. This breccia carries a variety of angular melt rock fragments of shard-like appearance that, in part, show schlieren (fluidal texture; Fig. 2.3b). Dark gray and brown melt fragments are also observed. All melt fragments are suspended in a microcrystalline to cryptocrystalline groundmass (Fig. 2.3b). Melt fragments are generally larger in this unit - (~2 cm on average, but up to 9 cm in diameter) - than in Unit 1. Recognizable lithic inclusions are derived from limestone, siltstone, and granite.

2.5.1.4. Unit 3

Unit 3, between 846 and 861 m depth, displays a gradational upper contact but a sharp lower contact. This material (Fig. 2.3c) consists of subrounded/subangular melt particles that locally display shard forms and a range of colors (brown, gray, and green), and commonly show distinct, beige, reaction rims. Average fragment size is similar to that in Unit 2, at 2 cm, but larger

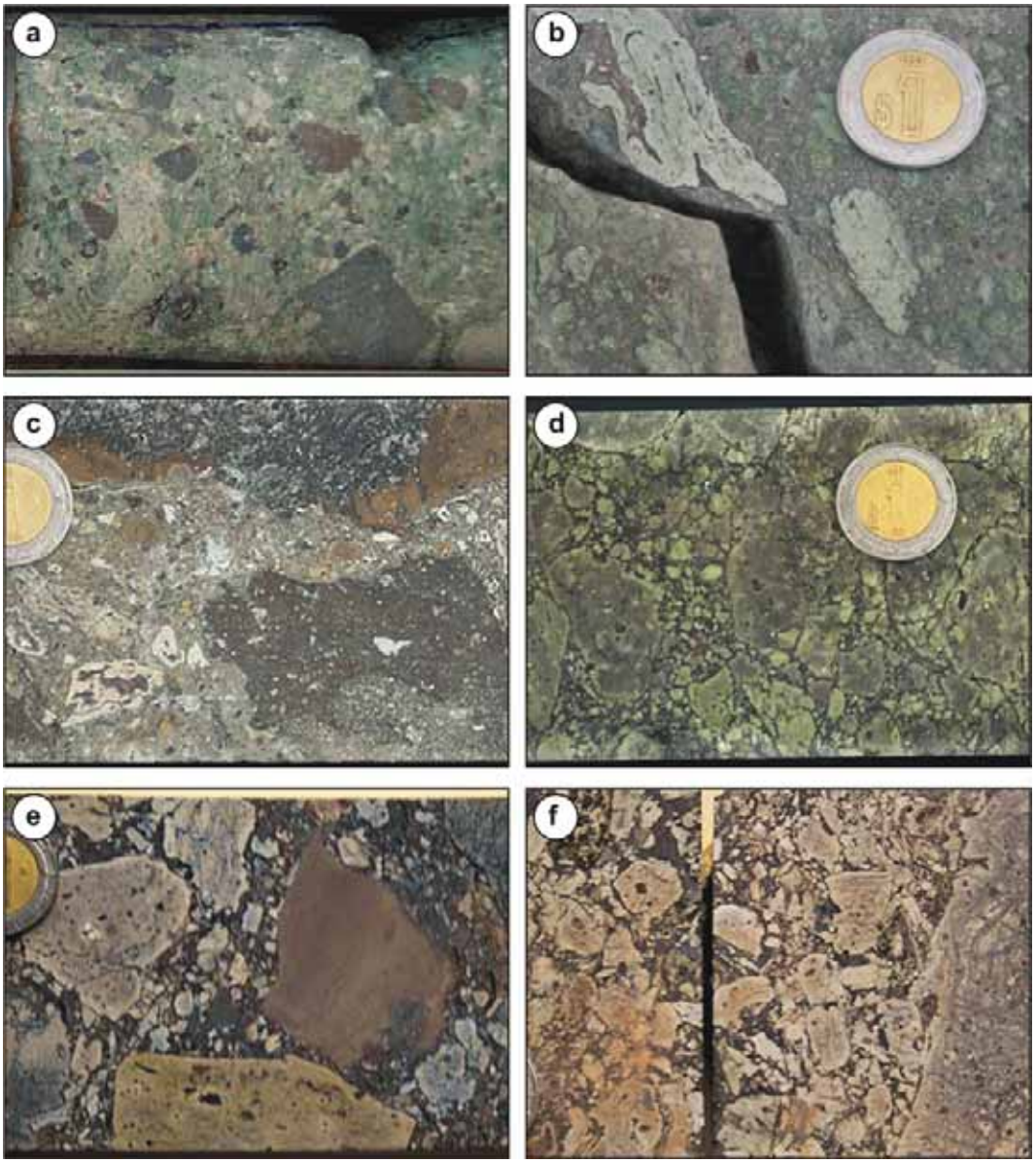

Fig. 2.3. Photographs of the various lithological units taken in the impactite interval of the Yaxcopoil-1 borehole, core width = 6.35 cm, coin diameter = 2 cm: a) Unit 1, reworked suevite, depth = 811.55 m; b) Unit 2, un-reworked suevite, depth = 835.31 m; c) Unit 3, variegated melt rock rich suevite, depth = 851.85 m; d) Unit 4, brecciated green impact melt rock , depth = 862.81 m; e) Unit 5, variegated polymictic impact melt breccia, depth = 889.88 m; f) Unit 5, undulating contact between coarse- and a fine-grained breccia, image height = 6.2 cm, depth = 892.55 m. See text for detail.

fragments occur in relatively greater abundance. The proportion of brown melt rock particles increases with depth (as discussed in detail below). Lithic fragments are rare and generally comprise small (5-10 mm), rounded limestone clasts, besides a few silicate (granite, schist) inclusions. Calcite veins permeate the groundmass and anastomose around melt shards.

2.5.1.5. Unit 4

Unit 4, from 861 to 885 m, is a massive green unit dominated by large, angular to subangular, melt fragments (Fig. 2.3d). The shard-like melt fragments display internal fluidal textures and the jigsaw-like arrangement of fragments indicates that this melt experienced *in situ* brecciation. The material interstitial to the shards is fine-grained, dark gray, and cannot be resolved in hand specimen.

2.5.1.6. Unit 5

The lowermost impactite unit, between 885 and 895 m, displays a locally variable population of lithic fragments and melt particles. A 34 cm wide granitic clast was observed at 889.59 m depth. Other lithic fragments that can be recognized macroscopically represent dolomite and limestone. Sub-angular and relatively large (2-5 cm) melt particles, often with internal flow structures, are suspended within a fine-grained, carbonate-dominated groundmass (Fig. 2.3e). Sharp undulating contacts were also observed within the brecccia (Fig. 2.3f; at 892.55 m depth).

2.5.2. Micro-analysis

In total, 52 polished thin sections of samples from the impactite interval were prepared for petrographic analysis. It is important to bear in mind the small sample size: only specimens between 8 to 16 cm^3 were provided. In the light of lithic and melt fragment diversity, as well as the large variation of grain sizes observed, the representivity of our sample suite must be considered. In point-counting analysis, 1000 counts were recorded per thin section, at 0.25 mm increments and 1 mm line spacing. Cathodoluminescence (CL) properties were observed using an Olympus BH-2 petrographic microscope connected to a cold-cathode CITL MK3a CL apparatus at 10 ± 2 kV and 300 ± 25 μA operating conditions, with the vacuum maintained at 0.3-0.7 mTorr. Backscattered electron imaging and energy-dispersive X-ray analysis were carried out, at 15-20 kV, 20 nA, and 39 to 15 mm working distances, with a JSM-840 scanning electron microscope (SEM) at the Electron Microscope Unit of the University of the Witwatersrand. Additional imaging was done at the Council for Geoscience,

Pretoria, with a Leica 440 Stereoscan instrument with attached LINK OXFORD energy-dispersive X-ray analysis system, at 20 kV, 2 nA, and 25 mm working distance. Quantitative electron microprobe analyses were collected for the elements Si, Ti, Al, Cr, Fe, Mn, Mg, Ca, and Na in wavelength-dispersive mode on a JEOL 733 Superprobe, at 15 kV, 20 nA, and 39 mm working distance, also at the Council for Geoscience in Pretoria. Electron-beam widths ranged from 3 to 10 μm, with peak count times of 10 seconds and 5 seconds each on symmetrical background positions. The standard K-H, a hornblende from Kakanui, New Zealand (USNM 143965, see Jarosewich et al., 1980) was used for SiO_2, Al_2O_3, FeO_{tot}, CaO, Na_2O, and K_2O analysis, synthetic rutile for TiO_2, natural rhodonite for MnO, and the chromite standard USNM 117075 for Cr_2O_3 standardization. Data reduction was done with the JEOL Fortran program (FZAFOC). X-ray diffraction analyses on bulk rock powders were carried out with the PW 1710 instrument at the X-ray analytical facility of the School of Geosciences at the University of the Witwatersrand.

2.5.3. Microscopic observations

A summary of the key micro-petrographic observations made on samples of the various impactite units is given in this section.

2.5.3.1. Unit 1

Thin sections of Unit 1 breccia reveal relatively small lithic clasts, as well as melt fragments that commonly have shard-like forms. These particles range in size from 0.1 to 4 mm, and have an estimated average size of 2 mm. The melt particles are primarily angular to subangular. They are self-supported. The fragments are surrounded primarily by an interstitial network of fine-grained carbonate veins and/or by a microcrystalline (<0.05 mm) groundmass containing small carbonate grains interspersed with a very fine-grained silicate cement (Fig. 2.4a), as also observed by Ames et al. (2003) and Kring et al. (2003a). Melt fragments are extensively altered; they are predominantly green but can also be grayish-brown or colorless. With increasing depth, the color of the altered melt fragments shifts from a dominant greenish-yellow to more yellowish-green hues.

Microscopic perlitic fractures characterize the melt fragments, dividing the fragments into domains of typically <0.05 mm width. The samples also contain rare, very small, brown to dark gray, fluidal-structured, altered melt fragments, and even more rare, orange-red melt particles (Fig. 2.4b). An increasing abundance of large (5-15 mm), angular, fluidal-textured, dark gray and brown melt particles is noted with increasing depth. Lithic inclusions are rare and include, with decreasing relative abundance, limestone, dolomite, shale, quartzite, granite, and schist fragments. Mineral fragments are very rare and include, again in decreasing abundance, calcite, dolomite, quartz and feldspar. The abundance of microscopic calcareous shells and foraminiferous limestone (Fig. 2.4c) is a key characteristic of Unit 1 (compare Table 2.3). They are found within carbonate clasts or freely suspended in the groundmass. Numerous melt fragments have small blebs of carbonate that represent either infilled vesicles or evidence of liquid immiscibility of a carbonate melt phase in silicate melts. Fine-grained (~1 mm) and relatively wide (2 mm) carbonate veins commonly cut through the fine-grained carbonate-rich groundmass and meander around lithic and melt fragments. Samples from the section between 808 and 823 m and from close to the gradational contact with Unit 2 contain more angular and vesiculated green melt fragments, and rarer fluidal-structured shard-like melt fragments (size range 0.5-5 mm, average size 2.5 mm) than elsewhere in this unit. These fragments are also self-supported and are set in a vein network of very fine-grained (<0.05 mm) to, in patches, fine-grained (~0.5-1.0 mm), white to light gray interstitial carbonate. Small (~0.25 mm) lithic (quartzite/chert, limestone, dolomite) inclusions and large (up to 15 mm), brown or dark gray, melt fragments are also present. Quartz grains are usually found with one set of planar deformation features (PDFs), sometimes with more, and may display an unusual, angular fracture pattern similar to the “cracked tile” texture known from cristobalite (Deer et al., 1996). Melt fragments can be disaggregated, brecciated, or shattered, and are generally extensively altered. In this interval, larger melt particles with fewer perlitic fractures are found with increasing depth.

Table 2.3. Modal analyses of selected samples from units 1 to 5 (data in vol. %).

	Unit	1	1	1	1	2	2	2	2	2
	Depth (m)	803.4	805.3	810.8	821.4	825.4	827.1	835.1	840.3	843.5
	Description**	Sue.	Sue.	Sue.	Sue.	Sue.	Sue.	Sue.	B.M.R.	B.M.R.
Melt particles, rocks, and matrix	Green		1.5	9.9	1.8	1.2		0.5		
	Brown	1.9	3.7	4.0	4.7	31.4	0.4	3.3		
	Brown, microlite rich						12.0	3.3	61.5	34.8
	Yellow					0.9	12.2			3.1
	Yellow, microlite rich						8.6			
	Colorless, microlite rich	0.3			1.8		11.5	17.4	19.4	20.9
	Orange/red	0.1	0.3	0.5		0.2				0.7
	Multi-colored		0.3	6.1		0.3		0.1		
	Colorless	13.7	31.4	34.3	36.0	25.2	6.5	34.0		10.2
	Perlitic fractured	39.5	18.4	18.4	5.3		1.4			
	Siliceous matrix	10.4	2.6	0.5	1.9	2.3	12.0	11.2		
Carbonate	Carbonate, microcrystalline	18.7	15.7	7.7	28.4	7.0	12.0	19.8		
	Carbonate crystal or patch, med.-grained	7.7	6.1	2.8	3.6	6.6	0.7	3.7	1.7	1.0
	Carbonate bleb, immiscible in glass	0.9	1.4	0.8	2.8		3.1	1.5	0.5	1.9
Carbonate/ sulfate clastic	Limestone/dolomite fragment	2.9	2.8	5.0	1.6	4.1	0.1	0.1		0.2
	Foraminifer/shell	0.6	1.3	0.3						
	Anhydrite	0.1			0.3	0.2		0.1		
	Carbonaceous siltstone		0.7	0.2		1.7		0.7		
Unshocked silicate clasts	Clinopyroxene		0.2	0.2		0.1				
	Apatite	0.1				0.1				
	Opaques	0.2				2.5			0.2	0.1
	Quartzite					0.1				6.7
	Quartz	0.3	0.5	0.2	0.6	1.2	0.7		2.3	1.5
	Feldspar	0.2				0.1				0.3
Shocked clast content	Ballen quartz	0.4	1.3	0.1				0.3		
	Quartz, 1 set of PDFs	0.2	0.2		0.1	0.1	0.5	0.1		0.6
	Quartz, 2 sets PDF of PDFs	0.1			0.1	0.1	0.6			0.2
	Quartz, 3 sets of PDFs									
	Checkerboard feldspar					0.1				
	Plagioclase with PDFs	0.7			0.3	0.1		0.4		
Secondary phases	Carbonate veining		8.6	5.6	3.1	2.6	16.0		1.4	1.8
	Opaque vein (hydrocarbon)					3.6				
	Opaque patch	1.2	3.0	3.4	7.7	4.6	1.7	3.7	12.7	12.9
	Acicular yellow crystal aggregate or bleb					8.4	0.2		0.3	2.7
Totals	Melt particles	55.4	55.6	73.2	49.6	59.1	52.6	58.6	80.9	69.7
	Microlite	0.2			0.9	0.0	16.1	10.4	40.5	27.9
	Groundmass	36.8	24.4	11.0	33.9	15.9	24.7	34.7	1.7	1.0
	Carbonate matrix	26.4	21.8	10.5	32.0	13.6	12.7	23.5	1.7	1.0
	Clastic carbonate	3.6	4.8	5.5	1.9	6.0	0.1	0.9		0.2
	Carbonate content	30.8	36.6	22.4	39.8	19.9	31.8	25.9	3.6	4.9
	Clastic silicate	2.2	2.2	0.5	1.1	4.4	1.8	0.8	2.5	9.4
	Secondary silicate & opaque	1.2	3.0	3.4	7.7	19.1	17.9	3.7	14.4	15.6
	Total	100.0	100.0	100.0	100.0	100.0	100.0	100.0	100.0	100.0

*Note count duplication at 875.8 m and 886.8 m depths per sample.

**Abreviations are: Sue. = Suevite, B.M.R. = Brown Melt Rock, G.M.R. = Green Melt Rock

***Patches or vein fillings

Table 2.3. Continued

3	3	3	3	4	4 Dup.*	4	4	4	5	5 Dup.*	5	5	5	5
846.0	846.8	851.2	860.4	875.8	875.8	878.1	879.0	882.5	886.8	886.8	888.1	890.5	892.6	894.1
Sue.	Sue.	Sue.	B.M.R.	G.M.R.	G.M.R.	G.M.R.	G.M.R.	G.M.R.	Sue.	Sue.	Sue.	Sue.	Sue.	Sue.
	0.3							0.1	0.3	0.9	0.8			
7.4	9.2			0.1										
22.2	21.4	5.4	9.8	0.6		0.5	11.2	2.2			0.2	6.4		
		1.5												
2.3	0.1	0.8					0.4							
17.0	16.8	34.6	60.5	72.6	72.9	70.1	47.0	73.1	7.9	11.2	18.2	54.4	39.6	
	0.1	0.6												
	0.7													
0.1	0.8	21.6	5.6	0.9	6.3	3.6	3.4	1.9	9.4	2.7			2.3	12.0
7.6		0.1												
21.3	20.0	6.6					4.0		44.2	59.3	67.5	19.7	50.0	70.2
	1.5	2.5	4.9				0.4	0.1	0.7	0.9	5.2	2.0	1.3	0.4
5.0	4.3	2.1	0.1							0.9	0.1	1.8	1.0	
0.1			0.1						18.6	15.0		1.5		10.8
									0.6	0.7	0.1			1.5
		0.1										0.2		
	0.3													
		0.1						0.1						
	0.1			0.1				0.3	0.3					
		0.2												
2.9	3.6	0.6	2.0	0.5		1.2	2.0	0.7	4.0	1.4	0.4	1.4	0.8	
0.3		0.4	0.2	1.3	1.4	0.8	0.3					1.5		
0.1	0.2	0.7	0.6	0.5	0.6	0.2		0.5	0.3	0.3	0.2	0.1	0.1	
0.2		0.3	0.2	0.2		0.1		0.2	0.1	0.1	0.4		0.5	
			0.1	0.2			0.1		0.2	0.3	0.2		0.4	
			0.2	0.4	0.8	0.6	2.4	1.4			0.1	0.2	0.1	
0.2			0.7	0.1		0.4	2.2			0.4				
8.9	15.0	8.2	2.4				0.7		6.3	0.5	0.4	4.6	0.4	0.4
	0.4		2.2	7.6	6.3	4.7	3.8	12.0	6.5	3.9	5.6	3.1	1.0	4.8
3.8	3.1	1.3	2.8	0.5	1.1	1.3	2.5	3.9		0.8	0.6	1.0	2.3	
0.6	2.1	12.4	7.6	14.7	10.6	16.5	19.7	3.5	0.6		0.2	2.3	0.1	
49.0	49.5	64.5	75.9	74.2	79.2	74.2	62.0	77.3	17.6	14.8	19.1	60.8	41.9	12.0
20.8	19.2	20.4	35.2	36.6	36.5	35.3	29.3	37.7	4.0	5.6	9.2	30.4	19.8	
28.9	21.4	9.2	4.9				4.4	0.1	44.9	60.2	72.6	21.7	51.3	70.6
21.3	21.4	9.1	4.9				4.4	0.1	44.9	60.2	72.6	21.7	51.3	70.6
0.1	0.3	0.1	0.1						19.2	15.7	0.1	1.7		12.3
35.3	41.1	19.6	7.5				5.1	0.1	70.4	77.3	73.2	29.7	52.7	83.3
3.7	3.9	2.3	4.0	3.1	2.8	3.3	7.0	3.2	4.9	2.5	1.3	3.2	1.9	
13.3	20.5	13.7	12.6	22.7	18.0	22.5	26.6	19.4	13.5	4.7	6.8	10.9	3.4	5.2
100.0	100.0	100.0	100.0	100.0	100.0	100.0	100.0	100.0	100.0	100.0	100.0	100.0	100.0	100.0

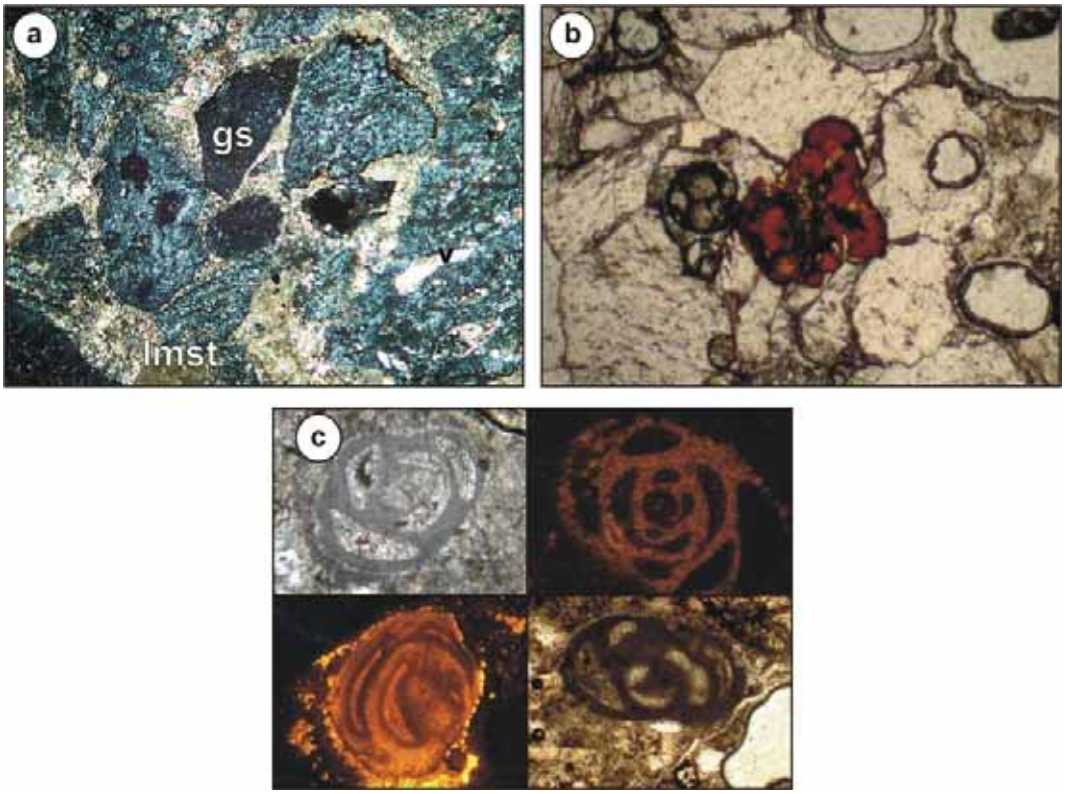

Fig. 2.4. Photomicrographs of unit 1: a) Fragmental, angular to rounded, and vesiculated clast-supported glass shards (gs) set into a microcrystalline carbonate groundmass; note the limestone (lmst) fragment at the bottom of image; image width = 4 mm, cross polarized light (CPL), sample depth = 803.44 m. b) Botryoidal red glassy bleb in a medium-grained calcite patch; image width = 1.5 mm, plane polarized light (PPL), sample depth = 809.70 m. c) Various foraminifera fossils: top-right foraminifera width = 0.65 mm, cathodoluminescence image (CL), sample depth = 809.70 m; bottom-right foraminifera width = 2 mm, PPL, sample depth = 803.48 m; bottom-left foraminifera width = 2 mm, CL, sample depth = 809.70 m; top-left foraminifera width = 1.5 mm, PPL, sample depth = 803.48 m.

2.5.3.2. Unit 2

Melt fragments in this unit are angular to sub-rounded and locally display internal fluidal structures. Some melt fragments are vesiculated and display frothy (Fig. 2.5a) morphologies. Melt fragment size is one to two orders of magnitude larger than in Unit 1, ranging from 0.5 to 6 mm (averaging at 4 mm). In contrast to the melt fragments of Unit 1, melt fragments in Unit 2 contain abundant microlites. The long axes of microlites are frequently aligned, indicating flow within the melts at the time of crystallization (Figs 2.5b and c). Most of these fragments are groundmass-supported. As seen in Figure 2.5a, vesicles can be filled with calcite, whereas others are filled with the very fine-grained groundmass material. Locally, carbonate blebs with ovoid shapes are observed in melt fragments; they

may be extended parallel to the prevailing microlite orientation (Fig. 2.5b), indicating flow. Melt fragments observed by backscattered electron imaging reveal patches of varying gray value, indicative of diverse melt particle compositions (Fig. 2.5c).

The Unit 2 breccia is supported by a groundmass that represents a mixture of microcrystalline carbonate grains and very fine-grained silicate matter (Fig. 2.5d). It has not been possible, even with the use of the SEM, to conclude what the nature (and origin) of this silicate material is, but it is thought that it represents, to a large degree, altered melt particles. Secondary fibrous and, as yet unidentified, minerals can be discerned at a < 5 μm scale in an otherwise unresolved silicate phase. The microscopic calcite grains range in size from 10 to

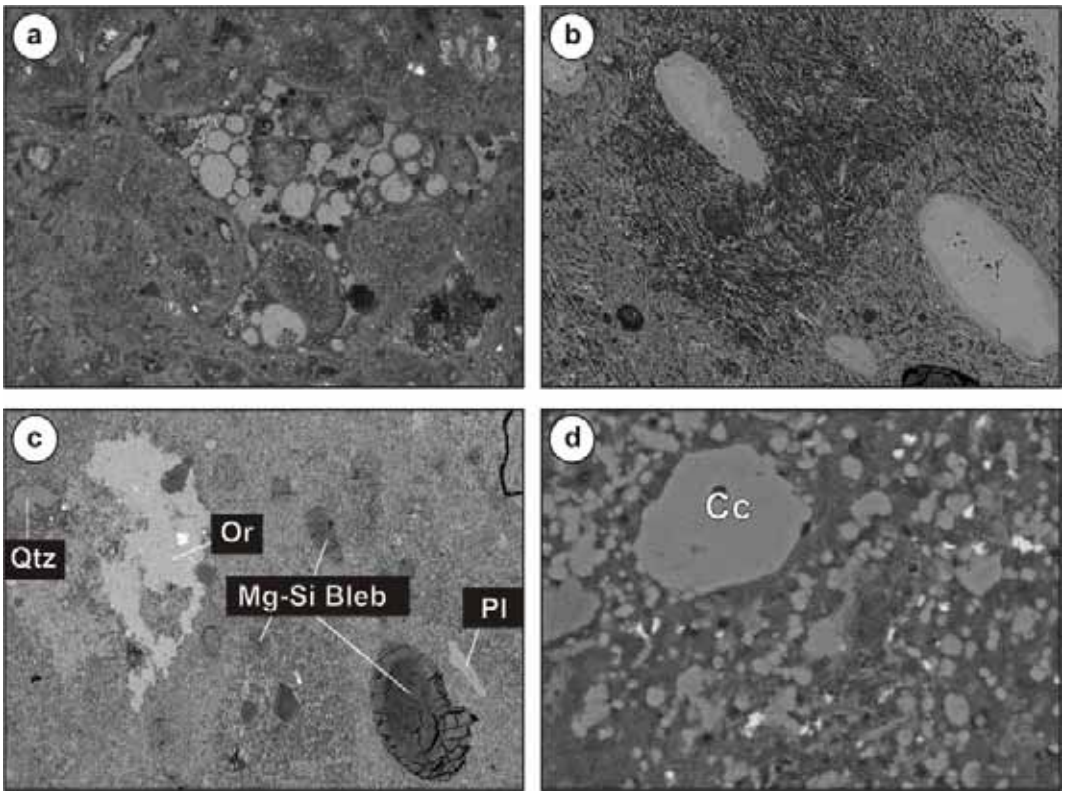

Fig. 2.5. Backscattered electron images (BSE) of unit 2: a) Highly angular and vesiculated, melt particle-rich breccia; note that most of the vesicles in the large melt rock fragment are infilled by calcite, whereas remaining vesicles contain groundmass material; image width = 2.4 mm, sample depth = 835.18 m. b) Primary immiscible fine-grained carbonate blebs set in a microlite-rich melt rock fragment. Note the similar allignment of the blebs to the microlites; image width = 1 mm, sample depth = 844.82 m. c) Microlite-bearing melt rock with magnesium-silica rich blebs (dark ovoid), and orthoclase (Or) and quartz (Qtz), as well as a partially assimilated plagioclase crystal (Pl); image width = 2 mm, sample depth = 844.82 m. d) Mixed groundmass: calcite (Cc) crystals set in altered mesostasis; image width = 0.1 mm, sample depth = 835.14 m.

40 μm. Younger irregularly shaped carbonate veins, 0.5 – 2.5 mm wide, cut across the groundmass and meander around fragments. The lithic clast content is similar to that of Unit 1, comprising limestone, dolomite, shale, quartzite and quartz, granite, and schist fragments, but with significantly fewer carbonate inclusions. Rare weakly shocked feldspar fragments with kink bands and micro-shear planes have also been observed. An ~3 cm wide quartz-plagioclase-biotite-apatite-sphene schist clast occurs at 824 m depth. The plagioclase in this clast was melted; this melt phase is now mostly devitrified and altered.

2.5.3.3. Unit 3

Many microscopic characteristics of Unit 3 are similar to those of Unit 2. The most noticeable differentiating feature is the multi-colored (variegated) nature of the melt fragments in Unit 3. Under plane polarized light, the dominant colors of these fragments are patchy brown and orange. Again, lath-shaped microlites are common in melt fragments, at noticeably greater abundance than in Unit 2. Melt fragments are typically sub-rounded to sub-angular and can display prominent alteration rims (Fig. 2.6a). The groundmass is carbonate-rich and appears similar, but slightly coarser-grained (0.05 - 0.2 mm) than that of the upper units (Fig. 2.6b). A similar observation – i.e., increase of matrix grain size from the uppermost unit to the second interval - was made by Claeys et al. (2003) for the impactites from the Y6 borehole. The clast population in Unit 3 is the same as that described for Unit 2. However, specific to Unit 3, many feldspar grains have checkerboard texture (Fig. 2.6c). Other feldspar clasts show deformation features that are indistinguishable from those formed by conventional tectonic deformation processes, i.e., extensive fracturing that was most likely produced in a brittle deformation regime. Shock metamorphic effects in clasts are similar to those in clasts of the overlying units, but an increase in the number of sets of PDFs per quartz grain is apparent (see below, section on modal analysis, Table 2.3). Rare anhydrite blebs, interpreted here as clasts, are observed in melt fragments. They have radiating acicular growth textures (Fig. 2.6d), which could indicate that they are crystallized melt phases. Irregular carbonate blebs are also common in melt fragments.

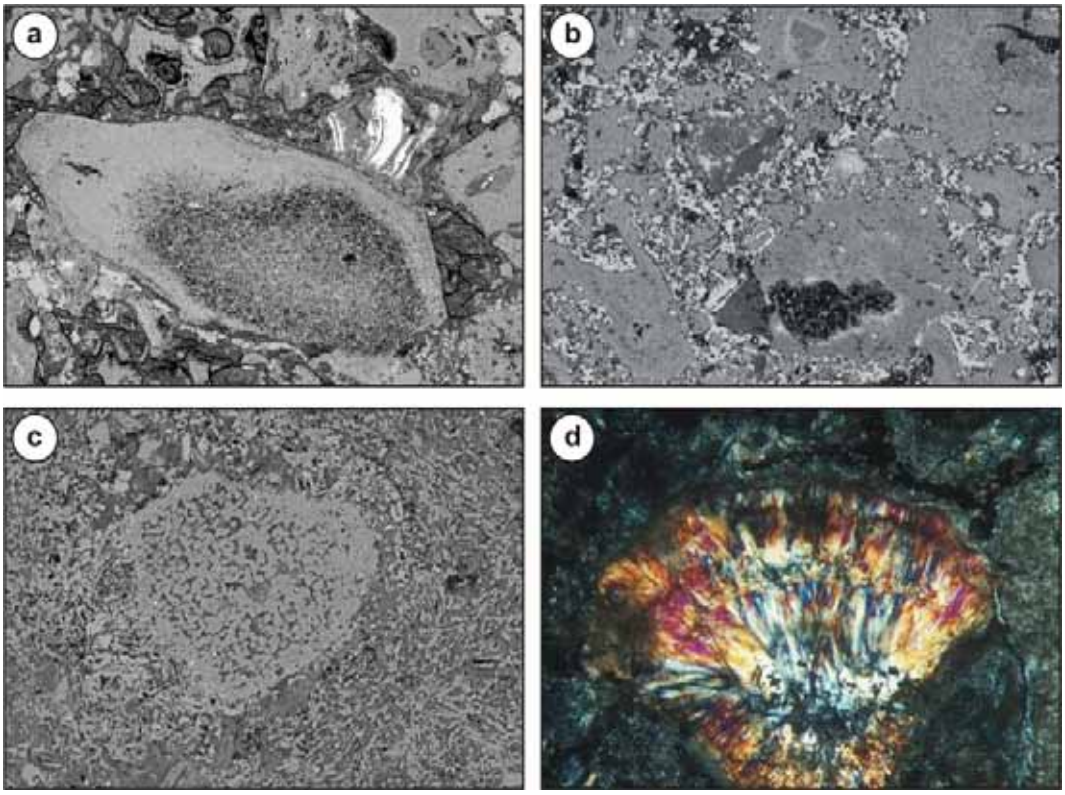

Fig. 2.6. Photomicrographs of unit 3: a) Subrounded to subangular melt particles, notice the alteration corona surrounding the large melt particle; image width = 1.0 mm, sample depth = 846.80 m. b) Melt particles suspended in carbonate rich groundmass, image width = 2mm, sample depth = 851.15m, c) Checkerboard plagioclase in microlite-rich melt rock; image width = 0.4 mm, BSE, sample depth = 851.15 m. d) Patch of radiating crystals of anhydrite in melt rock; image width = 0.5 mm, CPL, sample depth = 846.80 m.

2.5.3.4. Unit 4

Unit 4 has a very large (75 – 80 vol %) melt fragment component. These fragments usually contain abundant microlites that may be localized in specific bands. This banding is further accentuated by compositional and alteration heterogeneities (Fig. 2.7a; also Ames et al., 2003). In contrast to the overlying units that show a more diverse lithological variation in the clast content (see also point count analyses – Table 2.3), lithic and mineral clasts in Unit 4 comprise primarily quartz, feldspar, and granite. Feldspar grains show signs of thermal overprint, and commonly display checkerboard textures. Quartz grains have undergone extensive recrystallization as observed by characteristic mosaic textures. Where recrystallization or mosaicism have not affected entire crystals,

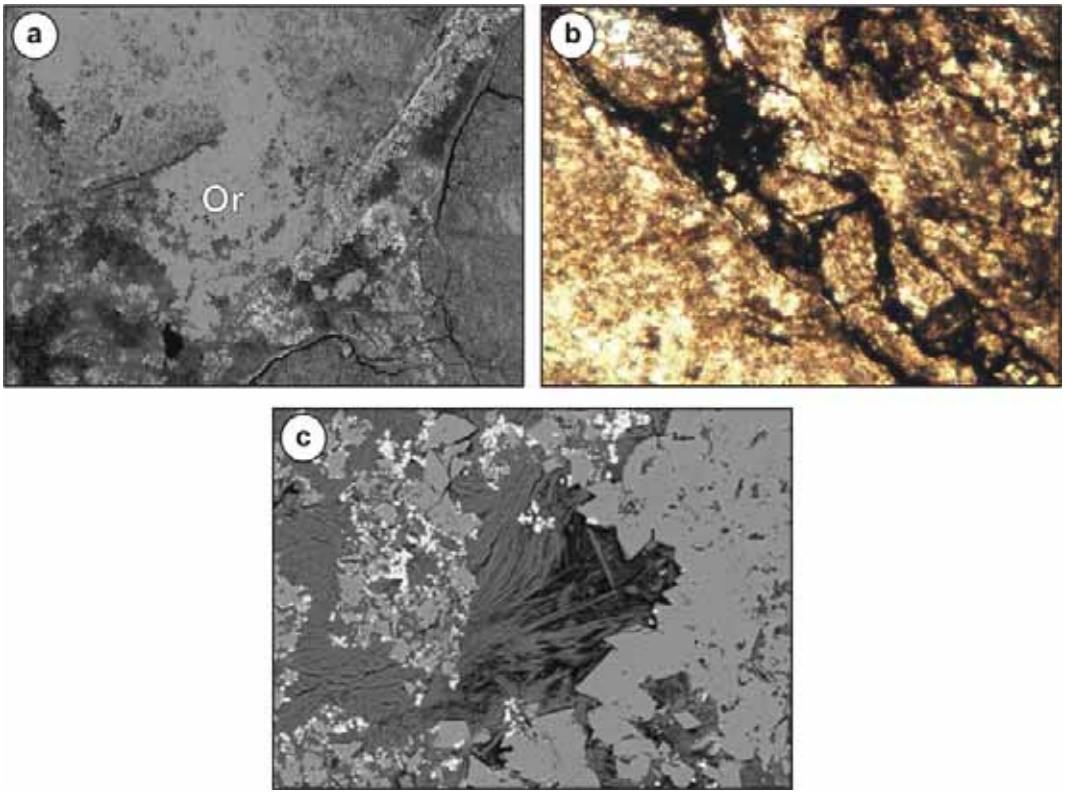

Fig. 2.7. Photomicrographs of unit 4: a) Orthoclase (Or) secondary crystallization growth; image width = 1.5 mm, BSE, sample depth = 875.79 m. b) Altered microlite-bearing melt rock with fluidal texture intertwined with dark opaque veins thought to be filled with hydrocarbons; image width = 4 mm, PPL, sample depth = 875.79 m. c) Secondary acicular phyllosilicate needles (saponite) in porous vein, image width = 0.6 mm, BSE, sample depth = 875.79 m.

the remnants sometimes display one or two sets of PDFs. This unit is pervaded by a network of anastomosing and undulating opaque veins that are hydrocarbon-rich (Fig. 2.7b). Black oil was observed oozing out of some thin section cut-offs and a distinct oily odor was detected during sample preparation. Rare green and brown blebs observed within melt fragments are thought to represent an alteration product, likely of an original mafic component. The main and most obvious alteration product of the melt particles comprises prominent, acicular crystal aggregates and veins (Fig. 2.7c). Zurcher et al., (2003) suggested that this phase could have been chlorite that is now altered to other phyllosilicate phase(s); our XRD study failed to detect any chlorite. Microprobe analyses and SEM observations indicate that the material in such veins comprises acicular clay minerals such as saponite. The presence of these phyllosilicate phases produces a

cloudy gray overprint on many light colored melt particles. In contrast to the overlying units, veins and isolated patches of carbonate are rare to totally absent.

2.5.3.5. Unit 5

Unit 5 has the highest carbonate content of all impactite units (see Table 2.3). Similar to units 2 and 3, melt particles are totally suspended in a carbonate-dominated groundmass (Fig. 2.8a). As observed in hand samples, the melt particles are mostly subangular. The microlite content in these melt fragments is variable, ranging from abundant to totally absent (see Table 2.3). This is in contrast to the overlying units where microlites in melt fragments are generally of uniform abundance on a thin section scale. As in the two immediately overlying units, melt fragments contain various lithic and monomineralic inclusions, predominantly of granitoid origin, including much quartz. In the matrix, small, subrounded to subangular, clasts of sedimentary precursors, including dolomite, limestone, calcareous siltstone, and quartz-rich siltstone, can be discerned. The groundmass also contains granitic, limestone, and siltstone clasts, as well as rare limestone clasts with foraminifera microfossils. Carbonate fragments are optically almost indistinguishable from the groundmass, but they are readily discerned by cathodoluminescence (see cathodoluminescence section below). Backscattered electron imaging reveals that the carbonate-dominated groundmass contains numerous inclusions of quartz and barite, silicate melt particles, and euhedral dolomite crystals (Fig. 2.8b). The carbonate groundmass has a variable grain size, ranging from microcrystalline to fine-grained (<0.05–2 mm). It also reveals a unique texture: subangular to subrounded microcrystalline (<0.05 mm) carbonate aggregates that appear to be enclosed by larger carbonate crystals, similar to a poikilitic texture in igneous rocks. The apparent host crystals can be in optical continuity for up to 2 mm and display interlocking grain boundaries (Fig. 2.8c). This texture could, of course, represent a sedimentary feature of target carbonates, resulting from dissolution and recementation. Vesicles in melt clasts contain euhedral barite growths, and occasionally vugs are observed that are rimmed by iron oxides.

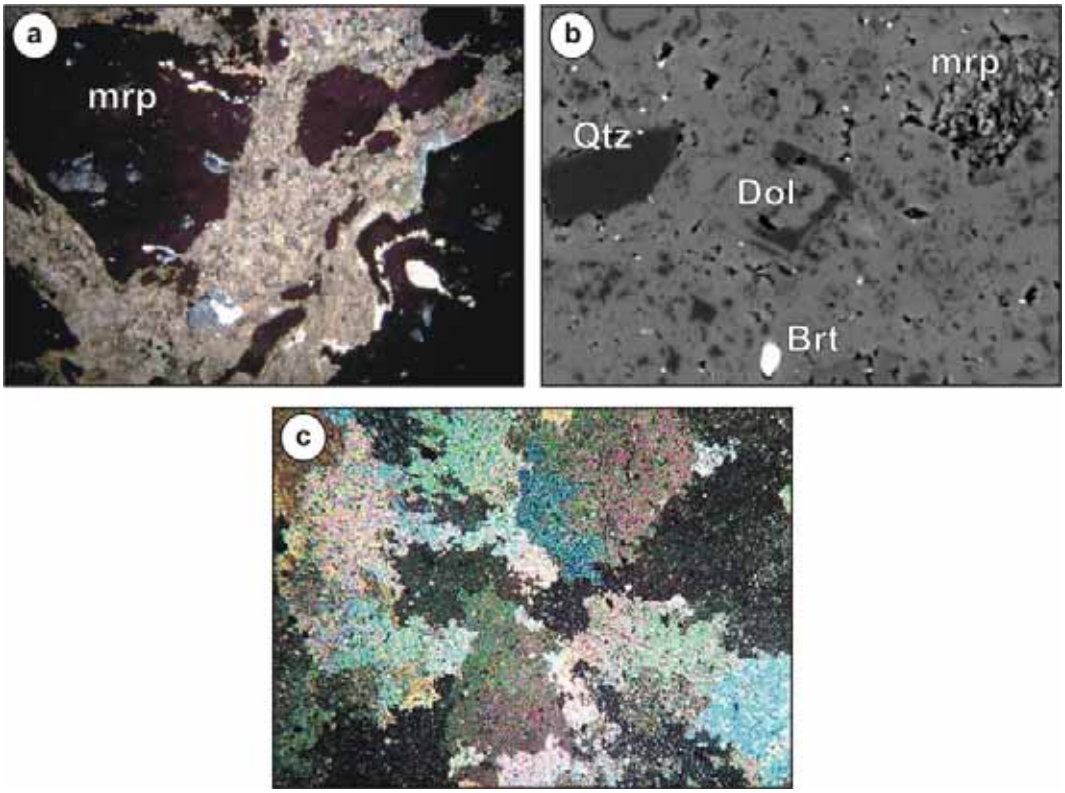

Fig. 2.8. Photomicrographs of unit 5: a) Semi-isotropic melt rock particles (mrp) set in microcrystalline carbonate groundmass; image width = 5 mm, CPL, sample depth = 892.55 m. b) Carbonate groundmass showing numerous microscopic inclusions of melt rock particles (mrp), quartz (Qtz), and barite (Brt), with a euhedral dolomite (Dol) crystal; image width = 0.19 mm, BSE, sample depth = 892.55 m. c) Carbonate groundmass with interlocking, internally fine-grained calcite patches, scale = 1 mm, CPL, sample depth = 886.79 m.

2.5.3.6. Brown melt fragments

Brown melt fragments (up to >10 cm in size) occur throughout the breccia package, but are most abundant at the base of Unit 3. They are found sporadically, though in increasing numbers with depth, throughout Unit 2, but only occur as small and rare fragments in Unit 1. As with other melt fragments found in units 2 to 4, the brown melt fragments are also fluidal-textured and have angular morphologies, and commonly contain abundant microlites that are typically flow-aligned. Schlieren occur commonly as brown patches that may appear totally opaque and that enclose small tabular microlites of pyroxene and feldspar. Rounded and ovoid carbonate blebs, 0.5 to 3 mm in size, and small

monomineralic inclusions (mostly quartz and plagioclase) are also found within this melt. The brown melt particles at the base of Unit 3 texturally resemble the green monomict melt breccia of Unit 4. Melt fragments locally fit together in a jigsaw puzzle-like arrangement.

2.5.4. Shock metamorphism

Numerous clasts in the impactites of the Yax-1 borehole display shock metamorphic features. Quartz grains with planar deformation features (PDFs) are ubiquitous. They are generally found as small grains, 1-5 mm in size, and typically have 1 to 3 sets of PDFs (Fig. 2.9a) that are indicative of shock pressures of 15 to ~30 GPa (e.g., Stöffler, 1974; Langenhorst and Deutsch, 1994; Huffman and Reimold, 1996). Point count analyses indicate that the proportion of quartz grains with multiple sets of PDFs appears to increase with depth in the impactite interval (Table 2.3). Ballenquartz (Fig. 2.9b) forms <1.5 vol% of the quartz in samples from all units. If ballenquartz is the result of recrystallization of diaplectic glass, it indicates a minimum shock pressure of about 30 GPa (Bischoff and Stöffler, 1984). Unit 4, however, appears to contain more ballenquartz and checkerboard-textured feldspar particles than the other units (c.f., Table 2.3). Checkerboard-textured particles reveal remnants of both plagioclase and alkali feldspar precursors. Bischoff and Stöffler (1984) suggested that the checkerboard texture reflects preferential melting along important crystallographic orientations in feldspars and was indicative of shock pressures in excess of 35 GPa.

A large granitic clast was observed within Unit 5 at 889.59 m depth. All plagioclase and feldspar minerals show partial isotropization, occasional PDFs, and undulating contacts indicative of melting. Quartz minerals are rare but can reveal two to three sets of PDFs and extensive mosaicism (recrystallization). Amphibole crystals have also been observed and reveal shattered and highly fractured morphologies. Apatite crystals have been observed under cathodoluminescence and appear relatively unshocked, as euhedral morphologies are still preserved. These, however, display outer concentric zonations that may have been produced by post-shock thermal metamorphism.

The most striking characteristic of the Yax-1 impactites is the high proportion of melt fragments. A few fragments still preserve evidence of the crystalline precursor material, as seen in relict polysynthetic plagioclase twins in small parts of such clasts. As discussed below (see electron microprobe analysis section), both individual mineral and mineral combination compositions are represented in this melt component. Thus, this component represents the entire shock pressure range between mineral melting (from ca. 35-40 GPa shock pressure) to bulk rock melting (from ca. 50 GPa) (Bischoff and Stöffler, 1984).

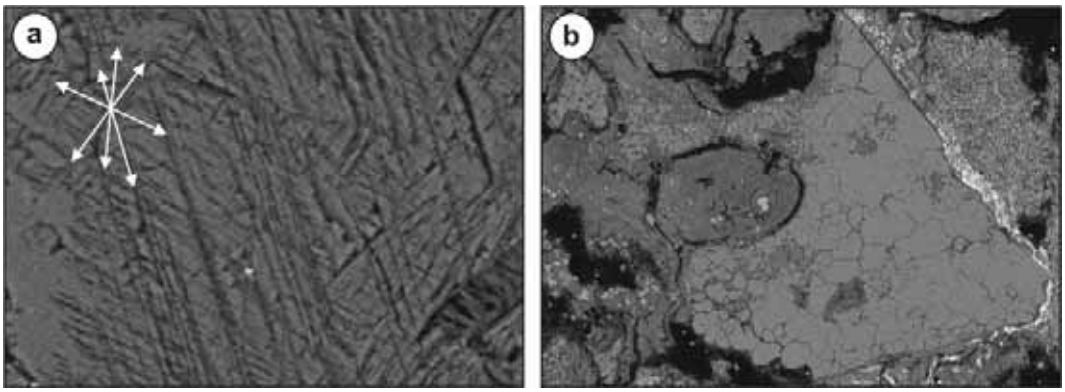

Fig. 2.9. Shock metamorphic features: a) Shocked quartz grain with 4 sets of PDFs, image width = 0.13 mm, BSE, sample depth = 916.36 m. b) Ballen quartz in microlite-bearing melt rockfragment; note narrow (bright) iron-oxide rim around the grain and the phyllosilicate rich vesicle infill to the center-left of the image; image width = 1.15 mm, BSE, sample depth = 878.09 m.

2.5.5. Modal analyses

The results of modal analysis by point counting of selected thin sections from each unit of the impactite sequence are presented in Table 2.3. The major components identified are melt particles, various lithic and mineral clast types, and secondary phases. Among the clastic component, carbonate, silicate, and shocked silicate inclusions have been distinguished. From Table 2.3 it is obvious that the various samples of a specific unit have highly variable modes. This is obviously related to the small sample sizes that are clearly unrepresentative for these highly varied lithologies.

Various types and proportions of melt particles are found throughout the impactites. Altered green melt, predominantly with intense perlitic fracturing, is the important type in Unit 1. Orange/red and uniformly devitrified melt particles are restricted to units 1 to 3. Microlite-bearing melt particles are dominant in

units 2 to 5. An increase in the proportion of brown melt particles in the suevite samples occurs with depth, but they are totally absent in Unit 5. Large microlite-bearing brown melt particles occur at 840.3 m and 843.5 m depth in Unit 2 and at 860.4 m depth in Unit 3. Unit 4 has the highest abundance of microlite-bearing melt.

Several trends are observed with respect to the clast content. Lithic carbonate inclusions are found predominantly within Unit 1 (1.9 to 5.5 vol.%), in one sample in the upper segment of Unit 2 (825.4 m depth, 6 vol.%), and in Unit 5 (0.1 to 19 vol. %). Foraminifera are only found in these samples. Anhydrite fragments are rare and are restricted to units 1 and 2. Siliceous clasts (shocked and unshocked) occur throughout the impactites; Unit 4 samples have characteristic checkerboard feldspar.

Carbonate veins and blebs in melt fragments (the blebs possible representing vesicle infilling) occur in all units besides Unit 4. The brown and green melt-rich samples in units 3 and 4 reveal extensive alteration in the form of veins and patches filled by fine-grained acicular crystals. Dark, opaque patches were found throughout the impactite sequence and may represent hydrocarbon-bearing material with oxide alteration products.

Various totals are tabulated at the bottom of Table 2.3. The total melt particle value represents the sum of melt fragment abundances. The microlite total is determined on the assumption that their mean abundance equals half that of the microlite-bearing melt rock particles (c.f., Fig. 2.5c). While the microlite values presented in Table 2.3 only constitute estimates, their relative variation from unit to unit appears meaningful. For the carbonate matrix total, the proportions of the fine- and medium-grained carbonate groundmass were added. The clastic carbonate value is a straightforward addition of all the clastic carbonate components. The total carbonate content is the sum of the matrix, clastic, and secondary carbonate components, and the clastic silicate total is the sum of all monomineralic and lithic silicate components. It is important to note that the tabulated results measured from thin sections 840.3, 843.5, and 860.4 m actually represent large particles of brown melt and are, therefore, not representative of the unit that they have been grouped with.

Overall trends can be inferred from the tabulated totals. The total melt particle content from units 1 to 3 is highly variable, ranging from 49 to 73 vol.%. The massive brown melt particles and the Unit 4 samples gave the highest melt contents, ranging from 70 to 81 vol.%, with one highly altered sample containing 62 vol.%. In contrast, Unit 5 has the most variable melt particle content with values ranging from 12 to 61 vol.%. Groundmass proportions in the suevites are also highly variable. Units 1 to 3 have a groundmass content ranging from 11 to 37 vol.%. The Unit 4 and brown melt particles samples contain minor proportions of groundmass due to their massive nature, ranging from 0 to 5 vol.%. The groundmass proportions of units 1 to 3 and 5 correlate negatively with the melt content, ranging from 22 to 73 vol.%. Because of the multi-component nature of the groundmass in units 1 to 3 (Fig. 2.5e, f), the calcite grain, siliceous matrix, and lithic mineral fragment constituents have been tabulated according to the corresponding major components. The total carbonate content fluctuates between 4 and 41 vol.% in Unit 1, is almost completely absent in Unit 4, and varies dramatically in Unit 5 between 30 and 83 vol.%. In Unit 5, most of the carbonate is found in the groundmass. The total clastic silicate and secondary silicate contents are generally high throughout the impactites. It is important to note that these modal proportions, especially with regards to the carbonate content, provide not only a basis for discussion of mixing of different melt and target rock components, but also for the discussion of geochemical trends (e.g., Tuchscherer et al., 2004).

2.5.6. Electron microprobe analysis of melt phases

Electron microprobe analyses were performed on a large number of melt fragments in 10 samples from units 2 to 5. The samples analyzed are from 827.13 m (2 sections), 835.18 m, 844.82 m, 846.01 m, 860.40 m (2 sections), 878.09 m, 890.52 m, and 892.55 m depths. As shown in Figure 2.10 and Tables 2.4 and 2.5, the analyses cover a wide range of compositions. Because altered melt particles should have high volatile contents, only the results with weight percent totals close to 100 wt% are considered to represent reasonably unaltered material. Alkali element- and silica-rich melt particles have varied concentrations of SiO2

(54-67 wt%), TiO2 (0-2.8 wt%), Al2O3 (17-27 wt%), FeOtot (0-3.55 wt%), MgO (0-2.35 wt%), CaO (0-10 wt%), Na2O (0-11 wt%), and K2O (0-16 wt%) (only those results that yielded total weight % values between 97 and 103 wt%). Small amounts of iron and magnesium are present in many of the alkali element-silica-rich melts. Mafic melt particles generally have a high volatile content and, thus, low analytical totals. The electron microprobe analyses indicate that these particles also commonly have high proportions of alkali elements - up to 5 wt% Na_2O and CaO, and up to 10 wt% K_2O, despite high FeO_{tot} (i.e., Fe as FeO) and MgO contents.

Selected major oxides were converted into molecular proportions and plotted on a modified four-component ACF-A'FK diagram (after Eskola, 1939; Fig. 2.10). Modifications to the methodology of Eskola (1939) were required because the total iron content is plotted in the F apex instead of only the ferrous iron (Fe^{2+}) content. Phosphorus was not analyzed and, thus, the C apex does not incorporate this component. The apices are defined as follows: A and A' = Al_2O_3 – (Na_2O + K_2O), C = CaO, F = FeO_{tot} + MgO + MnO, K = K_2O. Although the diagram was originally intended for metamorphic rocks, it can serve to compare the melt fragment compositions with those of possible precursor minerals. The already mentioned strong variability of compositions is obvious in Figure 2.10. Most analyses fall into two broad trends, namely mafic and alkaline. Note the heterogeneous composition of the melt particles. Heterogeneity (mixing) in the ACF diagram is observed primarily between the A and F apex. In the A'FK diagram, alkali rich melt particles plot throughout the ternary diagram. Mafic melt particles cluster towards the F apex in both diagrams of Figure 2.10a. Alkali element-rich melt particles, on the ACF diagram, also fall onto a strong trend that produces a constant ratio of molecular calcium oxide towards the A and F apex, clustering between 40 and 50 mole%. In the A'FK diagram, alkali-element-rich melts scatter throughout the ternary diagram, but plot notably away from the F apex, where a distinct grouping of mafic compositions is located. As the diagram does not account for silica, the analyses do not represent any quartz-derived melt or melt compositions with significant silica admixture. It is, however, important to note that, to date, no silica-rich melt that could be derived from a

predominantly quartz precursor or that incorporated a significant quartz component has been analyzed (the highest SiO_2 contents measured are in the order

Table 2.4. Averaged electron microprobe analyses of various melt particle types (data in weight %)

	1. Green Fsp. melt particle		2. Green Fsp. melt particle		3. Green biotitic melt particle		4. Brown Fsp. melt particle		5. Green Fsp. melt particle		6. Beige K-Fsp. melt particle	
Depth (m)	827.13		827.13		827.13		860.4		878.09		892.55	
Beam Width	10 µm		10 µm		10 µm		10 µm		10 µm		3 µm	
	Avg. (n=20)	2 σ	Avg. (n=14)	2 σ	Avg. (n=33)	2 σ	Avg. (n=25)	2 σ	Avg. (n=16)	2 σ	Avg. (n=20)	2 σ
SiO_2	60.51	0.82	56.97	3.55	50.09	0.66	58.43	0.57	51.78	4.50	59.35	5.47
TiO_2	0.73	0.26	0.77	0.54	0.48	0.06	0.28	0.17	0.71	0.87	0.52	0.66
Al_2O_3	18.70	0.76	20.10	0.69	15.24	0.38	21.23	0.57	15.85	2.73	18.00	1.29
Cr_2O_3	n.d.	n.d	n.d.	n.d	0.01	0.01	0.01	0.01	n.d.	n.d	0.08	0.26
FeO_{tot}	1.05	0.22	4.23	2.43	5.19	0.32	1.67	0.19	2.43	0.78	5.05	6.68
MnO	n.d.	n.d	0.03	0.03	0.01	0.01	n.d.	n.d	n.d.	n.d	0.03	0.05
MgO	1.23	0.43	0.33	0.11	6.52	0.40	0.57	0.24	3.76	2.02	0.19	0.22
CaO	4.36	0.82	4.32	1.28	0.75	0.27	5.43	0.61	4.39	1.58	0.88	0.13
Na_2O	1.31	0.33	2.34	1.22	0.47	0.14	3.87	0.74	1.47	0.55	1.18	0.17
K_2O	11.17	1.01	1.76	0.92	3.83	0.23	7.10	0.76	7.05	2.08	12.66	1.26
Total	99.06		95.76		82.58		98.58		87.45		97.95	

n.d. = not detected, Fsp = Feldspar

Table 2.5. Averaged electron microprobe analyses of microlite, host altered melt and checkerboard plagioclase (data in weight %)

	1. Plagioclase microlites		2. Host Melt		3. Checkerboard plagioclase	
Depth (m)	890.52		890.52		878.09	
Beam width	3 µm		3 µm		10 µm	
	Avg. (n=38)	2 σ	Avg. (n=20)	2 σ	Avg. (n=26)	2 σ
SiO_2	54.43	0.26	43.31	0.50	57.39	1.42
TiO_2	0.10	0.07	0.19	0.08	0.27	0.24
Al_2O_3	25.88	0.35	8.23	0.83	24.09	1.18
Cr_2O_3	n.d.	n.d.	0.01	0.01	n.d.	n.d.
FeO_{tot}	1.72	0.10	5.58	0.77	1.28	0.29
MnO	n.d.	n.d.	n.d.	n.d.	n.d.	n.d.
MgO	0.51	0.13	17.88	2.00	0.26	0.33
CaO	10.02	0.32	1.03	0.17	6.79	0.88
Na_2O	5.07	0.13	0.42	0.28	3.79	0.45
K_2O	0.57	0.09	1.12	0.38	5.15	1.13
Total	98.32		77.77		99.03	

n.d. = not detected

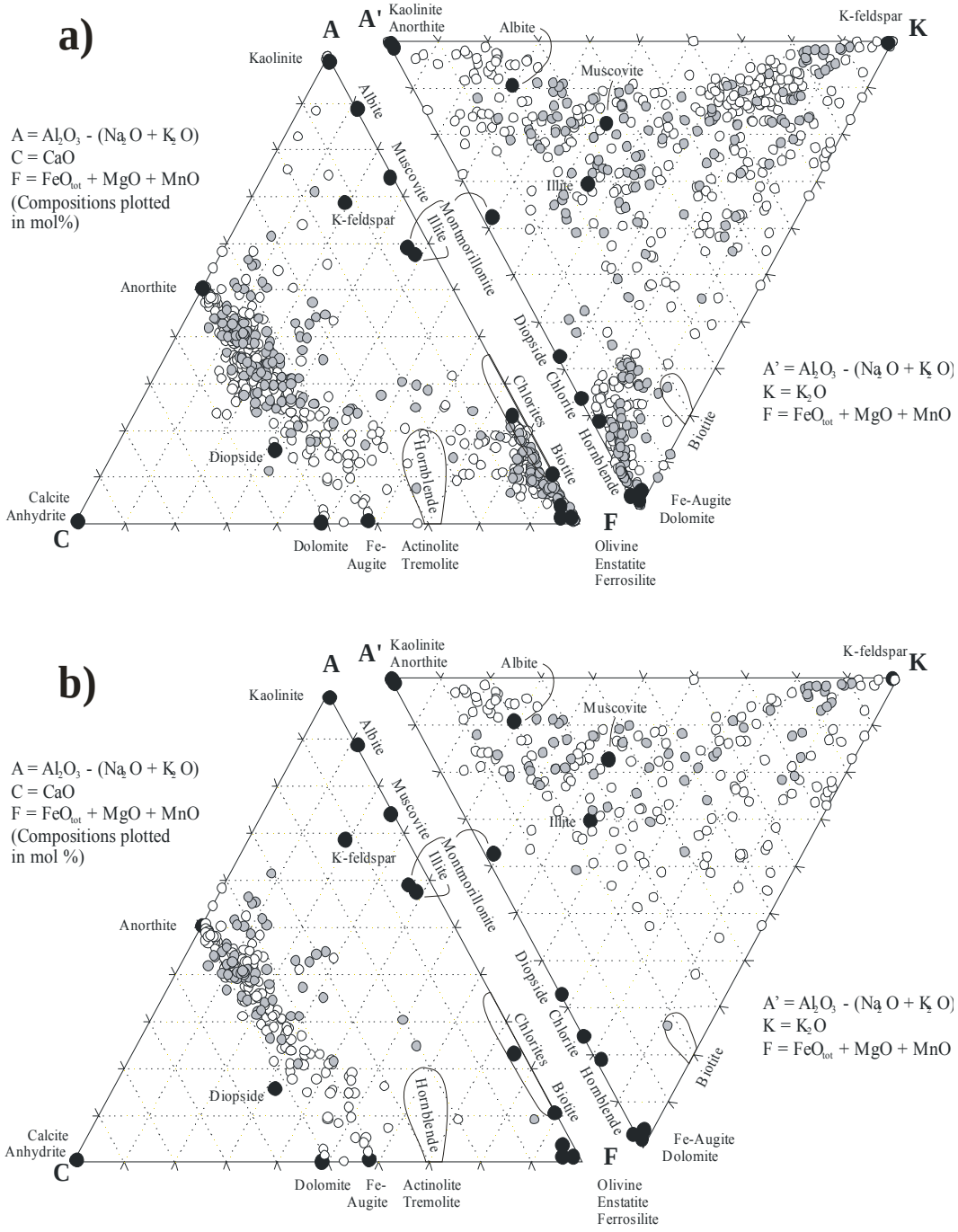

Fig. 2.10. ACF and A'FK diagrams (after Eskola 1939) with Yaxcopoil-1 melt particle compositions (electron microprobe analyses), plots are based on molecular proportions of the weight %: a) Plot showing all melt particle analyses (n = 555): gray circles represent focused beam analyses with 3 µm beam diameter, white circles represent defocussed beam analyses at 10 µm beam diameter. b) Plot showing only melt particle analyses with weight oxide totals between 103 and 97 wt% (n = 202). Note that none of the mafic analyses illustrated in Fig. 2.10a is retained, as all of these have totals < 97 wt% - indicative of extensive secondary alteration.

of 60-63 wt%).

The distribution of the melt analyses, against the rock types known to have been sampled in the clast contents of impactites, i.e., carbonates, granitoids and amphibolites (Kettrup et al., 2003), as well as some sedimentary and metamorphic rocks such as siltstones and schists (this work) - indicates precursor minerals included primarily feldspars, amphibole (a likely Ca contributor), biotite, muscovite, and presumably quartz. Our petrographic analysis did reveal the presence of traces of clinopyroxene in the clast content, but at minute proportions. The compositional boundary observed above 50 mole% C, in the ACF diagram, suggests no mixing occurred between alkali element-rich melt and extensive amounts of calcium carbonate or sulfate (in agreement with the petrographic observation of possible exsolution of carbonate melt blebs from silicate dominated melt).

Considering the petrographic finding that melts generally are strongly altered and/or devitrified and as many totals of the EMP analyses fall far short of 100 wt%, it must be established whether the trends identified in Figure 2.10a are significant or are the result of secondary overprint. As two data sets were collected, with electron beam widths of 10 and 3 μm, respectively, it had to be investigated whether beam size effects play a role. It became obvious, however, that this is not the case. The two different data suites display similar trends. When plotting only the analyses that have totals between 97 and 103 wt%, it can be shown that all mafic melts are eliminated from the ACF and A'FK diagrams (Fig. 2.10b). Obviously all mafic melts are highly altered (see also Table 2.4). This is expected as mafic minerals (biotite, amphibole, pyroxene), or as in this case, melts, are the first to undergo alteration and weathering when exposed to extensive hydrothermal activity (e.g., Freyssinet, 2000). Mafic minerals are also the first to react with meteoric waters. However, element mobility during weathering favors the removal of alkali elements, silica, and Mg^{2+} ions, whereas Al and Fe^{3+} typically remain behind as relatively inert cations (e.g., Righi and Meunier, 1995).

When all melt compositions (in weight %) are plotted onto an AFM diagram (Fig. 2.11a), these data also reveal the characteristic divide between

mafic and alkali-rich compositions. Two distinct trends are observed that suggest A plus F+M mixing and M plus A+F mixing (i.e., A = $Na_2O + K_2O$, F = FeO_{tot}, M = MgO). When the mafic melt compositions are plotted on a (Na + Ca) – Fe – Mg ternary diagram (Fig. 2.11b), no extensive mixing between the alkaline and the mafic components is obvious. When the mafic melt compositions are plotted on a K – Fe – Mg ternary (Fig. 2.11c), a distinct linear compositional trend is observed that corresponds to K-metasomatism, with K substituting for a constant proportion of Fe^{2+}.

The composition (in mol %) of feldspathic melts is presented on an An-Ab-Or plot (Fig. 2.12a). Several feldspar microlites (Fig. 2.12b, in a sample at 890.52 m) were analyzed in relatively less altered melt fragments. In addition, two checkerboard plagioclase crystals (Fig. 2.12c) were analyzed in a sample from 878.09 m depth. The averaged microlite and checkerboard compositions are given in Table 2.5 (analyses 1 and 3, respectively). A hydrated mafic melt (analysis 2 of Table 2.5) hosts the microlites analyzed. The feldspathic melts have compositions of $An_{<50}$ (Fig. 2.12a), but exhibit a rough trend towards the Or apex. This could be indicative of either the strong K-metasomatism, also shown by the mafic melts (Fig. 2.11c), or variable K-feldspar and plagioclase mineral melt mixing. A few analyses plot at ~An_{20}; they were obtained along a traverse of 10 melt analyses in a sample from 827 m depth. The albitic compositions indicate the composition of the pre-cursor plagioclase mineral. Conversely, it can be deduced that mineral melt mixing was not pervasive.

Individual microlite analyses from the sample from 890 m depth (Unit 5) are shown in the ternary feldspar diagram of Figure 2.12b. All results fall into a tight group around An_{55}. The average composition of microlites analyzed in this study is $An_{51}Ab_{46}Or_3$ and falls within the range of feldspar microlite compositions for Unit 5 samples reported by Kring et al. (2003a,b). The microlites analyzed do not appear to be extensively altered as indicated by the good totals and the rather low mole% Or content (low K content, precluding extensive K-metasomatism).

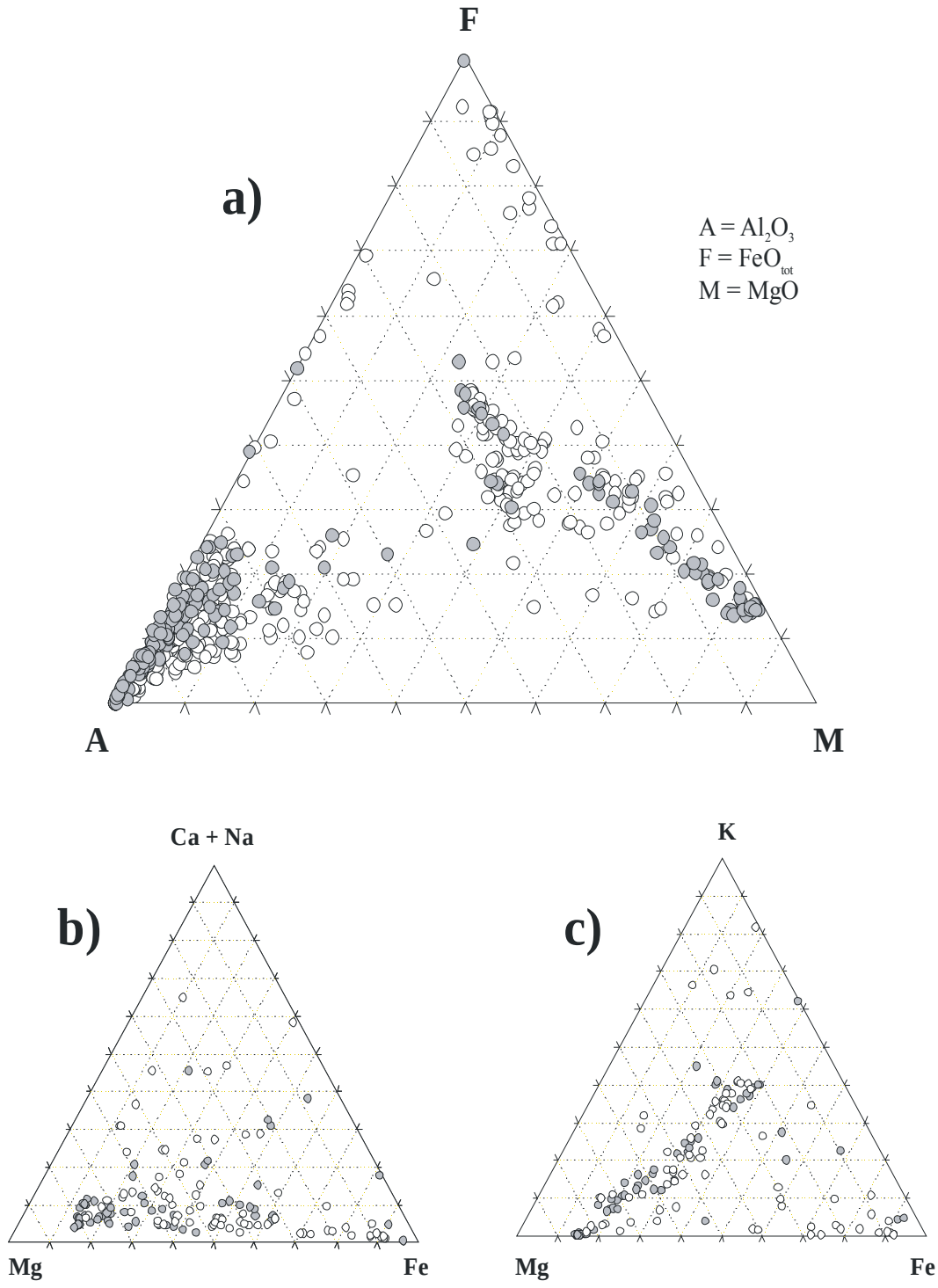

Fig. 2.11. a) AFM diagram of all the Yaxcopoil-1 melt particle analyses (n = 555): Gray circles represent focused beam analyses with 3 µm beam diameter, white circles represent defocussed beam analyses witht 10 µm beam diameter. Plot based on weight oxide results. See text for discussion. b) Ternary diagram showing the mafic melt particle analyses (n = 139) according to their Fe – Mg – Ca + Na contents. Plot based on calculated weight % abundances of the elements. Notice the lack of a strong Ca + Na overprint. c) Ternary diagram showing the mafic melt particle analyses (n = 139) according to their Fe – Mg – K contents. Plot based on calculated cationic abundances. Note the distinct trend towards elevated K contents.

Electron microprobe analyses of two checkerboard plagioclase crystals yielded unusual "feldspar" compositions. When the data are plotted on an An-Ab-Or diagram, it is observed that the tiny melt pockets produced from a primary plagioclase crystal of $An_{52}Ab_{48}$ composition are characterized by a significant potassium content (Fig. 2.12c) but with the original An:Ab ratio preserved. The diameter of the electron beam used for these analyses was about 10 μm, and, thus, it is not impossible that some of these results represent mixtures of the remnant crystalline material plus interstitial melt (compare Fig. 2.6c), but this does not affect the interpretation of these data. These results are in agreement with observations on checkerboard plagioclase grains from the Lappajärvi impact crater where an increase in K_2O and SiO_2 and a decrease in Na_2O were discerned (Bischoff and Stöffler, 1984). These authors determined - based on theoretical, compositional, and textural observations - that checkerboard plagioclase grains formed above the solidus temperature of the impact melt and could reach thermal equilibrium in the span of one to two hours.

It is interesting to note that probe analyses on shocked feldspar clasts from the Y6, Y2, and Y5A drill cores, as well as feldspar grains from the Raton basin of New Mexico, do not show anorthite contents exceeding An_{58} (Izett, 1990; Sharpton et al., 1996). The An concentrations reported here also fall into this plagioclase compositional range.

2.5.6.1. Electron microprobe traverses across melt fragments

A dozen melt particles were analyzed by EMPA along traverses across the entire particles, in samples at various depths (805.34, 810.84, 827.13, 835.18, 843.46, 844.82, 846.01, 846.08 851.15, 860.04, 860.40, 886.79, 878.09, 890.52, 892.55). Melt fragments selected all are characterized by differently colored schlieren. All traverses show that these fragments have highly heterogeneous compositions, with quite variable totals (65 to 103 wt%) measured from schlieren to schlieren. In general, low totals correspond to high iron and magnesium contents, which, in turn, are generally – but not always – correlated. Several fragments yielded good totals throughout; they had variable alkali element and calcium contents. Other fragments revealed that a substantial amount of iron and

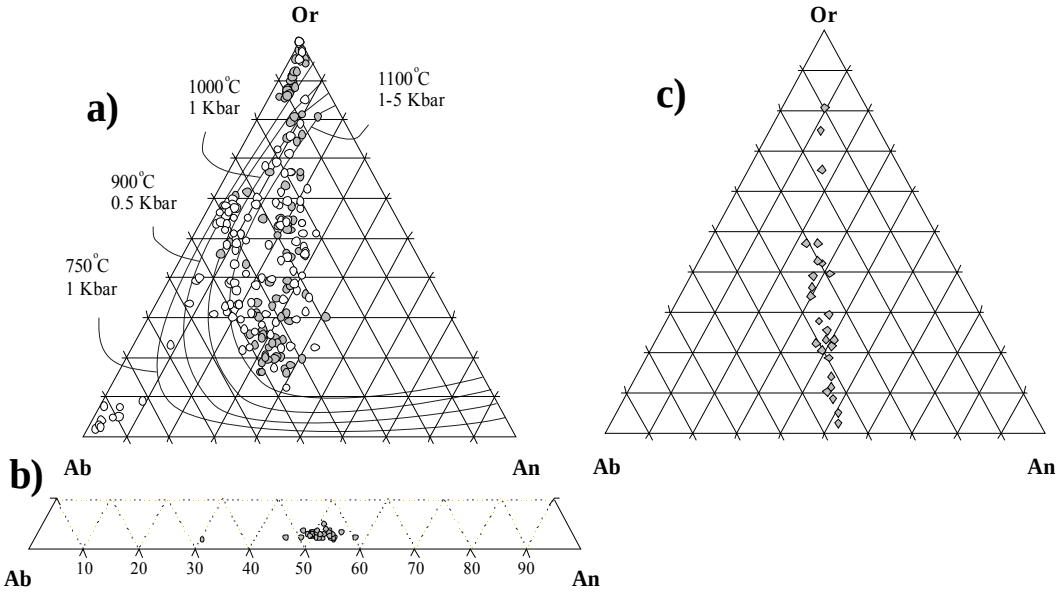

Fig. 2.12. An – Ab – Or diagram illustrating the composition of various feldspathic melt particles, microlites, and checkerboard grain. All plots based on calculated An – Ab – Or molecular proportions. a) An – Ab – Or diagram of all alkali rich melt particles with good totals between 103 and 97 wt% (n = 202). Note that the analyses all plot on the left of the ternary with compositions restricted to $An_{<50}Ab_{0-100}Or_{0-100}$; isograds after Fuhrman and Lindsley (1988). b) Portion of the An – Ab – Or diagram with plagioclase microlite compositions that cluster between An_{50} and An_{56} (labradorite). c) An – Ab – Or diagram with checkerboard plagioclase compositions. Note the strong trend towards the Or corner, with constant An/Ab ratio that would correpsond to a primary plagioclase composition of ~An_{52}.

magnesium was mixed with the feldspathic component. Several mafic melt fragments were observed to contain unusual K abundances (3 to 5 wt%).

It was determined that the distinctive zonation in the melt particle shown in Figure 2.6a is characterized by variable alkali element and CaO concentrations; both zones yielded good wt% totals (~98 wt%). The results for this grain suggest remobilization of alkali elements and Ca towards the periphery of the particle. On one occasion, a uniform and clearly pristine composition was observed for a particle that appears to have a characteristic orthoclase composition (K_2O = 14 wt%) with low Na_2O (~1 wt%) and CaO (~0.8 wt%) contents.

Overall, these traverse data emphasize that alteration – especially of mafic schlieren – has had a major effect on the melt fragments in these impact breccias. K-metasomatism is variable but widespread. The melts analyzed have highly variable compositions, with melt formation from individual minerals (K-feldspar, biotite) or mineral combinations (e.g., feldspar plus a mafic mineral). The

particles analyzed do not represent homogenized melt, but have, from spot to spot or schlieren to schlieren different compositions, on a ~0.01 mm scale.

2.5.6.2. Electron microprobe traverses across carbonate groundmass

Two traverses were analyzed across carbonate groundmass in unit 2 and 5 samples. The Unit 2 groundmass represents a mixed carbonate/silicate groundmass as shown in Figure 2.5e. The SiO_2 and CaO contents are highly variable and are negatively correlated (i.e., the higher the silica, the lower the calcium oxide, and vice-versa). Regions of high CaO produce the lowest oxide totals, as expected for carbonate analyses. Relatively high concentrations of Na_2O and K_2O are observed in high-SiO_2 areas, indicating feldspathic component. Ca and Mg are typically not correlated, as one would expect if a dolomite component were present. The Unit 5 groundmass reveals a generally higher CaO content than that in Unit 2 groundmass. Discrete SiO_2 peaks, correlated with Al_2O_3, Na_2O, K_2O, and relatively high oxide totals are observed locally and represent small melt fragments or lithic clasts (as imaged in Fig. 2.8b). Some of the magnesium peaks that do not correlate with SiO_2 or Al_2O_3 could represent isolated dolomite crystals (compare Fig. 2.8d).

2.5.7. X-ray diffraction data

Bulk powders of 22 impactite samples were subjected to X-ray diffractometry. These samples included one from the upper reworked limestone interval (791.71m), nine samples from Unit 1 (800.35 m, 805.34 m, 809.00 m, 809.70 m, 811.55 m, 815.80 m, 816.62 m, 821.39 m), four from Unit 2 (825.43 m, 835.14 m, 835.18 m, 840.30 m, 843.46 m), two from Unit 3 (851.15 m, 860.40 m), two from Unit 4 (875.79 m, 882.45 m), and four from Unit 5 (886.79 m, 888.92 m – two subsamples, 890.52 m). In general, highly variable proportions of calcite and dolomite are indicated, with calcite usually dominant. An additional minor carbonate phase identified in the upper reworked limestone is ankerite. Besides calcite and dolomite, Unit 1 samples reveal the presence of a phyllosilicate phase, likely an illite/montmorillonite/sepiolite at 7.07^o 2θ, obviously representing the product of alkali and mafic melt alteration. Other

minor phases identified are quartz, plagioclase, orthoclase, mica group minerals (biotite and muscovite), and traces of ilmenite. Unit 2 contains the same minerals but also minor pyrite. Samples from Unit 3 contain the same minerals as the overlying units; however, relatively more plagioclase feldspar is present than in units 1 and 2. Unit 4 samples displayed distinct spectra with the main quartz and feldspar peaks having very similar intensities and being dominant over those for calcite and dolomite. This is in agreement with the modal analyses of Unit 4 samples that indicate relatively small (<5.1 vol%) carbonate contents (compare Table 2.3). The phyllosilicate peaks (illite/smectite and sepiolite) are also very strong for these samples, consistent with the generally strong devitrification or alteration of melt particles. Unit 5 samples yielded variable XRD spectra, as the melt and carbonate contents are clearly variable (see Table 2.3). However, the calcite peak intensity always dominates over the intensities of main peaks for all other phases. Dolomite and feldspar peaks are also quite strong, whereas the phyllosilicate peaks are subdued.

Chlorite peaks were not detected by our XRD analysis, in keeping with our petrographic observations, as well as in agreement with Zurcher et al. (2003), who suggested that all chlorite possibly formed during alteration of melt was transformed to other phyllosilicate phases (e.g., saponite).

2.5.8. Cathodoluminescence observations

Several samples were studied with cathodoluminescence (CL) microscopy. This included one sample from the sedimentary rocks above the impactites (from 791.71 m depth), three from Unit 1 (809.7 m, 818.33 m, 821.39 m), three from Unit 2 (824.03 m, 840.30 m, 843.46 m), one from Unit 3 (851.15 m), three from Unit 4 (875.79 m, 879.03 m, 882.45 m), and two from Unit 5 (886.79 m, 888.09 m).

The upper limestone sample revealed typical orange luminescence, a characteristic of calcite (e.g., Marshall, 1988; Pagel et al., 2002). The calcite crystals contain disseminated, small (~0.1 mm), euhedral, non-luminescent rhombohedra zones (Fig. 2.13a). The calcite rims reveal variable intensities of

orange luminescence, suggesting episodic overgrowths. Foraminifera fossils typically <0.2 mm in diameter are present locally (Fig. 2.13a).

Several distinctive features were observed in the Unit 1 samples. As in the upper sedimentary rock, foraminifera fossils are present, but are much scarcer (Fig. 2.4d). They have rather variable sizes, ranging from 1 to 0.1 mm. Cathodoluminescence was useful for identification of the foraminifera, as a strong alteration overprint made them almost invisible in optical microscopy. Secondary calcite veins are also more visible by this method, as they are characterized by a stronger orange luminosity with respect to the host material. This higher luminescence intensity is attributed to the paucity of "quenching" cations, such as iron, that typically subdues the luminescence of calcite (Meldin, 1963). Melt particles are typically non-luminescent, however rare green and faint blue luminescent flow textures and minerals are sometimes observed (Fig. 2.13b). As observed in optical microscopy, cathodoluminescence also shows that some melt particles contain carbonate blebs that may be preferentially aligned, indicative of flow. Units 2 and 3 reveal similar cathodoluminescence features. Bright orange luminescent secondary calcite veins are observed cutting through a heterogeneous groundmass that comprises a mixture of carbonate, siliceous material, and silicate clasts (Fig. 2.13c). The clasts do not show luminescence, whereas the carbonate in the groundmass commonly shows light orange luminescence. As in Unit 1, secondary veins are of stronger orange luminosity. Melt fragments in these units contain well-preserved green luminescent crystals (Fig. 2.13c). This CL color is characteristic of apatite, with Mn^{2+} as the principle activator that produces a broad emission band between 562 nm and 580 nm. This has been shown to be diagnostic of apatite crystals of various igneous, hydrothermal, and metamorphic origins, as well as synthetic fluorapatite (Mariano, 1988). Energy-dispersive X-ray analysis confirmed that these green luminescent crystals are apatite. This mineral is found in abundance within a quartz-plagioclase mica-schist inclusion sampled at 824 m and in small amounts in a large granitic inclusion from 888 m depth. Groundmass is sometimes seen to protrude into the fluidal-textured melt fragments within these samples. This could be a primary fluidal feature or the result of local thinning of a particle and grinding into groundmass during thin

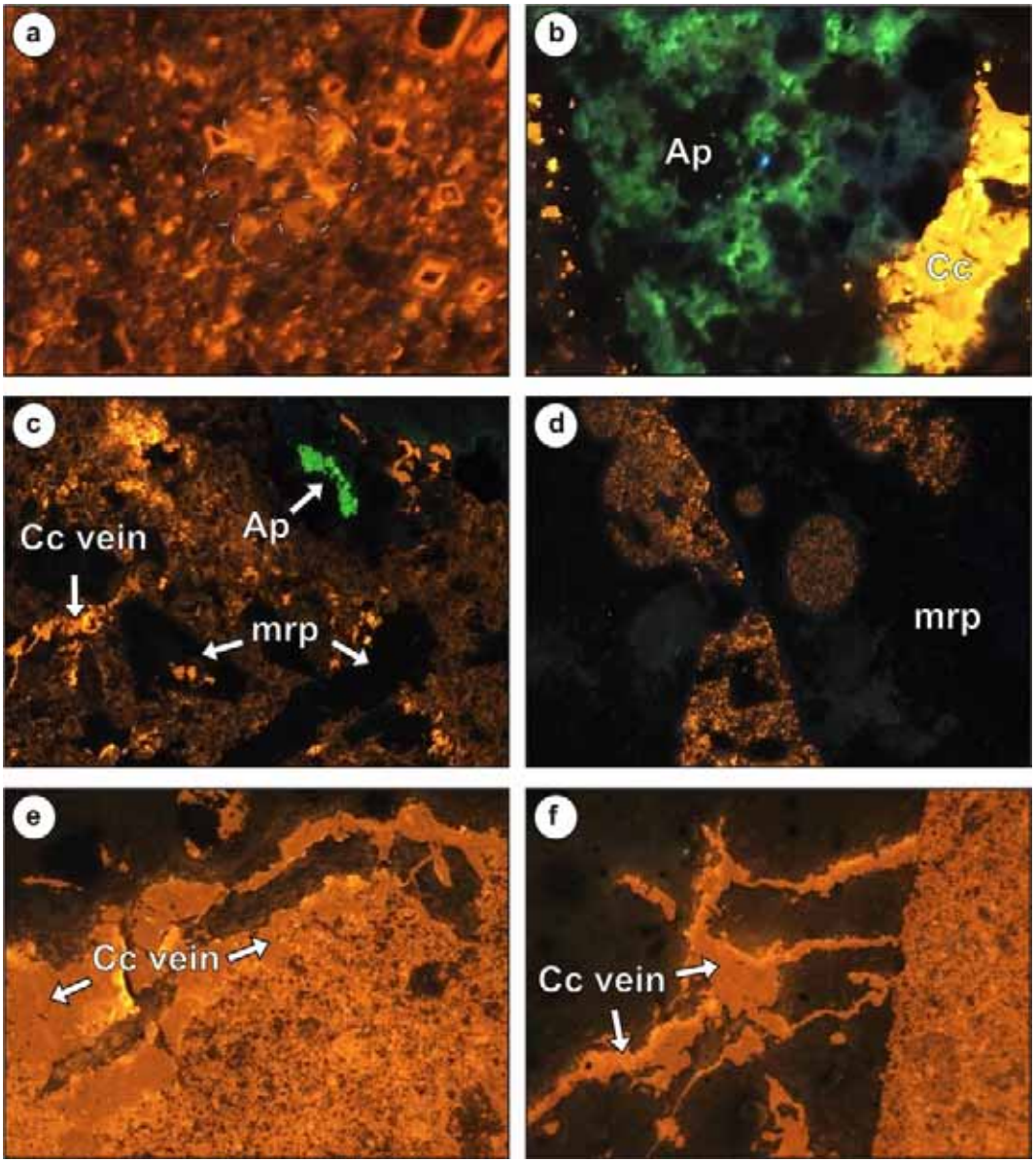

Fig. 2.13. Various cathodoluminescence photomicrographs of Yaxcopil-1 impactites: a) Foraminifera bearing Tertiary limestone with oscillatory zoned calcite/dolomite rhombohedra image width = 0.5 mm, sample depth = 791.71 m. b) Green luminescent (melted apatite, Ap), and patchy texture within melt rock fragment; image width = 4 mm, sample depth = 821.39 m. c) Mixed carbonate-silica groundmass with angular melt rock particles (mrp, no luminescence) showing well preserved, fractured, green luminescent apatite (Ap) crystal; note the high luminosity of secondary carbonate veining; image width = 4 mm, sample depth = 822.90 m. d) Vesicle in melt rock fragment, filled with mixed carbonate/altered glass groundmass material; image width = 2 mm, sample depth = 825.43 m. e) Melt rock fragment with lining of high luminescent secondary calcite (Cc) vein (arrow); image width = 4 mm, depth = 886.79 m; f) Melt rock fragment cross-cut by carbonate vein. Note the vein does not cross-cut the groundmass indicating it is younger, image width = 4 mm, sample depth = 886.79 m.

section preparation. Groundmass is also found as fills within round or ovoid blebs in melt fragments (Fig. 2.13d). Irregular calcite blebs, usually with bright orange luminescence, are commonly found dispersed throughout melt fragments.

Because Unit 4 is practically devoid of calcite, cathodoluminescence features for samples from this unit are subdued. Rare disseminated calcite crystals were only observed along a 6 mm wide shear zone, suggesting migration of carbonate-bearing fluids along such deformation zones. The dark, opaque, possibly hydrocarbon-bearing veins that are commonly found within this unit lack any luminescence.

Various cathodoluminescence features and textures were observed within Unit 5 that has the highest carbonate content of all impactite units. Sub-angular to sub-rounded melt fragments are typically found suspended in the carbonate groundmass. The groundmass contains numerous non-luminescent, euhedral dolomite crystals (Fig. 2.13e,f). SEM-EDS analysis confirmed that the groundmass is rich in dolomite (Fig. 2.8d). Fine-grained carbonate veins with relatively high luminescence compared to the nearby groundmass are found lining melt fragments (Fig. 2.13e). Similar veins were noted in units 1 to 3. Pure calcite veins also cut silicate melt particles (Fig. 2.13f) but do not seem to continue into the surrounding groundmass.

2.6. Discussion

The petrographic observations on the 100 m thick impactite interval intersected in the Yaxcopoil-1 borehole are discussed with respect to the following key issues: 1) stratigraphic relationship with other boreholes, 2) the variation of petrographic features found throughout the impactite sequence, 3) the chemical composition of melt fragments, 4) the nature of the groundmass of the five units, 5) implications for the emplacement of the various impactite units, and 6) classification of the impactites.

2.6.1. Stratigraphic relationship with other boreholes

When compared to previous drilling, the 100 m thick impactite horizon of Yax-1 is much thinner than the intervals of impact breccia of 470 to 930 m thickness in the C1, S1, and Y6 drill cores (Ward et al., 1995; Sharpton et al., 1996; Stöffler et al., 2003b). Unfortunately no seismic profiles were obtained for the Yax-1 site before drilling. Cretaceous rocks intersected by the boreholes

towards the center of the impact crater, but still near Yax-1, occur at a much lower stratigraphic level (Fig. 2.2). The Y6 borehole was terminated in evaporitic rocks, i.e., dolomite and anhydrite, at 1630 m depth, whereas the C1 and S1 boreholes ended in melt rocks and breccias at 1581m and ~1530m, respectively (Ward et al., 1995; Sharpton et al., 1996; Stöffler et al., 2003b). Farther away from the center of the impact crater, the T1 borehole intersected Cretaceous rocks also at shallower depth, i.e., ~900 m depth. The relative position of the Cretaceous rocks in the Yax-1 borehole is thought to be the result of slumping around the crater periphery, an area that is characterized by a prominent gravity low (Ebbing et al., 2001). With respect to the correlation of impactites from other boreholes, i.e., the Y-6 borehole, we correlate our units 1 to 3 with the units 1 to 3 of Claeys et al. (2003). However, units 4 and 5 from the Yax-1 borehole do not seem to have equivalent subunits according to the observations of Claeys et al. (2003). A lower melt layer is suggested to occur below Unit 3 in the Y6 borehole.

2.6.2. Features common to the entire impactites sequence

Before discussing the intrinsic details that characterize each unit, it is important to keep in mind that some features have been found that are typical for the entire impactite sequence. Units 2, 3, and 5 all contain melt fragments suspended in a groundmass, whereas Unit 1 is composed of mostly self-supported melt rock and lithic fragments. Unit 4 has undergone *in situ* brecciation. Melt fragments are typically found as fluidal-textured, irregularly formed blebs or angular, shard-like particles. Lithic clasts are found throughout the entire sequence at relatively lower proportions than those of melt fragments (Table 2.3).

Some microscopic features are ubiquitous. Irregularly shaped carbonate blebs in silicate melt fragments can be alternatively interpreted as the result of immiscibility of a carbonate melt in silicate melt or as secondary carbonate-filled vesicles. They are common in melt particles of all units. Shock metamorphic features in lithic or mineral fragments, such as ballenquartz and quartz grains with PDFs, are also ubiquitous. Our statistics of shock-metamorphosed clasts do not indicate a substantial change of shocked mineral clast content or average shock degree with core depth/unit; however, a greater average number of PDFs in quartz

grains is observed towards Unit 5 (c.f., Table 2.3). Unit 4 has by far more checkerboard feldspar than all other units. For such incipient melting to occur, shock pressures must have been in excess of 45 GPa, with post-shock temperatures between 900 and 1300°C (Stöffler, 1974; Bischoff and Stöffler, 1984).

Clast compositions suggest that the lithic and mineral clast content of these impactites involved material from the upper carbonate platform and the underlying Pan-African basement. Lithic clasts are observed throughout the impactites. Inclusions that originate from the crystalline basement comprise primarily granitoid-derived fragments, schist and metapelite, quartzite, and rare amphibolite. Lithic inclusions that originate from the pre-impact sedimentary column comprise limestone, dolostone, fossiliferous limestone, calcareous sandstones, and quartzites. Anhydrite, which has been reported in abundance within the Cretaceous rocks of the Chicxulub structure (Ward et al., 1995, Dressler et al., 2003a), and as clasts in other impactite drill core intersections (Urrutia-Fucugauchi et al., 1996, Sharpton et al., 1999), only occurs in very small quantities (<1.5 vol%) throughout the Yax-1 sequence. The lithic and mineral clasts observed range from unshocked and weakly shocked material likely derived from the edge of the transient cavity to stronger shocked and, particularly, much melted material from closer to the point of impact. Unit 4 appears to be a brecciated impact melt rock that is interpreted to originate from melting of primarily crystalline basement. Our point count analysis reveals that only secondary carbonate occurs within this interval. Unit 4 comprises a massive melt rock unit and as such must have originated from a different region of the impact crater than Units 1 to 3. Units 1 and 5 contain foraminifera fossils that could have originated from outside the transient cavity. They are essentially undeformed.

Secondary carbonate veins are observed throughout the impactite interval and indicate pervasive hydrothermal overprint on the entire breccia sequence. However, there are distinctly more fractures with authigenic carbonate fill in units 2 and 3, between 823 and 861 m depth, than in the other units.

2.6.2.1. Characteristics of the overlying reworked interval

The upper reworked and suevitic material-bearing sedimentary interval between 793 and 795 m depth contains several lenses (0.5 – 1.5 cm thick) of green, altered, suevitic material (similar to the underlying upper suevite) that is intercalated with grayish-white carbonate-rich rock. Distinct cross-lamination/bedding planes and rare drop stones of suevitic material are found within these sedimentary rocks. The cross-beds all have the same attitude (orientation) and, thus, indicate that the current followed a similar direction throughout deposition of this interval. The cross-beds typically appear as straight-crested small-scale ripples and have a relatively high angle of repose that indicates good sedimentation rates with respect to ripple migration (Allan, 1972). Because suevitic material is incorporated into the ripples, we suggest that the underlying impactite deposit was unconsolidated and, thus, easily reworked at the time of deposition of these sediments. However, the presence of rare suevite drop stones ("pebbles") indicates that some of the suevite was sufficiently lithified to be transported by current without disaggregation. These observations are more consistent with the suggestions of a tsunami/high-energy current (Goto et al., 2003) origin for this interval than with normal sedimentation (Keller et al., 2003b; Stinnesbeck et al., 2003). Apparently, the reworking of suevitic material took place immediately after cratering, i.e., after emplacement of the crater fill.

2.6.2.2. Unit 1

Several petrographic features are distinct to Unit 1. Most strikingly, the average grain size of the fragmental lithic or melt material in this unit is much smaller (Fig. 2.2a) than that for the impactite units below. The primarily clast-supported character of this interval is also characteristic. The rocks, to a depth of 808 m, are very friable and poorly consolidated. Melt fragments are subrounded, without complex fluidal or angular morphologies that are typically observed in the lower units. A poor, but distinct, grading occurs from the top to the bottom of this unit. Overall, these features indicate progressive sorting with stratigraphic height, as also suggested by Dressler et al. (2003a, b), Kring et al. (2003a), and Stöffler et al. (2003a). Laminations were also reported by Dressler et al. (2003b).

The clast content is characterized by a distinctly greater proportion of microfossils and sedimentary clasts than observed in the lower units – with exception of lowermost Unit 5 (Table 2.3). The superb preservation of these fossils (Fig. 2.3c), along with the greater proportion of carbonate clasts, could indicate detrital input from outside of the impact crater. The ratios of limestone to other clast proportions for samples of this unit is similar to that for the upper unit of the Y6 borehole (5 to 1), as observed by Claeys et al. (2003). Melt particles do not have microlites but strong perlitic fracturing (Fig. 2.3b), which can be interpreted as the result of relatively faster cooling of late fall-out into relatively cooler ocean water (perlitic fracturing indicates that the once glasses interacted with water - Ross and Smith, 1955). Because the entire upper package between 795 and 823 m has similar features, including subrounded to subangular clast morphologies, presence of carbonate clasts, plus foraminifera microfossils, and a clast-supported character, the two upper units as defined by Dressler et al. (2003a) are here grouped together into Unit 1. We suggest that these common characteristics far outweigh the differences reported by Dressler et al. (2003a) for the intervals 795–808 m and 808–823 m, specifically the unconsolidated and fine-grained nature of the uppermost (795–808 m) segment in contrast to a more coherent nature of the lower interval.

We propose that this upper interval has been reworked by high-energy sedimentary processes in the form of a turbulent back-surge of seawater into the impact basin. The influx of seawater would have been responsible for transport and deposition of unshocked detritus into the impactite material, as observed by foraminifera microfossils and the unusually high carbonate clast content. This interpretation relates to the turbulent reworking invoked for several proximal Chicxulub ejecta sites around the Caribbean Sea (Bourgeois et al., 1988; Smit et al., 1992; Smit et al., 1996; Smit, 1999; Takayama et al., 2000; Tada et al., 2002; Goto et al., 2002; Claeys et al., 2003). The resurge process has been recognized at several impact craters formed in the shallow marine realm, i.e., the Lockne (Ormö and Miyamoto, 2002), Kaluga (Masaitis, 2002) and Wetumpka (King et al., 2002) impact craters.

2.6.2.3. Units 2 and 3

The variegated character of the melt particles of Unit 3 compared to the uniform green color of melt fragments in Unit 2 is the main characteristic that differentiates these two units (Fig. 2.2b,c). Fragment size and morphological features are similar. A progressive increase in melt fragment size is observed with depth and may indicate a primary sorting effect. Another observation made on Unit 2 by Dressler et al. (2003a) indicated that the groundmass had a "chocolate-brown" color as it was retrieved from the borehole, but that the color had changed since to medium gray upon drying of the core. This temporary coloration was also used to determine the extent of this unit. Macroscopically, some of the melt particles reveal fluidal and undulating contacts with the host groundmass, which is indicative of a primary deposit or that it was, at least, not mechanically reworked as the unit above. Kring et al. (2003a) reported that Unit 2 was, in part, clast-supported and showed an increase in matrix content, from 15 to 24 vol%, between 823 and 846 m. We report modal proportions of 3 to 25 vol% for matrix in this unit. Our modal data do not indicate whether there is indeed an increase in matrix proportion with depth. In agreement with Kring et al. (2003a), we recognize that the melt fragment content in units 2 and 3 is high (between 50 and 80 vol%). It was also reported that the groundmass of this interval was most likely of secondary origin as it comprises abundant alkali elements (Na and K) and well defined carbonate crystals (Kring et al., 2003a). It is, thus, supposed that carbonate probably replaced a clastic matrix (Stöffler et al., 2003a). With respect to the emplacement mechanism of units 2 and 3, we favor fallout of primary ejecta from an impact-induced debris cloud/plume, as large and small melt particles display fluidal and undulating morphologies (Fig. 2.3b, c). We suggest that the uniform green color of Unit 2 represents a hydrothermal overprint and that this material likely represents rocks, from which the reworked Unit 1 material was derived.

2.6.2.4. Unit 4

Unit 4, between 861 – 885 m depth, represents a massive, brecciated, green melt rock unit. Macroscopic observations indicate that brecciation occurred

in situ, as fragments fit together like the parts of a jigsaw puzzle. The fractures between fragments appear to be filled by a dark opaque material that, under the microscope, is non-reflective and, thus, could represent hydrocarbons. The melt is locally extensively altered, and veins filled with acicular crystals (thought to have been chlorite, now totally converted to sepiolite) are found throughout, commonly in close association with the opaque veining. The heat derived from this melt rock unit is suggested to have thermally metamorphosed and dehydrated the overlying Unit 3, preserving its variegated character. This metamorphism is also believed to have increased the grain size character of Unit 3 groundmass, similar to the thermal effect on the so-called "thermometamorphic breccia unit" observed in the Y6 borehole (Claeys et al., 2003).

Because this unit contains hardly any carbonate material, no carbonate inclusions or foraminifera, and numerous silicate mineral fragments and inclusions (see Table 2.3), it is suggested that it must represent an allogenic deposit formed entirely from siliceous, crystalline basement-derived material. Any carbonate observed in this unit is restricted to some secondary veins. As the Yax-1 borehole is thought to be located just outside (~ 10 km, Morgan et al., 1997) the limits of the now collapsed transient cavity, transport from the source region is constrained to approximately 10 to 60 km, which is the maximum radial distance to the crater center. As Unit 4 represents the second unit to be deposited in the impactite interval, it must have been deposited relatively early during the impact process. We suggest that Unit 4 could either be an isolated melt pod or an outer part of a greater, perhaps coherent, melt sheet (see also Kring et al., 2003b).

2.6.2.5. Unit 5

Unit 5, at the base of the impactite sequence, comprises a complex mixture of lithic and melt fragments suspended in a fine- to medium-grained, carbonate-dominated groundmass. The polymict nature of the unit and the high content of carbonate clasts indicate that extensive mixing occurred between a diversity of target rock types, including Cretaceous carbonate. The presence of foraminifera microfossils within carbonate fragments (Table 2.3) indicates complete melting, or dissociation of carbonates, was not achieved in this unit. This is in contrast to

units 2 through 4 where no fossils or preserved carbonate inclusions were found.

The stratigraphic position of Unit 5 indicates that it was the first impactite deposited. Stöffler et al. (2003a) suggested that the rocks might have been emplaced as an initial ground-surge deposit. We agree with this interpretation because of the diverse lithic content and the high carbonate versus silicate content, likely derived from the excavation and mixing of carbonate rocks of the upper stratigraphy of the area around the transient cavity.

There is conflicting evidence regarding the hydrothermal or primary impact melt origin of the carbonate groundmass to this unit. Unequivocal evidence for hydrothermal activity is indicated by the growth of euhedral barite grains in vesicles and the presence of iron-oxide lined vugs. Nevertheless, in support of a primary impact melt origin, Kring et al. (2003a) pointed out that melt fragments in this unit are groundmass-supported. The groundmass appears to contain at least 12 vol% melt fragments and numerous monomineralic clasts (Fig. 2.8b). Microprobe analyses indicate that melt fragments in the groundmass have high wt % totals and, thus, are volatile poor and relatively unaltered. Also, macroscopic textural observations indicate fluidal contacts are locally preserved (Fig. 2.2f). In contrast, a secondary origin of the groundmass carbonate is favored by the lack of clear cross-cutting relationships between the groundmass and carbonate veining. No calcite crystals with quenched acicular radiating textures were observed that could indicate that this groundmass is a melt phase, as observed by Claeys et al. (2003). Carbonate veins are observed cutting through melt fragments and not the groundmass, suggesting that the veins could be older than the groundmass (Fig. 2.13f). In contrast, carbonate veins meandering around melt fragments indicate that these veins are younger than the groundmass (Fig. 2.13e). Because of this conflicting evidence, it is still premature, if not eventually impossible, to determine accurately the hydrothermal or impact melt origin of this groundmass.

2.6.3. Microprobe analysis of melt

The composition of many melt fragments from the entire impactite sequence was determined by electron microprobe spot and traverse analysis (Fig.

2.10). These results indicate that the melt particles are of extremely variable composition, both between fragments and between zones within individual fragments. This is in agreement with the studies of Sharpton et al. (1992), Kettrup et al. (2000), and Claeys et al. (2003) of melts from the Y6 and C1 cores. Based on composition, at least three types of melt particles were identified: mafic, mafic-alkali element-rich, and alkali element-rich, the latter occurring in greater abundances. In contrast to Hecht et al. (2003a), we did not analyze any silica-dominated melt particles. The feldspathic component-rich melt fragments show variable degrees of hydration with a significant proportion of analysed fragments still yielding high total wt% values that are interpreted as evidence for relative "freshness" (e.g., Fig. 2.10b). Some fragments are of unusually high CaO contents that coincide with high K_2O concentrations and, thus, yielded non-stoichiometric normative feldspar compositions. The high K contents can be attributed to K-metasomatic overprint (e.g. Hecht et al. 2003b), primary mixing of plagioclase and alkali feldspars, or to the incorporation of lime from decomposed carbonates into siliceous melt rock particles. We have been able to observe that at least some of the melt analyses indicate the presence of unaltered mineral melts, as indicated, for example, by K-feldspar composition and stoichiometric plagioclase melts (e.g., albite). Many fragments, however, and especially all mafic melt particles, show variable degrees of alteration, in accordance with the pervasive interaction of fluid phases after deposition. Such alteration has been observed at several impact sites, notably at the Ries, Lonar, and Mistastin Craters, where the impact melt particles and glasses were converted to saponite and montmorillonite (e.g., Osinski, 2003; Hagerty and Newsom, 2003). Variable degrees of K-metasomatism are also indicated by the K contents of mafic particles (Fig. 2.11c), alkali element-rich fragments (Fig. 2.12a), and melt phases in some checkerboard plagioclase grains (Fig. 2.12c). The melt fragment analyses indicate that the melt phases did not undergo extensive homogenization, and that, instead, mineral or mineral combination melts form schlieren within the variegated melt fragments.

2.6.4. Classification of Yax-1 impactite interval

According to the proposed impactite classification scheme of Stöffler and Grieve (1994), the entire sequence intersected in the Yaxcopoil-1 section can be defined as suevitic breccia and impact melt rock. Suevite is defined as containing melt particles suspended within a matrix dominated by clastic material (e.g., Stöffler, 1974; Dressler and Reimold, 2001). Macroscopic observations alone would suggest that units 1 to 3 represent suevitic rocks. However, microscopy cannot resolve the exact nature of the groundmass of units 1 to 3. Our SEM investigations are generally in agreement with the features noted by Kring et al. (2003a) with the groundmass comprising calcite, alkali element-rich phases. It is difficult to support a total hydrothermal origin for this groundmass, as well preserved monomineralic inclusions and small melt particles are quite abundant.

Unit 4 is an obvious impact melt rock, as it comprises a zone of now altered melt with abundant microlites. Unit 5 contains melt particles and a minor component of lithic debris suspended in the carbonate-dominated groundmass; however, conflicting evidence concerning the nature of the groundmass (secondary or primary?) also prohibits accurate classification. If Unit 5 contains a secondary carbonate groundmass that replaced or overprinted a primary lithic-plus-melt-fragment matrix, then the rock should be classified as a suevite (Stöffler et al., 2003a). If the groundmass indeed represents a carbonate melt, then the rock is basically an impact melt rock with a minor lithic clast content.

2.7. Summary

The Yaxcopoil-1 borehole, at a distance of ca. 60 km from the crater center, intersected an about 100 m thick section of impactites. Similar to the impactite sections in the boreholes located closer to the center of the impact structure (C1, S1, Y6, and T1 boreholes), large quantities of melt fragments with minor proportions of lithic or mineral inclusions were observed throughout the sequence. We subdivide the 100-m-sequence into five units, namely based on the melt particles' morphology, size, color, and abundance. Microscopic shock deformation such as PDFs in quartz and ballenquartz occurs throughout the impactite interval, in addition to the presence of checkerboard feldspar mainly in

Unit 4. The melt fragment compositions are highly variable and they have undergone a substantial amount of alteration to phyllosilicate phases. All mafic melt particles are strongly hydrated, in comparison to alkali element-Si rich melt particles that, at least in part, still yield good analytical totals and, thus, presumably original compositions. Both alkaline and mafic melt fragments show evidence for a K-metasomatic event that affected the entire sequence of impactite.

The conflicting evidence observed does not allow resolving the impact melt or authigenic origin of the carbonate component in the groundmass of Unit 5. This unresolved issue arises from the fact that alteration and hydrothermal processes have been pervasive throughout the impactite sequence and that textural observations, such as possible liquid immiscibility features that might be interpreted to indicate impact melting of carbonate, are not conclusive.

Dressler et al. (2003a) subdivided the impactite sequence into 6 units, based on the variable proportions of glass, lithic fragments, and groundmass; in contrast, we prefer a five-fold subdivision. We argue that units 1 and 2 of Dressler et al. (2003a) belong to the same unit that records a distinct mode of origin, but does not have a uniform preservation state. Our Unit 1 (795 – 823 m) represents a reworked fallout deposit, units 2 (823 – 846 m) and 3 (846 – 861 m) represent a pristine fallout suevite deposit, Unit 4 (861 – 885 m) an allogenic siliceous melt rock body, and Unit 5 (885 – 895 m) could represent an early suevitic or impact melt deposit. Further work is needed in order to elucidate the still unresolved origin of the carbonate groundmass in some of the Yax-1 impactites.

2.8. Acknowledgments

We gratefully acknowledge the comprehensive financial support for this project from the Petroleum Research Fund (grant PRF # 37299-AC8) of the American Chemical Society. Our analytical work has been generously supported by the Director of the South African Council of Geosciences, Pretoria. C. K. was supported by the Austrian Science Foundation (Y58-GEO). This is University of the Witwatersrand Impact Cratering Research Group Contribution No. 77.

3. Major and trace element characteristics of impactites from the Yaxcopoil-1 borehole, Chicxulub Structure, Mexico[2]

3.1. Abstract

Approximately 100 m of impactites were retrieved from the ICDP borehole Yaxcopoil-1 (Yax-1), located ca. 60 km SSW from the center of the Chicxulub impact crater on the Yucatán peninsula of Mexico. Here, we characterize and discuss this impact breccia interval according to its geochemical characteristics.

Chemical analysis of samples from all five recognized breccia units reveals that the impactites are of heterogeneous composition with regard to both major and trace elements at the single sample (8-16 cm^3) scale. This is primarily due to a strong mixing relationship between carbonate and silicate fractions. However, averaged compositions for suevitic units 1 to 3 are similar and the silicate fraction (after removal of the carbonate component) indicates thorough mixing and homogenization. Analysis of the green melt breccia horizon, Unit 4, indicates that it contains a distinct mafic component. Large brown melt particles (in units 2, 3 and 4) represent a mixture of feldspathic and mafic components, with high CaO abundances. Unit 5 shows the greatest compositional diversity, with highly variable abundances of SiO_2, CaO, and MgO.

Inter-sample heterogeneity is the result of small sample size combined with inherent heterogeneous lithological compositions, highly variable particle size of melt and lithic components, and post-depositional alteration. In contrast to samples from the Y6 borehole from closer to the center of the structure, Yax-1 impactites have a strong carbonate component. Elevated Loss on Ignition, Rb, and Cs contents in the upper two impactite units indicate strong interaction with

[2] Tuchscherer M. G., Reimold W. U., Koeberl C., and Gibson R. L. 2004. Major and trace element characteristics of impactites from the Yaxcopoil-1 borehole, Chicxulub Structure, Mexico. Meteoritics & Planetary Science 39:955-978.

seawater. The contents of the siderophile elements, including Ni, Co, Ir, and Cr, do not indicate the presence of a significant extraterrestrial component in the Yax-1 impactites.

3.2. Introduction

The 195-km-wide Chicxulub impact structure (e.g., Morgan et al. 1997; Grieve and Therriault 2000) is located on the northeastern margin of the Yucatán Peninsula (Fig. 3.1, inset). It was drilled by the International Continental Scientific Drilling Program (ICDP) between December 2001 and February 2002 (e.g., Dressler et al. 2003). Previous drilling by the Mexican oil company Pemex and by the Universidad Nacional Autónoma de México (UNAM) yielded only limited core and cuttings. The core retrieved from the borehole Yaxcopoil-1 (Yax-1, Fig. 3.1) located 60 km SSW from the center of the structure is the subject of extensive scientific investigation by a number of research groups (e.g., Ames et al. 2003; Keller et al. 2003; Kring et al. 2003a; Stöffler et al. 2003a; Vermeesch et al. 2003; Tuchscherer et al. 2003; this volume). The Yax-1 borehole made a 100 m thick sequence of impact melt breccia and suevite from the Chicxulub crater accessible for analysis. This impactite interval comprises various units of suevite and impact melt. Results of petrographic analysis of our sample suite from all these units are discussed by Tuchscherer et al. (2004). Here, we present the first geochemical results for this impactite sample suite.

The borehole was first described by Dressler et al. (2003). It extends to a depth of 1511 m (Fig. 3.2) and intersected, from top to bottom, 795 m of upper Tertiary sedimentary rocks, 100 m of impactites between 795 and 895 m depth, and 616 m of Cretaceous sedimentary rocks (Table 3.1). The impactites were subdivided by Dressler et al. (2003) into six units, based primarily on fragment size, color, and morphological criteria such as clast types and shapes. Most workers investigating this interval have adopted this stratigraphic division (e.g., Stöffler et al. 2003a), whereas Tuchscherer et al. (2004) have recognized only 5 units (Fig. 3.2).

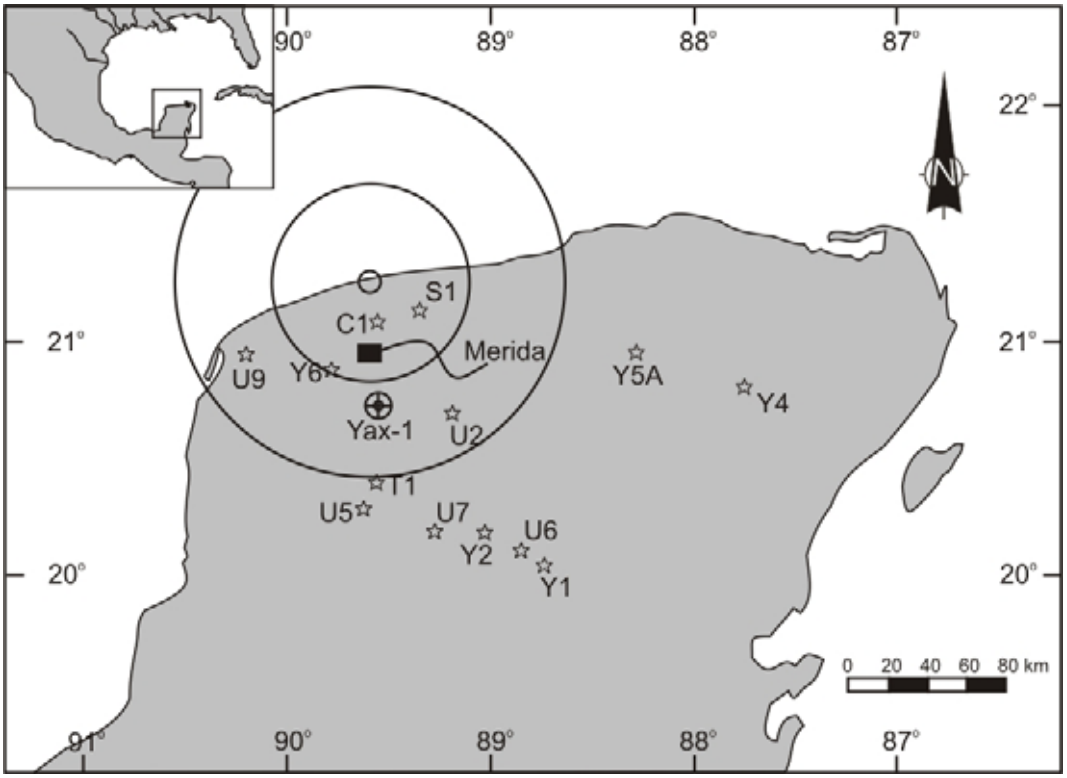

Fig. 3.1. Location of the Chicxulub impact structure on the northwestern part of the Yucatán Peninsula of Mexico. The ICDP borehole is located ~60 km towards the SSW of the crater center. The circles shown here represent the extent of the postulated transient cavity at ~100 km (Morgan et al. 2002) and the postulated crater diameter at ~195 km from the outermost, most significant inward-facing scarp (after Morgan et al. 2002). Also shown are all well localities (localities from Persaud and Sharpton, 1998).

3.2.1. Short review of the Yaxcopoil-1 stratigraphy

A short description of the various lithologies intersected by the Yax-1 borehole is presented here. The upper Tertiary rocks comprise calcarenite, calcareous siltstone, minor chert, and rare conglomeratic deposits. The impactites represent a succession of suevite and impact melt breccia deposits of varying degrees of alteration. The Cretaceous rocks are primarily composed of interlayered dolomite, limestone, and anhydrite that are occasionally truncated by thin (8 to 80 cm) breccia zones and melt breccia veins (Dressler et al. 2003; Wittmann et al. 2004, this volume). Rare oil-bearing horizons have also been recorded (Kenkmann et al. 2003; Gilmour et al. 2003, Zurcher et al. 2004). The anhydrite content of the Cretaceous interval has been estimated at 27.4 vol% (Dressler et al. 2003).

Table 3.1. Yaxcopoil-1 impactite lithological units (after Tuchscherer et al., 2004) and summary of key lithological characteristics.

Depth (m)	Units		Lithological characteristics
794 – 822	1	Reworked suevite	Fining upward, sorted, reworked, and clast supported breccia deposit. Contains limestone and fossil fragments. Melt particles are typically green.
822 – 845	2	Suevite	A fine-grained carbonate groundmass-supported breccia that contains green, fluidal textured, angular melt particles.
845 – 861	3	Variegated suevite	A fine-grained, carbonate groundmass-supported breccia that contains variegated, angular, and rounded melt particles. Large brown melt masses increase in abundance with depth with decreasing alteration.
861 – 884	4	Green impact melt breccia	A massive but strongly brecciated green melt unit. The melt rock displays flow-textures.
884 – 894	5	Variegated, polymict, impact melt breccia/suevite	A melt breccia comprising variegated melt particles and polymict lithic/mineral clasts suspended in a fine-grained carbonate groundmass.

Our five-fold stratigraphic subdivision of the impactites is based on texture, melt particle size, morphology, color, groundmass type, and lithic mineral clast content of these breccias, as discussed in detail in Tuchscherer et al. (2004). The uppermost unit, Unit 1, is defined according to its comparatively finer grain size, obvious clast-supported character, the subrounded morphological character of melt and lithic fragments, and the occurrence of clasts with/of foraminifera, as observed in thin section. This unit corresponds to the combined units 1 and 2 of Dressler et al. (2003). Units 2 and 3 (units 3 and 4 of Dressler et al. 2003) are both groundmass-supported and contain fluidal melt particles. Unit 2 has a uniformly green melt particle population. Unit 3 has a variegated character and a comparatively higher proportion of melt fragments. Unit 4 (Unit 5 of Dressler et al. 2003) comprises a massive green melt rock horizon that displays internal fluidal textures indicative of flow, but that experienced *in situ* brecciation, as indicated by the jigsaw pattern of the subangular to angular fragments. The lowermost Unit 5 (Unit 6 of Dressler et al. 2003) displays a locally variable population of lithic fragments and melt particles that are supported by a fine-grained carbonate-rich groundmass that may either be a primary carbonate melt or a secondary matrix.

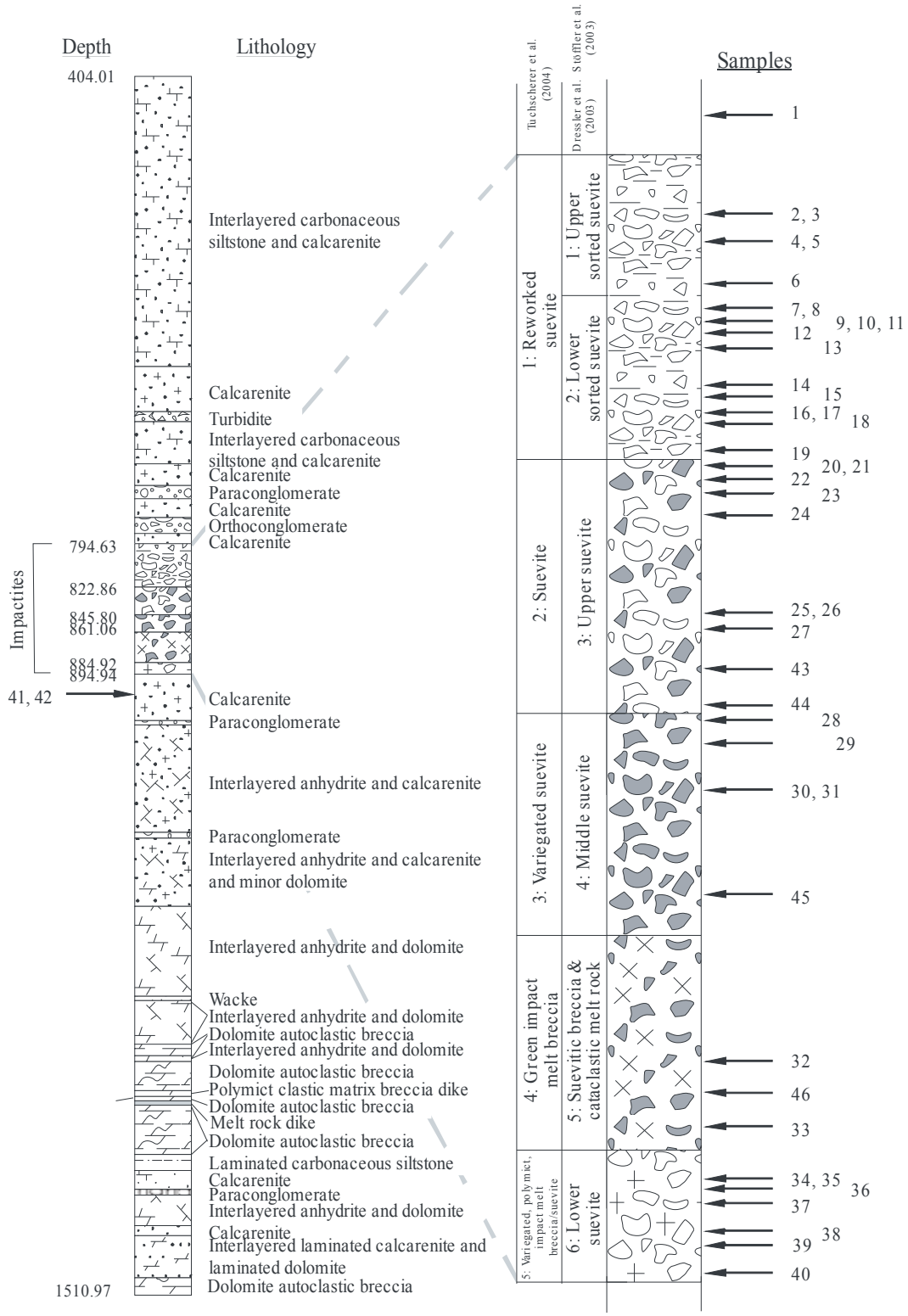

Fig. 3.2. Stratigraphic column of the Yax-1 borehole (after Dressler et al. 2003 and impactites terminology of Stöffler et al. 2003a), with sample positions on enlarged impactite interval. Sample 1 is a Cretaceous limestone, samples 2 to 19 are reworked suevite from Unit 1, samples 20 to 28 are green suevite from Unit 2, samples 29 to 31 are variegated suevite from Unit 3, samples 32 and 33 are from Unit 4, samples 34 to 40 are from Unit 5, samples 41 and 42 are Cretaceous limestone lithic breccias, and samples 43 to 46 are brown melt particles from 840, 843, 860, and 879 m depth.

With respect to the six-fold subdivision of Dressler et al. (2003), we do not recognize their uppermost two subdivisions. We found that the foraminifera content, the fine-grain size, the presence of primarily subrounded clasts, and the clast-supported character of both upper units support their combination as one unit. All these rocks have undergone variable degrees of alteration in the form of chloritization, alleged K-metasomatism (see Discussion below), and carbonatization (Zurcher et al. 2003; Hecht et al. 2003). Alkali element-rich melt particles and lithic inclusions have undergone variable but extensive conversion to phyllosilicate phases, and the mafic melt particles to saponite. For a detailed overview of the modal compositions and petrographic features of the various impactite constituents, see Tuchscherer et al. (2004).

We interpret the five units distinguished by us, from top to bottom, as (1) a sorted and reworked suevite, (2) fallout suevite, (3) a variegated fallout suevite, (4) a green impact melt breccia that was derived primarily from crystalline basement components, and (5) a polymict impact melt breccia that includes a possible carbonate melt matrix, deposited as either an ejecta or ground-surge deposit.

3.2.2. Comparison with previous boreholes

The Yax-1 impactites must be compared to impactites retrieved from previously drilled boreholes. Impactite samples from boreholes located at the center of the Chicxulub impact crater, the Y6, C1, and S1 sites, as well as a sample from the Y2 site outside of the impact structure (Fig. 3.1), were described as igneous and microcrystalline by Hildebrand et al. (1991). Hildebrand et al. (1991) described the stratigraphy of the impactites in wells C1, S1, and Y6 as comprising an upper, coarse, clastic breccia underlain by impact melt, the latter described as an andesitic igneous rock. According to Hildebrand et al. (1991) andesitic glass underlies the breccia in boreholes C1 and S1, whereas microcrystalline andesitic rocks were observed in well Y6 and below the andesitic glass in well C1. In wells C1 and S1, the upper breccias comprised limestone and bentonite fragments interbedded with marl, shale, and rare occasional dolomitic limestone, whereas the upper breccia of well Y6 comprised sandstone interbedded

with shale, marl, and bentonite. The Y6 samples contained numerous cm-sized silicate inclusions including granitic-gneiss, quartz-mica schist, and metaquartzite (Hildebrand et al. 1991; Claeys et al. 2003). In contrast, samples from the Y6 borehole were described by Schuraytz et al. (1994) as being comparatively richer in clasts derived from platform-sedimentary target rocks, whereas the C1 melt rocks originated from a more siliceous basement source.

The UNAM 7 borehole, which is located relatively farther from Yax-1 than Y6, was reported to have a somewhat different impactite stratigraphy (Sharpton et al. 1999). It contains two distinct breccia intervals where the upper segment comprised abundant allogenic basement clasts above an anhydrite and gypsum clast rich breccia. Impactites from the UNAM-6 borehole, at a distance still farther from the center of the structure (Fig. 3.1) than UNAM 7, were described to contain variegated (white to gray), evaporitic, limestone, dolomitized limestone, gypsum, and anhydrite fragments up to 4 cm in diameter (Urrutia-Fucugauchi et al. 1996). A geochemical study on impactite samples recovered from the UNAM 5 to 7 boreholes by Sharpton et al. (1999) revealed that impactites sampled further away from the center of the Chicxulub impact structure are more depleted in silica relative to materials from closer to the center of the structure.

A detailed investigation of impactite samples from the Y6 borehole was undertaken by Claeys et al. (2003). These authors observed three distinct subdivisions within the impactites: i) an upper, fine-grained, carbonate-rich, fossil-bearing suevite; ii) a middle, relatively coarser-grained, suevite rich in altered silicate melt particles and silicate basement clasts; and iii) a lower, so-called “thermometamorphic” suevite rich in melt fragments, large evaporite clasts, and shocked basement clasts. Claeys et al. (2003) also observed that the CaO and SiO_2 content of the Y6 impactites produce a negative correlation, as described by Stöffler et al. (2003) for Yax-1 and Kettrup et al (2000) for Y6 and C1. Claeys et al. (2003) also observed that the suevitic rocks decreased in MgO, Sr, and CaO but increased in TiO_2, Na_2O, K_2O, and Fe_2O_3 with depth.

The recent geochemical investigations of Kettrup et al. (2000) indicated that a mafic to intermediate component (e.g., diabase, pyroxenite, or amphibolite)

is required in order to model the variation between C1 melt rock and Haitian impact glasses; however, no clasts of such rocks have so far been found in any of the Chicxulub drill cores. These authors also determined that the melt rocks and ejecta deposits had isotopic and major element characteristics that are different from each other and, thus, indirectly revealed the complex geological character of the Yucatán crust. Kettrup et al. (2003) suggested the Chicxulub impact might have sampled Gondwanan and Laurentian crust.

3.3. Samples and analytical methods

Forty three bulk impactite samples, two Cretaceous footwall limestone breccias, and one Tertiary limestone sample were analyzed for major and trace element contents by X-ray fluorescence (XRF) and instrumental neutron activation analysis (INAA). Fourteen samples were additionally analyzed for their iridium content using the γ-γ iridium coincidence spectrometry (ICS) technique that allows detecting concentrations in the ppt range (Koeberl and Huber 2000). The bulk impactite sample suite represents all five stratigraphic units as defined by our group (Table 3.1). Eighteen samples originate from Unit 1, nine from Unit 2, three from Unit 3, two from Unit 4, and seven from Unit 5. In addition, four samples of brown melt sampled in units 2, 3, and 4 at 840, 843, 860, and 879 m depths (Fig. 3.2) were analyzed. The samples selected for ICS also represent the entire Yax-1 impactite interval (Table 3.3)

Major element contents were determined by standard X-ray fluorescence spectrometry (XRF) at Setpoint Laboratories in Johannesburg, South Africa. Samples were carefully pulverized using an automated agate mill. Approximately 8 g of powder was used per analysis; the powders were fused in Spectroflux 105 (Li Tetraborate/Li Carbonate/La Oxide). Calibration curves were determined with a series of reference rock materials from the South African Bureau of Standards. Precision and accuracies (determined by sample and standard duplicate analysis) for major element analyses were determined (in wt%) at: Si, ± 0.1; Ti, ± 0.05; Al, ± 0.3; Fe, ± 0.2; Mn, ± 0.04; Mg, ± 0.1; and Ca, Na, and K ± 0.02. The analyses were performed on an ARL 9800 XP spectrometer. Trace element analyses of ~150 mg sample aliquots were determined by INAA at the Department of

Geological Sciences in Vienna, Austria. The samples were irradiated with known standards, including the international granite standards AC-E and USGS G-2 (Govindaraju et al. 1989), the Allende meteorite standard (Jarosewich et al. 1987) for Au and Ir, and the mineralized gabbro PGE standard WMG-1 (CANMET 1994). Irradiation took place at the TRIGA Mark II reactor at the Atominstitut der Österreichischen Universitäten in Vienna for 7 hours at a flux of ~2×10^{12} n/cm^{2}s. For further details regarding the INAA technique, i.e., isotope decay measurement times, accuracy, and precision, refer to Koeberl (1993b). Samples analyzed using the ICS technique were irradiated with the Allende meteorite standard (Jarosewich et al. 1987) for 48 hours at the ASTRA reactor of the Forschungszentrum Seibersdorf, Austria at a flux rate of ~7×10^{13} n/cm^{2}s. For additional details regarding the ICS technique, refer to Koeberl and Huber (2000). Sulfur analyses were performed at the University of the Witwatersrand using a LECO sulfur determinator SC132 instrument. Both precision and accuracy on these analyses were calculated at ± 0.02 wt%. As suspected by the high degree of alteration and the high carbonate content of the rocks (Dressler et al. 2003; Kring et al. 2003b; Stöffler et al. 2003a; Tuchscherer et al. 2004), most analyses have a high loss on ignition (LOI), ranging from 5 to 45 wt%.

Several factors influence the variability of these analyses (Appendix A.5). Sample sizes were restricted and ranged in volume from 8 to 16 cm^3, as supplied by the staff at the Universidad Nacional Autónoma de México (UNAM). Considering the highly variable grain sizes of the various components in these impactites that range from <1 mm to several cm and the heterogeneous lithological make-up of these rocks, it can only be speculated at this stage how far individual samples should be considered representative for a given unit. The high variability of the compositions of individual samples is, thus, attributed to the small sample size, variable grain sizes, alteration effects, and the highly compositional heterogeneous character of the Yax-1 impactites.

3.4. Results

3.4.3. Major elements

The analyses of forty-six bulk samples from the Yax-1 borehole are presented in Appendix A.5. Major element concentrations were plotted versus depth (Fig. 3.3) to investigate the respective compositions of the five stratigraphic impactite units. Notwithstanding the scatter of the individual data, the alkali elements (Na_2O and K_2O) show a subtle yet consistent increase in concentration from units 1 to 4. The SiO_2, TiO_2, Al_2O_3, MgO, and CaO contents remain relatively uniform throughout this interval. However, Unit 4 and brown melt particles show the greatest abundances of SiO_2, Al_2O_3, and K_2O.These trends can also be observed in the tabulated average compositions for the five respective units (Table 3.2). Data scatter is particularly evident for samples from the upper three units. The total iron contents of units 1 and 2 are very variable, ranging from 3.0 to 5.5 wt%, whereas the 3 samples from Unit 3 only range from 3.7 to 2.9 wt%. The two melt samples from Unit 4 display the highest FeO_{tot} and relatively high MgO contents, indicating a possible mafic component. Four brown melt samples from various depths in units 2 to 4 have similar compositions to the samples from the upper units. The lower sample from Unit 4, from 879.0 m depth, has the highest TiO_2 content among all analyzed samples, at 1.1 wt%; this could be caused by a possible nugget effect from any of the following observed minerals, either sphene, ilmenite, or Ti-rich melt particles.

Unit 5 is distinct from all other units, as it shows the greatest compositional variability and has a geochemical character that does not follow the afore-mentioned trends, with regard to SiO_2, TiO_2, Al_2O_3, FeO_{tot}, MnO, CaO, and Na_2O. This lowermost unit also displays an unusual abundance of MnO (values between 0.08 and 0.39 wt%, compared to all other analyzed samples with less than 0.15 wt%). Overall, the phosphate contents in the impactite interval are low, < 0.4 wt%, with the exception of one Unit 3 sample from 851.2 m depth (0.74 wt %). This is most likely the product of slight enrichment of apatite in this sample, a nugget effect, as this mineral is commonly observed in granitic and schistose

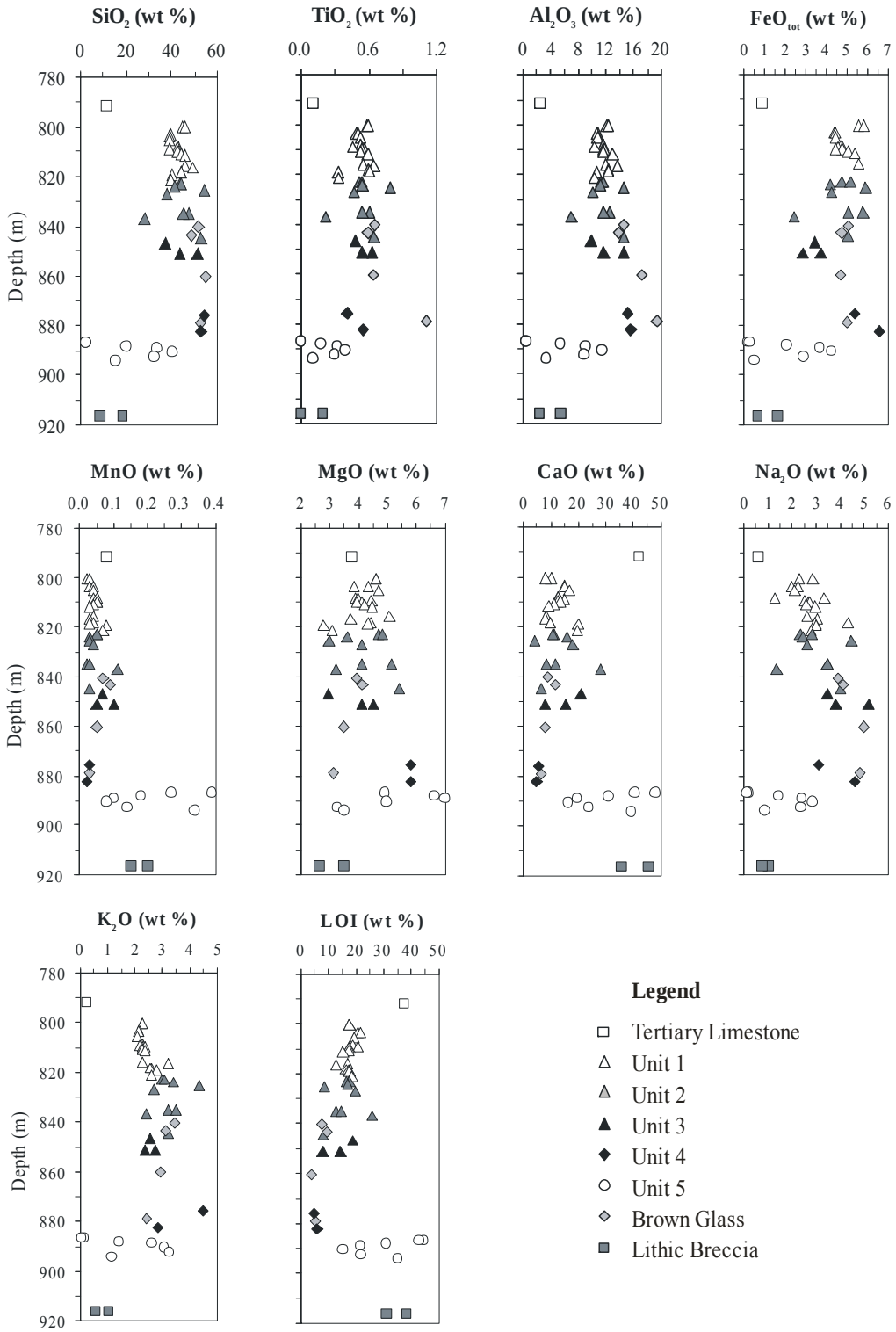

Fig. 3.3. Major element and LOI abundances versus depth for the Yax-1 impactites and selected Tertiary and Cretaceous rocks.wt%).

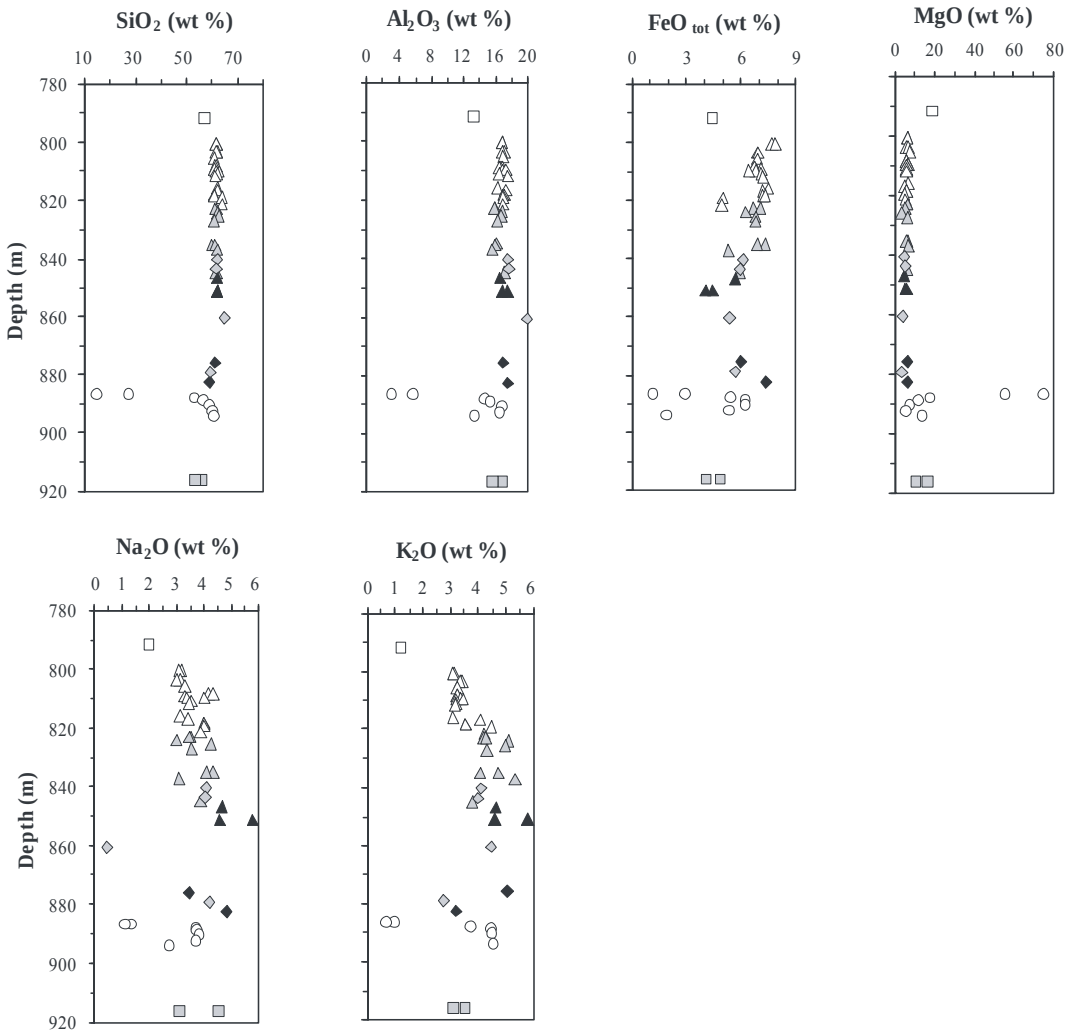

Fig. 3.4. Recalculated (CaO and LOI free) major element data versus depth for the Yax-1 impactites and selected Tertiary and Cretaceous rocks, refer to Fig. 3 for legend.

inclusions in Yax-1 impactites. The chlorine content is relatively uniform throughout the impactite interval ranging from 0.1 to 0.7 wt%.

In order to gain a better understanding of the chemical signature of the silicate fraction in the impactite samples, major element abundances have been recalculated on a volatile- and CaO-free basis (Fig. 3.4). As shown in Figure 3.5a, actual carbonate modal proportions determined for a number of impactite samples (see Tuchscherer et al. 2004) and respective CaO abundances for these samples are very well correlated. This suggests that by far the majority of all CaO analyzed resides in the carbonate component, in agreement with our petrographic

Table 3.2. Average chemical compositions (wt %) and 2σ standard deviation for the Yax-1 impactite units.

Units	1		2		3		4		5		Brown Glass	
Depth range	794 – 822 m	2 σ	822 – 845 m	2 σ	845 – 861 m	2 σ	861 – 884 m	2 σ	884 – 894 m	2 σ	843, 843, 860, 879 m	2 σ
Major Oxides	n=18		n=9		n=3		n = 2		n=7		n=4	
SiO_2	42.86	1.37	43.91	4.96	43.99	6.78	53.72	1.31	20.95	10.71	52.13	2.53
TiO_2	0.52	0.04	0.54	0.10	0.55	0.07	0.48	0.10	0.26	0.08	0.74	0.21
Al_2O_3	11.65	0.42	11.60	1.43	12.03	2.19	15.37	0.33	5.61	3.06	16.23	2.14
FeO_{tot}	4.78	0.36	4.73	0.66	3.33	0.41	5.96	0.83	1.97	1.19	4.86	0.18
MnO	0.07	0.05	0.04	0.02	0.07	0.02	0.03	0.01	0.21	0.08	0.06	0.02
MgO	4.13	0.26	4.22	0.53	3.84	0.77	5.80	0.01	5.92	1.91	3.67	0.39
CaO	12.60	1.69	12.77	4.51	14.60	6.27	5.20	0.33	31.26	8.28	8.73	1.92
Na_2O	2.47	0.16	2.67	0.47	3.60	1.00	3.70	0.85	1.31	0.70	2.68	1.33
K_2O	2.38	0.13	3.20	0.34	2.55	0.18	3.68	1.17	1.67	0.93	3.22	0.52
P_2O_5	0.04	0.01	0.06	0.02	0.38	0.30	0.11	0.05	0.07	0.02	0.18	0.12
Cl	0.42	0.05	0.46	0.08	0.43	0.05	0.45	0.07	0.21	0.08	0.28	0.11
L.O.I	17.74	0.91	15.50	3.48	13.69	5.20	5.40	0.60	30.20	7.88	6.77	1.81
Total	99.67		99.72		99.26		99.89		99.70		99.57	
Sulfur content (wt %)												
S_{tot}	0.02	0.01	0.02	0.01	0.03	<0.01	0.02	<0.01	0.02	<0.01	0.03	<0.01
SO_3	0.05	0.02	0.05	0.02	0.04	0.03	0.05	0.01	0.03	0.01	0.04	0.03
Trace Elements (ppm, except where noted)												
Sc	16.4	1.0	15.2	2.7	13.4	1.4	15.1	1.6	5.2	3.0	23.1	6.3
Cr	51.8	4.7	43.2	11.8	49.6	11.7	39.3	3.1	15.4	7.3	37.6	17.4
Co	7.8	0.6	7.6	1.0	6.4	0.9	9.2	0.4	3.4	2.0	8.6	1.0
Ni	22	3	25	7	16	2	8	4	13	8	32	7
Zn	71	3	570	10	46	3	52	4	18	8	100	48
As	0.27	0.03	0.26	0.09	0.69	0.22	0.85	0.15	0.48	0.53	0.50	0.29
Se	0.3	<0.1	0.2	0.1	0.3	0.1	0.4	0.1	0.2	0.1	0.2	0.1
Br	12.9	1.7	14.8	5.5	2.6	0.3	13.1	13.9	4.0	3.3	24.6	8.6
Rb	57.3	3.2	55.0	8.2	32.2	6.2	42.2	13.8	16.8	9.5	30.8	8.7
Sr	205	28	259	107	402	55	328	371	333	74	495	257
Zr	139	25	110	18	142	19	88	4	82	62	143	48
Sb	0.18	0.02	0.14	0.03	0.22	0.07	0.14	0.05	0.11	0.04	0.13	0.04
Cs	2.21	0.16	1.45	0.24	0.60	0.15	0.68	0.09	0.22	0.13	0.68	0.27
Ba	98	17	148	76	358	182	210	157	194	129	235	45
La	15.6	2.0	17.9	7.9	30.7	12.2	20.4	4.9	11.7	6.6	28.7	16.0
Ce	32.2	3.0	49.0	42.5	49.7	17.1	44.9	8.9	20.9	12.6	49.9	30.3
Nd	14.3	1.5	15.0	5.4	26.6	10.5	17.2	4.0	9.4	5.0	23.6	12.9
Sm	2.86	0.30	2.82	0.79	5.06	2.02	3.12	0.26	1.70	0.91	5.24	3.71
Eu	0.80	0.08	0.79	0.26	1.27	0.45	0.76	0.09	0.39	0.23	1.56	1.09
Gd	2.91	0.31	2.92	0.72	5.73	2.75	2.74	0.33	1.78	0.97	4.83	3.45
Tb	0.49	0.05	0.48	0.10	0.90	0.39	0.42	0.04	0.27	0.15	0.76	0.48
Tm	0.27	0.03	0.32	0.09	0.39	0.13	0.21	0.08	0.15	0.08	0.41	0.22
Yb	1.91	0.22	1.92	0.43	2.85	1.15	1.35	0.52	1.01	0.56	2.80	1.55
Lu	0.29	0.04	0.27	0.06	0.44	0.17	0.20	0.09	0.16	0.09	0.43	0.24
Hf	3.64	0.74	2.66	0.41	2.74	0.44	2.85	0.51	0.88	0.49	4.17	1.15
Ta	0.49	0.07	0.38	0.09	0.41	0.06	0.67	0.28	0.24	0.18	0.64	0.20
W	0.87	0.15	0.79	0.26	0.30	0.00	0.46	0.06	5.95	7.24	0.60	0.12
Ir (ppb)	<1.1	<0.1	<0.8	<0.1	<1.2	<0.3	<1.0	<1.0	<0.5	<0.2	<1.2	<0.5
Au (ppb)	0.90	0.22	0.43	0.23	0.40	0.23	0.4	0.21	0.3	0.20	0.77	0.61
Th	6.28	0.51	5.56	1.41	6.68	2.00	11.0	0.14	3.5	2.07	7.94	4.17
U	0.79	0.17	0.62	0.09	1.08	0.17	0.52	0.37	1.83	0.48	1.19	0.08
Elemental Ratios												
CIA	70	1	65	1	64	2	68	1	65	3	69	3
K/U	35402	12117	45488	5676	21922	4804	104103	107603	11049	6955	18445	5422
Zr/Hf	30.5	10.4	36.1	14.9	52.1	5.7	31.1	4.3	138	92	25.9	14.1
La/Th	12.1	7.4	11.4	9.0	5.01	2.26	1.85	0.47	8.63	8.56	16.0	14.0
Th/U	10.7	4.0	8.99	1.93	6.12	0.99	28.3	20.4	2.52	1.85	6.56	3.48
LaN/YbN	5.44	0.47	6.19	2.06	7.4	0.81	10.5	1.6	7.7	1.7	7.1	1.1
Eu/Eu*	0.88	0.09	0.83	0.07	0.74	0.06	0.79	0.02	0.63	0.10	0.98	0.14

findings that Ca-bearing feldspar is very rare (< 1 vol%). It can be observed in Figure 3.4 that the compositional variability previously observed is dramatically decreased with respect to all major elements, in particular SiO_2, Al_2O_3, FeO_{tot}, MgO, Na_2O, and K_2O. However, the recalculated Na_2O and K_2O data still reveal a distinct increase in abundance with depth, and the FeO_{tot} data a slight decrease in abundance with depth.

In terms of the volatile content, the LOI content correlates positively with increasing CaO abundance (Appendix A.5). It is obvious that the total LOI values comprise CO_2 from carbonate, SO_x from sulfate, as well as H_2O and hydroxide from secondary alteration phases and, to an extent, from hydrous ferromagnesian minerals (biotite, amphibole, chlorite, and phyllosilicate phases, up to 20 vol%. Although the observed secondary silicate is high in some samples, e.g., Unit 4 and brown melt particles, it is important to note that these have the lowest LOI values as they do not contain appreciable quantities of carbonate (see Tuchscherer et al. 2004). In general, SO_3 values are very low at < 0.15 wt%, in comparison to sulfate abundance determined for impactite samples from other Chicxulub boreholes, e.g., UNAM 5, where values between 5 and 25 wt% anhydrite (Sharpton et al. 1999) were determined, and also the anhydrite content of the pre-impact target, which was estimated at 25 to 30 vol% (Ward et al., 1995). Slightly decreasing SO_3 contents with depth are noticed for upper units 1 to 3 (Appendix A.5) that correlate with observed modal abundances of anhydrite.

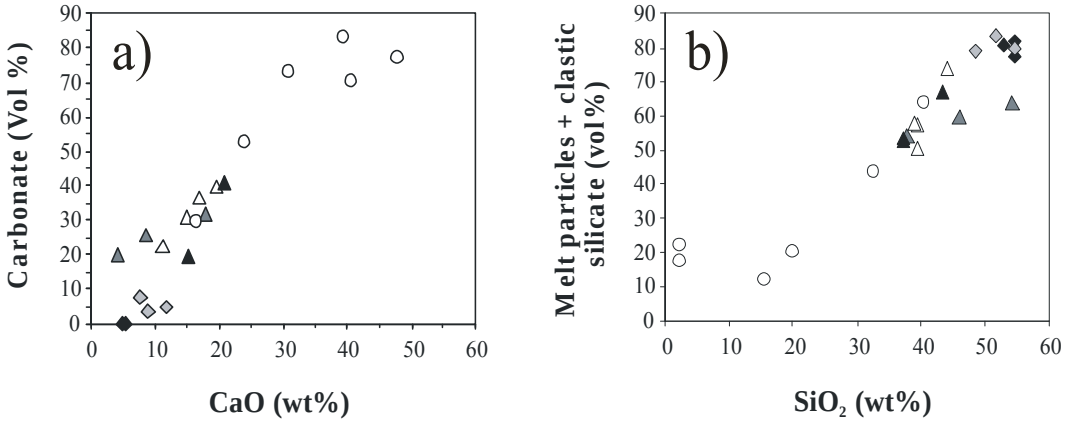

Fig. 3.5. Correlations between modal data (in vol%) and selected major element abundances: a) total carbonate content (calcite and dolomite) versus CaO (wt%) and b) total melt particle and clastic silicate content versus SiO_2, refer to Fig. 3 for legend.

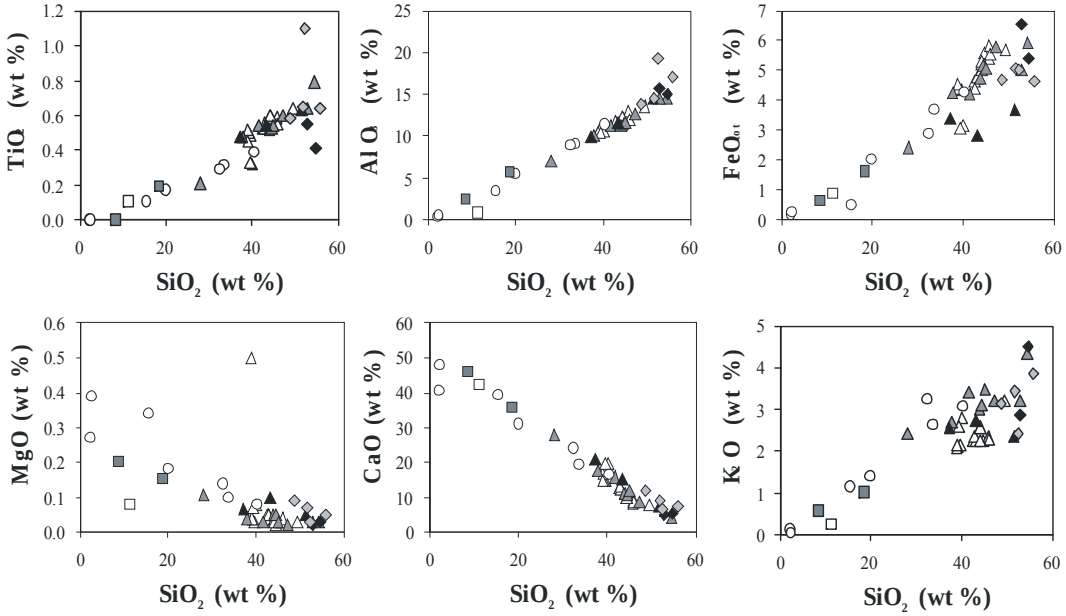

Fig. 3.6. Harker variation diagrams for Yax-1 impactite samples and selected Tertiary and Cretaceous rocks, refer to Fig. 3 for legend.

Binary plots of major element abundances versus silica indicate reasonable correlations for TiO_2, Al_2O_3, FeO_{tot}, Na_2O, and K_2O (all correlated positively with increasing silica abundance), and MnO, MgO, and CaO contents that are negatively correlated (examples shown in Fig. 3.6). A similar negative correlation between CaO and SiO_2 was reported by Kettrup et al. (2000), Claeys et al. (2003), and Stöffler et al. (2003). The LOI is also observed to be negatively correlated to silica. The trends are very well defined for TiO_2, Al_2O_3, LOI, and Na_2O, whereas significant scatter is observed in the MnO and MgO trends. Compared to other units, Unit 5 contains the highest CaO contents (16.5 - 47.9 wt%), whereas a brown melt particle from 860 m depth contains the highest SiO_2 content (55.8 wt%). The silica contents vary in units 1 to 3 between 54.4 and 28.1 wt%, in Unit 4 and the brown melt samples from 55.8 to 48.7 wt%, and in Unit 5 from 40.4 to 2.2 wt%. Samples from Unit 5 with relatively high LOI have MgO values that are constant but slightly above those of units 1 to 4. Based on our petrographic findings (Tuchscherer et al. 2004), these MgO contents are related to the presence of dolomite in Unit 5. This dolomitic component is best revealed in the LOI- and CaO-free recalculated data shown in Figure 3.4, whereas Unit 5 reveals significantly higher MgO content in some samples relative to others.

A ternary plot of the major element oxides (K_2O+Na_2O) – CaO – (FeO_{tot}+MgO) for Yax-1 impactite samples from all 5 units, together with data for selected Y6 (Kettrup et al. 2000) and C1 (Schuraytz et al. 1994) impactites, Haitian impact glasses (Koeberl and Sigurdsson, 1992), and several target rock compositions (Koeberl 1993a) is shown in Figure 3.7. All Yax-1 samples show a small and limited ratio of (K_2O+Na_2O) to (FeO_{tot}+MgO) values and highly variable abundances of CaO. It can be seen that units 1 to 3 display the greatest variation in composition, with no particular grouping forming over a specific field. However, it can also be seen that the Yax-1 brown melt data fall into the fields for Y6 and C1 impact melt and Haitian black glass. The green monomict melt breccia, Unit 4, plots into the meta-sedimentary rock field, relatively close to the mafic apex. Once again, Unit 5 data are distinct, with these samples plotting near the CaO apex close to the two limestone samples from Yax-1, an evaporite (Kettrup and Deutsch 2003), Haitian yellow glass (Koeberl and Sigurdsson 1992), and the Y6 melt breccia field (Kettrup and Deutsch 2003).

Average compositions for units 1 to 5 are presented in Table 3.2. The average compositions of units 1 to 3 are relatively similar, within the variability given by the 2σ standard deviations. The sole exception is the slightly elevated K_2O content of Unit 2 (3.2 wt%) compared to the lower abundances of units 1 and 3 (2.38 and 2.55 wt%, respectively). The composition of Unit 4 is similar to the average composition of the brown melt but has higher FeO_{tot} (i.e., all Fe as FeO), MgO, Na_2O and lower CaO contents, all of which are also variable beyond the 2σ standard deviation limits. Unit 5 has a unique composition, as it contains the lowest SiO_2 and the highest CaO, MgO, and LOI abundances. Average LOI contents of units 1 to 3 are similar. Unit 4 has the lowest LOI. Average SO_3 values are similar for all units. In order to investigate any possible alkali element and CaO exchange, a plot of the major element ratios, K_2O/CaO versus Na_2O/CaO was generated (Fig. 3.8). This produces a relatively linear trend that indicates that the proportions of K, Na, and Ca throughout the impactites remain relatively uniform with depth. It does, however, indicate a significant spread between the two analyses available for Unit 4 samples.

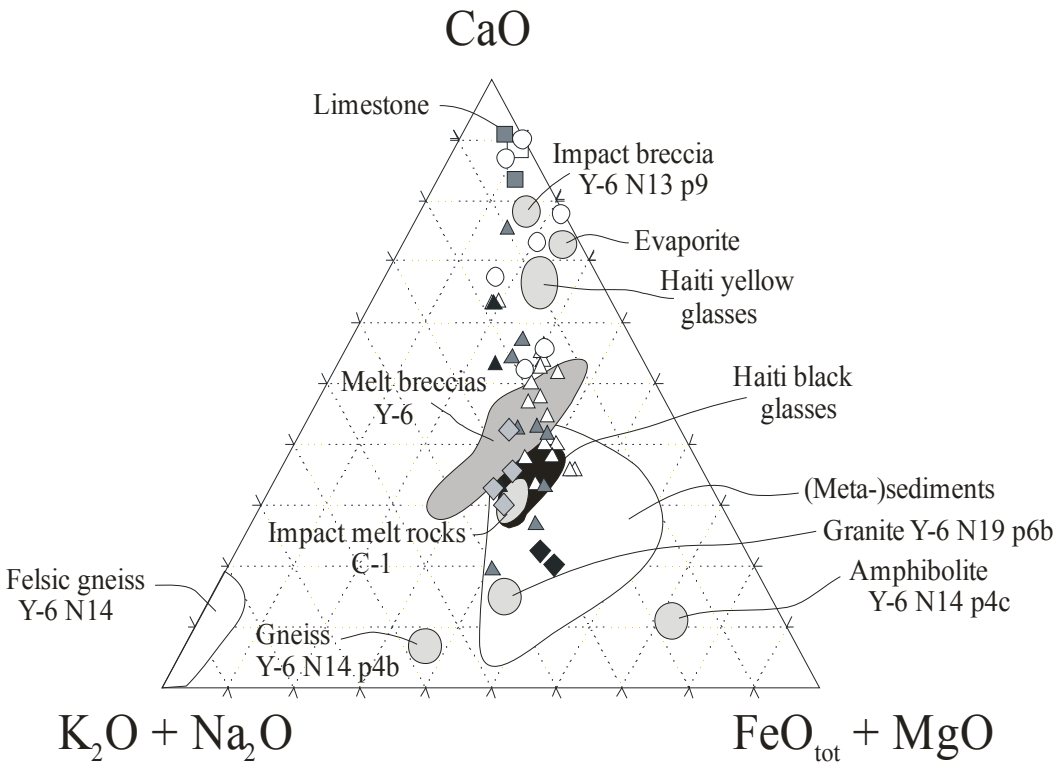

Fig. 3.7. Ternary K_2O+Na_2O – CaO – FeO_{tot}+MgO diagram (modified from Kettrup and Deutsch, 2003) showing the relative composition of the Yax-1 impactites with impactites and lithic samples from the Y6 (Kettrup and Deutsch, 2003) and C1 (Schuraytz et al. 1994) boreholes. Sample Y6-N14 is a pinkish granitic gneiss, Y6-N14-p4c a banded amphibolite, Y6-N14-p4b a melanocratic partially banded gneiss fragment, Y6-N19-p6b is a quartz, plagioclase, and K-feldspar rich granitic fragment, and Y6-N13-p9 is a layered foraminifera bearing clastic breccia with a calcitic matrix (Kettrup and Deutsch, 2003). Black and yellow Haitian glasses (Koeberl and Sigurdsson, 1992) are also plotted for comparison. The Yax-1 impactites display relatively constant proportions of K_2O+Na_2O and FeO_{tot}+MgO with variable CaO, refer to Fig. 3 for legend.

3.4.4. Trace elements

Trace element abundances plotted versus depth indicate some trends: Zn, Rb, and Cs are observed to decrease in concentration with depth, whereas Ni, Sr, Ba, Th, and U show increasing concentrations with depth (Fig. 3.9, Appendix A.5). As observed with the major elements, Unit 5 is also different from the other impactite units, with regard to observed wide ranges of trace element abundances. The concentrations of Sc, Cr, Co, Zn, Rb, Zr, Hf, Ta, and Th in Unit 5 are relatively lower, whereas U is present in relatively greater abundance, than in the other units. Rubidium, Sr, Ba, and Th show the greatest variability.

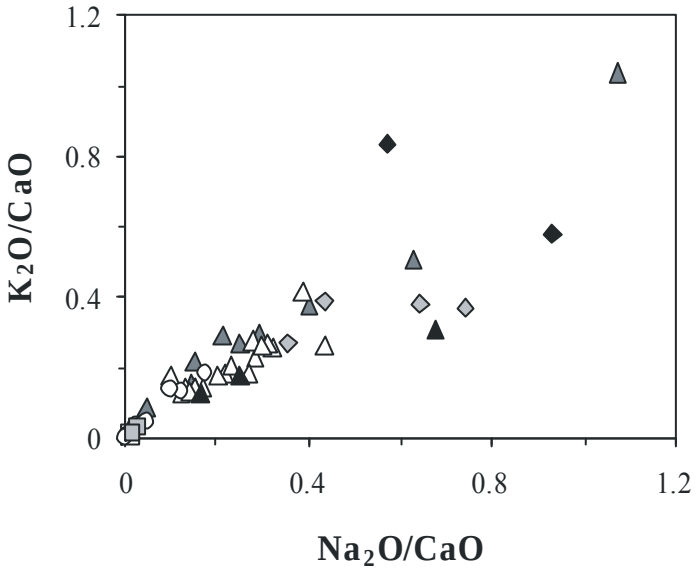

Fig. 3.8. K_2O/CaO versus Na_2O/CaO for Yax-1 impactites and selected Tertiary and Cretaceous rocks, refer to Fig. 3 for legend. The data plots along a linear trend, indicating K for Na and/or Ca exchange occurred under relatively constant proportions.

Chondrite-normalized (Taylor and McLennan 1985) rare earth element (REE) patterns for samples from the various units are illustrated in Figure 3.10. All plots show an enrichment of the light rare earth elements (LREE) that is typical of upper crustal rocks. The impactites have variable chondrite-normalized REE concentrations, typically between 100 and 10 times chondritic values. No clear distinction between the impact melt breccia (Unit 4) and the suevites can be observed. Many samples display relatively significant negative Eu anomalies with only a few with positive Eu anomalies. Most samples have REE patterns that are typical for those of upper continental crust. In some of the low REE abundance samples the crustal pattern is diluted by carbonate, which has low REE abundances (see "Target rocks" in Fig. 3.10). Samples of melt from Unit 4 and of brown melt display relatively smoother REE patterns, similar to the smooth patterns of sampled granodioritic and gneissic inclusions. In comparison with the suevite samples, the range of abundances is similar. What is fairly obvious, though, is the range of positive and negative Ce anomalies, with positive anomalies being more common in Units 1 and 2 and negative anomalies dominating in the lower units. These anomalies indicate alteration and interaction with hydrothermal fluids.

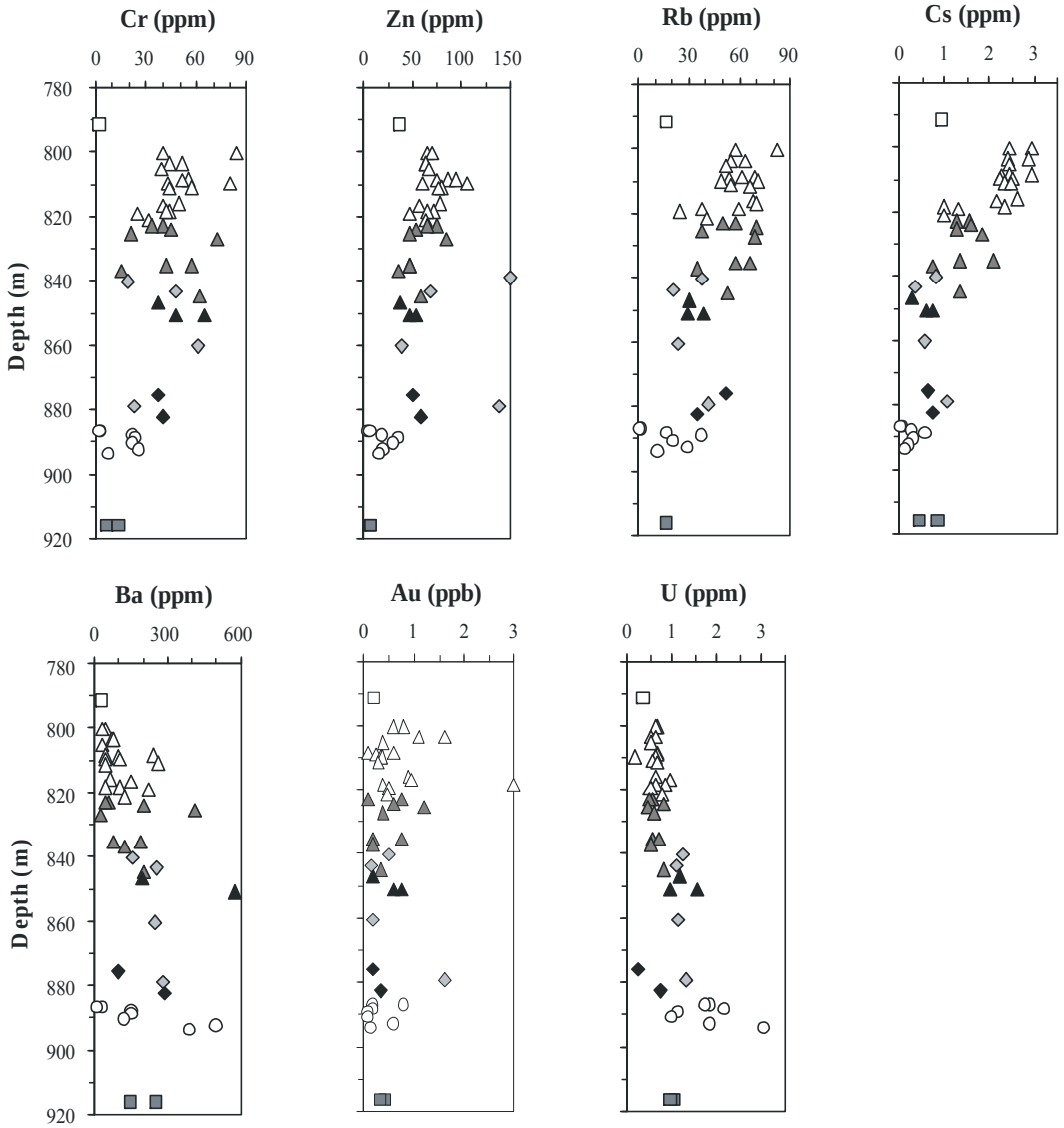

Fig. 3.9. Abundances of selected trace elements versus depth for the Yax-1 impactites and several Tertiary and Cretaceous rocks, refer to Fig. 3 for legend.

Several Cretaceous target rock samples from the Yucatán subsurface have been analyzed for their trace element and REE abundances, including two limestone lithic breccia samples from 916 m depth and granodioritc and gneissic inclusions in this study (Appendix A.5). Normalized REE patterns for these samples, along with results from a previous study by Koeberl (1993a), are also shown in Figure 3.10. It can be observed that the REE abundances of these samples range between 1 and 100 times chondrite, the lowest values being from an evaporite sample of Koeberl (1993a). The only impactite unit that displays such a range of REE abundances seen in these target rocks is Unit 5, which is cha-

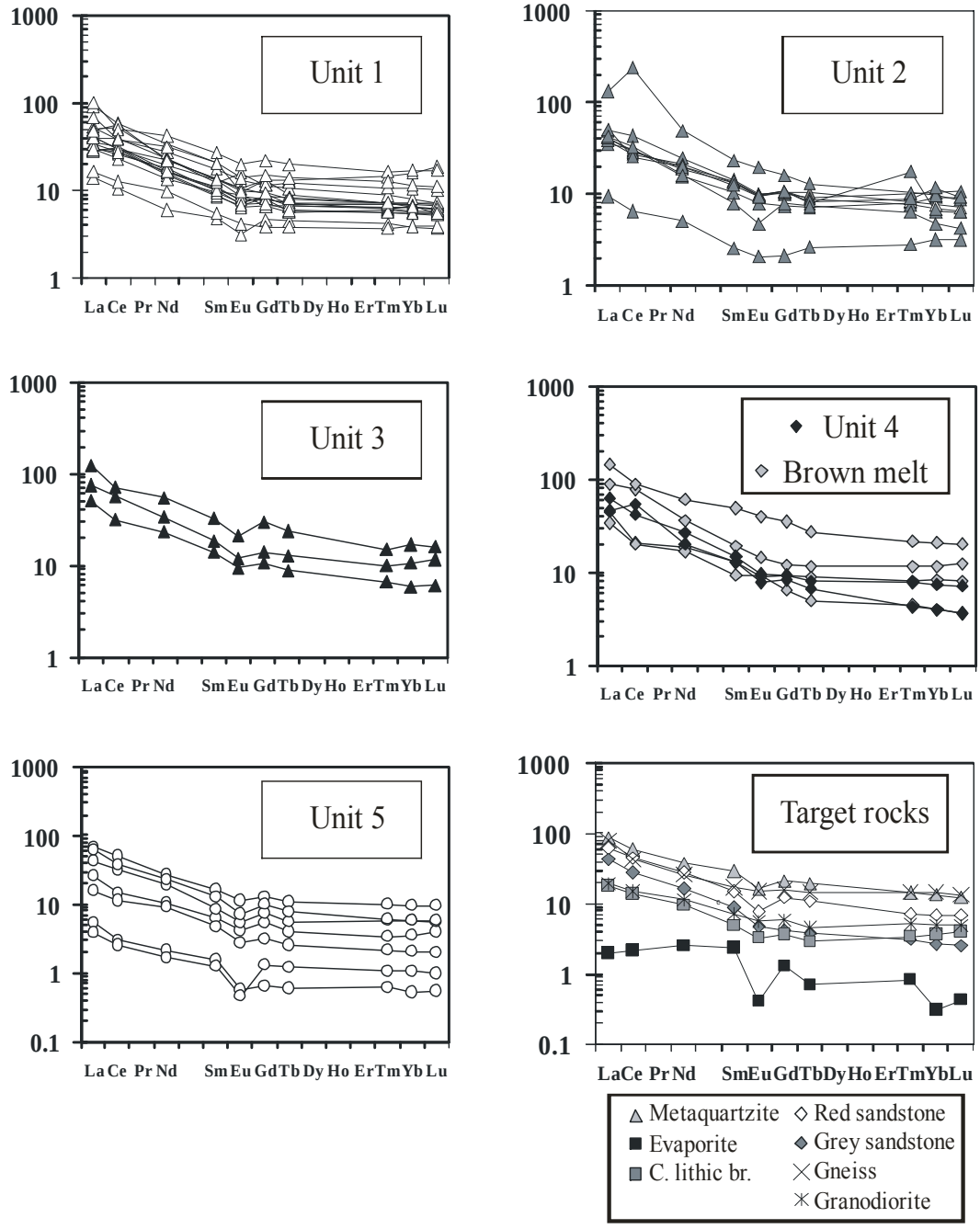

Fig. 3.10. Chondrite-normalized rare earth element abundance diagrams for the Yax-1 impactite and selected Tertiary and Cretaceous samples (metaquarztite, red sandstone, gray sandstone, and evaporite from Koeberl (1993a), gneissic and granodioritic inclusions from Tuchscherer et al. (2004) unpublished data). Normalization factors from Taylor and McLennan (1989).

racterized by variable and, in part, significant carbonate contents. The gneissic basement inclusion, compared to the granodiorite sample, produces a much more elevated REE pattern.

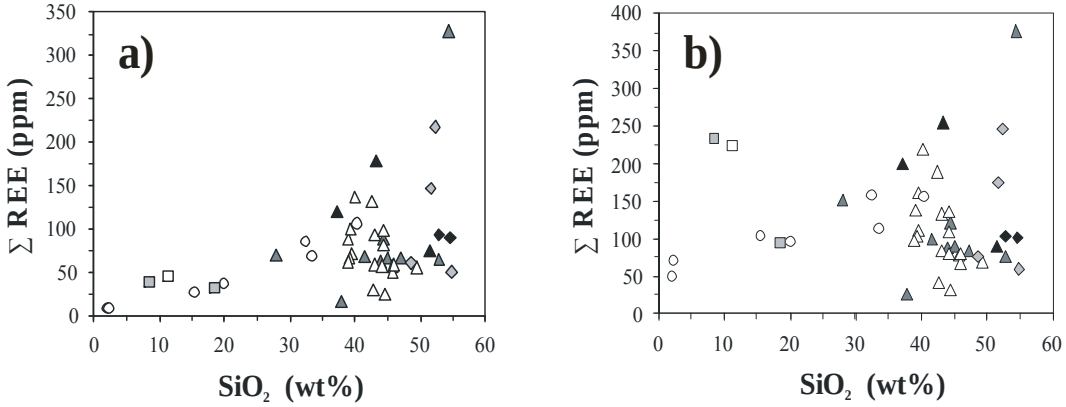

Fig. 3.11. ∑REE (ppm) versus SiO2 (wt%) abundances for the Yax-1 impactites and selected Tertiary and Cretaceous rocks. a) Bulk elemental abundances, and b) abundances corrected for carbonate content, showing that only two low SiO_2 samples have a silicate fraction with REE abundances similar to those of high-SiO_2 samples. Other low-SiO_2 samples have low REE abundances; the hyperbolic trend seen in (a) is absent, indicating that the REE contents are diluted by the carbonate fraction, and that the REE reside in the silicate fraction (accessory minerals), refer to Fig. 3 for legend.

Figure 3.11a represents a plot of the sum of the REE versus SiO_2. This plot indicates a hyperbolic correlation, with strong scatter of data for those samples with relatively high silica content. As discussed before, some of the lowest silica values are from samples that contain quite a large amount of carbonate. The dilution effect of carbonates is clearly shown in Figure 3.11b that shows that samples with recalculated REE abundances (based on the carbonate dilution factors derived from CaO and LOI free recalculated major elements) with low SiO_2 do indeed contain high REE abundances. A plot of Eu/Eu* versus Gd_N/Yb_N values (Fig. 3.12) shows that most samples have a calculated Eu anomaly value less than 1, and all samples have Gd_N/Yb_N ratios between 1 and 2.

A binary plot of the two LIL incompatible trace elements Rb and Cs indicates increasing abundances with stratigraphic height, where these two elements follow a relatively linear correlation trend (Fig. 3.13). However, when plotting Rb versus La, the latter being a high field strength (HFS) and a relatively less incompatible element, a divergent trend is observed, where the Rb rich samples of units 1 and 2 have low La abundances in contrast to the remaining samples. It is interesting to note that this trend was also observed for Rb versus Lu, which is a HFS element that is still less incompatible. However, when the Rb content is plotted versus the Zr, Th, Sc, and Hf contents the observed split trends become progressively linear in the sequence of the listed elements, because of a

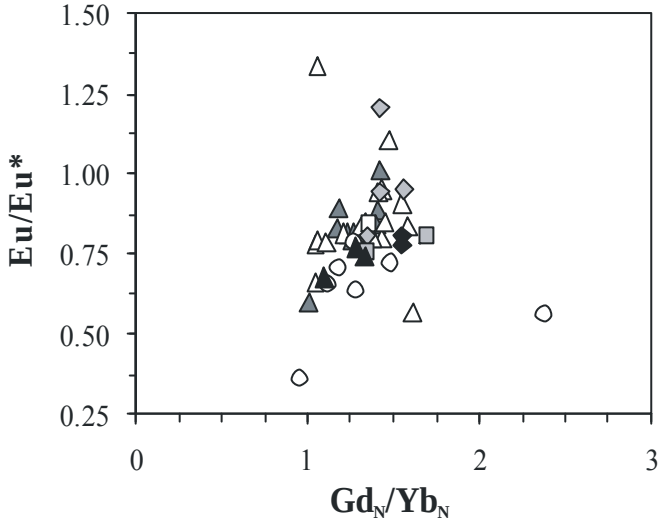

Fig. 3.12. Calculated Eu/Eu* versus Gd_N/Yb_N values for the Yax-1 impactites and selected Tertiary and Cretaceous rocks. Notice that besides 3 samples all Eu/Eu* values fall below 1.0, indicating to Eu depleted target rocks. The Gd_N/Yb_N ratio falls primarily between 1 and 2, indicating to the enrichment of normalized Gd versus normalized Yb, as seen for all samples in Fig 11 ($Eu/Eu^* = Eu_N/(Sm_N \times Gd_N)^{0.5}$, values <0.95 indicate depletion, >1.05 indicate enrichment, Gd_N/Yb_N = chondrite-normalized Gd over Yb abundances), refer to Fig. 3 for legend.

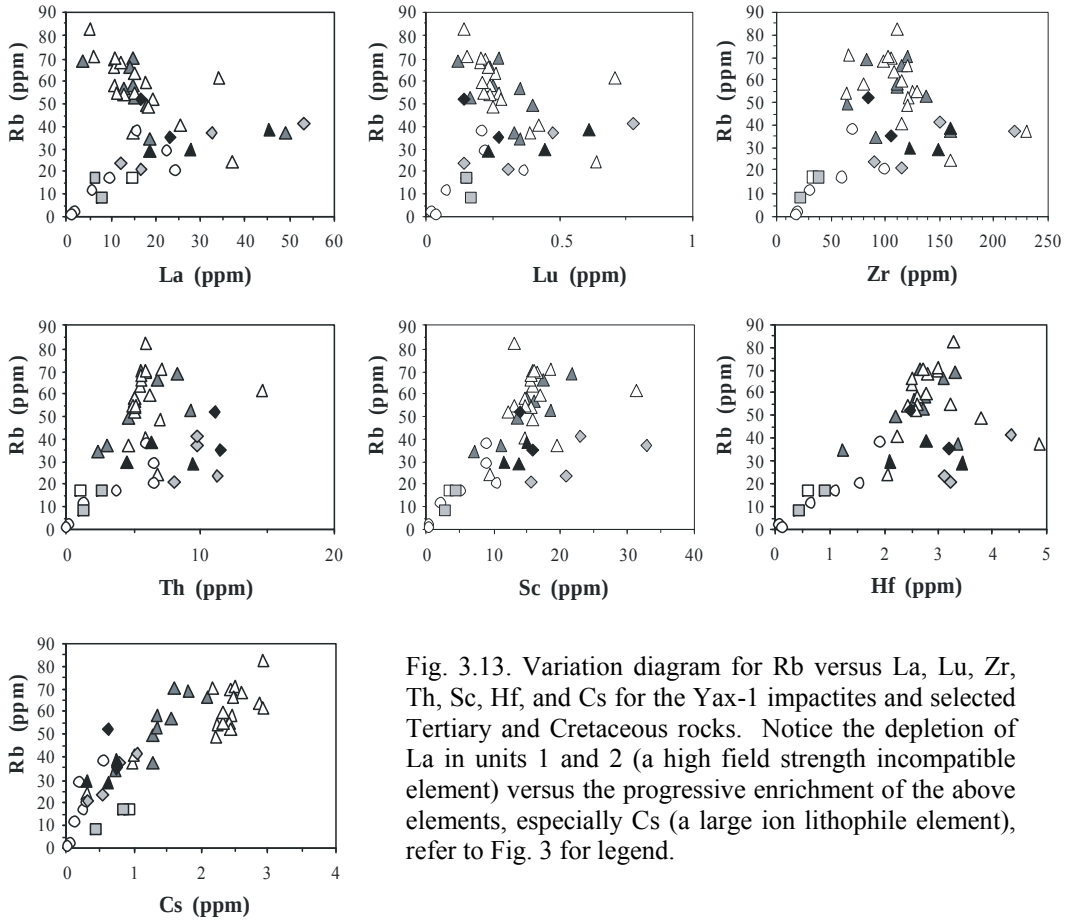

Fig. 3.13. Variation diagram for Rb versus La, Lu, Zr, Th, Sc, Hf, and Cs for the Yax-1 impactites and selected Tertiary and Cretaceous rocks. Notice the depletion of La in units 1 and 2 (a high field strength incompatible element) versus the progressive enrichment of the above elements, especially Cs (a large ion lithophile element), refer to Fig. 3 for legend.

proportional increase of the abundances of these elements in Unit 1 and 2 (Fig. 3.13).

All samples have been analyzed for siderophile element abundances, i.e., those of Cr, Co, Ni, Ir, and Au. The concentrations of these elements are slightly elevated when compared to the concentrations of the Tertiary and Cretaceous limestone samples. However, silica-rich impactites, or those that contain a mixture of silica and carbonate, produce siderophile element concentrations that are rather uniform throughout the impactites interval (compare Appendix A.5 with Tale 3.2). All iridium results by INAA fall below the detection limit. Precisely determined Ir abundances by the γ-γ technique are presented in Table 3.3. It can be seen that the analyses do reveal some variation in the Ir abundances, ranging from approximately 92 to 400 ppt. For comparison with the Ir abundance of carbonate-rich samples, the single analyzed Cretaceous carbonate-rich lithic breccia (sample 41) contains 100 ppt Ir.

Table 3.3. Iridium abundances for impactites and one Cretaceous rock of the Yaxcopoil-1 borehole, Chicxulub impact structure.

Sample No.	Units	Description	Depth (m)	Ir (ppt)
2	1	Reworked suevite	800.4	250 ± 31
13	1	Reworked suevite	811.6	<162
14	1	Reworked suevite	815.8	<233
15	1	Reworked suevite	816.6	<242
23	2	Suevite	825.4	<229
25	2	Suevite	835.1	<274
43	2	Brown melt particle	840.3	<257
28	2	Suevite	844.8	132 ± 23
45	3	Brown melt particle	860.0	<241
32	4	Green impact melt breccia	875.8	<168
46	4	Brown melt particle	879.0	92 ± 19
33	4	Green impact melt breccia	882.5	<103
38	5	Variegated polymict melt breccia/suevite	890.5	399 ± 39
42	Cretaceous Rock	Limestone lithic breccia	916.4	100 ± 20

3.5. Discussion

The impactite compositions reflect, primarily, mixtures of various components from the pre-impact target stratigraphy. This comprises an ~3 km thick carbonate platform on top of a lithologically varied metamorphic crystalline

basement of Pan-African age (Ward et al. 1995; Krogh et al. 1993). Here we discuss the geochemical data for the Yax-1 impactites in order to help elucidate the characteristics of target lithologies, the degree of mixing of different target components, the alteration history, and the contamination from an extra-terrestrial source.

3.5.5. Compositional variation of the impactites units

It has been shown that the compositions of the Yax-1 impactites appear to be quite variable. However, when the major element and trace element data are recalculated on a CaO- and LOI-free basis (Fig. 3.4), they are actually quite uniform with respect to depth (Fig. 3.4). This suggests that the silicate component of the impactites has been relatively well homogenized (also compare average unit compositions, Table 3.2) and that the variability is largely a function of variable proportions of carbonate (a dilution effect). Evidence for homogenization of target rock material in impactites has been observed at many impact structures, as for example reviewed by Dressler and Reimold (2000).

The influence of the carbonate component on the Yax-1 impactites is also evident when comparing Harker diagrams for selected major elements versus SiO_2 (Fig. 3.6). Most major elements have a positive linear correlation with SiO_2 contents, with the exception of CaO and MgO that are primarily controlled by the presence of calcite and dolomite, respectively. The silicate fraction is primarily held by siliceous feldspathic melt particles and clastic silicates (Fig. 3.5b). The compositional heterogeneity of the impactites can be well discerned in Figure 3.7, which clearly illustrates the effect of carbonate-hosted Ca on the alkali elements and mafic components of the impactites. The range of alkali elements to the mafic component appears limited, in agreement with the interpreted homogenized silicate fraction seen in the recalculated data of Figure 3.4. This obvious relationship between the silicate and carbonate fractions is the result of mixing that occurred during and immediately after cratering, but also relates to post-depositional carbonate hydrothermal activity.

When analyses for the respective units are averaged, compositional uniformity is observed on the unit scale (Table 3.2). This is particularly valid for

units 1, 2 and 3, for which the resultant averaged compositions do not differ beyond the 2σ standard deviations. Unit 4 and the brown melt samples reveal some compositional similarities with respect to SiO_2, Al_2O_3, and the LOI; however, the brown melt contains comparatively lower abundances of FeO_{tot}, MgO, and Na_2O, and greater abundances of CaO and K_2O. Unit 5 shows the greatest compositional variability and is distinct from the remaining units in composition due to its inherently high carbonate and dolomite contents.

Our sulfur analyses (Appendix A.5) indicate that the Yax-1 impactite samples must be considered depleted when compared to estimated values of anhydrite in Cretaceous target rocks (Ward et al. 1995; Dressler et al. 2003). These results suggest that the subsurface target composition could be heterogeneously distributed or that anhydrite nearly completely devolatilized upon cratering (cf., Gupta et al. 2001; Osinski and Spray 2003). These results are in agreement with the low estimated anhydrite content derived for the source of Haitian yellow glasses (Blum and Chamberlain 1992).

The trace element results show much compositional variability. Generally, samples with high SiO_2 abundances contain the highest trace element concentrations. This indicates that the trace elements are primarily held within silicate, oxides, and phosphate-bearing accessory mineralogical phases, e.g., observed zircon, ilmenite, apatite, and barite. Chondrite-normalized REE abundances also reveal the wide compositional variability found within the Yax-1 impactites (Fig. 3.10). Our results indicate that the varied impactite REE compositions are a reflection of the subsurface target rock compositions and that the impactites represent variable mixtures of these components.

3.5.6. Secondary alteration

Secondary alteration effects on the impactites of the Yax-1 borehole have been extensively described and a multi-stage paragenetic sequence has been determined to comprise: (1) Na–Ca exchange between primary feldspars, (2) extensive K-metasomatism of melt and lithic fragments, (3) chloritization of pyroxenes, amphiboles, and more mafic melt fragments, (4) conversion to phyllosilicates of chlorite, and (5) late calcite veining or carbonatization (Zurcher

et al. 2003; Hecht et al. 2003; Kring et al. 2003b). Kring et al. (2003b) also described variation of hydrothermal alteration with depth in the borehole: from top to bottom of the sequence, a decrease of Na concomitant with an increase of Ca exchange. As demonstrated in Figs 3.3 and 3.4, we observe similar trends between the alkali elements, i.e., increasing elemental abundances with depth towards Unit 4. These trends coincide with our observation of (in thin section) decreasing proportions of orbicular perlitic fractures, the uniformly decreasing amount of devitrification, and the increasing microlite content of melt particles with depth (cf. Table 3.2, Tuchscherer et al. 2004). We suggest that these petrographic observations can be attributed to the interaction of hot rocks with water (Ross and Smith 1955), rapidly cooling the upper impactite units. The major element analyses also allow us to suggest that a significant fluid to rock ratio affected the upper units, preferentially leaching soluble alkali elements from melt particles and clastic mineral fragments. As a consequence of this effect, alkali elements are especially depleted in Unit 1 and the total iron content is observed to increase with height compared to samples from units 2 to 4. This effect is most likely the product of the greater solubility of alkali elements versus iron typically associated to weathering (Nesbitt and Young 1984).

Detailed petrographic observations were initially interpreted to suggest that the impactites had undergone a substantial K-metasomatism (Ames et al. 2003; Hecht et al. 2003; Zurcher et al. 2003; Kring et al. 2004b; Tuchscherer et al. 2004). Our K abundances throughout this interval are variable between ca. 0.2 and 4.5 wt%. Unit 1 seems to be slightly depleted in comparison to the other units (Fig. 3.3). In order to determine any possible exchange of K for Na and/or Ca, a plot of K_2O/CaO versus Na_2O/CaO was generated (Fig. 3.8). The data show a relatively linear correlation, indicating that the proportions of K to Ca and Na to Ca have remained constant, i.e., no alkali element or CaO exchange is supported.

In order to better understand the weathering/alteration of the impactites, the Chemical Index of Alteration (CIA) of Nesbitt and Young (1982) has been calculated for each major element analysis (Appendix A.5). It can be seen that Unit 1 samples yield the highest average CIA value, whereas units 2, 3, and 5 show similar values within 2σ statistical limits (Table 3.2). The green impact melt

unit (Unit 4) and brown melt samples also produce fairly constant values, slightly lower than the value from Unit 1. These results indicate that Unit 1 has been subjected to the most intense alteration of all the impactites. With regards to the possible K-metasomatism previously inferred, for example, in the form of secondary adularia observed in thin section throughout the impactite interval (e.g., Hecht et al. 2003), no distinct mass exchange can be noticed in the bulk rock geochemistry. This suggests that alteration was essentially isochemical at our bulk sampling scale, i.e., the K-exchange was limited to the sub-centimeter scale.

Among the trace elements, obvious trends can be observed for the following elements: Cr, Zn, Rb, Cs, Ba, Au, and U. Chromium, Zn, Rb, Cs, and Au decrease in abundance with depth, whereas Ba and U contents increase. These trends suggest that the upper and lower portions of the impactite sequence, namely units 1, 2, and 5 have been most affected by hydrothermal conditions. A plot of Rb versus La and Rb versus Cs abundances illustrates the preferential accumulation of these LIL incompatible elements in units 1 and 2 (Fig. 3.13). Because of their large ionic radius, it is suggested these elements preferentially accumulate in secondary phyllosilicate phases during weathering (Kronberg et al. 1979; Taylor and McLennan 1985). The uniformly green color of the melt particles is, thus, due to the presence of illite/smectite/sepiolite phyllosilicate phases that formed from the conversion of melt particles as a result of fluids. We indicate that these results are in agreement with the geochemical investigation of Kettrup et al. (2000) and Kettrup and Deutsch (2003), who indicated that the Rb/Sr isotopic system was reset by hydrothermal alteration. It is interesting to note that the abundances of Rb, when plotted against La, Lu, Zr, Th, Sc, and Hf, are progressively enriched in units 1 and 2. However, the specific groupings observed in the Rb versus Cs plot is not observed. This may indicate that these elements progressively behave in a similar fashion to the large ion lithophile elements, Cs and Rb, i.e., being progressively more immobile but due to increasing ionic charge effects instead of large radii.

We attribute the high Ba concentration of Unit 5 to high modal barite abundance (Tuchscherer et al. 2004). Barite deposition has been associated with hydrothermal activity, as this mineral is typically observed as authigenic vug

infillings (e.g., Zurcher et al. 2003a; Kring et al. 2003a). In the presence of even low concentrations of aqueous sulfate, Ba is insoluble and is precipitated as barite (e.g., Huston and Logan 2004). Thus, the presence of barite indicates oxidizing conditions in seawater-dominated fluids/brines. The precipitation of such minerals under hydrothermal conditions led to changes in the redox conditions (and the pH), which can also help to explain the high Mn and U abundances in samples of Unit 5 due to the redox chemistry of U (e.g., McLennan and Taylor 1980; Greinert et al. 2002).

3.5.7. Comparison with other impactites from Chicxulub

In order to investigate the possible target components for these impactites, our results have been plotted on a (K_2O+Na_2O) – CaO – (FeO_{tot}+MgO) ternary diagram (Fig. 3.7, modified from Kettrup and Deutsch 2003). The Yax-1 impactites display a range in compositions corresponding to variable mixtures of carbonate with mafic and felsic target rock components such as felsic gneiss and diorite/amphibolite. It is interesting to note that the observed Yax-1 impactite trend is different from that for the melt breccia samples of the Y6 borehole (Kettrup et al. 2003). These impact breccias follow a linear trend where the alkali element abundances are variable, with uniform proportions of CaO and FeO_{tot}+MgO. This suggests that melt samples from the Y6 borehole correspond to a different mixture of target rocks from the Yax-1 impactites, i.e., admixing of supracrustal carbonate does not seem to be as important for the Y6 melt breccias (see Kettrup and Deutsch 2003). This observation, however, may be a biased result due to the limited sampling of the Y6 borehole, as Claeys et al. (2003) report binary mixing relationships of major elements versus SiO_2 for Y6 samples that are similar to our results and those of Stöffler et al. (2003) for Yax-1 samples.

3.5.8. Extraterrestrial component

Only two geochemical studies have so far attempted to constrain an extraterrestrial component in the Yax-1 impactites. Tagle et al. (2003) analyzed the contents of the platinum group elements and found no or only very little enrichment compared to the contents in upper crustal terrestrial rocks, and Gelinas

et al. (2003) studied the Os isotopic compositions of Yax-1 samples. Isotopic analyses using the highly sensitive $^{187}Os/^{188}Os$ system by Koeberl et al. (1994) (see also Koeberl and Shirey 1997), as well as Ir analyses by Schuraytz et al. (1996), indicated the presence of a (extremely heterogeneous) extraterrestrial component in some melt rock samples of the C1 and Y6 cores. However, in Yax-1, Gelinas et al. (2003; and this volume) found variable ratios of $^{187}Os/^{188}Os$, with a few samples showing indications of a minor extraterrestrial component of significantly less than 1 wt%.

In this study, we analyzed the Cr, Co, Ni, Ir, and Au contents to investigate the possible presence of an extraterrestrial component in the Yax-1 impactites, but found only slightly elevated abundances of Cr, Co, and Ni in impactite samples in comparison with Cretaceous or Tertiary limestone samples – which is not sufficient evidence for the presence of an extraterrestrial component. The INAA Ir abundances are only two orders of magnitude greater than those of the Cretaceous carbonate target rocks, which suggests the Cr, Co, and Ni are mostly derived from a mixture of carbonates and crystalline basement components. The ICS analyses for Ir have much better detection limits and do show variable contents up to 0.4 ppb, which is significantly higher (by a factor of up to 50) compared to other suevite values and typical carbonates and crustal values. This agrees with data of Gelinas et al. (2004), who found Os contents of 0.01 to 0.4 ppb, and initial $^{187}Os/^{188}Os$ ratios of about 2.3 to 0.2, inversely correlated with the Os content. This clearly indicates the presence of a very small, heterogeneously distributed, but still measurable extraterrestrial component even in Yax-1 rocks (less than about 0.1 percent by weight of a chondritic component), which is, however, smaller than that found in C1 and Y6 samples. In contrast, the PGE data of Tagle et al. (2003) are not sensitive enough to allow the determination of the projectile type, which has, however, already been determined from ejecta analyses to be of carbonaceous chondrite type (Shukolyukov and Lugmair 1998).

3.5.9. Implications for cratering dynamics

The interpretation for the emplacement mechanism of the Yax-1 impactites cannot be solely based on geochemical results. Additional information from macro- to microscopic observations is required in order to establish a coherent and logical sequence of events. Here we discuss these geochemical results in unison with petrographic observations in support of a comprehensive emplacement model for these rocks.

Geochemical observations indicate that the alkali elements are depleted and the LIL elements are of high abundance in units 1 and 2, suggesting an interaction with water (Kronberg et al. 1979; Taylor and McLennan 1985, Figs 3.3, 3.4, and 3.13). These results are in agreement with our petrographic observations that indicate units 1 and 2 interacted with seawater, i.e., as observed by prominent orbicular fractures in melt particles, their lack of microlites, and their highly altered state. Based on these results and petrographic observations, we maintain our proposed interpretation for the origin of Unit 1 as a suevitic deposit that has been reworked by seawater. The evidence from petrographic observations indicates that this unit contains a characteristic foraminifera fossil content and a distinct clastic lithic carbonate component that may have been introduced from outside the impact basin. It is important to note that this clastic component is not observed in units 2 to 4. We also observed that melt particles are self-supported, subrounded, and are of a finer grain size compared to units 2 and 3. We, thus, propose this reworking was the product of high-energy aquatic activity instead of passive erosion, as 20 m of material is observed to have been redeposited (Fig. 3.2).

The high LIL element concentrations (Rb and Cs) found in units 1 and 2 (Fig. 3.13) indicate that despite being reworked or not, these units were extensively altered (Kronberg et al. 1979; Taylor and McLennan 1985). Because our dataset includes only three samples from Unit 3, we cannot conclusively determine the geochemical characteristics of this unit. However, samples from this unit do not reveal any increased Rb and Cs abundances, suggesting it has been relatively unaffected by hydrothermal fluids.

The similar major element compositions of units 1 to 3, within the 2σ confidence interval, are in support of our petrographic observations that indicate these units are of common origin as fallback deposits from a collapsing impact induced debris cloud. This is consistent with our petrographic observations that classify these rocks as suevites.

Our geochemical results for Unit 4 and the brown melt particles indicate a silicate-rich origin for these samples, as these compositions record the lowest CaO abundances, the lowest LOI values, and similar subdued REE profiles (no Eu anomalies) to sampled silicate inclusions. These results are in agreement with our petrographic observations that indicate Unit 4 and the brown melt particles represent impact melt that was almost wholly derived from the siliceous crystalline basement. For example, all lithic clasts are derived from siliceous, feldspathic-rich precursors.

Our geochemical observations indicate that Unit 5 samples have highly variable compositions and contain some of the highest CaO, MgO, MnO and U abundances (Fig. 3.2). This suggests that a large Cretaceous carbonate component could be involved (Koeberl 1993a; Dressler et al. 2003), that this unit was altered by post-impact hydrothermal activity, and that the carbonate and silicate fractions were poorly mixed, compared to units 1 to 3, during deposition. These results are in agreement with the suggestion that this unit represents an initial ejecta/groundsurge deposit (Stöffler et al. 2003a; Tuchscherer et al. 2004). Petrography confirms the origin of hydrothermal barite and a characteristic Cretaceous poorly distributed carbonate lithic component.

3.6. Summary and conclusions

The main results from major and trace element analysis of Yax-1 impactite samples include: The highly variable composition of this sample suite can be attributed to 1) the compositionally heterogeneous pre-impact stratigraphy that comprises an ~ 3 km thick carbonate platform overlying a siliceous crystalline metamorphic terrane, and incomplete mixing thereof; 2) the small sample size, 3) the variable grain or melt particle size, and 4) post-depositional alteration processes.

The variable composition of the Yax-1 impactites is primarily the result of variable mixing between a carbonate component and the silicate fraction during cratering and also by the effects of post-impact hydrothermal activity. This variability is observed in both major and trace element content, i.e., the silicate and carbonate contents are negatively correlated and the REE are diluted by the carbonate fraction.

Secondary processes have been discerned and contribute to the compositional heterogeneity of the impactites, especially as in the case for hydrothermal carbonate. It is suggested that secondary processes were also responsible for the redistribution and removal of alkali elements and enrichment of iron in Unit 1. The LIL elements, Cs and Rb, and several compatible elements, Cr, Zn, Au, are observed to occur in greater abundances in units 1 and 2. This is attributed to a high fluid/rock interaction in units 1 and 2. In Unit 5, anomalous U and Mn abundances are believed to be characteristic of Cretaceous evaporitic carbonate rocks or correspond to high Ba concentrations that are attributed to hydrothermal authigenic barite crystal growths. Despite the extensive petrographic observation indicating to a K-metasomatic event, our geochemical data do not reveal any strong substitution of K for Na or Ca. This indicates that K redistribution occurred at a scale of less than sample size, unlike, for example, at the Kärdla crater, where a distinct K-feldspar enrichment was observed exchanging for Ca and Na feldspars (see Puura et al. 2004).

Average major and trace element contents indicate that units 1 to 3 are of similar composition. The composition of Unit 4 and the brown melt particle samples suggests that these impact melt rocks formed from fused Yucatán crystalline basement. The more mafic composition of Unit 4 samples suggests they involved a comparatively larger mafic component than the brown melt particles and suevitic samples. The lowermost unit, Unit 5, reveals the greatest compositional variability and represents a mixture of supracrustal carbonate with siliceous melt particles that underwent secondary hydrothermal alteration (anomalous U concentrations).

Our Cr, Co, Ni, and Ir data do not allow unambiguous identification of an extra-terrestrial component, although Ir values of up to 0.4 ppb were found. This

agrees with Os abundance and isotope data of Gelinas et al. (2004), which can be interpreted to indicate the presence of a small (<0.1 wt%) and heterogeneously distributed chondritic component.

These geochemical results, in combination with detailed petrographic observations (cf., Tuchscherer et al. 2004), support the interpretation of units 1 to 3 as fallout suevite, with units 1 and 2 having been influenced by a hydrothermal overprint. Unit 4 is suggested to have originated as an impact melt derived entirely from the crystalline basement but is of a more mafic composition that brown melt particles. The lowermost unit, Unit 5, displays the greatest compositional variability. It contains a distinct dolomitic component (high MgO) and was also subjected to hydrothermal activity as indicated by the anomalous Mn, U, and Ba concentrations.

3.7. Acknowledgments

We would like to gratefully acknowledge the comprehensive financial support that this project has received from a Petroleum Research Fund grant (PRF # 37299-AC8) of the American Chemical Society. Two anonymous reviewers are also thanked for their concise and helpful comments. Funding for CK's work was obtained from the Austrian Science Foundation project Y58-GEO. This work forms part of a Ph.D. thesis by M.G.T. This is University of the Witwatersrand Impact Cratering Research Group Contribution No. 81.

4. Geochemical and petrographic characteristics of impactites and Cretaceous target rocks from the Yaxcopoil-1 borehole, Chicxulub impact structure, Mexico: implications for target composition[3]

4.1. Abstract

We present major and trace element data, as well as petrographic observations, for impactites (suevitic groundmass, bulk suevite, and melt rock particles) and target lithologies, including Cretaceous anhydrite, dolomite, argillaceous limestone, and oil shale, from the Yaxcopoil-1 borehole, Chixculub impact structure. The suevitic groundmass and bulk suevite have similar compositions, largely representing mixtures of carbonate and silicate components. The latter are dominated by melt rock particles. Trace element data indicate that dolomitic rocks represented a significant target component that became incorporated into the suevites; in contrast, major elements indicate a strong calcitic component in the impactites. The siliceous end-member requires a mafic component, in order to explain the low SiO_2 content. Multi-component mixing of various target rocks, the high alteration state, and dilution by carbonate complicate the determination of primary melt particle compositions. However, two overlapping compositional groups can be discerned - a high-Ba low-Ta group and a high-Fe, -Zn, and -Hf group.

Cretaceous dolomitic rocks, argillaceous limesone, and shale are typically enriched in U, As, Br, and Sb, whereas anhydrite contains high Sr contents. The oil shale samples have abundances that are similar to the North American Shale Composite (NASC), but with a comparatively high U content. Clastic sedimentary

[3] Tuchscherer M. G., Reimold W. U., Koeberl C., and Gibson R. L. 2005. Geochemical and petrographic characteristics of impactites and Cretaceous target rocks from the Yaxcopoil-1 borehole, Chicxulub impact structure, Mexico: implications for target composition: Meteoritics & Planetary Science 40:1513-1536.

rocks are characterized by relatively high Th, Hf, Zr, As, and Sb abundances. Petrographic observations indicate that the Cretaceous rocks in the Yaxcopoil-1 drill core likely register a multi-stage deformation history that spans the period from pre- to post-impact. Contrary to previous studies that claimed evidence for the presence of impact melt breccia injection veins, we have found no evidence in our samples from 1347-1348 m depth that would support this possibility. Instead, we suggest that these breccia veinlets occur in a sheared and altered zone that underwent intense diagenetic overprint prior to the impact event.

4.2. Introduction

Chicxulub (Yucatán Peninsula, Mexico) is the Earth's third largest known impact structure (Grieve and Therriault 2000). Its formation is widely accepted to have been responsible for the dramatic environmental changes at the Cretaceous/Tertiary (K/T) boundary (e.g., Hildebrand et al. 1991; Swisher et al., 1992; Blum et al. 1993; Ryder et al. 1996; papers in Koeberl and McLeod 2002). Because of its great scientific importance for the understanding of impact cratering processes in general and those related to the K/T mass extinction in particular, the structure was recently drilled by the International Continental Scientific Drilling Program (ICDP; see Dressler et al. 2003). The resulting Yaxcopoil-1 (Yax-1, Fig. 4.1) drill core contains a ca. 100 m long, continuous section of impact breccias. Impactite samples are of particular interest, as they can provide constraints on the pressures and temperatures experienced by target rocks and can give clues to the mode of impactite formation and deposition during impact cratering. Chemical analysis of impactites also constrains mixing between the various target rocks and the bolide, and provide information on post-impact alteration processes.

The major and trace element compositions of target rocks and their contribution to the various units of the Chicxulub impactites, as well as of the suevitic groundmass, bulk suevite, and melt rock particle fractions, are the prime focus of this paper. This work was done in order to constrain the dominant geochemical components that are part of the impactite composition and to investigate their distribution and mixing throughout the interval. As part of our

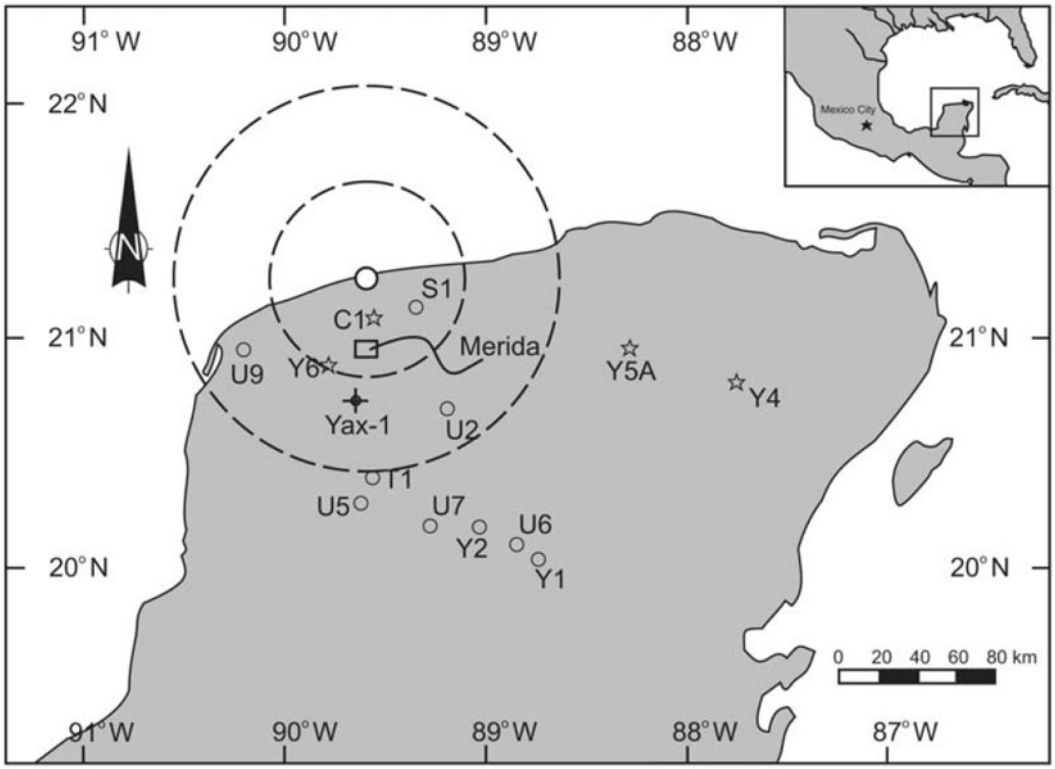

Fig. 4.1. Location of the Yaxcopoil-1 (Yax-1) and other boreholes within and around the Chicxculub impact structure on the northeastern segment of the Yucatán Peninsula of Mexico. Boreholes mentioned in the text are shown as stars. The innermost dashed circle represents the inferred extent of the initial transient cavity as postulated by Morgan et al. (2002). The outer dashed circle represents the estimated crater edge (rim), as determined by seismic surveying of the outermost inward facing scarp (Morgan et al. 2002).

investigation of the Cretaceous section below the impactite interval, crystalline veinlets in the 1347-1348 m depth interval were investigated with regard to their possible origin as impact melt.

4.3. The Yaxcopoil-1 borehole

Drilling into the Yucatán subsurface extended to a depth of 1511 m and intersected approximately 795 m of post-impact Tertiary carbonate rocks, 100 m of impactites, and 615 m of pre-impact Cretaceous rocks (Fig. 4.2). The impactites are composed of suevitic and impact melt breccias, both of which have undergone significant alteration (Dressler 2004; Ames et al. 2004; Kring et al. 2004b; Hecht et al. 2004; Kenkmann et al. 2004; Schmitt et al. 2004; Stinnesbeck

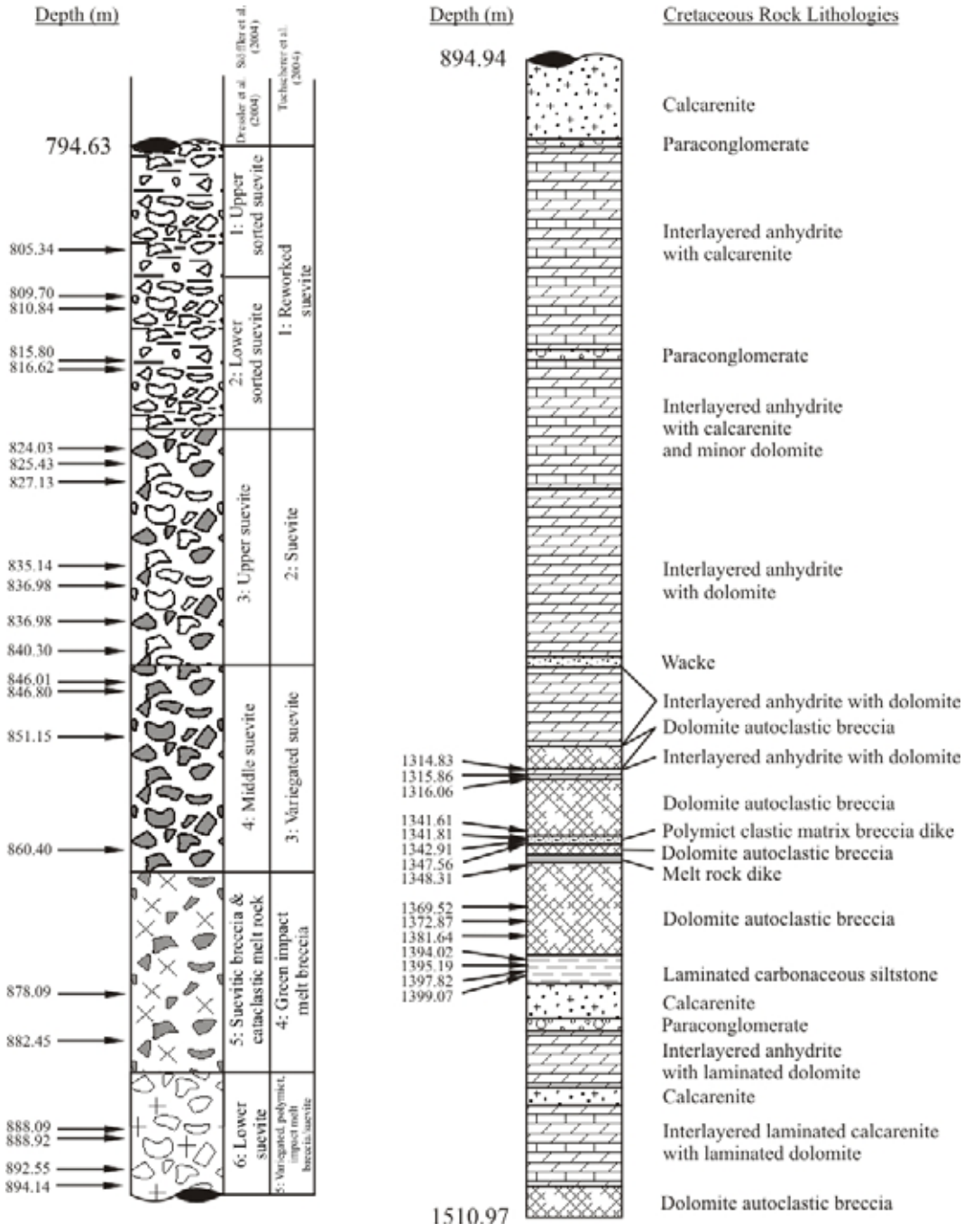

Fig. 4.2. Core-log and stratigraphy of the Yaxcopoil-1 borehole, with depths of samples used in this study. The stratigraphic subdivisions after Dressler et al. (2004), Stöffler et al. (2004), and Tuchscherer et al. (2004) are also shown and juxtaposed to the log.

et al. 2004; Stöffler et al. 2004; Wittman et al. 2004; Zurcher et al. 2004). While most research groups have adopted the original six-fold impactite stratigraphy of Dressler et al. (2003) (compare Fig. 4.2), we subdivide the Yax-1 impact breccias into five units based on macro- and microscopic observations (according to Tuchscherer et al. 2004a).

The uppermost Unit 1, between 795 and 823 m, is defined as a reworked suevite deposit that contains foraminifera and lithic carbonate clasts with numerous self-supported melt rock particles. The melt particles are subrounded to subangular, green when palagonized, and contain distinct perlitic devitrification textures. A subtle coarsening of the lithic clasts and melt rock particles is noticed with depth. Similar to Unit 1, all Unit 2 (822.86 – 845.80 m) melt rock particles are altered green; pervasive conversion of glass and clastic components to phyllosilicates is characteristic of these units. Units 1 and 2 contain high abundances of the large ion lithophile (LIL) elements Rb and Cs. This alteration feature is typical of palagonized volcanic glasses (Staudigel and Hart 1983; Jercinovic et al. 1990). In contrast, Unit 3 (845.80 – 861.06 m) has variegated melt particles that are less altered. The groundmass of units 2 and 3 is rich in volatiles, silicon, and alkali elements and contains disseminated calcite grains (see Tuchscherer et al. 2004a, for more detail). The calcite grains have comparatively larger grain sizes towards Unit 3, possibly indicating a thermal effect from the underlying mass of green impact melt rock (Unit 4, 861.06 – 884.92 m). Similar metamorphism has also been observed in the so-called “lower suevite” of the Y-6 borehole (Claeys et al. 2003). Unit 4 represents a uniform green, brecciated, massive impact melt rock. It does not have the LIL element signature that characterizes the upper altered units, indicating its overall green color may represent its primary composition (see, e.g., Tuchscherer et al. 2004b). Geochemical investigations indicated this melt rock has a composition that is slightly more mafic than brown melt particles found in units 1 to 3, i.e., it contains more FeO_{tot}, MgO, but less CaO (Tuchscherer et al. 2004b). The impact melt rock has abundant microlites, small lithic and monomineralic clasts derived from the crystalline basement, and abundant fractures and veins filled with phyllosilicate. It also displays fluidal textures (schlieren). The lowermost unit, a variegated polymict impact melt breccia or suevite (Unit 5, 884.92 – 894.94 m)), comprises discrete siliceous melt particles that are fluidal to angular in shape. They are suspended in a fine-grained calcitic and dolomitic groundmass that could represent either authigenic carbonate or a crystallized impact melt (e.g., Dressler et al. 2004; Tuchscherer et al. 2004a).

The Tertiary rocks overlying the impactite sequence are composed of interlayered carbonaceous siltstones, calcarenite, and rare conglomerate and turbidite (Dressler 2002, pers. communication). The underlying (895 – 1511 m), presumably Cretaceous (Kenkmann et al. 2004; Stinnesbeck et al. 2004; Wittmann et al. 2004) rocks consist of anhydrite, dolomite, and argillaceous limestone, with small intervals of conglomerate (Fig. 4.2). Several breccia horizons have been observed at 909-910, 916, 1035-1036, and 1347-1348 m; lithic breccias at 1314-1316, 1341, 1398-1399 m; and black oil-bearing shale layers at 1350, 1369, 1372, 1382, 1394, 1397, 1399, 1420 m depths. Several thick, brittle deformation zones between 1310 and 1400 m and from 1496 to 1511 m have also been identified (Kenkmann et al. 2004; Stinnesbeck et al. 2004; Wittmann et al. 2004, for further background on the Cretaceous interval).

4.4. Samples

Thirty-six samples from the impactite interval and 27 samples from the Cretaceous interval (Fig. 4.2) were analyzed. This includes eight suevitic groundmass samples (from 825.43, 825.43, 827.13, 835.14, 836.98, 836.98, 888.92, and 892.55 m depths), 15 bulk suevite samples (from 2 x 805.34, 809.7, 810.84, 815.8, 816.62, 827.13, 846.01, 2 x 846.80, 2 x 851.15, 860.4, 888.09, and 894.14 m depths), 10 individual melt rock particles (from 809.7, 810.84, 825.43, 835.14, 840.3, 840.30, 851.15, 878.09, 882.45, and 892.55 m depths), and three lithic clasts (from 824.03, 888.09, and 888.92 m depths) from the impact breccia. The Cretaceous samples comprise one anhydrite (1314.83 m), 15 dolomite (1314.83, 2 x 1315.86, 2 x 1316.06, 1341.61, 1341.82, 1342.91, 1347.56, 2 x 1348.31, 1369.52, 1372.87, 1381.64, 1397.82 m), five argillaceous limestone and argillaceous dolomite (2 x 1381.64, 1397.82, 1398.25, 1399.07 m), four oil shale (1369.52, 1372.87, 1394.02, and 1397.82), and four dolomite plus oil shale (1369.52, 1381.64, 1395.19, and 1399.07 m) samples. The dolomite samples, in particular, originate from sections of massive dolomite between 1372.87 m and 1381.64 m, fractured dolomite from 1314.83, 1315.86, and 1369.52 m, and a monomictic dolomitic breccia from 1316.06 m. A polymict breccia was also sampled from an interval between 1341.82 and 1342.91 m, as well as a brecciated

blue-green alteration zone with anhydrite veining from the interval between 1347 and 1348 m.

Hand sample descriptions and some microscopic observations are summarized in Appendix A.1 to A.3, and selected images of off-cuts are also shown in Figure 4.3. The groundmass from Unit 1 could not be separated due to its clast-supported character (Fig. 4.3a). The analyzed bulk suevite samples have abundant but variable amounts of melt rock particles (Appendix A.2). This group of samples is green to variegated in color, depending on which unit the samples originated from. Examples are shown in Figs 4.3a, d, g, h, and j. Duplicate analyses were obtained for samples from 805.34, 846.80, and 851.15 m depths. Samples that have few melt particles are generally gray, and are dominated by the carbonate-rich groundmass (Figs 4.3c, e, and j).

Three individual clast samples, a finely laminated gneiss (Fig. 4.3b), a dolomitic limestone (Fig. 4.3h), and a granodioritic clast (Fig. 4.3i; lithologies classified according to hand sample observation), were separated from the suevitic groundmass. For petrographic characteristics of these inclusions, see Appendix A.1 and Tuchscherer et al. (2004a). Cretaceous rocks illustrated in Figure 4.3 include anhydrite (Fig. 4.3k), a highly brecciated dolomite (Fig. 4.3l), a thin oil-shale vein (Fig. 4.3m), and an argillaceous dolomite sample showing stylolitic dissolution texture (Fig. 4.3n).

4.5. Analytical methods

Trace element as well as major Na, K, and Fe abundances were obtained by Instrumental Neutron Activation Analysis (INAA, see Koeberl 1993b for methodology, precision, and accuracy details). Ten Cretaceous samples (one anhydrite, six dolomite, one oil shale, and two argillaceous limestone samples) were analyzed for their major element compositions by standard X-ray fluorescence spectrometry (XRF) at Setpoint Laboratories in Johannesburg, South Africa, whereas the remaining samples were too small to allow full major element analysis. For major element precision and accuracy values see Tuchscherer et al. (2004b). Sulfur contents were determined by direct combustion analysis using a LECO sulfur determinator SC132 instrument at the University of the Wit-

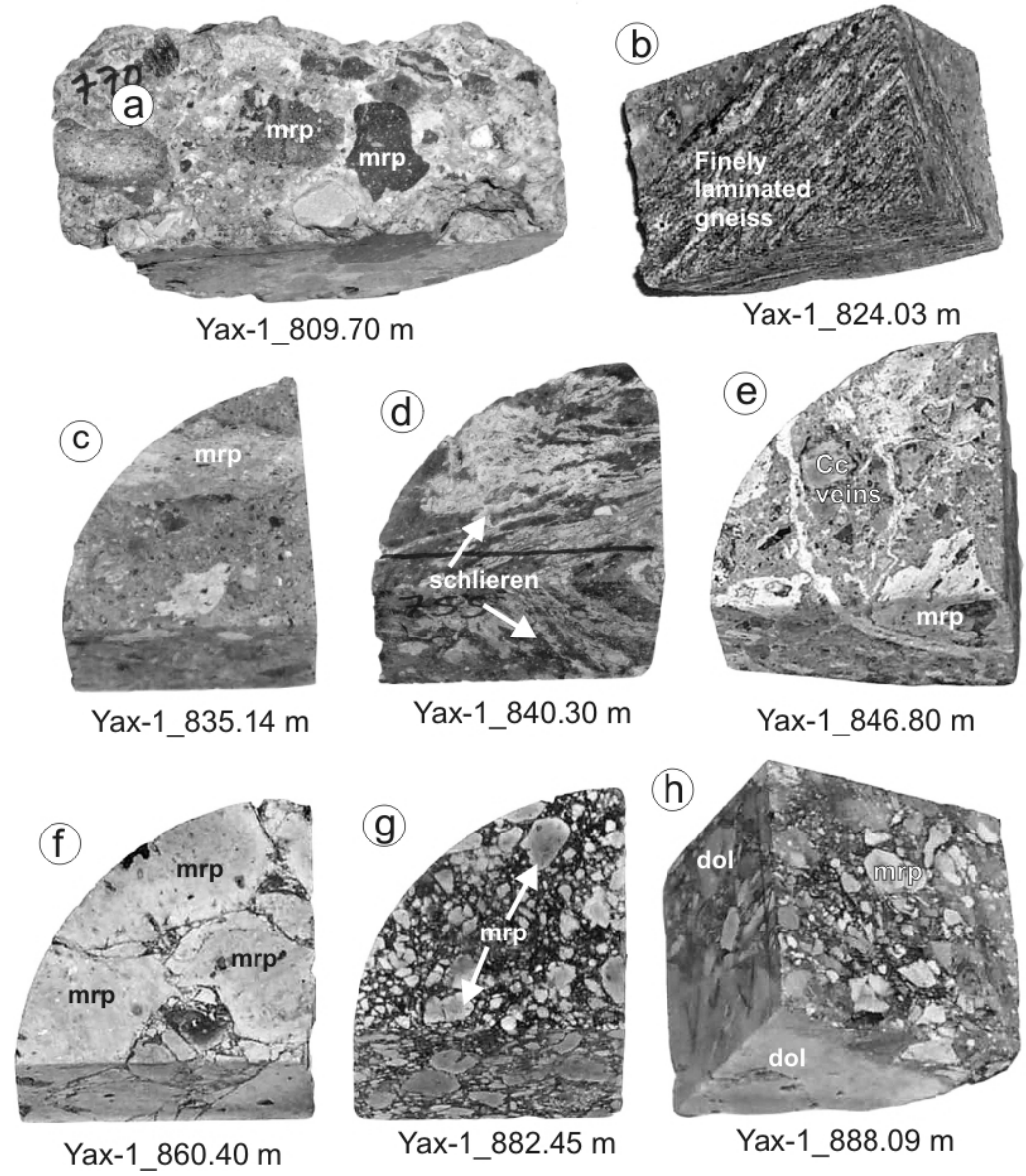

Fig. 4.3. Images of selected impactite samples used in this study. (a) Suevite of Unit 1 showing various reworked subrounded melt rock particles and lithic clasts of variable size that are self-supported (sample long axis = 6.35 cm). (b) A finely laminated gneiss clast suspended in suevitic groundmass of Unit 2 (sample long axis ~3 cm). (c) Unreworked suevite containing numerous melt rock particles of variable sizes and alteration state that are groundmass-supported. Melt rock particles show schlieren textures, are subrounded and elongate indicative of flow, Unit 2, core radius ~ 3 cm (d) A massive brown melt particle showing schlieren textures indicative of flow and incomplete mixing of felsic and mafic components. Small undigested lithic clasts of <0.5 cm size can be discerned suspended in the melt rock particle, Unit 2, core radius ~3 cm. (e) Unreworked suevite of Unit 3 containing variegated melt rock particles of variable sizes that are subangular to subrounded and are groundmass supported. Numerous calcite veins <0.5 cm wide cut across the groundmass (core radius ~ 3 cm). (f) A massive impact melt rock agglomerate from the bottom of Unit 3, similar to the massive impact melt rock of Unit 4. The dark veins are rich in phyllosilicate and calcite and represent individual melt particle boundaries (core radius ~ 3 cm). (g) Subrounded to rounded, melt particles suspended in a dark gray, fine-grained, calcite-rich groundmass from Unit 4 thought to represent an impact melt (core radius ~ 3 cm). (h) Various melt rock particles and lithic clasts that are subrounded and supported by a dark gray, calcite-rich groundmass from Unit 5 (core radius ~ 3 cm).

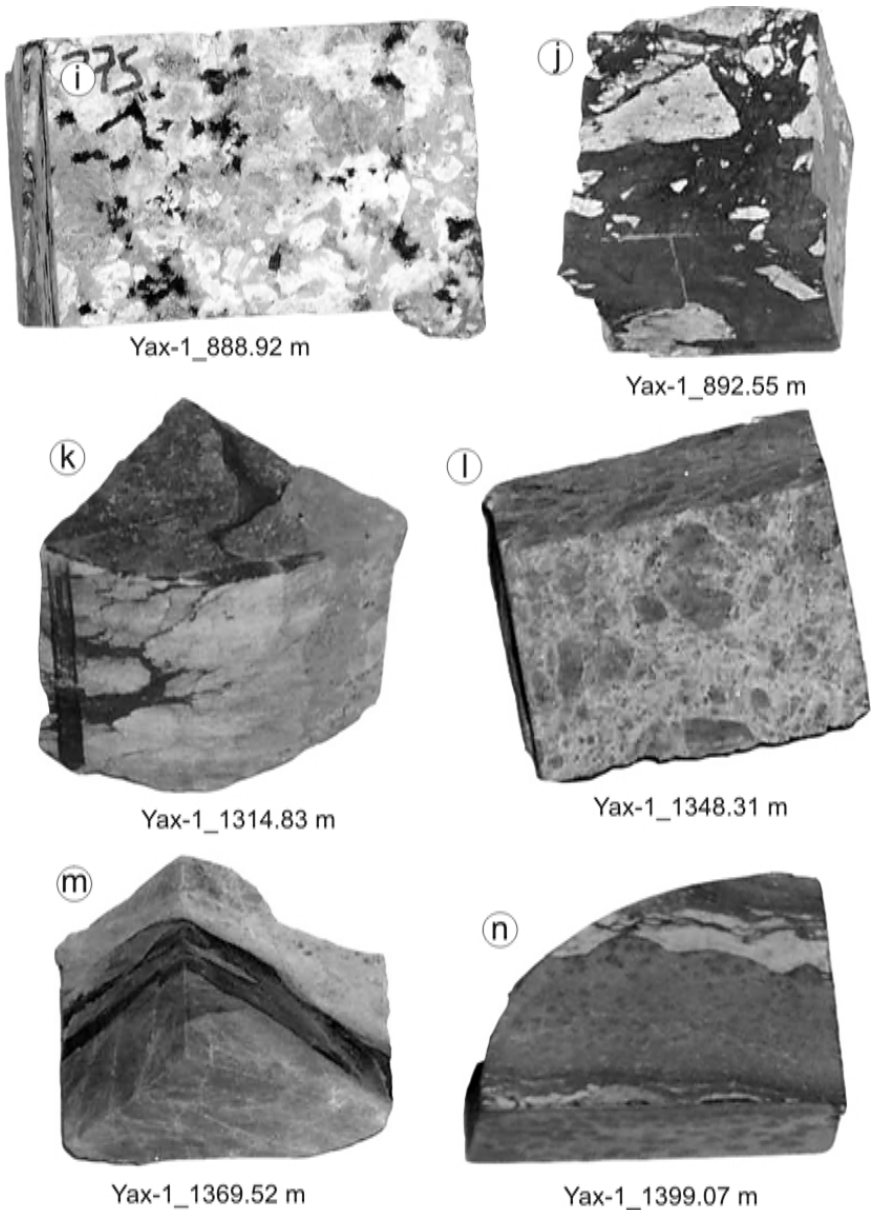

Fig. 4.3 *Continued*. (i) A medium-grained granodiorite clast from Unit 5 (sample long axis ~3 cm). (j) Groundmass supported angular melt particles of Unit 5. The groundmass comprises fine-grained calcite that may be an impact melt (sample width ~2.5 cm). (k) Anhydrite intergrown with phyllosilicates in dolomite (core radius ~ 3 cm). (l) Highly fractured and brecciated dolomite (sample long axis ~ 4 cm). (m) Thin oil shale horizon in dolomite (sample width ~ 4cm). (n) Argillaceous limestone with dissolution features (stylolite; sample long core axis ~ 3 cm). Abbreviations: anh = anhydrite, Cc = calcite, dol = dolomite, mrp = melt rock particles, os = oil shale.

watersrand (also see Tuchscherer et al., 2004b for details concerning methodology, precision, and accuracy). Scanning electron microscopy (SEM) was done at the Council for Geoscience, Pretoria, with a Leica 440 Stereoscan instrument equipped with a LINK OXFORD EDS X-ray analysis system operating at 20 kV and 2 nA working conditions at 25 mm working distance. Two

bulk sample powders from 1347.56 and 1348.31 m were also analyzed for their mineralogical content by X-ray diffraction (XRD) with the University of the Witwatersrand's Phillips PW 1710 instrument.

4.6. Calculation of end-member and Cretaceous target rock interval compositions

End-member compositions for the suevite section of the Yax-1 borehole were calculated by linear regression analysis of the major and trace element compositions of the impactites from the data of Tuchscherer et al. (2004b). This was done using the "LINEST" function in Microsoft Excel. The carbonate end-member of the Yax-1 impactites (denominated "CEMY") was derived by plotting all elements versus SiO_2, extrapolating a best-fit linear regression line for each element, and calculating the respective element abundance for a silica content of 4 wt%. This silica value was used, as it represents our best estimate of the average silica abundance of the Cretaceous target rock interval of the Yax-1 borehole (denominated "CTIY") and, thus, provides a good means for comparing all major and trace element abundances of carbonate-dominated and silicate components. The siliceous end-member of the Yax-1 impactites ("SEMY") was calculated by plotting all elements versus CaO, and extrapolating the best-fit linear regression line for each element, also based on the results of Tuchscherer et al. (2004b). The respective element abundances were then calculated for a CaO content of 5.2 wt%. This CaO value was used, as it is identical to the average CaO composition of Unit 4 and the CaO content in previously analyzed impact melt rock samples from other Chicxulub boreholes, e.g., from the C1 borehole (Sharpton et al. 1992; Kring 1997). Although higher CaO values have been reported for impact melt rocks from the Y6 and Yax-1 boreholes (Schuraytz et al. 1994; Claeys et al. 2003; Ames et al. 2004; Schmitt et al. 2004), we used the lowest published CaO abundances of bulk rock samples in order to provide a good SEMY composition. This is also done in order to reduce the diluting effects that any minor carbonate presence may cause. The calculated end-member compositions are listed in Table 4.1. Correlation coefficients (R^2), slopes (m), y-intercepts (b), respective least-

square standard errors, and y-estimate least-square standard errors for the elements plotted against SiO_2 and CaO are presented in Table 4.1.

An average composition for CTIY (Table 4.1) was estimated based on a detailed core log provided by B.O. Dressler (pers. commun., 2002) with the following lithological proportions: dolomite (63 vol%), anhydrite (27 vol%), and argillaceous limestone (10 vol%). The averaged dolomite composition from this work, two anhydrite analyses from Schmitt et al. (2004), and the average argillaceous limestone of this study were used.

4.7. Results

4.7.1. Petrography of Cretaceous Rocks

Petrographic observations were made on selected samples in order to understand the mineralogy and, thus, the compositions of the rocks. Detail on our Cretaceous samples is presented in Appendix A.2. In brief, anhydrite is grayish-white in hand sample (Figs 4.3k and 4.4) and has moderate birefringence under cross-polarized light. Crystals are usually tabular and elongate and some occur in seemingly fluidal arrangements. Grains can be up to 1 mm wide along crystal short axis. Dolomite is beige/brown in hand sample and shows very high birefringence. Crystals are typically fine-grained, <0.05 mm, but locally euhedral and of larger size (~0.2 mm), where they are found in association with phyllosilicates. Argillaceous dolomite samples are typically grayish-black and locally finely laminated. In such cases, dolomite crystals are very fine-grained and occur in dark-gray phyllosilicate.

The Yax-1 borehole is located in a major deformation zone that comprises a series of slumped blocks between 40 and 65 km from the crater center, as determined by seismic profiling (e.g., Morgan et al. 1997). Selected photographs of core samples from the intersected Cretaceous rocks show some characteristic deformation features. Figures 4.4a and b show several anhydrite samples from various depths that have fluidal textures that may be typical of solution collapse. The dolomitic host rocks and the anhydrite are not fractured (Fig. 4.4b). This may indicate that the rock is younger than the intense brecciation observed in dolomitic

Table 4.1. List of statistical (R^2, S.E.)† and equation variables (m, b)†, derived from linear regression analysis from all elements against SiO_2 and CaO, used when calculating the CEMY and SEMY end-member compositions.

	Values of R^2, S.E., m, and b (derived against SiO_2)						Values of R^2, S.E., m, and b (derived against CaO)						CEMY†	SEMY†	CTIY‡
	R^2	m	S.E.	b	S.E.	y-est.† S.E.	R^2	m	S.E.	b	S.E.	y-est.† S.E.			
SiO_2	n/a	n/a	n/a	n/a	n/a	n/a	0.96	-1.18	0.03	58.56	0.71	2.68	4.00	52.54	4.01
TiO_2	0.80	0.01	<0.01	-0.09	0.04	0.10	0.81	-0.02	<0.01	0.75	0.03	0.10	-	0.66	0.08
Al_2O_3	0.95	0.29	<0.01	-0.63	0.40	0.87	0.91	-0.34	0.02	16.42	0.33	1.25	0.44	14.68	1.14
FeO_{tot}	0.84	0.11	<0.01	-0.29	0.30	0.65	0.92	-0.14	0.01	6.36	0.13	0.48	0.16	5.65	0.69
MnO	0.44	-0.01	<0.01	0.28	0.04	0.08	0.43	0.01	0.01	-0.01	0.02	0.08	0.27	0.02	-
MgO	0.06	-0.02	0.02	5.34	0.62	1.36	0.01	0.01	0.02	4.16	0.37	1.39	5.51	4.23	13.62
CaO	0.96	-0.83	0.03	49.28	1.04	2.27	n/a	n/a	n/a	n/a	n/a	n/a	45.83	5.20	31.78
Na_2O	0.74	0.08	0.01	-0.36	0.29	0.64	0.66	-0.09	0.01	4.21	0.19	0.73	0.18	3.75	0.36
K_2O	0.73	0.06	0.01	0.10	0.23	0.50	0.66	-0.07	0.01	3.57	0.15	0.56	0.38	3.22	0.55
Cr_2O_3	<0.01	<0.01	<0.01	$2.2x10^{-3}$	0.01	0.02	<0.01	<0.01	<0.01	$4.6x10^{-3}$	<0.01	0.02	-	-	-
P_2O_5	0.03	<0.01	<0.01	0.02	0.05	0.12	0.01	-0.01	0.01	0.10	0.03	0.12	-	0.10	0.01
V_2O_5	0.14	<0.01	<0.01	$2.7x10^{-3}$	<0.01	0.01	0.09	-0.01	<0.01	0.01	<0.01	0.01	-	0.00	-
Cl	0.30	<0.01	<0.01	0.15	0.05	0.12	0.35	-0.01	<0.01	0.49	0.03	0.11	0.16	0.46	0.25
SO_3	0.01	<0.01	<0.01	0.03	0.02	0.04	0.01	-0.01	<0.01	0.04	0.01	0.04	0.03	-	14.30
L.O.I	0.96	-0.69	0.02	45.59	0.90	1.97	0.87	0.78	0.05	5.50	0.90	3.42	42.71	9.55	32.06
Total													99.67	100.06	98.85
Sc	0.59	0.38	0.05	-1.2	1.98	4.35	0.59	-0.45	0.06	21.4	1.16	4.39	1.33	19.1	2.60
Cr	0.35	0.98	0.20	1.3	8.24	18.1	0.40	-1.22	0.22	60.2	4.61	17.5	5.1	53.8	13.6
Co	0.55	0.15	0.02	1.03	0.83	1.81	0.54	-0.17	0.02	9.66	0.48	1.83	1.88	8.76	3.10
Ni	0.25	0.42	0.11	4.3	4.53	9.93	0.19	-0.43	0.13	27.9	2.72	10.3	7	28	10
Zn	0.41	1.46	0.26	-0.2	10.83	23.8	0.43	-1.76	0.31	86.5	6.18	23.4	12	77	8
As	0.06	-0.01	0.01	0.79	0.21	0.47	0.10	0.01	0.01	0.23	0.12	0.46	0.54	0.28	2.89
Se	0.03	<0.01	<0.01	0.1	0.077	0.17	0.03	-0.01	<0.01	0.3	0.05	0.17	0.2	0.3	0.3
Br	0.30	0.37	0.08	-1.7	3.48	7.63	0.26	-0.40	0.10	19.5	2.08	7.88	1.4	17.4	18.1
Rb	0.38	0.96	0.18	6.1	7.58	16.61	0.47	-1.25	0.20	64.5	4.07	15.4	12.2	63.2	7.7
Sr	<0.01	0.74	2.09	244	86.3	189.2	<0.01	0.59	2.46	264	49.9	188.9	291	267	551
Zr	0.47	2.40	0.38	7	15.7	34.39	0.44	-2.73	0.46	147	9.37	35.5	38	133	28
Sb	0.11	<0.01	<0.01	0.09	0.03	0.06	0.12	-0.01	<0.01	0.18	0.02	0.06	0.10	0.17	0.12
Cs	0.15	0.03	<0.01	0.31	0.39	0.86	0.24	-0.04	0.011	2.01	0.22	0.82	0.37	1.81	0.21
Ba	0.03	3.82	3.18	45	131.2	287.7	0.02	-3.06	3.78	246	76.6	290	108	230	22
La	0.18	0.37	0.12	3.2	4.81	10.54	0.13	-0.36	0.14	23.6	2.88	10.9	5.5	21.8	1.7
Ce	0.18	1.06	0.34	-5.5	14.2	31.15	0.16	-1.17	0.41	55.8	8.33	31.6	1.3	49.7	3.0
Nd	0.23	0.32	0.09	2.9	3.62	7.94	0.17	-0.32	0.11	20.6	2.17	8.24	4.6	18.9	1.9
Sm	0.18	0.06	0.02	0.61	0.80	1.76	0.13	-0.06	0.02	4.04	0.48	1.81	0.97	3.72	0.48
Eu	0.21	0.02	0.01	0.08	0.23	0.50	0.16	-0.02	0.01	1.14	0.14	0.52	0.19	1.04	0.10
Gd	0.17	0.06	0.02	0.68	0.81	1.78	0.13	-0.06	0.02	4.02	0.48	1.83	1.01	3.70	0.39
Tb	0.19	0.01	<0.01	0.11	0.12	0.27	0.14	-0.01	0.01	0.65	0.07	0.28	0.17	0.60	0.06
Tm	0.22	0.01	<0.01	0.07	0.06	0.14	0.18	-0.01	<0.01	0.37	0.04	0.14	0.09	0.34	0.04
Yb	0.16	0.03	0.01	0.62	0.44	0.97	0.12	-0.03	0.01	2.37	0.26	0.99	0.78	2.21	0.23
Lu	0.15	0.01	<0.01	0.09	0.07	0.15	0.12	<-0.01	<0.01	0.36	0.04	0.16	0.11	0.33	0.03
Hf	0.16	0.07	0.02	0.11	1.02	2.23	0.17	-0.09	0.03	4.36	0.59	2.22	0.18	4.39	0.50
Ta	0.30	0.01	<0.01	-0.02	0.11	0.24	0.29	-0.01	<0.01	0.64	0.06	0.24	0.08	0.57	0.09
Th	0.48	0.16	0.02	-0.41	1.03	2.27	0.44	-0.18	0.03	8.82	0.62	2.34	0.65	7.88	0.51
U	0.12	-0.02	0.01	1.66	0.29	0.64	0.13	0.02	<0.01	0.62	0.17	0.64	1.55	0.73	1.57

†Abbreviations: R^2 = correlation coefficient, S.E. = standard error, m = slope, b = y – intercept, y-est = y – estimate, n/a = not available, CEMY = Cretaceous end-member for the Yax-1 borehole, SEMY = siliceous end-member for the Yax-1 borehole, ‡CTIY = Cretaceous target rock interval of the Yax-1 borehole, Cretaceous interval calculated according to 27 vol% anhydrite, 63 vol% dolomite, 10 vol% calcarenite from the Dressler (2002) Yax-1 core log, ‡see methodology section for explanation, major elements are reported in wt %, trace elements reported in ppm.

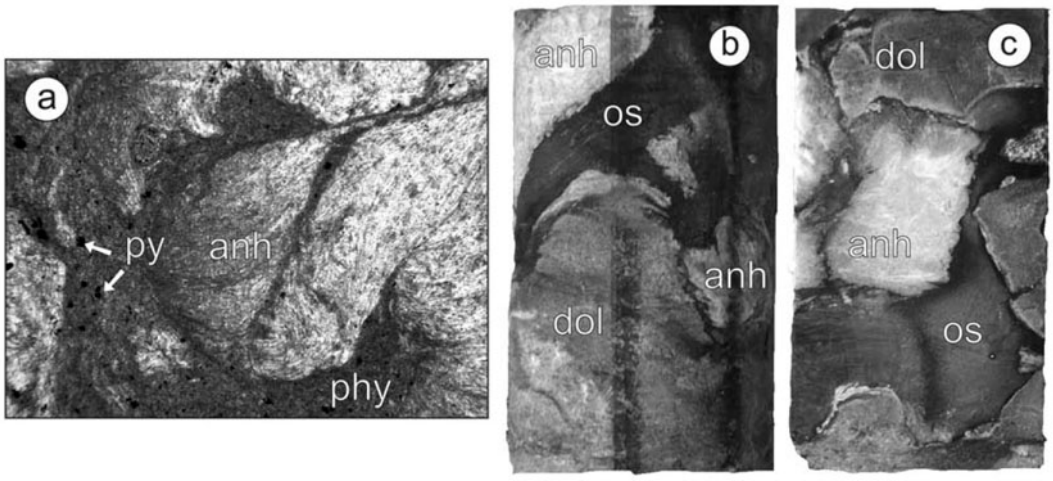

Fig. 4.4. Anhydrite in the Yax-1 borehole: a) Fluidal-textured anhydrite (anh) intercalated with phyllosilicates (phy). Note the disseminated pyrite (py) in the phyllosilicates. Sample depth = 1314.80 m, field of view ~4 mm (long axis), plane polarized light. b) Anhydrite interlayered with dark opaque oil shale (os) hosted by dolomite (dol); sample depth = 1394.02 m, core width = 6.35 cm (short axis). c) Blocky anhydrite and dolomite in oil shale groundmass; sample depth = 1394.12 m, core width = 6.35 cm (short axis).

rocks. The anhydrite sample shown in Fig. 4.4a (also Appendix A.1) displays crystals (<0.05 mm) that seem to be part of a fluidal pattern. Anhydrite is intercalated with a brownish mixture of dolomite and phyllosilicates, with some fine-grained, disseminated pyrite. The sample from 1394.02 m also shows this fluidal-textured anhydrite, but also has a black hydrocarbon vein (Fig. 4.4b). Figure 4.4c reveals anhydrite and dolomite clasts that are contained in an oil shale. Again, no extensive brittle fracturing, as seen in the dolomite, can be discerned. Thus, it is reasonable to interpret the occurrence of fluidal anhydrite (Figs 4.4a, b) and the anhydrite clasts in Figure 4.4c as the product of dissolution-related processes, in agreement with the observations of Stinnesbeck et al. (2004). However, we note that several-centimeter-thick monomictic breccias, with sharp contacts to the footwall that could be indicative of high strain rates unique to a single slip event typical of impacts (e.g., Kenkmann 2002) have been found in at least one massive anhydrite horizon at 1314.83 m. This indicates that not all anhydrite dissolution features post-date the pervasive brittle deformation event.

Massive dolomite intervals are common in the Cretaceous section. On a macroscopic scale, they are typically shattered and locally faulted (e.g., Figs 4.5a and b). This brittle deformation is observed as finely fractured dolomite crystals occurring along thin (0.2-1 mm) hairline fissures. Under the SEM (Figs 4.5c and d), fracturing is pervasive to the micrometer scale. No evidence for dissolution and recrystallization of the fine-grained dolomite is observed, at this scale, in this sample. However, fracturing may have enhanced the porosity of the rock, enabling the infiltration of K-rich fluids, as observed in the form of patches of secondary illite (as determined by XRD). This fracturing can be so pervasive that fine-grained, subrounded dolomitic fragments (Fig. 4.5c) may be suspended in a groundmass composed of smaller fragments of dolomite (Fig. 4.5d).

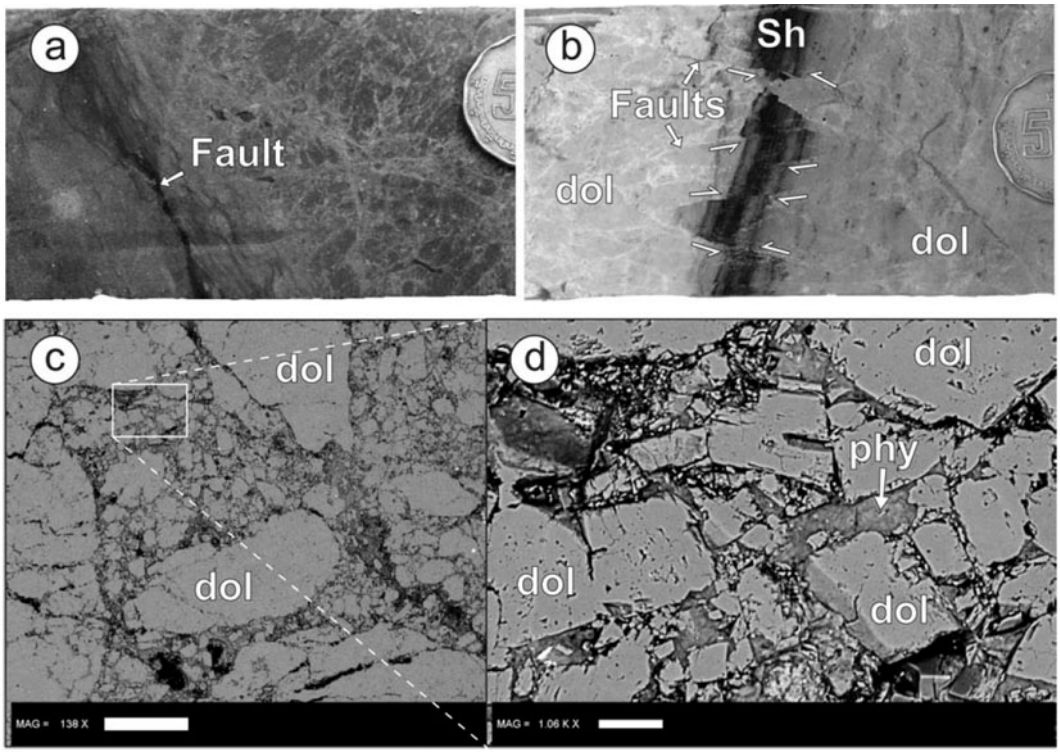

Fig. 4.5. Brittle deformation in dolomitic rocks: a) Highly fractured dolomitic rocks; sample depth = 1342.13 m, core width = 6.35 cm (short axis). b) Highly faulted shale (Sh) horizon bounded by shattered dolomite (dol); sample depth = 1315.86 m, core width = 6.35 cm (short axis). c) Backscattered electron image of brittle brecciated dolomite. Sample depth = 1348.30m, scale bar = 1 mm; d) Close-up of shattered dolomite in c); note the occurrence of phyllosilicates (phy) in interstices; scale bar = 50 μm.

A sample of the massive polymict clastic breccia carries fragments of various compositions and is bounded by a highly fractured dolomitic rock (Figs 4.6a and b). The breccia itself does not register any post-emplacement deformation. It comprises sub-angular fragments of anhydrite, dolomite, and argillaceous limestone or shale, and the groundmass consists primarily of similar, yet smaller, lithic fragments (Figs 4.6a and b).

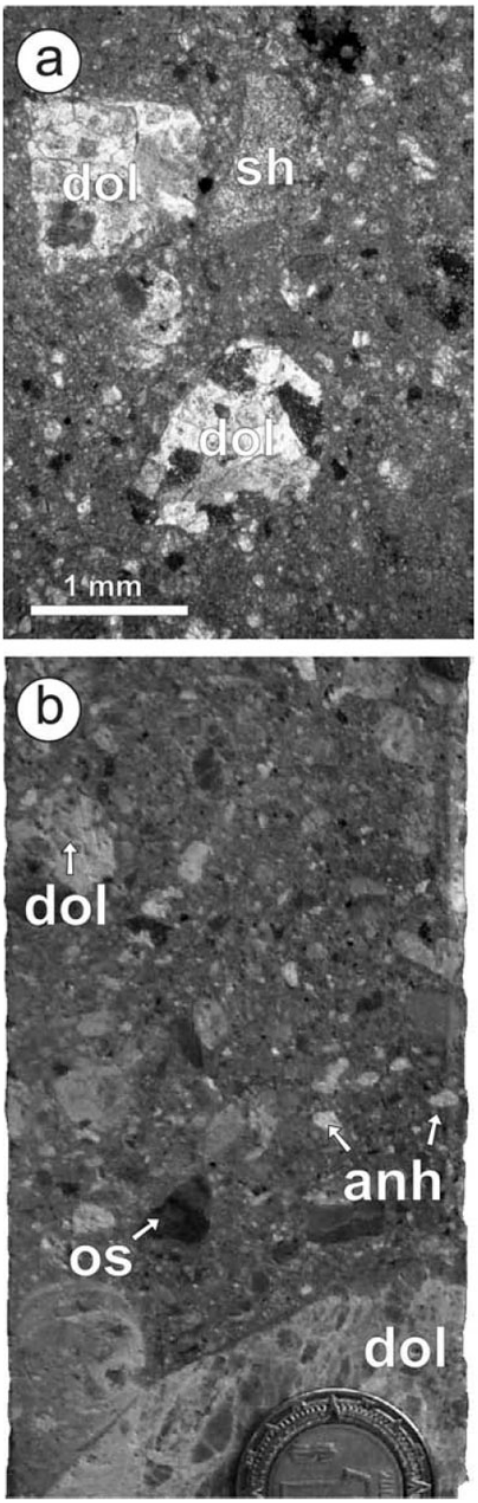

Fig. 4.6. Polymict lithic breccia from 1342.91 m depth; dol = dolomite, sh = shale, os = oil shale, anh = anhydrite. a) Microscopic image of the polymict lithic breccia dike; crossed polarizers, field of view ~4 mm (long axis); note the breccia nature of the groundmass and the heterogeneous composition of lithic fragments. b) Macrophotograph of the same breccia: note the heterolithic nature and subangular character of individual fragments; coin diameter = 2 cm.

Figure 4.7a reveals numerous fractures (outlined in white) and undulating discontinuities (stylolites) that cross-cut a dolomite, anhydrite, and phyllosilicate rich breccia. Associated with this interval is a highly brecciated dolomite that is pervaded by interstitial anhydrite (Fig. 4.7b). The brecciated alteration zone is characterized by an unusual blue color. Thin repetitive bands, that are blue in the actual hand sample, can be discerned in Fig. 4.7c. These bands are characterized by alternating concentrations of interstitial illite and dolomite (Fig. 4.7d). The occurrence of illite was determined by X-ray diffractometry on samples 219 and 226.

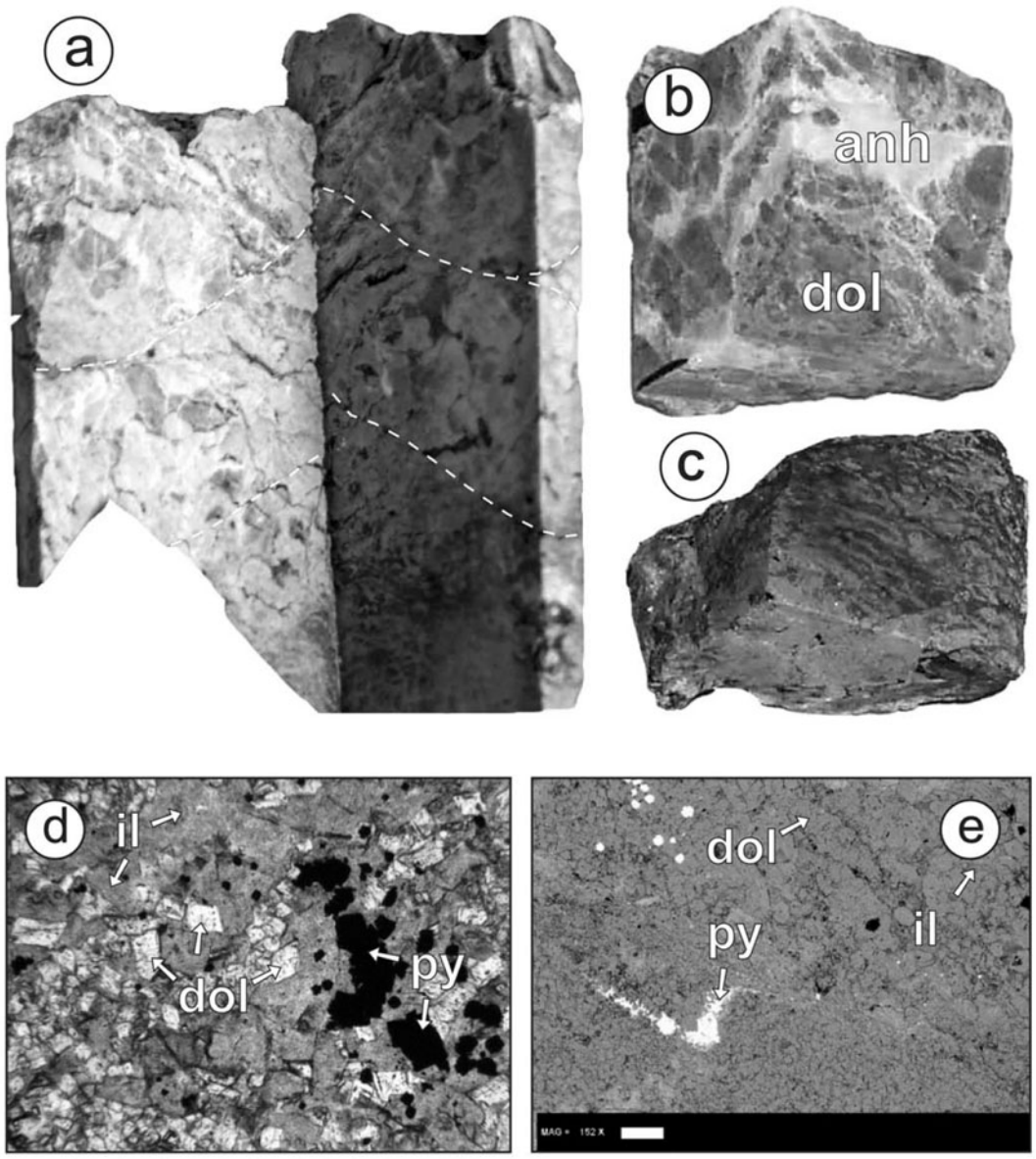

Fig. 4.7. Samples from the brecciated interval between 1347 and 1348 m: a) Macrophotograph of the halved core from 1347.5 m depth, showing the heterogeneous and fragmental nature of clasts within the interval. Dashed lines indicate fault zones; core width = 6.35 cm (short axis). b) Anhydrite (anh) veinlets pervading highly brecciated dolomite (dol) interval; sample depth = 1348.30 m, sample height and width is ~ 2 cm. c) Core off-cut showing fluidal, dark bands between lighter dolomitic layers. Sample depth = 1347.60 m, sample width ~ 3 cm (short axis). d) Microscopic image of the undulating, dark banded sample shown in Figure 4.7a**,** with illite (il) relationship with dolomite grains and euhedral pyrite (py) crystals; sample depth = 1347.60, field of view ~4 mm (long axis), plane polarized light. e) Backscattered electron image of very fine-grained dolomite with pyrite (same sample as in Fig. 4.7d). Towards the top-right, dolomite crystals are observed interspersed with phyllosilicate minerals. Sample depth = 1347.60 m; scale bar = 200 μm.

Euhedral crystals of pyrite and zoned dolomite are suspended in this groundmass (Figs 4.7d and e). The dolomite crystals pictured are characteristically euhedral and of the same size, i.e., planar and unimodal, or idiotopic (Warren 2000). The

characteristic zonation is defined by cloudy centers and clear rims. This texture is apparently typical of primary crystal growth at temperatures below 50 ^{o}C (Gregg and Sibley 1984). Our microscopic observations did not reveal any impact-related micro-features.

Several argillaceous limestone samples were analyzed from below 1381 m depth (Fig. 4.2). They contain small calcite crystals (~0.025 mm) intercalated with abundant phyllosilicate and opaques. Locally, black, oil-bearing veins truncate fresh samples of this argillaceous limestone. The oil-bearing horizons throughout the Cretaceous interval of the Yax-1 borehole vary in width from ~5 mm to 1 cm; examples are shown in Figures 4.8a-c. In hand sample, this material is very fine-grained, and locally it contains small, subangular dolomite fragments that could originate from the immediate host rock (Fig. 4.8b). SEM analysis shows that the veins contain disseminated euhedral adularia crystals and spherical pyrite framboids in a phyllosilicate matrix (Figs 4.8d and e). Such pyrite framboids are typical of kerogen-rich rocks such as oil shales (e.g., Combaz 1970), but also occur in sedimentary rocks formed in reducing environments (e.g., Wilkin et al. 1996; Butler and Rickard 2000). Each pyrite crystal is coated by a thin film of organic material, and the framboids may act as a trace element trap (Tissot and Welte 1978).

4.7.2. Impactite geochemistry

Major and trace element data of impactites are shown in Appendix A.6, and in Table 4.2 averages for the suevitic groundmass, bulk suevite, and melt rock particles are given. For comparison, the impactite carbonate and silicate end-member compositions, calculated according to the procedures outlined in the previous section, are shown in Figs 4.9 to 4.14.

The major elements Na_2O, K_2O, and FeO_{tot} show considerable compositional variation (Appendix A.6). The melt particles have the highest Na_2O, K_2O, and FeO_{tot} abundances, followed by the groundmass, and the bulk suevite samples (Table 4.2, Figs 4.9a, b). However, much overlap exists, especially for the Na_2O and K_2O abundances of the bulk suevite samples and groundmass fractions. The FeO_{tot} content of melt particles is well constrained, as

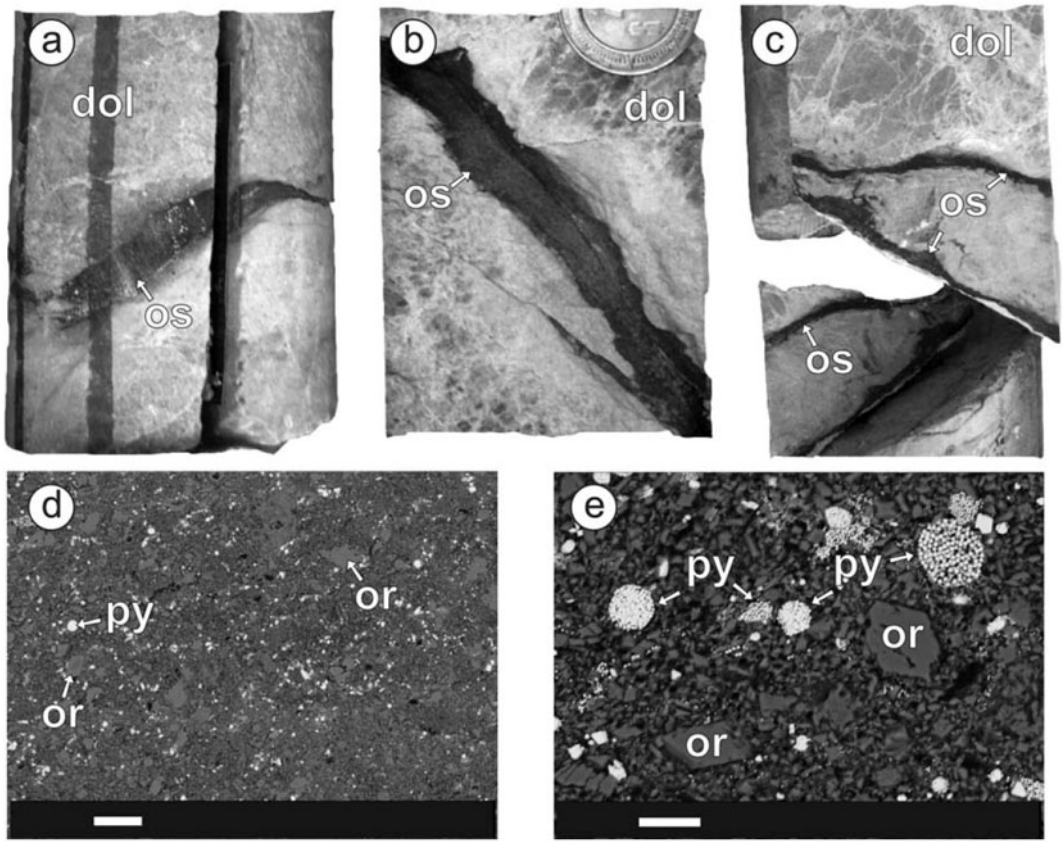

Fig. 4.8. Black, oil-bearing shale layers within the Cretaceous sequence of the Yaxcopoil-1 borehole: a) Undulating oil-shale (os) vein within dolomite (dol); sample depth = 1369.52 m, core width = 6.35 cm (short axis). b) A 1 cm thick oil-bearing shale vein; note the offshoot at the lower right, and the fractured character of the host dolomite; sample depth = 1373.59 m, core width = 6.35 cm (short axis). c) Anastomosing network of oil-bearing shale layers, ~0.5 cm thick; sample depth = 1372.87 m, core width = 6.35 cm (short axis). d) Backscattered electron image of a typical oil-bearing shale. Note the disseminated pyrite (py) and orthoclase (or); sample depth = 1394.00 m, scale bar = 100 μm. e) Backscattered electron image of spherical pyrite aggregates (framboids) and orthoclase within oil-shale; sample depth = 1394.00 m, scale bar = 10 μm.

seen in the 2σ standard deviation (Table 4.2) when compared to the suevitic groundmass and the bulk suevite (Figs 4.9b, 10b, and 12). Amongst the target rock clasts, the gneiss has the highest iron content (4.7 wt%), followed by the granodiorite (2.11 wt%) and the dolomite (0.08 wt%). The granodiorite has the highest potassium content (4.18 wt%) followed by the gneiss (2.70 wt%) and dolomite (0.23 wt%).

The LIL elements show variable concentrations (Table 4.2, Fig. 4.10). Comparing the suevitic groundmass, bulk suevite, and melt particle suites, no specific trends can be established. Several melt particles are enriched in Ba (Appendix A.6), having contents ranging from ~150 to 1280 ppm, compared to numerous samples having concentrations <150 ppm. Samples with relatively high

Table 4.2. Average major and trace† element compositions for sample suites of suevitic groundmass, suevite, and melt rock particles from the Yax-1 borehole, Chicxulub impact structure.

Groups	Groundmass free of visible clasts				Suevite with clasts					Melt particles			
	AVG n = 8	MAX	MIN	2σ	AVG n = 15	MAX	MIN	2σ	correlation gmass/ suevite	AVG n = 10	MAX	MIN	2σ
Na_2O	2.83	5.04	0.47	1.01	2.63	4.21	0.22	0.58	1.08	3.76	5.58	1.92	0.64
K_2O	3.06	4.41	0.76	0.83	2.57	4.64	0.65	0.52	1.19	3.48	6.23	2.01	0.87
Sc	10.2	15.3	5.3	2.8	12.1	15.6	2.1	2.0	0.84	19.6	34.2	5.9	5.9
Cr	26.1	43.9	10.3	9.0	38.8	75.8	5.4	7.7	0.67	53.0	121.0	17.1	20.2
FeO_{tot}	3.04	5.16	1.38	0.97	3.19	5.04	0.21	0.55	0.95	5.83	12.18	3.02	1.80
Co	6.10	9.65	2.05	1.95	5.55	7.54	1.04	0.83	1.10	8.16	10.70	3.38	1.43
Ni	33	73	4	19	23	39	8	5	1.47	26	50	10	9
Zn	45	72	14	15	50	90	3	12	0.90	84	160	25	30
As	0.26	0.37	0.06	0.07	0.52	2.02	0.09	0.28	0.50	0.48	1.16	0.24	0.19
Se	0.2	0.2	0.1	0.0	0.2	0.6	0.1	0.1	0.89	0.3	0.7	0.1	0.1
Br	15.6	27.5	3.7	6.7	17.5	31.9	3.0	4.6	0.89	20.8	50.0	5.1	9.1
Rb	40.5	65.9	7.8	13.6	41.9	73.5	6.1	9.4	0.96	49.2	79.5	32.5	10.3
Sr	293	525	38	155	180	544	27	94	1.63	219	903	48	171
Zr	79	120	50	20	115	190	40	18	0.68	147	245	85	31
Sb	0.14	0.24	0.04	0.05	0.16	0.53	0.06	0.06	0.85	0.12	0.24	0.03	0.05
Cs	1.43	2.77	0.11	0.66	1.22	2.66	0.17	0.52	1.17	1.28	2.32	0.23	0.54
Ba	117	194	60	33	130	453	20	60	0.90	405	1280	60	260
La	17.1	29.2	13.4	3.6	19.4	41.3	5.6	5.1	0.88	20.0	33.7	10.5	5.0
Ce	35.3	54.9	24.0	8.3	37.8	92.4	10.7	11.2	0.93	45.1	75.8	21.0	13.3
Nd	16.1	28.8	10.3	4.2	17.9	40.4	5.3	4.7	0.90	17.0	26.6	10.2	3.5
Sm	3.10	5.59	1.81	0.94	3.64	9.04	1.07	1.08	0.85	3.13	4.49	2.09	0.52
Eu	0.81	1.53	0.36	0.27	0.96	2.01	0.22	0.26	0.85	0.91	1.31	0.58	0.18
Gd	2.79	4.70	1.65	0.79	3.30	8.20	0.70	1.00	0.85	2.77	4.37	1.70	0.46
Tb	0.47	0.80	0.25	0.13	0.53	1.16	0.14	0.15	0.87	0.47	0.76	0.27	0.09
Tm	0.28	0.48	0.19	0.07	0.30	0.55	0.09	0.07	0.94	0.28	0.47	0.15	0.07
Yb	1.93	3.37	1.35	0.45	1.97	3.51	0.73	0.41	0.98	1.90	3.52	0.90	0.58
Lu	0.29	0.52	0.21	0.07	0.29	0.53	0.12	0.06	0.99	0.30	0.57	0.12	0.10
Hf	1.85	3.20	1.19	0.52	2.37	4.15	0.26	0.46	0.78	4.06	5.98	2.31	0.97
Ta	0.31	0.61	0.11	0.15	0.33	0.55	0.04	0.07	0.93	0.65	0.94	0.24	0.15
W	0.5	0.8	0.3	0.2	1.0	2.4	0.4	0.4	0.52	0.6	1.1	0.2	0.2
Ir (ppb)	b.d.	b.d.	b.d.	b.d.	b.d.	b.d.	b.d.	b.d.	n/a	0.40	0.40	0.40	b.d.
Au (ppb)	0.6	2.0	0.1	0.4	1.2	6.9	0.2	0.9	0.48	1.1	5.2	0.2	0.9
Th	3.48	5.84	1.31	1.34	4.93	6.63	0.82	0.69	0.71	9.17	14.10	3.50	2.06
U	1.43	6.42	0.25	1.45	1.06	2.47	0.49	0.28	1.35	0.98	2.33	0.26	0.42
K/U	42510	109600	4782		25416	76327	2186			46542	180000	14121	
Zr/Hf	43.7	52.6	28.9		56.0	153.8	33.7			37.5	51.9	25.1	
La/Th	6.68	11.45	2.69		4.11	7.10	1.44			2.32	3.37	1.35	
Hf/Ta	7.69	12.91	3.89		7.36	9.39	4.00			7.00	15.33	2.86	
Th/U	4.42	7.79	0.60		6.02	13.53	0.33			13.29	42.69	5.30	
La_N/Yb_N	6.06	7.51	5.46		6.41	7.95	4.93			8.12	14.34	2.02	
Gd_N/Yb_N	1.16	1.59	0.85		1.27	1.89	0.67			1.34	2.08	0.57	
Eu/Eu*	0.83	1.00	0.59		0.91	1.91	0.70			0.96	1.77	0.78	

†Trace elements in ppm except where indicated, Na_2O, K_2O, and FeO_{tot} in wt%, Eu/Eu* = $Eu_N/(Sm_N \times Gd_N)^{0.5}$, b.d. = below detection limit, N = chondrite normalized (Taylor and McLennan, 1985), gmass = groundmass. Averages are taken from the following samples: groundmass = 210B, 211B, 212A, 212B, 225A, 769A, 769B, 775B; Suevite = 215A, 215B, 218B, 244A, 244B, 752B, 759, 762, 763, 768, 768 duplicate, 770A, 771, 772, 774; melt particles = 211A, 225B, 242, 241, 242, 752A, 755A, 755A duplicate, 756, 769C, 770B.

Rb and Cs concentrations are exclusively from units 1 and 2 (Fig. 4.10a). When Rb+Cs, Sr, and Ba are compared against K+Na, no specific trends are evident, indicating that this effect is not controlled by specific alkali element-rich phases. However, when Rb+Cs values are plotted against FeO_{tot}, a rough correlation is observed (Fig. 4.10b). As with Rb and Cs, the enrichment of FeO_{tot} appears to be restricted to the upper impactite units (Appendix A.4, also see Tuchscherer et al. 2004b). It is also observed that the greatest abundances of the LIL elements are held by the melt particle samples (Fig. 4.10b).

The high field strength elements (HFSE) Zr, Hf, Ta, Th, and U analyzed in this suite of impactites also have highly variable concentrations (Fig. 4.11, Table 4.2). Because of the incompatible behaviour of these elements in silicate phases,

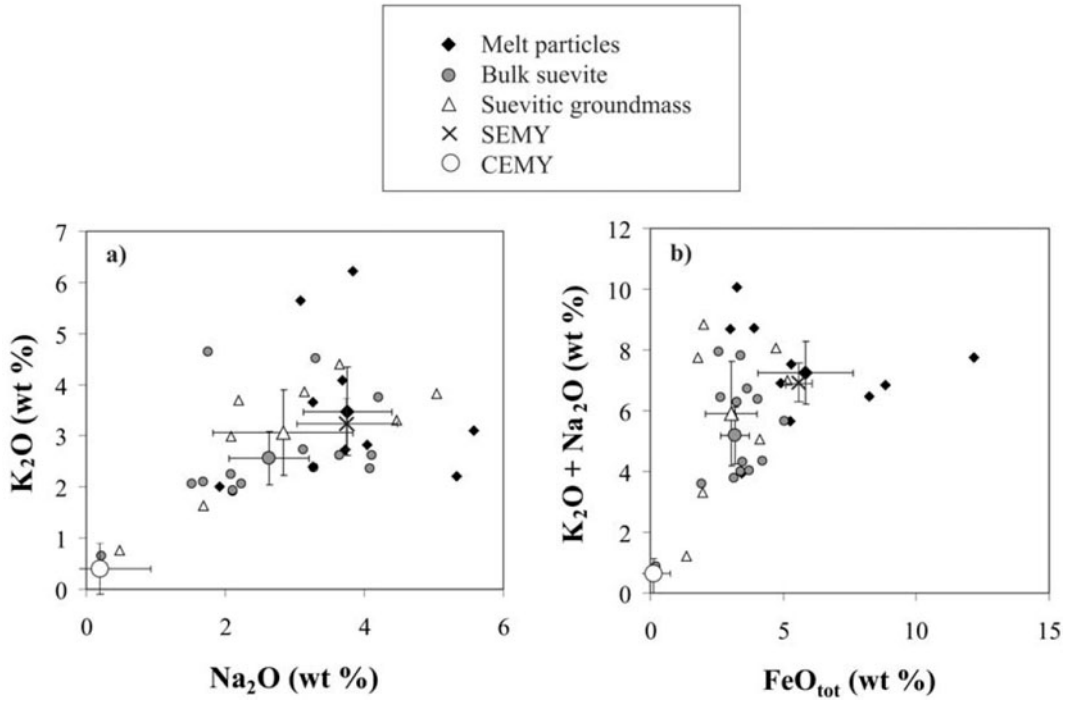

Fig. 4.9. Binary major element plots showing elemental abundances in all suevitic and melt particle samples analysed here, as well as for the average compositions for the suevitic groundmass (n = 8), bulk suevite (n = 15), melt particles (n = 10), SEMY (siliceous end-member for the Yax-1 impactites), and CEMY (carbonate end-member for the Yax-1 impactites) of the Yax-1 impactites. Error bars represent 2σ standard deviation plotted for averaged compositions (melt particles, bulk suevite and suevitic groundmass) whereas error bars for the end-member compositions represent calculated least-square standard errors for the y-estimate standard error presented in Table 4.1: a) K_2O versus Na_2O, b) $K_2O + Na_2O$ versus FeO_{tot}, data in wt%.

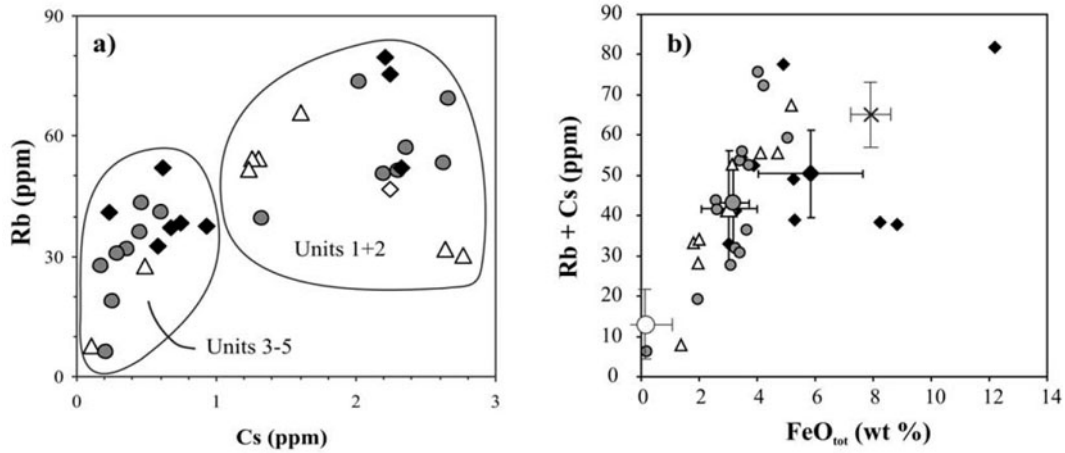

Fig. 4.10. Binary diagrams for selected large ion lithophile (LIL) elements: a) Rb versus Cs plot for melt particles, suevitic groundmass, and suevitic samples of the Yax-1 impactite interval (see Fig. 9 for legend); b) Rb+Cs versus FeO_{tot} plot showing all samples, averaged compositions for the suevitic groundmass (n = 8), bulk suevite (n = 15), melt particles (n = 10), SEMY (siliceous end-member for the Yax-1 impactites) and CEMY (carbonate end-member for the Yax-1 impactites); error bars represent 2σ standard deviations for averaged compositions and the least square y-estimate standard errors (Table 4.1) for the end-member compositions.

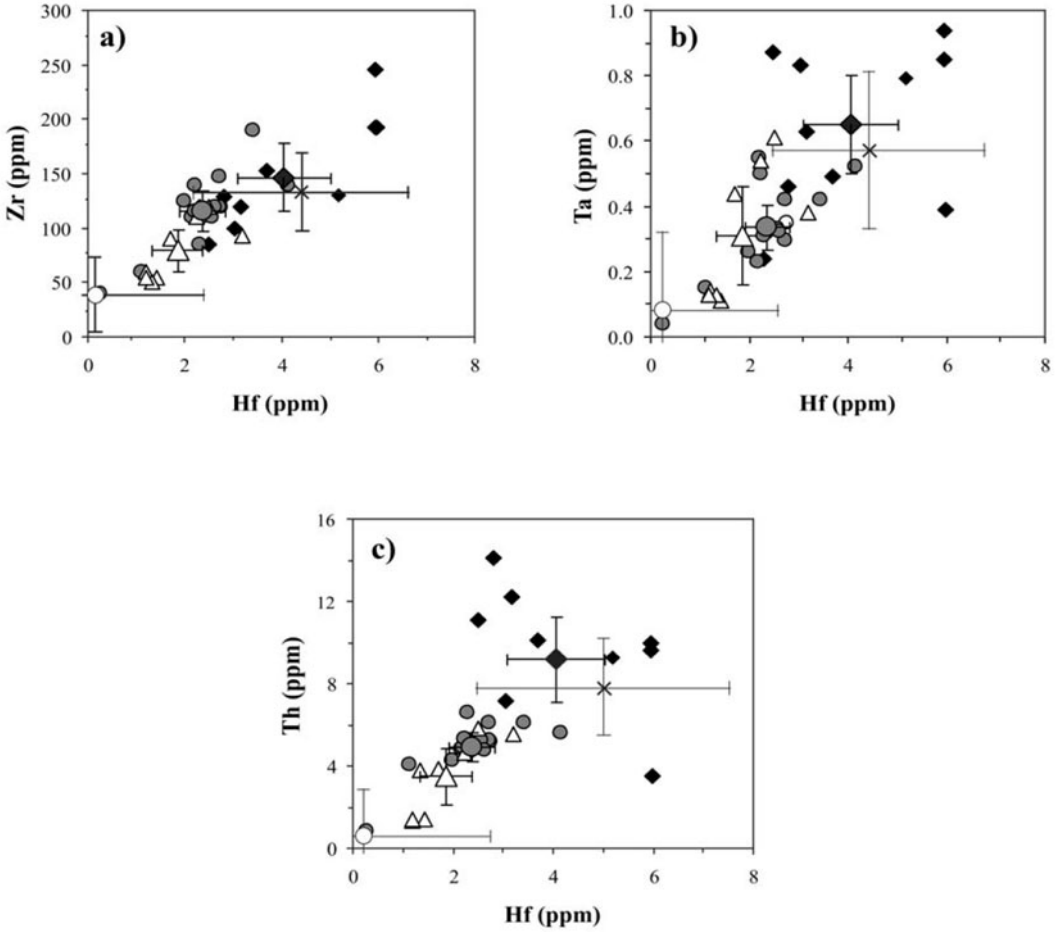

Fig. 4.11. Binary diagrams for abundances of selected high field strength elements (HFSE), for all suevitic, melt particle samples, and averaged compositions of suevitic groundmass (n = 8), bulk suevite (n = 15), melt particles (n = 10), SEMY (siliceous end-member for the Yax-1 impactites) and CEMY (carbonate end-member for the Yax-1 impactites) compositions of the Yax-1 impactite interval; error bars represent 2σ standard deviations for averaged compositions and least square y-estimate standard errors (Table 4.1) for the end-member compositions: a) Zr versus Hf, b) Ta versus Hf; c) Th versus Hf. Note the progressive enrichment of these HFSE towards the average melt particle composition.

plots of Ta, Zr, and Th versus Hf indicate positive linear correlations (Figs 4.11a-c). When U concentrations are plotted against the other HFSE, inverse relationships are observed. With the exception of U, the melt particles are enriched in the HFSE, compared to the suevitic groundmass and bulk suevite (Table 4.2). The melt particles also have the largest compositional variability with regard to trace elements.

When plotted against Fe, the transition metals Sc, Co, and Zn give positive linear correlation trends (Figs 4.12a-c), whereas Cr and Ni contents scatter (not shown). This behavior of Cr and Ni indicates that the distribution of a mafic component in the impactites is very heterogeneous. The compositional variation

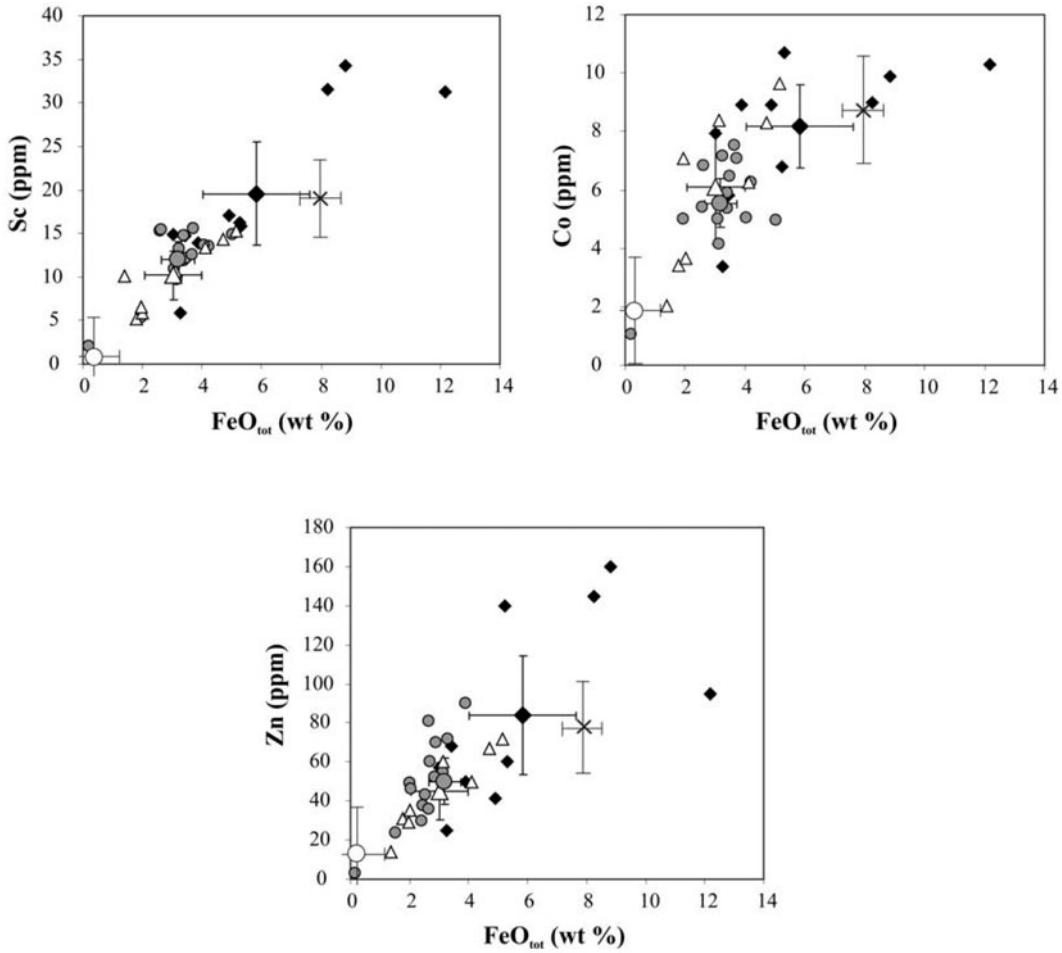

Fig. 4.12. Binary diagrams for selected transition trace metals versus FeO_{tot} showing all suevitic, melt particle samples and averaged compositions for suevitic groundmass (n = 8), bulk suevite (n = 15), melt particles (n = 10), SEMY (siliceous end-member for the Yax-1 impactites) and CEMY (carbonate end-member for the Yax-1 impactites) of the Yax-1 impactite interval; error bars represent 2σ standard deviations for averaged compositions (large symbols) and least square y-estimate standard errors (Table 4.1) for the end-member compositions: a) Sc versus Fe, b) Co versus Fe, and c) Zn versus Fe. Note the relative enrichment of these selected elements against Fe towards the melt particle composition.

and range of abundances of the transition metals are greatest for the melt particle suite.

Figure 4.13a shows that the heavy rare earth elements (HREE) for the SEMY of the Chicxulub impactites match the UCC composition well, whereas the light rare earth element abundances (LREE) are lower than those for the UCC composition. SEMY shares a negative Eu anomaly with the UCC. The CEMY and CTIY compositions are significantly depleted in the REE, in comparison with UCC and SEMY compositions. The carbonate end-member reveals a pronounced negative Ce anomaly. The averaged melt rock particles, bulk suevite, and suevitic groundmass all show normalized abundances that are a good match for the bulk CC

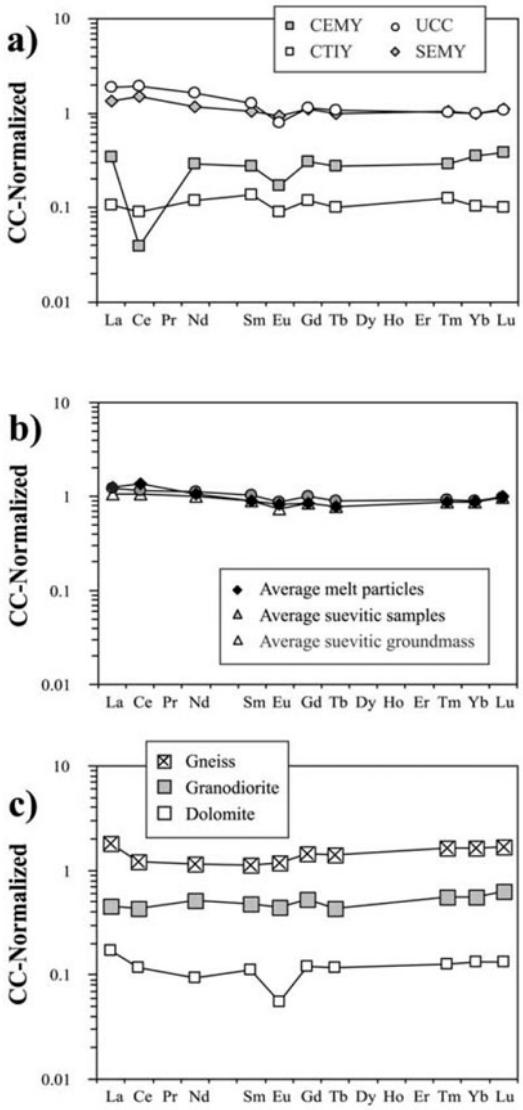

Fig. 4.13. Bulk continental crust (CC) normalized (values from Taylor and McLennan 1985) rare earth element (REE) patterns for a) upper continental crust (UCC), calculated siliceous (SEMY) and carbonate (CEMY) end-members for the Yax-1 impactites, and calculated average Cretaceous target rock interval composition of Yax-1 (CTIY); b) averaged suevitic groundmass (n = 8), bulk suevitic (n = 15), and melt rock samples (n = 10); c) individual clasts from the impactites: gneiss (824.03 m), granodiorite (88.92 m), and dolomite (888.09 m).

composition, yet they are slightly enriched in LREE (Fig. 4.13b). The average melt particle, suevite, and groundmass compositions are very similar to, and intermediate between, the calculated SEMY and CEMY compositions (Fig. 4.13b). Amongst the lithic clasts (Fig. 4.13c), the gneissic sample reveals the highest REE normalized abundances, followed by those of the granodiorite and the dolomite. The dolomite has a pronounced negative Eu anomaly.

To compare compositional differences between the average impactite sample suites, clasts, and calculated end-members, the available data set has been normalized against the composition of bulk CC and is compared against the trends for UCC and lower continental crust (LCC, Fig. 4.14). Figure 4.14a shows that the calculated SEMY is primarily intermediate between the UCC and the bulk CC. An upper-crustal signature can be observed, as defined by the similar normalized abundances of K, Th, Hf, Zr, Sr, Na, Sb, Zn, Fe, Sc, Co, Cr, and Ni to those of the UCC. A complex pattern is defined by positive K, Th, Hf, and Zr, and negative U, Ba, Ta, and As anomalies. The lower crust, also shown in Fig. 4.14a, has considerably lower abundances of the alkali elements and HFSE, but is characteristically enriched in the transition metals. Figure 4.14b

shows that the average for melt rock particles, the average bulk suevite, and average suevitic groundmass values produce relatively similar trends when normalized to the bulk CC, with the suevitic groundmass having the lowest normalized abundances. The average suevitic groundmass does not show a positive Th anomaly, but has a positive Sr anomaly. Figure 4.14c compares the compositions of the calculated CEMY and the dolomite clast with the bulk CC. These two phases have similar trends and overlapping abundances primarily below those of bulk CC. The trend is characterized by strong positive U, Sr, and Sb anomalies. The granodiorite clast (Fig. 4.14d) is strongly enriched in K, Ba, and to a lesser extent Zn, compared to the gneissic clast. The gneiss shows only relative enrichments of K and Zr, and, to a lesser extent, of Th and Na, compared to the bulk CC. However, the high Th abundances observed in the SEMY and melt particle compositions are not characteristic for these clasts. Thus, a Th-rich target rock component is still to be identified. The SEMY and average melt particle compositions have Th values of 7.9 and 14.1 ppm, respectively. The highest Th content from a sampled clast originates from the finely laminated gneiss, at 4.5 ppm Th.

A pronounced negative As anomaly is observed when comparing the SEMY and all the impactite samples to the bulk CC (Fig. 4.14a, b). Bromine abundances of these samples (Appendix A.6, 50-3 ppm) are unusually enriched when compared against the bulk CC (0.88 ppm, after Rudnick and Gao 2003). The chemical variation of impactites versus depth shows that, for Cs, Rb, Ni, Zn, Cr, and Sb, abundances are moderately enriched in the upper interval of the impactites, between 795 and 846 m depth (Fig. 4.2, Appendix A.6). The samples from Unit 5 yield the highest U and the lowest Cs, Rb, Hf, Zn, Sc, Cr, and Ni abundances. For a perspective on the carbonate content of the impactites, the HFSE, Sc and Hf, show low abundances in Unit 5. Scandium and Hf are preferentially enriched in silicate phases. Thus, low concentrations of these elements indicate high carbonate abundances.

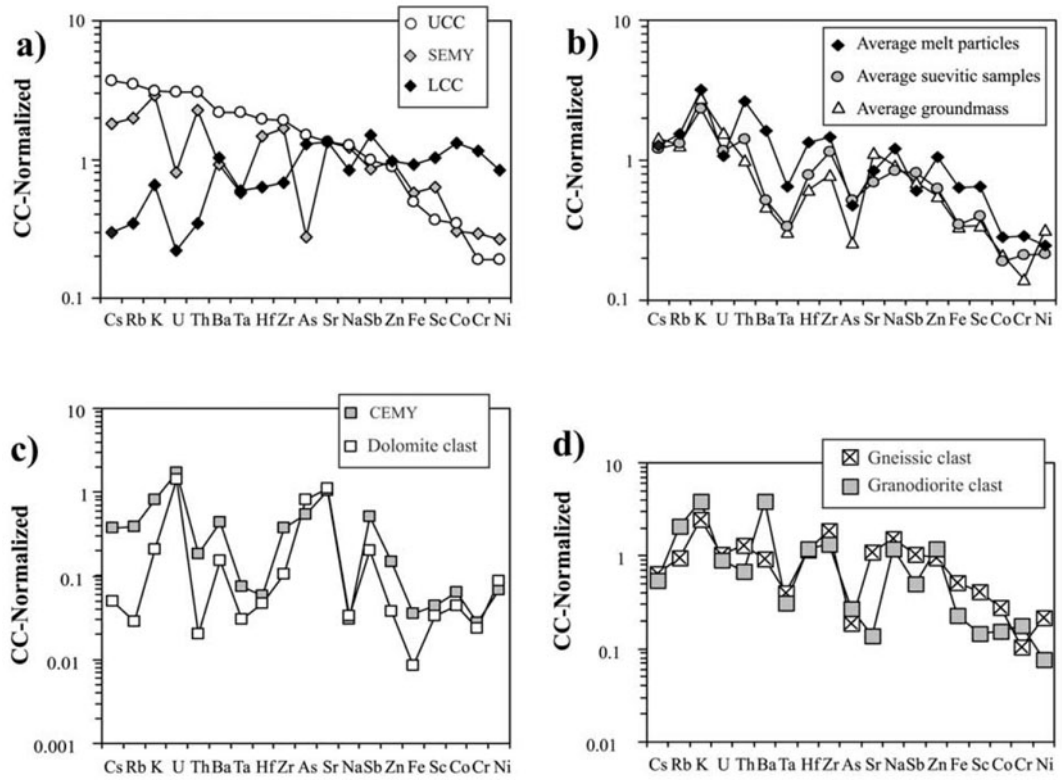

Fig. 4.14. Bulk continental crust (CC) normalized (values from Taylor and McLennan 1985) abundances of selected major elements, LIL elements, HFSE, volatile, and transition metals in impactites and clasts from the Yax-1 borehole. Elements are arranged according to their decreasing compatibility in the upper continental crust. a) Upper continental crust (UCC), calculated siliceous end-member of the Yax-1 impactite (SEMY), and lower continental crust (LCC); b) averaged melt particle composition, bulk suevite, and suevite groundmass; c) dolomite clast (depth = 888.09 m) and calculated carbonate end-member for the Yax-1 impactites (CEMY); d) siliceous crystalline clasts: granodiorite (depth = 888.92 m) and gneiss (depth = 824.03 m).
is comparatively significantly enriched in CaO.

4.7.3. Geochemistry of Cretaceous rocks

Results of major and trace element analyses for these lithologies are presented in Appendix A.7. In Table 4.3, average compositions for dolomite, argillaceous dolomite, and oil shale are presented. The Cretaceous lithologies have high loss on ignition (LOI) values due to their high carbonate/sulfate contents and phyllosilicate presence. Silica and Al_2O_3 can also be quite elevated in certain samples, depending on the amounts of modal phyllosilicate. Oil shale samples and, to a lesser extent, the argillaceous dolomite samples, have high K_2O concentrations (higher than any impactite samples - up to 13.73 wt% K_2O, Appendix A.7, Fig. 4.15a), and relatively high Al_2O_3 and FeO_{tot} abundances. The blue, brecciated dolomite from 1347.56 m contains slightly higher K_2O than the

Table 4.3. Averaged major and trace† element compositions for dolomitic rocks, argillaceous limestone, and oil shale, all from the Yax-1 borehole, Chicxulub impact structure.

Litho-logies	Dolomitic rocks				Argillaceous dolomite				Oil Shale			
	AVG n=4	Max	Min	2σ	AVG n=3	MAX	MIN	2σ	AVG n=3	Max	Min	2σ
SiO_2	2.57	4.80	0.97	1.74	25.33	39.40	14.70	12.70				
TiO_2	0.04	0.10	-	0.05	0.67	0.88	0.53	0.19				
Al_2O_3	0.86	1.41	0.30	0.50	6.90	10.40	4.10	3.21				
FeO_{tot}	0.44	0.84	0.16	0.29	4.40	5.25	3.06	1.17	4.73	5.44	3.72	
MnO	-	-	-	-	0.01	0.02	0.00	0.01				
MgO	18.90	19.80	16.90	1.36	5.40	15.30	0.42	8.58				
CaO	30.30	33.50	28.20	2.44	26.07	35.10	19.50	8.09				
Na_2O	0.50	0.79	0.19	0.28	0.32	0.45	0.14	0.16	1.02	1.36	0.53	
K_2O	0.19	0.43	0.08	0.16	4.85	7.94	2.58	2.77	8.01	13.73	3.00	
Cr_2O_3	-	-	-	-	-	0.01	-	0.01				
P_2O_5	-	0.01	-	0.01	0.08	0.10	0.06	0.02				
V_2O_5	-	-	-	-	0.01	0.03	-	0.02				
Cl	0.37	0.50	0.08	0.20	0.17	0.20	0.10	0.06				
SO_3	3.29	11.00	0.04	5.22	2.28	3.00	0.83	1.25				
L.O.I	42.38	44.60	36.30	4.05	22.17	33.00	11.60	10.70				
Total	99.83				98.64							
	AVG n=15	Max	Min	2σ	AVG n=4	MAX	MIN	2σ	AVG n=3	Max	Min	2σ
Sc	2.1	9.3	0.2	1.2	13.0	23.6	2.5	10.0	5.7	10.0	3.2	3.7
Cr	5.5	10.4	1.5	1.5	99.7	247	13.1	102	65	111	18.3	46.4
Co	1.87	5.01	0.39	0.66	20.4	38.3	1.88	15.3	14.0	24.9	4.87	10.0
Ni	8	22	3	3	38	61	18	18	74	91	52	20
Zn	8	21	1	4	22	28	16	5	59	79	31	25
As	2.62	7.73	0.13	1.41	12.7	43.9	1.42	20.8	25.5	32.9	21.3	6.4
Se	0.4	1.1	0.1	0.2	1.0	1.9	0.1	1.2	1.9	2.2	1.7	0.3
Br	23.9	60.5	4.4	8.7	29.5	57.2	12.8	20.3	86.7	90.4	82.4	4.0
Rb	5.5	17.7	0.7	2.7	29.8	54.1	1.3	23.9	31.2	48.0	0.9	26.3
Sr	155	373	43	51	163	283	41	130	117	146	75	37
Zr	25	97	5	12	126	414	13	193	232	330	125	103
Sb	0.12	0.51	0.01	0.06	0.41	1.37	0.06	0.64	1.00	1.77	0.06	0.87
Cs	0.20	0.64	0.04	0.10	0.12	0.34	0.01	0.15	0.53	1.02	0.22	0.43
Ba	19	57	5	7	65	200	5	91	74	148	5	72
La	1.7	3.2	0.6	0.4	4.6	14.4	0.9	6.6	4.5	7.6	2.2	2.8
Ce	2.9	6.4	0.3	1.0	6.6	20.5	0.6	9.3	6.7	9.0	4.4	2.3
Nd	1.9	3.4	0.8	0.5	5.9	17.6	1.5	7.8	5.4	7.0	2.9	2.2
Sm	0.44	0.87	0.17	0.12	1.78	5.30	0.28	2.36	1.85	2.57	0.98	0.80
Eu	0.11	0.29	0.03	0.04	0.31	0.72	0.08	0.28	0.20	0.23	0.17	0.03
Gd	0.39	0.80	0.14	0.11	1.25	2.60	0.30	0.97	1.40	1.80	0.81	0.52
Tb	0.06	0.15	0.02	0.02	0.22	0.43	0.05	0.16	0.22	0.26	0.15	0.06
Tm	0.04	0.09	0.01	0.01	0.11	0.20	0.03	0.07	0.11	0.14	0.08	0.03
Yb	0.24	0.62	0.05	0.08	0.69	1.01	0.20	0.37	0.67	0.87	0.48	0.20
Lu	0.03	0.09	0.01	0.01	0.10	0.14	0.03	0.05	0.09	0.12	0.07	0.03
Hf	0.37	1.60	0.04	0.21	2.06	6.34	0.09	2.90	3.63	6.96	1.09	3.01
Ta	0.09	0.25	0.02	0.03	0.28	0.81	0.03	0.36	0.70	1.04	0.21	0.43
W	0.3	1.5	0.1	0.2	n.d.	n.d.	n.d.	n.d.	0.2	0.4	0.1	0.2
Ir (ppb)	b.d.	b.d.	b.d.	b.d.	b.d.	b.d.	b.d.	b.d.	b.d.	b.d.	b.d.	b.d.
Au (ppb)	0.3	0.7	0.1	0.1	0.5	0.8	0.1	0.3	0.3	0.3	0.2	0.1
Th	0.39	1.25	0.05	0.19	1.69	6.43	0.07	3.16	6.57	11.50	0.78	5.41
U	1.39	3.64	0.10	0.58	6.37	23.50	0.46	11.42	13.59	16.80	9.17	3.96
K/U	4612	15862	412		33062	76471	213		4677	7703	2715	
Zr/Hf	99.5	221.5	20.1		79.9	146.7	26.1		82.1	114.7	47.4	
La/Th	7.04	17.29	2.38		9.65	16.86	2.24		1.37	2.77	0.32	
Hf/Ta	4.34	12.50	0.73		6.22	7.83	3.00		5.08	6.69	3.35	
Th/U	0.34	0.74	0.04		0.20	0.27	0.12		0.42	0.68	0.09	
LaN/YbN	6.03	13.80	1.83		3.97	9.63	1.02		4.23	5.86	3.04	
GdN/YbN	1.49	2.55	0.86		1.39	2.09	0.96		1.70	2.24	1.37	
Eu/Eu*	0.83	2.30	0.37		0.73	0.85	0.59		0.45	0.72	0.29	

Trace elements in ppm except where indicated, $Eu/Eu^* = Eu_N/(Sm_N \times Gd_N)^{0.5}$, b.d. = below detection limit, n.d. = not detected, †Cretaceous interval calculated according to 27 vol% anhydrite, 63 vol% dolomite, 10 vol% calcarenite, from the Dressler (2002) Yax-1 core log, ‡see methodology section for explanation, note: ratios presented are averaged from the sample population and not derived from the averaged composition presented in this table. Averages are taken from the following samples: dolomite major elements = 228, 229, 236, 237; dolomite trace elements = 220B, 221, 233B, 223A, 223B, 225C, 226, 227A, 227B, 228A, 229A, 235, 236, 237, 238B; argillaceous dolomite major elements = 220A, 220B, 224, 231; argillaceous dolomite trace elements = 220A, 224, 231, 238A; oil shale major and trace elements = 228B, 229B, 230.

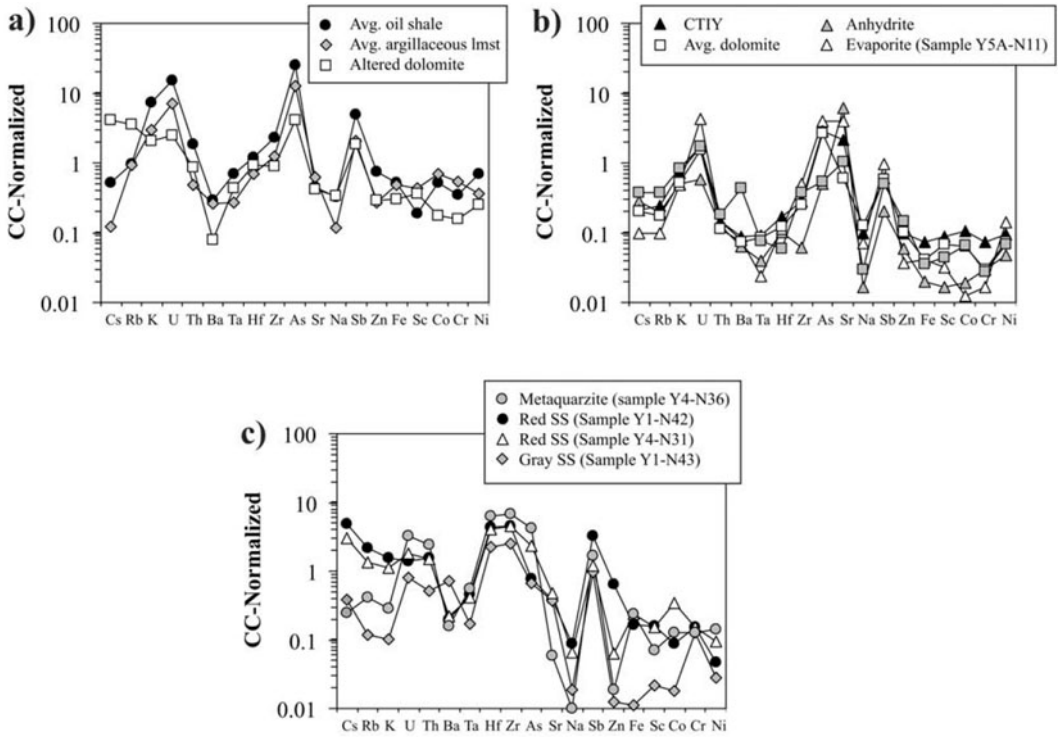

Fig. 4.15. Bulk continental crust (CC) normalized (values from Taylor and McLennan [1985]) data for major and LIL elements, HFSE, volatile elements, and transition metals in Yax-1 lithologies. Elements are arranged according to their decreasing compatibility in the upper continental crust. a) Average oil shale (n = 3), average argillaceous limestone (n = 4), and alteration zone sample from 1347.60 m; b) Yax-1 aggregate Cretaceous target composition (CTIY), average Yax-1 dolomite (n = 15), anhydrite, and evaporite data (the latter after Koeberl 1993a). c) Clastic sedimentary rock metaquartzite, red sandstone (SS), and gray SS, after data by Koeberl (1993).

other dolomite samples. The Na_2O content is quite low for all these samples. The MgO and SO_3 abundances calculated for the CTIY composition do not correlate with those of the CEMY calculated from the impactite compositions (Table 4.1), which as with the impactites above, the analytical data for the Cretaceous samples have been normalized against the composition of bulk CC. Abundances for the LILE, HFSE, transition trace metals, and selected volatile elements are presented in order of decreasing compatibility with respect to UCC in Fig. 4.15. Lithologies have been grouped according to their similar geochemical signatures. Figure 4.15a shows that the average oil shale, argillaceous dolomite, and the alteration zone (see Table 4.3 for selected samples used in the averages) all have similar positive U, As, and Sb anomalies. The oil shale is highly enriched in these elements. The alteration zone is rich in Cs and Rb. In Fig. 4.15b, the calculated CTIY composition is plotted and shows similar chemical characteristics to the dolomite and anhydrite lithologies, obviously representing a mixture of these rocks.

Compared to the rock types plotted in Fig. 4.15a, the CTIY composition, as well as the anhydrite and the evaporite, show similar chemical signatures but with significantly higher abundances of Sr, which is directly related to the anhydrite content. Analyses for several sandstones and a metaquartzite from the Y1 and Y4 boreholes, respectively (Koeberl 1993a), are presented for comparison in Fig. 4.15c, showing that these rocks are all rich in U, Th, Hf, Zr, As, and Sb. The volatile elements, As and Br, in the oil shale, argillaceous dolomite, the blue alteration zone, the evaporite (data of Koeberl 1993a), the average dolomite, and the CEMY are also strongly enriched when compared to the impactite samples and the bulk CC.

The average oil shale and average argillaceous dolomite show similar REE trends, with pronounced negative Ce and positive Sm anomalies (Fig. 4.16a). The alteration zone, however, is relatively enriched in LREE and shows a pattern that is similar to that of average dolomite (Fig. 4.16b). This illustrates also that the calculated CTIY composition is almost identical to the average dolomite pattern, with respect to REE systematics, despite 27.4 vol% anhydrite in the calculated CTIY composition contains. The anhydrite sample No. 233A has the lowest REE normalized abundances, compared also to the evaporite sample (Y5A-N11, from borehole Y5) of Koeberl (1993b). This latter analysis most likely represents a mixture of argillaceous limestone and/or oil shale with anhydrite, as it shows characteristic negative Ce and Eu, and positive Sm anomalies (Fig. 4.16a), as well as relatively high Sr abundance (Fig. 4.16b). In general, all dolomite samples are characterised by a negative Ce anomaly. The clastic sediments (Fig. 4.16c) all show similar REE trends at distinctly variable abundances.

4.8. Discussion

4.8.1. Compositions of end-member components of Yax-1 impactites

4.8.1.1.Siliceous end-member

When the siliceous end-member of the Yax-1 borehole (SEMY) composition is compared to the averaged melt rock particle composition (Figs 4.13 and 4.14), nearly identical patterns are observed. The only significant differences are that the average melt particle composition has a lower Sr but a higher Ba content than SEMY. SEMY has a REE geochemical signature that is similar to that of the UCC. This is obvious on a bulk continental crust (CC)-normalized REE diagram (Fig. 4.13a), where the HREE pattern is identical to that of the upper continental crust (UCC), and the LREE are only slightly depleted. The spider diagram of Fig. 4.14a shows that K, Th, Hf, Zr, Sr, Na, Sb, Zn, Fe, Co, Cr, and Ni of the SEMY composition have abundances that are nearly identical to those of the UCC. On the other hand, Cs, Rb, U, Ta, and As have abundances that are significantly more variable and intermediate between those of the UCC and the bulk CC. These results show that the crust struck by the Chicxulub impactor was deficient in Cs, Rb, and Ta, but slightly enriched in Sc, Cr, and Ni.

The discrepancy between the impactite composition and the UCC can be explained by a variety of processes. A high loss on ignition (LOI) value is evident from the major element composition; this affects the bulk silicate composition. High LOI is attributed to the high secondary and clastic carbonate contents of the impactites. Alteration has also resulted in extensive conversion of melt particles into phyllosilicates, with accompanying change of the composition of the bulk impactite material.

High LOI of impact crater fill must be expected to result from a wet impact, i.e., hydrous target rocks and interaction with seawater. A minor positive Ce anomaly is noted for SEMY, which indicates strong interaction with seawater. This may occur through the preferential microbially mediated oxidation of dissolved Ce^{3+} to the insoluble form Ce^{4+} in seawater. The anomaly is believed to

originate from the enrichment of insoluble Ce^{4+} in residual authigenic minerals, i.e., clay minerals and Ca-phosphates (e.g., Guy et al. 1999; Utzmann et al. 2002). Even if the major element abundances are recalculated on a LOI-free basis, the resultant composition does not equate to that of the UCC, having relatively lower SiO_2 (58.05 wt%) and higher CaO (5.74 wt%) contents. SEMY was calculated assuming a CaO content of 5.2 wt%, which is identical to the CaO content of Unit 4 (Tuchscherer et al. 2004b) and previously reported compositions of the Yucatán crystalline basement (e.g., Kring 1997). This CaO content is slightly higher than that of the average UCC, i.e., 4.2 wt% (Taylor and McLennan 1985), which might be influenced by the incorporation of lime from the target carbonate rocks. Secondary processes have, thus, had a strong influence on the present composition of the impactite.

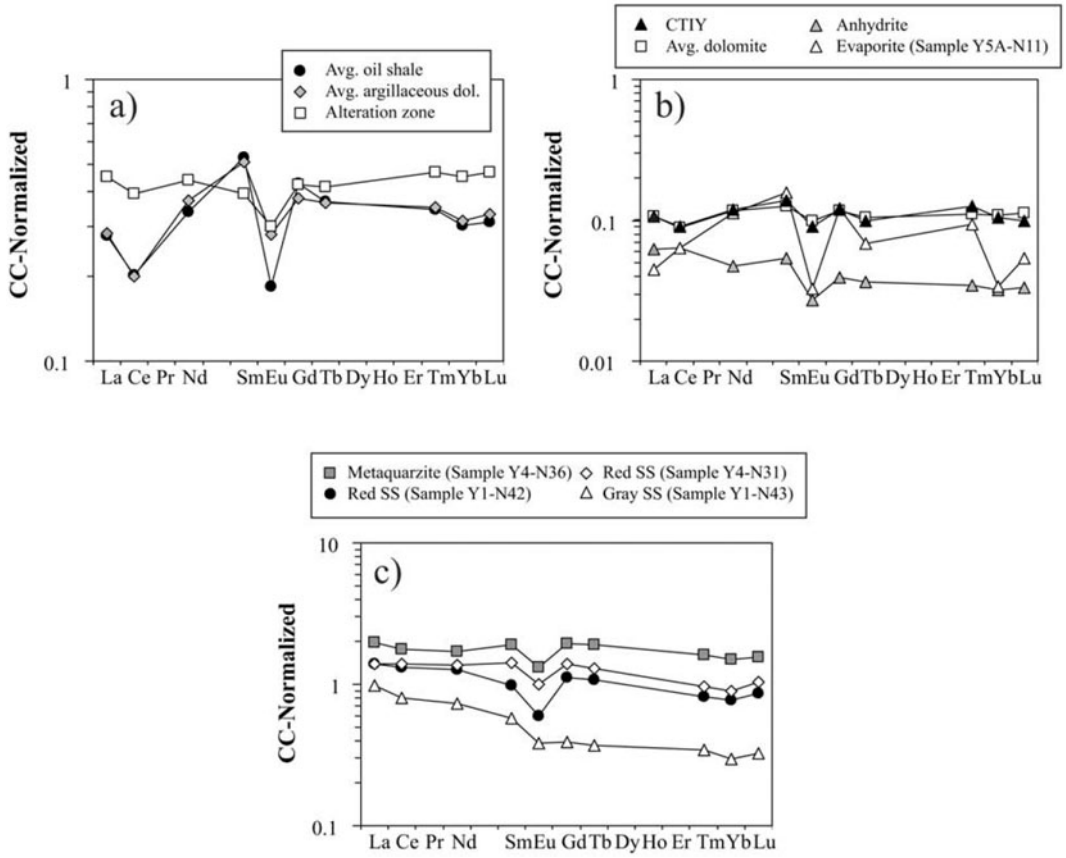

Fig. 4.16. Bulk continental crust (CC) normalized (values from Taylor and McLennan [1985]) REE abundances for: a) Average oil shale (n = 3), average argillaceous limestone (n = 4), the alteration zone sample from 1347.60 m depth. b) Yax-1 aggregate Cretaceous rock composition (CTIY), average Yax-1 dolomite (n = 15), anhydrite, and evaporite compositions (the latter from Koeberl 1993a). c) Clastic sedimentary rocks (metaquartzite, red sandstone (SS), and gray SS) from Koeberl (1993).

Based on the calculated SEMY composition, we suggest that the crust struck by the Chicxulub impactor was more mafic than the UCC estimate of Taylor and McLennan (1985). In agreement with this finding, a significant mafic target rock component to the Chicxulub impactite has been invoked by Kettrup et al. (2000) in order to explain their Sr and Nd isotope data. Our petrographic findings (Tuchscherer et al. 2004a) include observation of some clasts of mafic rocks (gabbroic and mica schist clasts) throughout the impactite interval, albeit in very small volume percentages (i.e., total clastic content, siliceous and mafic << 2.5 vol%). Furthermore, abundant altered mafic melt rock particles have been found in the Yax-1 suevites (Tuchscherer et al. 2004a).

4.8.1.2. Carbonate end-member

The carbonate end member (CEMY) for the impactites of the Yax-1 borehole has a trace element geochemical signature that differs slightly from that of the calculated Cretaceous target rock interval in Yax-1 (CTIY). Figure 4.13a shows that the calculated CEMY has a normalized REE pattern that is almost identical to that of the CTIY composition, but with pronounced negative Ce and Eu anomalies. According to Elderfield et al. (1981), the negative Ce anomaly is a characteristic of seawater-precipitated sedimentary rocks and minerals, e.g., limestone, dolomite, and anhydrite (cf. Figs 4.16a,b). With regard to the normalized trace element patterns (Fig. 4.14c), the pattern for the CEMY overlaps with that for a dolomite clast in the impactite. The average dolomite composition shows similar peaks of U, As, and Sb, but with lower Ba and Sr (Fig. 4.15b). The high Ba and Sr in the CEMY can be attributed to the presence of authigenic barite, which indeed has been observed abundantly by several groups, e.g., Hecht et al. (2004) and Tuchscherer et al. (2004a). The calculated CTIY, plotted on a similar multi-element diagram (Fig. 4.15b), is slightly different from that of the CEMY, showing a pronounced positive As anomaly and relatively higher U and Sr normalized abundances. The differences in the calculated CTIY composition and that of the CEMY can be attributed to an incomplete record of Cretaceous – and possibly older – lithologies of the target volume that was sampled by the Yax-1 borehole (e.g., the borehole did not intersect any clastic sedimentary rocks), to the

devolatilization of anhydrite and other highly volatile phases (e.g., As) during the impact event (as postulated by, e.g., Sigurdsson et al. 1992 or Ivanov et al. 1996), and to the presence of quite a significant amount of calcite and barite in the impactites.

Petrographic observations have demonstrated that numerous secondary calcite veins with barite crystals occur in the impactite interval**,** in particular in units 3 and 4 (Hecht et al. 2004; Tuchscherer et al. 2004a)**.** With regards to the devolatilization of anhydrite, Ames et al. (2004), Schmitt et al. (2004), and Tuchscherer et al. (2004b) have demonstrated that the Yax-1 impactites have very low sulfate (from <0.02 to 0.15 wt% SO_3). This has been observed in the impactites of the Y6 drill core (Claeys et al. 2003). This effect is also obvious when the sulfate abundance of the calculated carbonate end-member is compared with the calculated Cretaceous target rock composition (Table 4.3).

From the calculated compositions of CTIY, it is also noted that CEMY is more calcitic than expected on the basis of the prominence of dolomite in the Cretaceous stratigraphy (Table 4.3). This can be explained in several ways: (1) Pervasive secondary calcite has entered the impactites in significant proportion. (2) Our calculated CTIY composition does not adequately represent the bulk Cretaceous (and older) carbonate rocks at Chicxulub, i.e., a more limestone-rich, rather than dolomitic target rock component was incorporated into the Yax-1 impactites. (3) Lime may have preferentially been taken up into the impactites compared to MgO (in dolomite) due to the fast back-reaction of CO_2 with CaO and the comparatively poor reactivity of MgO (Agrinier et al. 2001). MgO does not appear to have been preferentially incorporated into the impactites as both the SEMY and the CEMY do not show substantial concentrations of MgO (4.23 and 5.51 wt%, respectively) compared to the CTIY (13.62 wt%). The unusual and unique MgO-rich composition of magnesiowüstite spinels found in K/T boundary ejecta layers of the Pacific Ocean compared to all other K/T boundaries (Kyte et al. 1996; Ebel and Grossman 2005) may account for some of this missing MgO.

4.8.2. Comparisons of suevitic groundmass and bulk suevite

The average suevitic groundmass and average bulk suevite compositions are similar (Table 4.2, Figs 4.9a and b, 4.10b, 4.11a-c, 4.12a-c, and 4.14b) and clearly contain similar proportions of silica-rich and carbonate components. In the case of bulk suevite, these components are primarily melt particles and suevitic groundmass. In the suevitic groundmass, the principal components are calcite, dolomite, microscopic melt particles, lithic clasts, and an altered alkali element-, Ca-, and Si- rich cement (Tuchscherer et al. 2004a). The lithic clasts and melt particles, in both bulk suevite and suevitic groundmass, have been extensively converted to phyllosilicates (cf. Tuchscherer et al. 2004a).

The average groundmass composition is enriched in Sr and the average suevite in Th. The Sr could originate from anhydrite preserved in the groundmass (Figs 4.14b and 4.15b) or the presence of Sr-rich barite (Hecht et al. 2004). Conversely, the positive Th anomaly observed in the average suevite composition could originate from melt particles that were originally clastic sedimentary rocks (Lopez Ramos 1975; Koeberl 1993a; Ward et al. 1993) or as yet unsampled granitoid lithologies.

4.8.3. Melt particle compositions

Melt particles have variable chemical compositions (Appendix A.6, Table 4.2, Figs 4.9a and b, 4.10b, 4.11a-c, 4.12a-c, 4.14b; Tuchscherer et al., 2004a). Amongst the 10 newly analyzed individual melt particle compositions, several geochemical groupings can be discerned. The gray melt particle samples 755A, 755AD, 769C, and 770B, (Appendix A.6) show high Zn, Fe, and Hf concentrations. This group is also distinguished by its overall low element abundances of certain elements, especially of K and Th, which do not exceed three times the bulk CC values. This group of melt particles is similar to the type 4 melt particles identified by Hecht et al. (2004) based on the low K content and their opaque petrographic characteristics. The second group of melt particles has high Ba and low Ta concentrations and includes the samples 752A, 769C, 756, 241, and 225B (Appendix A.6). Based on these data, these samples could represent melted granodiorite, which also contains high Ba and low Ta (Appendix

A.6, Fig. 4.14d). However, these groupings are not entirely separated compositionally; for example, sample 769C shows characteristics from both groups. Because the second melt particle population possesses variable textural attributes, such as variegated colors and fluidal to shard-like morphologies, we cannot correlate these samples with any of the groups defined by Hecht et al. (2004).

The difficulty of trying to decipher the protolith composition of melt particles stems from the fact that the Chicxulub situation includes impact-induced mixing as well as alteration of different degrees (i.e., open system behaviour), and the samples are diluted by secondary carbonate. To further investigate potential protolith compositions of melt particles, element ratios, especially those involving immobile HFSE, e.g., Zr/Hf and Hf/Ta ratios, were applied. From Appendix A.6 and A.7, and data from Koeberl et al. (1993), it is seen that the currently known target rock compositions have Hf/Ta ratios that only bracket the upper range of the melt particle composition. When considering Zr/Hf ratios, the melt particles produce unusually low ratios that cannot be accounted for by any currently known siliceous target rock. Thus, other means are required in order to discern the protolith composition(s) of melt rock particles. The lack of geochemical data from any mafic target lithology prohibits any mixing calculations, at this stage.

4.8.4. Cretaceous rock geochemistry: implications

Certain aspects of the geochemical results for Cretaceous lithologies merit further discussion. Most Cretaceous rocks, i.e., the oil shale, average argillaceous limestone, average dolomite, evaporite (from Koeberl 1993a), and a few clastic, silicate-rich, sedimentary rocks (samples Y4-N36, Y4-N31 – from Koeberl 1993a) have relatively high U abundances compared to the bulk CC (Fig. 4.15). The U, as well as K and Th, contents of these rocks are well documented in the downhole gamma ray log for Yax-1 (Kenkmann et al. 2004; Wohlgemuth et al. 2004). The high U abundances may be explained by either a high-U provenance for these sedimentary deposits, or the preferential affinity of U towards organic matter in sedimentary rocks, preserved in the form of stable organo-uranyl compounds during diagenesis (e.g., Nakashima et al. 1984). This most likely

occurs through the transport of highly soluble $[UO_2]^{2-}$ ions (McLennan and Taylor 1980). Our single sample of Tertiary limestone and the North American Shale Composite (NASC, Gromet et al. 1984), however, do not show anomalous U abundances when normalized to bulk CC. This may indicate that high U concentrations are typical of the Cretaceous target rocks. Unit 5 impactites have the highest U abundances, and, thus, record a strong Cretaceous rock component.

Potassium abundances sampled in oil shale horizons in the Yax-1 borehole are anomalously high (Appendix A.7 and Table 4.3). Increased illitization, i.e., increased K-content, with depth, in carbonate rocks associated with a major oil-producing basin, has been recently documented by Iftikhar et al. (2004) from the Hibernia oil field off the coast of Newfoundland, Canada. These authors suggested that the illitization occurred as the result of K-rich fluids migrating along fault zones, which were also exploited by migrating hydrocarbons. This study suggests that such pathways may occur in the form of our sampled oil-shale horizons (Fig. 4.8). As the oil shales occur below 1500 m in the Yax-1 borehole, this depth interval appears to be consistent with the onset of catagenesis in oil-producing carbonate rocks (Tissot and Welte 1978).

The altered rock located at 1347-1348 m appears to coincide with slightly elevated K and U gamma ray intensities (Kenkmann et al. 2004). Whole-rock analyses (Appendix A.7 and data in Schmitt et al. 2004) indicate this rock contains high SiO_2, Al_2O_3, K_2O, and Na_2O abundances, and the abundances for the trace elements Sc, Cr, Co, Ni, Zn, Rb, Zr, Sb, Cs, REE, Th, and U are also elevated in comparison to the host dolomitic rocks (Fig. 4.15b). The alteration zone displays a similar trace element profile and abundances to the average argillaceous dolomite and average oil shale, but has higher Cs and Rb (Fig. 4.15a). The REE, however, are not similar to the average argillaceous dolomite and average oil shale; they are LREE enriched. Considering our inability to identify bona fide shock metamorphic characteristics in this interval, an endogenic origin as part of the target sequence is, thus, more likely for this rock type, i.e., an illite-rich dolomitic rock (see next section).

4.8.5. Cretaceous rocks: impact-induced deformation?

Several Cretaceous rock samples located between 1315 and 1399 m from the Yax-1 borehole have distinct deformation features in the form of extensive brittle fractures and breccias. This deformation evidence must be discussed with regard to impact versus endogenic deformation. The brittle deformation fractures (Figs 4.3i, 4.5, 4.6) were probably produced by the Chicxulub impact event. As also suggested by Kenkmann et al. (2004), brittle deformation appears to be lithologically controlled, being more dominant in the dolomitic rocks (Figs 4.5, 4.6, and 4.8) than in anhydrite and argillaceous dolomites. Several breccia horizons are found in the Cretaceous rocks, which indicate extensive faulting with pervasive fragmentation (Figs 4.5 and 4.6). However, the paucity of shock metamorphic deformation effects in the limited amount of silicate minerals, due to the carbonate-dominated composition of the target rocks, makes the correlation of this deformation with the Chicxulub impact difficult (Kenkmann et al. 2004).

The extensive fracturing that characterizes the polymict breccia (Fig. 4.6) is difficult to reconcile with typical dissolution of carbonate/sulfate, as extensive translation is required to produce such a fault. Even if the dissolution of carbonate/sulfates had produced the brittle deformation observed in the dolomite, a later extensive deformation event would have to be invoked in order to explain the formation of this rather thick polymict breccia horizon. Based on these arguments, the formation of this polymict breccia is most likely the result of the Chicxulub impact event.

Other petrographic criteria were defined by Kenkmann et al. (2004) in order to link the observed deformation with the impact, i.e., the identification of fine-grained, low-porosity faults atypical of solution collapse produced in an extensional regime. Kenkmann et al. (2004) showed that the displacement to thickness (D/T) ratio of the brittle fault zones is not typical of tectonic shear zones but that the thickness of some of these faults indicates “dynamic shock loading before shear zone formation”. Most of the faults in the dolomite are indicative of “oscillating” conditions atypical of the incremental nature of endogenic faults, as no visible offset is observed (Kenkmann et al. 2004). Thus, we believe, in conjunction with our observations of brittle fractures, that the extensive fracture

pattern observed in Yax-1 Cretaceous dolomitic rocks (Figs 4.2 and 4.5) is most likely a product of the energy transfer that occurred immediately after impact.

In keeping with the observations by Kenkmann et al. (2004) and Wittmann et al. (2004), we have not found any *bona fide* shock metamorphic silicate mineral deformation or impact melt particles in our samples from the 1314 to 1399 m interval. This also refers to the so-called "impact melt rock" samples described by these authors from the interval between 1347 and 1348 m (see Appendix A.1 to A.3). *Bona fide* PDFs and melt particles have been identified in the suevitic dikes at 909 and 916 m depths, and PDFs alone in the meta-paraconglomerate at 1036 m (also described by Kenkmann et al. 2004). Stinnesbeck et al. (2004) also indicated that they had not found evidence for impact-induced deformation of the Cretaceous target rocks (they referred to overturned bedding, steeply dipping lithologies, major mechanical fragmentation, and shock metamorphism). These authors suggested the observed deformation was more likely the result of intraformational processes, i.e., the "dissolution of evaporites". We do not agree with Stinnesbeck et al. (2004) that the observed deformation in the Cretaceous rocks is primarily a product of dissolution. We suggest the Cretaceous rocks record a multi-stage history of deformation that encompasses impact-induced brittle deformation that overprints traditional dissolution-related carbonate deformation, i.e., dissolution related anhydrite is cross cut by a monomictic breccia dike at 1314.83 m (sample 233) and brittle fractures cross-cutting stylolites observed in the 1347 to 1348 m interval (Fig. 4.7).

The location of the Yax-1 borehole with respect to the crater center and the associated attenuated shock wave have to be considered in order to provide insight into the formation of shock deformation features and melt production. Because the Yax-1 borehole is located at quite a distance from the crater center, it might not have been subjected to significant shock levels required to produce, locally, characteristic (e.g., PDFs) shock microdeformation or impact melt. Already at >10 km radial distance downrange from the crater center, shock levels have been estimated by numerical modelling at less than 10 GPa, for impact angles between 90^{o} and 45^{o} (Pierazzo and Melosh 1999), the minimum required for planar deformation feature (PDF) formation (e.g., French 1998). Furthermore, at a

distance of 60 km from the center of the Sudbury impact crater, shock levels, also determined by numerical modelling, were shown to be <10 GPa (Ivanov and Deutsch 1999), and at 20 km from the heavily eroded center of the Vredefort impact crater of South Africa, shock levels have been recorded to be <10 GPa (Gibson and Reimold, 2005). These numerical and field studies agree with our observation regarding the paucity of shock-related micro-deformation features such as PDFs in the clastic Cretaceous components (Tuchscherer et al. 2004a) and on the endogenic origin of the altered dolomitic interval between 1347 and 1348 m. We suggest this horizon was likely a section of intense dissolution.

4.9. Conclusions

1) Melt particles in Yax-1 impactites represent mixtures of various siliceous target rocks, therefore, the use of element ratios cannot constrain the melt particle precursor compositions. This is also hindered by the paucity of analyzed mafic target rocks.

2) The average bulk suevite and suevitic groundmass compositions are similar to each other and, thus, must be composed of similar proportions of precursor components. Minor siliceous and carbonate target rock geochemical characteristics can be observed in the suevite and groundmass, respectively.

3) The siliceous end-member of the Yax-1 impactites has a trace element signature that is similar to that of the upper continental crust, i.e., it has similar abundances of Sr, Na, Sb, Zn, Fe, Co, Cr, Ni. When the siliceous end-member composition is calculated on a LOI-free basis, a significant mafic component becomes apparent in the Yucatán target volume.

4) The calculated carbonate end-member of the Yax-1 impactites indicates that the impactites are anomalously rich in calcite when compared to the calculated Cretaceous target rock composition. This indicates that our estimate of the Cretaceous target rock composition is either not a true representation of the Cretaceous rocks, and/or secondary calcite occurs in proportions great enough to significantly alter the carbonate end-member composition. The trace element signature of the carbonate end-member indicates that dolomitic rocks must have been a major component in the impactites and that U is a ubiquitous component.

5) Deformation features observed in the investigated interval between 1315 and 1399 m of the Cretaceous target rock indicate a multi-stage deformation history from pre- to post-impact times. A detailed microscopic investigation did not document any characteristic shock-related deformation micro-features. This makes the correlation of deformation features with the Chicxulub impact difficult. However, using cross-cutting relationships between the target rocks and brecciated intervals, at least one episode of deformation can be constrained that must be related to the Chicxulub impact.

6) We find no conclusive evidence that would suggest the brecciated interval between 1347 and 1348 m is an impact melt breccia. Mineralogical and textural indicators are more consistent with this breccia being interpreted as an alteration horizon that underwent extensive dissolution through the migration of K-rich fluids associated to brine reflux. The occurrence of oil-bearing shale below this impermeable horizon is also consistent with the onset of catagenesis, i.e., the oil-window. High concentrations of K were found in the oil-shale, which indicates that these layers may have been adequate pathways for the migration of fluids and hydrocarbons.

4.10. Acknowledgements

We gratefully acknowledge the comprehensive financial support that this project has received from a Petroleum Research Fund grant (PRF #37299-AC8) of the American Chemical Society. Detailed reviews by Phillip Claeys and Ralf Schmitt, and input from Ulrich Riller have significantly improved the manuscript. Thanks are also due to Maria Anastova, at the Council for Geosciences (Pretoria), who provided valuable support with the SEM investigations. C. Koeberl's work was funded by the Austrian Science Foundation project P17194-N10. This is University of the Witwatersrand Impact Cratering Research Group Contribution No. 94.

5. Major and trace element compositions of melt particles and associated phases from the Yaxcopoil-1 drill core, Chicxulub impact structure, Mexico[4]

5.1. Abstract

Melt particles found at various depths in impactites from the Yaxcopoil-1 borehole into the Chicxulub impact structure (Yucatán) have been analyzed for their major and trace element abundances. A total of 176 electron microprobe and 45 LA-ICP-MS analyses from 8 different melt particles were investigated. The main purpose of this work was to constrain the compositions of precursor materials and secondary alteration characteristics of these melt particles. Individual melt particles are highly heterogeneous, which makes compositional categorization extremely difficult. Melt particles from the uppermost part of the impactite sequence are Ca- and Na-depleted and show negative Ce anomalies, likely a result of seawater interaction. Various compositional groupings of melt particles are determined with ternary element and binary element-ratio plots involving major and trace elements. This helps to distinguish the degree of alteration versus primary heterogeneity of melt phases. Comparison of the trace element ratios Sc/Zr, Y/Zr, Ba/Zr, Ba/Rb and Sr/Rb with compositions of known target rocks provides some constraints on protolith compositions; however, melt compositions analyzed exceed the so far known compositional diversity of possible target rocks. Normalized REE patterns are unique for each melt particle, likely reflecting precursor mineral or rock compositions. The various discrimination techniques indicate that the highly variable compositions are the products of melting of individual minerals or of mixtures of several minerals. Small, angular shards that are particularly abundant in units 2 and 3 represent rapidly quenched melts, whereas larger particles (>0.5 mm) that contain microlites and have fluidal, schlieric textures cooled over a protracted period. Angular,

[4] Tuchscherer M. G., Reimold W. U., Gibson R. L., de Bruin D., and Späth A. 2006. Major and trace element compositions of melt particles and associated phases from the Yaxcopoil-1 drill core, Chicxulub impact structure, Mexico. *Meteoritics & Planetary Science* 41:1361-1379.

shard-like particles with microlites in Unit 5 likely crystallized below the glass transition temperature, or underwent fragmentation during or after deposition.

5.2. Introduction

In 2002 the International Continental Scientific Drilling Program (ICDP) retrieved the Yaxcopoil-1 (Yax-1) drill core about 60 km south-southwest of the center of the Chicxulub impact structure (Fig. 5.1; Dressler et al. 2003). This project was carried out because the retrieval and study of impactites from the Chicxulub impact structure was considered of prime scientific importance with regard to a plethora of aspects involving impact cratering processes. The Yax-1 core has provided a complete crater fill intersection, including a thick layer of impact melt rock. The melt rock particles at Chicxulub are believed to be the vitrification product of bulk rock and/or mineral melts. However, no adequate constraints have been obtained yet that would allow determining the degree of melting and mixing in Chicxulub melt rock particles. Impact melts are produced under extreme temperatures and pressures atypical of traditional endogenic processes (e.g., Melosh 1989; French 1998). The study of impact melt rock particles, thus, provides valuable information about cratering dynamics (e.g., Dressler et al. 1996; Hörz et al. 2002). Impact melt particles are commonly found as part of either fallback deposits in impact structures, fallout deposits of impact breccia, and even as clasts in injection dikes within the crater floor (Dressler and Reimold 2001).

The Yax-1 drill core recovered 100 m of continuous impactites between 795 and 895 m depth. Dressler et al. (2003) recognized 6 stratigraphic subdivisions, which have since been adopted by many Yaxcopoil-1 researchers. Our group, in contrast, has only recognized 5 subdivisions (Tuchscherer et al. 2004a, b), as we prefer to combine the upper two units of Dressler et al. (2003) into one unit (compare stratigraphic column of Fig. 5.2). Initial petrographic and geochemical information about the impactites and their stratigraphy has been published in two special Yax-1 issues of Meteoritics and Planetary Sciences (vol. 39, Nos. 6 and 7; in particular, the contributions by Ames et al. 2004; Dressler et al. 2004; Hecht et al. 2004; Kring et al. 2004b; Schmitt et al. 2004; Stöffler et al.

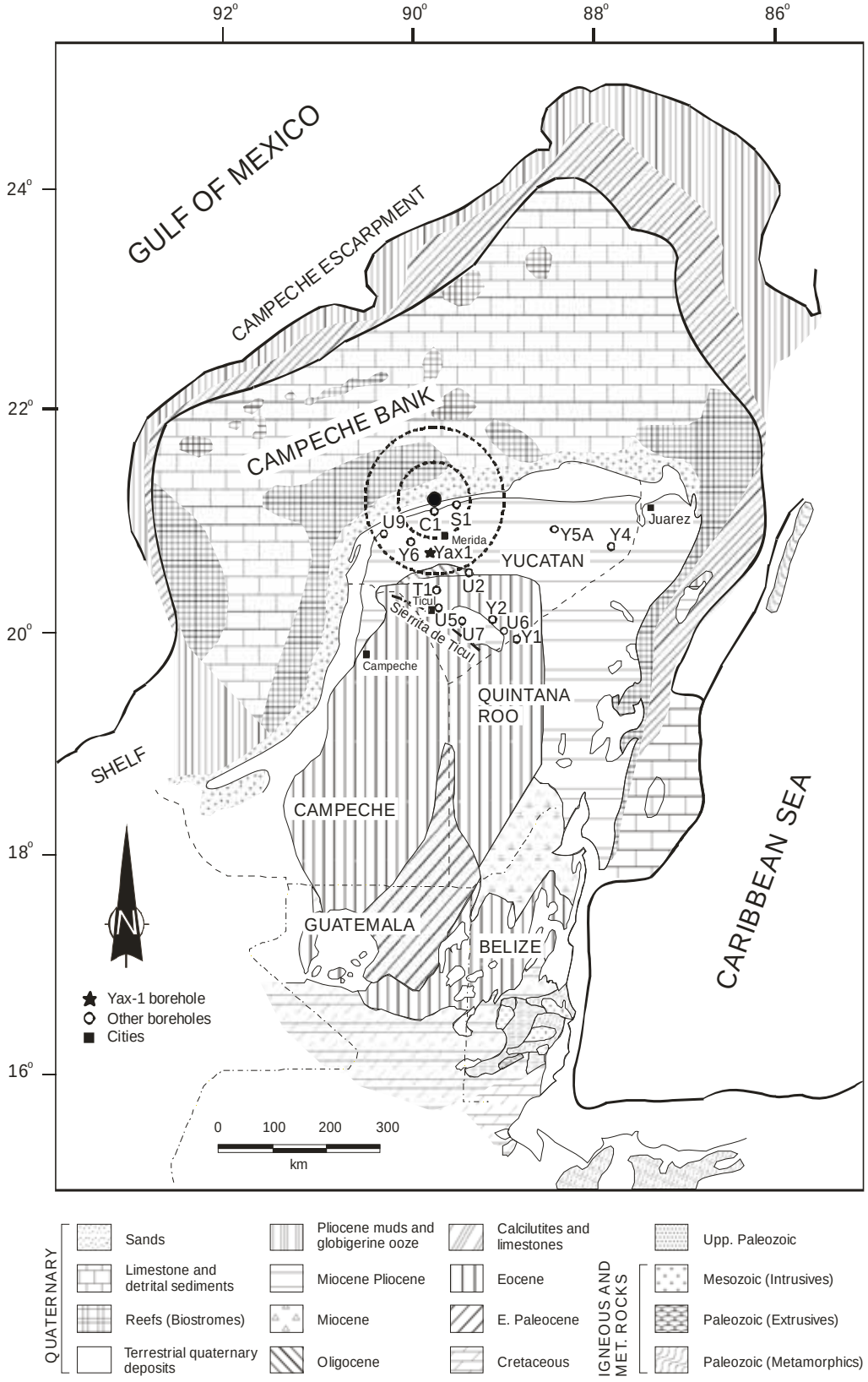

Fig. 5.1. Surface and offshore geology of the Yucatán Peninsula of Mexico with location of the Chicxulub impact structure, as well as the Yaxcopoil-1 (Yax-1) and other boreholes (modified after Lopez-Ramos 1975). Note that the nearest exposures of Cretaceous target rocks occur in Belize and Guatemala, several hundred kilometers from the impact structure.

2004; Tuchscherer et al. 2004a, b, also 2005; Wittmann et al. 2004; Zurcher et al. 2004). In the Yax-1 core, the retrieved impactites are believed to represent a depositional sequence of ejecta, massive melt rock, and a sequence of fallback suevite that have been preserved in the outer part of the impact structure (Stöffler et al. 2004; Tuchscherer et al. 2004a,b; 2005). The uppermost unit of suevitic breccia is believed to have been reworked by the resurge of seawater (suevite is defined as a clastic matrix, melt particle-bearing impactite – e.g., Dressler and Reimold 2001).

Previous studies on Yax-1 melt rock particle compositions, mostly obtained by EMPA, were reported by Ames et al. (2004), Dressler et al. (2004), Hecht et al. (2004), Kring et al. (2004b), Tuchscherer et al. (2004a), and Zurcher et al. (2004). They showed that the impactites are compositionally heterogeneous, which was attributed to incomplete mixing of compositionally diverse target rocks in the formation of melts, dilution with a large secondary carbonate component, and hydrothermal as well as seawater alteration that converted silicate phases into phyllosilicates. Ames et al. (2004), and others, showed that a great proportion of melt rock particles had been converted to phyllosilicate phases, as a result of low temperature seawater alteration. Dressler et al. (2004) concluded that melt particle compositions were generally homogeneous when recalculated on a L.O.I. free basis. They found a bimodal compositional distribution that they attributed to the melting and mixing of felsic/intermediate and mafic silicate target rocks. Hecht et al. (2004) recognized 4 types of melt particles based on petrographic characteristics, i.e., the degree of crystallization, color, shape, vesiculation, and clast content. Three types of alteration phases (sm1, sm2, and sm3) were also identified. Tuchscherer et al. (2004a) distinguished three types of melt particles (1 - mafic, 2 - mafic-alkali element-rich, and 3 - alkali element-rich) that all registered a K overprint. All mafic particles are thoroughly altered, whereas the more felsic particles analyzed commonly yield analytical totals near 100 wt%. Tuchscherer et al. (2004b) also analyzed bulk impact melt rock samples and noted that the green impact melt rock of Unit 4 (Fig. 5.2) has a composition involving a significant mafic component. Brown melt particles show similar compositions but a higher CaO content. Tuchscherer et al. (2005) analyzed melt particles for trace

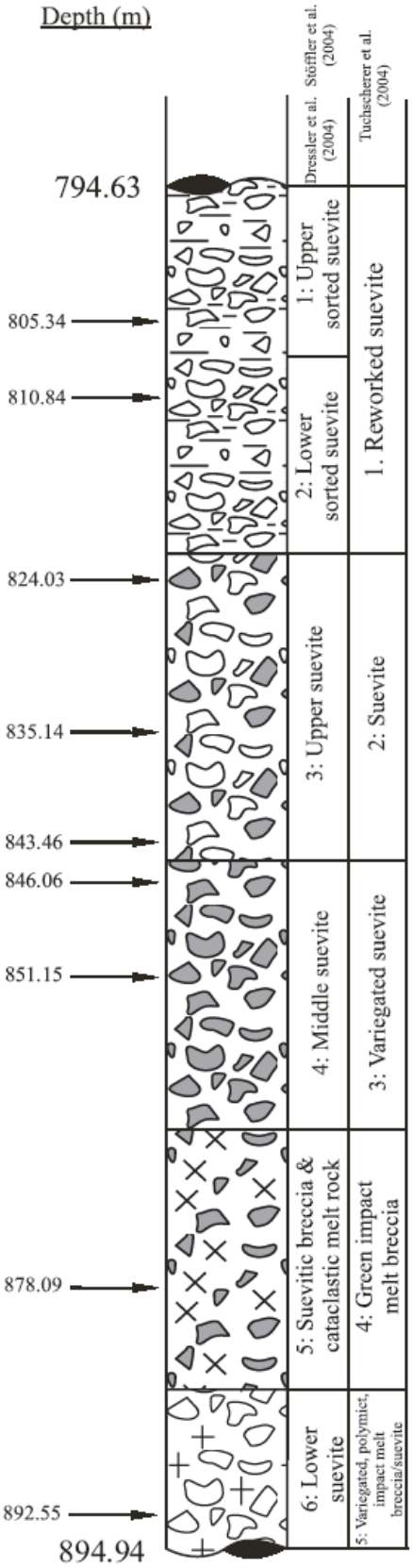

Fig. 5.2. Stratigraphy of the continuous impactite sequence retrieved from the Yax-1 borehole; sample depths are indicated as well. The stratigraphy of Dressler et al. (2004) and Stöffler et al. (2004) is shown for comparison.

element abundances and found that they represent mixtures of known target rocks (clastic supracrustals, granitic gneiss, granodiorite) with a mafic component (possibly amphibolite, as reported by Kettrup and Deutsch 2003).

For this contribution, we obtained major and trace element compositions for selected melt rock particles from different units of the Yax-1 core by electron microprobe (EMP) and laser-ablation-inductively coupled plasma-mass spectrometry (LA-ICP-MS). The results allow us to comment on the extent of melting involved during melt particle generation (mineral melting, bulk rock melting), mixing dynamics, cooling rates, and the effects of secondary alteration processes.

5.3. Geology

The Chicxulub impact structure is centered on the northwestern region of the Yucatán Peninsula (Fig. 5.1) that has a poorly known subsurface regional geology. The best geological compilation for the area was given by Lopez Ramos (1975). Geological observations at surface show that Tertiary and Quaternary rocks overlie the Chicxulub structure. Offshore rocks comprise Quaternary limestone with extensive biostromes. The nearest surface exposure of Cretaceous and Upper Paleozoic sedimentary/crystalline target rocks is found to the south of the Yucatán Peninsula, in Belize and Guatemala, where Chicxulub ejecta also occur (e.g., Pope et al. 2005). These deposits also provide insight into the composition of the Yucatán basement: The distal fallout breccias are generally carbonate-rich; clasts are composed of micritic and coarse crystalline limestone, laminated dolomite and calcareous mudstone. Detailed studies on buried ejecta deposits sampled by the UNAM 5-7 boreholes sampled closer towards the crater center show a progressively - towards the crater center - increasing proportion of silicate clasts (e.g., Sharpton et al. 1999). Other fallout deposits in NE Mexico contain melt spherules that are mafic to intermediate in composition, which likely reflects compositionally varied target rocks (Schulte and Kontny 2005). Zircons sampled in K/T boundary ejecta from the Raton basin of Colorado and Saskatchewan indicate Pan-African ages (544 ± 5, 548 ± 6 Ma; Kamo and Krogh 1995) for the crystalline basement in the Chicxulub target region. Various lithic

clasts were observed in the impactites of the Yax-1 borehole. Sedimentary rocks comprise limestone, dolomite, quartzite grains, and argillaceous limestone. Rocks from the silicate basement consist of granite, gabbronorite, gneiss, and schists (Tuchscherer et al. 2004a, 2005).

5.4. Methodology

Polished sections of ~150 µm thickness were prepared from samples that originated from 805.34, 824.03, 835.14, 843.46, 846.06, 878.09, and 892.55 m depths (Fig. 5.2). These "thick sections" were investigated with a petrographic microscope and a scanning electron microscope (SEM) in order to describe the various melt particles present. Once melt particle characteristics of a given unit had been identified, a backscattered electron (BSE) study was undertaken in preparation of quantitative EMPA and LA-ICP-MS work. Backscattered electron imaging was done at the Council for Geoscience, Pretoria, with a Leica 440 Stereoscan instrument with a LINK OXFORD energy-dispersive X-ray analysis system, at 20 kV, 2 nA, and 25 mm working distance. Quantitative electron microprobe analyses were collected for the elements Si, Ti, Al, Cr, Fe, Mn, Mg, Ca, and Na in wavelength-dispersive mode on a JEOL 733 Superprobe, at 15 kV, 20 nA, and 39 mm working distance, also at the Council for Geoscience. The electron-beam width was 3 µm, and peak counting times were 10 sec, with 5 sec counting times on symmetrical background positions. The standard K-H (USNM 143965; Jarosewich et al. 1980) was used for SiO_2, Al_2O_3, FeO_{tot}, CaO, Na_2O, and K_2O analysis, synthetic rutile for TiO_2, natural rhodonite for MnO, and the chromite standard USNM 117075 for Cr_2O_3 standardization. Data reduction was done with the JEOL Fortran program FZAFOC.

The concentrations of 26 trace elements (Sc, Ti, V, Cr, Ni, Co, Rb, Sr, Y, Zr, Nb, Ba, La, Ce, Pr, Nd, Sm, Eu, Tb, Gd, Dy, Ho, Er, Tm, Yb, Lu) were determined by LA-ICP-MS at the University of Cape Town (UCT) in particles previously analyzed by EMP. The UCT instrument is a Perkin Elmer ELAN6000 ICP-MS equipped with a CETAC LSX-200 laser ablation module. The frequency quadrupled Nd-YAG laser produces radiation with a wavelength of 266 nm and was operated at an energy level of approximately 5 mJ per pulse and at a

frequency of 5 Hz. Ablation pits of 100 μm diameter were excavated. Each analysis comprised the acquisition of three replicate analyses from 85 sweeps each across the selected mass range, at dwell times of 10 μs per mass peak. Calibration was done by hourly external standardization of all trace elements using the NIST 610 and 612 glass standards with background limits obtained by analysis of the carrier argon gas. Internal standardization was used to correct for instrument drift and differences in ablation yield from spot to spot. Calcium was used as an internal standard, based on Ca concentration results from EMPA. Off-line computer software (such as GLITTER) was not used to reprocess the data. Oxide levels were minimized by ensuring that Th/ThO was < 0.005 during daily instrument optimization. Isobaric interference corrections based on the knowledge of naturally occurring isotopes abundances (e.g., ^{144}Sm on ^{144}Nd) were made automatically by the instrument software. Typical precision and accuracy values for such analyses range from 1 to 10% (Grégoire et al. 2002). Repeat analysis of a UCT in-house glass standard (V40-56) produced 2σ error variations of <5% for Sc, Ni, Rb, Sr, Y, Zr, Nb, Ba, the rare earth elements (REE), Th, and U. For this instrument, Le Roux et al. (2002) indicated lower limits of detection (LLD) for all elements at less than 0.2 ppm, except for Ni (<1 ppm), and Sc and Ba (<0.4 ppm). Theoretical LLD ranges from 10 to 20 ppb were predicted for the REE, Ba, Rb, Nb, Sr, Zr, and Y to 100 ppb for V, Sc, and to 2 ppm for Ti, Ni and Cr (Grégoire et al. 2002). Le Roux et al. (2002) determined (for ablation craters of 100 μm diameter) the LLD for these major and trace elements at: Sc (0.36), Ni (1.06), Rb (0.12), Sr (0.08), Y (0.07), Zr (0.19), Nb (0.11), Ba (0.41), La (0.08), Ce (0.06), Nd (0.23), Sm (0.19), Eu (0.08), Gd (0.21), Dy (0.19), Er (0.14), Yb (0.13) (all values in ppm). LLD for the other trace elements were published by Potts et al. (1995), for a LA-ICP-MS operating at 7 Hz, at 100 sweeps, 320 μs dwell time, and ablation pits of 150 μm: Ti (0.03), V (0.06), Cr (0.30), Co (0.08), Pr (0.02), Tb (0.009), Ho (0.007), Tm (0.009), Lu (0.02) (values in ppm).

5.5. Samples studied

Table 5.1 summarizes the petrographic characteristics of the selected melt particles and their overall modal abundances in the various units. As discussed,

the melt particles throughout the impactite sequence all register variable degrees of alteration (Ames et al. 2004; Hecht et al. 2004; Tuchscherer et al. 2004a; and Zurcher et al. 2004). More petrographic detail about these melt particles is provided in Table 5.2 and in the following unit description sections. Figure 5.3 shows backscattered electron (BSE) images of these melt particles, with analytical traverses and LA-ICP-MS spots also shown.

Table 5.1. Petrographic characteristics and abundances (from Tuchscherer et al. 2004a) of melt rock particles found in the various impactite units of the Yax-1 borehole.

Unit	**1**	**2**	**3**	**4**	**5**
Abundance	63 vol %	62 vol %	66 vol %	94 vol %	33 vol %
Shape	Rounded to subangular	Subrounded to subangular	Subrounded to subangular	Subangular to angular	Subrounded to subangular
Schlieren	No	No	Yes, common	Yes, occasional	Yes, occasional
Hand sample color	Mostly green	Mostly green	Variegated, green, beige, brown, red	Mostly green with yellow, brown, green tinges	Variegated, green, beige, brown
Micro-scopic light color	Yellow to brown green (altered)	Yellow green	Dark to med. brown red and gray	Green gray	Yellow gray
Perlitic fractures	Yes	Rare	No	No	No
Vesicles	Yes	Yes	Yes	No	No
Microlites	No	Yes	Yes	Yes	Yes
*Inclusions**	Cc, qtz, fs	Cc, qtz, fs	Cc, qtz, fs, ap	Qtz, fs, bio	Cc, qtz

*Abbreviations: Cc = Calcite, qtz = quartz, fs = feldspar, bio = biotite, ap = apatite.

Table 5.2. General description of melt particle material analyzed by EMPA and LA-ICP-MS for this study.

Thin section depth (m)	Unit	Type of melt particle material analyzed
805.34	1	Reworked green melt particle with secondary calcite intergrowths replacing altered mesostasis.
824.03	2	Small, altered, green, vesiculated melt shard with no microlites.
835.14	2	Altered, subrounded, gray melt particle with detrital quartz inclusions and other noticeable compositional heterogeneities.
843.46	2	Altered, brown melt particle with quartz clast and microlites.
846.06	3	Two altered, zoned, beige melt particles with microlites.
878.09	4	Altered crystalline patch overprinting melt particle and microlite bearing melt particle.
892.55	5	Traverse through a melt shard with microlites.

5.5.1. Unit 1

From this unit, a sample from 805.34 m depth was selected for analysis (Fig. 5.3a). It is a reworked suevite that comprises an amalgamated mass of highly altered and fractured melt particles. No significant groundmass material is observed macroscopically owing to the compacted nature of the melt particles. Highly altered lithic clasts (gneiss, carbonate, and monomineralic quartz) are present. The melt particle boundaries are irregular. Fracturing is strong, and, accordingly, the sample is highly friable. The analyzed melt particle region is characterized by well preserved, often circular, cross-sections of vesicles, only partially filled by calcite (Fig. 5.3a). The original mesostasis is partially replaced by authigenic intergrowths of calcite and K-feldspar (Fig. 5.3a).

5.5.2. Unit 2

Three melt particles were analyzed from Unit 2, from 824.03, 835.14, and 843.46 m depths (Figs 5.3b to d, respectively). The shard-shaped particle in Figure 5.3b is highly altered, shows a subangular morphology, and is partially replaced by calcite. Holes (irregularly shaped, dark regions) are visible in the BSE image and thought to have been plucked during thin sectioning. The melt particle at the center of Figure 5.3c is well-preserved and subrounded. The particle is zoned, having a narrow margin defined by a somewhat lighter gray color compared to the mottled interior. The BSE image of Figure 5.3d is of a large, brown melt particle (>3 cm) and displays a patchy texture that is primarily controlled by sectors rich in K-feldspar (see EMPA section 4.1).

5.5.3. Unit 3

Both melt particles analyzed from Unit 3 are from 846.06 m depth (Figs 5.3e, f). Figure 5.3e shows melt particles with sub-rounded to sub-angular shapes that contain vesicles. The particle analyzed (at left in the image) contains several BSE dark gray patches that are enclosed in a rather homogeneous, medium gray matrix. A bright (iron-rich) BSE region is noted in the bottom right of the particle. Figure 5.3f shows the second particle, which is sub-rounded and zoned as defined by medium gray BSE intensity towards the margin, compared to the darker gray

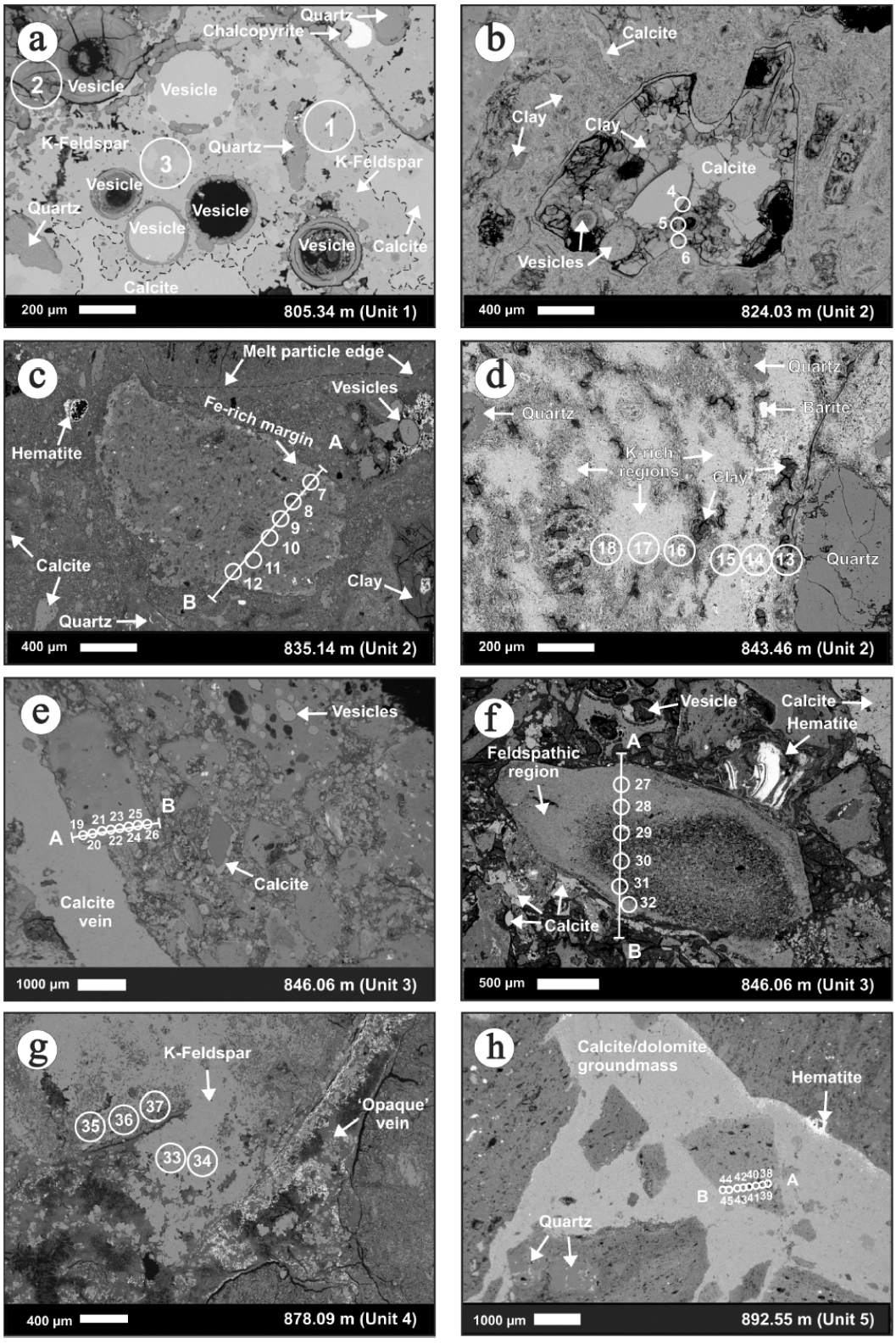

Fig. 5.3. Backscattered electron (BSE) images of melt particles analyzed in this study. The location of LA-ICP-MS ablation pits with analysis numbers are shown as large circles: a) Melt particle mrp_805.34, Unit 1. Note the well rounded cross-sections of vesicles, some infilled by calcite whereas others empty. b) Melt particle mrp_824.03, Unit 2. The interior region of the particle has been replaced by calcite. c) Melt particle mrp_835.14, Unit 2. The margins of the particle are of higher BSE intensity, being rich in iron. d) Melt particle mrp_843.46, Unit 2. The

(*Fig.5.3 caption continued from previous page)* particle displays a patchy texture defined by bright BSE K-feldspar rich regions that are surrounded by phyllosilicate rich margins. e) Melt particle mrp1_846.06, Unit 3. Note that a much lower proportion of groundmass is noted compared to the grains in Figures 5.3c and d. f) Melt particle mrp2_846.06, Unit 3. The particle shows marginal zonation defined by heavier elements compared to the core. g) Melt particle mrp_878.09, Unit 4. h) Melt particle mrp_892.55, Unit 5. Note the angular and shard-like character of the melt particles, which are groundmass-supported.

core. Melt particles are well compacted and contain vesicles (Fig. 5.3e), as well as calcite grains and veins. The groundmass is dark gray, suggesting it is composed of light elements (volatile-rich phyllosilicates).

5.5.4. Unit 4

Figure 5.3g represents the sample from 878.09 m depth in Unit 4. A number of medium gray patches are discernable. High-magnification shows radiating acicular phyllosilicates, elongate and stubby microlites, and equant crystals of either adularia or orthoclase. Cross-cutting relationships between the microlites and larger equant crystals suggest the microlites crystallized first. The phyllosilicates do not cut the equant crystals, which suggests that the latter formed last. An opaque vein, typical of veining in the green monomict melt breccia, contains disseminated μm-sized hematite and radiating acicular phyllosilicate crystals. The radiating crystal habit suggests rapid crystallization in open spaces.

5.5.5. Unit 5

Angular melt particles are typically suspended in the carbonate groundmass (Fig. 5.3h). The particles contain monomineralic quartz inclusions, dark alteration patches, BSE bright hematite patches, and numerous microlites. The latter may be preferentially aligned, indicative of flow prior to melt particle solidification and subsequent fragmentation. In the groundmass, hematite is observed at the margins of melt particles. Numerous small (<10 μm), angular melt particles occur disseminated in the groundmass carbonate minerals (see also Tuchscherer et al. 2004a).

5.6. Geochemical results

Great care was taken to ensure that the LA-ICP-MS pits overlapped the much smaller EMPA spots in order to attempt correlation. The numbered circles shown in Figure 5.3 represent ablation pits with corresponding LA-ICP-MS analysis numbers. The results are given in Appendix A.9 to A.11. In order to discuss the compositions of the melt particles, major elements have been plotted on an ACF-A'FK diagram (Fig. 5.4) and compositional profiles have been drawn (Fig. 5.5). With regards to the trace element data, chondrite-normalized REE patterns are compared (Fig. 5.6), and selected ternary diagrams (Fig. 5.7) and element ratio plots (Fig. 5.8) are used to illustrate compositional variation. The elements Zr, Sc, Nb, Y, Cr, Ni, and Co are all relatively immobile and, thus, most useful for the investigation of possible protolith/proto-mineral chemical characteristics. The elements La, Sm, and Yb are incompatible and, thus, provide good comparison between severely altered and less altered melt particles, as they preferentially migrate into a fluid phase. The large ion lithophile elements (LILE) Ba, Sr, and Rb are also incompatible, but because of their low ionic potential will behave during alteration differently from, for example, the rare earth elements (REE) (Guy et al. 1999). As observed in units 1 and 2 (Tuchscherer et al. 2004b), the LILE are preferentially enriched, as they have not been leached out due to their large ionic radii in comparison to the REE. The refractory elements Cr, Ni, and Co (Fig. 5.7c) also provide insight into the presence, or admixture, of mafic phases in the melt particles. For the identification of possible target components in the melt particle population, all currently known target rock compositions are compared in Figures 5.7 and 5.8 with the melt particle data. For a similar correlation with the chondrite-normalized REE abundances and target rocks (Fig. 5.6), see REE plots in Koeberl (1993) and Tuchscherer et al. (2004b, 2005).

5.6.1. Unit 1

The results of EMPA on the melt particle from 805.34 m depth have generally low wt% totals (analyses #1–19, Table A.9), indicative of a high volatile content. The particle is characterized by low Ca and Na abundances but enriched in Fe, Mg, and K compared to compositions of melt particles from other

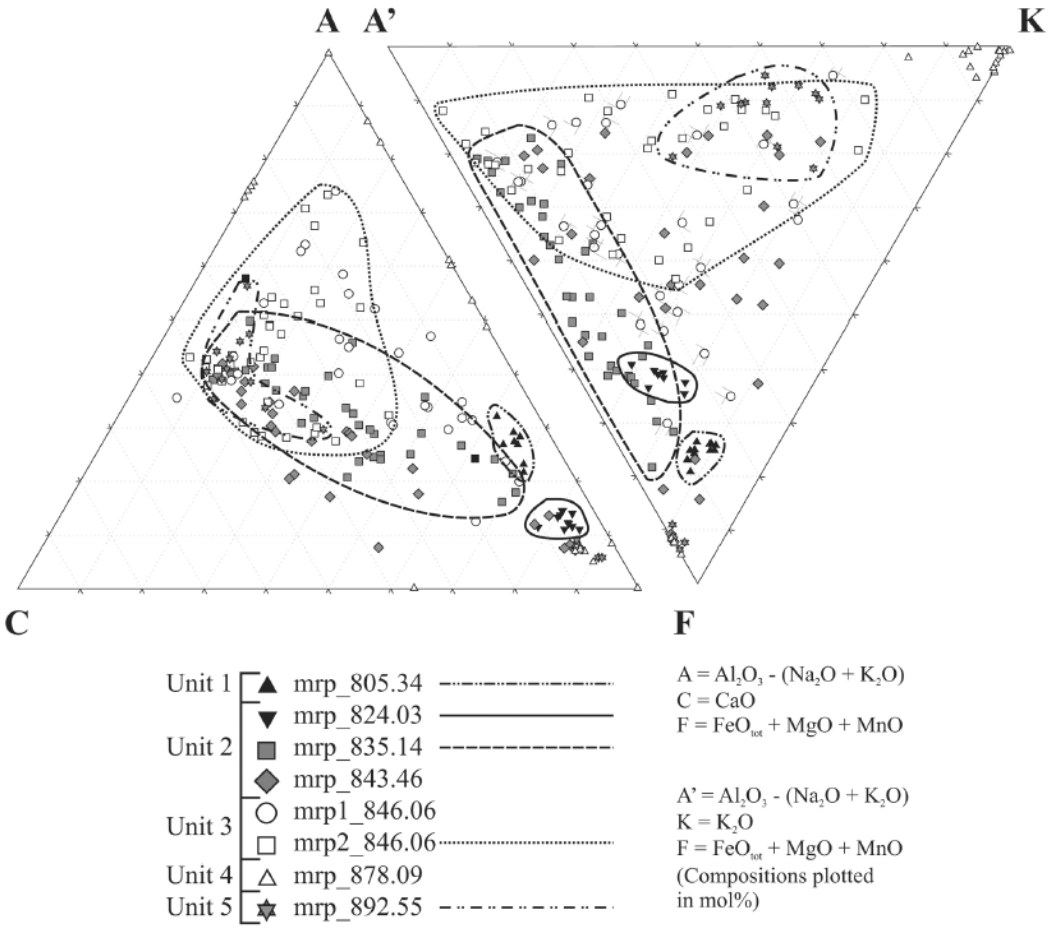

Fig. 5.4. ACF–A'FK diagram (after Eskola, 1939) of Yax-1 melt particle compositions determined by EMPA (data from Table A.9) plotted based on molecular proportions.

units (with exception of the particle from 824.03 m). In Figure 5.4, the data for this particle plot in a discrete group near the F apex of the ACF–A'FK diagram. Apart from this grouping, all major elements show some variation, especially regarding Ti, Al, and Fe. Trace element results for the 805.34 m particle show some of the lowest trace element abundances obtained in this investigation, especially with regards to Ti, V, Co, Sr, Y, Nb and the REE. The REE (Fig. 5.6a) abundance for this particle is almost chondritic; slight negative Ce and positive Eu anomalies are noted. Specific groupings can be discerned in the incompatible trace element data (Fig. 5.7a): the analyses form a high Zr and low Sc plus Y group. Lanthanum, Sm, and Yb (Fig. 5.7b), and Cr, Ni, and Co (Fig. 5.7c) do not yield groupings. Cr was not detected in most of these analyses, which, therefore, do not plot meaningfully in Figure 5.7c. A plot of the LILE Rb, Sr, and Ba (Fig. 5.7d) also produces good compositional separation; the particle is low in Sr and high in Rb and Ba. Ratios of selected trace elements distinguish 2 data groups

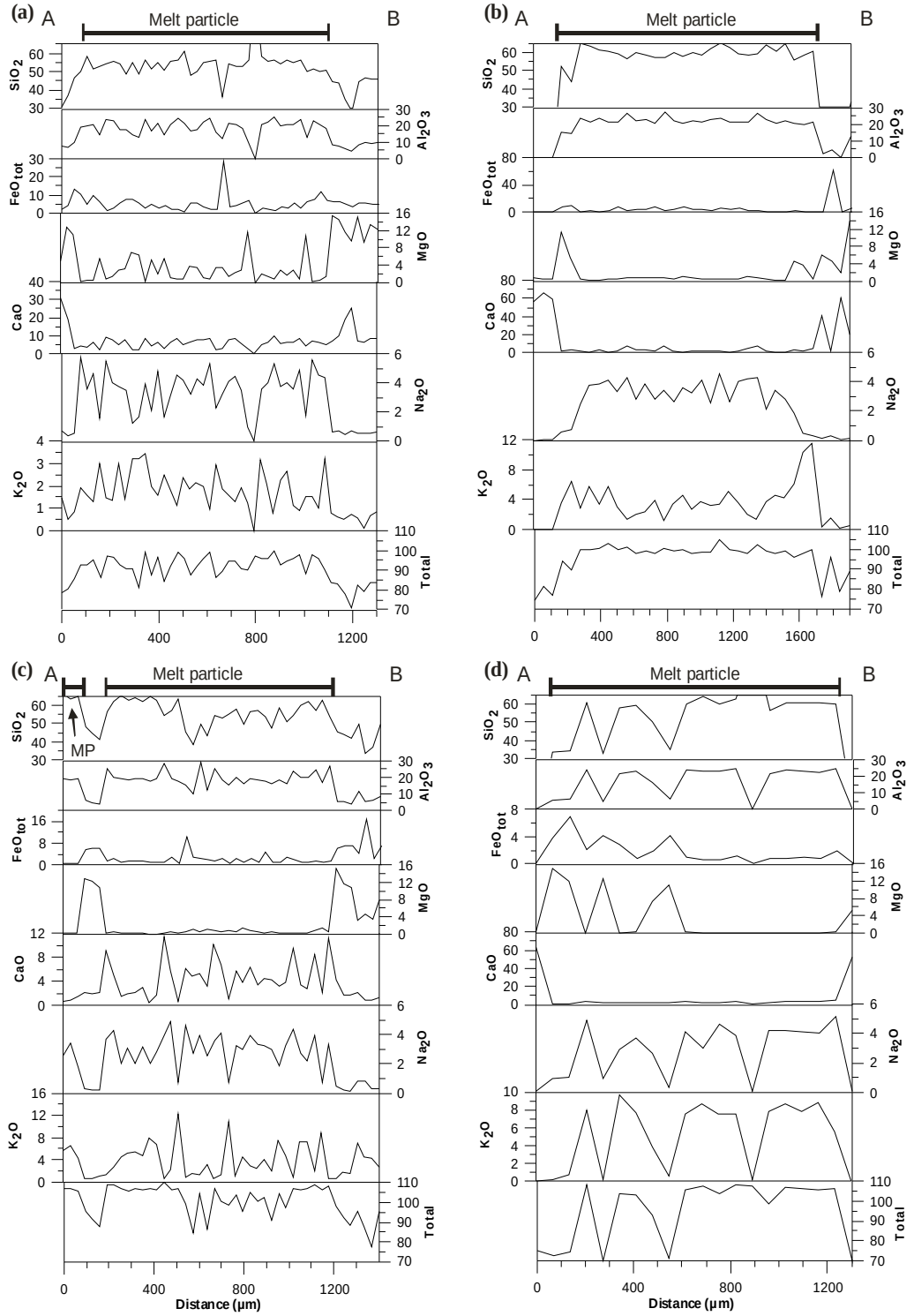

Fig. 5.5. a) Electron microprobe traverse through melt particle mrp_835.14: analyses # 20-55 in Table A.10 and analyses #1-11 of Table A.11. b) Electron microprobe traverse through particle mrp1_846.06: analyses #86-114 of Table A.10 and analyses # 12-28 of Table A.11. c) Electron microprobe traverse through particle mrp2_846.06: analyses # 115-147 of Table A.10 and analyses #29-38 of Table A.11. Note that the zonation observed in Figure 3f is best defined by SiO_2 and the wt.% totals. d) Electron microprobe traverse through particle mrp_892.55: analyses #155-172 of Table A.10 and analyses #39 and 40 of Table A.11. Note that mafic phyllosilicates are most prevalent towards the "A" margin; the groundmass is calcite rich.

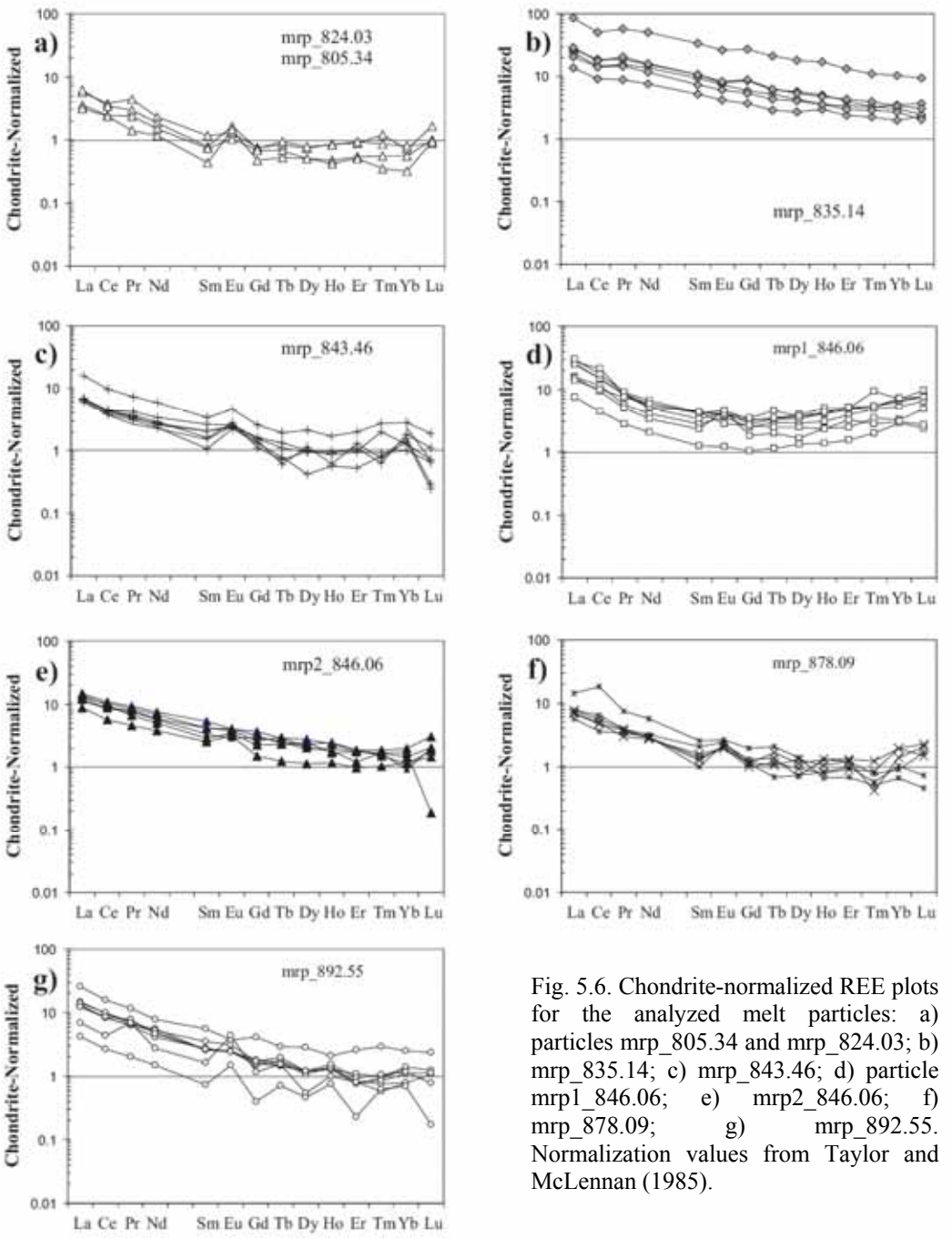

Fig. 5.6. Chondrite-normalized REE plots for the analyzed melt particles: a) particles mrp_805.34 and mrp_824.03; b) mrp_835.14; c) mrp_843.46; d) particle mrp1_846.06; e) mrp2_846.06; f) mrp_878.09; g) mrp_892.55. Normalization values from Taylor and McLennan (1985).

(Figs 5.8a-d). When comparing individual analyses with the sampled area (Fig. 5.3a), it is noted that there are no obvious compositional discrepancies between the altered melt particle and the orthoclase replacement intergrowths, with the exception of Ti that locally can be several orders of magnitude above average and signifies the presence of small inclusions.

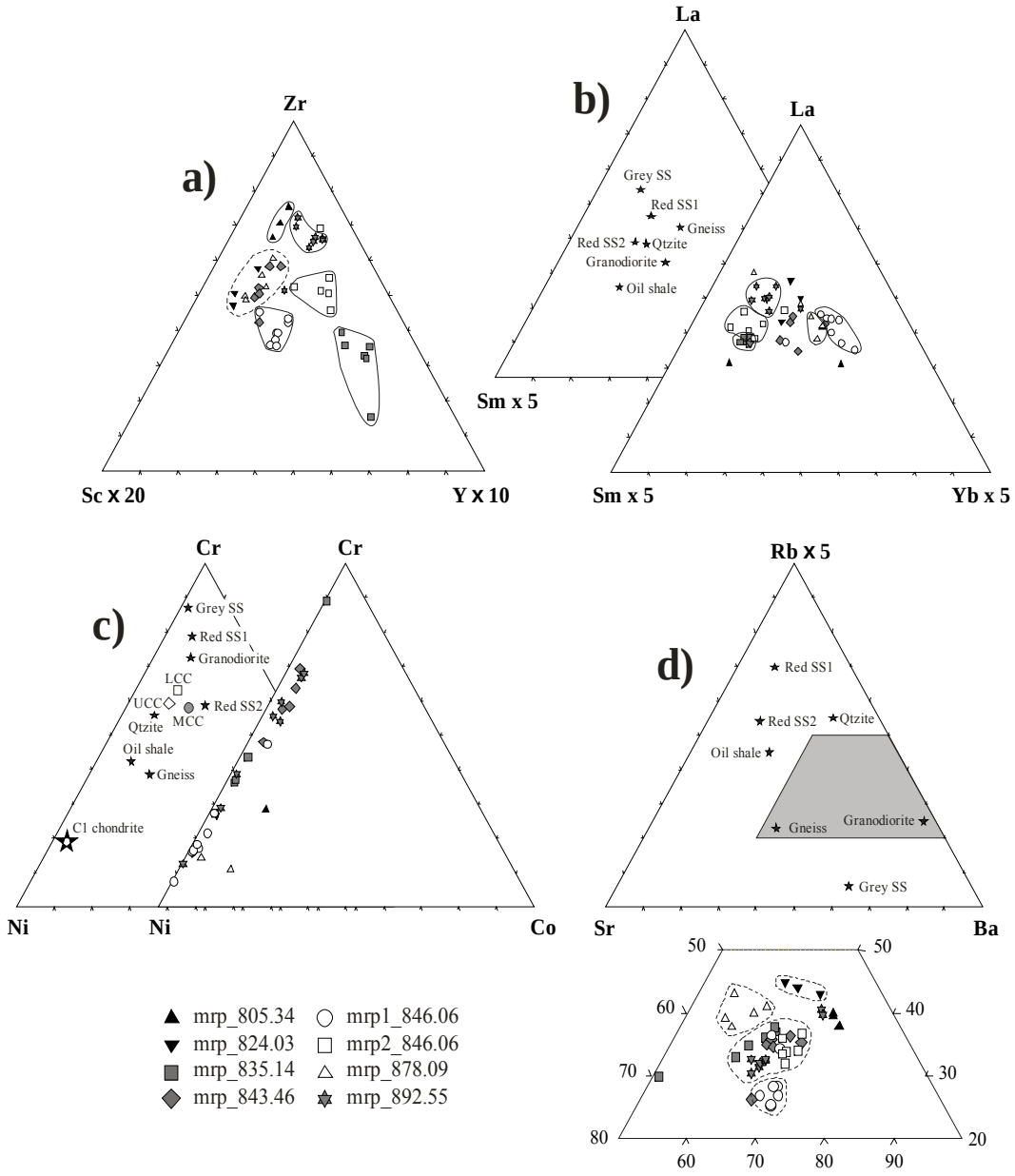

Fig. 5.7. Trace element ternary diagrams showing melt particle and known target rock compositions. Dashed areas indicate clusters of uniform melt particle compositions: a) Zr-Sc-Y ternary; in order to accentuate the melt particle fields, Sc and Y were factored by 20 and 10, respectively; b) La-Sm-Yb ternary; in order to accentuate the melt particle fields, Sm and Yb were both factored by 5; c) Cr-Ni-Co ternary, UCC = upper continental crust, MCC = middle continental crust, LCC = lower continental crust (crustal values from Rudnick and Gao, 2003; CI chondrite values from Palme and Jones, 2003); d) Rb-Sr-Ba ternary; in order to accentuate the melt particle field, Rb was factored by 5.

5.6.2. Unit 2

The particle from 824.03 m depth has similar compositional characteristics as the particle from Unit 1. Particle mrp_835.14 is rich in Si, Al, Ca, Na, and K (# 20–55, Table A.9) and has an iron-rich margin, as observed in elevated BSE

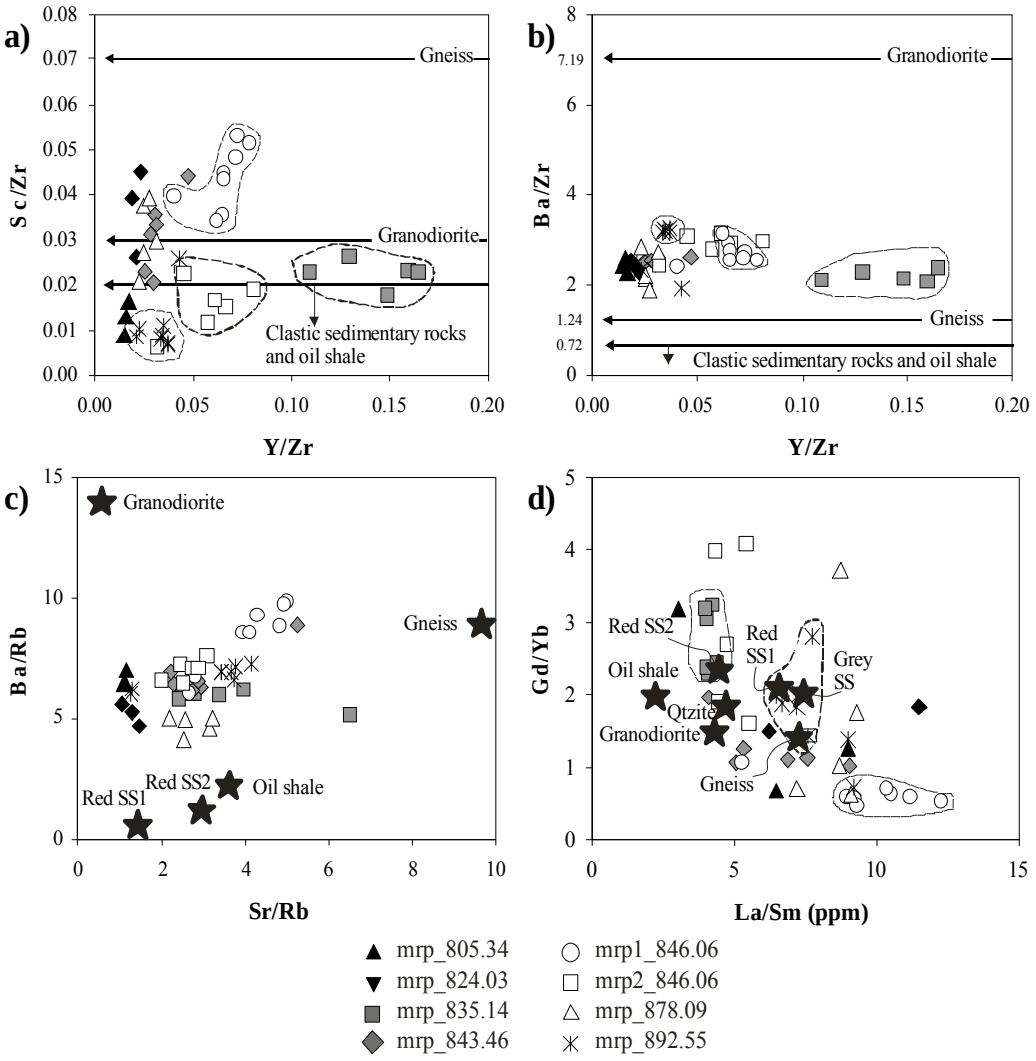

Fig. 5.8. Binary diagrams for melt particle and known target rock trace element ratios: a) Sc/Zr versus Y/Zr; b) Ba/Zr versus Y/Zr; c) Ba/Rb versus Sr/Rb; d) Gd/Yb versus La/Sm. See text for discussion.

intensity (Fig. 5.3c) at the edges of the traverse (Fig. 5.5a). The surrounding groundmass is highly enriched, compared to the melt particle, in Ca, Mg, and Fe (# 1–11, Table A.10, Fig. 5.5a). Abundances throughout the particle are highly variable (Fig. 5.5a). Only a single analysis produced an analytical total near 100 wt%, consistent with an andesine composition of $An_{49}Ab_{47}Or_4$ (# 48, Table A.9).

Most adjacent analyses are similar but contain some K and have low totals. In the ACF diagram (Fig. 5.4), most analyses fall between 30 and 50 % C component, but some analyses scatter widely and trend towards the F apex; they originate from the Fe-rich margin of the particle. In the A'FK diagram, all analyses plot along the A'–F tie line, between 0 and 20% of the K component. Trace element results for particle mrp_835.14 (#7 – 12, Table A.11, Unit 2) record some of the highest abundances in the whole data suite. The chondrite-normalized REE patterns show abundances up to 100x chondritic (Fig. 5.6b). Negative Ce but no Eu anomalies are noted. Specific groupings can be observed in the Zr–Sc–Y and La–Sm–Yb ternary diagrams (Figs 5.10a, b), but more scatter is obvious in the Rb–Sr–Ba ternary (Fig. 5.7d). Particle mrp_835.14 is enriched in Y (Fig. 5.7a) and Sm (Fig. 5.7b) compared to all other analyzed particles. High Sm is indicated by the shallower slope of the LREE (Fig. 5.6b) and lower La/Sm ratios (Fig. 5.8d), also when compared to other melt particles. No grouping can be identified in the distribution of Cr–Ni–Co (Fig. 5.7c), but reasonable groupings are observed in the element ratio plots (Figs 5.8a, b, and d).

Microprobe analyses obtained from a brown melt particle (mrp_843.46, Fig. 5.3d) have in their majority (18/29) analytical totals near 100 wt%, indicating the particle is relatively volatile-poor (# 56–85, Table A.9). These analyses correspond to a *pseudo*-feldspar composition of $An_{33}Ab_{32}Or_{35}$. Other EMP analyses rich in volatiles are consistent with a mixed mafic and alkaline composition. The analyses plot in the ACF diagram similar to particle mrp_835.14; however, because of the relatively high K abundances, these data scatter widely in the A'FK diagram (Fig. 5.4). The particle is not very trace element-rich (#13–18, Table A.11, Unit 2). Chondrite-normalized REE patterns are mostly above chondritic, but with some HREE analyses falling below or straddling the chondrite line (Fig. 5.6c). The LREE are preferentially enriched and a positive Eu anomaly is characteristic. Data for this particle are best separated from the analyses of other melt particles in the Zr–Sc–Y plot (Fig. 5.7a), but show much scatter in the La–Sm–Yb plot (Fig. 5.7b). A reasonable grouping occurs in the Rb–Sr–Ba plot; however, extensive overlap with data from other particles is

noted. Trace element ratios produce relatively good groupings in Figures 5.8a-c, but not in 5.8d.

5.6.3. Unit 3

The melt particle mrp1_846.06 (Fig. 5.3e, Unit 3) has a generally feldspathic composition (# 86–114, Table A.9). Along the EMPA traverse the particle is relatively homogeneous with respect to silica (Fig. 5.5b) but has much variation of Fe, Ti, Ca, Na, and K. Similar to the particle in Figure 5.3c (mrp_835.14), this melt fragment is enriched in Si, Al, Na, and K compared to surrounding groundmass that is a carbonate/phyllosilicate mixture (# 12–28, Table A.10). The melt particle analyses plot throughout the central areas of the ACF and A'FK diagrams, but not above 50 % C component. This is attributed to low concentrations of Ca with increasing K (Fig. 5.4). Eight LA-ICP-MS analyses were obtained from this particle (analyses #19–26, Table A.11). Overall abundances are relatively uniform, except for analysis #25 with a relatively lower concentration of the lithophile trace elements due to a local hematite patch of likely secondary origin. The chondrite-normalized REE diagram shows a concave (saddle) pattern, with all normalized abundances above chondritic values (Fig. 5.6d). In ternary plots the analyses fall into well-defined fields (Figures 5.10a, b, and d). The siderophile elements (Fig. 5.7c) do not show any good compositional grouping. Other trace element ratios produce good groupings in Figures 5.11a, c, and d, whereas three outliers are seen in Figure 5.8b (variable Ba contents in #19, 24, 26), two outliers in Figure 5.8c due to low Sr abundances, and one outlier in Figure 5.8d due to a low La/Sm ratio.

The zoned particle mrp2_846.06 is less volatile-rich in its marginal zone than in the core (Fig. 5.3f, Unit 3). It is enriched in Si, Al, Ca, Na, and K (# 115–147, Table A.9) compared to the groundmass, which is rich in Fe and Mg (# 29–38, Table A.10). Figure 5.5c shows an EMPA traverse across the particle. In the central part, Si abundances are lower and more variable than at the margins, and Mg abundances are slightly higher in the core. The abundances of Fe, Ca, Na, and K are variable throughout the particle but relatively more so in the core. The particle is volatile-rich but, despite this, has a composition that resembles alkali

feldspar. The melt particle does not contain much Fe or Mg; thus all analyses plot below 50 % of the F components in both the ACF and A'FK diagrams; the data scatter (Fig. 5.4). Six trace element analyses were obtained for this particle (analyses #27–32, Table A.11). REE patterns do not show much variation (Fig. 5.6e). The patterns are similar to those of mrp_835.14 but, in comparison, do not show a Ce anomaly and contain both positive and negative Eu anomalies. With regards to the observed zonation (Fig. 5.3f), analysis #30 in the central region of the melt particle shows slightly lower trace element abundances of P, Sc, Ti, V, Sr, and Y than the spots closer to the edge of the grain. Compositional groupings are observed in Figures 5.10a, b, and d. No Cr was detected; thus, the particle can not be plotted in Figure 5.7c. The LILE data yield a tight grouping, which overlaps with other melt particle compositional fields (Fig. 5.7d). Trace element ratio plots show good groupings in Figure 5.8a, b, c, but scatter is prominent in Figure 5.8d due to variable Gd/Yb ratios that are especially high at the edges of the particle. The lower trace element abundances in the central region of the particle correlate with lower EMPA totals.

5.6.4. Unit 4

A melt particle from 878.09 m depth represents the green impact melt breccia (Figs 5.3g). Several EMP analyses were obtained in a relatively unaltered region, towards the top-left of Figure 5.3g, where plagioclase microlites of $An_{49-39}Ab_{57-44}Or_{7-3}$ composition occur. The particle also contains euhedral, equant orthoclase-like patches believed to represent secondary adularia from K-metasomatic overprint. In the A'FK diagram, these data all cluster towards the K apex (Fig. 5.4). In the ACF diagram, however, individual analyses plot along the A–C and A–F tie-lines, because Ca is either very low or absent, and Fe and Mg can also be absent. Several acicular diopside crystals of $En_{45-46}Fs_6Wo_{48-49}$ composition were found. This particle represents a specific melt type that is Ca and Mg rich enough to produce diopside microlites. The remainder of the particle, i.e., the altered mesostasis surrounding the orthoclase crystals, contains phyllosilicates rich in Mg (# 148–154, Table A.9). The particle has relatively low trace element abundances (#33–37, Table A.11). The LREE are enriched, but do

not exceed 10x chondritic values (Fig. 5.6f). The HREE scatter about the chondrite line, and all patterns have a positive Eu anomaly. Analysis #34 shows a strong positive Ce anomaly. Analyses of the immobile elements from the medium gray region (#33 and 34) cluster together with the melt particle analyses (# 35–37) in the Zr–Sc-Y ternary diagram (Fig. 5.7a). The REE ternary plot shows more scatter for the orthoclase patch than the melt particle analyses, the latter plotting together (Fig. 5.7b). No grouping occurs for Cr, Ni, and Co results (Fig. 5.7c), but the LILE analyses all plot together (Fig. 5.7d). Trace element ratio plots show much scatter in Figures 5.8a, b, and d, and a relatively good grouping in Figure 5.8c.

5.6.5. Unit 5

Particle mrp_892.55 is alkali-rich and characterized by a variable volatile content, (total major element contents range from 60 to 97 wt%; # 155–169, Table A.9). This is primarily the result of mafic phyllosilicates interspersed with alkali-rich melt. The Al, Na, and K abundances are anti-correlated with Fe and Mg contents. A traverse shows that the mafic patches are located mostly at the A margin (Fig. 5.5d). This produces two data groupings in the ACF diagram, one near the F apex and another closer to the A–C tie line (Fig. 5.4). In the A'FK diagram, the alkali-rich phases plot close to the K apex. Trace element results are variable (# 38–45, Table A.11). REE concentrations vary widely from below chondritic values to 20 times above. Six patterns have positive Eu anomalies (Fig. 5.6g). Compositional groupings occur in Figures 5.7a, b, and d. Variable ratios of Cr and Ni are noted (Fig. 5.7c). Analysis # 40 has high P, Sc, Ti, V, Cr, Ni, Co, Y, Zr, Nb, REE, low Ba, and a high Sc/Zr ratio. These high abundances most likely reflect the local presence of titanite. This analysis also forms a compositional outlier in Figures 5.7a and 5.8a. Two analyses, # 38 and 39, have relatively low trace element abundances, especially for Sr, and, thus, plot away from the other analyses (Figs 5.7d, 5.11b, c). These aberrant data were obtained close to the right margin labelled "A" (Fig. 5.3h), which is rich in mafic phyllosilicate phases, as determined by optical examination and EMPA (Fig. 5.5d).

5.7. Discussion

EMPA and LA-ICP-MS analysis has provided new insight into the composition of melt particles of the Yax-1 drill core, especially with regard to the trace element distribution at the microscopic scale. Several previous investigators noticed the heterogeneous and pervasive alteration signature in the Yax-1 impactites (see geochemistry background in the Introduction section). However, because the melt particles were subjected to variable degrees of alteration, other techniques have to be used to unmask the melt formation process(es). Here, we discuss how LA-ICP-MS trace element data can help decipher the genetic history of these highly altered melt phases.

5.7.1. EMPA constraints on secondary alteration

Besides the limited number of EMP analyses from this and earlier studies that yielded analytical totals near 100 wt%, the data base suggests that all remaining melt particle analyses with low analytical totals represent compositions that have been overprinted by secondary hydrothermal processes and/or were devitrified through diagenetic hydration (e.g., Ames et al. 2004; Hecht et al. 2004; Tuchscherer et al. 2004a and b 2005; Zurcher et al. 2004). The Chicxulub impactor struck a wet and carbonate-rich target that inevitably promoted the formation of volatile-rich melt particles and their alteration after cratering. Melt particles from units 1 and 2 are depleted in Ca and Na, but enriched in Fe, Mg, and K, in comparison with melt particles from greater depth. Because of their stratigraphic location at the top of the impactite section and the similar geochemical alteration signature as that of palagonized volcanic rocks (e.g., Guy et al. 1999), we believe that the upper impactites interacted with seawater. This has promoted compositional homogeneity of the melt particles in the upper two units, which are of more uniform composition compared to particles from the lower units (see compositional fields and sample depths in Fig. 5.4). This homogenization effect can also be observed in the whole rock major and trace element data for this unit (Tuchscherer et al. 2004b).

Electron microprobe analyses with low analytical totals, indicative of strong alteration, have also been obtained from melt particles and groundmass

phases from below Unit 2 (e.g., .analyses with low wt% totals and rich in Mg and Fe from particles mrp_843.46, mrp_878.09, and mrp_892.55; Tables A.9 and A.10). These analyses also typify the preferential leaching of Na and K observed throughout the impactite sequence, but not as thoroughly as in units 1 and 2. The zonation in melt particle mrp_846.06 is representative of this process, which most likely is the result of diffusion of Na and K from the adjacent volatile-rich groundmass (Fig. 5.3f).

Other secondary phases encountered here are adularia and calcite, which are commonly found in melt particles throughout the impactite sequence (also Hecht et al. 2004; Zurcher et al. 2004). Anomalous Fe abundances along melt particle margins have been observed in melt particle mrp_835.14 and mrp_892.55 and testify to the mobility of this element. This was shown by Pilkington et al. (2004), who recognized the dominant magnetization in Yax-1 impactites originated from secondary magnetite. The occurrence of secondary alteration phases and the redistribution of Fe, Na, K, and volatiles all contribute to the heterogeneity of melt particle compositions at the micro-scale, as successfully investigated by EMPA. However, this technique alone, thus far, has not been able to succeed in deciphering any primary formation processes for these melt particles.

5.7.2. Linking EMPA and LA-ICP-MS results

Our EMPA and LA-ICP-MS results indicate that melt particles are of highly diverse compositions, which renders melt particle compositional classification difficult. Some LA-ICP-MS analyses yield abundances orders of magnitude greater than adjacent analyses (e.g., analyses #11, 14, 27, 40 of particle mrp_835.14, mrp_843.46, mrp_846.06, and mrp_892.55), which we attribute, at least partially, to a “nugget” effect from trace-element-rich accessory phases such as zircon, apatite or titanite, the presence of which was ascertained by individual EMP analyses. Cathodoluminescence observations also show the presence of apatite schlieren that are poorly mixed with the enclosing melt and/or isolated apatite and zircon grains within melt particles (Tuchscherer et al. 2004a). Conversely, analyses with relatively lower trace element abundances may be

attributed to microscopic phases that are inherently poor in trace elements, i.e., calcite, hematite, or areas rich in phyllosilicates (e.g., analyses from units 1 and 2, and # 25, 30, 38, and 39).

Only two trace elements, titanium and chromium, were analyzed with both techniques. Their abundances in the two data sets do not, however, correlate with the LA-ICP-MS results typically having much lower values than the corresponding EMPA data. This is likely a result of the different volumes of material analyzed. For example, melt particle mrp_835.14 contains two areas with high Ti (see Table A.9). The only LA-ICP-MS analysis that shows any high Ti is analysis #11 (Table A.11), which does not overlap with the EMPA Ti-rich area near the A point of the traverse. The EMPA compositional heterogeneities can only serve to explain suspected heterogeneities observed in the LA-ICP-MS data. Any direct correlation is coincidental; i.e., high LA-ICP-MS trace element results do not necessarily correspond to high EMPA Ti/Cr results.

5.7.3. Trace element constraints on secondary alteration

In order to further investigate the nature and degree of alteration of the melt particles, variations between the immobile elements Sc, Zr, Y, the more mobile incompatible REE, and the very mobile LILE are considered. Melt particles that show good compositional groupings of the immobile, REE, and mobile trace elements (LILE) may be interpreted as relatively unaltered and are also homogeneous in composition, on the LA-ICP-MS scale (compare Figs 5.7 and 5.8). This includes particles mrp_835.14, mrp1_846.06, and mrp_878.09, and this signature is referred as type 1 composition. If a particle shows groupings of immobile elements but not in the REE or LILE plots, this suggests that the particle is altered to a degree; this refers to particles mrp_805.34 and mrp2_846.06 and is referred as type 2 composition. Particles that show much variation in the immobile, REE, and LIL elements can be interpreted to have primary compositional heterogeneity, and are called type 3. Particle mrp_843.46 belongs to this category. A melt particle that shows variations in the immobile elements but reasonable groupings with regard to either the REE or LILE was likely subjected to secondary overprint, like particles mrp_824.03 and

mrp_878.09; this is termed type 4. The difference between types 2 and 4 is that the former has been leached by seawater, whereas the latter has been metasomatised by a K, LILE, and/or REE rich fluid. This systematic approach can not, however, determine whether melt particles of type 3 composition are either of primary or secondary compositional diversity.

For melt particle mrp_835.14 with the highest recorded overall trace element abundances, the EMPA results are highly variable and mostly indicate a high volatile content. There does not appear to be a relationship between high trace element abundances and the alteration state of melt particles. Negative Ce anomalies in REE analyses of unit 1 and 2 melt particles indicate leaching by seawater through preferential removal of Ce^{3+} (Guy et al. 1999; Utzmann et al. 2002). This anomaly is observed in all analyzed particles to a sample depth of 835.14 m. Cerium has a partitioning coefficient 4 times greater than that of La (Guy et al. 1999; Utzmann et al. 2002) and will, thus, be mobilized into an aqueous phase more readily than the other REE. However, this does not appear to correlate with results from bulk rock REE analyses (Tuchscherer et al. 2004b), which suggest some of the remobilized Ce must be contained in either the groundmass or secondary phases in these units. This is consistent with small-scale mobilization of Ce. The carbonate component of the impactites, inferred by the carbonate end-member composition of Tuchscherer et al. (2005), shows a strong negative Ce anomaly. It implies that the leached Ce should be accommodated by a silicate phase similar to zeolites and saponite in altered basalt (Guy et al. 1999). Analyses enriched in Ce are also found in lower impactites (particles mrp1_846.06 and mrp_878.09), perhaps indicative of precipitation of insoluble Ce^{4+} in a recharge zone characterized by Ce^{3+} oxidation.

5.7.4. Protoliths/proto-minerals and mixing of precursor phases

Because of the highly heterogeneous composition of the melt particles, it is apparent that they do not explicitly represent bulk rock melts, but possibly mixtures of anything between mineral melts and mixed rock melts. This interpretation is supported by the fact that stoichiometric plagioclase of andesine ($An_{49}Ab_{47}Or_4$) composition has been measured in particle mrp_835.14 and a K-

feldspar-plagioclase mixed composition of $An_{33}An_{32}Or_{35}$ was found in particle mrp1_846.06. We do not believe these melt particles were subjected to extensive alkali metasomatism, as they are both of type 1 composition based on our trace element alteration discrimination technique. A mixed orthoclase with iron melt composition is suggested by melt particle mrp_843.46, but it can not be excluded that this is due to secondary overprint. For the remaining analyses, which mostly have low major element totals, it is difficult to discern their original composition and then extend the interpretation to possible precursor phase(s). Heterogeneous melt particle compositions have been interpreted to be characteristic of suevites formed by impacts in lithologically varied target rocks (Dressler and Reimold 2001). If the Yax-1 melt particles are interpreted as melts of individual minerals or of mixtures of minerals, compositions can even exceed the complexity of the target, due to incomplete mixing of individual melts. Of course, secondary alteration processes are a further complication.

Another method that can be used to constrain possible precursor materials involves the use of trace element ratios (Fig. 5.7 and 5.8). Compositions of known target rocks (granodiorite, gneiss, clastic sedimentary rocks, and oil shale) can be used for comparison with the compositions of the melt particles (Table 5.3). It is observed that the Sc/Zr ratios of the melt particles (Fig. 5.8a) are constrained between the ratio of gneiss from the Yax-1 borehole and various clastic sedimentary rock compositions (Koeberl 1993). This must also include a mafic component (likely amphibolite - Kettrup et al. 2003). The highest known target rock value of Ba is 7.19 for a granodiorite clast (Fig. 5.8b). Therefore, the low Ba/Zr ratios of melt particles could indicate a predominant metasedimentary or gneissic protolith with Ba/Zr ratios <1.24. However, the preferential remobilization and leaching of Ba cannot be excluded.

LILE ratios Ba/Rb and Sr/Rb show relatively good compositional groupings for the individual melt particles, and these values are also constrained by currently known target rock compositions, i.e., all melt particle compositions are intermediate between known target rock compositions (Figs 5.7d, 5.8c). REE data show significant scatter and, thus, appear to have been affected by secondary alteration (Figs 5.6, 5.10b, 5.11). Also, no currently known target rock

composition can account for the high La/Sm and Gd/Yb ratios observed in the melt particles (Fig. 5.8d). Combinations of target rocks also cannot account for the observed melt particle REE characteristics, as combinations by averaging or

Table 5.3. Selected trace element concentrations for known target rocks related to the Chicxulub impact crater (in ppm).

	Grano-diorite**	Gneiss**	Avg. oil shale**	2 σ	Red SS1*	Red SS2*	Gray SS*	Qtzite*
Sc	4.4	12.5	5.7	3.7	4.74	4.61	0.66	2.13
Cr	32.9	19.5	65	46.4	27.8	28.1	23.3	23.4
Co	4.48	8.08	14	10	2.52	9.89	0.53	3.62
Ni	8	23	74	20	5	10	3	15
Rb	66.5	30.5	31.2	26.3	68.3	42.9	3.72	13.2
Sr	36	287	117	37	100	125	95	<30
Zr	135	185	232	103	460	450	250	670
Ba	970	229	74	72	50	55	180	40
La	7.2	29.2	4.5	2.8	22.4	22.3	15.7	31.6
Sm	1.66	3.98	1.85	0.8	3.43	4.98	2.01	6.67
Gd	1.75	4.8	1.4	0.52	3.7	4.6	1.3	6.4
Yb	1.21	3.61	0.67	0.2	1.71	1.96	0.65	3.31
Ratios								
Sc/Zr	0.03	0.07	0.02	-	0.01	0.01	0	0
Ba/Zr	7.19	1.24	0.32	-	0.11	0.12	0.72	0.06
Ba/Rb	14.59	7.51	2.37	-	0.73	1.28	48.39	3.03
Sr/Rb	0.54	9.41	3.75	-	1.46	2.91	25.54	n/a
La/Sm	4.34	7.34	2.43	-	6.53	4.48	7.81	4.74
Gd/Yb	1.45	1.33	2.09	-	2.16	2.35	2	1.93

Data from *Koeberl 1993 and **Tuchscherer et al. (2005); Avg. = average, SS = sandstone, Qtzite = quartzite.

direct addition of ratios cannot exceed any current target rock compositions. Ratios of trace elements can only be modified by primary differentiation processes or the preferential hydrothermal remobilization of certain elements.

Our analyses are generally Co poor, compared to Ni and Cr that show an apparent mixing trend (Fig. 5.7c), which can not, however, be attributed to any currently known Ni-bearing target rocks. This likely confirms that the mafic component of the target stratigraphy has not been sampled properly. A small proportion of projectile matter could also contribute to this trend; the projectile contribution to the suevitic impact breccias was estimated by Gelinas et al. (2004) at ca. 0.1%. This would result in a contribution of some 0.5 ppm Co, 10.8 ppm Ni and 2.6 ppm Cr from a CI meteorite (Palme and Jones 2003), the type inferred for the K/T bolide by Shukolyukov and Lugmair (1998) from Cr isotopic analysis.

The highest siderophile element abundances in the Yax-1 borehole have been determined in narrow shale horizons (Tuchscherer et al. 2005), which make up an insignificant proportion of the Yucatán pre-impact target rocks (Ward et al. 1995). These samples do not possess an adequate Ni/Cr ratio to account for the observed trend. However, known values for the upper, middle, and lower continental crust (Rudnick and Gao 2003), as well as for average CI chondrite, plotted in Figure 5.7c may explain the observed trend by a mixture of continental crust and the projectile.

5.7.5. Melt particle formation

Petrographic observations of melt particles yield clues to their formation. It is suggested that small particles (< 0.5 mm) cooled rapidly and, thus, were deposited as quenched shard-like fragments that were then enclosed by the groundmass. Vesicular nature, angular morphologies, and small sizes testify to formation in a volatile-rich and extremely turbulent environment prior to deposition and/or consolidation with the groundmass. Rapid quenching is also necessary to maintain the heterogeneous compositions of individual melt particles. Melt particles larger than 0.5 mm could have kept enough latent heat to allow them to be deposited while in a semi-plastic state, i.e., above the glass transition temperature. This semi-molten state would have allowed melt particles below Unit 2 to flow and solidify with schlieren textures. However, it is possible that schlieren could also have formed through the agglomeration of various melts while in transit through the air. The protracted cooling period also allowed the crystallization of microlites, which increase in proportion with core depth (Tuchscherer et al. 2004a) - likely because melt particles lower in the impactite sequence took longer to cool. The melt particles from Unit 5, however, all show angular morphologies but lack vesicles, which indicates rapid cooling and extensive fragmentation prior to deposition in a relatively dry or higher pressure environment. Most particles in Unit 5 also show well preserved microlites. This indicates that once the shard-like particles were deposited, microlite growth persisted under slower cooling conditions. This may have been induced by thermal conduction from the overlying impact melt rock of Unit 4. Engelhardt et

al. (1995) showed experimentally that quenched melt particles in the Ries crater could continue to crystallize plagioclase microlites below the glass-transformation temperature to a temperature of 550 ^{o}C at 600 bar water pressure. Similar conditions may have been present here to allow microlites to crystallize in the angular melt particles of Unit 5.

Melt particles from Unit 1, on the other hand, are all subrounded, with only rare particles revealing well preserved vesicles and shard-like morphologies. As indicated by Goto et al. (2004) and discussed by Tuchscherer et al. (2004a,b, 2005), these particles were most likely redeposited and reworked by seawater resurge into the crater basin, minutes after impact and suevite deposition. This idea is in contrast to Stöffler et al. (2004), who did not consider aquatic reworking. The melt particles must have quenched rapidly, as no microlites are observed in this unit.

Volatiles in the target rocks at Chicxulub appear to have been essential for preserving the heterogeneous compositions of melt particles. Volatiles (H_2O, CO_2, SO_x) would have enabled the dispersion of the particles, thus, inhibiting homogenization (Kieffer and Simonds 1980; Hörz et al. 2002). The Yax-1 suevites have a large carbonate component, but no significant SO_3 concentrations have been found despite the significant anhydrite component of the target. This suggests all sulfates were devolatized upon impact (Tuchscherer et al. 2004b). Evidence for the melt particles having interacted with volatiles can be found in their extensively altered nature, such as the conversion to phyllosilicate phases, and the occurrence of abundant filled vesicles in the upper three units. The dispersion of fallback suevite also facilitated the rapid cooling of melt particles, producing heterogeneous melt particle compositions.

5.7.6. Comparison with melt rocks from other impact structures

Impacts into lithologically diverse targets can produce compositionally heterogeneous melt particles in suevite, especially at the micro-scale (see Dressler and Reimold 2001). Large impacts can access quite heterogeneous crust. For example, Dressler et al. (1996) showed that melt particles obtained from the Onaping Formation, widely considered the suevite deposit of the Sudbury

Structure, have compositions that are highly heterogeneous and represent diaplectic and liquid-state glasses that quenched rapidly after shock melting of the lithologically varied target sequence. A recent study of Ries melt particles and glasses by Osinski (2003) showed that various types of glasses exist in the Ries suevite, which also originated from the melting of different target lithologies. A detailed EMPA investigation of ballistically dispersed melt particles from Meteor Crater resulted in the recognition of heterogeneous melt particle compositions (Hörz et al. 2002). These authors suggested that efficient mixing was hindered by the devolatilization of CO_2 from the shock melting of target carbonate rocks – an important target component in the case of the Ries and the Chicxulub structures as well. Thus, our results are consistent with suevite deposits that are found in large impact structures that have heterogeneous target rocks.

5.8. Summary and conclusions

Constraints from this study provide insight into the formation of melt particles, mixing characteristics between various melts and lithic inclusions, and alteration characteristics. The main results are:

1. Stoichiometric feldspar and plagioclase compositions found in melt particles indicate mineral melting during cratering, whereas mixed alkali feldspar and plagioclase compositions show mixing of mineral melts.
2. The compositional heterogeneity of melt particles can exceed the compositional diversity of the target rocks because of incomplete mixing between mineral melts and/or rock melts.
3. Melt particles that have been leached by seawater (units 1 and 2) are of a more homogeneous composition than particles located lower in the impactite sequence; they show negative Ce anomalies.
4. Heterogeneous trace element compositions are the product of alteration, the incomplete melting of precursor phases (nugget effect), incomplete mixing of melts (schlierens), and the presence of small clasts.
5. Correlation of the EMPA and LA-ICP-MS data is problematic due to the disparate beam widths of the two techniques.

6. Trace element results allow the compositional discrimination of melt particles based on groupings for immobile elements, REE, and LILE data. Four type compositions have been assigned on trace element basis that help determine the variable degrees of alteration.
7. Trace element ratio plots for data obtained from melt rock particles overlap with all known target rock compositions and, thus, support that these melt particles represent various target rock mixtures. No such overlap can be observed with ratios of the REE (Gd/Yb and La/Sm), either because of secondary remobilization or an incomplete target rock trace element geochemical record.
8. Siderophile element, especially Ni and Cr, data indicate mixing involving Cr-,Ni- rich components. No trace element data currently exist for the postulated mafic target rocks. A small contribution could originate from the bolide.
9. Small shard-like melt particles in units 1 to 3 quenched rapidly in a volatile-rich environment prior to solidification with the host groundmass. Larger fluidal melt particles that contain microlites underwent protracted cooling. Shard-like melt particles in Unit 5 contain microlites and are believed to have crystallized below the glass transformation temperature or were fragmented after crystallization.

The presence of volatiles in target rocks helped disperse and cool melt particles during cratering. Impacts that occur in target rocks of variable composition and that are rich in volatiles (Chicxulub, Sudbury, Ries, Meteor Crater) are more likely to develop suevite deposits with heterogeneous melt particle compositions.

5.9. Acknowledgments

We gratefully acknowledge the comprehensive financial support by the American Chemical Society Petroleum Research Fund (grant PRF # 37299-AC8), and the support of the Director of the Council for Geoscience (CGS), Pretoria. Maria Anastova and Annabe Walliser (CGS) provided helpful guidance during SEM and EMP analysis, respectively. We are also very grateful for the insightful and constructive editorial reviews of Pierre Beck, Paul Sylvester, and John Spray

that significantly improved this article. MGT thanks, in particular, his wife Libby Sharman-Harris for her continuous support. This is Impact Cratering Research Group Contribution No. 98.

6. Summary and Discussion

A summary of the most important research findings and discussion thereof are presented in this chapter in terms of the research objectives stated in Chapter 1. In brief, the objectives of this investigation were to provide new observations from Chicxulub impactites retrieved from the Yax-1 borehole, discuss and interpret these findings with regards to the current understanding of impact cratering, and provide new conclusions about this process. Specifically, the impact cratering processes to be discussed include the extent of melting and mixing of the various target rock components, interpret the emplacement mechanism(s) of the various impactite units, describe and interpret the variation and occurrence of shock metamorphic features, characterize the contribution from a meteoritic source, and evaluate the source and extent of subsequent hydrothermal and diagenetic alteration processes. These observations also allow commenting on the classification of the impactites with regards to the scheme proposed by Stöffler and Grieve (1994) and with respect to their mode of formation.

Results obtained from the four central chapters of this thesis (Chapters 2-5) are reviewed in section 6.1. These results are then discussed with regards to the scientific objectives sought, i.e., the distribution of ejecta and the meteorite with regards to collapse of the impact plume (section 6.2), a comprehensive emplacement mechanism for the various units (section 6.3), impact related features identified in the Cretaceous target rock and their relevance with the modification stage of cratering (section 6.4), alteration features as they relate to melt rock particles and their host groundmass (section 6.5), melt rock particle petrographic, morphological, and geochemical characteristics (section 6.6), and shock metamorphic features (section 6.7).

6.1. Summary of main research results

The following summarizes the main results as presented in the four result chapters (Chapters 2-5) of this thesis.

6.1.1. Summary of Chapter 2: First petrographic results

Prior to this work, the only published results on the Yax-1 impactites were available in the form of abstracts presented at the 2003 Lunar and Planetary Science Conference in Houston, Texas (e.g., Dressler et al. 2003; Stöffler et al. 2003; Kring et al. 2003a; Tuchscherer et al. 2003; Zurcher et al. 2003) and the initial review with core log lithostratigraphic descriptions of Dressler et al. (2002). The impactites had been subdivided into six units based solely on the macroscopic observations of Dressler et al. (2002). Petrographic observations from this work (Chapter 2, Tuchscherer et al. 2004a) reassessed the initial impactite stratigraphic subdivision of Dressler (2002, see Table 2.1). In contrast to the 6 units of Dressler (2002) only 5 units were recognized. It was observed that the original units 1 and 2 had similar characteristics and that the preservation state of Unit 1, i.e., its poor degree of lithification (see Appendix A.3 sample 248 at 800.35 m depth), was the only distinctive difference between them. Key petrographic characteristics for each of these units in the impactites were defined at the macro- and microscopic scales, i.e., based on melt particle and clast morphology, size, color, and abundance. Modal proportions, based on the point counting of thin sections from selected samples of all impactite units, also provided key information for each unit, e.g., percentage of clasts, melt particles, microlites, groundmass, carbonate content, and secondary phases (Table 2.3). Shock metamorphic characteristics, i.e., planar deformation features (PDFs), ballenquartz, checkerboard feldspar and melt particle abundances, revealed that the impactites registered a wide range of shock pressures and temperatures (Fig. 2.9). Electron microprobe analysis (EMPA) showed that melt particles have highly heterogeneous compositions (Fig. 2.10). All mafic melt particles are rich in volatiles, whereas alkaline and felsic particles retain good analytical totals. EMPA showed that melt particles were affected by an extensive potassium metasomatic event. XRD analyses of bulk sample powders confirmed the optical observations that the impactites contain a substantial amount of phyllosilicates (illite/smectite/saponite), consistent with the obviously volatile-rich nature of the melt particles indicated by the EMPA results. This work also indicated that Unit 5 has an unusual calcite/dolomite-rich groundmass that locally displays fluidal

textures when in contact with large fluidal melt rock particles. Although inconclusive, this may represent a shocked carbonate melt (Fig. 2.3f).

6.1.2. Summary of Chapter 3: Major and trace element characteristics of impactites

This work (Chapter 3, Tuchscherer et al. 2004b) indicated that the impactites are compositionally heterogeneous at the bulk sampling scale (8-16 cm^3, Fig. 3.3). When compositions of individual samples were averaged for the extent of the respective lithological units, the impactites showed similar average compositions for units 1 to 3, with some minor variations due to secondary alteration effects on individual samples (Table 3.2). When the carbonate fraction (CaO and the loss on ignition [L.O.I.]) are subtracted from the impactite compositions, the remaining silicate fraction revealed remarkable homogeneity (Fig. 3.4). In contrast to the suevitic units, Unit 4, the green impact melt breccia, contains a distinct mafic component indicated by enrichment in FeO and MgO. The large brown melt particles that are dispersed throughout the impactites have a combined feldspathic–mafic composition, and also show higher TiO_2 and Al_2O_3 abundances than all other units. Unit 5 displays the greatest compositional variability amongst the Yax-1 impactite units (especially between SiO_2 and CaO), which is largely the product of large melt rock fragments occurring in variable proportions in a carbonate groundmass. This result is also enhanced by the small sample sizes (8-16 cm^3) from this unit that were available for study (see Appendix A.3, sample depths between 886.79 and 894.14 m). Alteration effects were observed in the form of comparatively high Rb and Cs concentrations in units 1 and 2 (Fig. 3.9). High L.O.I. in these units is also ascribed to their strong alteration. With regards to the possible presence of traces of the meteoritic projectile in the Yax-1 impact breccias, this study identified only one sample with an Ir content that is 4 times greater than background levels (Table 3.3). The highly siderophile elements Ni and Co, as well as Cr, do not occur in unusual (with regard to indigenous, i.e., target concentrations) abundances, although the nature of the target is only poorly constrained.

6.1.3. Summary of Chapter 4: Geochemical and petrographic characteristics of impactites and Cretaceous target rocks

This chapter aimed to describe the geochemical, in particular trace elements, and petrographic characteristics of sub-samples obtained from the Yax-1 core. This study was possible due to the small volume requirements for INAA. These subsamples include individual melt rock particles, massive melt rock, groundmass, lightly to moderately shocked target rock lithic clasts, suevite samples (mixed groundmass and melt rock particles), and Cretaceous target rocks sampled below the impactite unit. The trace element results (Chapter 4, Tuchscherer et al. 2005) indicated that the carbonate end-member of the Yax-1 impactites is dominated by a dolomitic component. This is supported from the finding that the impactite carbonate end-member composition has similar transition trace element and similar rare earth element (REE) pattern to dolomitic samples (Figs 4.13 and 4.14). The siliceous end-member has a composition that is similar to the averaged melt rock particle component, which also best matches the composition of a sampled gneiss clast (Figs 4.13 and 4.14). The suevitic groundmass and bulk suevite are similar in composition, having trace element abundances that are lower than the average melt rock particle composition. The average melt rock particle composition shows two compositional groupings - a high-Ba, low-Ta group and a high-Fe, -Zn, and -Hf group. Melt rock particles also have transition and REE compositions that are similar to those from a mixture of target rocks, i.e., granitoids, gneiss, schists, and quartzite (Fig. 4.14). These rocks are therefore likely precursors to the melt rock particles. Mixing calculations that might help to further constrain the proportion of these target rocks in the melt rock particles could not be performed owing to the incomplete nature of the target rock geochemical inventory.

The petrographic characteristics of selected Cretaceous target rocks reveal a multi-stage deformation history that spans the period from before to after the impact. Extensive fracturing is observed in the Cretaceous rocks that appear to be lithologically restricted to dolomitic horizons. The pervasive fracturing observed is suggestive of intense seismic shaking that is unusual of dissolution processes. Centimeter(s) wide polymict breccia horizons observed in the Cretaceous rocks

also indicate to extensive slip movements that most likely occurred during the modification stage of the Chicxulub impact event. Brittle and sharp offsets are observed that support this interpretation, not typical of dissolution features (Fig. 4.5b). Petrographic observations did not reveal any bona-fide impact-related shock metamorphic features in the so-called impact melt injection veins in the 1347 – 1348 m interval as reported by Wittman et al. (2004) and Wittmann (2006) (Fig. 4.7). It is suggested the "melt rock" veinlets actually comprise phyllosilicates (mainly illite) that were formed as a result of traditional diagenetic processes associated to brine reflux in a recharge zone instead of shock melting.

6.1.4. Summary of Chapter 5: Major and trace element compositions of melt particles and associated phases

This work aimed to understand the formation of melt rock particles through a combined detailed backscattered scanning electron microscope and micro-analytical geochemical investigation. The results revealed that major element compositions vary widely both within individual melt rock particles and between particles (Fig. 5.4). This variation is attributed primarily to secondary alteration, the influx of volatiles and alkali–FeO metasomatism. Melt particles in the topmost units 1 and 2 are depleted in K, Na and Ca and have high L.O.I.; they are clearly affected by seawater alteration involving primarily leaching of alkalis (Fig. 5.4). Leaching is dependent on the active removal of mobile elements by a fluid, which is also evidenced by negative Ce anomalies in melt rock particles of Unit 2 (Fig. 5.6e). The use of mobile versus immobile trace element discriminant plots provided insight into the degree of alteration and primary compositional characteristics. It is suggested that when multiple results obtained from an individual melt rock particle reveal variable mobile element but consistent immobile trace element compositions, the particle is variably altered. In this case, fluids are suggested to have remobilized compatible elements and not immobile ones. Results from a particle that showed uniform mobile and immobile compositions indicated that it is largely unaltered and that it has a homogeneous composition. A melt rock particle that showed heterogeneous immobile trace element characteristics is believed to represent a primary unaltered and

heterogeneous composition. In order to characterize potential protoliths, trace element ratios for known target rocks were correlated with those of melt rock particles. The compositional diversity of melt rock particles when compared to the current target rock geochemical database on discriminant diagrams exceeds the range of presently-known target rock compositions (Figs 5.7 and 5.8). A binary mixing relationship between Cr and Ni in melt rock particles is observed (Fig. 5.7c), which may indicate mixing between a meteoritic component and upper crustal rocks.

6.2. Processes associated with ejecta plume collapse

A review of the processes involved during impact ejecta plume collapse is presented in this section in order to provide a background for the formation of the Yax-1 impactites. The formation of an ejecta plume and its subsequent collapse is dependent on the second and third fundamental stages of cratering that include: stage 2 – excavation and stage 3 – modification. The first stage, contact/compression, is not involved in this process. More details concerning these stages of cratering are presented in section 1.4. The actual collapse of the ejecta plume and, thus, the formation of impactites, begin at the onset of the excavation stage and continue through the modification stage. In the Chicxulub plume, physical and chemical conditions are believed to have been extreme and unique owing to the composition of the target rocks and the energy released by the event.

6.2.1. Plume characteristics obtained from target rocks

The impact of the Chicxulub projectile on the Yucatán Peninsula is estimated to have ejected vast amount of dust and volatiles into the atmosphere. Dust estimates range from as high as 3 x 10^{17} grams to < 10^{16} grams (e.g., O'Keefe and Ahrens 1982; Pope et al. 2002). Dust concentrations in excess of ~10^{16} grams would have been enough to inhibit photosynthesis (Gerstl and Zardecki 1982; Toon et al. 1982). Enormous quantities of CO_2 (200-100000 Gt, Ivanov et al. 1996; Ivanov and Deutch 2002; Takata and Ahrens 1994), H_2O (200-5000 Gt, Siret et al. 2000), and SO_2 (100-1000 Gt, Brett 1992; Pierazzo et al.

2003) are known to have been produced from the melting, dissociation, and vaporization of wet sulphate and carbonate target sedimentary rocks. The amount of sulfur released into the atmosphere is suggested to have been 100 times worse on the climate than the Pinatubo volcanic eruption and is believed to have considerably cooled the planet following impact (Pierazzo et al. 2003). The release of CO_2 from carbonate rocks contributed towards a subsequent greenhouse event (e.g., Lomax et al. 2001). The release of these volatiles in the atmosphere is most likely responsible for the associated global mass extinction event (e.g., Kring 2003, 2005). It is believed that it is not the size of the impact that caused the associated mass-extinction event, but the composition of the target rocks. Numerous large impact events have occurred throughout geological times that are not linked to any mass-extinction event (Morgan et al. 2004; Keller 2005).

6.2.2. The fate of the projectile

Pierrazzo et al. (1998) and more recently Artemieva et al. (2003) numerically modelled the cratering conditions and the fate of the projectile specific to the Yax-1 borehole impactites. The model revealed that the projectile is primarily vaporized, melted, and with decreasing angle against towards the horizon the simulation shows the projectile is preferentially ejected out of the crater and back into the atmosphere/stratosphere. This is in agreement with the oblique impact simulations of Pierazzo and Melosh (2000). The model of de Niem et al. (2007) predicts that only 10% of the projectile can be expected to be redistributed globally and that the proportion of meteoritic material compared to crustal components in the fallout deposits increases with distance from the crater. Whatever is left of the projectile is extensively dispersed by vapor emanating out from shocked sedimentary rocks (Artemieva et al. 2003). Artemieva et al. (2003) also suggested this is why no significant meteoritic component has been detected in the Yax-1 impactites (e.g., Tagle et al. 2003; Tuchscherer et al. 2004). According to Alvarez et al. (1995) most of the projectile should have been concentrated in the rapidly ascending “hot fireball”. The fact that the Ir layer occurs worldwide and that the Yax-1 impactites only have a slight meteoritic component supports the suggestion by Alvarez et al. (1995) that a plume doublet

was indeed produced at Chicxulub. The refracted projectile may also be ejected out of the impact site at velocities of up to 10 km/s (Stöffler et al. 2004). In the case of an oblique impact, Pierazzo and Melosh (2000) showed that the projectile should have a greater ejection velocity with decreasing incidence against the surface of the Earth.

6.2.3. Meteoritic component in the Yax-1 impactites

The contamination of the Yax-1 impactites by an extraterrestrial component, i.e., the bolide, has been investigated by several authors (Gelinas et al. 2004; Tagle et al. 2004; and Tuchscherer et al. 2004b, 2006). In brief, these studies have been unsuccessful and could not constrain a significant extraterrestrial component. Tagle et al. (2004) noted that the role of abundant volatiles found in the target rocks and its response during cratering is poorly understood and may have played a role in dissipating/diluting the extraterrestrial component. Gelinas et al. (2004) constrained the proportion of the bolide in the Yax-1 impactites with Re-Os isotope systematics to no greater than 0.1% by mass. Tagle et al. (2004) published similar findings based on platinum group element analyses, suggesting no more than 0.05% of the impactites could be attributed to an extraterrestrial component.

No significant Iridium abundance, with respect to published indigenous components (Koeberl 1993), has been found in the whole-rock INAA results for the Yax-1 impactites (Tuchscherer et al. 2004b, 2005). The most Ir-rich Yax-1 impactite sample analyzed by iridium γ-γ coincidence spectrometry originates from Unit 5 and contains 0.4 ppb Ir. This is 50 times greater than the Ir concentrations analyzed in a Tertiary limestone sample above the impactites and in some of the impactite samples themselves (Table 3.3). This indicates a slight contribution from the projectile that would also be heterogeneously distributed in the Yax-1 impactites. This finding is similar to the results obtained from analyzed samples of the C1 borehole (Koeberl et al. 1994).

Melt rock particles investigated by LA-ICP-MS (Tuchscherer et al. 2006) show a mixing trend for Ni and Cr abundances that may indicate a contribution from the projectile (Fig. 5.7c). However, this trend may also be the product of

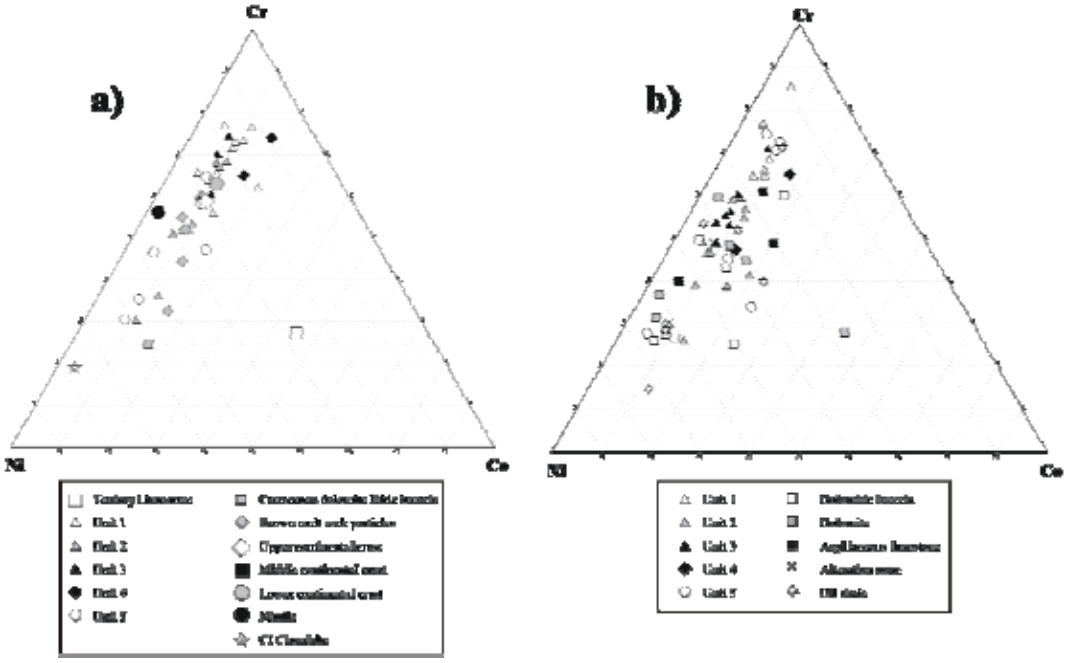

Fig. 6.1. Cr – Ni – Co ternary diagram: a) Whole rock trace element data for impactites, brown melt rock particles, country rocks (data from Tuchscherer et al. 2004b), upper continental crust, middle continental crust, lower continental crust, mantle (data from Rudnick and Gao 2004); b) Trace element data obtained from sub-samples (data from Tuchscherer et al. 2005).

inferred mafic target rocks (Kettrup and Deutsch 2003), for which no trace element data currently exists. Despite this lack of known mafic rocks, spinel grains have been known to occur in fallout deposits linked with the Chicxulub impact event (Bohor et al. 1990; Kring and Boynton 1992; Kring et al. 1994). A similar trend between Ni and Cr can also be observed for bulk rock samples (Fig. 6.1a) and subsamples obtained from the Yax-1 impactites and Cretaceous target rocks (Fig. 6.1b, whole rock data from appendix A.6, subsample data from appendix A.7, A.8). Interestingly, Figure 6.1b shows that an individual oil shale sample contains high proportions of Ni. Although occurring in thin lenses in the Yax-1 borehole, oil-laden, heavy metal-rich rocks may have existed in greater proportions in the Chicxulub target rocks (Ward et al. 1995). Their incorporation in the impactites may also account for this trend.

Current research suggests that the projectile responsible for the Chicxulub impact structure was a carbonaceous chondrite of either CI or CM2 composition (Shukolyukov and Lugmair 1998; Trinquier et al. 2006). For a crater the size of Chicxulub, it is suggested the bolide was completely vaporized upon impact (Melosh 1989) and its vapor may have been preferentially redistributed back into

the atmosphere if the impact angle was oblique (e.g., Schultz and D'Hondt 1996; Pierrazo and Melosh 1999). A recent study on the distribution of shocked quartz grains from K/T boundary deposits around the Chicxulub Structure suggests an uprange direction towards the southeast for the incoming bolide (Morgan et al. 2006). Condensates of the vaporized bolide would have been deposited around the world, creating the famous K/T boundary Ir anomaly (Alvarez et al. 1980).

6.3. Constraints on the emplacement of the impactites

The petrographic and geochemical data accumulated from the four central chapters of this thesis enable the construction and interpretation of a comprehensive emplacement model for the 5 impactite units intersected by the Yax-1 borehole. In order to appreciate the scale of the Chicxulub impact event, which is responsible for the deposition of these impactites, energy constraints are briefly reviewed here. The best constraint on the size of the Chicxulub impact event in terms of energy released can be determined from the crater diameter. The currently accepted diameter for Chicxulub is 185 km diameter (Morgan et al. 1997). Knowing that the transient cavity diameter (D_{tc}) follows an empirical relation $D_{tc} \approx 0.5$ to $0.65D$ (Grieve et al. 1981), the Chixculub transient cavity should have had a diameter between 92.5 and 120.25 km. According to the generally agreed transient cavity depth-to-diameter ratio, which range between 0.24 and 0.32 (Melosh 1989), the transient cavity must have been between 22.5 and 38.5 km deep before collapse. The estimated energy required to produce such a cavity is equivalent to 87,000,000 tons of TNT (French 1998). The 5 impactite units intersected by the Yax-1 borehole, which have been described in detail during this work, are the final product of this event. In the following sections, their emplacement is interpreted temporally, from the first unit deposited to the last, based on the findings of this study.

6.3.1. Unit 5 – Variegated, polymict, impact breccia

Unit 5 represents the lower-most impactite deposit. The fact that no medium to small sized fluidal-shaped melt rock particles can be found in this unit indicates that this unit is not a fallback suevite. Instead, it is believed to have been

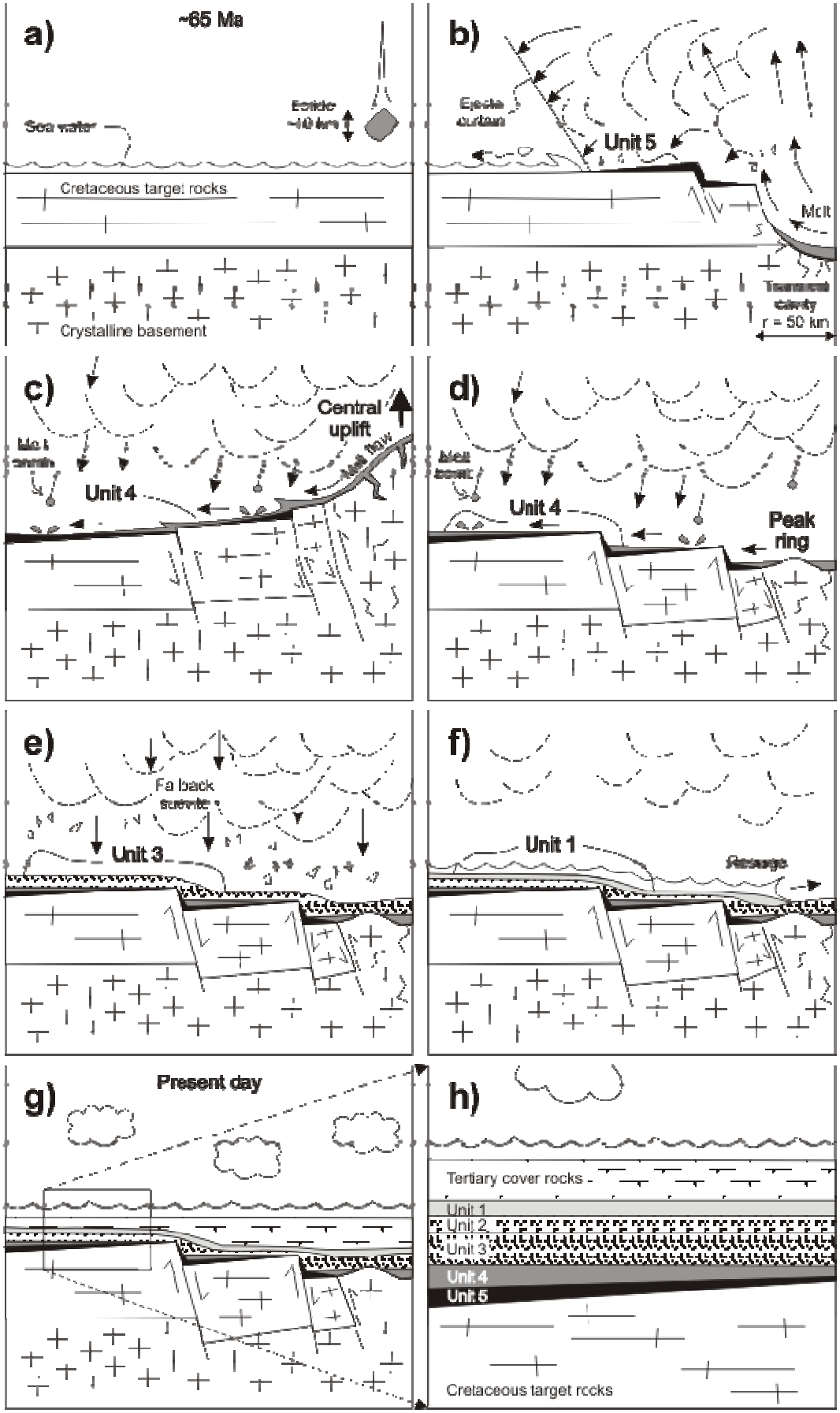
a)
~65 Ma
Sea water
Cretaceous target rocks
Crystalline basement
b)
Unit 5
Melt
r = 50 km
c)
Central uplift
Unit 4
d)
Unit 4
Peak ring
e)
Unit 3
f)
Unit 1
g)
Present day
h)
Tertiary cover rocks
Unit 1
Unit 2
Unit 3
Unit 4
Unit 5
Cretaceous target rocks

Fig. 6.2 (*previous page*). Emplacement mechanism schematic for the 5 Yax-1 impactite units; note that the cross-section is not to scale (the carbonate rock thickness appears greater than expected). a) Idealized cross-section prior to impact, note the presence of seawater overlying Cretaceous carbonate overlying crystalline basement; the bolide is estimated at 10 km diameter. b) Deposition of Unit 5 following the passage of the ejecta curtain and during the excavation stage of the transient cavity. c) Emplacement of Unit 4 by outward flow away from the central uplift during rebound and collapse of the transient cavity. d) Emplacement of Unit 4 by fallout deposition of large melt bombs following the collapse of the central uplift. Note melt rocks are found in greater proportions in troughs between the crest of collapsed terraces and in the center of the impact basin between the inner peak ring. e) Emplacement of Unit 3 by fallout/fallback of suevite. f) Formation of Unit 1 by the mechanical reworking of the pre-existing suevite deposit during resurge of seawater into the impact basin. g) Present day idealized cross-section of the Chicxulub impact structure. h) Close up of the 5 impactite units as intersected by the Yax-1 borehole.

deposited from or immediately after the initial ejecta curtain, which was first produced following the contact/compression stage of cratering (Fig. 6.2b). Allogenic carbonate clasts that are mixed with variable proportions of melt rock particles and highly shocked quartz grains support this interpretation. This unit contains the greatest proportion of carbonate clasts, which are believed to have originated from the initial excavation of supracrustal rocks. The clasts have sharp contacts with the groundmass in both hand sample (Fig. A.1.41, A.1.43) and in thin section (Fig. A.4.103-111). The melt rock particles are generally angular, which suggests they must have either cooled rapidly and have been shattered or they were brecciated immediately after deposition, possibly by immediate seismic activity associated to ongoing excavation/modification stage processes. Rapid cooling could have been enhanced by turbulent mixing along the edge of the ejecta curtain. Dressler et al. (2004) and Stöffler et al. (2004) suggested this unit is typical of pyroclastic ground-surge deposits and that the shard-like character of melt rock particles is the result of movement during deposition. With the limited data available from nearby boreholes to correlate with, this emplacement interpretation remains loosely constrained.

Based on textural observations of flow in the carbonate-rich groundmass (see Fig. 7 of Dressler et al. 2004) and between the groundmass and large fluidal melt rock particles (Tuchscherer et al. (2004a, see Fig. 2.3f), it is proposed that the groundmass hosting the melt clasts may represent a crystallized impact melt. Basal ejecta deposits found in the UNAM 5 and 7 boreholes also contain felsic melt rock particles in a carbonate matrix (Salge 2007). The matrix of UNAM 5 and 7 has been documented by Salge (2007) to also show textural evidence

indicative of deposition while in a liquid state. It is known that carbonatite lavas can remain molten to at least 544 ^{o}C and can have viscosities that are one order of magnitude lower than the most mobile basaltic lavas (Dawson et al. 1990). If the matrix in Unit 5 is indeed a crystallized carbonate melt, then this unit should be reclassified as an impact melt breccia and not a suevite-type deposit. Brecciation of the silicate melt rock particles may have also occurred while this groundmass melt was still liquid. However, Tuchscherer et al. (2004a) suggested that the presence of foraminifera fossils in clasts of Unit 5 is at odds with this interpretation because this infers incomplete melting of the carbonate target rocks. However, these may have been incorporated in the deposit as poorly shocked lithic clasts that originated outside the region of shock melting. Dressler et al. (2004) suggested that partially digested lithic clasts could be observed in their Unit 5 samples. This is consistent with the various degree of melting typically observed in impact melt rocks.

The contact of Unit 5 with Unit 4 has been described by Dressler et al (2004) and Tuchscherer et al. (2004a) as abrupt. This would imply the two units are of distinct origin and were deposited by two different processes. However, Kring et al. (2004) suggested the lower Unit 5 may represent a "more disaggregated portion of the green melt unit". If Unit 5 is indeed an impact melt rock that has a rich fused carbonate component, it could very well have a similar orign as Unit 4. However, until the nature of the carbonate groundmass is Unit 5 is resolved, this interpretation is still loosely constrained.

6.3.2. Unit 4 – Green impact melt breccia

The green impact melt breccia is believed to have been formed primarily by fusion of the crystalline basement. This interpretation is supported by the carbonate-poor character of this unit, the occurrence of monomineralic silicate and felsic lithic inclusions, and by its geochemical characteristics. The green impact melt rock has REE and transition trace element abundances that are similar to the siliceous end-member of the impactite, which is also compositionally similar to sampled silicate inclusions (granodiorite, granite). This melt is suggested to have been emplaced in two possible ways, 1- outward lateral flow of impact melt away

from the collapsing central uplift (Fig. 6.2c) or 2- ballistic deposition of a large fragment(s) of impact melt (Fig. 6.2d). A lateral flow of impact melt rocks has also been documented at the Ries impact crater (Osinski 2004; Kring 2005) and is suggested to have been emplaced during rebound of the transient cavity floor. A similar process is called upon for the emplacement of Unit 4 (Fig. 6.2c). It was suggested by Kring and Boynton (1992) and Claeys et al. (2003) that melt flowed away from the rising central uplift of the Chicxulub Structure and that significant amount may have been captured in the moat feature around the central peak, as shown by the 380 m thick intersection of impact melt in the Y6 borehole (see Fig. 1.1 and 1.8 for the location of the Y6 borehole). With regards to the lateral continuity of Unit 4, which is still unknown, it could also be argued that individual melt bodies became isolated during late-stage readjustments of the crater (Fig. 6.2d). In this instance, the continuity of the melt sheet is interrupted by the inner peak ring and between the crest of collapsed terraces (Kring et al. 2004b). This interpretation supports the fact that variable proportions of melt rock have been identified in various boreholes (C1, S1, Y6, and Yax-1). If Unit 4 was deposited as a ballistic body that travelled through the air, isolated melt bodies could also be found laterally. However, Kring et al. (2004b) indicated that the impact melt rocks found in Unit 4 have chemical and textural similarities to siliceous impact melt rock from the Y6 borehole, implying that these originate from similarly fused target rocks and a continuous impact melt sheet. Brecciation of the massive melt rock seemingly occurred *in situ* by either immediate seismic activity, late-stage tectonic modification processes, or by explosive action from steam emanations from the underlying carbonate-rich Unit 5 (see also Wittmann 2006). Further drilling of the Chicxulub impactites should help determine whether Unit 4 is indeed laterally continuous, or occurs as isolated melt pods.

Dressler et al. (2004) suggested that units 4 and 5 represent an overturning of the target stratigraphy, implying that crystalline basement derived siliceous impact melt rocks presently overlie supracrustal carbonate rocks. This compositional inversion by impact is similar to what is observed at the Sudbury impact structure, where mafic rocks of the Sudbury Igneous Complex are suggested to represent a partial inversion of the continental crust (Mungall et al.

2005). In the latter case, granitic target rocks of the Cartier batholith are juxtaposed and overlain by mafic norite, a differentiated impact melt rock.

6.3.3. Units 2 and 3 – Variegated and green suevite

The fluidal texture of numerous melt rock particles and their vesiculated and lithic groundmass-supported character suggests these units represent a primary suevite deposit. For fluidal textures to remain preserved, melt rock particles must have been deposited in a semi-plastic state, i.e., their temperatures must have been just below the glass transition temperature. Melt rock particles also contain numerous vesicles, indicative of the high volatile content present in the melt phase. Volatiles (CO_2, H_2O, SO_x) are believed to have been ubiquitous in the Chicxulub impactites since the target was water-, carbonate-, and sulphate-rich. In general, volatiles are believed to enhance dispersion of the ejecta (Kieffer and Simonds 1980; Osinski 2006). However, despite this dispersion, the silicate component of the suevite deposit is rather well homogenized on a bulk rock sampling scale probably due to mixing while in the turbulent impact plume (Fig. 3.4). The average geochemical composition of units 2 and 3 is also very similar; within error limits (compare Table 3.2). However, mixing was not efficient on the micro-scale since melt rock particles are documented as being of a heterogeneous composition (Tuchscherer et al. 2004a, 2006). Numerical modelling of the Yax-1 suevite emplacement suggests that roughly half of the ejecta should comprise sedimentary material, with the other half comprising crystalline basement material (Stöffler et al. 2004). This is not in agreement with the documented proportions of the actual silicate versus carbonate clastic material in the Yax-1 impactites, which is ~1:2, as shown in the modal proportions presented in Table 2.3. This observation suggests most of the volatiles should have originated from the sedimentary target rocks. Impact craters in sedimentary target rocks are typically characterized by vesiculated melt rock particles, e.g., Ries (Engelhardt et al. 1995) Houghton (Osinski 2003). Vesicule-poor melt rock particles typically occur in crystalline target rock impact craters, e.g., Mistastin Lake crater (Grieve 1975).

With regards to the emplacement of these units, unanimity exists among Yaxcopoil-1 researchers on the fallback origin of units 2 and 3 (Fig. 6.2e).

However, different ideas have been presented regarding the fashion in which the deposit was generated. Dressler et al. (2004) suggested that the chocolate brown melt breccia (his Unit 3) and variegated, glass-rich suevitic breccia (his Unit 4) were deposited in a similar fashion to a pyroclastic flow deposit, i.e., a *nuée ardente*. Stöffler et al. (2004) suggested that these units represent continuous collapse of the ejecta plume, i.e., Unit 2 is a late-stage suevite deposit, whereas Unit 3 is an early-stage deposit. This study is in agreement with the continuous fallback origin of units 2 and 3, as Unit 2 shows similar textural characteristics to Unit 3. A slight modal increase in the clastic carbonate content is observed from Unit 3 to Unit 2. This may be due to the late fallback of early ejected carbonate clasts. Differences between Unit 2 and Unit 3 include the variegated character and the more compacted nature of melt rock particles in Unit 3. No breccia-in-breccia textural characteristics, as noted by Wittmann (2006), have been observed in these units. The green color of Unit 2 was likely caused by seawater alteration that converted melt rock particles to secondary phyllosilicates such as illite/smectite/saponite (Tuchscherer et al. 2004a).

The suevite found in the Yax-1 borehole is genetically related to those found in the upper segments of the C1, Y6, UNAM 5, 6, 7 boreholes, and in localities found in southern Quintana Roo and central Belize (Pope et al. 2005; Kenkmann and Schönian 2006, see Fig. 1.8 for location). Distal suevite deposits have also been identified at the El Guayal site, which is located 520 km west of the Chicxulub impact site (Salge 2007). The Y6 suevite is geochemically very similar to that of the Yax-1 core (Claeys et al. 2003; Schmitt et al. 2004). However, with increasing distance from the center of the Chicxulub impact, it has been observed that the UNAM borehole suevite contains a greater proportion of carbonate material (Sharpton et al. 1999). The Chicxulub ejecta deposit also decreases in thickness with distance. Below the suevite of the UNAM 6 and 7 boreholes, Bunte Breccia type deposits, i.e., breccias that are poor in melt rock particles and rich in sedimentary (in this case carbonate) lithic clasts analogous to the breccia at its type locality, the Nördlinger Ries, have been identified (Kring 2005; Salge 2007). These suevite deposits are all believed to belong to a continuous suevite ejecta blanket (Pope et al. 2005; Kenkmann and Schönian

2006; Salge 2007). At the El Guayal site, Salge (2007) suggested that the suevite ejecta was carried beyond 6 crater radii by the expansion of volatiles in the impact plume. This process of volatile rich suevite deposition is believed to be similar to the fluidized ejecta deposits observed at pedestal craters on the surface of Mars (Kenkmann and Schönian 2006; Osinski 2006). The suevite at El Guayal is overlain by spherules that are also more common in Northeastern Mexico (Schulte and Kontny 2005). These spherules are believed to have been deposited in highly turbulent conditions in two different temperature regimes (Salge 2007). A cool regime (~100^{o}C) is required for the condensation of steam onto relatively high-temperature carbonate nuclei in order to form accretionary lapilli. Schulte and Kontny (2005) do not exclude the formation of the distal deposits by pyroclastic-like flows that "glided" over the sea surface. Irrespective of the exact mechanism, the processes involved in the deposition of distal Chicxulub ejecta are believed to have involved highly turbulent conditions in a vapour phase (Salge 2007). It should be mentioned that no spherules have been found in this investigation in any of the Yax-1 impactites, as reported by Wittmann (2006) in the upper suevite deposit or by Dressler et al. (2004) for his Unit 3. The spherules found by these researchers indicate that conditions of the late ejecta plume could have been similar to those at the El Guayal site, where spherules are more common.

6.3.4. Unit 1 – Reworked suevite

Unit 1 is interpreted to have been reworked by the resurge of seawater into the impact basin (Fig. 6.2f). The presence of foraminifera plus coral fossils, carbonate clasts, and the overall subrounded and self-supported character of melt rock particles supports this interpretation. It is stressed here that these biogenic features have only been observed in this unit. It is suggested that detritus, e.g., fossils and carbonate clasts (e.g., Figs 2.4c and A.4.4 to A.4.8, A.411, A.4.14 to A.4.19), were transported into the impact basin from outside during the resurge of seawater into the crater cavity. The high energy associated with resurge is consistent with the subrounded morphology and the self-supported character of the melt rock particles (e.g., Figs 2.3a and 2.4a). The groundmass is suggested to have been mechanically removed during this activity. Seawater was also

responsible for the severe alteration of Unit 1, i.e., all melt rock particles are thoroughly altered to phyllosilicates, the unit is leached of alkali elements, and melt rock particles show negative Ce anomalies (Fig. 5.6). This emplacement mechanism is corroborated by the findings of Goto et al. (2004) who described several graded bed units and the occurrence of late Campanian to early Maastrichtian foraminifera fossils in the 794 to 823 m immediate post-impact sediment interval and extending into Unit 1. A similar resurge/reworking process has been documented at the Lockne and Chesapeake Bay impact craters (Von Dalwigk and Ormö 2001; Horton et al. 2005) and in the UNAM 5 core (B.O. Dressler pers. comm. 2008).

Stöffler et al. (2004) and Wittmann (2006), in contrast to this study, suggested another mechanism for the deposition of Unit 1. Using computer generated numerical modelling, they proposed that the atmosphere overlying the Chicxulub impact site had been temporarily excavated. By the time Unit 1 was deposited, their simulation suggests the atmosphere was re-established and, thus, that it would have enhanced sorting of fine impact melt particles. This is consistent with findings at the top of the impactite sequence observed in borehole LB-5A of the Bosumtwi impact structure (Koeberl et al. 2007). However, this plume-sorting model does not account for the occurrence of foraminifera fossils and carbonate clasts in Unit 1 as demonstrated in this investigation (Tuchscherer et al. 2004a).

6.4. Crater collapse

The collapse of the 33 km deep Chicxulub transient cavity is predicted to have taken as little as 6-10 minutes (Collins et al. 2002; Stöffler et al. 2004). Rebound of target rocks at the base of the transient cavity led to the formation of a large 40 km wide central uplift (Morgan et al. 2000). Based on numerical modelling, the central uplift is believed to have overshot the surface of the target rocks up to an altitude of 20 km (Collins et al. 2002; Stöffler et al. 2004). This overshooting of the central uplift would have benefited the lateral and outwards flow of Unit 4, as previously discussed (Fig. 6.2c). Numerical modelling of the Chicxulub event also shows that the final crater rim likely had a height of

approximately 800 m relative to the surrounding surface and that the crater floor had a final depth of 1 km below the pre-impact Cretaceous surface (Stöffler et al. 2004). Because of this high rim, Stöffler et al. (2004) suggested that no violent post-impact resurge activity could have occurred in the impact basin, as previously proposed for Unit 1 (section 6.3.4.). The water depth prior to impact is estimated to have only been several tens of meters deep based on fossil coral and foraminifera assemblages (Sharpton et al. 1996). This simulation has to be revised based on the findings obtained from this study.

6.4.1. Deformed and altered Cretaceous rocks

Several deformation zones have been documented in the Cretaceous target rock interval of the Yax-1 borehole at various depths. Several cm wide (2.5 to 33 cm), brittle deformation zones have also been identified (for specific depth intervals refer to Chapter 4). These sections have been investigated by various researchers in order to understand their formation by crater collapse or shock melting (Kenkmann et al. 2004; Stinnesbeck et al. 2004; Wittmann et al. 2004). Because the Cretaceous target rocks are carbonate dominated, shock metamorphic effects that are usually recorded in silicate minerals are rare. Only one shock metamorphic feature has been documented in the form of a checkerboard feldspar grain by Wittmann et al. (2004, see their Fig. 13). This grain was found in a heterolithic breccia at 1341.97 m depth. The breccia was allegedly produced by mechanical activity during the modification stage of cratering (Wittmann et al. 2004). Kenkmann et al. (2004) reported several shocked quartz grains in a diamictite at 1036.52 m depth. It should be stressed here that no such features were observed throughout this investigation (Tuchscherer et al. 2005). According to the scheme of Stöffler and Grieve (1994) and taking into consideration the various petrographic observations for this interval (Kenkmann et al. 2004, Wittmann et al. 2004, Tuchscherer et al. 2004) these rocks are therefore classified as authigenic shocked rocks, and/or parautochthonous polymict (lithic) breccias. However, based on petrography and compositions obtained by EMPA, Wittmann et al. (2004) reported an impact melt rock dike at 1347.8 m depth in the Yax-1 borehole. A detailed SEM investigation of this interval was undertaken by

Tuchscherer et al. (2005). It was determined by X-ray diffraction analysis and EMPA that the so-called "impact melt breccia" described by Wittmann et al. (2004) consists of a mixture of illite and dolomite. Tuchscherer et al. (2005) found no evidence for any shock metamorphism in their sample from 1347.8 m depth. It is therefore suggested that this interval be reclassified as an autochthonous monomict lithic breccia. As previously suggested in the review section 6.1.3, the fracture system prevalent in the Cretaceous dolomitic rocks of the Yax-1 borehole (Kenkmann et al. 2004) enabled the migration of secondary diagenetic fluids during burial of the structure. These fluids promoted the crystallization of illite in the interstitial pore space between dolomite crystals (see Figs 4.5, A.4.161-164, A.4.167, A.4.171).

6.5. Impactite alteration characteristics

The alteration of the Yax-1 impactite has been determined to be extensive and pervasive, as previously mentioned in the review section of this chapter. Various petrographic observations and analytical measures have been used to characterize this process, i.e., XRD, EMPA, XRF, INAA, and LA-ICP-MS. Here the alteration characteristics of the impactites are discussed with regards to the vast amount of geochemical and petrographic data accumulated in this investigation, i.e., melt rock particle petrographic and geochemical characteristics, whole rock major and trace element geochemical analyses, and groundmass alteration characteristics. With regards to the latter, the implication of groundmass alteration towards the suevite classification of units 2, 3, and 5 is discussed.

6.5.1. Melt rock particle secondary alteration

The high temperatures produced during impact cratering typically produce extensive hydrothermal systems. Examples of impact-related hydrothermal activity have been documented at various craters, e.g., the Haughton, Kärdla, Popigai, Puchezh-Katunki, and Sudbury impact structures (e.g., Ames et al. 1998; Naumov 2002; Osinski et al. 2005). In this section, the alteration characteristics of the melt rock particles from the Yaxcopoil-1 borehole are discussed.

6.5.1.1. Petrographic observations indicative of alteration

Hand sample observations testify to the altered nature of the Yax-1 impactites. At this scale, networks of calcite veins permeate the impactites and melt rock particles. Lithic clasts are not cross cut by calcite veins because of their competent nature. Under the microscope, these veins are associated with various secondary minerals including analcime, K-feldspar, barite, and dolomite (e.g., Figs A.4.10, A.4.38, A.4.74, A.4.151). These phases indicate that a pervasive hydrothermal system was active subsequent to the deposition of the impactites (also observed by Dressler et al. 2004; Hecht et al. 2004; Kring et al. 2004a,b; Stöffler et al. 2004; Tuchscherer et al. 2004a; Zurcher et al. 2004, 2005). Calcite veins are more prominent in Unit 3 than in units 1 and 2 (see Table 2.3). Units 1 and 2 show an overall characteristic green coloration, indicating thorough alteration. The green coloration of units 1 and 2 is interpreted to originate from the conversion of melt rock particles to phyllosilicates, namely illite/smectite/saponite, as determined by X-ray diffraction analysis (Tuchscherer et al. 2004a). Unit 3 melt rock particles are variegated, suggesting a lower degree of alteration. It is suggested that Unit 3 was better preserved because it directly overlies Unit 4, which was at the time of deposition a hot and massive impact melt body. It is also lower in the impactite sequence and would have been protected from circulating fluids by the above units. Unit 3 is similar to the "thermometamorphic" lower suevite unit observed in the Y6 borehole (Claeys et al. 2003). This latent heat emanating from Unit 4 better preserved Unit 3 by driving off volatiles upwards, hence, producing the extensive calcite vein network observed in the uppermost units. Cooling of the impactites was slower with depth, as observed by the increasing proportion of microlites in melt rock particles with depth (Table 2.3). Unit 4 does not contain as many calcite veins as the upper units because it was less porous, impermeable and significantly hotter than the overlying suevites. Melt rock particles in Unit 5 are variably altered, with some being partially replaced, surrounded, and cross-cut by calcite (Figs A.4.112-115, A.4.126-129, A.4.136). Dolomite core samples located immediately below Unit 5 show extensive dissolution features (Fig. A.1.50).

6.5.1.2. Geochemical evidence indicative of alteration

Electron microprobe analysis of melt rock particles obtained from Unit 1 generally produced low totals. This coincides with whole rock analyses that show this unit is characterized by higher loss on ignition (L.O.I.) values compared with other units (Table 2.3), as also determined by other researchers (Dressler et al. 2004; Hecht et al. 2004; Kring et al. 2004b). EMPA results for Unit 1 also reveal lower compositional variability than other units, which has been suggested by Tuchscherer et al. (2006) to be a product of secondary alteration. This is believed to occur through the localized remobilization of elements, thus, producing an overall homogenization of elemental abundances down to the 3 μm EMPA beam width scale. Electron microprobe analyses obtained throughout the impactite sequence showed that all mafic melt rock particles are thoroughly altered, i.e., they all have low major element totals (compare Figs 2.10a versus 2.10b). All mafic melt rock particles also show an obvious K-overprint (Fig. 2.11c). Laser-ablation inductively-coupled plasma mass-spectrometry results for melt particles from Unit 1 also show negative Ce anomalies, indicating that the melt rock particles were leached by seawater (Guy et al. 1999; Utzmann et al. 2002).

6.5.2. Alteration constraints obtained by whole-rock geochemical analyses

Whole-rock analyses show that Unit 1 is depleted in alkali elements and, as with Unit 2, is enriched in iron compared with the underlying units (See Fig. 3.3, Table 3.2). Unit 1 also shows an enrichment of the Large Ion Lithophile elements (LILE, Cs and Rb) and also of some compatible elements (Zn and Au), in comparison to the underlying units. Unit 2 shows similar major and trace element characteristics to Unit 1, but is slightly richer in the alkali elements. These observations show that units 1 and 2 were severely altered. It is suggested that these units were more altered because they are close to the top of the impactites, i.e., closer to circulating seawater and, thus, the suevite pile in this interval was preferentially infiltrated by alteration fluids. Unit 3, which is petrographically considered the less altered upper suevite unit, contains the lowest FeO_{tot} values and the highest Na_2O content. Compared to the overlying suevites, it also has lower L.O.I. values, indicative of its less altered state. Unit 3 is less

altered than units 1 and 2 because it is lower in the impactite sequence and took longer to cool. The heat of Unit 4 is believed to have helped better preserve Unit 3 through the driving upwards of volatiles. Zurcher et al. (2005) found a decreasing water/rock ratio with depth. Although Unit 4 is also green, similar to units 1 and 2, whole rock major element analysis shows it has comparatively low L.O.I. values. The green coloration could therefore be a compositional product or simply the result of the reduction of Fe^{3+} to Fe^{2+} with time during burial, e.g., anoxia by bacterial activity. The average Unit 4 composition presented in Table 3.2 has a relatively higher MgO and FeO_{tot} content compared to other units, with the exception of Unit 5 that has a greater MgO content because of the inherently higher dolomitic content in the groundmass (determined by EMPA traverses through the groundmass and cathodoluminescence observations, Section 2.5.6.2. and 2.5.8., respectively) and as lithic clasts (see modal percentages in Table 3.3). Unit 5 also has the highest whole-rock loss on ignition values because of this high carbonate content. This lowermost unit shows the greatest compositional variability among samples, not only by alteration, but because of the highly variable proportions of melt rock particles, carbonate clasts, and groundmass.

With regards to the extent of element transport, whole-rock major element data accumulated for the entire impactite sequence do not show any substitution of Na or Ca for K (see Fig. 3.8). This suggests remobilization of K happened on a microscopic scale, i.e., not over meters or across units. This localized alteration is also supported by the work of Newsom et al. (2006) who found limited transport of mobile elements (Li, Be, B) in the groundmass of the Yax-1 impactites.

When comparing the calculated carbonate end-member of the Yax-1 impactite (CEMY) with the calculated Cretaceous target rock interval of the Yax-1 borehole (CTIY), Tuchscherer et al. (2005) observed that the CEMY composition was unusually calcite-rich. This could suggest the impactites were pervaded by calcite-rich fluids, thus altering the CEMY composition. Conversely, it could be that the CTIY composition determined by Tuchscherer et al. (2005) is not a good compositional representation of the target Cretaceous rocks. It could also be argued that limestone-rich regions in the target rocks were excavated by the Chicxulub impact and currently may not have been ground-truthed by drilling.

6.5.3. Classification problems due to groundmass alteration

The impactites of Units 1 to 3 (see section 1.5 for description of the impactite units in the Yaxcopoil-1 borehole and Fig. 1.13 for stratigraphic column) are all classified as allogenic suevites, as they contain discreet melt rock particles suspended in an altered clastic groundmass (Dressler et al. 2004b; Stöffler et al. 2004; Tuchscherer et al. 2004b). However, because of this alteration, the presumed lithic nature of the groundmass in these units has remained controversial (Kring et al. 2004b; Dressler et al. 2004; Stöffler et al. 2004; Tuchscherer et al. 2004a) due to its fine-grain size and, thus, poorly resolvable state (see groundmass descriptions for each units in section 2.5.3., Figs 2.5d and 2.6b). Because the groundmass in Unit 1 is generally highly altered and is suggested to have been reworked by the resurge of seawater into the impact basin (Tuchscherer et al. 2004a), it is assumed that it was originally similar to units 2 and 3. In units 2 to 3, the groundmass is composed primarily of microcrystalline calcite grains suspended in a phyllosilicate matrix (Fig. 2.5d). It has been suggested that pervasive multi-stage hydrothermal alteration has masked the lithic and, in part, glassy character of the groundmass (Stöffler et al. 2004; Tuchscherer et al. 2004b). If this groundmass was once glassy in origin, these suevites should then be reclassified as impact melt breccias.

The nature of the groundmass in Unit 5 is also still problematic. It represents either an authigenic carbonate-rich phase that formed by extensive post-depositional hydrothermal activity or an impact-generated carbonate impact melt (Tuchscherer et al. 2004a). Textural observations and geochemical results have not been able to resolve this issue. The carbonate groundmass shows fluidal textures (see Figs 2.3f, A.1.43-45 and Fig. 7 of Dressler et al. 2004), locally replaces felsic melt rock particles (Figs A.4.126-129), and is cross-cut by secondary calcite veins (Figs A.4.112-113). If this groundmass represents an impact melt, Unit 5 should be classified as an impact melt breccia. However, if it is an authigenic phase that has replaced a lithic precursor, it should be classified as a suevite.

The original nature of the groundmass observed in various units (units 1-3, and 5, see Fig. 1.2 and Table 2.1 for stratigraphic column and description thereof)

of the Yaxcopoil-1 borehole impactites was studied by detailed SEM investigation and is discussed below. Original results were presented in chapter 2. Unit 4 is not discussed here as it comprises a massive impact melt breccia.

6.5.3.1. Unit 5 groundmass

The groundmass of Unit 5 is of ambiguous origin. It is dominated by fine- to medium-grained calcite with interspersed dolomite crystals arranged in an interlocking nature (Figs 2.8b,c; A.4.103; A.4.116-121). The groundmass is also host to melt rock particles, lithic clasts, and authigenic barite crystals (Figs 2.8a; A.4.104-111; A.4.116-117; A.4.122-123; A.4.130; A.4.132-136). Tuchscherer et al. (2004a) identified foraminifera fossils in some of the dolomite clasts. However, these fossils might just represent relatively unshocked carbonate lithic clasts that were captured during the transport and deposition of Unit 5. Various authors have shown that this groundmass displays a fluidal texture indicative of flow (see Figs 7 of Dressler et al. 2004; Tuchscherer et al. 2004a) and fluidal contacts with melt rock particles or other melt phases (see Figs 2.3f, A.1.43- 45). The fluidal textures indicate the groundmass was not crystalline at the time of deposition. These observations remain open to interpretation; they could suggest the groundmass is either a primary carbonate impact-melt or that hydrothermal carbonate minerals replaced a pre-existing lithic matrix. Evidence of hydrothermal activity is indicated by the numerous calcite veins that cross-cut melt rock particles and that originate from the groundmass (Figs A.4.112- 115). However, carbonate textures indicative of melt have been observed in impactites of the UNAM 7 borehole and at the El Guayal site by Salge (2006). If carbonate melts have been observed farther away from the center of the Chicxulub crater and the Yax-1 site, it is not unreasonable to suggest the shock melt origin for the groundmass of Unit 5.

6.5.3.2. Groundmass of units 2 and 3

In units 2 and 3, the groundmass is composed of microcrystalline calcite grains that are suspended in a phyllosilicate matrix (Figs 2.5d, 2.6b, A.4.50, A.4.52, A.4.70, A.4.71). The modal proportion of calcite, compared with the

amount of phyllosilicate matrix in the groundmass, increases downwards towards Unit 3. Conversely, the modal proportion of groundmass decreases from Unit 2 to Unit 3 (see Table 2.3). This groundmass is analogous to cement, i.e., a glue. Dressler et al. (2004) described it as fine-grained to aphanitic, since crystalline components are barely discernable with the unaided eye. The only true lithic grain observed in this study is imaged in Figure A.4.52: it is a deformed, sheared feldspar grain. It has been previously suggested by various authors (Stöffler et al. 2004; Tuchscherer et al. 2004a) that this groundmass was originally a lithic matrix that was thoroughly converted to phyllosilicates and carbonates by extensive hydrothermal activity. Dressler et al. (2004) suggested the microscopic carbonate crystals enclosed by the phyllosilicate matrix are clastic. Recent geochemical investigation of the Yax-1 matrix using mobile elements (Li, B) indicates limited fractionation of these elements at low temperatures (Newsom et al. 2006). According to these authors this suggests that no extensive hydrothermal system can be accountable for the origin of the groundmass, as previously suggested by Stöffler et al. (2004) and Tuchscherer et al. (2004a). The petrographic and geochemical characteristics of the groundmass are therefore still open to interpretation. The original character of the groundmass, whether it was glassy or lithic, is still unknown. This issue still has serious implications on the classification of the impactite and the amount of melt produced.

6.5.3.3. Unit 1 groundmass

The groundmass found in the interstitial spaces between melt particles of Unit 1 is primarily made up of secondary phases, i.e., it represents veins of fine-grained calcite (Figs A.4.9, A.4.12, A.4.23). Rare occurrences of the original matrix can still be discerned in the interstitial space between melt rock particles (Figs 2.4a, A.4.9). Backscattered electron imaging also shows that the Unit 1 groundmass contains aggregates of highly altered melt particles (Figs A.4.8, A.4.10, A.4.18, A.4.19, A.4.21). The strong alteration of Unit 1 groundmass and melt particles is also obvious from the depletion of alkali elements and incompatible elements (see Fig. 3.3 and Table 3.2). This alteration is attributed to Unit 1 having being in contact with seawater and, thus, having been subjected to

alteration with the greatest fluid/rock ratio compared to lower units. It is suggested that seawater was able to circulate between the poorly consolidated suevite material. Geochemical evidence in support of seawater alteration is observed by the negative normalized Ce anomalies in melt rock particles of Unit 1 (see Figs 3.10 and 5.6a). Stable isotopic analysis of the silicate fraction also indicates relatively high (0.57 to 1.05) fluid/rock ratios for this unit (Zurcher et al. 2005). However, these authors have found that samples in the interval between 823 and 846 m (Unit 2 of this work) have even greater fluid/rock ratios (0.46 to 2.02). This discrepancy might be attributed to the lack of equilibrium alteration assemblages in Unit 1 required for the fluid/rock isotopic calculations.

6.5.4. Alteration characteristics observed by other research groups

Extensive evidence has been accumulated during this study that points to a pervasive hydrothermal system at Chicxulub, preserved in the Yax-1 impactites. Other researchers have also described extensive alteration features in the Yax-1 impactites. Ames et al. (2004), Hecht et al. (2004), Lüders and Rickers (2004), and Zürcher et al. (2004) have specifically described the hydrothermal alteration of the impactites. It is generally agreed between these groups that all siliceous melt rock particles have been thoroughly converted to phyllosilicates and are anomalously K-rich when compared to samples from other Chicxulub boreholes. It is noted that these geochemical features are similar to the seawater alteration describe in volcanic glasses, i.e., palagonization (e.g., Stroncik and Schmincke 2002). Ames et al. (2004) suggest the Yax-1 impactites were located in a Mg-K-rich seawater recharge zone that was probably driven by higher temperatures closer to the central region of the impact basin. Hecht et al. (2004) indicated that the lowermost unit, Unit 5 (their Unit 6), has been affected by extensive K-metasomatism. Fluid inclusions were observed in secondary quartz and calcite veins by Lüders and Rickers (2004). These authors suggested that the compositions of fluids were not homogeneous in space and time after the impact. Inclusions within quartz grains have high salinities and contain bitumen. These are suggested to have formed during boiling at temperatures up to 285 ^{o}C. In contrast, inclusions found within secondary calcite crystals do not contain

bitumen. Their $\delta^{13}C$ isotopic signatures do not suggest any significant interaction with organic matter; thus, they indicate a formational temperature no greater than 100 ^{o}C. Based on mineralogical observations and isotope constraints, Zurcher et al. (2004, 2005) also concluded that saline brine-like fluids permeated the impactites. They suggested that the heat driving the hydrothermal system was not derived from the immediate impact melt rocks, but from heat flow that originated closer to the center of the impact basin, as invoked by Ames et al. (2004). In terms of mineral paragenesis, Hecht et al. (2004) and Zurcher et al. (2004) both concluded feldspathic minerals first crystallized followed by phyllosilicates, zeolites, and barite. This hydrothermal activity allegedly generated an extensive hydrothermal plume into the Tertiary ocean (Ames et al. 2004; Rowe et al. 2004). This interpretation is supported by a suite of anomalous elements, i.e., Mn, Fe, P, Ti, Al, Ni, Ag, Au, Bi, and Te in the overlying Tertiary carbonate sedimentary rocks. Computer-assisted numerical modelling indicates that this hydrothermal system may have taken between 1.5 and 2.3 Myr to completely cool (Abramov and Kring 2007).

6.5.5. Conclusions regarding the alteration of the impactites

Alteration processes observed in the Yax-1 impactites are a testimony of the dynamic conditions that prevail after the deposition of hot suevite and impact melt rock breccias in a volatile rich environment. This alteration is pervasive and provides serious constraints on the hydrothermal history of the Yax-1 impactites.

Based on petrographic and geochemical observations, the following can be concluded. Units 1 and 2 have been thoroughly altered by the circulation of seawater through the impactite pile. This alteration is witnessed by the overall green alteration character of these units, their lower compositional variability (which compared to the underlying units is an alteration characteristics), and negative Ce anomalies in melt rock particles. Units 1 and 2 also show an enrichment of the large ion lithophile elements that can be attributed to alteration.

Unit 3 is the least altered of the fallback suevite units, i.e., units 1 to 3. This is obvious by its overall variegated character, as originally observed by Dressler (2002). This enhanced preservation state is attributed to the unit's

location, which is stratigraphically above Unit 4. The heat of the underlying impact melt breccia, Unit 4, is suggested to have been sufficicent to drive away volatiles and therefore preventing the pervasive conversion of melt rock particles to phyllosilicates. This is similar to the thermometamorphic unit observed by Claeys et al. (2003).

Additional constraints on the degree of alteration can be obtained from melt rock particle characteristics. Melt rock particles show a pervasive conversion to phyllosilicates. All mafic melt rock particles are thoroughly altered and show a K overprint. However, whole rock analyses do not show extensive exchange between K and Na. This suggests the impactite sequence was water saturated and the hydrothermal system at Yax-1 was not pervasive enough to enable the extensive remobilization of alkali elements or create characteristic alteration haloes.

Despite the overwhelming alteration characteristics that prevail in the Yax-1 impactites, several issues remain inconclusive. It is not possible to determine whether the hydrated mafic melt rock particles were hydrated during impact cratering processes, or if they were hydrated subsequent to their formation. It also cannot be determined whether alkali, felsic-rich melt rock particles that retain good totals were produced during melt formation and represent primary melt phases or if they are the product of secondary Ca-Na-K localized metasomatism. This is problematic as it prevents differentiating impact melt processes from secondary alteration processes.

6.6. Melt rock particles

Petrographic and geochemical information obtained from melt rock particles has been useful in the investigation and interpretation of the genetic history of the Yax-1 impactites. Melt rock particles can help discern the extent of melting (whether homogeneous versus heterogeneous) and provide constraints on the target rock protoliths.

6.6.1. Petrographic observations

6.6.1.1. Macroscopic morphological characteristics

Extensive petrographic observations have been made on the Yax-1 melt rock particles (Appendices A.1–A.4) and their key features are presented in Tables 2.2, 5.1, and 5.2. The melt rock particles in Unit 1 have sub-rounded morphologies, are self-supported, and display a fining-upward sorting. This indicates they have been subjected to some sort of sorting process, possibly by the atmosphere as suggested by (Stöffler et al. 2004). However, highly energetic post-depositional activity in the form of resurge may also account for these features. Melt rock particles from units 2 and 3 are groundmass-supported and show fluidal and angular morphologies (e.g., Fig. 2.3). The melt rock particles in Unit 3 are better compacted than those of Unit 2, indicating these units were deposited as part of a continuous fallback deposit. Unit 4 is a massive green melt rock that shows *in situ* brecciation, i.e., massive fragments fit together like pieces of a jigsaw puzzle. In Unit 5, melt rock particles are all groundmass-supported and show angular morphologies. The sub-angular to fluidal morphologies combined with the groundmass-supported character of units 2-3 and 5 suggest these are primary features. The massive yet brecciated character of Unit 4 indicates it underwent brecciation *after* deposition. Because Unit 1 shows features consistent with reworking, it is not to be a primary deposit.

6.6.1.2. Microscopic characteristics

Several microscopic features assist in establishing the genetic history of the melt rock particles. Melt rock particles in units 1 and 2 show numerous perlitic fractures (Table 2.3, Fig. A.4.9). This feature is consistent with devitrification under aqueous conditions (Ross and Smith 1955). Combined with the lack of microlites in this unit, this indicates rapid cooling in a wet environment. With depth, it is observed that melt rock particles from Unit 2 downwards show a marked increase in microlite content compared with Unit 1. This is consistent with relatively slower cooling with depth. Schlieren textures are commonly observed in melt rock particles from units 2-3 and 5. This suggests incomplete

mixing of mineral and/or rock melts. In Unit 3, numerous melt rock particles have alkali-element-enriched zones along their margins (e.g., Fig. 5.3f). This is believed to be the product of the localized remobilization of alkali elements. Another important feature is the common occurrence of carbonate blebs in melt rock particles (e.g., Figs A.4.54, A.4.65-66, A.5.71-73, A.4.90). This feature has been argued by Graup (1999) and Osinski and Spray (2001) at the Ries and Haughton impact craters to represent the presence of carbonate melt as an immiscible phase in silicate melt. However, the features observed in the Yax-1 impactites, although superficially similar to those at Ries and Haughton, could result from the infilling of vesicles by secondary calcite during hydrothermal activity. No conclusive evidence exists that can characterize such features as carbonate impact melt, especially when considering the highly altered state of the Yax-1 impactites

Wittmann et al. (2004) defined 5 different melt rock particle types based on petrographic characteristics. The details of these melt rock particle types are presented in Table 6.1. It is important to comment on these melt rock particles as Wittmann (2006) presented extensive EMPA results obtained from these particles. The correlation between the major element compositions of these particles and their petrographic characteristics is discussed in section 6.6.2. It should be noted that the petrographic characteristics observed by Wittmann et al. (2004) have also been observed by Tuchscherer et al. (2004a). However, Tuchscherer et al. (2004a) did not discriminate melt rock particle characteristics based on lithology but on geochemistry (see section 2.6.3.). Tuchscherer et al. (2004a) showed that melt rock particles displayed a multitude of petrographic characteristics (see Table 2.3). Classifying the melt rock particle characteristics based on the variable colour, microlite content and morphology was therefore deemed questionable.

6.6.2. Geochemical characteristics

In this study, melt rock particles have been analysed by various techniques, including SEM, EMPA, INAA, and LA-ICP-MS. In Chapter 2 (Tuchscherer et al. 2004a) it was found that melt rock particles have heterogeneous chemical compositions and this was not dependent on the EMPA

beam width (beam width = 3 and 10 μm, see Fig. 2.10). This heterogeneity in melt rock particle compositions was corroborated by trace element analysis obtained by INAA (Chapter 4, Tuchscherer et al. 2005) and LA-ICP-MS data (Chapter 5, Tuchscherer et al. 2006).

Table 6.1. Melt rock particle petrographic characteristics according to the classification scheme of Wittmann (2006).

Melt rock particle type	Color	Morphology	Lithological characteristics
1	Dark green	Amoeboid to angular	Lack of phenocrysts indicates rapid quenching.
2	Light green	Vesicular, shard-like, aerodynamic morphologies	Variable phenocryst abundances noticed, indicative of variable cooling rates. Phenocrysts increase with depth.
3BMR	Gray-green	Angular	BMR = broken melt rock, contain numerous phenocrysts of plagioclase and clinopyroxene. Can contain Fe-oxide schlieren.
3S	Red-white	Sub-angular	S = schlieren, display corroded margins.
4	Dark brown - black	Sub-angular, vesicular	Contain variable abundances of plagioclase phenocryts with Fe-(Ti) oxide crystals.

In Figure 6.3a, the 176 EMPA data obtained with a beam width of 3 μm from the study of Tuchscherer et al. (2006, Fig. 5.4) have been combined with the 555 EMPA results obtained in the study of Tuchscherer et al. (2004, Fig. 2.10a). This combined dataset shows a greater compositional variation of the melt rock particles than before (Tuchscherer et al. 2004a). No major differences can be noted between the focused beam (3 μm) EMPA results and the defocused beam width (10 μm) EMPA results. The combined dataset shows melt rock particles have a wide range of compositions that most likely reflects melting of a range of, and combinations of, precursor minerals. In the ACF diagram (Fig. 6.3a), numerous analyses plot near the K-feldspar composition. In the A'FK diagram (Fig. 6.3a), several analyses fall between the illite and biotite compositions. These analyses show that the two compositional fields observed in Fig. 2.10a (in the ACF diagram, the field near the F apex and the field between the anorthite - diopside compositions, in the A'FK diagram the field near the F apex and the field between the anorthite – F-feldpsar, and illite compositions) are actually part of a continuous compositional trend (Fig. 6.3a).

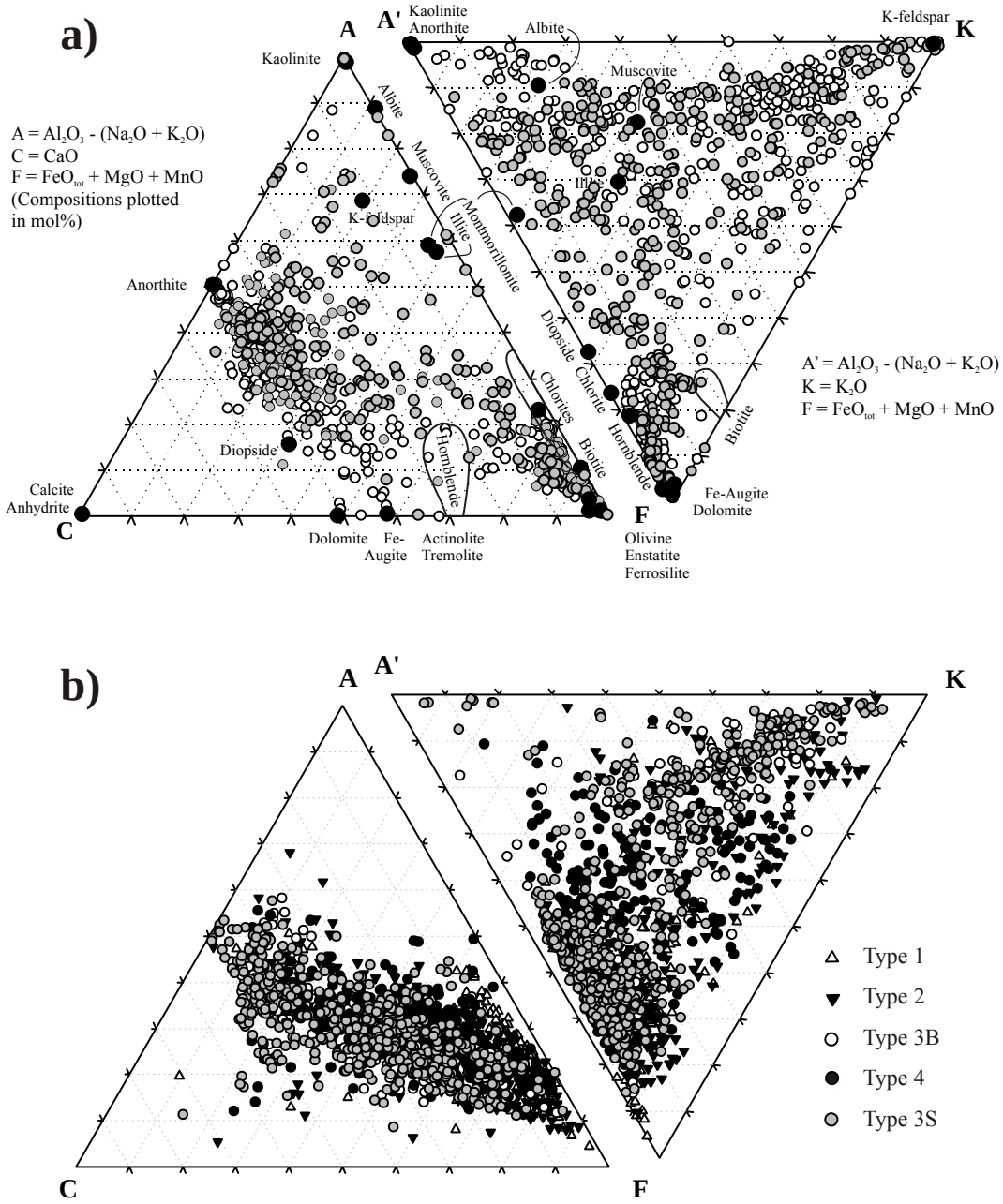

Fig. 6.3. ACF-A'FK diagram after Eskola (1939) with Yaxcopoil-1 melt particle compositions (electron microprobe analyses), plots are based on molecular proportions calculated from the weight % measurement results: a) All EMPA results obtained from this study (n = 731): gray circles represent focused beam analyses with 3 µm beam diameter, white circles represent defocused beam analyses at 10 µm beam diameter. b) all EMPA results obtained from the study of Wittmann (2006). Note the various particle types (see Table 6.1) and their heterogeneous compositions.

For comparative purposes, the 1673 EMPA results from Wittmann et al. (2006) have also been plotted on the ACF – A'FK diagram (Fig. 6.3b). The EMPA beam width from the study of Wittmann et al. (2006) was 20 μm. These data show a complete continuum between anorthite composition and the F apex in the ACF diagram and between the K-apex and the F-apex in the A'FK diagram (Fig. 6.3b). The melt rock particles have been plotted with different symbols according to the petrographic classification scheme of Wittmann (2006) presented in Table 6.1. Several differences can be observed between the plots obtained from the datasets of Wittmann (2006) and this study. In the ACF diagram of Figure 6.3b does not have data that plot near the A-apex, whereas several analyses plot towards the C-apex. In the A'FK diagram of Figure 6.3b, not one of the analysis plot on the F-K tie line. Also in this plot, none of Wittmann's data fall between 0-10% of the A-apex composition. The highly defocused EMPA beam width used by Wittmann (2006) is the only factor that could have caused this discrepancy compared to the results obtained in this work. This implies melt rock particle heterogeneities are greater on a scale that is lower than 20 μm. The phase(s) that contain components of the A apex (Al_2O_3, Na_2O, and K_2O) and that are responsible for this observed trend are most likely feldspar microlites. In general, this vast compilation of EMPA results shows that the melt particles are of heterogeneous composition irrespective of the melt rock particle type and mixture of microlite/altered glass analyzed. It is interesting to note that when plotting only analyses that have totals that range between 97 – 103 %, the data obtained by Wittmann (2006) also exclude any mafic melt rock particle compositions (Fig. 6.4).

With regards to EMPA results obtained from other researchers, Dressler et al. (2004) found two compositional groups (mafic and felsic groups) with relatively homogeneous compositions when recalculated on a volatile-free basis. Kring et al. (2004b) determined that the Yax-1 melt rock compositions were similar to those of the Y6 and C1 boreholes that originated primarily from the crystalline basement (Kring and Boynton 1992; Sharpton et al. 1992). Kring et al. (2004a) also suggested that the variegated character of Unit 3 melt rock particles may not be a function of heterogeneous compositions but rather the presence of

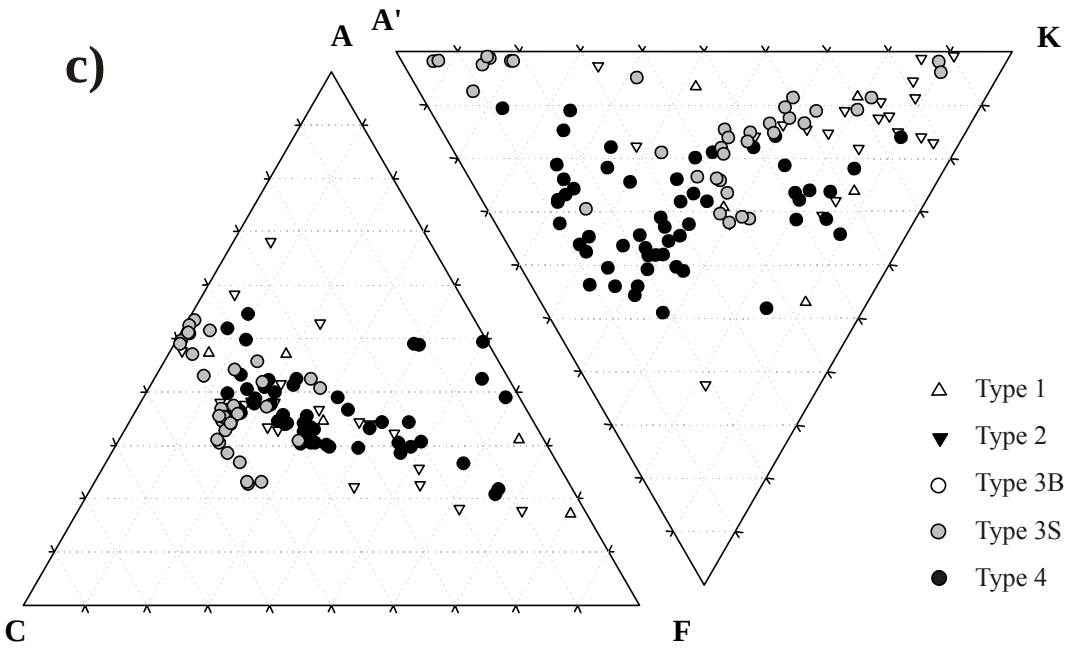

Fig. 6.4. ACF-A'FK diagram after Eskola (1939) with Yaxcopoil-1 melt particle compositions (electron microprobe analyses). Melt rock particle compositions are from Wittmann (2006) and comprise only melt rock particles with EMPA totals ranging between 97 – 103 wt%. Note that only 118 analyses can be plotted out of 1673 and that no analyses plot near the F-apex, as previously determined by Tuchscherer et al. (2004a) for mafic melt rock particles.

phyllosilicates and the variable oxidization state. Hecht et al. (2004) found 4 types of melt rock particles based on petrographic considerations. This scheme is essentially similar to the one found in the investigation of Wittmann (2006) presented in Table 6.1.

Extensive trace element data have been obtained by the INAA and LA-ICP-MS methods for melt rock particles (Tuchscherer et al. 2004b, 2005, 2006). This dataset shows that melt rock particles are generally trace element rich, whether altered or not. Carbonate minerals that are trace element poor dilute the overall concentrations (especially for INAA results that require ~150 μm). Although the trace element dataset for known target rocks is limited, Tuchscherer et al. (2005, 2006) showed that various geochemical characteristics observed in crystalline target rocks from the Chicxulub region are also found in Yax-1 melt rock particles. An analyzed granodiorite clast shows positive K, Ba, Zr, Na, and

Na anomalies and negative Sr, As, and Sb anomalies that are generally consistent with the averaged melt rock particle composition (Figs 4.14d, b). Melt rock particle compositions analyzed by LA-ICP-MS can also be linked to mixtures of known felsic crystalline target rock compositions (see Figs 5.7b, c, d). These results showed that melt rock particles are the product of fused felsic crystalline rocks. Their heterogeneous compositions are consistent with the incomplete melting of target minerals and rocks (or combinations of minerals). The negative geochemical anomalies (when normalized to the continental crust) observed in the melt rock particle compositions, i.e., U, As and Sb, can be accounted for by the lack of carbonate admixture to the melts. These elements are preferentially located in the dolomite, argillaceous limestone, and oil shale rocks of the Cretaceous carbonate platform (Fig. 4.15a, b).

6.7. Shock metamorphic features found in the Yax-1 impactites

Shock metamorphic features have been documented in the impactites of the Yax-1 borehole that are indicative of various shock pressures and temperatures (see section 2.6.4., Chapter 2). These range from unshocked rocks and minerals, weakly shocked, to bulk rock melting (from ca. 50 GPa, Bischoff and Stöffler 1984; Stöffler and Langenhorst 1994; Grieve et al. 1996). Shock metamorphic characteristics include quartz with reduced birefringence and/or mosaicism (Fig. A.4.146), quartz grains with single to multiple planar deformation features (PDFs, e.g., Fig. A.4.148), ballenquartz (Fig. 4.139, A.4.141), checkerboard textures (A.4.100) in feldspar minerals, the widespread occurrence of melt rock particles, and a massive impact melt rock. Although reduced birefringence and mosaicism are not key shock indicators, these textures are commonly observed in quartz found in impact structures and in the Yax-1 impactites (e.g., Fig. A.4.146).

The key shock indicator found in the Yax-1 impactite is the ubiquitous presence of PDFs in quartz. Planar deformation features were rarely observed in feldspar grains (see Table 2.3 for modal abundances). The formation of PDFs occurs in quartz when the crystal fails, i.e., develops crystallographic defects such as dislocations, after compression and release from the passage of a shock wave

(Stöffler and Langenhorst 1994; Grieve et al. 1996). The planar features usually have a spacing of >20 μm and follow important crystallographic planes. Up to 15 sets of PDFs can be recorded in highly shocked quartz grains (Grieve et al. 1996). A maximum of 4 sets of PDFs have been recorded in a quartz grain sampled at 878.09 m (Figs 2.9a, A.4.148-149). PDFs indicate shock pressures that range between 5 and 35 GPa (e.g., Stöffler and Grieve 1994; Grieve et al. 1996). Because the number of PDFs is known to increase with shock pressure (e.g. Robertson et al. 1968), it can be concluded that the Chicxulub impactites were subjected to pressures that range from at least 7.5 to >16 GPa.

Ballenquartz is another textural feature that is commonly associated with impact structures (Figs A.4.138-141; Grieve et al. 1996), although its origin is still not well understood. It has been suggested that ballenquartz forms from the recrystallization of quartz diaplectic glass to cristobalite primarily along grain boundaries (Bischoff and Stöffler 1984; Grieve et al. 1996). Its formation is believed to originate from a 7% volume contraction that occurs during the crystal structure inversion of β-cristobalite to α-cristobalite (von Engelhardt 1972). Because cristobalite is a high temperature quartz polymorph and is only stable at temperatures in excess of 1470^{o}C (Richet et al. 1982), its association with ballenquartz suggests shock pressures that extend between 30 and 65 GPa (Bischoff and Stöffler 1984). Metastable cristobalite has been found in association with ballenquartz in Fennoscandian impact craters and the Wanapitei and Popigai impact structures (Carsten 1975; Polsky and McHone 1998; Whitehead et al. 2002).

Interestingly, the occurrence of quartz glass, such as lechatelierite and quartz diapletic glass, has not been documented in the Yax-1 impactites. This may be due to the poorly ordered structural state of diaplectic glass in rapidly quenched melt, which makes it more susceptible to alteration. Lechatelierite may also be absent from the Yax-1 impactite owing to the lower proportions of sandstone and quartzite compared to the primarily carbonate-dominated target sedimentary rocks. Stöffler and Langenhorst (1994) indicated that highly shocked quartz-bearing rocks, e.g., granite, do not generally contain lechatelierite because the shock pressures required for whole-rock melting are below the peak pressures

required for the formation of lechatelierite. This latter condition is most likely the case for the Yax-1 impactites.

Checkerboard textures in feldspar grains have been documented throughout the impactites of the Yax-1 borehole (e.g., Fig. A.4.100). This texture has been interpreted as the product of preferential melting along crystallographic planes and indicates shock pressures in excess of 35 GPa (Bischoff and Stöffler 1984). It is important to note that despite the fact that ballenquartz and checkerboard feldspar are associated with specific shock pressures, their formation is not the product of the actual shock event (compression and release) but rather from the high post-impact temperatures (Langenhorst 2002).

Shock metamorphic variations with depth have been identified in the Yax-1 impactites (Table 2.3). Quartz grains that contain 2 to 3 sets of PDFs are most commonly found in units 4 and 5, whereas quartz grains with 1 to 2 sets of PDFs are most commonly found in units 1 to 3. Unit 4, a massive impact melt rock, shows the greatest occurrence of checkerboard feldspar. Unit 1 has some of the greatest proportions of melt rock particles but their high proportion here is the result of the resurge post-depositional activity. The original fine-grained groundmass of Unit 1 was removed during mechanical reworking during the resurge. Melt fragments were abraded during this process and are, thus, of smaller sizes compared to the underlying units. In brief, these observations show that the impactites have a greater modal proportion of shock metamorphic indicators with depth. If the groundmass found in Unit 5 is indeed a carbonate melt, which theoretically should have formed at temperatures of >1240^{o}C (Ivanov and Deutsch 2002), this would be in agreement with these observations. Additional petrographic observations obtained from other boreholes at Chicxulub may reveal greater insight to the response of carbonate rocks during shock melting.

7. Conclusions

Based on this detailed petrographic and geochemical investigation of the Yax-1 impactites, the following can be concluded:

1. The 100 m impactite interval intersected by the Yaxcopoil-1 borehole can be subdivided into 5 units based on the modal percentage of melt rock particles, their morphology, size, color, and alteration state.

2. Microscopic shock deformation features, e.g., planar deformation features, checkerboard feldspar and ballenquartz, occur throughout the interval, supporting the impact origin of these rocks. An increase in the number of planar deformation features per grain is noticed with depth. This indicates low shocked material was deposited subsequent to highly shocked material. Ballenquartz is found throughout the impactites, whereas checkerboard feldspar is generally restricted to melt rock particles and to the green impact melt rock (Unit 4).

3. Bulk rock major and trace element analysis obtained from individual samples shows that the impactites are compositionally highly heterogeneous. This heterogeneity is attributed to the poor mixing of target rock components at the sampling size, the variable lithic and melt rock particle size with variable groundmass proportions, and post-depositional alteration. Trace element ratios indicate the melt rock particles represent mixtures of various siliceous target rocks. The incorporation of a large carbonate component causes extensive dilution of the major and trace element concentrations. When the carbonate component (CaO and L.O.I.) is substracted from the impactite compositions, it can be shown the the silicate fraction has, however, an overall homogeneous composition.

4. Average chemical compositions calculated for the respective units reveal that units 1 to 3 are of relatively similar compositions. Unit 4 has a composition that suggests it formed primarily from fused Yucatán crystalline basement. Brown melt rock particles have a composition that is less mafic than that of Unit 4. Unit 5 shows the greatest compositional diversity, as it has variable melt rock particle, groundmass, and lithic clast proportions.

5. The calculated siliceous end-member of the Yax-1 impactites has a trace element signature similar to the average Upper Continental Crust (UCC) of

Rudnick and Gao (2003). The UCC also contains a mafic component when calculated on a L.O.I.-free basis.

6. The carbonate end-member calculated for the Yax-1 impactites is anomalously rich in calcite when compared to the calculated Cretaceous target rock composition that is dominated by dolomite. This indicates that the impactites have been subjected to extensive secondary carbonate metasomatic activity or that our calculated Cretaceous rock composition is not a true representation of the Yucatán target rocks.

7. Melt rock particles are compositionally (major and trace elements) highly heterogeneous. This result from the incomplete mixing and melting of target minerals and rocks combined with variable alteration. The melt rock particles have a compositional range that exceeds the compositional diversity of the suspected target rocks. Evidence supporting this interpretation originates from multidisciplinary (INAA, EMPA, LA-ICP-MS) analysis. The highly altered state of the melt rock particles is manifested by their conversion to phyllosilicates, especially in the upper units 1 and 2. All mafic melt rock particles are volatile-rich, whereas alkali element and Si-rich particles may still produce good major element totals. K-metasomatic activity has affected all particles, but on millimetre to micrometer scale. This is corroborated by major element analysis that does not show any exchange of Na and Ca for K.

8. The altered melt rock particles of units 1 and 2 are of a more homogeneous composition than their lower counterparts. Melt rock particles from these units are depleted in Na and K and enriched in Fe. Negative Ce anomalies in melt rock particles are indicative of alteration by seawater. It is suggested that the more intense alteration processes in the upper segment of the impactite unit smoothed over any pre-existing geochemical heterogeneities.

9. Small shard-like melt rock particles from units 1 to 3 quenched rapidly in a volatile-rich environment prior to crystallization with the host groundmass. Larger fluidal melt rock particles that contain microlites underwent protracted cooling. Microlite bearing shard-like melt rock particles in Unit 5 crystallized below the glass transformation temperature, or were fragmented after crystallization.

10. The volatiles present in the Chicxulub target rocks helped disperse and cool melt rock particles. Therefore, impacts that occur in heterogeneous target rocks that are volatile-rich are more likely to form compositionally heterogeneous suevite deposits.

11. The formation of the carbonate-rich groundmass in Unit 5 remains enigmatic as it could have formed by either shock melting of carbonate rocks or the replacement of a pre-existing clastic matrix. Apparent liquid immiscibility textures observed in melt rock particles cannot help solve this problem, as they could also have formed by the infilling of empty vesicles by precipitates from altering fluids.

12. A scenario consistent with the findings of this study is proposed for the successive deposition of the Yax-1 impactites: Unit 5 is interpreted as an early ejecta deposit that was emplaced following the passage of the initial ejecta curtain during the excavation stage of cratering. Unit 4 is an allogenic siliceous melt rock body that originated primarily from the fusion of the silicate crystalline basement. The origin of Unit 4 is based on geochemical and petrographic arguments, i.e., no carbonate component to the melt could be detected and only igneous/metamorphic mineral/rock fragments were observed in it. It is suggested Unit 4 was emplaced as an outward flow of fused crystalline basement rocks from the collapsing central uplift or it may have also been deposited from the fallback of a large melt bomb. Units 2 and 3 represent unreworked fallback suevite deposits. Unit 2 is the altered equivalent of Unit 3. Unit 1 represents a reworked fallback deposit.

13. Siderophile element analysis (INAA, γ-γ iridium coincidence spectrometry, and LA-ICP-MS) does not allow the unambiguous identification of traces of the extraterrestrial projectile component. This matter is further impeded by the as yet unknown composition of a postulated mafic target rock component.

14. Deformation features observed in the Cretaceous rocks testify to a multi-stage deformation history that extends from pre- to post-impact times. Detailed microscopic observations did not document any characteristic shock-related deformation features in the narrow breccia deposits of this core interval, even in the interval between 1347 and 1348 m depth that had been documented as an impact melt breccia occurrence by other researchers. Instead, this breccia has

been interpreted as a zone that experienced strong fluid alteration, involving the dissolution of dolomitic rocks by K-rich fluids associated with brine reflux. Oil shales documented below this interval are typical of oil-bearing rocks that form during diagenesis associated with the oil-window.

15. If the groundmasses of units 2-3 and 5 are indeed impact melt, this would have important implications in determining the amount of melt that was produced at Chicxulub and in impacts that occur in sedimentary target rocks in general (e.g., Osinski et al. 2005).

8. Recommendations

Several scientific objectives that are beyond the scope of this investigation still remain unresolved following this investigation. Questions regarding the nature of the groundmass in units 2, 3, and 5 and the lateral continuity of Unit 4 remain open. The groundmass in units 2 and 3 is extremely fine-grained, i.e., microcrystalline, requiring the usage of a scanning electron microscope to resolve its constituents. Additional samples, possibly from another site that is less altered than at Yax-1, may shed additional light on this issue. Further analytical investigation of this groundmass by SEM, LA-ICP-MS, and TEM should be beneficial in resolving this problem. It is still uncertain whether this material is truly clastic or represents entirely the alteration of previous melt rock/glass particles. How the carbonate groundmass of Unit 5 formed is still an unresolved issue, i.e., whether it represents a carbonate impact melt rock or a secondary authigenic phase. Additional sampling and analytical investigations are also necessary here. These unresolved issues have important consequences on the petrologic classification of the impactites, i.e., if the rocks of units 2, 3, and 5 are indeed impact melt rocks or clastic matrix suevites. This also has important implication regarding the extent of melting involved in impacts that occur in sedimentary target rocks and specifically at Chicxulub, help resolve the volume of melt produced, which is currently poorly constrained.

The resurge origin of Unit 1 is another unresolved issue that has originated from this study. Numerical cratering models have predicted this unit could originate by atmospheric drag and sorting from a re-established atmosphere at the Chicxulub impact site. Numerical models on crater collapse also suggest the final crater rim should have been too high to enable the resurge of seawater into the impact basin. These models are at odds with the findings of this study. It is suggested additional observations from either core samples or outcrop sections could provide additional insight into the origin of the topmost suevite deposit at Chicxulub. If truly a resurge deposit, numerical model simulations should then be recalibrated or reinterpreted to account for this finding.

It is proposed that answers to these issues can be obtained from the further study of Chicxulub impactites, especially through the description of impactite

deposits that occur laterally away from the Yax-1 borehole. Subtle lateral variations may provide insight and answers to these questions. Where outcrops are not present, future drilling of the Chicxulub impact structure is suggested. This should help determine the extent and lateral continuity of the units observed in the Yax-1 borehole and in earlier drillings. Correlation of specific lithological characteristics can already be made between samples obtained from the Y6 (Claeys et al. 2003, see Chapter 2) and the UNAM boreholes (Salge 2007). Additional samples should also provide further understanding in the distribution of target rock components, the attenuation of the shock wave in various target rocks, and constrain ejecta distribution of suevite during impact cratering. Future drilling of the Chicxulub impact structure has already been proposed through the International Ocean Drilling Program (IODP) and International Continental Drilling Program (ICDP).

References

Abramov O. and Kring D. A. 2007. Numerical modeling of impact-induced hydrothermal activity at the Chicxulub crater. Meteoritics & Planetary Science 42:93-112.

Agrinier P., Deutsch A., Schärer U., and Martinez I. 2001. Fast back-reactions of shock-released CO2 from carbonates: An experimental approach. Geochimica et Cosmochimica Acta 65:2615-2632.

Alegret L., Arenillas I., Arz J. A., Díaz C., Grajales-Nishimura J. M., Meléndez A., Molina E., Rojas R., and Soria A. R. 2005. Cretaceous-Paleogene boundary deposits at Loma Capiro, central Cuba: Evidence for the Chicxulub impact. Geology 33:721-724.

Allan J. R. L. 1972. A theoretical and experimental study of climbing-ripple cross lamination, with a field application to the Uppsala esker. Geographic Annals 53A:157-187.

Alvarez W. 1997. T. Rex and the Crater of Doom. Princeton: Princeton University Press. 185 p.

Alvarez L. W., Alvarez W., Asaro F., and Michel H. V. 1980. Extra-terrestrial cause for the Cretaceous-Tertiary extinction. Science 208:1095-1108.

Alvarez W., Asaro F., Michel H. V., Alvarez L. W. 1982. Iridium anomaly approximately synchronous with terminal Eocene extinctions. Science 216:886-888.

Alvarez W., Kauffman E. G., Surlyk F., Alvarez L. W., Asaro F. and Michel H. V. 1984. Impact theory of mass extinctions and the invertebrate fossil record: Science 223:1135-1141.

Alvarez W., Claeys P., and Kieffer S. W. 1995. Emplacement of K/T – boundary shocked quartz from the Chicxulub Crater. Science 269:930-935.

Ames D. E., Watkinson D. H., and Parrish R. R. 1998. Dating of a hydrothermal system induced by the 1850 Ma Sudbury impact event. Geology 26:447–450.

Ames D., Dressler B., Pope K. O., and Pilkington M. 2003. Chicxulub impact structure hydrothermal activity. Geophysical Research Abstracts 5. # 07331. CD-ROM.

Ames D. E., Kjarsgaard I., Pope K. O., Dressler B., and Pilkington M. 2004. Secondary alteration of the impactite and mineralization in the basal Tertiary sequence, Yaxcopoil-1, Chicxulub impact crater, Mexico. Meteoritics & Planetary Science 39:1145-1167.

Arenillas I., Arz J. A., Grajales-Nishimura J. M., Murillo-Muñetón G., Alvarez W., Camargo-Zanoguera A., Molina E., and Rosales-Domínguez C. 2006. Chicxulub impact event is Cretaceous/Paleogene boundary in age: New micropaleontological evidence. Earth and Planetary Science Letters 249:241-257.

Argyle E., Cisowski S. M., Fuller M., Officer C. B., and Ekdale A. A. 1986. Cretaceous extinctions and wildfires. Science 234: 261-263.

Artemieva N.A., Stöffler D., Hecht L., Schmitt R. T., and Tagle R. 2003. Interaction of the ejecta plume and the atmosphere during the deposition of the uppermost suevite layers at the Yax-1 drilling site, Chicxulub, Mexico. Large Meteorite Impacts Conference. Ries, Germany (Abstract # 4063) CD-ROM.

Argyle E., Cisowski S. M., Fuller M., Officer C. B., and Ekdale A. A. 1986. Cretaceous extinctions and wildfires. Science 234:261-263.

Bischoff A. and Stöffler D. 1984. Chemical and structural changes induced by thermal annealing of shocked feldspar inclusions in impact melt rocks from Lappajärvi crater, Finland. Journal of Geophysical Research, Supplement, 89:B645-B656.

Blum J. D. and Chamberlain C. P. 1992. Oxygen isotope constraints on the origin of impact glasses from the Cretaceous-Tertiary boundary. Science 257:1104-1107.

Blum J. D., Chamberlain C. P., Hingston M. P., Koeberl C., Marin L. E., Schuraytz B. C., and Sharpton V. L. 1993. Isotopic comparison of K/T boundary impact glass with melt rock from the Chicxulub and Manson impact structures. Nature 364:325-327.

Bohor B. F. 1990. Shocked quartz and more; Impact signatures in Cretaceous/Tertiary boundary clays. In Global catastrophes in Earth history, edited by Sharpton V. L. and Ward P. D. GSA Special Paper 247. Boulder: Geological Society of America. pp. 335-342.

Bohor B. F., Foord, E. E., Modreski P. J., and Triplehorn D. M. 1984. Mineralogic Evidence for an Impact Event at the Cretaceous-Tertiary Boundary. Science 224:867-869.

Bohor B. F., Modreski P. J., and Foord E. 1987. Shocked quartz in the Cretaceous-Tertiary boundary clays: evidence for a global distribution Science 236:705-709.

Bohor B. F., Betterton W. J., and Foord E. E. 1990. Shocked zircon and chromite in K/T boundary claystone. Meteoritics 25:350.

Bostwick J. A. and Kyte F. T. 1996. The size and abundance of shocked quartz in Cretaceous-Tertiary boundary sediments from the Pacific basin. In The Cretaceous-Tertiary event and other catastrophes in Earth history, edited by Ryder G., Fastovsky D. and Gartner S. GSA Special Paper 307. Boulder: Geological Society of America. pp. 403-415.

Bourgeois J., Hansen T. A., Wiberg., P.L., and Kauffman E. G. 1988. A tsunami deposit at the Cretaceous-Tertiary boundary in Texas. Science 241:567-570.

Bralower T. J., Paull-Charles K., and Leckie R. M. 1998. The Cretaceous-Tertiary boundary cocktail; Chicxulub impact triggers margin collapse and extensive sediment gravity flows. Geology 26:331-334.

Braman D. R. and Sweet A. R. 1999. Terrestrial palynomorph biostratigraphy of the Cypress Hills, Wood Mountain, and Turtle Mountain areas (Upper Cretaceous - Paleocene) of western Canada. Canadian Journal of Earth Sciences 36:725-741.

Brett R. 1992. The Cretaceous-Tertiary extinction: A lethal mechanism involving anhydrite target rocks. Geochimica et Cosmochimica Acta: 56:3603–3606.

Buffetaut E. 1990. Vertebrate extinctions and survival across the Cretaceous – Tertiary boundary. Tectonophyics 171:337-345.

Buseck P. R. 2002. Geological fullerenes: review and analysis. Earth and Planetary Science Letters.203:781-792.

Butler I. B. and Rickard D. 2000. Framboidal pyrite formation via the oxidation of iron (II) monosulfide by hydrogen sulphide. Geochimica et Cosmochimica Acta 64:2665-2672.

Carstens H. 1975. Thermal history of impact melt rocks in the Fennoscandian Shield. Contributions to Mineralogy and Petrology 50:145–155.

Carter N. L., Officer C. B., Chesner C. A., and Rose W. I. 1986. Dynamic deformation of volcanic ejecta from the Toba caldera: Possible relevance to Cretaceous/Tertiary boundary phenomena. Geology 14:380-383.

CANMET 1994. Catalogue of Certified Reference Materials. CCRMP 94-1E, 82p

Chaussidon M., Sigurdsson H., and Métrich N. 1996. Sulfur and boron isotope study of high-Ca impact glass from the K/T boundary: Constraints on source rocks. In The Cretaceous-Tertiary event and other catastrophes in Earth history, edited by Ryder G., Fastovsky D. and Gartner S. Special Paper 307. Boulder: Geological Society of America. pp. 253-262.

Chodas P.W. and Yeomans D.K. 1993. The upcoming collision of Comet Shoemaker-Levy 9 with Jupiter. 25th DPS Meeting of the American Astronomical Society. Bulletin of the American Astronomical Society 25: 1042.

Cisowski S. M. 1990. The significance of magnetic spheroids and magnesioferrite occurring in K/T boundary sediments. In Global catastrophes in Earth history, edited by Sharpton V. L. and Ward P. D. Special Paper 247 Boulder: Geological Society of America. pp. 359-365.

Claeys P., Kiessling W., and Alvarez W. 2002. Distribution of Chicxulub ejecta at the Cretaceous-Tertiary boundary. In Catastrophic events and mass extinctions: Impacts and beyond, edited by Koeberl C. and MacLeod K. G. Special Paper 356. Boulder: Geological Society of America. pp. 55-68.

Claeys P., Heuschkel S., Lounejeva-Baturina E., Sanchez-Rubio G., and Stöffler D. 2003. The suevite of drill hole Yucatán 6 in the Chicxulub impact crater. Meteoritics & Planetary Science 38:1299-1317.

Collins G. S., Melosh H. J., Morgan J. V., and Warner M. R. 2002. Hydrocode simulations of Chicxulub crater collapse and peak-ring formation. Icarus 157:24-33.

Combaz A. 1970. Microsphérule muriforms dans les roches mères du pétrole, hypothèse sur leur origine. Comptes Rendus Académie des Sciences (Paris) Série D 270:2240-2243.

Courtillot V., Jaeger J.-J., Yang Z., Féraud G., and Hofmann C. 1996. The influence of continental flood basalts on mass extinctions: Where do we stand? In The Cretaceous-Tertiary event and other catastrophes in Earth history, edited by Ryder G., Fastovsky D. and Gartner S. Special Paper 307 Boulder: Geological Society of America. pp. 513-525.

Courtillot V., Gallet Y, Rocchia R., Feraud G., Robin E., Hofmann C., Bhandari N., and Ghevariya Z. G. 2000. Cosmic markers, 40Ar/39Ar dating and paleomagnetism of the KT sections in the Anjar Area of the Deccan large igneous province. Earth and Planetary Science Letters 182:137-156.

de Cserna Z. 1989. An outline of the geology of Mexico. In: The geology of North America an Overview, edited by Bally A. W. and Palmer A. R. Boulder: Geological Society of America. Volume A, pp. 233 – 264.

Dawson J. B., Pinkerton H., Norton G. E., and Pyle D. M. 1990. Physicochemical properties of alkali carbonatite lavas: Data from the 1988 eruption of Oldoinyo Lengai, Tanzania. Geology 18:260-263.

Deer W. A., Howie R. A., and Zussman J. 1996. An introduction to the rock forming minerals, 2nd edition. Essex: Longman Scientific and Technical. 696 p.

Dressler B. O., Weisser T., and Brockmeyer P. 1996. Recrystallized impact glasses of the Onaping Formation and the Sudbury Igneous Complex, Sudbury Structure, Ontario, Canada. Geochimica et Cosmochimica Acta. 60:2019-2036.

Dressler B. O. and Reimold W. U. 2001. Terrestrial impact melt rocks and glasses. Earth Science Reviews 56:205-284.

Dressler B. O. 2002. Lithological report of Chicxulub/Yaxcopoil: Unpublished report for the Chicxulub Scientific Drilling Project and summary of the lithological report for ICDP/Chicxulub-Yax-1, ICDP/OSG-Geo-Forschungs-Zentrum Potsdam, Germany.

Dressler B. O., Sharpton V. L., Morgan J., Buffler R., Moran D., Smit J., Stöffler D., and Urrutia-Fucugauchi J. 2003a. Investigating a 65-Ma-old smoking gun: Deep Drilling of the Chicxulub Impact Structure. EOS Transactions of the American Geophysical Union 84:125, 131.

Dressler B. O., Sharpton V. L., and Marin L. E. 2003b. Chicxulub YAX-1 impact breccias: Whence They Come? (abstract # 1259). 34th Lunar and Planetary Science Conference. CD-ROM.

Dressler B.O., Sharpton V.L., Schwandt C.S., and Ames D. 2004. Impactites of the Yaxcopoil-1 drilling site, Chicxulub impact structure: Petrography, geochemistry, and depositional environment: Meteoritics & Planetary Science 39:857-878.

Ebel D. and Grossman L. 2005. Spinel-bearing spherules condensed from the Chicxulub impact-vapor plume. Geology 33:293-296.

Ebbing J., Janle P., Koulouris J., and Milkereit B. 2001. 3D gravity modelling of the Chicxulub impact structure. Planetary and Space Science 49:599- 609.

Elderfield H., Hawkensworth C.J., Greaves M.J., and Calvert S.E. 1981. Rare earth element geochemistry of oceanic ferromanganese nodules and associated sediments. Geochimica et Cosmochimica Acta 45:513-528.

Engelhardt W. v. 1972. Shock produced rok glasses from the Ries crater. Contribution to Mineralogy and Petrology 36:265-292.

Engelhardt W. v., Arndt J., Fecker B., and Pankau H. G. 1995. Suevite breccia from the Ries crater, Germany: Origin, cooling history and devitrification of impact glasses. Meteoritics 30:279-293.

Eskola P. 1939. Die Entstehung der Gesteine. Julius Springer, Berlin, 422 p.

Espindola J. M., Mena M., de la Fuente M., and Campos-Enriquez J. O. 1995. A model of the Chicxulub impact structure (Yucatán, Mexico) based on its gravity and magnetic signatures. Physics of the Earth and Planetary Interiors 92:271–278.

Evans N. J., Ahrens T. J., and Gregoire D. C. 1995. Fractionation of ruthenium from iridium at the Cretaceous-Tertiary boundary. Earth and Planetary Sciences Letters 134:141-153.

Fastovsky D.E. and Sheehan P.M. 2005. The extinction of the dinosaurs in North America. GSA Today 15:4-10.

Fleming R. F. and Nichols D. J. 1990 The fern-spore abundance anomaly at the Cretaceous-Tertiary boundary: A regional bioevent in western North America. In Extinction Events in Earth History. Springer, Berlin 30:347-349.

French B. M. 1998. Traces of catastrophe: A handbook of shock-metamorphic effects in terrestrial meteorite impact structures. Contribution 954. Houston: Lunar and Planetary Institute. 120 p.

French B. M. 2004. The importance of being cratered: The new role of meteorite impact as a normal geological process. Meteoritics & Planetary Science 39:169-197.

Freyssinet P. 2000. Geochemical mass balance and weathering rates of ultramafic schists in Amazonia. Chemical Geology 170:133-151.

Fuhrman M. L. and Lindsley D. H. 1988. Ternary-feldspar modeling and thermometry. American Mineralogist 73:201-215.

Galbrun B. 1997. Did the European dinosaurs disappear before the K-T event? Magnetostratigraphic evidence. Earth and Planetary Science Letters 148:569-579.

Gartner S. and Keany J. 1978. The terminal Cretaceous event: A geological problem with an oceanographic solution. Geology 6:708-712.

Gartner S. and McGuirk J. P. 1979. Terminal Cretaceous extinction scenario for a catastrophe. Science 206:1272-1276.

Gayraud J., Robin E., Rocchia R., and Froget L. 1996. Formation conditions of oxidized Ni-rich spinel and their relevance to the K/T boundary event. In The Cretaceous-Tertiary event and other catastrophes in Earth history, edited by Ryder G., Fastovsky D. and Gartner S. Special Paper 307. Boulder: Geological Society of America. pp. 424-443.

Gelinas A. Walker R. J., Kring D. A., and Zurcher L. 2003. Osmium isotope constraints on the proportions of bolide component in Chicxulub impact melts (abstract # 1359). 34th Lunar and Planetary Science Conference. CD-ROM.

Gelinas A., Kring D.A., Zurcher L., Urrutia-Fucugauchi J., Morton O., and Walker R.J., 2004, Osmium isotopic constraints on the proportion of bolide component in Chicxulub impact melts. Meteoritics & Planetary Science 39:1003-1008.

Gerstle S. A. W. and Zardecki A. 1982. Reduction of photosynthetically active radiation under extreme stratospheric aerosol loads. In Geological implications of impacts of large asteroids and comets on Earth, edited by Silver L. T. and Schultz P. H. Special Paper 190. Boulder: Geological Society of America. pp. 201-210.

Gibson R. L. and Reimold W. U. 2005. Shock pressure distribution in the Vredefort impact structure, South Africa. In Large meteorite impacts III, edited by Kenkmann T., Hörz F., and Deutsch A. Boulder: Geological Society of America Special Paper 384. pp. 329–349.

Gilmour I., Russell S. S., Arden J. W., Lee M. R., Franchi I. A., and Pillinger C. T. 1992. Terrestrial carbon and nitrogen isotopic ratios from Cretaceous-Tertiary boundary nanodiamonds. Science 258:1624-1626.

Gilmour I., Sephton M. A., and Morgan J. V. 2003. Organic geochemistry of a hydrocarbon-rich calcarenite from the Chicxulub scientific drilling program. (abstract # 1771). 34th Lunar and Planetary Science Conference. CD-ROM.

Glasby G. P. and Kunzendorf, H. 1996. Multiple factors in the origin of the Cretaceous/Tertiary boundary: the role of environmental stress and Deccan trap volcanism. Geologische Rundschau 85:191-210.

Goto K., Nakano Y., Tajika E., Tada R., Iturralde Vinent M.A., and Matsui T. 2002. Constraint on the depositional process of the K/T boundary proximal deep-sea deposit in northwestern Cuba based on shocked quartz distribution and its grain size (abstract). Geological Society of America Abstracts with Programs. Paper # 239-10.

Goto K., Tada R., Bralower T. J., Tajika E., and Matsui T. 2003. Probability of marine invasion into the Chicxulub crater and consequent generation of large tsunamis. Geophysical Research Abstracts 5, # 14413. CD-ROM.

Goto K., Tada R., Tajika E., Bralower T. J., Hasegawa T., and Matsui T. 2004. Evidence for ocean water invastion into the Chicxulub crater at the Cretaceous/Tertiary boundary. Meteoritics & Planetary Science 39:1233-1247.

Govindaraju K. 1989. 1989 compilation of working values and sample description for 272 geostandards. Geostandards Newsletter 13:1-113.

Graup G. 1999. Carbonate-silicate liquid immiscibility upon impact melting: Ries Crater, Germany. Meteoritics & Planetary Science 34:425-438.

Greinert J., Bollwerk S. M., Derkachev A., Bohrmann G., and Suess E. 2002. Massive barite deposits and carbonate mineralization in the Derugin Basin, Sea of Okhotsk: precipitation processes at cold seep sites. Earth and Planetary Science Letters 203:165-180.

Gregg J.M. and Sibley D.F. 1984. Epigenetic dolomitization the origin of xenotopic dolomite texture. Journal of Sedimentary Petrology 54:907–931.

Grégoire M., Bell D. R., and Le Roex A. P. 2002. Trace element geochemistry of phlogopite-rich mafic mantle xenoliths: their classification and their relationship to phlogopite-bearing peridotites and kimberlites revisited: Contribution to Mineralogy and Petrology 142:603-625.

Grieve R. A. F. 1975. Petrology and chemistry of the impact melt at Mistastin Lake crater, Labrador. Geological Society of America Bulletin 86:1617-1629.

Grieve R. A. F. and Therriault A. M. 2000. Vredefort, Sudbury, Chicxulub: Three of a kind?. Annual Reviews in Earth and Planetary Science 28:305-338.

Grieve R. A. F., Robertson P. B., and Dence M. R. 1981. Constraints on the formation of ring impact structures, based on terrestrial data. In Multi-Ring Basins: Formation and Evolution edited by Schultz P. H. and Merrill R. B., Proceedings of the Lunar Planetary Science, New York: Pergamon. 12A. pp. 37–57.

Gromet L.P., Dymek R.F., Haskin L.A., and Korotev R.L. 1984. The “North American Shale Composite”: its compilation, major and trace element characteristics. Geochimica et Cosmochimica Acta 48:2469-2482.

Grieve R. A. F., Langenhorst F., and Stöffler D. 1996. Shock metamorphism of quartz in nature and experiment: II. Significance in geoscience. Meteoritics & Planetary Science 31:6-35.

Gupta S. C., Ahrens T. J., and Yang W. 2001. Shock-induced vaporization of anhydrite and global cooling from the K/T impact. Earth and Planetary Science Letters 188:399-412.

Guy C., Daux V., and Schott J. 1999. Behaviour of rare earth elements during seawater/basalt interactions in the Mururoa Massif. Chemical Geology 158:21-35.

Hagerty J. J. and Newsom H. E. 2003. Hydrothermal alteration at the Lonar Lake impact structure, India: Implications for impact cratering on Mars. Meteoritics & Planetary Science. 38:365-381.

Hallam A. and Perch-Nielsen K. 1990. The biotic record of events in the marine realm at the end of the Cretaceous: calcareous, siliceous and organic-walled microfossils and macroinvertebrates. Tectonophysics 171:347-357.

Hallam A. and Wignall P. B. 1997. Mass Extinctions and their Aftermath. Oxford: Oxford University Press. 320 p.

Hecht L., Kenkmann T., Schmitt R. T., Stöffler D., Tagle R., and Wittmann A. 2003a. Petrography, composition, shock metamorphism, and geology of the impact formations of the ICDP drill core YAX-1, Chicxulub crater, Mexico (abstract). 66th Annual Meteoritical Society Meeting.

Hecht L., Schmitt R. T., and Wittman A. 2003b. Hydrothermal alteration of the impactites at the ICDP drill site Yax-1 (Chicxulub crater) (Abstract # 1583). 34th Lunar and Planetary Science Conference. CD-ROM.

Hecht L., Wittman A., Schmitt R. T., and Stöffler D. 2004. Composition of impact melt particles and the effects of post-impact alteration in suevitic rocks at the Yaxcopoil-1 drill core, Chicxulub crater, Mexico. Meteoritics & Planetary Science 39:1169-1186.

Heymann D., Chibante L. P. F., Brooks R. R., Woolbach W. S., and Smalley R. E. 1994. Fullerenes in the Cretaceous-Tertiary boundary layer. Science 256:645-647.

Heymann D., Chibante L. P. F., Brooks R. R., Woolbach W. S., Smit J., Korochantsev A., Nazarov M. A., and Smalley R. E. 1996. Fullerenes of possible wildfire origin. In The Cretaceous-Tertiary event and other catastrophes in Earth history, edited by Ryder G., Fastovsky D. and Gartner S. Special Paper 307. Boulder: Geological Society of America. pp. 453-464.

Hildebrand A. R. and Boynton W. V. 1990. Proximal Cretaceous-Tertiary boundary impact deposits in the Caribbean. Science 248:843-847.

Hildebrand A. R., Penfield G. T., Kring D., Pilkington M., Camargo A., Jacobsen S. B., and Boynton W. 1991. Chicxulub Crater: A possible Cretaceous-Tertiary boundary impact crater on the Yucatán peninsula, Mexico. Geology 19:867-871.

Hildebrand A. R., Pilkington M., Connors M., Ortiz-Aleman C., and Chavez R. E. 1995. Size and structure of Chicxulub crater revealed by horizontal gravity gradients and cenotes. Nature 376:415–417.

Horton J. W. Jr., Gohn G. S., Jackson J. C. Aleinikoff J. N., Sandford W. E., Edwards L. E., and Powars D. S. 2005. Results from a scientific test hole in the central uplift, Chesapeake bay impact structure, Virginia, USA. (Abstract # 2003) 36th Lunar and Planetary Science Conference. CD-ROM.

Hörz F. and Banholzer G. S. 1980. Deep-seated target materials in the continuous deposits of the Ries Crater, Germany. In Proceedings of the Conference on Lunar Highlands Crust, edited by Papike J. J. and Merrill R. B. New York: Pergamon Press. pp. 211–231.

Hörz F., Ostertag R., and Rainey D. A. 1983. Bunte Breccia of the Ries: Continuous deposits of large impact craters. Reviews of Geophysics and Space Physics. 21:1667–1725.

Hörz F., Mittlefehldt D. W., See T. H., and Galindo C. 2002. Petrographic studies of the impact melts from Meteor Crater, Arizona, USA. Meteoritics and Planetary Sciences. 37:501-531.

Hough R. M., Gilmour I., Pillinger C. T., Langenhorst F., and Montanari A. 1997. Diamonds from the iridium-rich K-T boundary layer at Arroyo el Mimbral, Tamaulipas, Mexico. Geology 25:1019-1022.

Hough R. M., Wright I. P., Sigurdsson H., Pillinger C. T., and Gilmour I. 1998. Carbon content and isotopic composition of K/T impact glasses from Haiti. Geochimica et Cosmochimica Acta 62:1285-1291.

Huffman A. R. and Reimold W. U. 1996 Experimental constraints on shock-induced microstructures in naturally deformed silicates. Tectonophysics 256: 165-217.

Huston D. L. and Logan G. A. 2004. Barite, BIFs and bugs: evidence for the evolution of the Earth's early hydrosphere. Earth and Planetary Science Letters 220:41-55.

Iftikhar A.A., Hesse R., and Harper J.D. 2004. Variations in mixed-layer illite/smectite diagenesis in the rift and post-rift sediments of the Jeanne d'Arc Basin, Grand Banks offshore Newfoundland, Canada. Canadian Journal of Earth Science 41:401-429.

Ivanov B.A., Badjukov O.I., Yakovlev M.I., Gerasimov M.V., Dikov Yu. P., Pope K.O., and Ocampo A.C. 1996. Degassing of sedimentary rocks due to Chicxulub impact: hydrocode and physical simulations. In The Cretaceous–Tertiary event and other catastrophes in Earth history, edited by Ryder G., Fastovsky D., and Gartner, S. Boulder: Geological Society of America. Special Paper 307. pp. 125–139.

Ivanov B. A. and Deutsch A. 1999. Sudbury impact event: Cratering mechanics and thermal history. In Large meteorite impacts and planetary evolution II, edited by Dressler B. O. and Sharpton V. L. Boulder. Geological Society of America. Special Paper 339. pp. 389-397.

Ivanov B. A. and Deutsch A. 2002. The phase diagram of CaCO3 in relation to shock compression and decomposition. Physics of the Earth and Planetary Interiors 129:131-143.

Izett G. A. 1990. The Cretaceous/Tertiary boundary interval, Raton Basin, Colorado and New Mexico, and its content of shock-metamorphosed minerals; Evidence relevant to the K-T boundary impact-extinction theory. Geological Society of America Special Paper 249, 100 p.

Izett G. A., Cobban W. A., Obradovich J. D., and Kunk M. J. 1993. The Manson impact structure: $^{40}Ar/^{39}Ar$ age and its distal impact ejecta in the Pierre shale in southeastern South Dakota. Science 262:729-732.

Jablonski D. 1994. Extinctions in the fossil record. Philosophical Transactions: Biological Sciences 344:11-16.

Jarosewich E., Nelen J. A., and Norberg J. A. 1980. Reference standards for electron microprobe analysis. Geostandards Newsletter 4:43-47.

Jarosewich E., Clarke R. S. Jr., and Barrows J. N. 1987. Allende meteorite reference sample. Smithsonian Contributions to the Earth Sciences 27:1-49.

Jercinovic M. J., Keil K., Smith M. R., and Schmitt R. A. 1990. Alteration of basaltic glasses from north-central British Columbia, Canada. Geochimica et Cosmochimica Acta 54:2679–2696.

Kajiwara Y. and Kaiho K. 1992. Oceanic anoxia at the Cretaceous/Tertiary boundary supported by the sulfur isotopic record. Palaeogeography, palaeoclimatology, palaeoecology 99:151-162.

Kamo S. L. and Krogh T. E. 1995. Chicxulub crater source for shocked zircon crystals from the Cretaceous-Tertiary boundary layer, Saskatchewan: Evidence from new U-Pb data. Geology 23:281-284.

Kamo S. L., Reimold W. U., Krogh T. E., and Colliston W. P. 1996. A 2.023 Ga age for the Vredefort impact event and a first report of shock metamorphosed zircons in pseudotachylitic breccias and Granophyre. Earth and Planetary Science Letters 144:369–388.

Keller G. 2005. Impacts, volcanism and mass extinction: random coincidence or cause and effect?. Australian Journal of Earth Sciences 52:725-757.

Keller G. and Lindinger M. 1989. Stable isotope, TOC and $CaCO_3$ record across the Cretaceous/Tertiary boundary at El Kel, Tunisia 73:243-265.

Keller G., Li L., and MacLeod N. 1995. The Cretaceous/Tertiary boundary stratotype section at El Kef, Tunisia: how catastrophic was the mass extinction? Palaeogeography, Palaeoclimatology, Palaeoecology 119:221-254.

Keller G. and Stinnesbeck W. 2000. Ir and the K/T boundary at El Caribe, Guatemala. International Journal of Earth Sciences 88:844-852.

Keller G., MacLeod N., Lyons J.B., and Officer C.B. 1993. Is there evidence for Cretaceous-Tertiary boundary-age deep water deposits in the Caribbean and Gulf of Mexico? Geology 21:776-780.

Keller G., Stinnesbeck W., Adatte T., Stüben D. 2003a. Multiple impacts across the Cretaceous - Tertiary boundary. Earth Science Reviews 62:327-363.

Keller G., Adatte T., Stinnesbeck W., Steben D., Kramar U., and Harting M. 2003b. The K/T transition at the Yaxcopoil-1 drillhole (abstract). Geophysical Research Abstracts 5, # 14415. CD-ROM.

Keller G., Adatte T., Stinnesbeck W., Rebolledo-Vieyra M., Urrutia Fucugauchi J., Kramar U., and Stüben D. 2004. Chicxulub impact predates the K-T boundary mass extinction. Proceedings of the National Academy of Sciences 101:3753-3758.

Kenkmann T. 2002. Folding within seconds. Geology 30:231-234.

Kenkmann T. and Schönian F. 2006. Ries and Chicxulub: Impact craters on Earth provide insights for Martian ejecta blankets. Meteoritics & Planetary Science 41:1587-1603.

Kenkmann T., Wittmann A., Scherler D., and Schmitt R. T. 2003. Deformation features of the Cretaceous units of the ICDP-Chicxulub drill core Yax-1 (abstract # 1368). 34th Lunar and Planetary Science Conference. CD-ROM.

Kenkmann T., Wittmann A., and Scherler D. 2004. Structure and impact indicators of the Cretaceous sequence of the ICDP drill core Yaxcopoil-1, Chicxulub impact crater, Mexico. Meteoritics & Planetary Science 39:1069–1088.

Kettrup B. and Deutsch A. 2003. Geochemical variability of the Yucatàn basement: Constaints from crystalline clasts in Chicxulub impactites. Meteoritics & Planetary Sciences 38:1079-1092.

Kettrup B., Deutsch A., Ostermann M., and Agrinier P. 2000. Chicxulub impactites: Geochemical clues to the precursor rocks. Meteoritics & Planetary Sciences 35:1229-1238.

Kieffer S. W. and Simonds C. H. 1980. The role of volatiles and lithology in the impact cratering process. Reviews in Geophysics and Space Physics 18:143-181.

King D. T. Jr., Neathery T. L., Petruny L. W., Koeberl C., and Hames W. E. 2002. Shallow-marine impact origin of the Wetumpka structure (Alabama, USA). Earth and Planetary Science Letters 202:541-549.

Kinsland G. L., Pope K. O., Cardador M. H., Cooper G. R. J., Cowan D. R., Kobrick M., and Sanchez G. 2005. Topography over the Chicxulub impact crater from Shuttle Radar Topography Mission data. In Large Meteorite Impacts III, edited by Kenkmann T., Hörz, F., and Deutsch A. Special Paper 384. Boulder: Geological Society of America. pp. 141-146.

Koeberl C. 1993a. Chicxulub crater, Yucatán: Tektites, impact glasses, and the geochemistry of target rocks and breccias. Geology 21:211-214.

Koeberl C. 1993b. Instrumental neutron activation analysis of geochemical and cosmochemical samples: A fast and reliable method for small sample analysis. Journal of Radioanalytical and Nuclear Chemistry 168:47-60.

Koeberl C. and Sigurdsson H. 1992. Geochemistry of impact glasses from the K/T boundary in Haiti: Relation to smectites and new type of glass. Geochimica et Cosmochimica Acta 56:2113-2129.

Koeberl C. and Shirey S. 1997. Re-Os isotope systematics as a diagnostic tool for the study of impact craters and distal ejecta. Palaeogeography, Palaeoclimatology, Palaeoecology 132:25-46.

Koeberl C. and Huber H. 2000. Multiparameter γ-γ coincidence spectrometry for the determination of iridium in geological materials. Journal of Radioanalytical Nuclear Chemistry 244:655-660.

Koeberl C. and MacLeod K. G., editors. 2002. Catastrophic events and mass extinctions: Impacts and beyond. Special Paper 356. Boulder: Geological Society of America. 746 p.

Koeberl C., Sharpton V. L., Schuraytz B. C., Shirey S. B., Blum J. D., and Marin L. E. 1994. Evidence for a meteoritic component in impact melt rock from the Chicxulub structure. Geochimica et Cosmochimica Acta. 58:1679-1684.

Koeberl C., Brandstätter F., Glass B. P., Hecht L., Mader D., and Reimold W. U. 2007. Uppermost impact fallback layer in the Bosumtwi crater (Ghana): Mineralogy, geochemistry, and comparison with Ivory Coast tektites. Meteoritics and Planetary Science 42:481-894.

Kring D.A. 1997. Composition of Earth's continental crust as inferred from the compositions of impact melt sheets (abstract # 1084) 28th Lunar and Planetary Science Conference. CD-ROM.

Kring D. A. 2003. Environmental consequences of impact cratering events as a function of ambient conditions on Earth. Astrobiology 3:133-152.

Kring D. A. 2005. Hypervelocity collisions into continental crust composed of sediments and an underlying crystalline basement: comparing the Ries (~24 km) and Chicxulub (~180 km) impact craters. Chemie der Erde 65:1-46.

Kring D. A. and Boynton W. V. 1992. Petrogenesis of an augite-bearing melt rock in the Chicxulub structure and its relationship to K/T impact spherules in Haiti. Nature 358:141-144.

Kring D. A. and Durda D. D. 2002. Trajectories and distribution of material ejected from the Chicxulub impact crater: Implications for postimpact wildfires. Journal of Geophysical Research 107:(6)1-22.

Kring D. A., Hildebrand A. R., and Boynton W. V. 1994. Provenance of mineral phases in the Cretaceous-Tertiary boundary sediments exposed on the southern peninsula of Haiti. Earth and Planetary Science Letters 128:629-641.

Kring D. A., Hörz F., and Zurcher L. 2003a. Initial assessment of the excavation and deposition of impact lithologies exposed by the Chicxulub scientific drilling project, Yaxcopoil-1, Mexico (abstract # 1641). 34th Lunar and Planetary Science Conference. CD-ROM.

Kring D. A., Zurcher L., and Hörz F. 2003b. Impact lithologies and post-impact hydrothermal alteration exposed by the Chicxulub scientific drilling project, Yaxcopoil, Mexico (abstract # 4112). 3rd International Conference on Large Meteoritic Impacts. CD-ROM.

Kring D. A., Zurcher L., Hörz F., and Mertzmann S. A. 2004a. Chicxulub impact melts: Geochemical signature of target lithology mixing and post-impact hydrothermal fluid processes. (abstract # 1701). 35th Lunar and Planetary Science Conference. CD-ROM.

Kring D. A., Hörz F., Zurcher L., and Urrutia Fucugauchi J. 2004b. Impact lithologies and their emplacement in the Chicxulub impact crater: Initial results from the Chicxulub Scientific Drilling Project, Yaxcopoil-1, Mexico. Meteoritics & Planetary Science 39:879-897.

Krogh T. E., Kamo S. L., Sharpton V. L., Marin L. E., and Hildebrand A. R. 1993. U-Pb ages of single shocked zircons linking distal K/T ejecta to the Chicxulub crater. Nature 366:731-734.

Kronberg B. I. Fyfe W. S., Leonardos O. H. Jr., and Santos A. M. 1979. The chemistry of some Brazilian soils: Element mobility during intense weathering. Chemical Geology. 24:211-229.

Kunk M. J., Izett G. A., Haugerud R. A., and Sutter J. F. 1989. $^{40}Ar/^{39}Ar$ Dating of the Manson Impact Structure: A Cretaceous - Tertiary Boundary Crater Candidate. Science 244:1565-1568.

Kyte F.T. 1998. A meteorite from the Cretaceous/Tertiary boundary. Nature 396:237-239.

Kyte F. T., Zhou Z., and Wasson J.T. 1980. Siderophile-enriched sediments from the Cretaceous-Tertiary boundary. Nature 288:651-656.

Kyte F. T. and Bostwick J. A. 1995. Magnesioferrite spinel in Cretaceous/Tertiary boundary sediments of the Pacific basin: Remnant of hot, early ejecta from the Chicxulub impact?. Earth and Planetary Science Letters 132:113-127.

Kyte F. T., Bostwick J. A., and Zhou L. 1996. The Cretaceous-Tertiary boundary on the Pacific plate: composition and distribution of impact debris. In The Cretaceous-Tertiary event and other catastrophes in Earth history, edited by Ryder G., Fastovsky D. and Gartner S. Boulder: Geological Society of America. Special Paper 307, pp. 389-401.

Langenhorst F. 2002. Shock metamorphism of some minerals: Basic introduction and microstructural observations. Bulletin of the Czech Geological Survey 77:265-282.

Langenhorst F. and Deutsch A. 1994. Shock experiments on pre-heated α- and β-quartz: I. Optical and density data. Earth and Planetary Science Letters 128:683-698.

Lawton T. F., Shipley K. W., Aschoff J. L., Giles K. A., Vega F. J. 2005. Basinward transport of Chicxulub ejecta by tsunami-induced backflow, La Popa basin, northeastern Mexico, and its implications for distribution of impact-related deposits flanking the Gulf of Mexico. Geology 33:81-84.

Le Roux P. J., Le Roex A. P., and Schilling J.-G. 2002. MORB melting processes beneath the southern Mid-Atlantic Ridge (40–55°S): a role for mantle plume-derived pyroxenite: Contribution to Mineralogy and Petrology 144:206-229.

Lomax B., Beerling D., Upchurch G. Jr., and Otto-Bliesner B. 2001. Rapid (10-yr) recovery of terrestrial productivity in a simulation study of the terminal Cretaceous impact event: Earth and Planetary Science Letters 192:137-144.

Lopez-Ramos E. 1975. Geological summary of the Yucatán Peninsula. In The ocean basins and margins, Vol. 3: The Gulf of Mexico and the Caribbean, edited by Nairn A. E. M. and Stehli F. G. New York: Plenum Press, pp. 257-282.

Lounejeva E., Elias-Herrera M., Ortega-Gutiérrez F., and Cedillo-Pardo E. 2003. Origin of epidote from the impact melt of the Chicxulub crater, México. Large Meteorite Impacts Conference. Ries, Germany (Abstract # 4054) CD-ROM.

Lüders V. and Rickers K. 2004. Fluid inclusion evidence for impact-related hydrothermal fluid and hydrocarbon migration in Creataceous sediments of the ICDP-Chicxulub drill core Yax-1. Meteoritics & Planetary Science 39:1187-1197.

Macdougall J. D. 1988. Seawater strontium isotopes, acid rain, and the Cretaceous-Tertiary boundary. Science 239:485-487.

Mariano A. N. 1988. Some further geological applications of cathodoluminescence. In Cathodoluminescence of geological materials, edited by Marshall D. and J. Winchester: Allen and Unwin Inc. pp. 94-123.

Marshall D. J. 1988. Cathodoluminescence of geological materials. Winchester: Allen and Unwin Inc. 146 p.

Maruoka T. and Koeberl C. 2003. Acid-neutralizing scenario after the Cretaceous-Tertiary impact event. Geology 31:489-492.

Masaitis V. L. 2002. The middle Devonian Kaluga impact crater (Russia): new interpretation of marine setting. Deep-Sea Research II 49:1157-1169.

Matsui T., Imamura F., Tajika E., Nakano Y., and Fujisawa Y. 2002. Generation and propagation of a tsunami from the Cretaceous-Tertiary impact event. In Large Meteorite Impacts III, edited by Kenkmann T., Hörz, F., and Deutsch A. Special Paper 384. Boulder: Geological Society of America. pp. 69–77.

McDonald M. A., Gulick S. P., Gorney D. L., Christeson G. L., Barton P. J., Morgan J. V., Warner M. R., Urrutia-Fucugauchi J., Melosh H. J., Vermeesch P. M., Surendra A. T., Goldin T., and Mendoza K. 2005. Terrace Zone Structure in the Chicxulub Impact Crater Based on 2-D Seismic Reflection Profiles: Preliminary Results From EW&35;0501. American Geophysical Union (Spring Meeting 2005). abstract #P21A-03.

McDonough W.F. 2003. Compositional Model for the Earth's Core. In Treatise on Geochemistry volume 2, edited by Carlson R.W. Amsterdam: Elsevier. pp. 547-568.

McHone J.F., Nieman R.A., Lewis C.F., and Yates A.M. 1989. Stishovite at the Cretaceous-Tertiary boundary, Raton, New Mexico. Science 243:1182-1184.

McLean D. M. 1982. Deccan volcanism and the Cretaceous-Tertiary transition scenario: a unifying causal mechanism. Syllogeus 39:143-144.

McLennan S. M. and Taylor S. R. 1980. Th and U in sedimentary rocks: crustal evolution and sediment recycling. Nature 285:621-624.

Meldin W. L. 1963. Emission centers in thermoluminescent calcite, dolomite, magnesite, aragonite, and anhydrite. Journal of the Optical Society of America 53:1276-1285.

Melosh H. J. 1989. Impact cratering: A geologic process. New York: Oxford University Press. 245 p.

Meyerhoff A. A., Lyons J. B., and Officer C. B. 1994. Chicxulub structure: A volcanic sequence of late Cretaceous age. Geology 22:3-4.

Morgan J. and Warner M. 1999. Chicxulub: The third dimension of a multi-ring impact basin. Geology 27:407-410.

Morgan J., Warner M., and the Chicxulub Working Group. 1999. The Chicxulub seismic experiment: Crater morphology. In Large meteorite impacts and planetary evolution II, edited by Dressler B. O. and Sharpton V. L. Boulder. Geological Society of America. Special Paper 339. pp. 269-279.

Morgan J., Warner M., The Chicxulub Working Group, Brittan J., Buffler R., Camargo A., Christeson G., Denton P., Hildebrand A., Hobbs R., MacIntyre H., MacKenzie G., Maguire P., Marin L., Nakamura Y., Pilkington M., Sharpton V. L., Snyder D., Suarez G., and Trejo A. 1997. Size and morphology of the Chicxulub impact crater. Nature 390:472-476.

Morgan J. V., Warner M. R., Collins G. S., Melosh H. J., and Christeson G. L. 2000, Peak-ring formation in large impact craters: geophysical constraints from Chicxulub. Earth and Planetary Science Letters 183:347-354.

Morgan J., Warner M., and Grieve R. A. F. 2002. Geophysical constraints on the size and structure of the Chicxulub impact crater. In Catastrophic events and mass extinctions: Impacts and beyond, edited by Koeberl C. and MacLeod K. G. Special Paper 356. Boulder: Geological Society of America. pp. 39-46.

Morgan J. P., Reston T. J., and Ranero C. R. 2004. Contemporaneous mass extinctions, continental flood basalts, and 'impact signals': are mantle plume-induced lithospheric gas explosions the causal link?. Earth and Planetary Science Letters 217:263-284.

Morgan J., Warner M., Urrutia-Fucugauchi J., Gulick S., Christeson G., Barton P., Rebolledo-Vierya M., and Melosh J. 2005. Chicxulub Crater Seismic Survey Prepares Way for Future Drilling, EOS Trans. AGU. 86(36):325.

Morgan J., Lana C., Kearsley A., Coles B., Belcher C., Montanari S., Díaz-Martínez, Barbosa A., and Neumann V. 2006. Analyses of shocked quartz at the global K-P boundary indicate an origin from a single, high-angle, oblique impact at Chicxulub. Earth and Planetary Science Letters 251:264-279.

Mungall J. E., Ames D. E., and Hanley J. J. 2005. Geochemical evidence from the Sudbury structure for crustal redistribution by large bolide impacts. Nature 429:546-548.

Nakashima S., Disnar J.R., Perruchot A., and Trichet J. 1984. Experimental study of mechanism of fixation and reduction of uranium by sedimentary organic matter under diagenetic or hydrothermal conditions. Geochimica et Cosmochima Acta 48:2321-2329.

Naumov M. V. 2002. Impact-generated hydrothermal systems: data from Popigai, Kara, and Puchezh-Katunki impact structures. In Impacts in Precambrian Shields edited by Plado J. and Pesonen L. J. Springer-Verlag, Berlin, pp. 117-171.

Nesbitt H. W. and Young G. M. 1982. Early Proterozoic climates and plate motions inferred from major element chemistry of lutites. Nature 299:715-717.

Nesbitt H. W. and Young G. M. 1984. Predictions of some weathering trends in plutonic and volcanic rocks based on thermodynamics and kinetic considerations. Geochimica et Cosmochimica Acta 48:1523-1534.

Newsom H. E., Nelson M. J., Shearer C. K., and Dressler B. O. 2006. Mobile element analysis by secondary ion mass spectrometry (SIMS) of impactite matrix samples from the Yaxcopoil-1 drill core in the Chicxulub impact structure. Meteoritics & Planetary Science 41:1929-1945.

de Niem D., Kührt E., and Motschmann U. 2007. Ejecta range : A simulation study of terrestrial impacts. Planetary and Space Science 55:900-914.

Norris R. D. and Firth J. V. 2002. Mass wasting of Atlantic continental margins following the Chicxulub impact event. In Catastrophic events and mass extinctions: impacts and beyond, edited by Koeberl C. and MacLeod K. G. Boulder: Geological Society of America Special Paper 356. pp. 79-95.

O'Keefe J. D. and Ahrens T. J. 1982. Impact mechanics of the Cretaceous – Tertiary extinction bolide. Nature 298:123-127.

Officer C. B. and Drake C. L. 1983. The Cretaceous-Tertiary transition. Science 219:1383-1390.

Ormö J. and Miyamoto H. 2002. Computer modelling of the water resurge at a marine impact: the Lockne crater, Sweden. Deep-Sea Research II 49:983-994.

Orth C. J., Gilmore S., Knight J. D., Pillmore C. L., Tschudy R. H., and Fasset J. E. 1981. An iridium abundance anomaly at the palynological Cretaceous-Tertiary boundary in northern New Mexico. Science 214:1341-1343.

Osinski G. R. 2003. Impact glasses in fallout suevites from the Ries impact structure, Germany: An analytical SEM study. Meteoritics & Planetary Science 38:1641–1667.

Osinski G. R. 2004. Impact melt rocks from the Ries structure, Germany: an origin as impact melt flows?. Earth and Planetary Science Letters 226:529-543.

Osinski G. R. 2005. Hydrothermal activity associated with the Ries impact event, Germany. Geofluids 5:202-220.

Osinski G. 2006. Effect of volatiles and target lithology on the generation and emplacement of impact crater fill and ejecta deposits on Mars. Meteoritics & Planetary Science 41:1571-1586.

Osinski G. R. and Spray J. G. 2001. Impact-generated carbonate melts: evidence from the Haughton structure, Canada. Earth and Planetary Science letters 194:17-29.

Osinski G. R. and Spray J. G. 2003. Evidence for the shock melting of sulfates from the Haughton impact structure, Arctic Canada. Earth and Planetary Science Letters 215:357-370.

Osinski G. R., Spray J. G., and Lee P. 2005. Impactites of the Haughton impact structure, Devon Island, Canadian High Arctic. Meteoritics & Planetary Science 40:1789-1812.

Oskarsson N., Helgason O., and Sigurdsson H. 1996. Oxidation state of iron in tektite glasses from the Cretaceous/Tertiary boundary. In The Cretaceous-Tertiary Event and Other Catastrophes in Earth History, edited by Ryder G., Fastovsky D., and Gartner S. GSA Special Paper 307. Boulder: Geological Society of America. pp. 445-452.

Owen M. R., Anders M. H., Barber A. A., Condon P. D., and Haughton M. G. 1990. A closer look at cathodoluminescence of shocked quartz at the K/T boundary. In Global catastrophes in Earth history, edited by Sharpton V. L. and Ward P. D. GSA Special Paper 247. Boulder: Geological Society of America. pp. 343-347.

Palme H. and Jones A. 2003. Solar system abundances of the elements. In Treatise on Geochemistry volume 1, edited by Davis A. M. Amsterdam: Elsevier. pp. 41-61.

Patterson C. C. 1956. Age of meteorites and the Earth. Geochimica et Cosmochimica Acta 10:230–237.

Penfield G. T. and Camargo Z. A. 1981 Definition of a major igneous zone in the central Yucatán platform with aeromagnetics and gravity (abstract). 51st Annual International Meeting of the Society of Exploration Geophysicists. p. 37.

Persaud P. and Sharpton V. L. 1998. Correlation of well data for the Chicxulub impact structure using gravity and magnetic anomalies. (abstract # 1876). 29th Lunar and Planetary Science Conference. CD-ROM.

Pierazzo E., Kring D. A., and Melosh H. J. 1998. Hydrocode simulation of the Chicxulub impact event and the production of climatically active gases. Journal of Geophysical Research 103:28607-28625.

Pierazzo E. and Melosh H. J. 1999. Hydrocode modelling of Chicxulub as an oblique impact event. Earth and Planetary Science Letters 165:163-176.

Pierazzo E. and Melosh H. J. 2000. Hydrocode modeling of oblique impacts: The fate of the projectile. Meteoritics & Planetary Sciences 35:117-130.

Pierazzo E., Hahmann A. N., and Sloan L. C. 2003. Chicxulub and climate: Radiative perturbations of impact-produced S-bearing gases. Astrobiology 3:99-118.

Pilkington M., Hildebrand A. R., and Ortiz-Aleman C. 1994. Gravity and magnetic modelling and structure of the Chicxulub crater, Mexico. Journal of Geophysical Research 99:13147–13162.

Pilkington M., Ames D. E., and Hildebrand A. R. 2004. Magnetic mineralogy of the Yaxcopoil-1 core, Chicxulub. Meteoritics and Planetary Sciences 39:831-841.

Polsky C. H. and McHone J. F. 1998. Raman spectroscopic confirmation of metastable cristobalite in melt samples from the Wanapitei impact structure. (abstract # 1471). 29th Lunar and Planetary Science Conference. CD-ROM.

Pope K. O. 2002. Impact dust not the cause of the Cretaceous-Tertiary mass extinction. Geology 30:99-102.

Pope K. O., Baines K. H., Ocampo A. C., and Ivanov B. A. 1994. Impact winter and the Cretaceous/Tertiary extinctions: Results of a Chicxulub asteroid impact model. Earth and Planetary Science Letters 128:719-725.

Pope K. O., Ocampo A. C., Kinsland G. L. and Smith R. 1996. Surface expression of the Chicxulub crater. Geology 24:527-530.

Pope K. O., Ocampo A. C., Fischer A. G., Vega F. J., Ames D. E., King, D. T. Jr., Fouke B. W., Wachtman R. J., and Kletetschka G. 2005. Chicxulub impact ejecta deposits in southern Quintana Roo, México, and central Belize. In Large Meteorite Impacts III, edited by Kenkmann T., Hörz, F., and Deutsch A. Special Paper 384. Boulder: Geological Society of America. pp. 171-190.

Potts P. J., Bowles J. F. W., Reed S. J. B., and Cave M. R. 1995. Microprobe Techniques in the Earth Sciences: Chapman & Hall, 419 pp.

Premo W. E. and Izett G. A. 1992. Isotopic signature of black tektites from the K – T boundary on Haiti – Implications for the age and type of source material. Meteoritics 27:413-424.

Puura V., Huber H., Kirs J., Kärki A., Suuroja K., Kirsimäe K., Kivisilla J., Kleesment A., Konsa M., Preeden U., Suuroja S., and Koeberl C. 2004. Geology, petrography, shock petrography, and geochemistry of impactites and target rocks from the Kärdla crater, Estonia. Meteoritics & Planetary Science 39:425-451.

Quezada Muñeton J. M., Marin L. E., Sharpton V. L., Ryder, G., and Schuraytz, B. C. 1992. The Chicxulub impact structure: Shock deformation and target composition (abstract). 23rd Lunar and Planetary Science Conference, pp.1121-1122.

Raup D. 1991. Extinction: Bad genes or bad luck?: New York, W.W. Norton & Co., 210 p.

Reimold W. U. 2003. Impact cratering comes of age. Science 300: 1888–1890.

Richet P., Bottinga Y., Deniélou L., Petitet J.P., and Téqui C. 1982. Thermodynamic properties of quartz, cristobalite, and amorphous SiO_2: drop calorimetry measurements between 1000 and 1800 K and a review from 0 to 2000 K. Geochimica et Cosmochmica Acta 46: 2639-2658.

Righi D. and Meunier A. 1995. Origin of clays by rock weathering and soil formation. In Origin and Mineralogy of Clays, edited by Velde B. Berlin. Springer-Verlag. pp. 43-161.

Robertson P. B., Dence M. R., and Vos M. A. 1968. Deformation in rock-forming minerals from Canadian craters. In Shock Metamorphism of Natural Materials, edited by French B. M. and Short N. M. Baltimore: Mono Book Corp. pp. 433-452.

Roddy D. J., Pepin R. O., and Merrill R. B. 1977. Impact and Explosion Cratering: Planetary and Terrestrial Implications. New York. Pergamon. 1301 pp.

Ross C. S. and Smith R. L. 1955. Water and other volatiles in volcanic glass. American Mineralogist 40:1071-1089.

Rowe A. J., Wilkinson J. J., Coles B. J. and Morgan J. V. 2004. Chicxulub: Testing for post-impact hydrothermal input into the Tertiary ocean. Meteoritics & Planetary Science 39:1223-1231.

Rudnick R. L. and Gao S. 2003. Composition of the Continental Crust. In Treatise on Geochemistry Volume 3, edited by Rudnick R. Amsterdam: Elsevier. pp. 1-64.

Ryder G., Fastovsky D., and Gartner S. 1996. The Cretaceous-Tertiary event and other catastrophes in Earth history. GSA Special Paper 307. Boulder: Geological Society of America. 580 p.

Salge T. 2007. The ejecta blanket of the Chicxulub impact crater, Yucatán, Mexico: Petrographic and chemical studies of the K-P section of El Guayal and UNAM boreholes. Ph.D. thesis, Humboldt University, Berlin, Germany.

Scasso R., Concheyro A., Kiessling W., Aberhan M., Hecht L., Medina F., and Tagle R. 2005. A tsunami deposit at the Cretaceous/Palaeogene boundary in the Neuquén Basin of Argentina. Cretaceous Research 26:283-297.

Schmitt R. T., Wittman A., and Stöffler D. 2004. Geochemistry of drill core samples from Yaxcopoil-1, Chicxulub impact crater, Mexico. Meteoritics & Planetary Science 39:979-1001.

Schmitz B. 1988. Origin of microlayering in world wide distributed Ir-rich marine Cretaceous-Tertiary boundary clays. Geology 16:1068-1072.

Schulte P. and Kontny A. 2005. Chicxulub impact ejecta from the Cretaceous-Paleogene (K-P) boundary in northeastern México. In Large Meteorite Impacts III, edited by Kenkmann T., Hörz, F., and Deutsch A. Special Paper 384. Boulder: Geological Society of America. pp. 191-221.

Schulte P., Speijer R., Mai H., and Konty A. 2006. More evidence that Chicxulub impact event coincided with K-P mass extinction. Sedimentary Geology 184:77-109.

Schultz P. H. and D'Hondt S. 1996. Cretaceous-Tertiary (Chicxulub) impact angle and its consequences. Geology 24:963-967.

Schuraytz B. C., Sharpton V. L., and Marin L. E. 1994. Petrology of impact-melt-rocks at the Chicxulub multiring basin, Yucatán, Mexico. Geology 22:868-872.

Schuraytz B. C., Lindstrom D. J., Marin L. E., Martinez R. R., Mittlefehldt D. W., Sharpton V. L., and Wentworth S. J. 1996. Iridium metal in Chicxulub impact melt: Forensic chemistry on the K-T smoking gun. Science 271: 1573-1576

Sharpton V. L. and Ward P. D. 1990. Global catastrophes in Earth history; An interdisciplinary conference on impacts, volcanism, and mass mortality. GSA Pecial Paper 247. Boulder: Geological Society of America. 631 p.

Sharpton V. L., Dalrymple G. B., Marin L. E., Ryder G., Schuraytz B. G., and Urrutia-Fucugauchi J. 1992. New links between the Chicxulub impact structure and the Cretaceous/Tertiary boundary. Nature 359:819-821.

Sharpton V. L., Burke K., Camargo-Zanoguera A., Hall S. A., Scott Lee D., Marin L. E., Suárez-Reynoso G., Quezada-Muñeton J. M., Spudis P. D., and Urrutia-Fucugauchi J. 1993. Chicxulub multiring impact basin: Size and other characteristics derived from gravity analysis. Science 261:1564-1567.

Sharpton V. L., Marin L. E., Carney J. L., Lee S., Ryder G., Schuraytz B. C. Sikora P., and Spudis P. D. 1996. A model of the Chicxulub impact basin based on evaluation of geophysical data and drill core samples. In The Cretaceous-Tertiary event and other catastrophes in Earth history, edited by Ryder G., Fastovsky D. and Gartner S. GSA Special Paper 307. Boulder: Geological Society of America. pp. 55-74.

Sharpton V. L., Corrigan C. M., Marin L. E., Urrutia-Fucugauchi J., and Vogel T. A. 1999. Characterization of impact breccias from the Chicxulub impact basin: Implications for excavation and ejecta emplacement (abstract #1515). 30th Lunar and Planetary Science Conference. CD-ROM.

Sharpton V. L. 2000. Exploring the Chicxulub impact basin through scientific drill-coring: Historical perspective and current plans. International Conference on Catastrophic Events and Mass Extinction: Impacts and Beyond, 9-12 July 2000, Vienna, Austria, Lunar and Planetary Institute Contribution No. 1053.

Shukolyukov A. and Lugmair G. W. 1998. Isotopic evidence for the Cretaceous-Tertiary impactor and its type. Science 282:927-929.

Sigurdsson H., D'Hondt S., Arthur M. A., Bralower T. J., Zachos J. C., Fossen van M., and Channell J. E. T. 1991 Glass from the Cretaceous/Tertiary boundary in Haiti. Nature 349:482-487.

Sigurdsson H., 'Hondt D., and Carey S. 1992. The impact of the Cretaceous/Tertiary bolide on evaporite terrane and generation of major sulfuric acid aerosol. Earth and Planetary Science Letters 109:543-559.

Siret D., Robin E., Le Guern F., and Cheynet B. 2000. Condensation in an Impact Vapor Plume: Estimates of Gas and Aerosol Emissions Generated by the Chicxulub Impact. International Conference on Catastrophic Events and Mass Extinctions: Impacts and Beyond, 9-12 July 2000, Vienna, Austria, Lunar and Planetary Institute Contribution No. 3124.

Smit J. 1999. The global stratigraphy of the Cretaceous-Tertiary boundary impact ejecta. Annual Reviews in Earth and Planetary Sciences 27:75-113.

Smit J. and Hertogen J. 1980. An extraterrestrial event at the Cretaceous-Tertiary boundary. Nature 285:198-200.

Smit J. and Romein A.J.T. 1985. A sequence of events across the Cretaceous-Tertiary boundary. Earth and Planetary Science Letters 74:155–70.

Smit J., Montanari A., Swinburne N. H. M., Alvarez W., Hildebrand A. R., Margolis S. V., Clayes P., Lowrie W., and Asaro F. 1992. Tektite-bearing, deep-water clastic unit at the Cretaceous-Tertiary boundary in northeastern Mexico. Geology 20:99-103.

Smit J., Roep B., Alvarez W., Montanari A., Claeys P., Grajales-Nishimura J. M., and Bermudez J. 1996. Coarse-grained, clastic sandstone comlex at the K/T boundary around the Gulf of Mexico: Deposition by tsunami waves induced by the Chicxulub impact? In The Cretaceous-Tertiary events and other catastrophes in Earth history, edited by Ryder G., Fastovsky D. and Gartner S. GSA Special paper 307. Boulder: Geological Society of Americ. pp. 151-182.

Staudigel H. and Hart S. R. 1983. Alteration of basaltic glass: Mechanisms and significance for the oceanic crust-seawater budget. Geochimica et Cosmochimica Acta 47:337–350.

Steuber T., Mitchell S. F., Buhl D., Gunter G., and Kasper H. U. 2002. Catastrophic extinction of Caribbean rudist bivalves at the Cretaceous-Tertiary boundary. Geology 30:999-1002.

Stinnesbeck W., Schulte P., Lindenmaier F., Adatte T., Affolter M., Schilli L., Keller G., Stüben D., Berner Z., Kramar U., Burns S. J., and López-Oliva J. G. 2001. Late Maastrichtian age of spherule deposits in northeastern Mexico: implication for Chicxulub scenario. Canadian Journal of Earth Sciences 38:229-238.

Stinnesbeck W., Keller G., Adatte T., Harting M., Kramar U., and Stüben D. 2003. D. 2003. Yucatán subsurface stratigraphy based on the Yaxcopoil-1 drillhole (abstract). Geophysical Research Abstracts 5, # 10868. CD-ROM.

Stinnesbeck W., Keller G., Adatte T., Harting M., Stüben D., Istrate G., and Kramar U. 2004. Yaxcopoil-1 and the Chicxulub impact. International Journal of Earth Sciences (Geologische Rundschau) 93:1042-1065.

Stöffler D. 1974. Deformation and transformation of rock forming minerals by natural and experimental shock processes: II. Physical properties of shocked minerals. Fortschritte der Mineralogie 51:443-458.

Stöffler D. and Langenhorst F. 1994. Shock metamorphism of quartz in nature and experiment: I. Basic observation and theory. Meteoritics 29:155-181.

Stöffler D. and Grieve R. A. F. 1994. Classification and nomenclature of impact metamorphic rocks: A proposal to the IUGS subcommission on the systematics of metamorphic rocks. 25th Lunar and Planetary Science Conference. p. 1347-1348.

Stöffler D., Hecht L., Kenkmann T., Schmitt R. T., and Wittmann A. 2003a. Properties, classification, and genetic interpretation of the allochthonous impact formation of the ICDP Chicxulub drill core Yax-1 (abstract # 1553). 34th Lunar and Planetary Science Conference. CD-ROM.

Stöffler D., Hecht L., Ivanov B. A., Kenkmann T., Salge T., Schmitt R. T., Schönian F., Tagle R., and Wittman A. 2003b. Characterisitcs of the multi-ring impact basin of Chicxulub, Mexico, as derived from drill core data and numerical modeling (abstract # 5241). 66th Annual Meeting of the Meteoritical Society. CD-ROM.

Stöffler D., Artemieva N. A., Ivanov B. A., Hecht L., Kenkmann T., Schmitt R. T., Tagle R. A., and Wittmann A. 2004. Origin and emplacement of the impact formations at Chicxulub, Mexico, as revealed by the ICDP deep drilling Yaxcopoil-1 and by numerical modeling. Meteoritics & Planetary Science 39:1035–1067.

Stroncik N. A. and Schmincke H.-U. 2002. International Journal of Earth Science (Geologische Rundschau) 91:680-697.

Stüben D., Kramar U., Harting M., Stinnesbeck W., and Keller G. 2005. High-resolution geochemical record of Cretaceous-Tertiary boundary sections in Mexico: New constraints on the K/T and Chicxulub events. Geochimica et Cosmochimica Acta 69:2559-2579.

Swisher III C. C., Nishimura G., Montanari A., Margolis S. V., Claeys P., Alvarez W., Renne P., Cedillo-Pardo E., Maurasse F. J. –M. R., Curtis G. H., Smit J., and McWilliams M. O. 1992. Coeval 40Ar/39Ar ages of 65.0 million years ago from Chicxulub crater melt rock and Cretaceous-Tertiary boundary tektites. Science 257:954-958.

Tada R., Nakano Y., Iturralde-Vinent M. A., Yamamoto S., Kamata T., Tajika E., Toyoda K., Kiyokawa S., Garcia Delgado D., Oji T., Goto K., Takayama H., Rojas-Consuegra R., and Matsui T. 2002. Complex tsunami waves suggested by the Cretaceous-Tertiary boundary deposit at the Moncada section, western Cuba. In Catastrophic events and mass extinctions: impacts and beyond, edited by Koeberl C. and MacLeod K. G. Boulder: Geological Society of America Special Paper 356. pp. 109-123.

Tagle R., Erzinger J., Hecht L., Stöffler D., Schmitt R. T., and Claeys P. 2003. Platinum group elements analysis of impactites from the ICDP Chicxulub drill core Yax-1: Are there traces of the impactor? (abstract # 1811). 34th Lunar and Planetary Science Conference. CD-ROM.

Tagle R., Erzinger J., Hecht L., Schmitt R. T., Stöffler D., and Claeys P. 2003. Platinum group elements in impactites of the ICDP Chicxulub drill core Yaxcopoil-1: Are there traces of the projectile?. Meteoritics & Planetary Sciences 39:1009-1016.

Takata T. and Ahrens T. J. 1994. Numerical simulation of impact cratering at Chicxulub and the possible causes of KT catastrophe. In Papers presented to New Developments regarding the KT event and other catastrophes in Earth History. Lunar and Planetary Institute Houston. (abstract) LPI Contribution. 825, 125–126.

Takayama H., Tada R., Matsui T., Irralde-Vinent M. A., Oji T., Tajika E., Kiyokawa S., Garcia D., Okada H., Hasegawa T., and Toyodo K. 2000. Origin of the Penalver formation in northwestern Cuba and its relation to the K/T boundary impact event. Sedimentary Geology 135:195-320.

Taylor S. R. 1982. Planetary Science: A lunar perspective. Houston: Lunar and Planetary Institute. 481 p.

Taylor S. R. 1992. Solar system evolution: A new perspective. New York: Cambridge University Press. 307 p.

Taylor S. R. and McLennan S. M. 1985. The continental crust: its composition and evolution. Oxford: Blackwell Scientific. 312p.

Tschudy R. H., Pillmore C. L., Orth C. J., Gilmore J. S., and Knight J. D. 1984. Disruption of the terrestrial plant ecosystem at the Cretaceous-Tertiary boundary, Western Interior. 225:1030-1032.

Terry K. D. and Tucker W. H. 1968. Biologic effects of supernovae. Science 159:421-423.

Tissot B.P. and Welte D.H. 1978. Petroleum formation and occurrence. Berlin: Springer-Verlag, 538 p.

Toon O. B., Pollack J. B., Ackermann T. P., Turco R. P., McKay C. P., and Liu M. S. 1982. Evolution of an impact-generated dust cloud and its effects on the atmosphere. In Geological implications of impacts of large asteroids and comets on Earth, edited by Silver L. T. and Schultz P. H. Boulder: Geological Society of America Special Paper 190. 187-200.

Trinquier A., Birck J.-L., and Allègre C. J. 2006. The nature of the KT impactor. A ^{54}Cr reappraisal: Earth and Planetary Science Letters 241:780-788.

Tuchscherer M. G., Reimold W. U., Gibson R.L., and Koeberl C. 2003. Petrographic observations and classification: Impactites from the Yaxcopoil-1 borehole, Chicxulub impact structure, Yucatán Peninsula, Mexico (abstract # 1310). 34th Lunar and Planetary Science Conference. CD-ROM.

Tuchscherer M. G., Reimold W. U., Koeberl C., Gibson R. L., and de Bruin, D. 2004a. First petrographic results on impactites from the Yaxcopoil-1 borehole, Chicxulub Structure, Mexico. Meteoritics & Planetary Sciences 39:899-930.

Tuchscherer M. G., Reimold W. U., Koeberl C., and Gibson R. L. 2004b. Major and trace element characteristics of impactites from the Yaxcopoil-1 borehole, Chicxulub Structure, Mexico. Meteoritics & Planetary Science 39: 955-978.

Tuchscherer M. G., Reimold W. U., Koeberl C., and Gibson R. L. 2005. Geochemical and petrographic characteristics of impactites and Cretaceous target rocks from the Yaxcopoil-1 borehole, Chicxulub impact structure, Mexico: implications for target composition: Meteoritics & Planetary Science 40:1513-1536.

Tuchscherer M. G., Reimold W. U., Gibson R. L. de Bruin D., and Späth A. 2006. Major and trace element compositions of melt particles and associated phases from the Yaxcopoil-1 drill core, Chicxulub impact structure, Mexico. Meteoritics & Planetary Science 41:1361-1379.

Urrutia-Fucugauchi J., Marin L., and Trejo-Garcia A. 1996. UNAM Scientific drilling program of Chicxulub impact structure – Evidence for a 300 kilometer crater diameter. Geophysical Research Letters 23:1565-1568.

Utzmann A., Hansteen T.H., and Schmincke H.-U. 2002. Trace element mobility during sub-seafloor alteration of basaltic glass from Ocean Drilling Program site 953 (off Gran Canaria). International Journal of Earth Sciences (Geologische Rundschau) 91:661-679.

Vajda V., Raine J. I., and Hollis C. J. 2001. Indication of global deforestation at the Cretaceous-Tertiary boundary by New Zealand fern spike. Science 294:1700-1702.

Vermeesch P.M., Morgan J.V., and King M.S. 2003 Chicxulub: physical property measurements on core samples from CSDP hole Yax-1. Geophysical Research Abstract 5 (Abstract #14418). CD-ROM.

von Dalwigk I. and Ormo J. 2001. Formation of resurge gullies at impacts at sea: The Lockne crater, Sweden. Meteoritics & Planetary Science 36:359-369.

Ward W. C., Keller G., Stinnesbeck W., and Adatte T. 1995. Yucatán subsurface stratigraphy: Implications and constraints for the Chicxulub impact. Geology 23:873-876.

Warren J. 2000. Dolomite: occurrence, evolution and economically important associations. Earth-Science Reviews 52:1–81.

Warren P. H., Claeys P. H., and Cedillo-Pardo E. 1996. Mega-impact melt petrology (Chicxulub, Sudbury, and the Moon): Effects of scale and other factors on potential for fractional crystallization and development of cumulates. In The Cretaceous-Tertiary event and other catastrophes in Earth history, edited by Ryder G., Fastovsky D. and Gartner S. Boulder: Geological Society of America Special Paper 307. pp. 105-124.

Weaver H.A., Feldman P.D., A'Hearn M.F., Arpigny C., Brown R.A., Helin E.F., Levy D.H., Marsden B.G., Meech K.J., Larson S.M., Noll K.S., Scotti J.V., Sekanina Z., Shoemaker C.S., Shoemaker E.M., Smith T.E., Storrs A.D., Yeomans D.K. and Zellner B. 1994. Hubble Space Telescope Observations of Comet P/Shoemaker-Levy 9 (1993e) Science. 263:787-791.

Whitehead J. 2002. Origin of “toasted” quartz in terrestrial impact structures. Geology 30:431-434.

Whitehead J. 2004. Earth impact database. PASSC. University of New Brunswick. http://www.unb.ca/passc/ImpactDatabase/images.

Wilkin R. T., Barnes H. L., and Brantley S. L. 1996. The size distribution of framboidal pyrite in modern sediments: An indicator of redox conditions. Geochimica et Cosmochimica Acta 60:3897-3912.

Wittmann A. 2006. Formation and emplacement of impactites from drill core Yaxcopoil-1, Chicxulub crater, Mexico. Ph.D. thesis, Humboldt University, Berlin, Germany.

Wittmann A., Kenkmann T., Schmitt R. T., Hecht L., and Stöffler D. 2004. Impact related dike breccia lithologies in the ICDP drill core Yaxcopoil-1, Chicxulub impact structure, Mexico. Meteoritics & Planetary Sciences 39:931-954.

Wittmann A., Kenkmann T., Schmitt R. T., and Stöffler D. 2006. Shock-metamorphosed zircon in terrestrial impact craters. Meteoritics & Planetary Sciences 41:433-454.

Wohlgemuth L., Bintakies E., Kück J., Conze R., and Harms U. 2004. Integrated deep drilling, coring, downhole logging, and data management in the Chicxulub Scientific Drilling Project (CSDP), Mexico. Meteoritics & Planetary Science 39:791-797.

Wolbach W. S., Lewis R. S., and Anders E. 1985. Cretaceous extinctions: evidence for wild fires and search for meteoritic material. Science 230:167-170.

Wolbach W. S., Anders E., and Nazarov M. A. 1990. Fires at the K/T boundary: Carbon at the Sumbar, Turkmenia, site. Geochimica et Cosmochimica Acta 54:1133-1146.

Zurcher L. and Kring D. A. 2003. Preliminary results on the post-impact hydrothermal alteration in the Yaxcopoil-1 hole, Chicxulub impact structure, Mexico (abstract # 1735). 34th Lunar and Planetary Science Conference. CD-ROM.

Zürcher L. and Kring D. A. 2004. Hydrothermal alteration in the core of the Yaxcopoil-1 borehole, Chicxulub impact structure, Mexico. Meteoritics & Planetary Science 39: 1199-1221.

Zurcher L., Kring D. A., Dettman D., and Rollog, M. 2003. Stable isotope record of post-impact fluid activity in the Chicxulub crater as exposed by the Yaxcopoil-1 borehole (abstract # 1728). 34th Lunar and Planetary Science Conference. CD-ROM.

Zurcher L., Kring D. A., Dettman D., and Rollog M. 2004. Stable isotope and hydrothermal fluid source in the Yaxcopoil-1 borehole, Chicxulub impact structure, Mexico (abstract # 1261). 35th Lunar and Planetary Science Conference. CD-ROM.

Zurcher L. Kring D.A. Barton M. D., Dettman D., and Rollog M. 2005. Stable isotope record of post-impact fluid activity in the core of the Yaxcopoil-1 borehole, Chicxulub impact structure, Mexico. In Large Meteorite Impacts III, edited by Kenkmann T., Hörz F., and Deutsch A. Boulder: Geological Society of America Special Paper 384. pp. 223-238.

Appendix A.1.
Photographs of the Yax-1core

Photographs of the Yax-1 core taken at the first UNAM sampling party in Mexico City in April 2002. For scale, the core is 76 mm wide. Core depths and brief petrographic descriptions are provided in each caption.

Fig. A.1.1. Stratified limestone with reworked impactites horizons overlying the Yax-1 impactites, the controverted Unit 0 (see Goto et al. 2004; Keller et al. 2004) at 794.10 – 794.60 m depth.

Fig. A.1.2. Close up of the unidirectional cross-laminations and green phyllosilicate rich layers at 794.20 – 794.30 m depth, for scale coin = 2 cm.

Fig. A.1.3. Unit 1 reworked suevite, note the fine-grained character, compacted nature, and light green colour of the impactite at ~ 803.48 m depth.

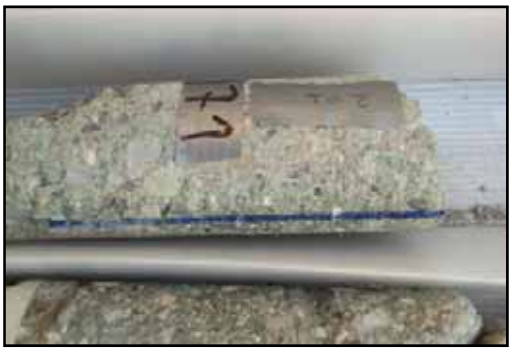

Fig. A.1.4. Unit 1 reworked suevite, note the fine to med.-grained character, compacted clasts and melt rock particles at 809.00 m depth.

Fig. A.1.5. Unit 1 reworked suevite, a slightly coarser grained impactite yet still self supported at 821.39 m depth.

Fig. A.1.6. Unit 2 suevite, note the groundmass supported large green melt rock particles and a laminated gneiss clast at 824.03 m depth showing a noticeable coarsening with depth compared to Fig. A.1.3.

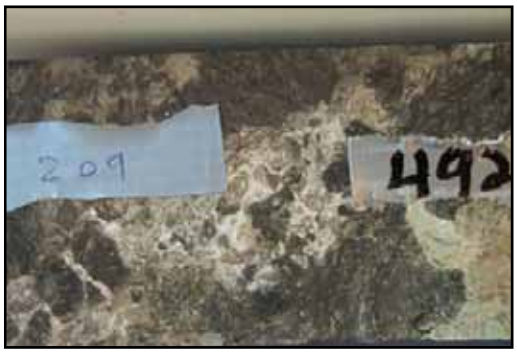

Fig. A.1.7. Unit 2 suevite, note the occurrence of large dark gray melt rock particles at 825.43 m depth.

Fig. A.1.8. Unit 2 suevite, note the abundance of groundmass supported angular green melt rock particles at 827.13 m depth.

Fig. A.1.9. Unit 2 suevite, note the fluidal to angular, groundmass supported melt rock particles and clasts at 830.29 m depth, coin = 2 cm.

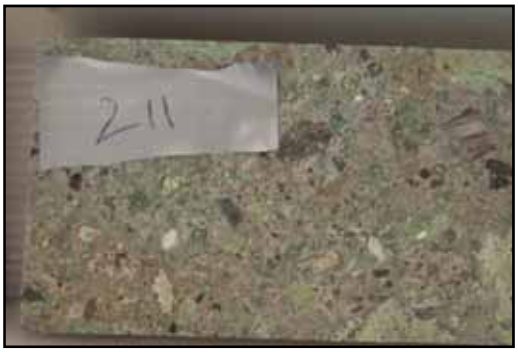

Fig. A.1.10. Unit 2 suevite characterized by numerous melt rock particles at 835.14 m depth.

Fig. A.1.11. Unit 2 suevite with a large fluidal green melt rock particle at 835.31 m depth, coin = 2 cm.

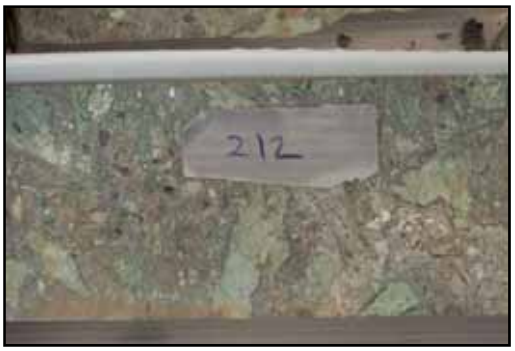

Fig. A.1.12. Unit 2 green suevite with numerous groundmass supported angular to fluidal melt rock particles at 836.98 m depth.

Fig. A.1.13. Unit 2 suevite with gray and dark gray/black melt rock particles, note the angular granitic clast near the right of the coin at 841.59 m depth.

Fig. A.1.14. Unit 2 suevite containing groundmass supported angular green melt rock particles at 842.78 m depth.

Fig. A.1.15. Unit 2 suevite showing a fluidal contact with a large brown melt particle containing obvious schlieren located at 843.46 m depth.

Fig. A.1.16. Unit 2 suevite showing numerous fluidal green and one brown melt rock particle at 843.08 m depth, note the beige reaction rims around the green particles.

Fig. A.1.17. Unit 2 suevite located at a depth of 844.48 m, similar to Fig. A.1.16.

Fig. A.1.18. Unit 2 suevite located at a depth of 844.82 m, similar to Fig. A.1.16.

Fig. A.1.19. Unit 2 suevite, close up of large green melt particles shown in Fig. A.1.18 and groundmass at a depth of 844.82 m.

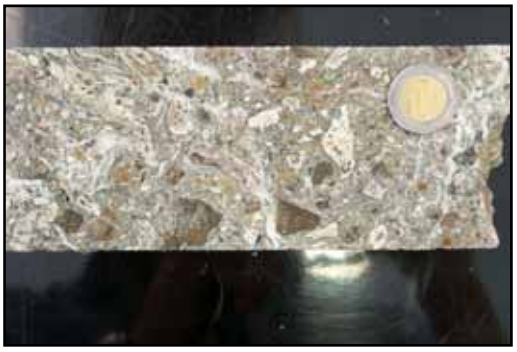

Fig. A.1.20. Unit 3 suevite, note the variegated (brown, beige, green, purple) melt rock particle character and gray groundmass located at a depth of 846.80 m.

Fig. A.1.21. Unit 3 suevite, similar to Fig. A.1.20 but with larger melt rock particles at the center of the core, located at a depth of 847.20 m.

Fig. A.1.22. Unit 3 suevite with large green melt rock particles located at a depth of 848.75 m.

Fig. A.1.23. Unit 3 suevite with a large green melt rock particle showing schlierens at a depth of 849.80 m.

Fig. A.1.24. Unit 3 suevite showing angular clasts, angular and fluidal melt rock particles at a depth of 851.00 m.

Fig. A.1.25. Unit 3 suevite showing variegated melt rock particles, and green groundmass at a depth of 851.15 m.

Fig. A.1.26. Unit 3 suevite showing variegated fluidal melt rock particles at 851.94 m depth.

Fig. A.1.27. Unit 3 suevite with fluidal brown melt rock particles, located at a depth of 853.05 m.

Fig. A.1.28. Unit 3 suevite with large angular melt rock particles, generally brown in colour, located at 857.22 m depth.

Fig. A.1.29. Unit 3 suevite, similar to Fig. A.1.27, with smaller brown fluidal melt rock particles at 857.36m

Fig. A.1.30. Unit 3 suevite with fluidal brown melt rock particles of various sizes located at a depth of 860.40 m.

Fig. A.1.31. Unit 4 suevite comprising shattered, angular, brown belt rock particles at 861.66 m depth.

Fig. A.1.32. Unit 4 suevite showing groundmass supported brown melt rock particles at 861.96 m depth.

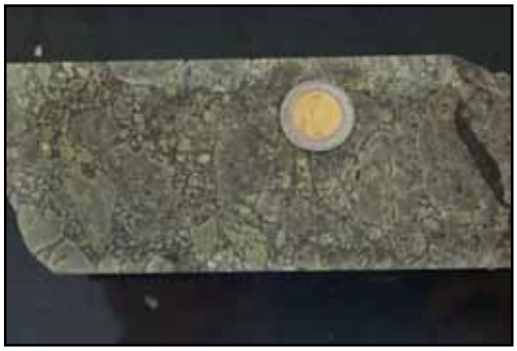

Fig. A.1.33. Unit 4 green impact melt rock, note the jig-saw like arrangement of the shattered melt rock particles, located at 862.81 m depth.

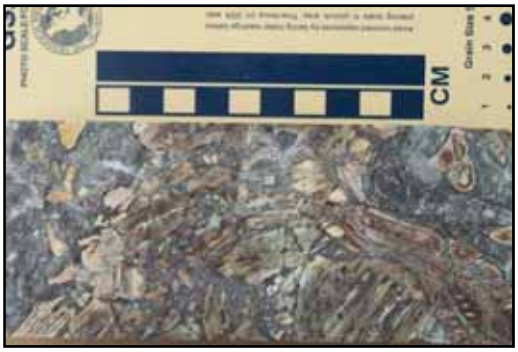

Fig. A.1.34. Unit 4 suevite showing angular, brown, melt rock particles with schlieren at 863.81 m depth.

Fig. A.1.35. Unit 4 green impact melt rock comprising large green/brown melt rock particles at 871.60 m depth.

Fig. A.1.36. Unit 4 green impact melt rock, showing large gray/green melt rock particles at 871.70 m depth.

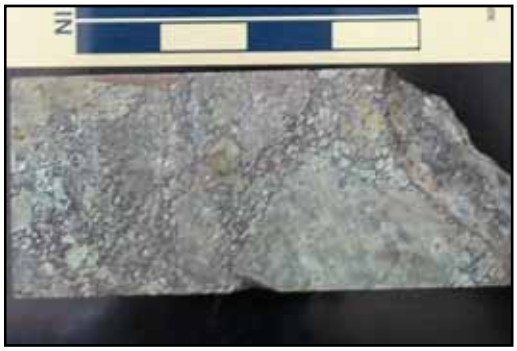

Fig. A.8.37. Unit 4 green impact melt rock showing large melt rock particles bound by smaller shattered melt rock particles at 874.13 m depth.

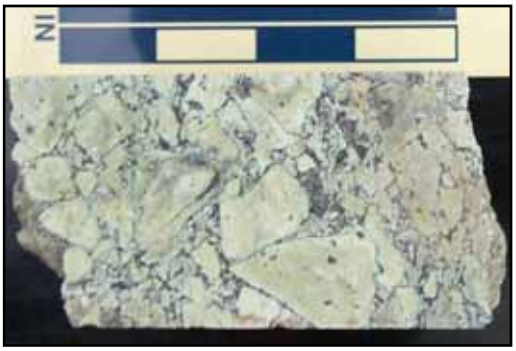

Fig. A.1.38. Unit 4 green impact melt rock located at a depth of 878.09 m, similar to Fig. A.1.37.

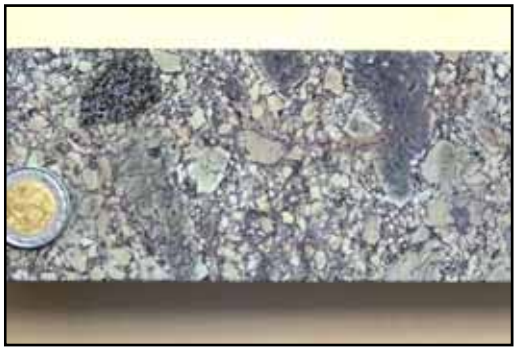

Fig. A.1.39. Unit 4 green impact melt rock with abundant rounded green and sporadic gray melt rock particles at 884.59 m depth.

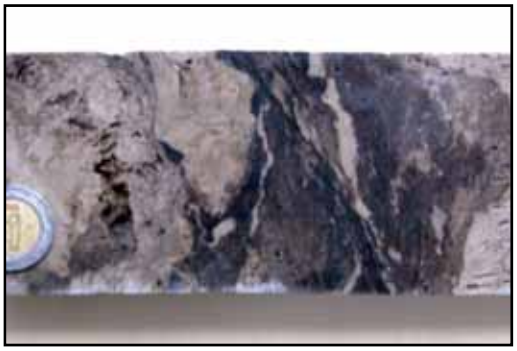

Fig. A.1.40. Unit 5 polymict impact melt breccia with highly altered dolomite clast (left) and a dark gray melt rock particle at 885.90 m depth.

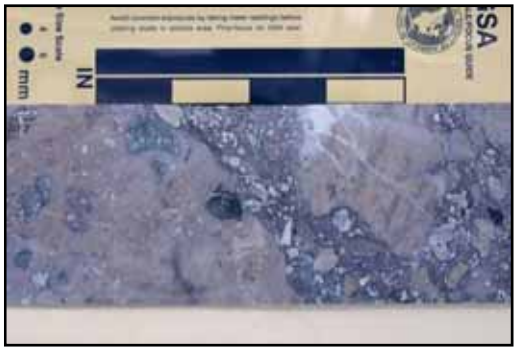

Fig. A.1.41. Unit 5 polymict impact melt breccia/suevite, located at 887.92 m depth, note the two generations of breccia.

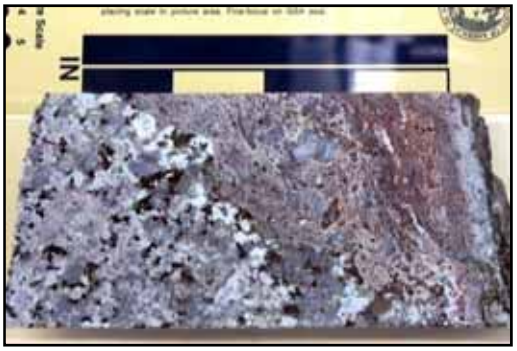

Fig. A.1.42. Unit 5 polymict impact melt breccia/suevite, note the granite clast towards the left and the melt schlieren textures at the right, located at 887.92 m depth.

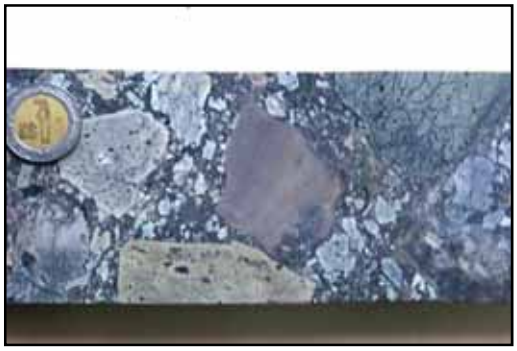

Fig. A.1.43. Unit 5 polymict impact melt breccia/suevite, note the variegated, angular, and large sizes of the melt particles and the dark gray colour of the carbonate rich

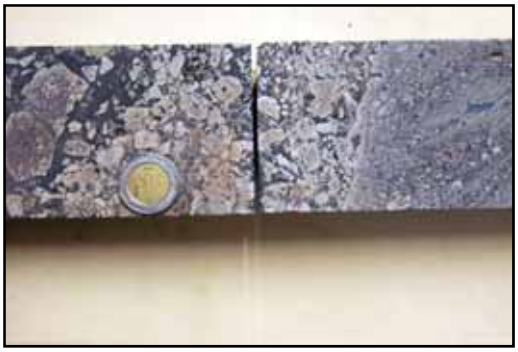

Fig. A.1.44. Unit 5 polymict impact melt breccia/suevite, note the breccia towards the left is similar to Fig. A.1.43, and the fluidal contact with a large melt rock particles towards the right at 892.55 m depth.

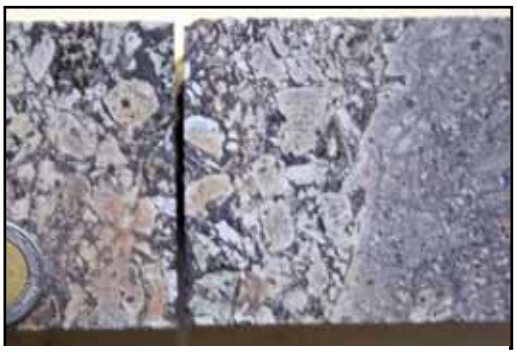

Fig. A.1.45. Unit 5, close up of fluidal contact shown in Fig. A.1.44, same depth. Note the schlieren texture of the angular melt rock particles at the left.

Fig. A.1.46. Unit 5 polymict impact melt breccia/suevite, close up of the melt particle shown in Fig. A.1.44 at a depth of 892.65 m.

Fig. A.1.47. Unit 5 polymict impact melt breccia/suevite, note the large, angular, schlieren textured groundmass supported melt rock particles at 892.90 m depth.

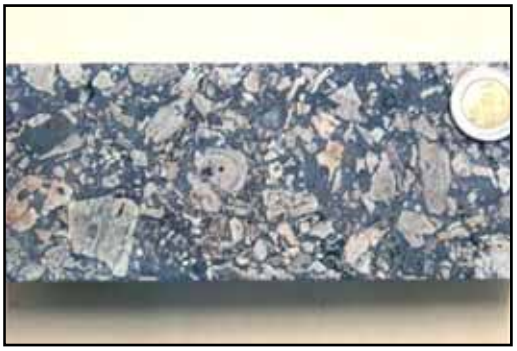

Fig. A.1.48. Unit 5 polymict impact melt breccia/suevite, note the abundance of groundmass supported angular melt rock particles with schlieren textures at depth of 893.94 m.

Fig. A.1.49. Polymict lithic breccia underlying impactite interval, note that the core has been submerged in water to bring out the brecciated fabric, located at 895.12.m depth.

Fig. A.1.50. Polymict lithic breccia underlying impactites with more massive clasts, similar to Fig. A.1.49 at 896.13 m depth.

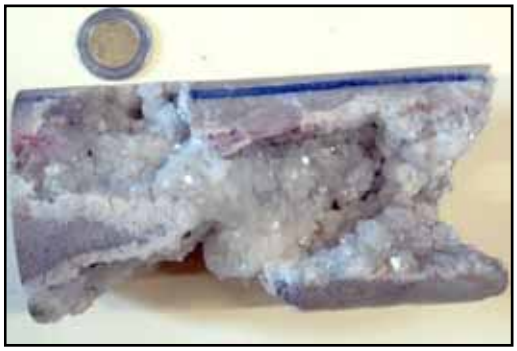

Fig. A.1.51. Dissolution vug lined with euhedral dolomite crystals at a depth of 896.92 m.

Fig. A.1.52. Suevitic injection dike located at 915.76 m depth, note the occurrence of several elongate fluidal melt rock particles.

Fig. A.1.53. Suevitic injection dike located at 916.36 m, note the large green-white melt rock particles with schlieren textures.

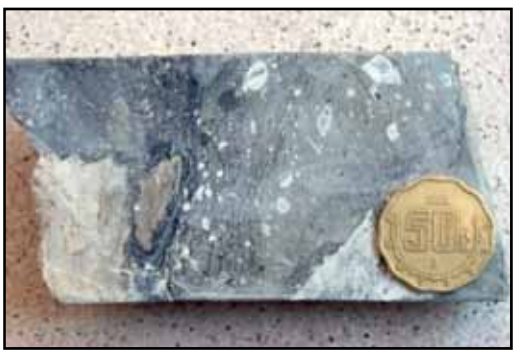

Fig. A.1.54. Heterolithic breccia with angular clasts and abundant lithic carbonate groundmass, located at 1,315.17 m depth.

Fig. A.1.55. Fine-grained monolithic breccia dike in dolomite at 1,315.86 m depth.

Fig. A.1.56. Faulted oil shale horizon in dolomite at a depth of 1,315.96 m.

Fig. A.1.57. Heterolithic breccia dike located at 1,316.06 m depth.

Fig. A.1.58. Heterolitic breccia (limestone, dolomite, shale) located at 1,341.61 m depth.

Fig. A.1.59. Heterolithic breccia located at 1,341.63 m depth.

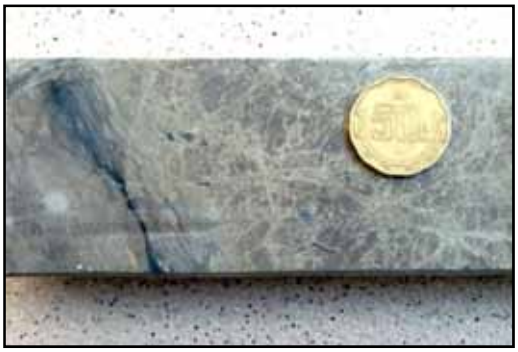

Fig. A.1.60. Faulted and shattered dolomite at a depth of 1,342.13 m.

Fig. A.1.61. Heterolithic breccia located at a depth of 1,342.91 m.

Fig. A.1.62. Altered dolomitic breccia rich with blue-green interstitial clays, located at a depth of 1,347.56 m.

Fig. A.1.63. Heterolithic breccia located at a depth of 1,348.32 m.

Fig. A.1.64. Thin oil-shale horizon in shattered dolomite located at a depth of 1,369.52 m.

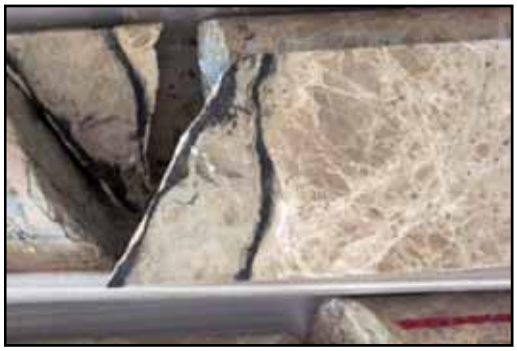

Fig. A.1.65. Thin oil-shale horizons in shattered dolomite at a depth of 1,372.87 m.

Fig. A.1.66. Oil-shale horizon in shattered dolomite located at a depth of 1,373.59 m.

Fig. A.1.67. Finely laminated oil shale in dolomite at a depth of 1,381.64 m.

Fig. A.1.68. Shattered dolomite, note the occurrence of thin blue clay found along some fractures, located at a depth of 1,383.62 m.

Fig. A.1.69. Dissolution breccia with anhydrite and dolomite clasts, located at a depth of 1,394.02 m.

Fig. A.1.70. Breccia horizon in shattered dolomite cross cut by calcite/anhydrite veins, located at a depth of 1,395.19 m.

Fig. A.1.70. Faulted shale in dolomite, located at a depth of 1,399.07 m.

Appendix A.2.
Petrographic descriptions

Table A.2. Petrographic description of all sampled Tertiary, impactite, and Cretaceous rocks, with sub-samples, from the Yax-1 borehole, Chicxulub impact structure, Yucatán Peninsula, Mexico.

Sample #	Depth (m)	Mag-netic	Run #	Box #	Description
250	791.71	N	132	176	Tertiary limestone, The rock is light beige to white and fine-grained. Core radius ~ 3 cm.
249	794.37	N	132	177	Tertiary limestone, The rock is light beige to white and fine-grained (no picture available).
248	800.35	N	136	180	Totally disaggregated altered greeen suevite.
767	800.35	N	136	180	Heterolithic green suevite, vesiculated, partially devitrified, ocassionally altered green, contains micro-clasts of Cpx, Qtz calcite, limestone and dolomite fragments, and fossil shells, contains shocked Qtz with 2 sets of PDF, microcrystalline, grain size <0.01mm, fine-grained carbonate crystals are observed intermixed with the silicate fraction, some fine-grained carbonate veins are also present, which is ocasionally observed as a groundmass. Picture width ~ 6 cm.
751	803.44	N	137	182	Heterogenous green-white suevite, the sample is not reworked and relatively unaltered, glass is vesiculated, partially devitrified, contains perlitic fractures, and trace monomineralic crystals of Qtz and orthoclase with some limestone fragments, cotnains undulatory Qtz, shocked Qtz with 1 set of PDF, grain size is microcrystalline <0.05 mm, The carbonate groundmass has a medium relief, shows a dirty appearance, appears pervasive, and infills vesicles.
201	803.48	N	137	182	Altered suevite, white-green matrix with white, brown, dark beige and gray shattered melt rock fragments. The suevite is relatively well sorted, elongate fragments are sorted perpendicular to the core axis, clasts comprise chert, shale, dolomite, and limestone.
768	805.34	N	137	182	Heterolithic green suevite, the sample contains melt particles (altered and subrounded) that are self-supported. Occasionally lithic clasts are observed, e.g., limestone, foraminifera fossils, and quartz (shocked, with planar deformation features, PDFs). The interstitial material is primarily microcrystalline to fine-grained calcite.
246	808.34	N	139	184	Fine-grained green suevite, white-green matrix with white, brown, dark beige and gray shattered melt rock fragments. Clasts comprise chert, shale, dolomite, and limestone.
765	808.34	N	139	184	Heterolithic green suevite.
202	809.00	N	139	184	Altered green suevite, same as above but with a greater concentration of melt rock shards.
203	809.7	N	140	185	Altered green suevite, vesiculated, devitrified, same as sampled 246 but melt rock particles are relatively larger and are not well sorted and show irregular contacts, melt particles contain clasts of chert, Qtz, shale, dolomite, and chalk, perlitic domains are suspended in 1 mm wide calcite grains.
770A	809.7	N	140	185	Light green-gray suevite, melt particles are partially devitrified, occasionally altered green, melt particles appear to comprise the dominant groundmass and do not appear to be reworked. Fine-grained carbonate crystals are observed intermixed with the silicate fraction, fine-grained hydrothermal carbonate melt veins are also present, carbonates are ocasionally observed as groundmass.
770B	809.7	N	140	185	A dark gray subrounded inclusion, 1cm x 2 cm in size. The particle is opaque and is totally composed of brown material (hematite, hydrocarbons?), Mg-rich phyllosilicates (determined by EMPA), it contains numerous monomineralic crystals: Qtz with oxidized myrmekitic intergrowth with a minor carbonate content.
752A	810.84	N	140	186	Suevite similar to sample 770B but bluish gray, fine-grained, and hard (chert?).
752B	810.84	N	140	186	Heterogeneous green-white suevite similar to sample 768.
204	811.55	N	140	186	Altered green suevite, whitish-green melt rock matrix with white, brown, dark beige and gray shattered melt rock fragments. Fragments are relatively larger and are not well sorted, contacts are highly irregular, melt particles contain visible clasts.
205	815.8	N	141	187	Altered green suevite, similar to sample 204 but well sorted, with fragments of smaller size.
771	815.8	N	141	187	Light green-gray suevite similar to 768, matrix is carbonate and silicate rich.
206	816.62	N	143	188	Altered green suevite with white-green-gray glass matrix and white, brown, dark beige and gray shattered glass fragments.
772	816.62	N	143	188	Light greenish gray suevite similar to sample 768

Table A.2. *Continued*

Sample #	Depth (m)	Mag-netic	Run #	Box #	Description
247	818.23	N	144	189	Green suevite, with green melt rock matrix and white, brown, dark beige and gray shattered rock and melt rock fragments.
766	818.33	N	144	189	Heterolithic green suevite similar to sample 768.
753	819.09	N	145	190	Medium gray heterolithic suevite showing fluidal textures.
207	821.39	N	145	190	Gray-brown suevite, with some minor green, yellow, beige, dark brown fragmental melt rock particles. The sample has a distinct medium to light gray colour and is chocked with fragmental melt rock particles.
245	822.9	N	146	191	Green suevite with whitie-green melt rock matrix, contains white, brown, dark beige and gray shattered melt rock fragments.
764	822.9	N	146	191	Green fluidal glass with minor brecciated fragments
773	824.03	N	146	191	Light gray suevite with carbonate matrix containing green fluidal melt rock fragments.
208A	824.03	N	146	191	Light to medium gray suevite with some minor green, yellow, beige, dark brown melt rock fragments.
208B	824.03	Y	146	191	Finely laminated gneiss clast, displays prominent layering and consists of altered diaplectic (isotropic) plagioclase, quartz (ballenquartz), biotite, apatite, sphene, ilmenite, and hematite. Clasts exhibits shock pressures < 35 GPa (Stöffler and Langenhorst, 1994)
209	825.43	Y	147	192	Dark brown to light gray suevite. Small <1 mm wide brown alteration veins are indicative of a high iron content.
769A	825.43	N	147	192	Light-med gray carbonate groundmass, the groundmass contains abundant secondary calcite (fine-grained), hematite, altered silicate melt particles, and minor limestone fragments and shocked quartz grains. Calcite crystals are found in a network of cross-cutting veins. Melt particles are groundmass supported.
769B	825.43	N	147	192	Med-dark gray carbonate groundmass, showing a greater proportions of melt particles than sample 769A, producing the darker gray color. Melt particles are groundmass-supported.
769C	825.43	Y	147	192	Medium to dark gray melt clast. Subrounded particle comprises microcrystalline, dark-brown to dark gray, and opaque, Mg-rich phyllosilicates (determined by EMPA), with a minor carbonate content.
774	827.13	N	147	193	Greenish white bulk suevite, The sample contains green melt particles (angular to fluidal) that are groundmass-supported. The groundmass is a mixture of microcrystalline calcite and devitrified glass that is crosscut by calcite veins. Occasionally mineral clasts, primarily quartz (shocked, with PDFs) and plagioclase grains, are observed.\
210A	827.13	N	147	193	Fluidal green melt rock fragment set in a light gray matrix, small slickensides at high angle, 60 degrees to core axis, are found within the sample. A small vug (4mm) with open space fillings, contaning euhedral calcite, is also observed. Calcite veins are seen to pervade parts of the sample. They are only found in the green melt rock and appear to originate from the gray groundmass.
210B	827.13	N	147	193	Medium gray suevitic groundmass comprising abundant secondary calcite (very fine-grained) and numerous, angular to fluidal, siliceous melt particles. The melt particles are groundmass-supported.
211A	835.14	N	150	196	Green melt particle, fluidal appearance, contains spherulites, microlites, perlitic fractures, detrital clasts, and is strongly vesiculated.
211B	835.14	N	150	196	Medium gray suevitic groundmass, similar to 210B.
212A	835.14	N	150	196	Dark gray suevitic groundmass, the groundmass exhibits greater proportions of melt particles than sample 212B, producing the darker gray color. Melt particles are groundmass-supported.
212 B	835.14	N	150	196	Two compositionally varied melt rock particles, a light-gray particle is intermingled with a medium gray particle. Contacts are irregular and contorted. Contacts between the two are defined by a fine black reaction rim.
754	835.18	Y	150	196	Medium gray groundmass with greenish melt rock particles.
212B	836.98	Y	150	196	Medium gray suevitic groundmass, Similar to 210B.

Table A.2. *Continued*

Sample #	Depth (m)	Mag-netic	Run #	Box #	Description
755A	840.3	Y	152	199	Dark gray brown, fine-grained, altered melt particle, the particle is thoroughly altered to phyllosilicates. The sample has carbonate blebs and quartz clasts showing undulatory extinction.
755B	840.3	Y	152	199	Brown fluidal melt rock particle with minor green melt rock particles
213	843.46	Y	152	199	Dark brown fluidal melt with patches (2-25mm) of elongated, stretched green melt rock. Green melt rock is elongated parallel to the core axis. Sample also contains a dark gray highly magnetic fragment.
214	844.82	N	153	201	Dark green fluidal melt rock particle set within a yellowish green groundmass. Preferential mineral lineation indicates flow. Numerous mineralogical inclusions: Qtz and Cc, have small 1 mm thin black reaction rims. Sample was oily upon crushing. Ballenquartz is observed.
763	846.01	N	154	202	Variegated melt particles in gray groundmass. The sample has variegated melt particles (angular to fluidal) that are groundmass-supported. The groundmass is a mixture of microcrystalline calcite and altered melt particles that are crosscut by calcite veins. Occasionally lithic clasts, primarily quartz (shocked, with PDFs) and plagioclase grains, are observed.
244A	846.8	N	154	202	Variegated melt particles in gray groundmass, similar to 763. The groundmass is pervaded by white calcite veins.
244B	846.8	N	154	202	Variegated melt particles in gray groundmass, similar to 763.
756	851.15	N	156	204	The green melt particle has a fluidal morphology and, in hand sample, is mixed with a brown melt phase. It contains abundant microlites, few lithic clasts, and small (0.25 - 0.5 mm) altered mafic melt pods. Thin phyllosilicate veins crosscut it.
215A	851.15	N	156	204	Variegated melt particles in gray groundmass, similar to 763. Small granitic and brown melt rock fragments are also present.
215B	851.15	N	156	204	Greenish white bulk suevite, similar to 774, but contains more green melt particles.
243	860.4	N	159	208	Highly contorted, fluidal, variegated melt rock particle. Carbonate fragments appear to have undergone partial melting and digestion showing irregular shapes.
762	860.4	N	159	208	Dark gray to yellow "dirty" breccia, suevite? Similar to 774, sample contains more green melt particles.
761	875.79	N	164	216	Green melt particle with minor carbonate veins, grain size is microcrystalline, <0.05mm, contains numerous small green pleochroic microlites (chlorite?), small, 0.10mm, fibrous crystals fill open spaces. Shock effects include 1 mm Qtz grain with 1 set of DPF, ballenquartz, mosaicism (annealing) in Qtz, and undulatory extinction.
242	878.09	N	164	216	Green melt fragment with dark veins, similar to above, but crosscut by phyllosilicate veins that contain opaques and hydrocarbons. Sample is very dark brown and is very magnetic. It is also similar to sample 213, but with green melt shards instead of elongated blebs.
216	879.03	Y	165	217	Dark green, brown, purple suevite.
241	882.45	N	166	218	Shattered green altered fragments or glass in dark groundmass. A massive green melt particle that contains abundant microlites, feldspathic and quartzitic fragments, and is cut by a network of opaques and hydrocarbon, and thin phyllosilicate veins.
760	882.45	N	166	218	Green melt rock, set in a medium gray carbonate melt, partially devitrified, semi-isotropic, yellowish-green in hand sample, contains crystals of partially melted feldspar and shocked/annealed Qtz, small veins are infilled by radial accicular needles (phyllosilicates), contains patches of opaque material as seen in brown glass and a preferential mineral lineation indicative of flow. Shock related effects are checker-board feldspar, 1 set of PDF in Qtz, undulatory extinction in Qtz.
217	886.79	N	167	220	Medium gray-beige polymict breccia, with a dark groundmass enclosing shattered angular beige to white angular fragments.
757	886.79	N	167	220	Lithic breccia (dolomite, some anhydrite) with some minor green melt rock particles.
218A	888.09	N	168	221	Dolomite clast, contains very fine-grained dolomite crystals with rare foraminifera fossils.

Table A.2. *Continued*

Sample #	Depth (m)	Mag-netic	Run #	Box #	Description
218B	888.09	N	168	221	Variegated melt particles in dark gray groundmass, the sample has numerous carbonate clasts with minor siliceous melt rock particles in a microcrystalline carbonate groundmass.
775A	888.92	N	168	221	Granodiorite or biotite-granite clast, comprises brecciated and recrystallized plagioclase, i.e., diaplectic glass, biotite, and quartz (ballenquartz), apatite, and magnetite. Clasts exhibits shock pressures < 35 GPa (Stöffler and Langenhorst, 1994).
775B	888.92	N	168	221	Med gray carbonate groundmass, similar to 210B.
240	890.52	Y	168	222	Polymict breccia in dark groundmass, Fragments within the breccia range in colour from light yellow, medium gray, to light brown. The groundmass is medium to dark gray.
225A	892.55	N	317	397	Black groundmass that contains fine-grained calcite crystals that are arranged in an interlocking relationship, are anhedral, with diffuse grain boundaries. Cathodoluminescence and SEM observations indicate a significant dolomite component is present with a minor volumes of microscopic melt particles. It is a potential impact melt rock.
225B	892.55	N	317	397	Beige shard-like melt particle. Displays an internal fluidal morphology defined by the preferential undulating alignment of microlites. Shocked Qtz contains 2 sets of PDF, annealing, and undulatory extinction.
239	894.14	N	169	224	Green and gray suevite that consists of dark gray to medium green melt rock particles with bleached white limestone/dolomite clasts.
759	894.14	N	169	224	The sample consists of carbonate clasts in a fine-grained carbonate groundmass. Occasionally melt rock particles and quartz clasts are observed.
222	916.36	N	177	234	The suevite consists of a dark to medium gray dolomite and limestone clasts with green melt rock particles. The suevite was injected from above.
758A	916.36	N	177	234	Medium gray, interstitial carbonate groundmass.
758B	916.36	N	177	234	Green fluidal melt rock particle.
233A	1314.83	N	308	387	Anhydrite vein, small (avg. 0.05 mm) crystals of anhydrite in fluidal pattern between med. brown oil patches that contain small (<0.05 mm) opaques (pyrite), brownish dolomite, and calcite crystals.
233B	1314.83	N	308	387	Dolomitic breccia, contains microcrystalline (<0.05 mm) dolomite with small (< 0.1 mm) pyrite blebs.
223A	1315.86	N	308	387	Dolomitic breccia that contains medium gray, microcrystalline carbonate groundmass enclosing fluidal textured, bluish blebs (phyllosilicates) and opaques.
223B	1315.86	N	308	387	Dolomite, crystals are microcrystalline (<0.05 mm). Thin fractures (0.2 to 0.05 mm) occasionally cut through sample.
227A	1316.06	N	308	387	Dolomite, crystals are microcrystalline (~0.05 mm). Fine layering characterized by interstitial brown (phyllosilicate) content that surrounds small (0.2 to 0.1 mm) quartz grains.
227B	1316.06	N	308	387	Dolomitic breccia showing medium gray microcrystalline carbonate groundmass enclosing anhydrite clasts.
235	1341.61	N	317	397	Dolomitic breccia showing subrounded dolomite fragments (4 to 0.2 mm in diameter) in a fractured, carbonate groundmass.
236	1341.81	N	317	397	Dolomitic breccia, same as sample 235, but with less groundmass.
225C	1342.91	N	317	397	Polymictic breccia, the breccia contains subangular lithic fragments (1 to 2 cm) of anhydrite, dolomite, and argillaceous limestone suspended in a fractured carbonate groundmass.
219	1347.56	N	n/a	399	Alteration zone (blue color), small euhedral dolomite crystals (0.2 to 0.05 mm) pervaded by biotite (determined by XRD). Occasionally, small pyrite blebs (avg ~0.05 mm) may coalesce into larger (up to 0.6 mm) patches.
226	1348.31	N	n/a	399	Alteration zone (blue color), dolomite fragments of variable sizes (>4 mm to 0.025 mm) and shapes (rounded to angular) are separated by numerous fractures and fractured groundmass.

Table A.2. *Continued*

Sample #	Depth (m)	Mag-netic	Run #	Box #	Description
237	1348.32	N	n/a	399	Dolomitic breccia, the sample contains dolomite and anhydrite fragments of variable sizes (>4 to 0.025 mm) that are more angular than in sample 226. Anhydrite appears distinctly less shattered than in sample 225C and only occurs sporadically. The crystals are tabular and elongate preserved in fluidal texture.
228	1369.52	N	325	407	Dolomite with some oil shale, brownish gray dolomite (0.1 to 0.025 mm) that is rarely fractured compared to the above samples (e.g., 237). Thin (0.1 to 0.025 mm) brownish-red veins are observed intermingling between dolomite crystals, emanating away from a larger oil-shale vein. This latter comprises clear euhedral adularia crystals (~0.1 mm), dolomite grains (<0.025 mm), small (<0.012) rounded to square pyrite grains that coalesce into aligned pervasive brown to opaque stringers.
228A	1369.52	N	325	407	Beige dolomite, dolomite (see 228 above for description).
228B	1369.52	N	325	407	Oil shale, oil shale (see 228 above for description).
229	1372.87	N	326	408	Beige dolomite with some oil shale, comprises crystalline dolomite (0.1 to 0.025 mm), similar to sample 228, but with trace anhydrite. It is weakly fractured. Dolomite is anhedral to subhedral and forms massive crystal mosaics. Brownish gray color originates from interstitial phyllosilicate. The oil rich horizons appear to be concentrated in distinct sheared and brecciated regions.
229A	1372.87	N	326	408	Beige dolomite, dolomite (as in 229).
229B	1372.87	N	326	408	Oil shale (as in 229)
220	1381.64	N	329	411	Argillaceous dolomite, the dolomite is interlayered with finely laminated (< 1 mm) oil shale. Dolomite crystals are euhedral to subhedral and display interlocking grain boundaries, typically with triple point junctions.
220A	1381.64	N	329	411	Argillaceous dolomite, the argillaceous limestone has sharp contacts with the dolomite. The silicates (predominantly adularia) are pervaded by interstitial phyllosilicate. The adularia crystals are euhedral to subhedral and of various sizes (0.2 to 0.025 mm).
220B	1381.64	N	329	411	Dolomite (as in 220 A+B)
230	1394.02	N	333	415	Oil shale, the sample consists of some anhydrite and minor dolomite immersed in hydrocarbons.
221	1395.19	N	333	416	Dolomitic breccia, the sample is shattered (brittle) with numerous fractures cutting across crystalline, massive and interlocking crystals of dolomite. Some of these fractures contain hydrocarbons.
238A	1397.82	N	334	417	Argillaceous limestone with some oil shale, the oil-bearing shale comprises numerous, subrounded to subangular crystals of dolomite and anhydrite. Some euhedral adularia is also found. The grains are surrounded by dark hydrocarbons.
238B	1397.82	N	334	417	Whitish beige dolomite, the dolomite is microcrystalline (<0.025 mm) and is locally contains disseminated pyrite crystals.
231	1398.25	N	234	417	Speckled argillaceous limestone, the sample consists of illite and minor dolomite fragments (0.3 to 1 mm) and small crystals (~0.075 mm) that are pervaded by hydrocarbons and phyllosilicates; few anhydrite crystals and pyrite grains are also observed.
224	1399.07	N	334	417	Argillaceous limestone with oil shale, the sample comprises microcrystalline (<0.025 mm) phyllosilicates, dolomite, and anhydrite that are pervaded by disseminated pyrite. Undulating brown hydrocarbon stringers (~1 mm) are observed in parts of the section.

Appendix A.3.
Photographs of Yax-1 core samples

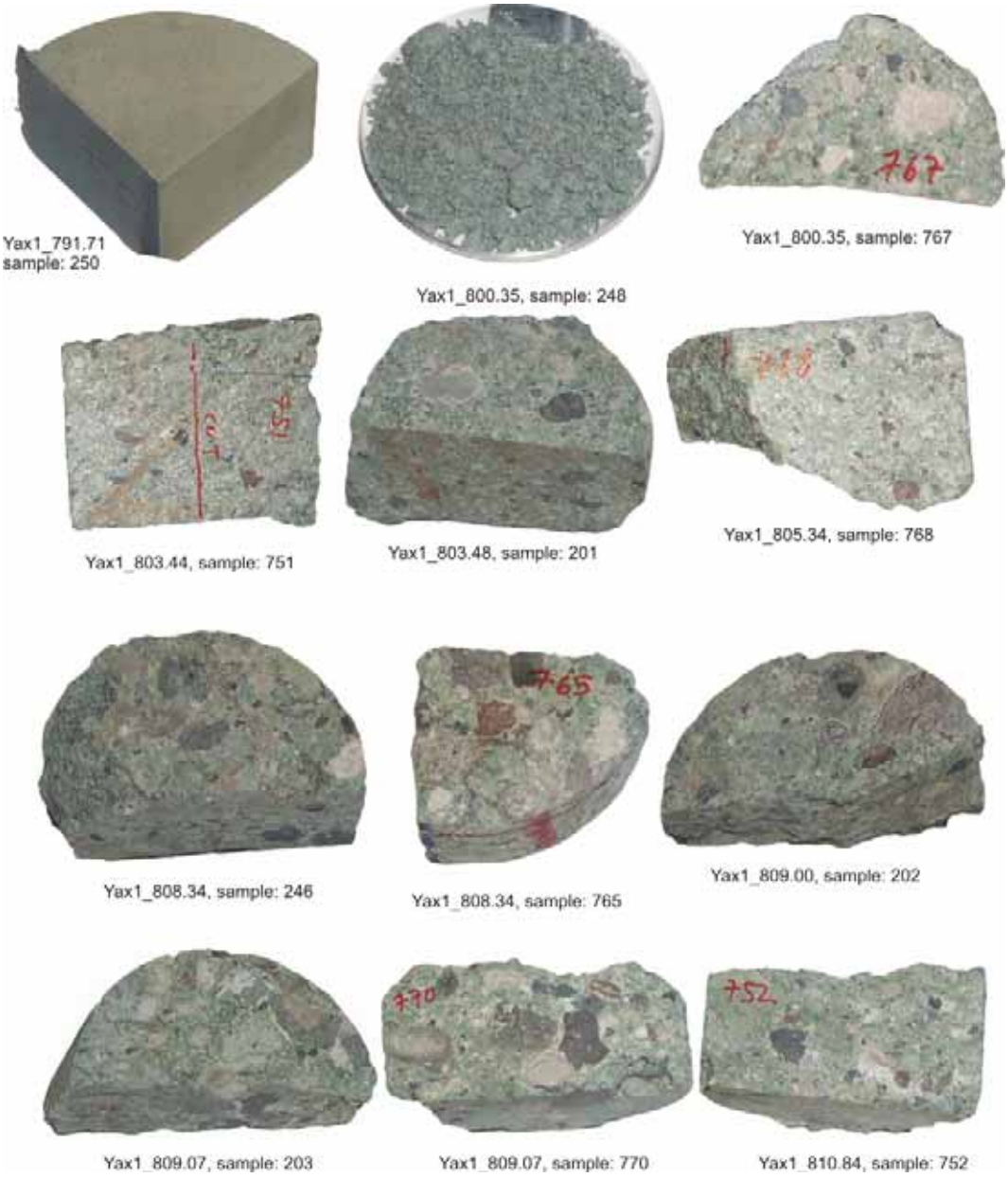
Yax1_791.71
sample: 250
Yax1_800.35, sample: 248
767
Yax1_800.35, sample: 767
751
Yax1_803.44, sample: 751
Yax1_803.48, sample: 201
Yax1_805.34, sample: 768
765
Yax1_808.34, sample: 246
Yax1_808.34, sample: 765
Yax1_809.00, sample: 202
770
752
Yax1_809.07, sample: 203
Yax1_809.07, sample: 770
Yax1_810.84, sample: 752

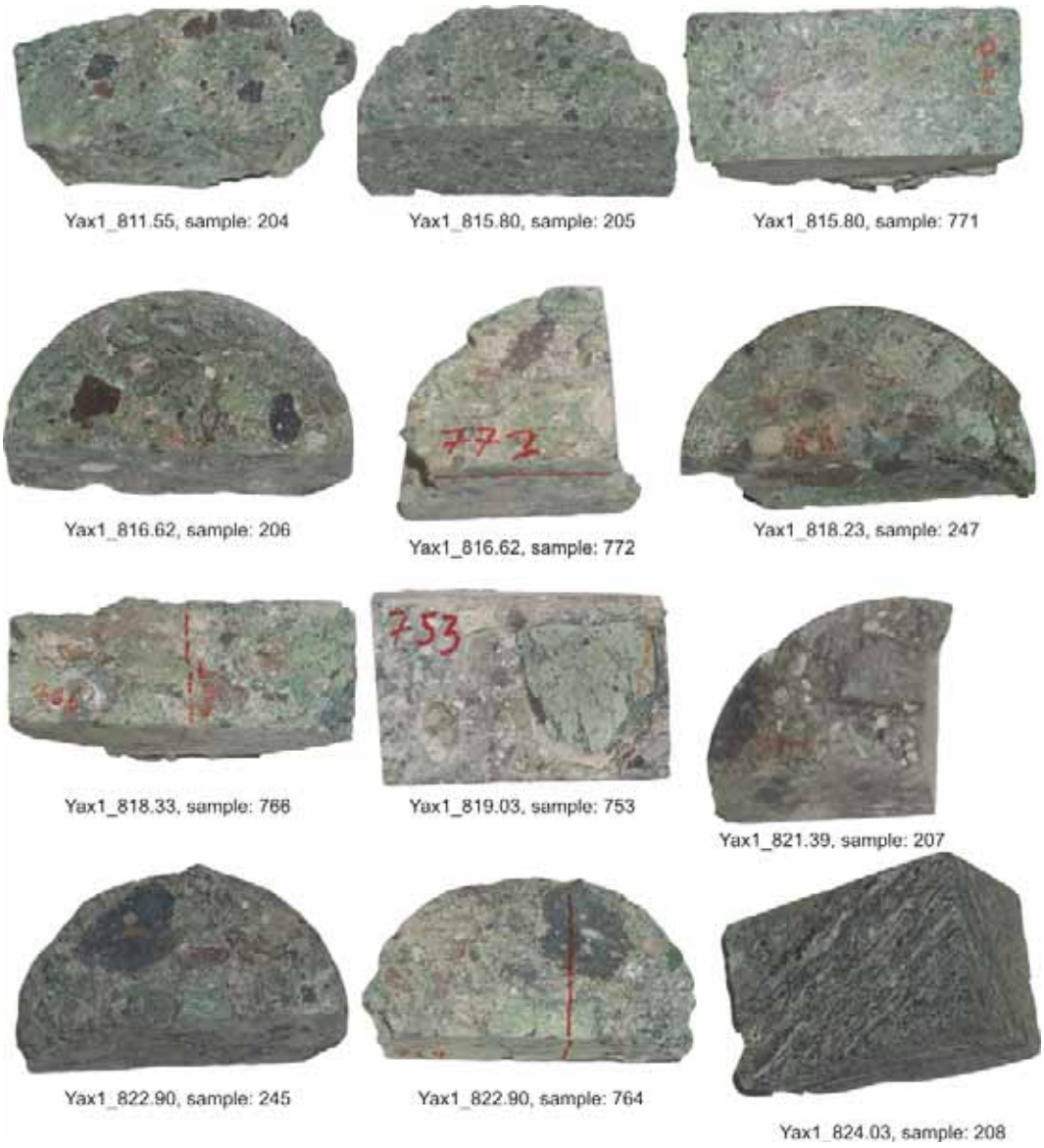
Yax1_811.55, sample: 204
Yax1_815.80, sample: 205
Yax1_815.80, sample: 771
Yax1_816.62, sample: 206
772
Yax1_816.62, sample: 772
Yax1_818.23, sample: 247
Yax1_818.33, sample: 766
753
Yax1_819.03, sample: 753
Yax1_821.39, sample: 207
Yax1_822.90, sample: 245
Yax1_822.90, sample: 764
Yax1_824.03, sample: 208

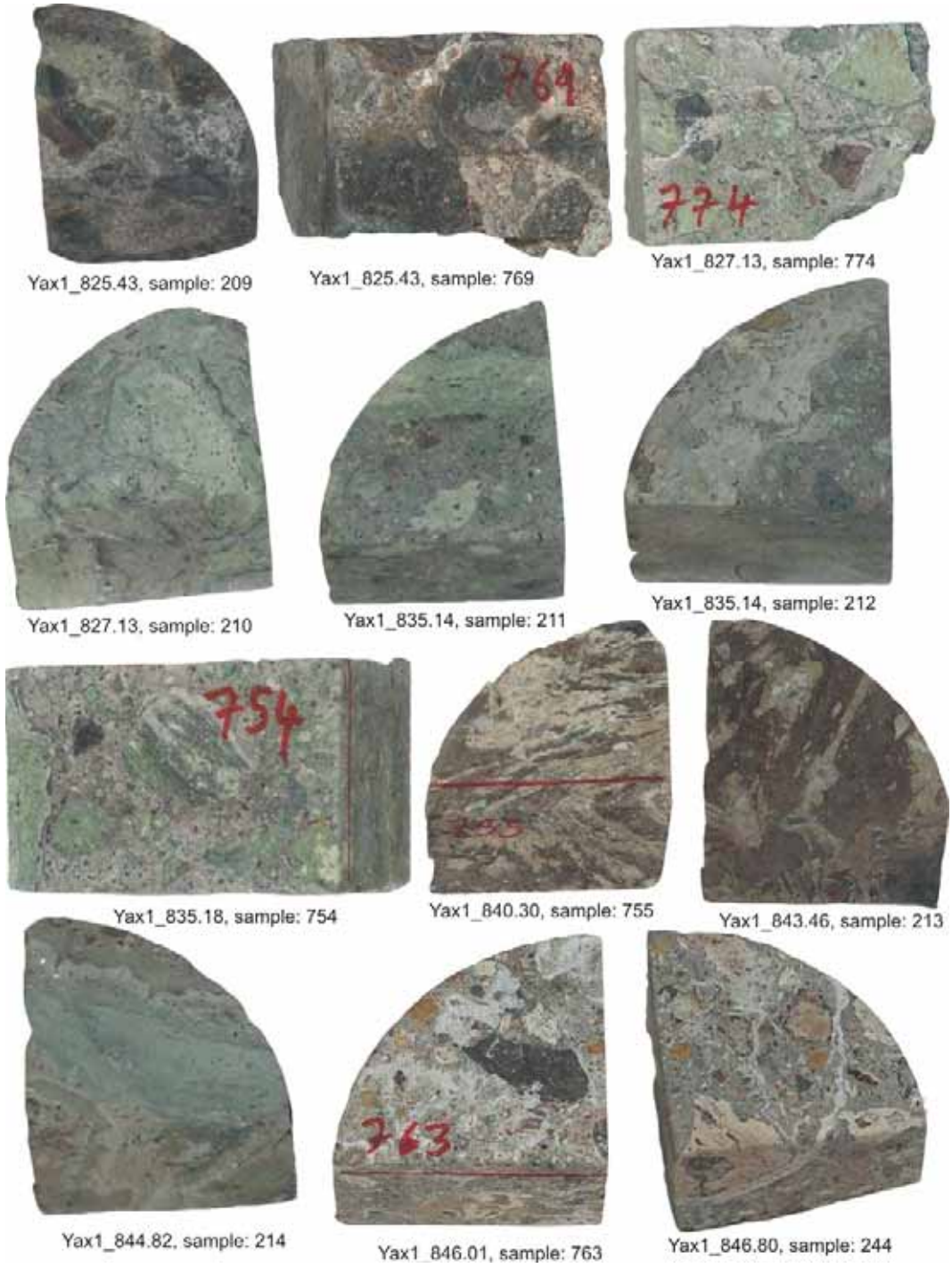
Yax1_825.43, sample: 209
769
Yax1_825.43, sample: 769
774
Yax1_827.13, sample: 774
Yax1_827.13, sample: 210
Yax1_835.14, sample: 211
Yax1_835.14, sample: 212
754
Yax1_835.18, sample: 754
Yax1_840.30, sample: 755
Yax1_843.46, sample: 213
Yax1_844.82, sample: 214
763
Yax1_846.01, sample: 763
Yax1_846.80, sample: 244

Yax1_851.15, sample: 756

Yax1_851.15, sample: 215

Yax1_860.40, sample: 243

Yax1_860.40, sample: 762

Yax1_875.79, sample: 761

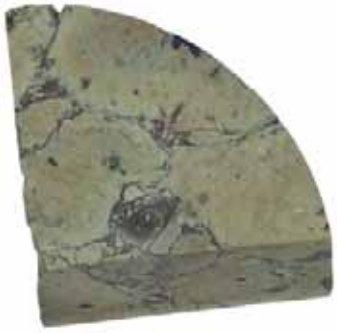

Yax1_878.09, sample: 242

Yax1_879.03, sample: 216

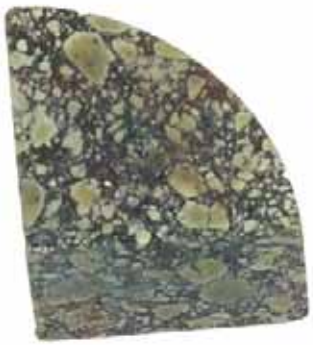

Yax1_882.45, sample: 241

Yax1_882.45, sample: 760

Yax1_886.79, sample: 217

Yax1_886.79, sample: 757

Yax1_888.09, sample: 218

Yax1_888.92, sample: 775

Yax1_890.52, sample: 240

Yax1_892.55, sample: 225

Yax1_894.14, sample: 239

Yax1_894.14, sample: 759

Yax1_916.36, sample: 222

Yax1_916.36, sample: 758

Yax1_1314.83, sample: 233

Yax1_1315.86, sample: 223

Yax1_916.36, sample: 758

Yax1_1341.61, sample: 235

Yax1_1341.81, sample: 236

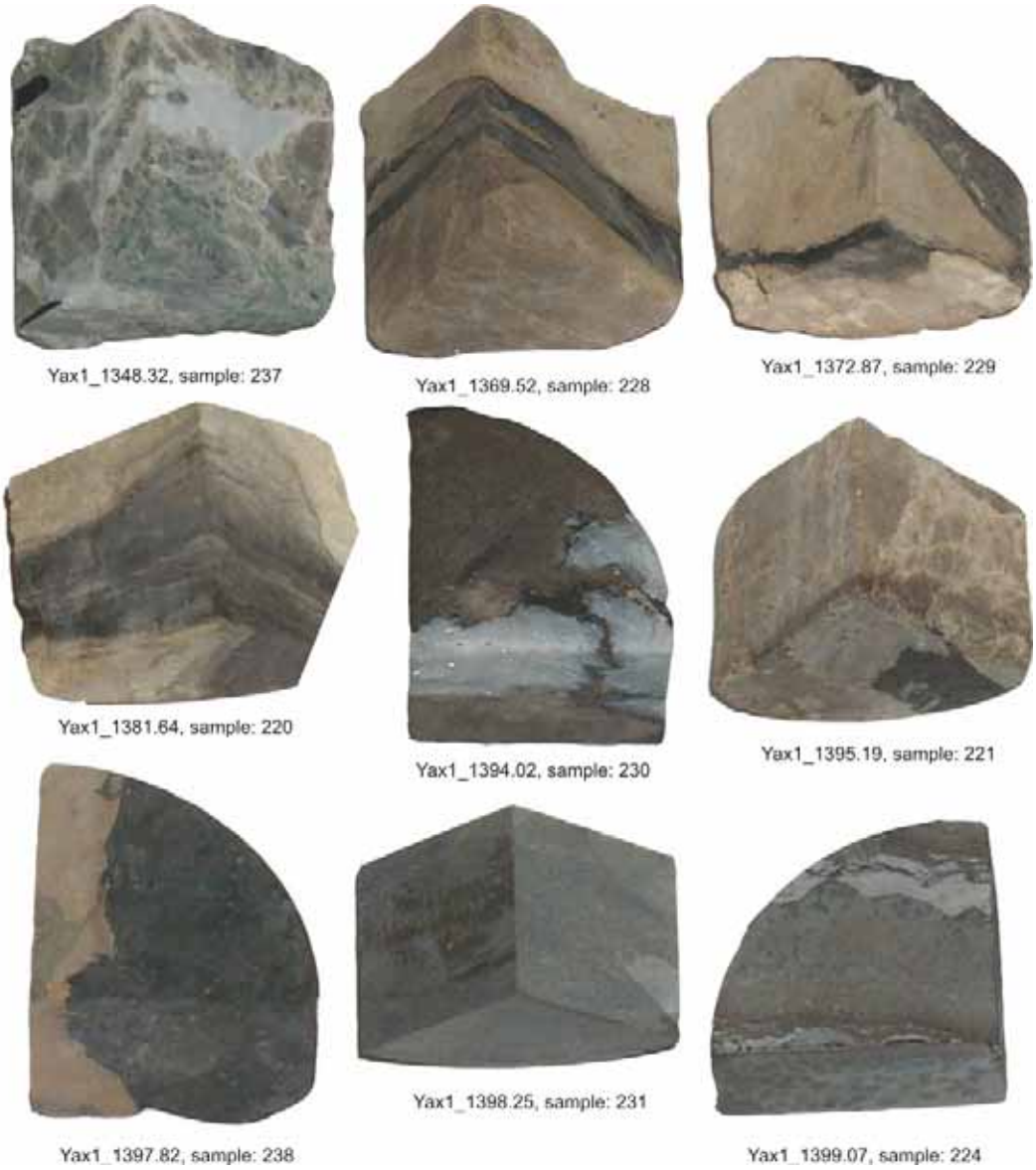
Yax1_1348.32, sample: 237
Yax1_1369.52, sample: 228
Yax1_1372.87, sample: 229
Yax1_1381.64, sample: 220
Yax1_1394.02, sample: 230
Yax1_1395.19, sample: 221
Yax1_1397.82, sample: 238
Yax1_1398.25, sample: 231
Yax1_1399.07, sample: 224

Appendix A.4.
Microphotographs of Yax-1 core samples

The following are representative photomicrographs of the various impactite units, including the hanging wall and footwall rocks found in the Yaxcopoil-1 borehole, arranged according to depth.

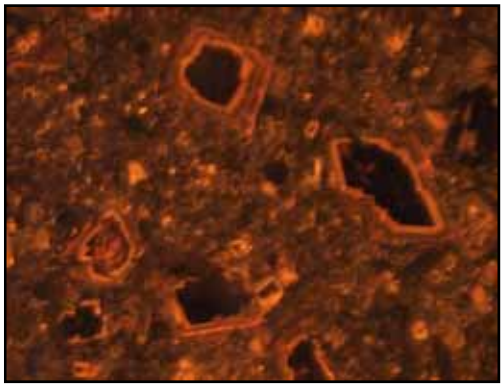

Fig. A.4.1. Cathodoluminescence image of calcite (orange) crystals with concentric intergrowths, 200 X , depth = 791.71 m.

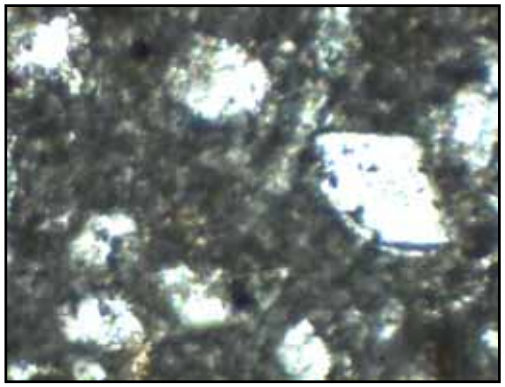

Fig. A.4.2. Plane polarized light image of calcite crystals, same area as Fig. A.2.1, 200 X , depth = 791.71 m.

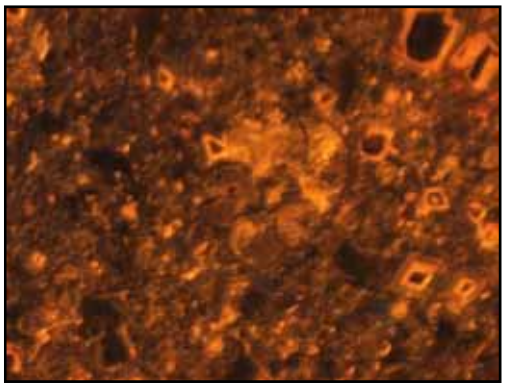

Fig. A.4.3. Cathodoluminescence image of foraminifora fossil (center of image) and zoned calcite crystals, 200 X, depth = 791.71 m.

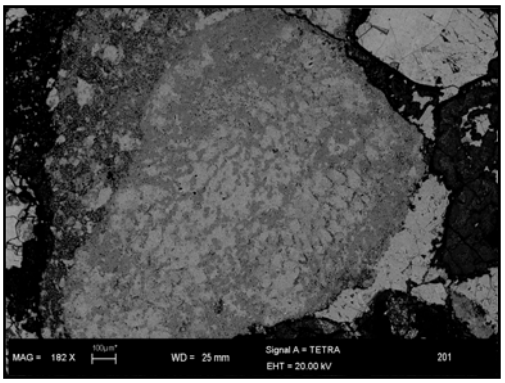

Fig. A.4.4. Backscatter electron (BSE) image of coral fragment, 182 X, depth = 803.48 m.

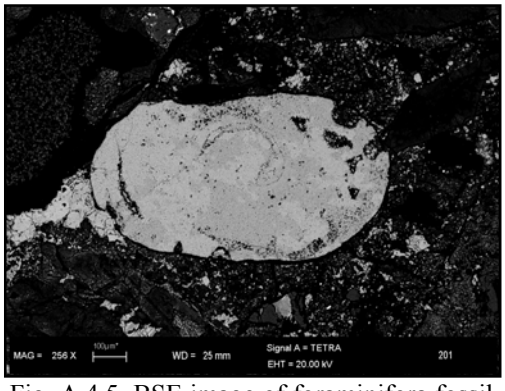

Fig. A.4.5. BSE image of foraminifora fossil, 256 X, depth = 803.48 m.

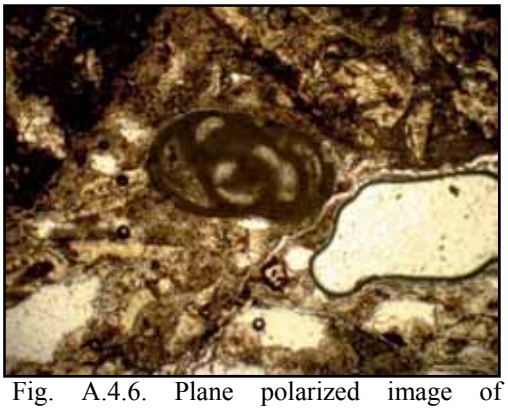

Fig. A.4.6. Plane polarized image of foraminifora fossil, 40 X, depth = 803.48 m.

Fig. A.4.7. Plane polarized image of foraminifora fossil, 100 X, depth = 803.48 m.

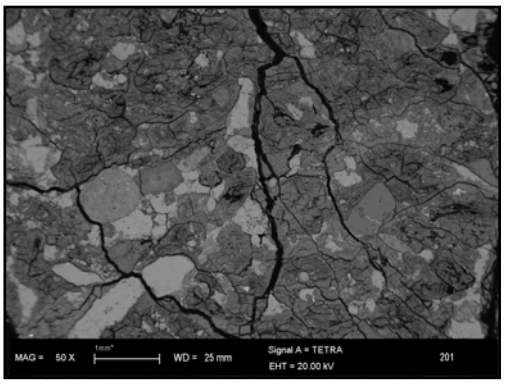

Fig. A.4.8. BSE image of the general character of Unit 1, note the inclusions at the left and right of the image 50 X, depth = 803.48 m.

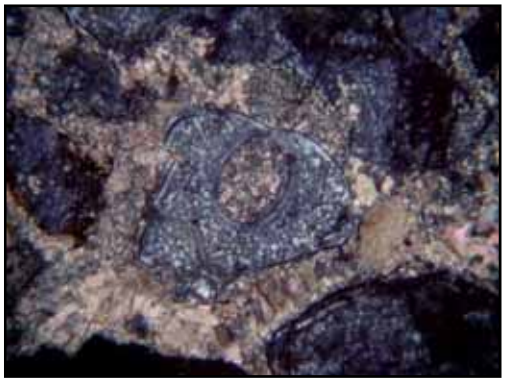

Fig. A.4.9. Cross polarized light image of devitrified melt particle with perlitic texture, 100 X, depth = 803.48 m.

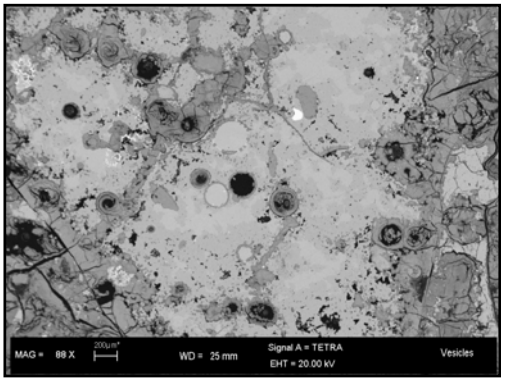

Fig. A.4.10. BSE image of altered melt particle replaced by calcite/K-feldspar, note the rounded vesicles, 88 X, depth = 805.34 m.

Fig. A.4.11. Plane polarized light image of foraminifera fossil, 50 X, depth = 808.34 m.

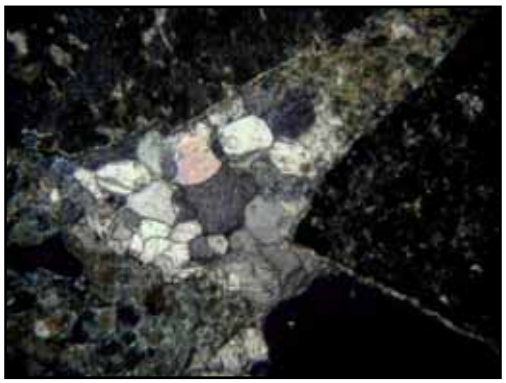

Fig. A.4.12. Cross polarized light image of dolomite crystals interstitial to melt rock particles, 25 X, depth = 809.70 m.

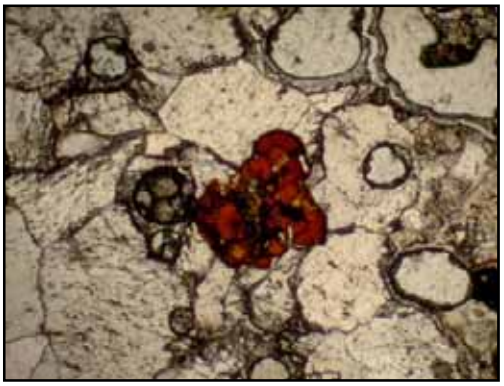

Fig. A.4.13. Plane polarized light image of red iron oxide melt particle, 100 X, depth = 809.70 m.

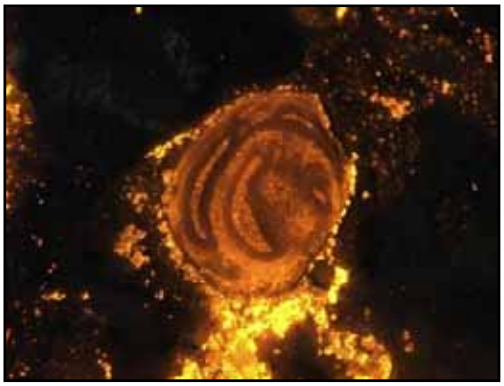

Fig. A.4.14. Cathodoluminescence image of foraminifera fossil, 50 X, depth = 809.70 m.

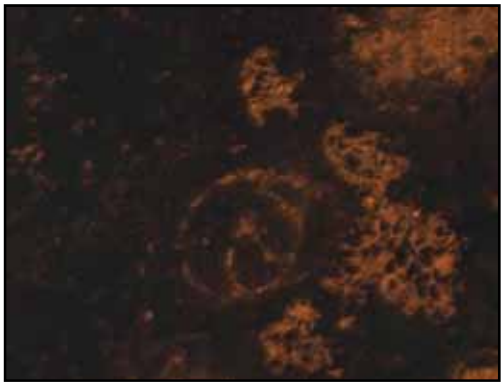

Fig. A.4.15. Cathodoluminescence image of foraminifera fossil, 200 X, depth = 809.70 m.

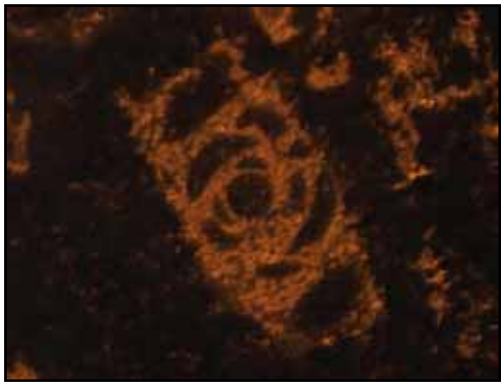

Fig. A.4.16. Cathodoluminescence image of foraminifera fossil, 200 X, depth = 809.70 m.

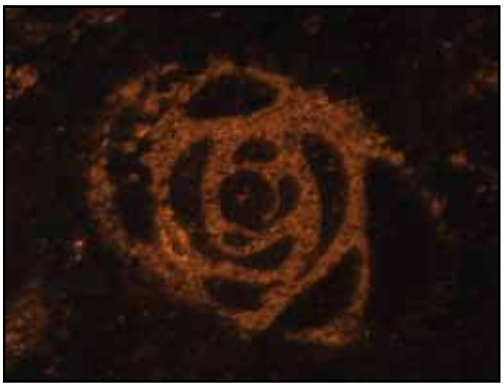

Fig. A.4.17. Cathodoluminescence image of foraminifera fossil, 200 X, depth = 809.70 m.

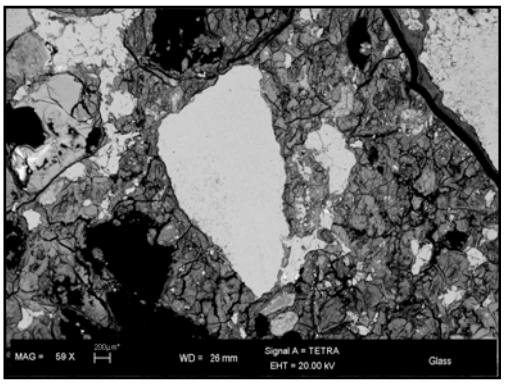

Fig. A.4.18. BSE image of dolomite clast in altered/reworked melt particle rich groundmass, 200 X, depth = 809.70 m.

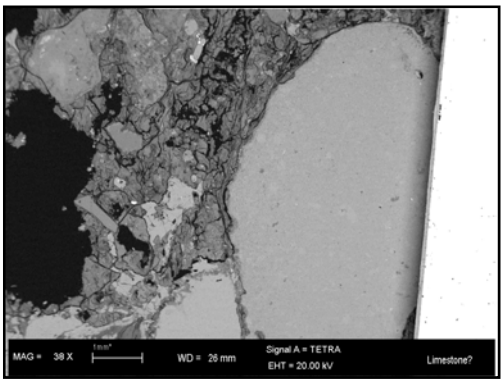

Fig. A.4.19. BSE image of argillaceous dolomite (right) and limestone (right) clasts in altered/reworked melt particle rich groundmass, 38 X, depth = 810.84 m.

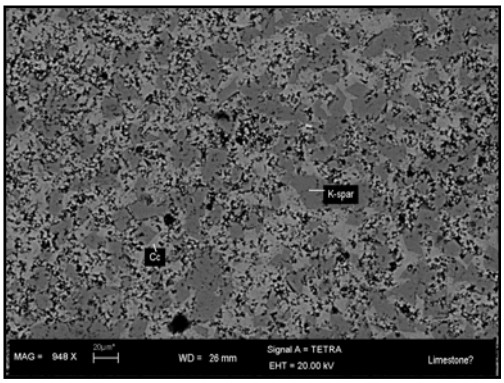

Fig. A.4.20. BSE image magnification of the argillaceous dolomite clast in Fig. A.2.19, note the intergrowth of K-feldspar and calcite, 948 X, depth = 810.84 m.

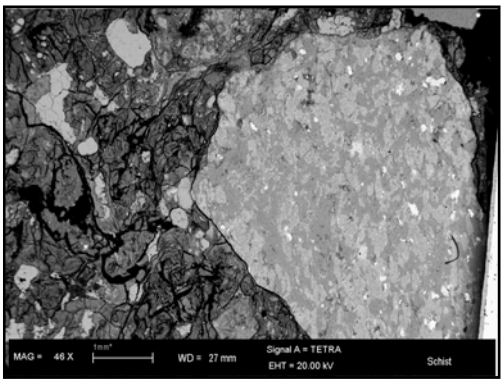

Fig. A.4.21. BSE image of schistose clast (right) in altered/reworked melt particle rich groundmass, 46 X, depth = 810.84 m.

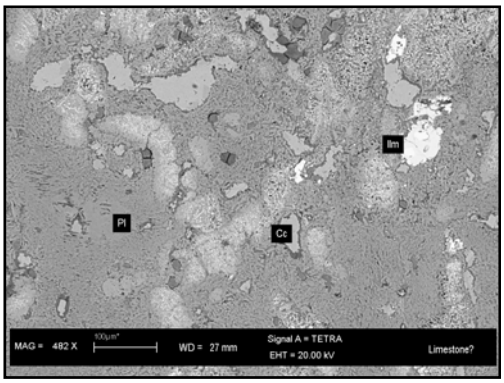

Fig. A.4.22. BSE image magnification of schistose clast in Fig. A.2.21, white patche at right = ilmenite, med. gray patches = calcite, dark gray groundmass = plagioclase, 482 X, depth = 810.84 m.

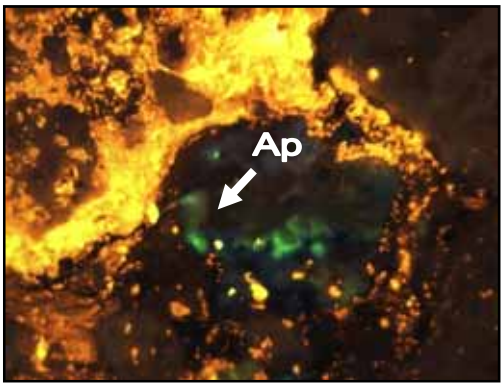

Fig. A.4.23. Cathodoluminescence image of melt particle with green schlieric apatite luminescence in carbonate groundmass, 50 X, depth = 821.39 m.

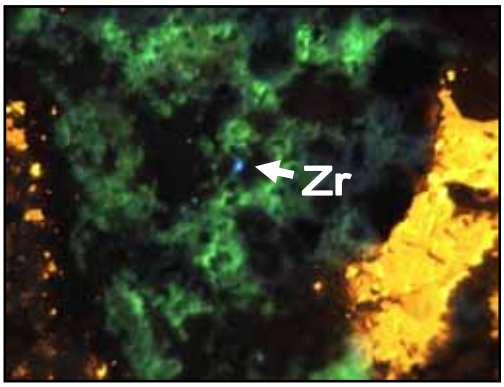

Fig. A.4.24. Cathodoluminescence magnified image of green luminescent apatite with blue luminescent zircon at its centre, 50 X, depth = 821.39 m.

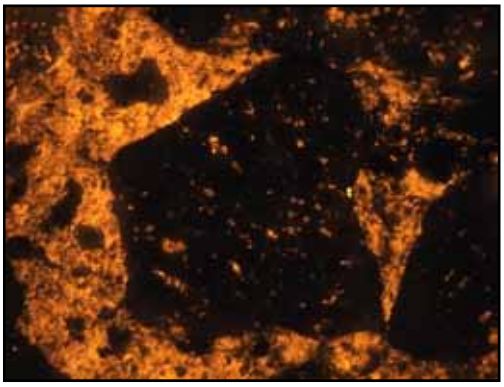

Fig. A.4.25. Cathodoluminescence image of angular melt particle in carbonate groundmass, note the alignment of inclusions in the particle, 50 X, depth = 821.39 m.

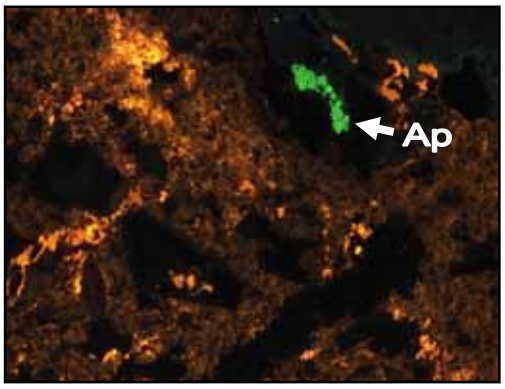

Fig. A.4.26. Cathodoluminescence image of melt particle in carbonate groundmass, note the green luminescent apatite crystal in the melt particle at the top right of the image. Calcite veins are brighter orange, 50 X, depth = 824.03 m.

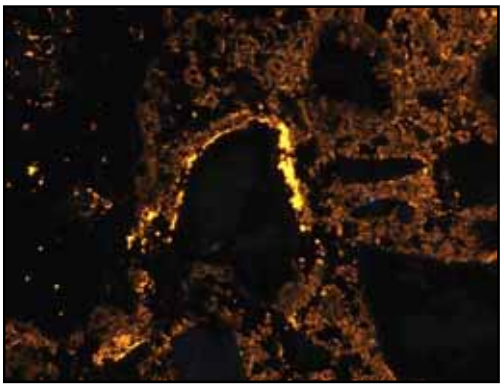

Fig. A.4.27. Cathodoluminescence image of subrounded melt particle in carbonate groundmass, note the carbonate rim around the inclusion at the center of the image, 50 X, depth = 824.03 m.

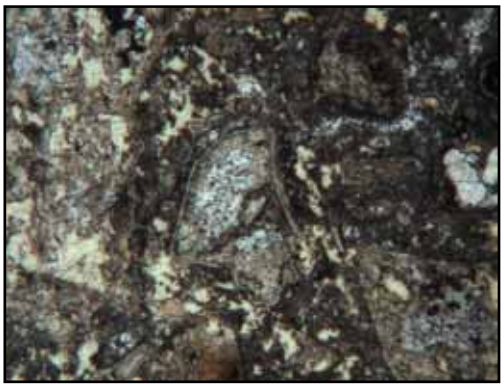

Fig. A.4.28. Plane polarized image of subrounded melt particle in carbonate groundmass, same region as Fig. A.2.27, 50 X, depth = 824.03 m.

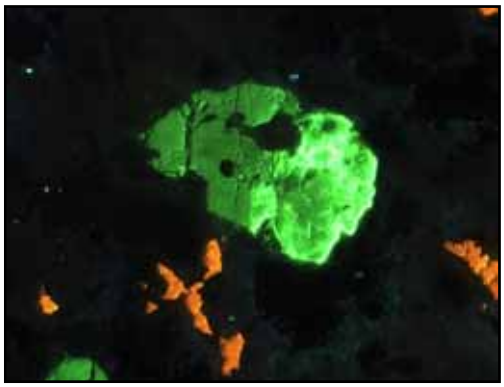

Fig. A.4.29. Cathodoluminescence image of green luminescent apatite crystal, 100 X, depth = 824.03 m.

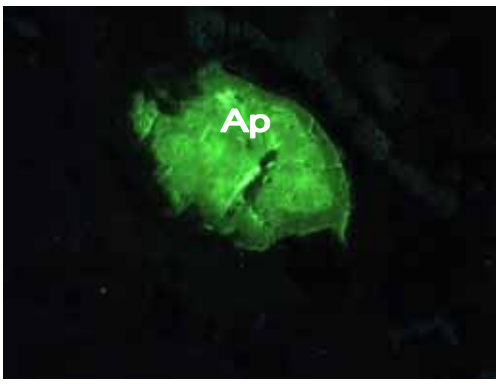

Fig. A.4.30. Cathodoluminescence image of green luminescent apatite crystal, note the darker green outside zonation, 100 X, depth = 824.03 m.

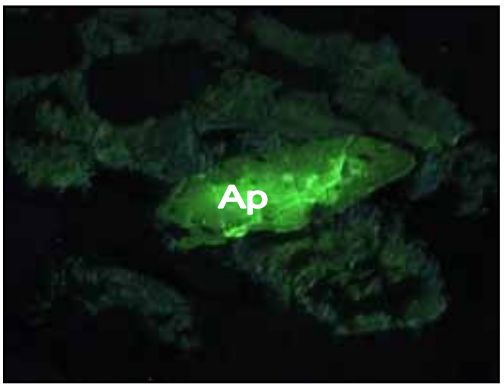

Fig. A.4.31. Cathodoluminescence image of green luminescent apatite crystal, 100 X, depth = 824.03 m.

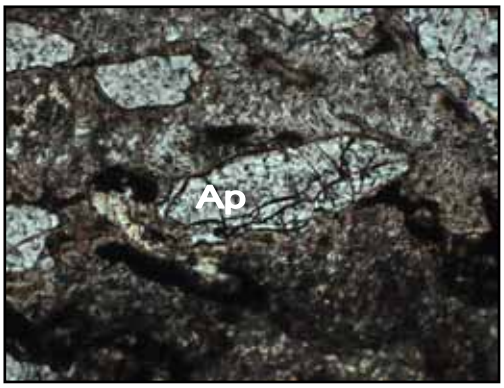

Fig. A.4.32. Plane polarized image of apatite crystal, note the crystal's fractured nature, 100 X, depth = 824.03 m.

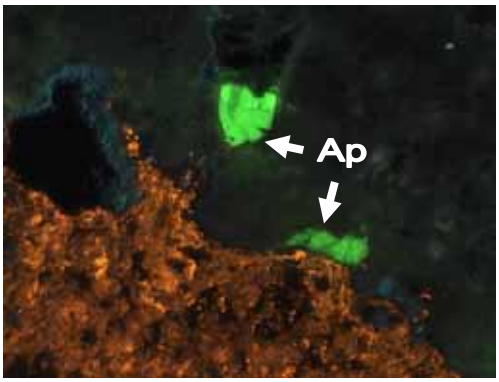

Fig. A.4.33. Cathodoluminescence image of green luminescent apatite crystals, 100 X, depth = 824.03 m.

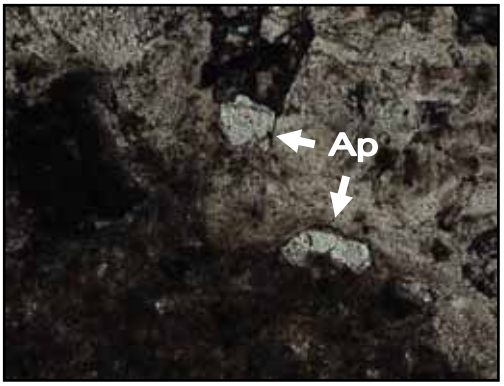

Fig. A.4.34. Plane polarized image of apatite crystals, same region as Fig. A.2.33, 100 X, depth = 824.03 m.

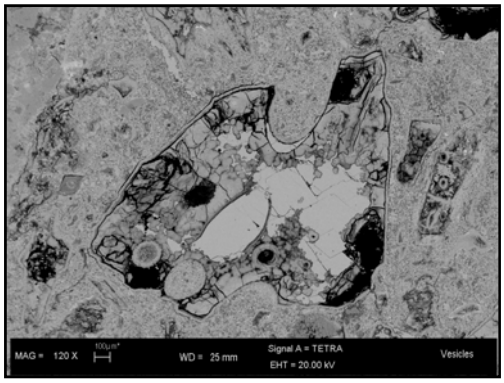

Fig. A.4.35. BSE image of angular melt rock particle replaced by calcite, 120 X, depth = 824.03 m.

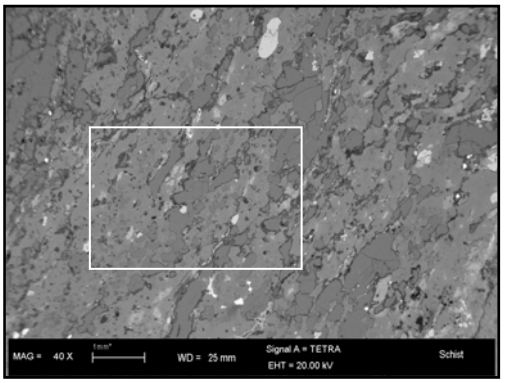

Fig. A.4.36. BSE magnified image of a schist inclusion, note the mineral lineation NE to SW, box is region imaged in Fig. A.2.37, 40 X, depth = 824.03 m.

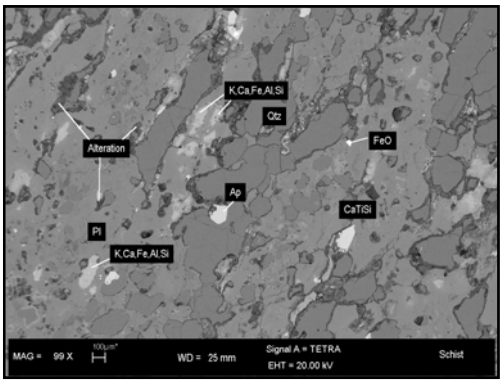

Fig. A.4.37. BSE magnified image of schist inclusion, a plagioclase, K-feldspar, apatite, ilmenite, magnetite, quartz schist, 99 X, depth = 824.03 m.

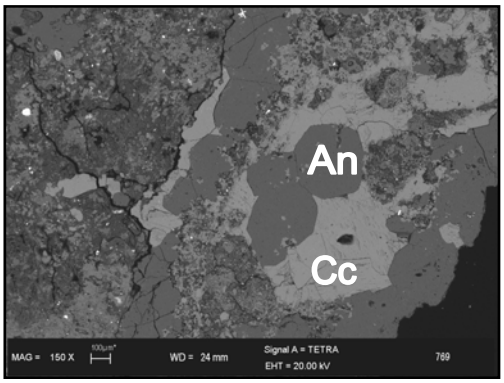

Fig. A.4.38. BSE image of calcite (light gray) and analcime (euhedral med gray) crystals found in a vein the interstices of melt rock particles, 150 X, depth = 825.43 m.

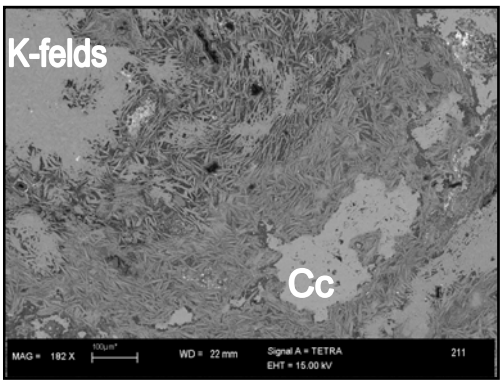

Fig. A.4.39. BSE image of microlite rich melt rock particle with K-feldspar and calcite rich patches, 182 X, depth = 835.14 m.

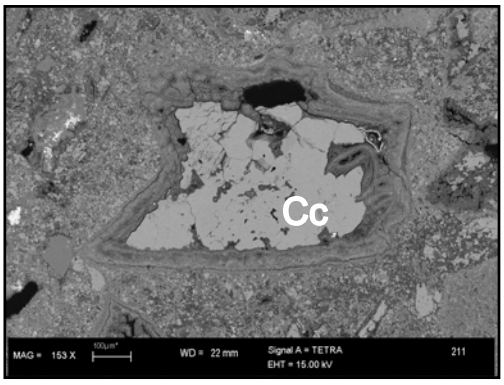

Fig. A.4.40. BSE image of melt rock particle replaced by calcite, 153 X, depth = 835.14 m.

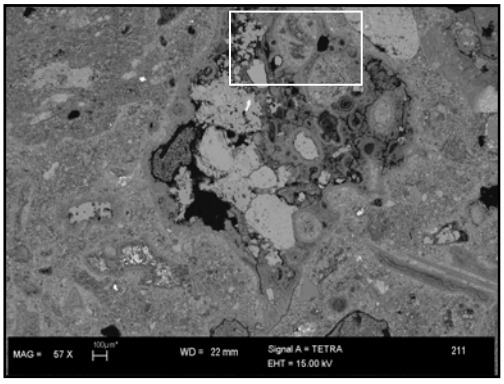

Fig. A.4.41. BSE image of vesiculated melt rock particle, box is region in Fig. A.2.42, 57 X, depth = 835.14 m.

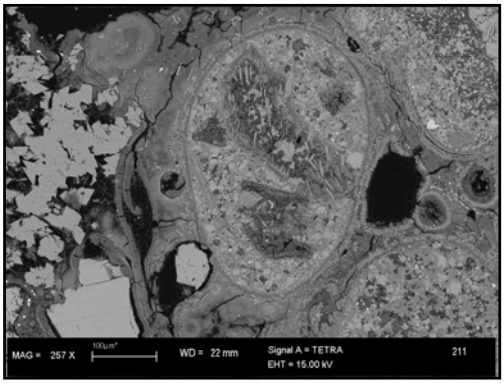

Fig. A.4.42. BSE magnified image of vesicle, 257 X, depth = 835.14 m.

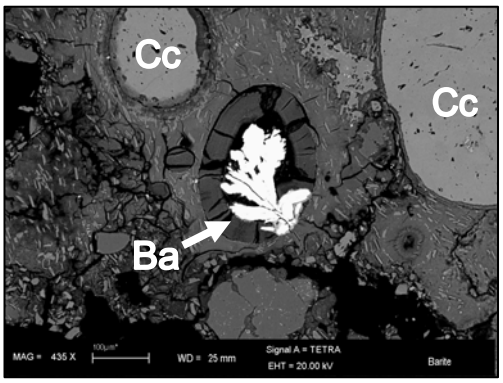

Fig. A.4.43. BSE magnified image of vesicles with barite and calcite infill, 435 X, depth = 835.14 m.

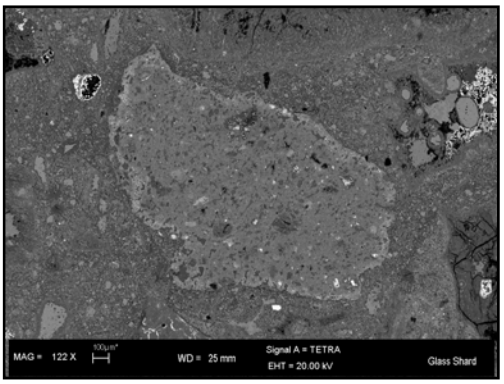

Fig. A.4.44. BSE magnified image of melt rock particle with zoned margin, 122 X, depth = 835.14 m.

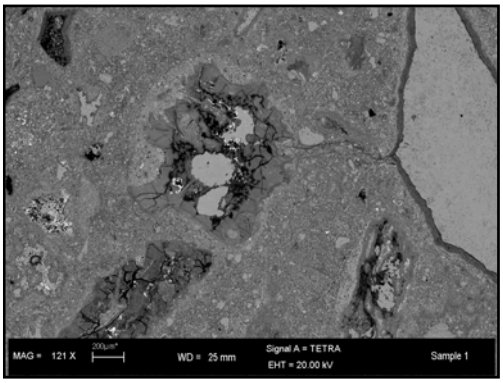

Fig. A.4.45. BSE image of suevite comprising groundmass supported angular melt rock particles and a limestone clast, 121 X, depth = 835.14 m.

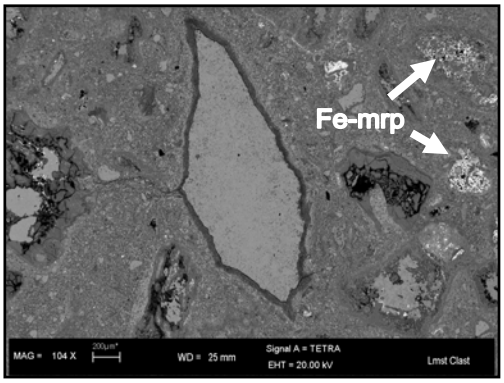

Fig. A.4.46. BSE image of suevite similar to Fig. A.2.45 but with iron rich melt rock particles at the right. 104 X, depth = 835.14 m.

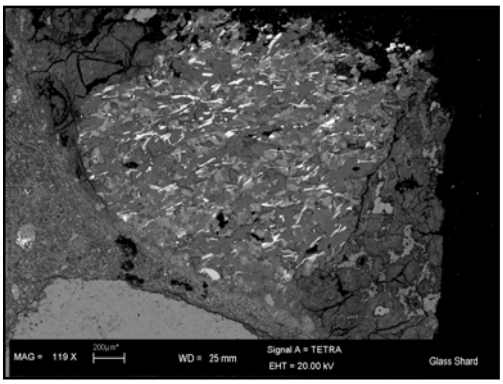

Fig. A.4.47. BSE image of schist clast, 119 X, depth = 835.14 m.

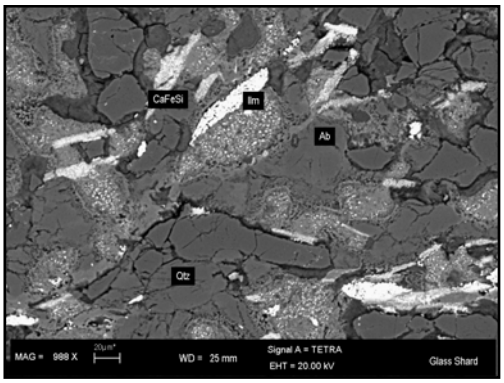

Fig. A.4.48. BSE image of quartz, albite, ilmenite, titanite schist clast, 988 X, depth = 835.14 m.

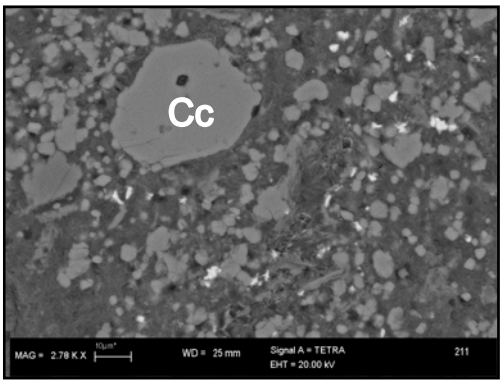

Fig. A.4.49. BSE image of suevite groundmass comprising calcite crystals in a phyllosilicate groundmass shown in Fig. 2.40, 2.41, 2.44, 2.45, 2.46, and 2.47, 2.78 KX, depth = 835.14 m.

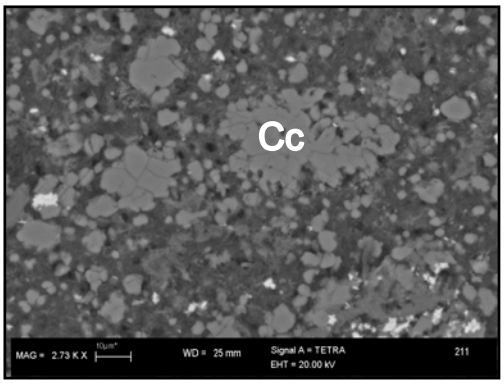

Fig. A.4.50. BSE image of suevite groundmass shown in Fig. 2.40, 2.41, 2.44, 2.45, 2.46, and 2.47, 2.73 KX, depth = 835.14 m.

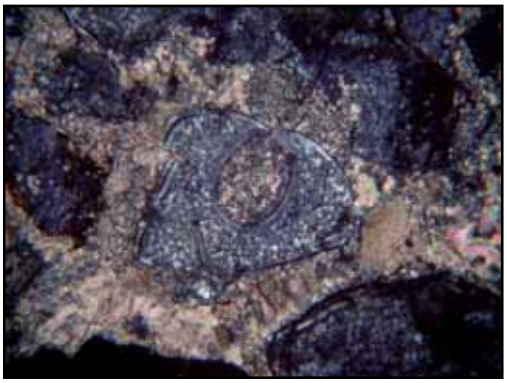

Fig. A.4.51. Cross polarized image of vesiculated melt rock particle with perlitic texture in carbonate groundmass, 50 X, depth = 835.14 m.

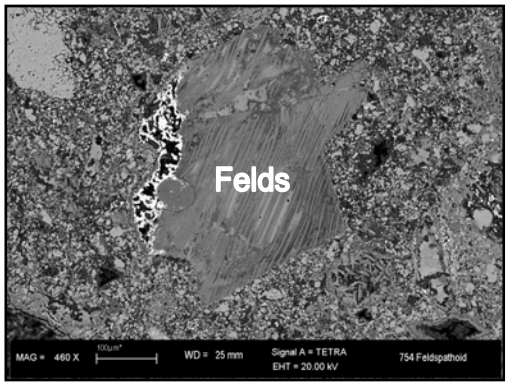

Fig. A.4.52. BSE image of strained feldspar crystal in mixed carbonate/phyllosilicate groundmass, 460 X, depth = 835.18 m.

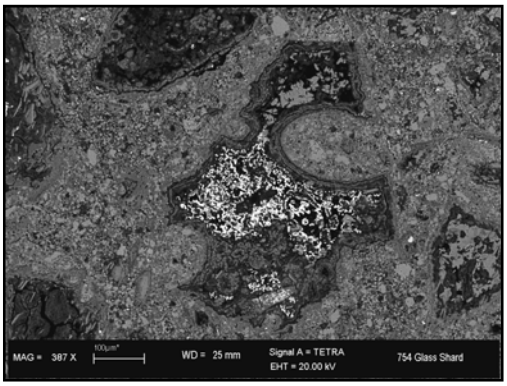

Fig. A.4.53. BSE image of vesiculated melt rock particle with iron rich patches in mixed carbonate/phyllosilicate groundmass, 387 X, depth = 835.18 m.

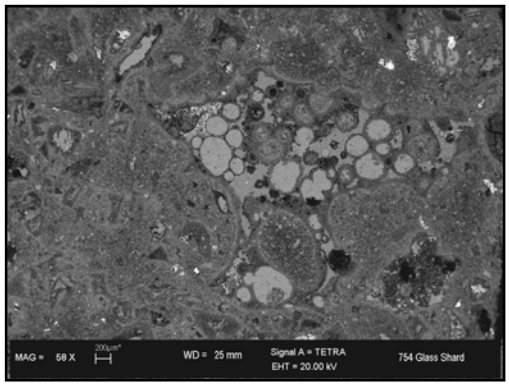

Fig. A.4.54. BSE image of vesiculated melt rock particle in mixed carbonate/ phyllosilicate groundmass, note vesicles are filled by calcite and groundmass material, 387 X, depth = 835.18 m.

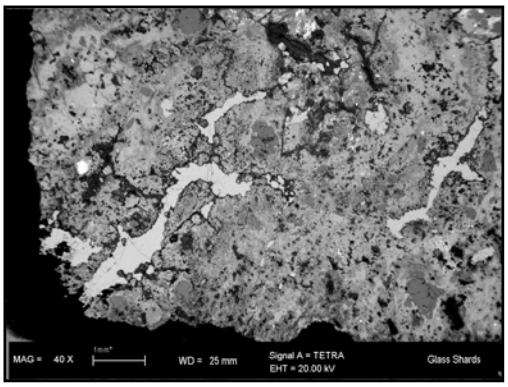

Fig. A.4.55. BSE image of large melt rock particle cross cut by several calcite veins (light gray), 40 X, depth = 843.46 m.

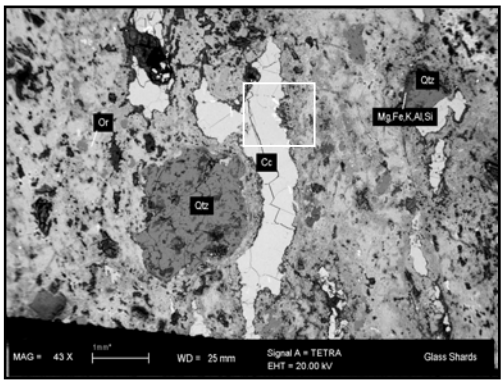

Fig. A.4.56. BSE image of large melt rock particle containing a quartz grain (no PDFs) cross cut by calcite veins (light gray), 43 X, depth = 843.46 m.

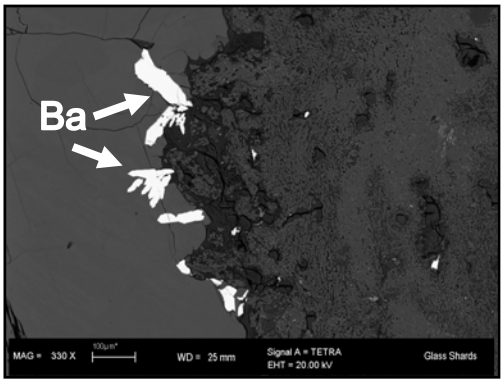

Fig. A.4.57. BSE magnified image of calcite veins shown in Fig. A.2.56 containing euhedral barite crystals (white), 330 X, depth = 843.46 m.

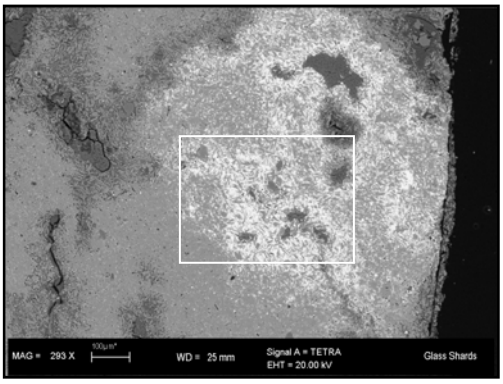

Fig. A.4.58. BSE image of melt rock particle showing interstitial magnetite between microlite laths , 293 X, depth = 843.46 m.

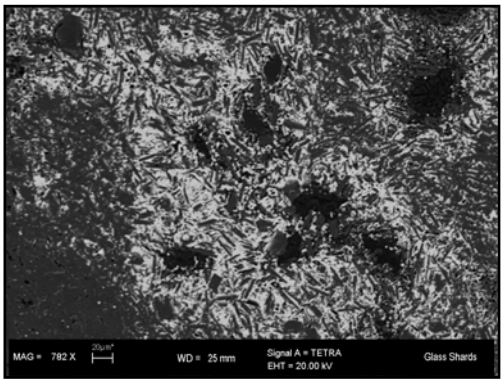

Fig. A.4.59. BSE magnified image of interstitial iron oxide shown in Fig. A.2.58, 782 X, depth = 843.46 m.

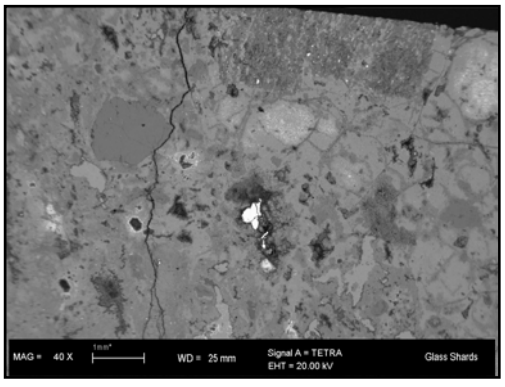

Fig. A.4.60. BSE image of large melt rock particle containing quartz and barite, note the polygonal alteration pattern towards the top right of the image, 40 X, depth = 843.46 m.

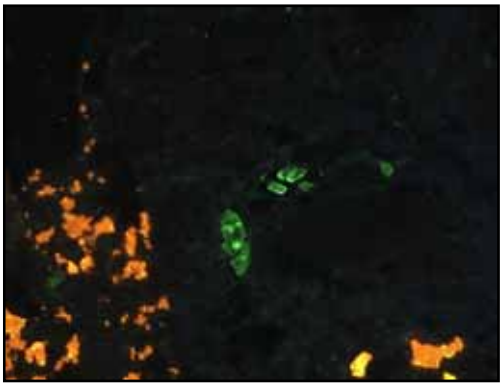

Fig. A.4.61. Cathodoluminescence image of calcite and apatite crystals, 50 X, depth = 843.46 m.

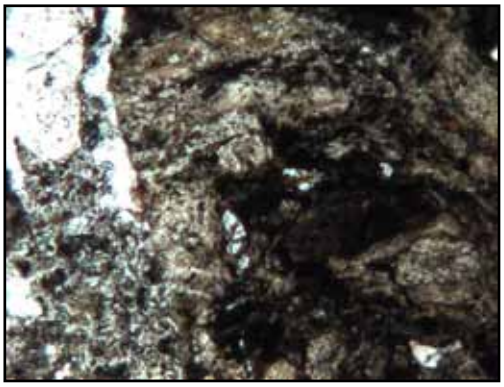

Fig. A.4.62. Plane polarized image of melt rock particle shown in Fig. A.4.61, 50 X, depth = 843.46 m.

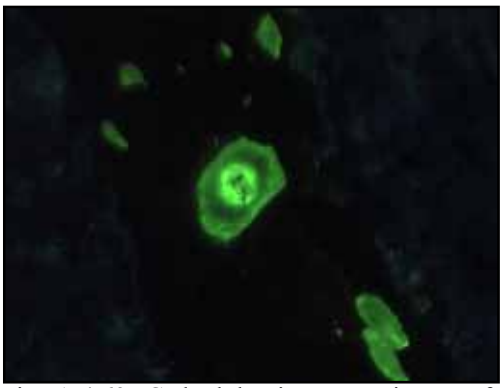

Fig. A.4.63. Cathodoluminescence image of zone apatite crystals, 200 X, depth = 843.46 m.

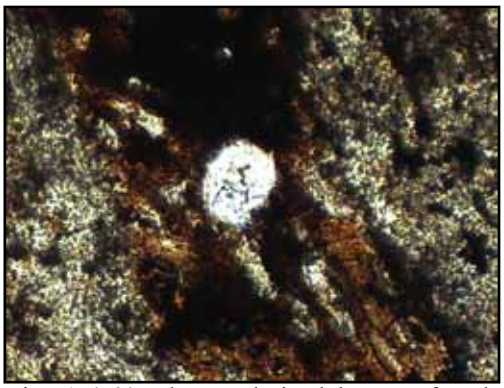

Fig. A.4.64. Plane polarized image of melt rock particle with apatite crystals shown in Fig. A.4.63, 200 X, depth = 843.46 m.

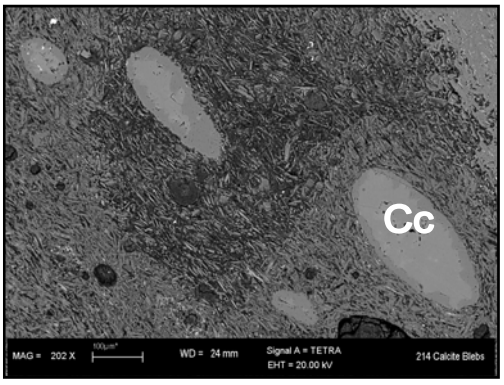

Fig. A.4.65. BSE image of melt rock particle with calcite filled vesicles, 202 X, depth = 844.82 m.

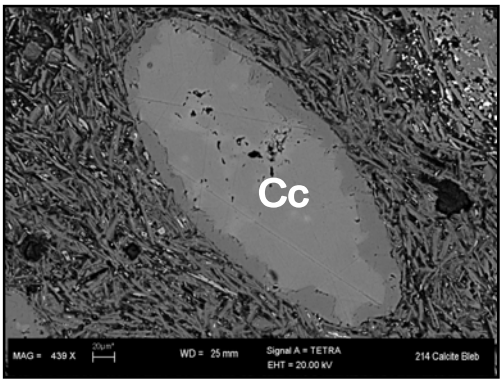

Fig. A.4.66. BSE magnified image of calcite filled vesicle shown in Fig. A.4.65. Note the irregular intergowth between calcite and the vesicle wall, 439 X, depth = 844.82 m.

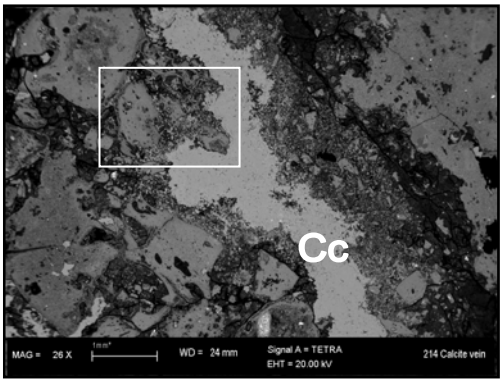

Fig. A.4.67. BSE image of calcite vein cross cutting suevite, 24 X, depth = 844.82 m.

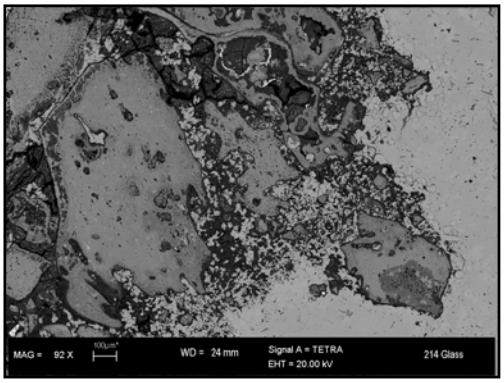

Fig. A.4.68. BSE magnified image of the left calcite vein wall contact as shown in Fig. A.4.67, note the diffuse nature of the contact, 92 X, depth = 844.82 m.

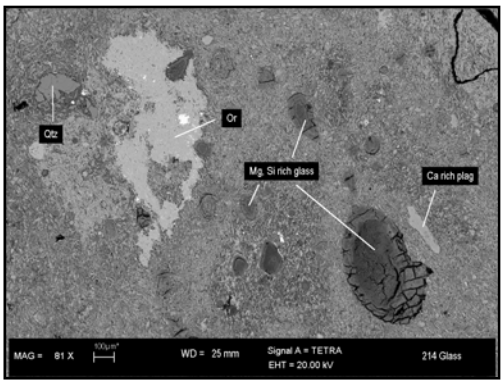

Fig. A.4.69. BSE image of a melt rock particle showing K-feldspar rich (light grey) and magnesium rich (dark grey) patches, 81 X, depth = 844.82 m.

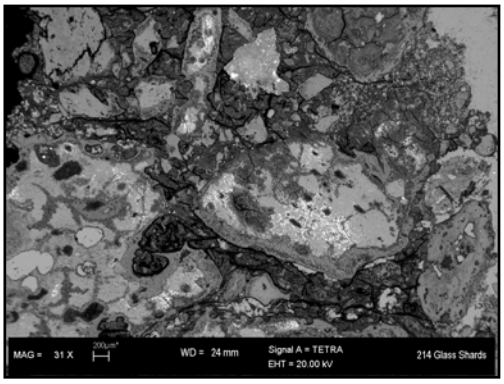

Fig. A.4.70. BSE image of melt rock particle aggregate, note the alkali bleaching of the particles' margins and dark BSE character of the enclosing groundmass, 31 X, depth = 844.82 m.

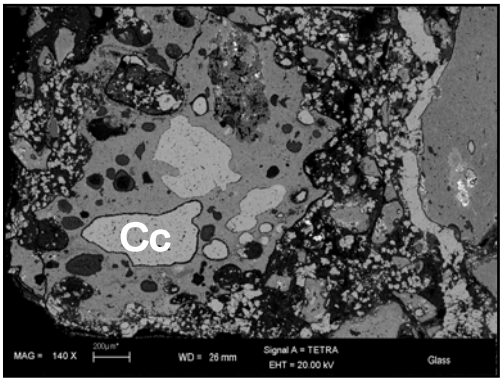

Fig. A.4.71. BSE image of an irregularly shaped melt rock particle, also note the irregular calcite blebs in the particle and the dark BSE character of the enclosing groundmass, 140 X, depth = 846.80 m.

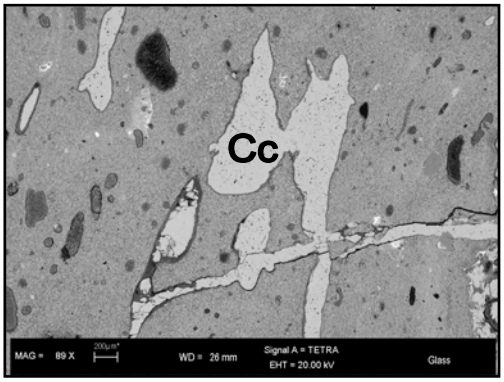

Fig. A.4.72. BSE image of an irregularly shaped calcite blebs in a melt rock particle, note the calcite vein cross cutting the particle and joining blebs, 89 X, depth = 846.80 m.

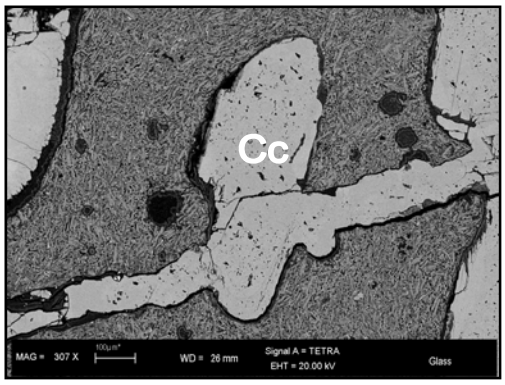

Fig. A.4.73. BSE magnified image of irregularly shaped calcite bleb and joining calcite vein, as shown in Fig. A.4.72, 307 X, depth = 846.80 m.

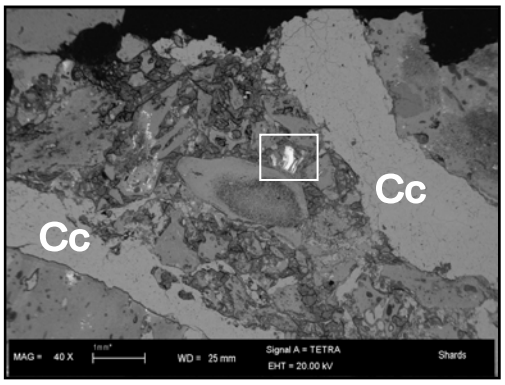

Fig. A.4.74. BSE image of zone melt rock particle in dark groundmass cross cute by calcite veins, note the fluidal shaped hematite patch towards the top right of the particle, 40 X, depth = 846.80 m.

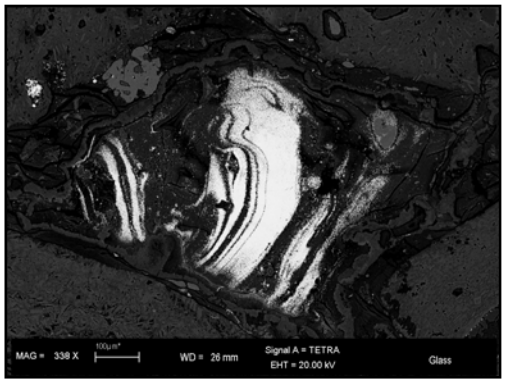

Fig. A.4.75. BSE magnified image of fluidal shaped hematite patch as shown in Fig. A.4.74, 338 X, depth = 846.80 m.

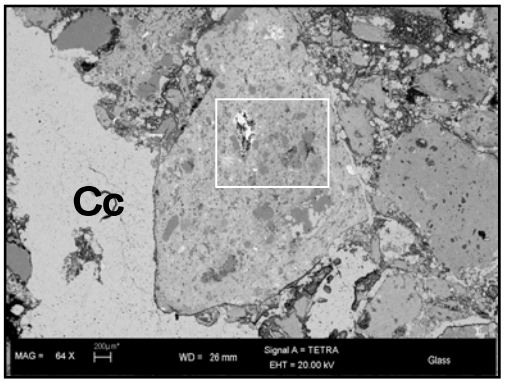

Fig. A.4.76. BSE image of compositionally heterogeneous melt rock particle, note the compacted nature of the suevite, 64 X, depth = 846.80 m.

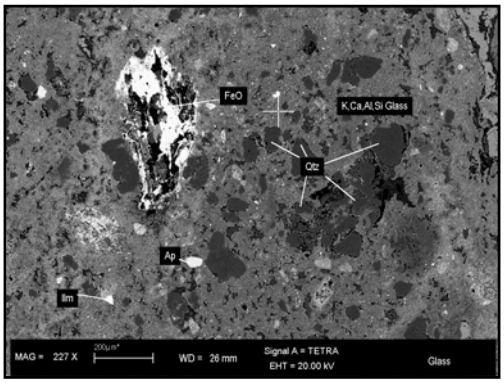

Fig. A.4.77. BSE magnified image of compositionally heterogeneous melt rock particle containing quartz (dark patch), apatite, ilmenite, and iron-oxides, in a feldspathic groundmass, 227 X, depth = 846.80 m.

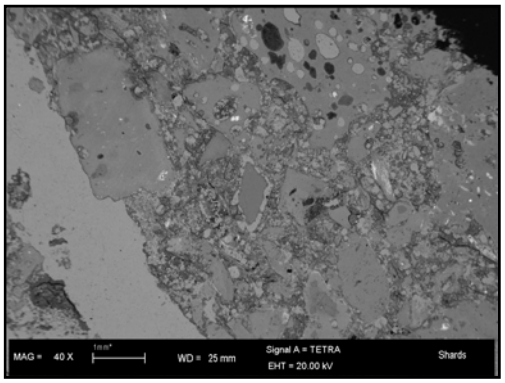

Fig. A.4.78. BSE image of melt rock particle aggregate, note the vesiculated nature of some of the melt rock particles, 40 X, depth = 846.80 m.

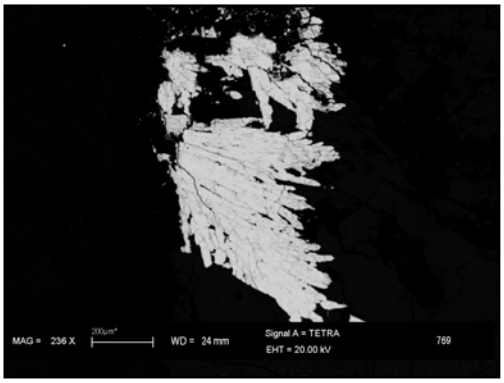

Fig. A.4.79. BSE image of euhedral barite crystals, 236 X, depth = 851.15 m.

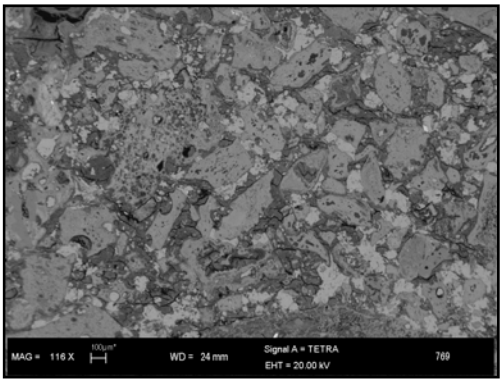

Fig. A.4.80. BSE image of melt rock particle aggregate, note the compacted nature of the particles and the dark coloured groundmass with calcite patches, 116 X, depth = 851.15

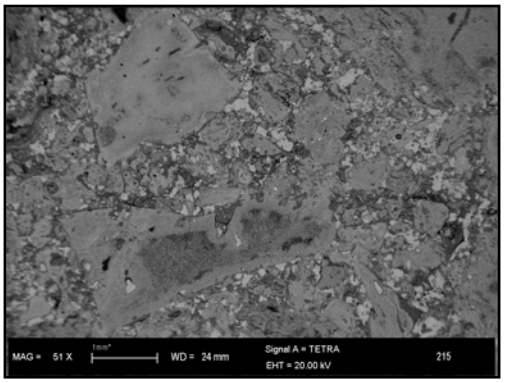

Fig. A.4.81. BSE image of melt rock particle aggregate, similar to Fig. A.4.80, note the zone melt rock particle, 51 X, depth = 851.15 m.

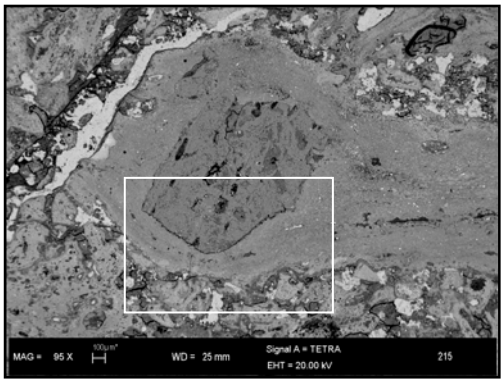

Fig. A.4.82. BSE image, note the cross cutting relationship of the melt rock flow with the enclosing suevite, indicating the former crystallized after the latter followed by the calcite vein, 95 X, depth = 851.15 m.

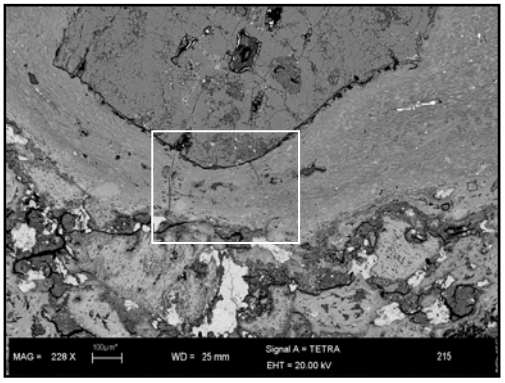

Fig. A.4.83. BSE magnified image of the melt rock shown in Fig. A.4.82, and contact with enclosing suevite, lithic fragment towards top of image is primarily quartz-rich, 228 X, depth = 851.15 m.

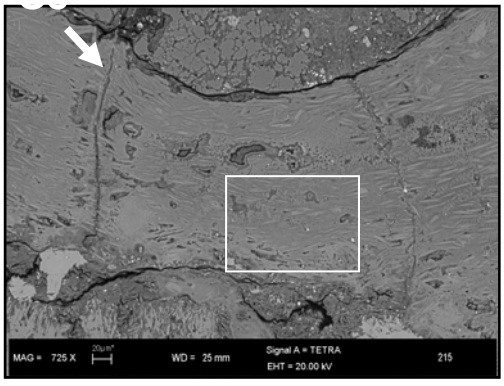

Fig. A.4.84. BSE magnified image of the melt rock shown in Fig. A.4.83, 725 X, depth = 851.15 m.

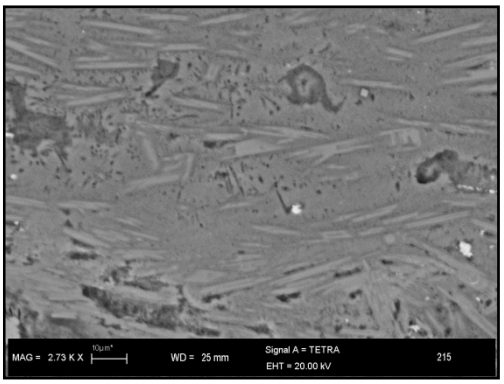

Fig. A.4.85. BSE magnified image of crystallites in melt rock shown in Fig. A.4.84, 2.73 KX, depth = 851.15 m.

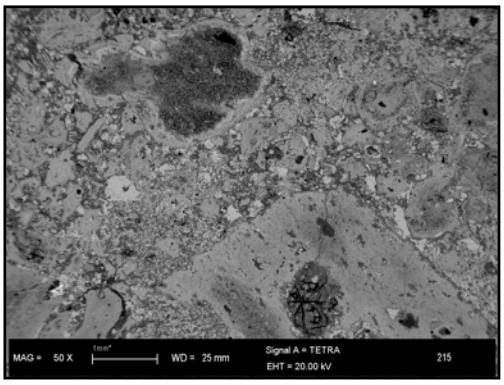

Fig. A.4.86. BSE image of suevite, note the pulverized and compacted nature of the groundmass, 50 X, depth = 851.15 m.

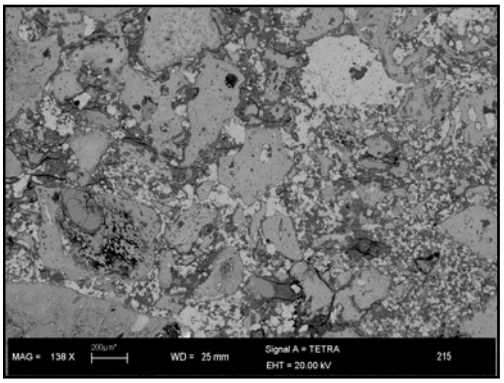

Fig. A.4.87. BSE image of suevite, note the angular and vesiculated character of melt rock particles, 138 X, depth = 851.15 m.

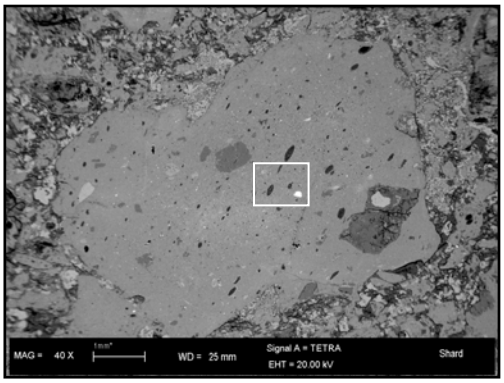

Fig. A.4.88. BSE image of large angular melt rock particle, note the aligned dark vesicles and quartz grain, 40 X, depth = 851.15 m.

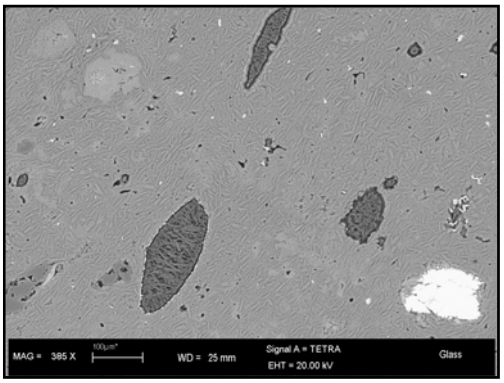

Fig. A.4.89. BSE magnified image of melt rock particle shown in Fig. A.4.88, note the microcrystalline, crystallite rich nature of the groundmass and dark grey vesicles, 385 X, depth = 851.15 m.

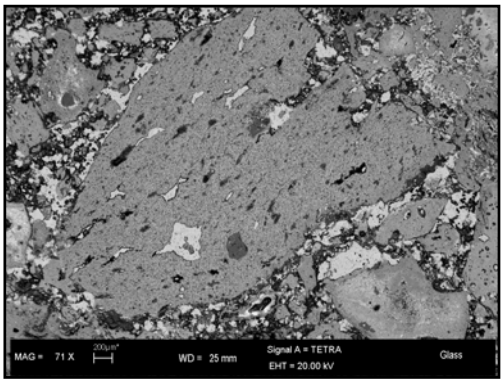

Fig. A.4.90. BSE image of melt rock particle, note the alignment of calcite blebs and inclusions, 71 X, depth = 851.15 m.

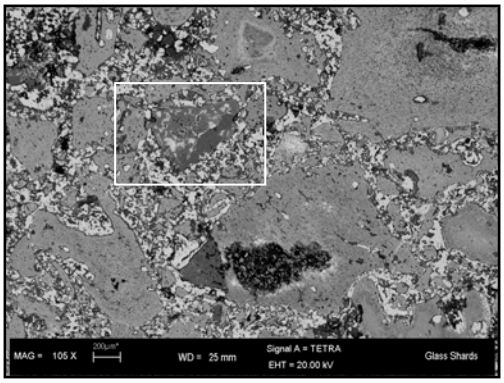

Fig. A.4.91. BSE image of suevite, note the compacted and angular nature of melt rock particles, 105 X, depth = 851.15 m.

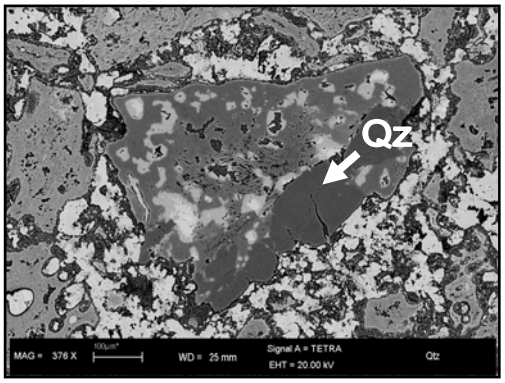

Fig. A.4.92. BSE magnified image of lithic fragment shown in Fig. A.4.91 comprising sodic plagioclase and quartz, 376 X, depth = 851.15 m.

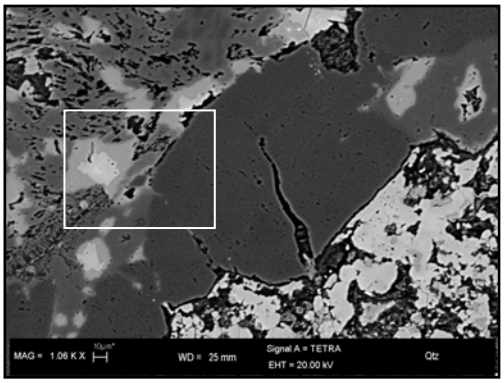

Fig. A.4.93. BSE magnified image of quartz mineral shown in Fig. A.4.92, note the calcite and K-feldspar alteration, 1060 X, depth = 851.15 m.

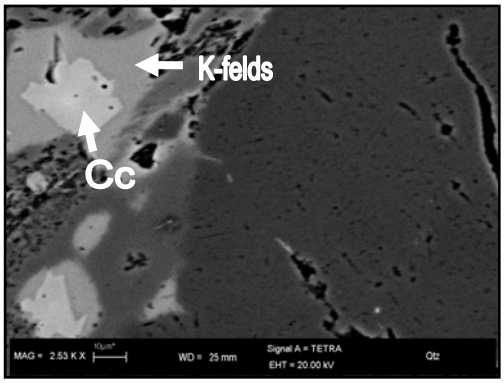

Fig. A.4.93b. BSE magnified image of quartz mineral shown in Fig. A.4.93, note the PDFs striations, 2530 X, depth = 851.15 m.

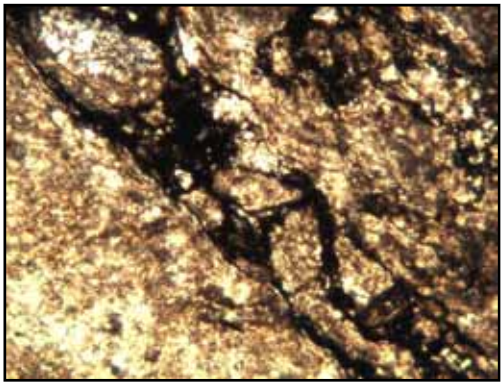

Fig. A.4.94. Plane polarized light image of opaque vein in massive melt rock (Unit 4), 50 X, depth = 875.79 m.

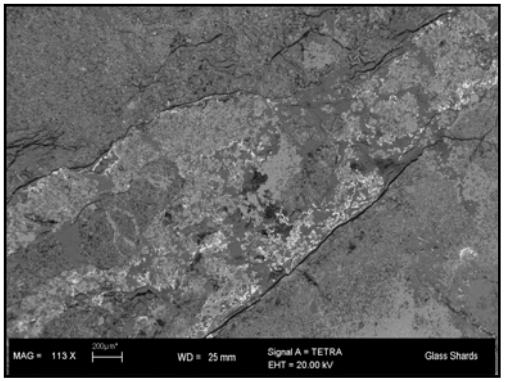

Fig. A.4.95. BSE image of opaque vein in massive melt rock (Unit 4), 113 X, depth = 878.09 m.

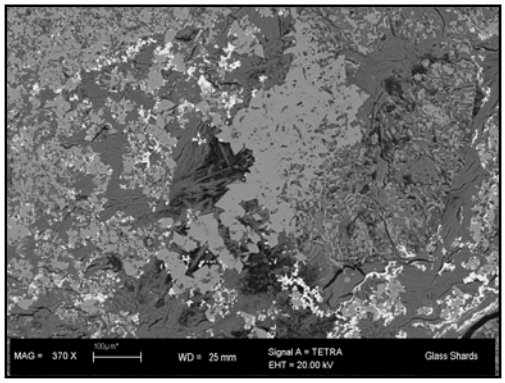

Fig. A.4.96. Magnified BSE image of opaque vein, as shown in Fig. A.4.97, in massive melt rock (Unit 4), note the euhdral K-feldspar crystals and radiating phyllosilicates in open vugs 370 X, depth =

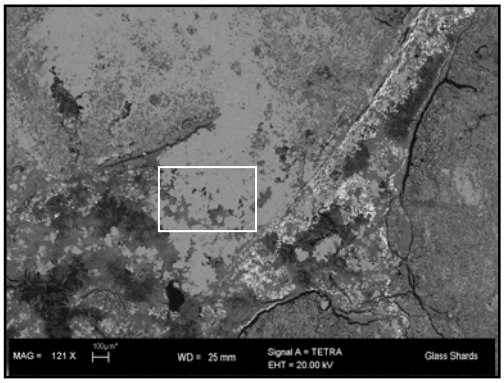

Fig. A.4.97. BSE image of opaque vein in massive melt rock (Unit 4), similar to Fig. A.4.96, 121 X, depth = 878.09 m.

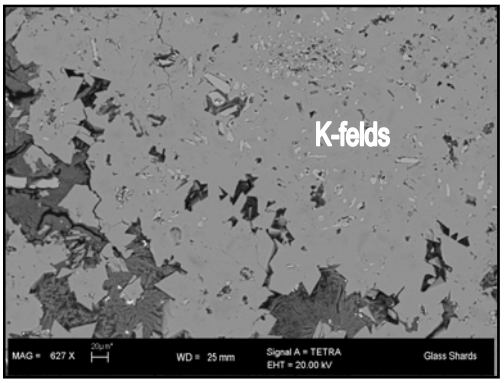

Fig. A.4.98. Magnified BSE image of euhedral K-feldpsar in massive melt rock (Unit 4) with small elongate laths of diopside, as shown in Fig. A.4.97, 627 X,

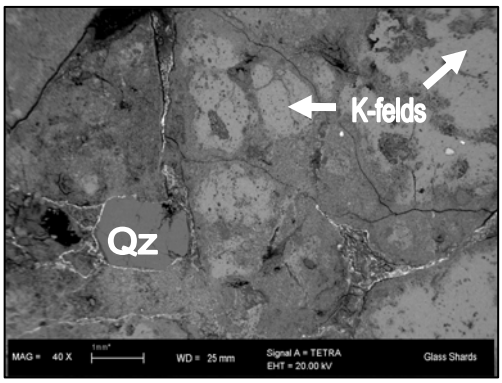

Fig. A.4.99. BSE image of massive melt rock (Unit 4). Note the quartz grain (1.5 mm in width), opaque (Fe) lined fractures, and K-feldspar rich sectors, 40 X, depth = 878.09 m.

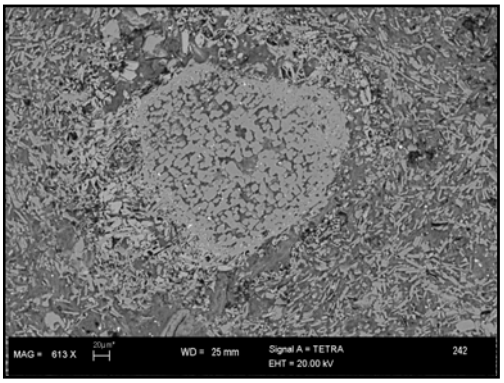

Fig. A.4.100. Magnified BSE image of checkerboard textured plagioclase in microlite rich massive melt rock (Unit 4), 613 X, depth = 878.09 m.

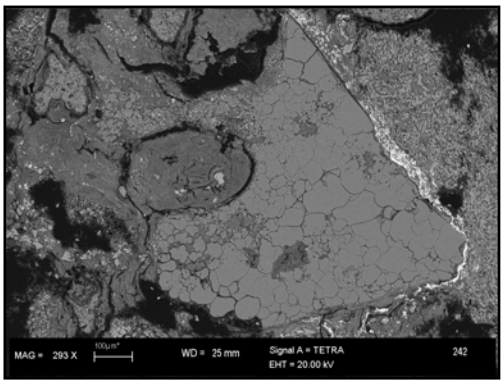

Fig. A.4.101. Magnified BSE image of ballenquartz texture in massive melt rock (Unit 4), 293 X, depth = 878.09 m.

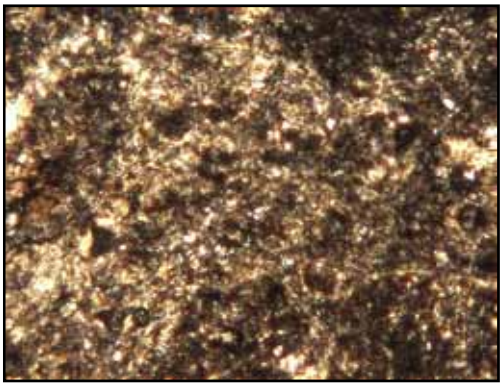

Fig. A.4.102. Plane polarized light image of massive melt rock, 50 X, depth = 879.03 m.

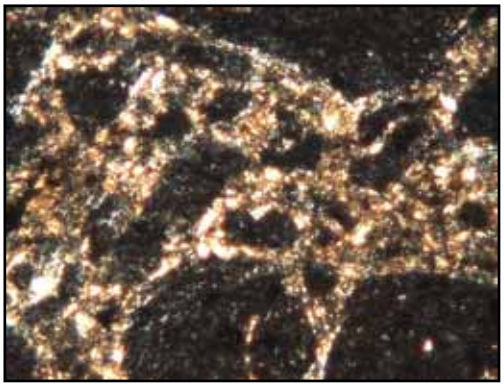

Fig. A.4.103. Cross polarized light image of massive melt rock, note the angular melt rock particles, same region shown in Fig. A.4.102, 50 X, depth = 879.03 m.

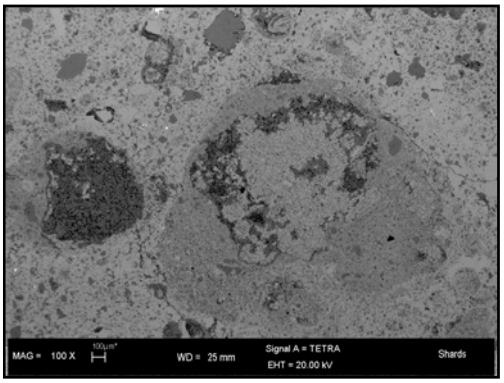

Fig. A.4.104. BSE image of breccia (Unit 5), note the subrounded heterogeneous lithic fragments, 100 X, depth = 886.79 m.

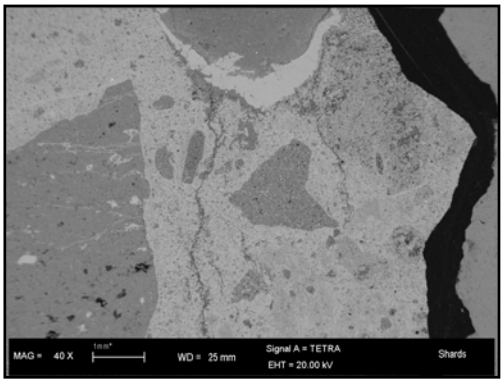

Fig. A.4.105. BSE image of breccia (Unit 5), note the heterogeneous angular melt particles and lithic fragments, 40 X, depth = 886.79 m.

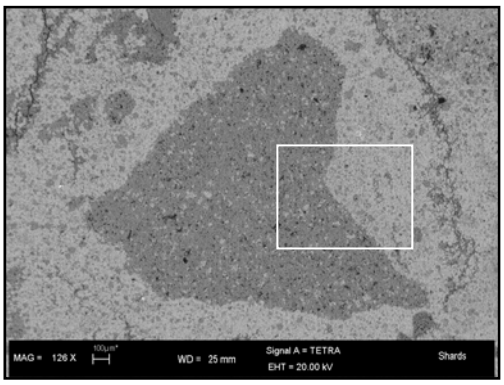

Fig. A.4.106. BSE image of angular dolomite clast in calcite/dolomite groundmass, 126 X, depth = 886.79 m.

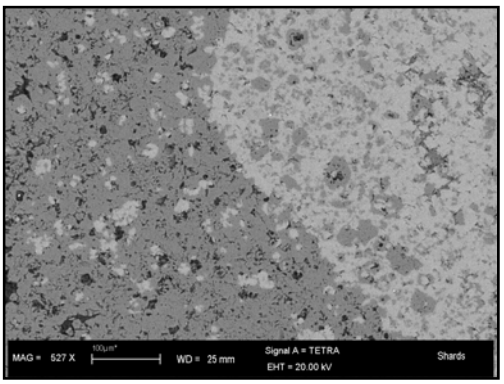

Fig. A.4.107. Magnified BSE image of dolomite clast contact with calcite/dolomite groundmass, as indicated in Fig. A.4.106, 527 X, depth = 886.79 m.

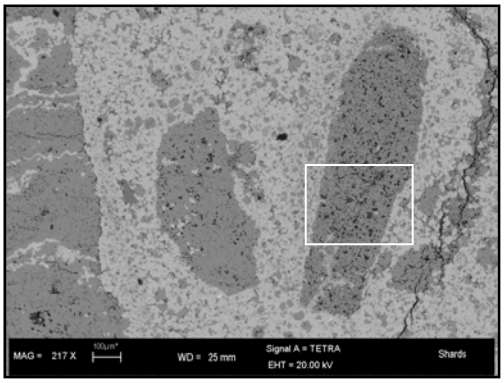

Fig. A.4.108. Magnified BSE image of dolomite clasts in calcite/dolomite groundmass, as shown in Fig. A.4.105, 217 X, depth = 886.79 m.

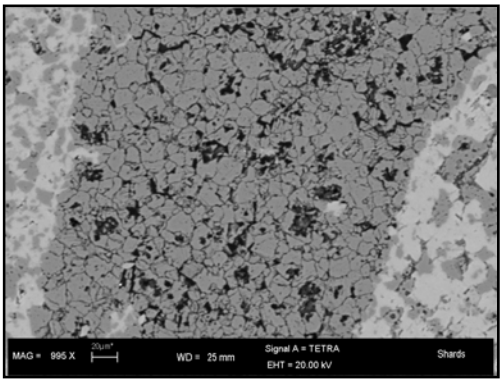

Fig. A.4.109. Magnified BSE image of dolomite clast texture, as shown in Fig. A.4.108, 995 X, depth = 886.79 m.

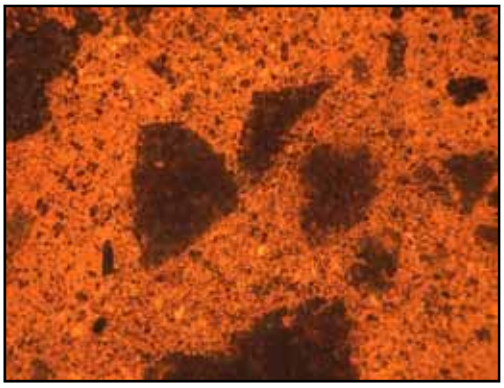

Fig. A.4.110. Cathodoluminescence image of dolomite clasts in calcite-rich groundmass, 50 X, depth = 886.79 m.

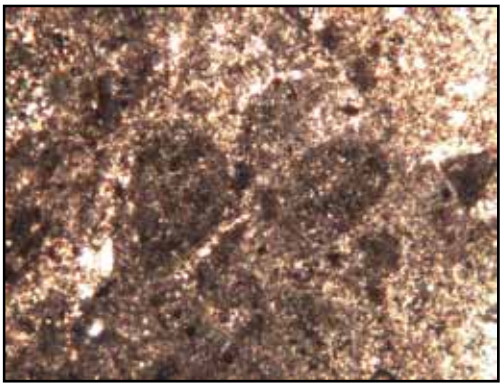

Fig. A.4.111. Plane polarized light image of lithic breccia, same region shown in Fig. A.4.110, 50 X, depth = 886.79 m.

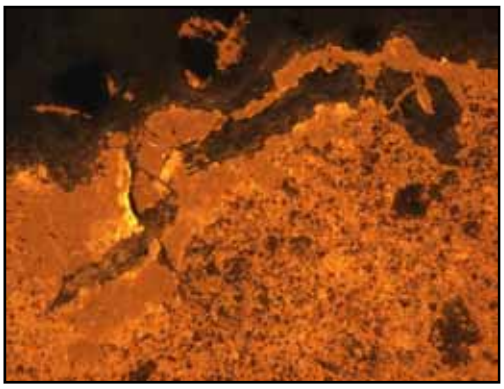

Fig. A.4.112. Cathodoluminescence image of carbonate rich lithic breccia, note the secondary calcite vein compared to the calcite/dolomite groundmass, 50 X, depth = 886.79 m.

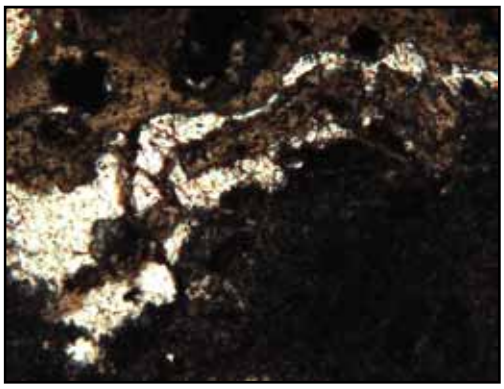

Fig. A.4.113. Plane polarized light image of lithic breccia, note the opaque nature of the carbonate/dolomite groundmass compared to the secondary calcite vein, same region shown in Fig. A.4.112, depth = 886.79 m.

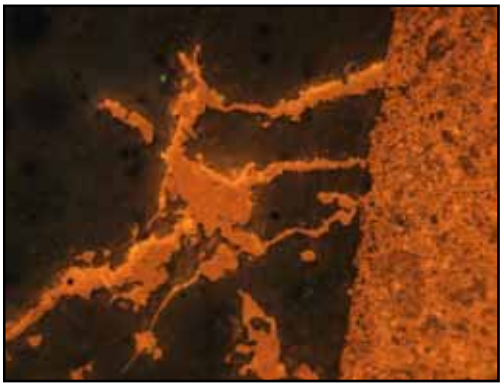

Fig. A.4.114. Cathodoluminescence image of melt rock particle in carbonate groundmass pervaded by calcite veins, 50 X, depth = 886.79 m.

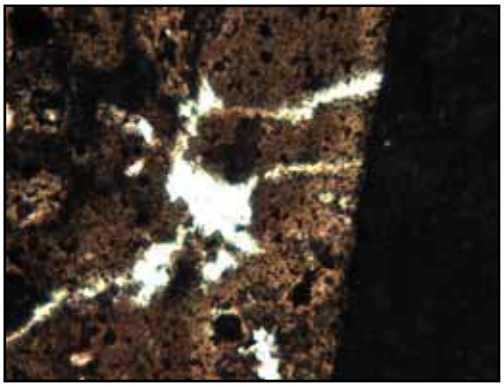

Fig. A.4.115. Plane polarized image of melt rock particle pervaded by calcite veins, same region as shown in Fig. A.4.114, 50 X, depth = 886.79 m.

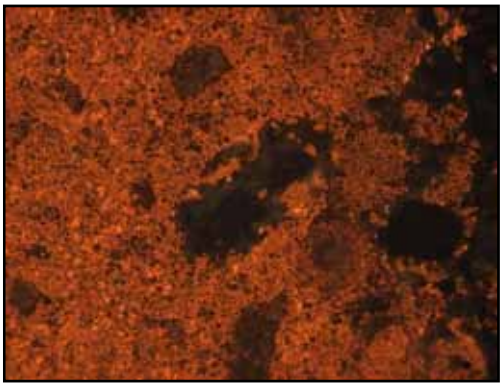

Fig. A.4.116. Cathodoluminescence image of Unit 5 carbonate groundmass, 50 X, depth = 886.79 m.

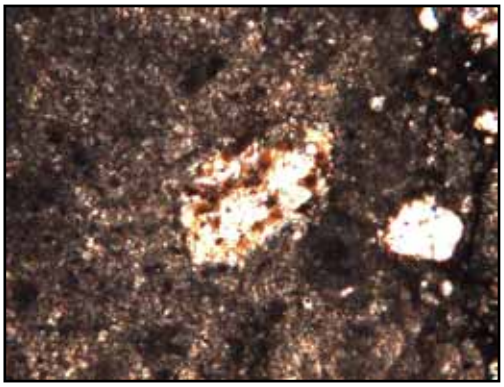

Fig. A.4.117. Plane polarized image of Unit 5 carbonate groundmass, same region as shown in Fig. A.4.116, 50 X, depth = 886.79 m.

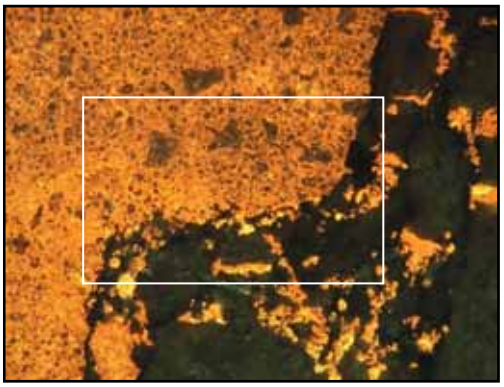

Fig. A.4.118. Cathodoluminescence image of Unit 5 carbonate groundmass, note the angular fragments in the groundmass, 50 X, depth = 888.09 m.

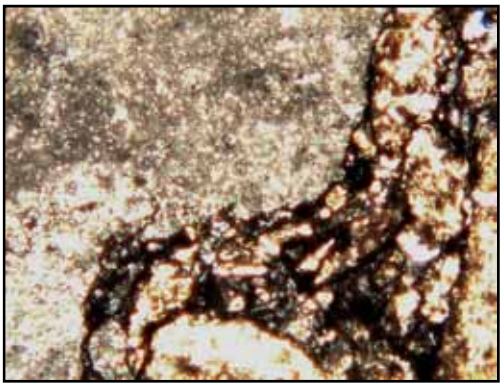

Fig. A.4.119. Plane polarized image of Unit 5 carbonate groundmass, same region as in Fig. A.4.118, note the angular fragments in the groundmass are not obvious, an opaque carbonaceous breccia is to the right, 50 X, depth = 888.09 m.

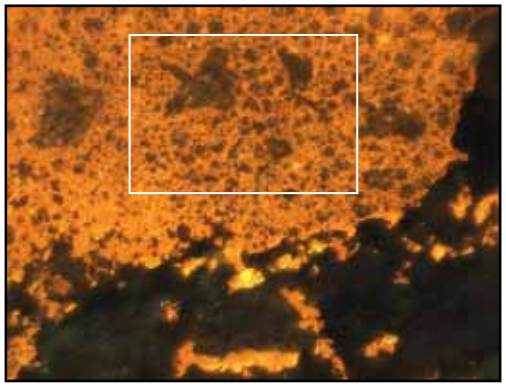

Fig. A.4.120. Cathodoluminescence close up image of Unit 5 carbonate groundmass, region indicated in Fig. A.4.118, note the angular fragments in the groundmass may be dolomite crystals, 100 X, depth = 888.09 m.

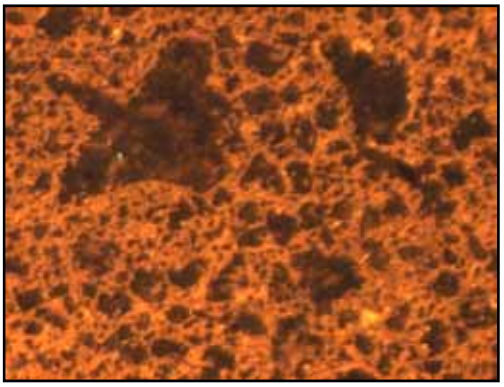

Fig. A.4.121. Cathodoluminescence close up image of Unit 5 carbonate groundmass, region indicated in Fig. A.4.120, note that the angular fragments in the groundmass are most likely dolomite crystals, 200 X, depth = 888.09 m.

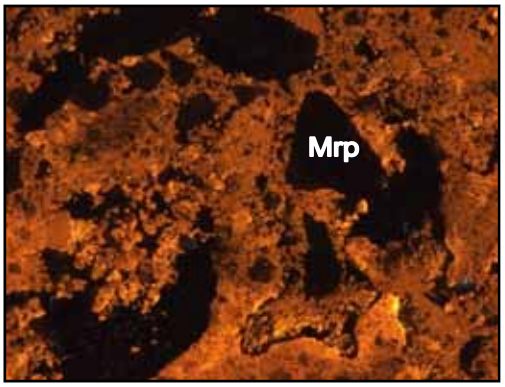

Fig. A.4.122. Cathodoluminescence image of Unit 5 carbonate groundmass, with melt rock particle fragments, 50 X, depth = 888.09 m.

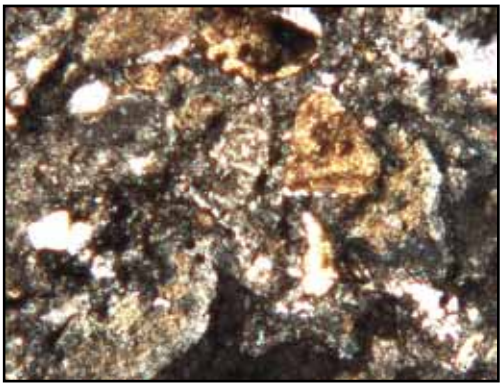

Fig. A.4.123. Plane polarized light image of Unit 5 carbonate groundmass, with melt rock particle fragments, same region as in Fig. A.4.122, 50 X, depth = 888.09 m.

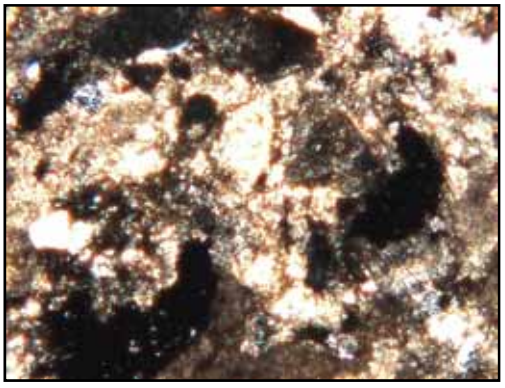

Fig. A.4.124. Cross polarized light image of Unit 5 carbonate groundmass, with isotropic melt rock particle fragments, same region as in Fig. A.4.122, 50 X, depth = 888.09 m.

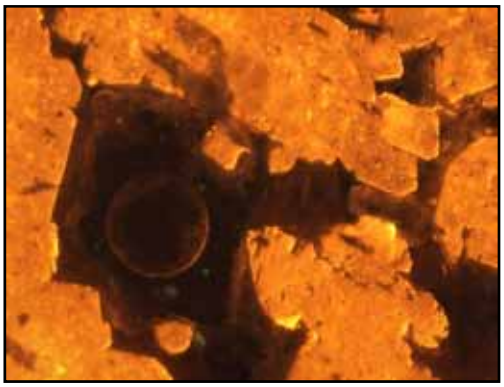

Fig. A.4.125. Cathodoluminescence image of Unit 5 carbonate groundmass with euhedral calcite crystals, 100 X, depth = 888.09 m.

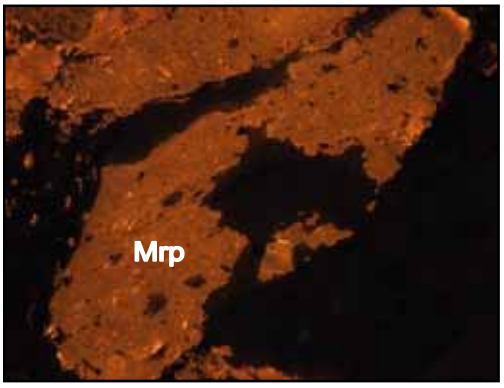

Fig. A.4.126. Cathodoluminescence image of subangular melt rock particle replaced by calcite in Unit 5, 100 X, depth = 888.09 m.

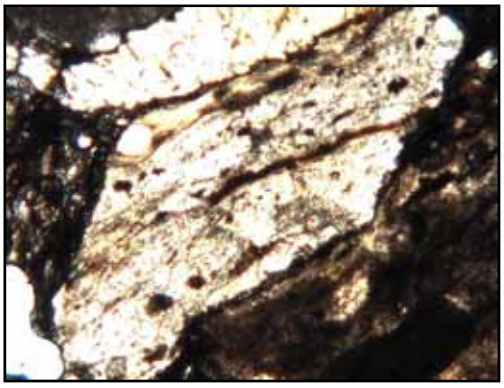

Fig. A.4.127. Plane polarized light image of melt rock particle shown in Fig. A.4.126, note the schlieren texture of the particle, 100 X, depth = 888.09 m.

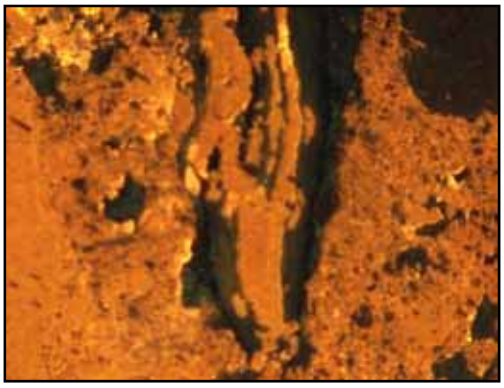

Fig. A.4.128. Cathodoluminescence image of melt rock particle replaced by calcite, 50 X, depth = 888.09 m.

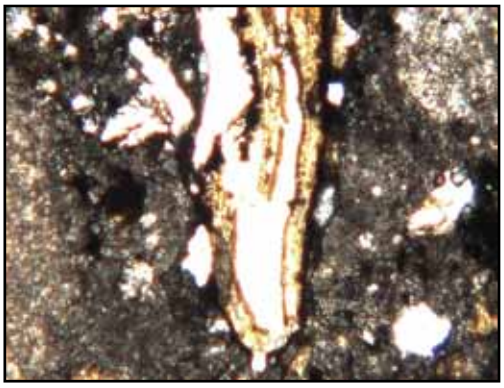

Fig. A.4.129. Plane polarized light image of melt rock particle replaced by calcite, same region as Fig. A.4.128, 50 X, depth = 888.09 m.

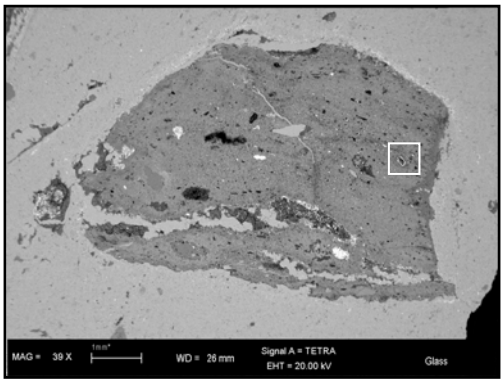

Fig. A.4.130. BSE image of melt rock particle in carbonate groundmass of Unit 5, 39 X, depth = 892.55 m.

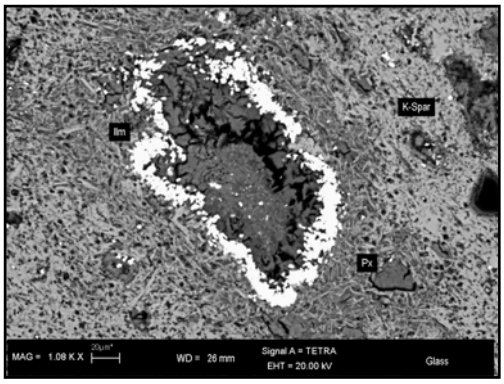

Fig. A.4.131. BSE close up image of fragment with ilmenite rim in melt rock particle shown in Fig. A.4.130, 1080 X, depth = 892.55 m.

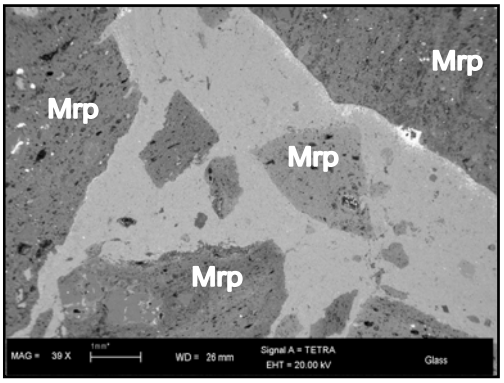

Fig. A.4.132. BSE image of angular melt rock particles in carbonate groundmass, 39 X, depth = 892.55 m.

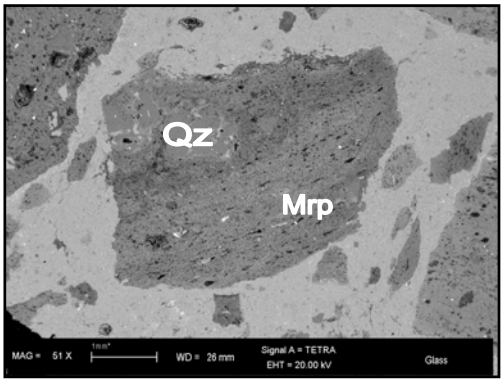

Fig. A.4.133. BSE image of angular melt rock particles in carbonate groundmass, note the large quartz crystals in the large particle, 51 X, depth = 892.55 m.

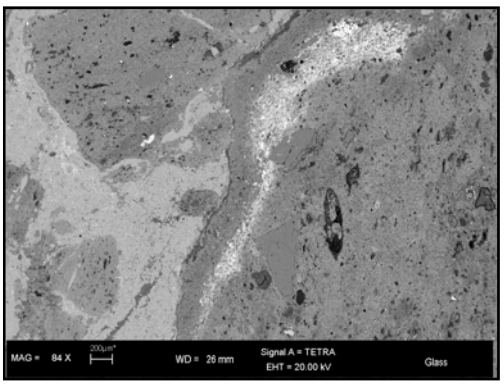

Fig. A.4.134. BSE image of melt rock particles with carbonate groundmass, note the iron-oxide schlieren texture in the large particle, 84 X, depth = 892.55 m.

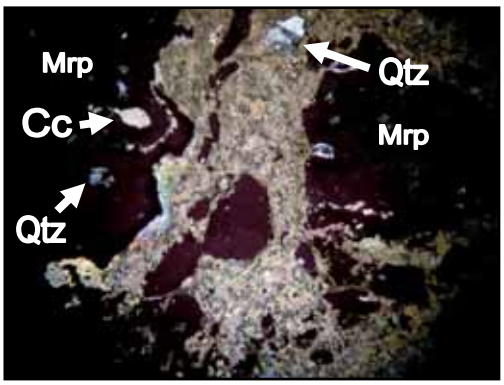

Fig. A.4.135. Cross polarized light image of melt rock particles with carbonate groundmass, note the numerous crystal inclusions in the particles and groundmass, 25 X, depth = 892.55 m.

Fig. A.4.136. Cross polarized light image of angular melt rock particles with carbonate groundmass, note the calcite veins cross cutting the particles, 25 X, depth = 892.55 m.

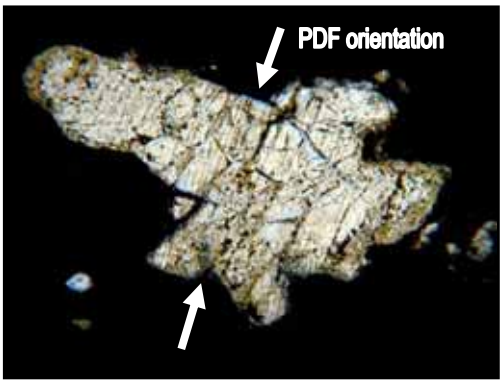

Fig. A.4.137. Cross polarized light image of shocked quartz crystal showing 1 set of PDFs, 100 X, depth = 892.55 m.

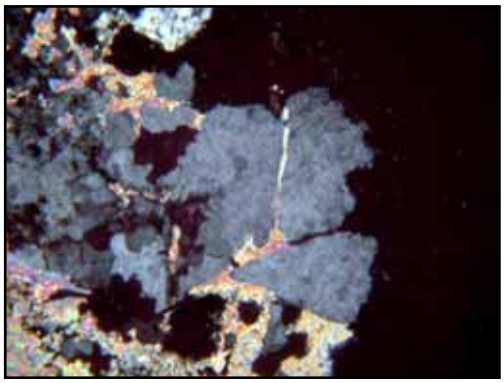

Fig. A.4.138. Cross polarized light image of ballenquartz crystal, 100 X, depth = 892.55 m.

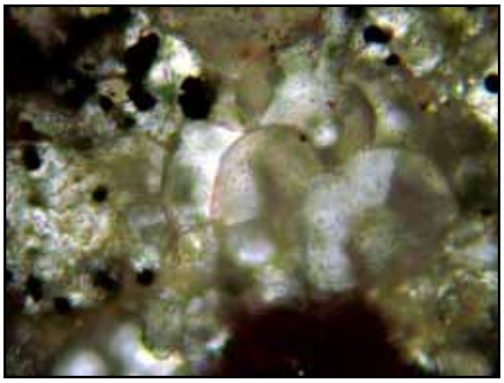

Fig. A.4.139. Plane polarized light image of ballenquartz crystal, 500 X, depth = 892.55 m.

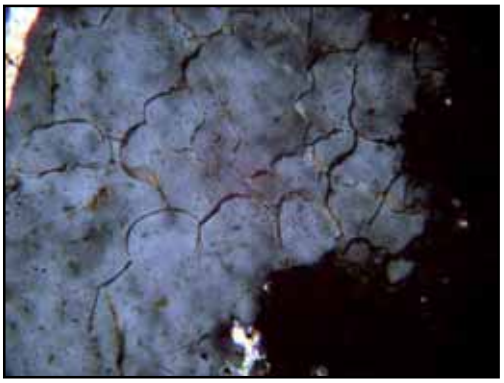

Fig. A.4.141. Cross polarized light image of ballenquartz crystal, 500 X, depth = 892.55 m.

Fig. A.4.142. Cross polarized light image of shocked quartz crystal showing 1 set of PDFs, 500 X, depth = 892.55 m.

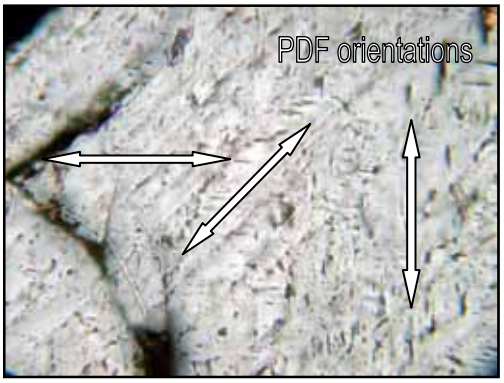

Fig. A.4.143. Cross polarized light image of shocked quartz crystal showing 3 sets of PDFs, 500 X, depth = 892.55 m.

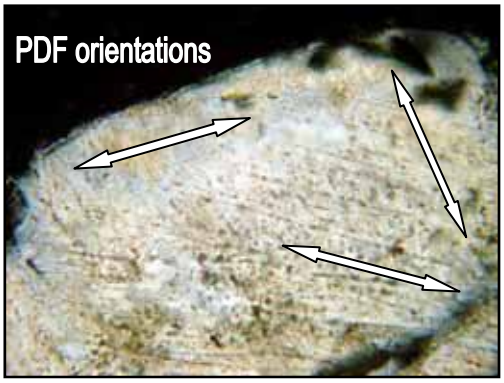

Fig. A.4.143. Cross polarized light image of shocked quartz crystal showing 3 sets of PDFs, 500 X, depth = 892.55 m.

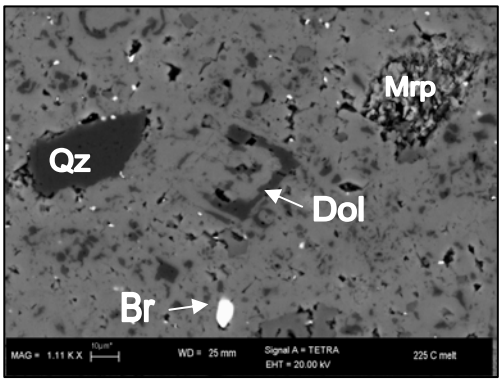

Fig. A.4.144. BSE magnified image of Unit 5 carbonate groundmass containing quartz, dolomite, a small melt rock particle, and barite, 1110 X, depth = 892.55 m.

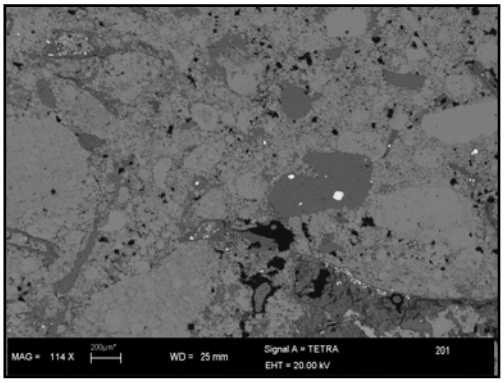

Fig. A.4.145. BSE magnified image of lithic breccia in injection dyke, 114 X, depth = 916.36 m.

Fig. A.4.146. BSE image of lithic breccia in injection dyke with melt rock particle, note the quartz crystal with shocked isotropic patches in the center of the image 50 X, depth = 916.36 m.

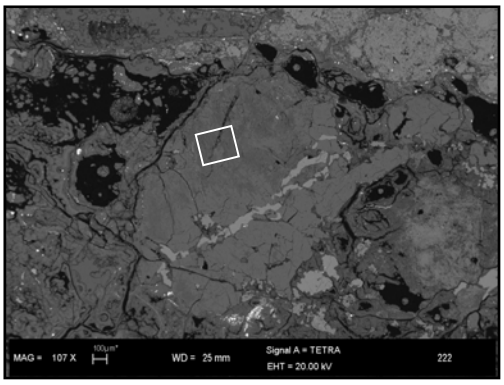

Fig. A.4.147. BSE image of quartz crystal imaged in Fig. A.4.146, 107 X, depth = 916.36 m.

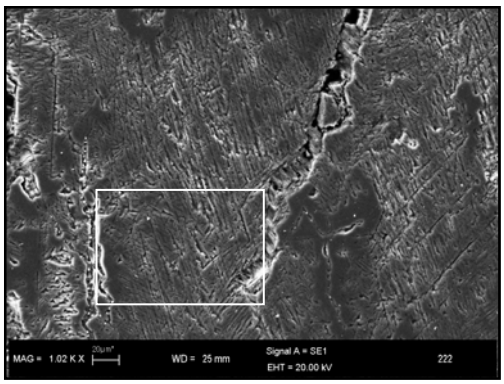

Fig. A.4.148. Scanning electron magnified image of quartz crystal imaged in Fig. A.4.147 showing 4 sets of PDFs, 1020 X, depth = 916.36 m.

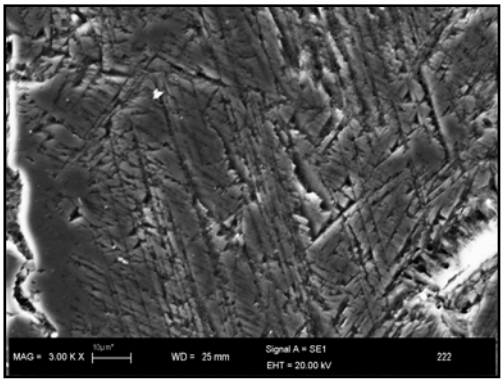

Fig. A.4.149. Scanning electron magnified image of PDFs in quartz crystal imaged in Fig. A.4.148 showing 4 sets of PDFs, 3000 X, depth = 916.36 m.

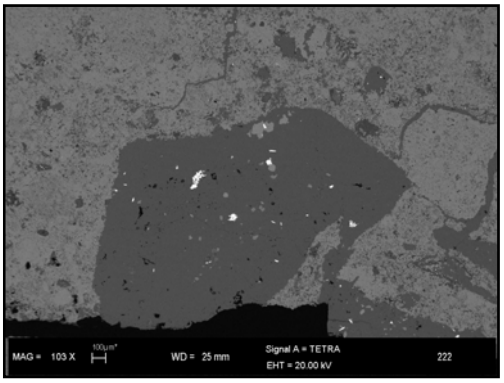

Fig. A.4.150. BSE image of analcime crystal (dark grey), 103 X, depth = 916.36 m.

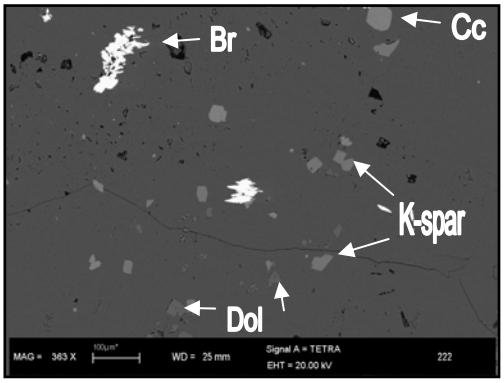

Fig. A.4.151. BSE magnified image of analcime crystal with barite, K-feldspar, calcite, dolomite secondary minerals in its interior, 363 X, depth = 916.36 m.

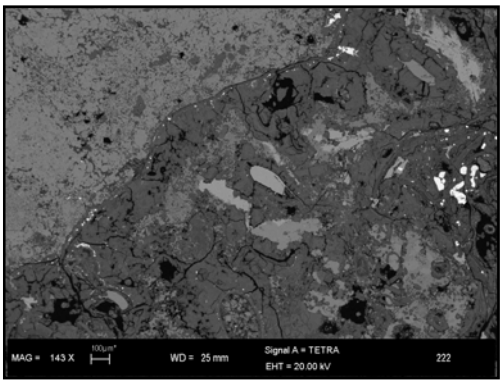

Fig. A.4.152. BSE image of melt rock particle in injection dyke, 363 X, depth = 916.36 m.

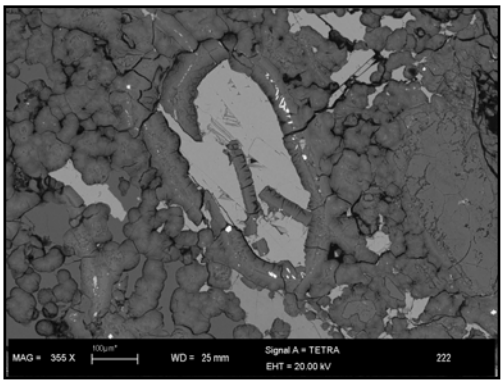

Fig. A.4.153. BSE magnified image of melt rock particle vesicle, note the perlitic devitrification texture, vesicle is infilled by anhydrite, 355 X, depth = 916.36 m.

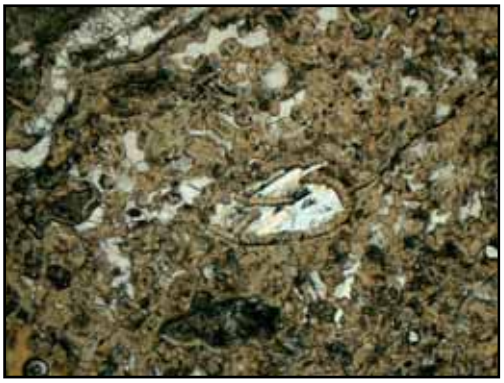

Fig. A.4.154. Plane polarized light image of melt rock particle vesicle, same region as Fig. A.4.153, 32 X, depth = 916.36 m.

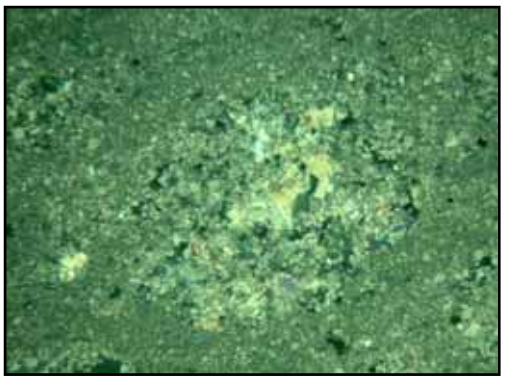

Fig. A.4.155. Cross polarized light image of dolomite with interstitial anhydrite, 100 X, depth = 1313.53 m.

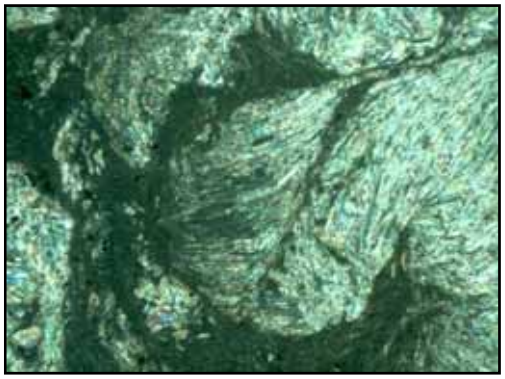

Fig. A.4.156. Cross polarized light image of flow textured anhydrite, 32 X, depth = 1314.83 m.

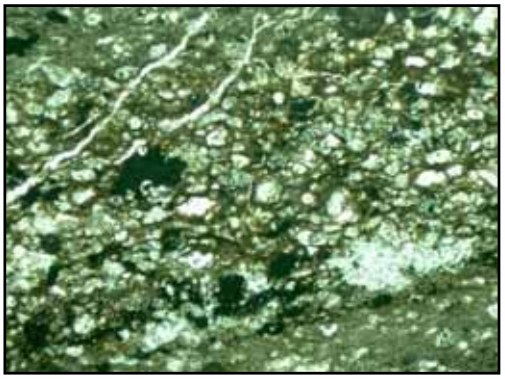

Fig. A.4.157. Plane polarized light image of oil shale, 32 X, depth = 1316.06 m.

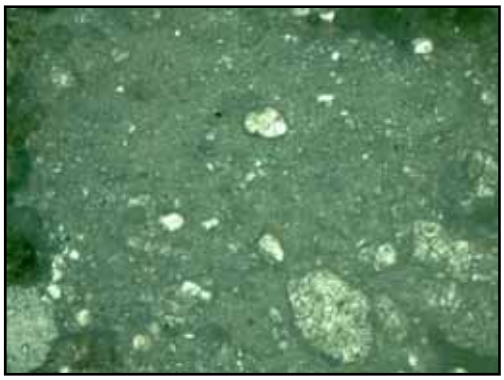

Fig. A.4.158. Plane polarized light image of lithic breccia, 32 X, depth = 1341.61 m.

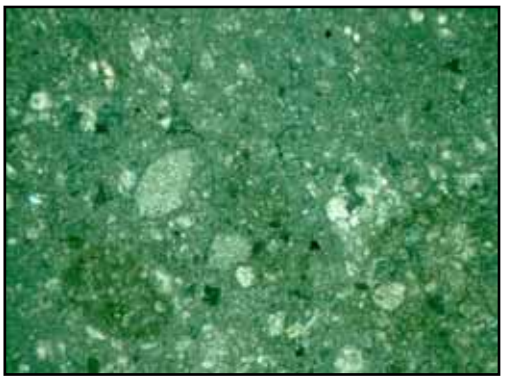

Fig. A.4.159. Plane polarized light image of heterolithic breccia, 32 X, depth = 1341.81 m.

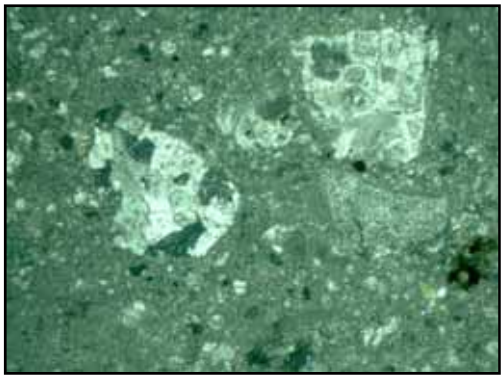

Fig. A.4.160. Plane polarized light image of heterolithic breccia, 32 X, depth = 1342.91 m.

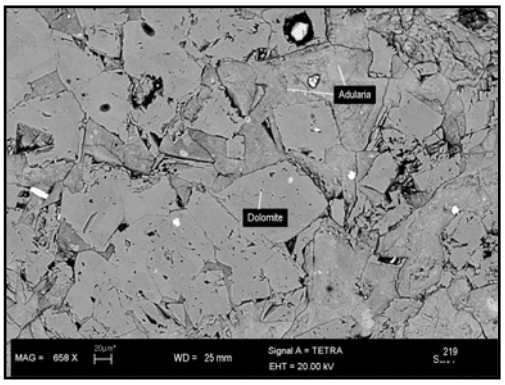

Fig. A.4.161. BSE image of illite with euhedral dolomite crystals, 658 X, depth = 1347.56 m.

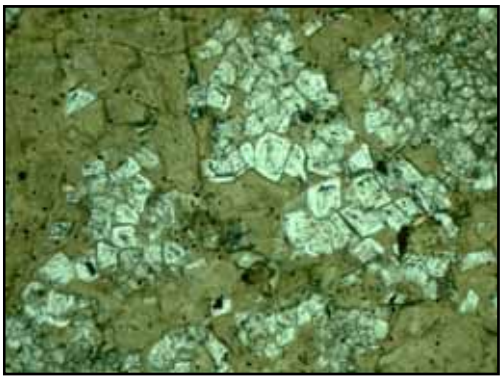

Fig. A.4.162. Plane polarized light image of illite with euhedral zoned dolomite crystals, 32 X, depth = 1347.56 m.

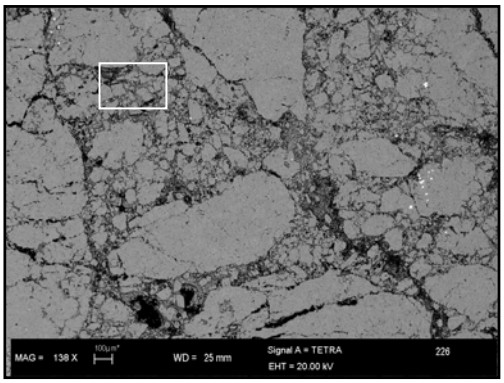

Fig. A.4.163. BSE image of lithic breccia, 138 X, depth = 1348.31 m.

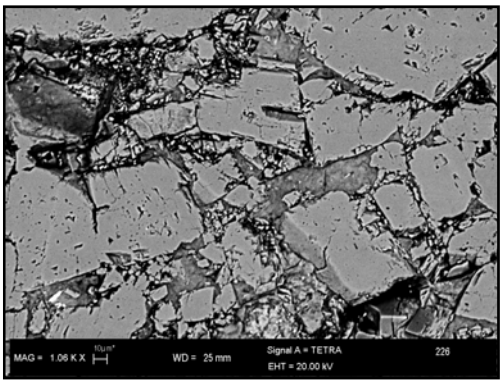

Fig. A.4.164. BSE magnified image of lithic breccia, shown in Fig. A.4.163, 1060 X, depth = 1348.31 m.

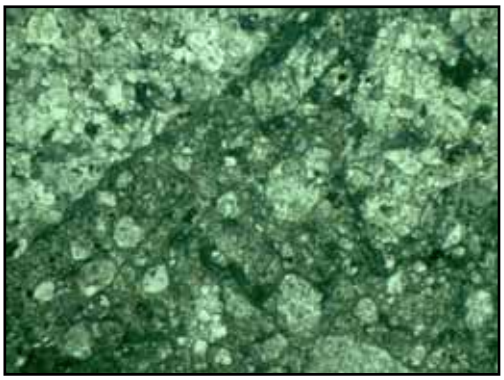

Fig. A.4.165. Cross polarized light image of lithic breccia, 32 KX, depth = 1348.31 m.

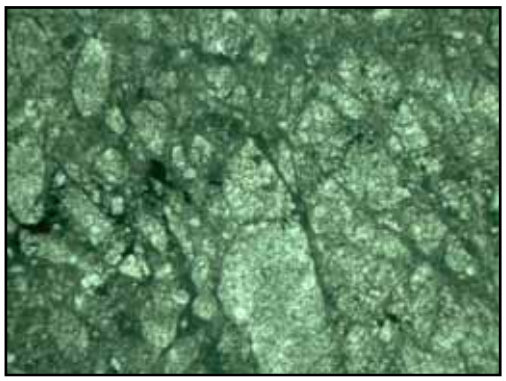

Fig. A.4.166. Cross polarized light image of lithic breccia, 32 X, depth = 1348.31 m.

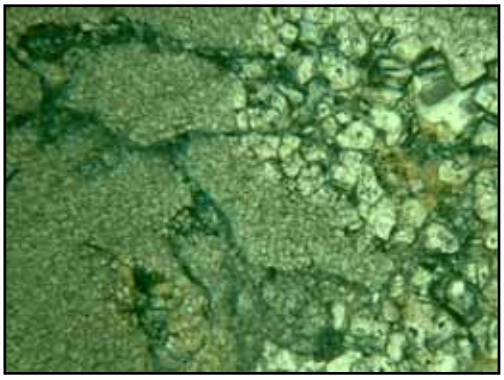

Fig. A.4.167. Cross polarized light image of lithic breccia with recrystallization texture (right of image), 100 X, depth = 1348.31 m.

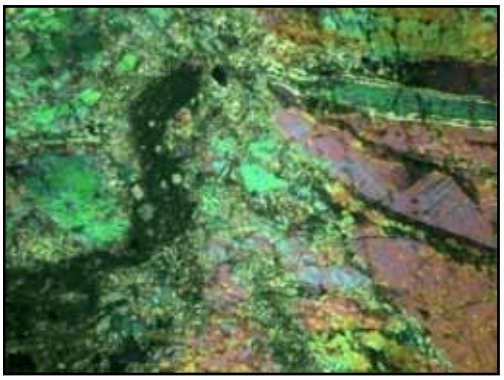

Fig. A.4.168. Cross polarized light image of shattered anhydrite crystals, 32 X, depth = 1348.32 m.

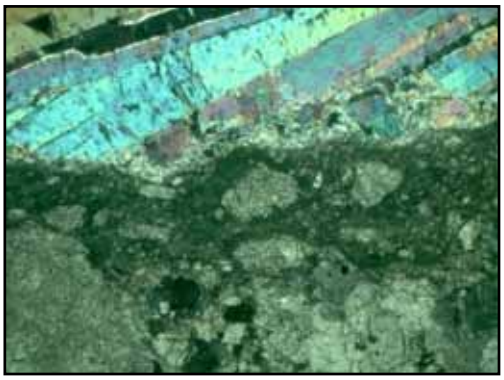

Fig. A.4.169. Cross polarized light image of lithic breccia along dolomite – anhydrite contact, 32 X, depth = 1348.32 m.

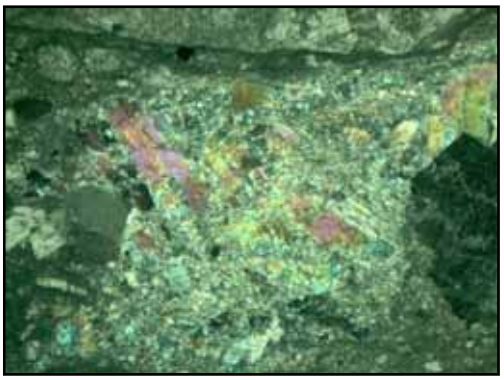

Fig. A.4.170. Cross polarized light image of lithic breccia along dolomite – anhydrite contact, 32 X, depth = 1348.32 m.

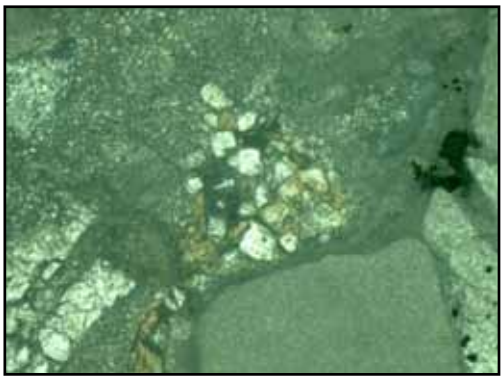

Fig. A.4.171. Cross polarized light image of lithic breccia with recrystallization texture, 32 X, depth = 1348.32 m.

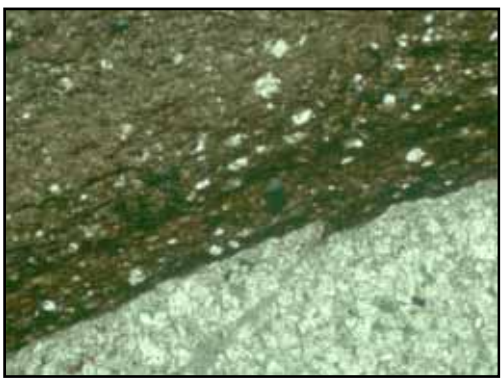

Fig. A.4.171. Plane polarized light image of oil shale with dolomite contact, note the small dextral fault offset, 32 X, depth = 1369.52 m.

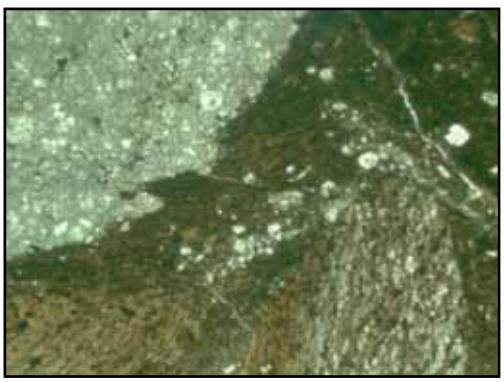

Fig. A.4.172. Plane polarized light image of oil shale with lithic breccia contact, 32 X, depth = 1372.87 m.

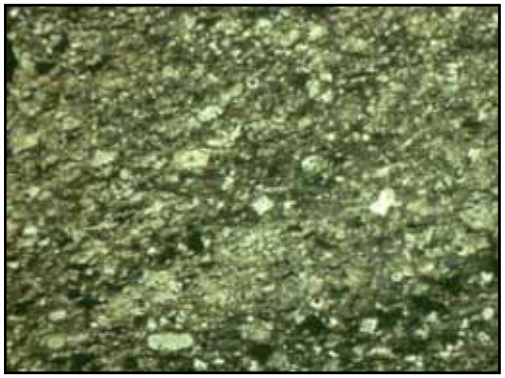

Fig. A.4.173. Plane polarized light image of oil shale, 32 X, depth = 1381.64 m.

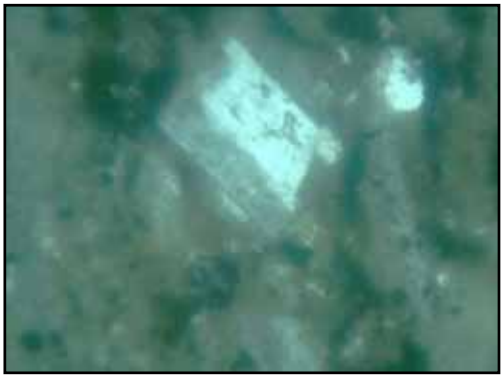

Fig. A.4.174. Cross polarized light magnified image of simple twinned plagioclase crystal in oil shale imaged in Fig. A.4.173, 32 X, depth = 1381.64 m.

Appendix A.5.
Electron microprobe results (Chapter 2)

EMPA spot ID abreviations

Br. M.R.P.	Brown melt rock particle
Cc	Calcite
Chck Pl	Checkerboard feldspar
Felds	Feldspar
Fe M.R.P.	Iron-rich melt rock particle
Gdm	Groundmass
K-felds	K-feldspar
Meso	Mesostasis
Mic	Microlite
Mf. gr.	Mafic grain
Mf. M.R.P.	Mafic melt rock particle
M.R.P.	Melt rock particle
Pl	Plagioclase
Vesc. fill	Vesicle fill
Vesc. rim	Vesicle rim

Table A.5. EMPA results used in Chapter 2

Analysis #	Sample #	Batch #	Depth (m)	Comment	SiO_2	TiO_2	Al_2O_3	Cr_2O_3	FeO_{tot}	MnO	MgO	CaO	Na_2O	K_2O	Total
1	210	1-1	827.13	M.R.P.	47.37	0.31	15.85	n.d.	3.62	n.d.	5.57	1.73	1.01	2.92	78.38
2	210	1-2	827.13	M.R.P.	47.67	1.30	16.54	n.d.	3.54	n.d.	5.45	2.51	1.14	2.52	80.67
3	210	1-3	827.13	M.R.P.	49.22	0.41	15.69	n.d.	4.66	0.11	5.71	0.79	0.17	3.71	80.47
4	210	1-4	827.13	M.R.P.	48.43	0.37	15.38	n.d.	3.95	n.d.	5.88	0.45	0.27	3.38	78.11
5	210	1-5	827.13	M.R.P.	63.87	0.05	18.10	n.d.	0.32	n.d.	0.32	0.57	0.11	16.08	99.42
6	210	1-6	827.13	M.R.P.	61.09	0.23	18.07	n.d.	1.14	n.d.	1.65	4.09	0.84	12.15	99.26
7	210	1-7	827.13	M.R.P.	61.86	0.39	18.95	n.d.	0.76	n.d.	0.93	2.99	1.33	12.31	99.52
8	210	1-8	827.13	M.R.P.	63.33	0.12	17.88	n.d.	0.63	n.d.	0.65	1.33	0.25	14.93	99.12
9	210	1-9	827.13	M.R.P.	46.24	0.65	15.23	n.d.	3.13	n.d.	6.61	3.91	2.33	2.30	80.40
10	210	1-10	827.13	M.R.P.	47.23	0.30	13.35	n.d.	4.59	n.d.	8.40	0.36	0.28	3.28	77.79
11	210	1-11	827.13	M.R.P.	48.03	0.68	13.28	n.d.	4.76	n.d.	9.20	0.38	0.18	3.30	79.81
12	210	1-12	827.13	M.R.P.	49.59	0.54	15.44	n.d.	5.04	n.d.	7.49	0.61	0.27	3.93	82.91
13	210	1-13	827.13	M.R.P.	53.54	0.51	16.64	n.d.	4.79	n.d.	6.22	0.20	0.21	4.26	86.37
14	210	1-14	827.13	M.R.P.	51.67	0.43	16.44	n.d.	4.80	n.d.	6.09	0.24	0.25	4.09	84.01
15	210	1-15	827.13	M.R.P.	53.04	0.41	16.44	n.d.	4.78	n.d.	6.00	0.19	0.25	4.22	85.33
16	210	1-16	827.13	M.R.P.	51.60	0.53	16.44	0.06	4.38	n.d.	5.79	0.29	0.27	3.84	83.20
17	210	1-17	827.13	M.R.P.	50.40	0.40	15.38	n.d.	5.35	n.d.	5.84	0.28	0.28	4.28	82.21
18	210	1-18	827.13	M.R.P.	48.71	0.37	15.36	n.d.	5.31	n.d.	5.64	0.23	0.23	4.13	79.98
19	210	1-19	827.13	M.R.P.	49.33	0.86	15.50	n.d.	5.35	n.d.	6.15	0.90	0.65	4.06	82.80
20	210	1-20	827.13	M.R.P.	51.79	0.46	16.54	n.d.	4.90	n.d.	5.68	0.31	0.28	4.40	84.36
21	210	2-1	827.13	K-felds	61.21	0.32	18.95	n.d.	0.72	n.d.	0.65	3.08	0.98	12.60	98.51
22	210	2-2	827.13	K-felds	61.70	0.60	18.45	n.d.	0.80	n.d.	0.85	3.08	0.97	12.44	98.89
23	210	2-3	827.13	K-felds	61.69	0.23	17.23	n.d.	0.88	n.d.	1.35	2.79	0.47	13.85	98.49
24	210	2-4	827.13	K-felds	62.89	0.07	17.51	0.05	0.44	n.d.	0.65	1.27	0.17	15.52	98.57
25	210	2-5	827.13	K-felds	58.81	0.27	16.82	n.d.	1.71	n.d.	2.12	5.99	1.18	10.09	96.99
26	210	2-6	827.13	Mic	49.34	0.09	20.52	n.d.	2.68	n.d.	1.83	7.77	3.66	1.18	87.07
27	210	2-7	827.13	Mic	51.87	1.37	23.91	n.d.	2.44	n.d.	1.44	8.54	3.62	1.36	94.55
28	210	2-8	827.13	Mic	50.66	0.78	23.70	n.d.	2.31	n.d.	1.27	9.16	3.89	0.99	92.76
29	210	2-9	827.13	Mic	53.37	0.81	24.44	n.d.	2.07	n.d.	0.96	9.32	3.94	1.40	96.31
30	210	2-10	827.13	Mic	46.46	0.87	18.79	n.d.	2.73	n.d.	3.77	5.92	2.44	1.79	82.77
31	210	2-11	827.13	Vesc. fill	41.69	n.d.	5.58	n.d.	3.67	n.d.	21.18	1.33	0.12	n.d.	73.57
32	210	2-12	827.13	Vesc. fill	40.23	n.d.	5.17	n.d.	3.44	n.d.	20.84	1.27	0.17	n.d.	71.12
33	210	2-13	827.13	Vesc. fill	47.08	0.09	14.35	n.d.	2.65	n.d.	7.32	1.49	0.41	1.98	75.37
34	210	2-14	827.13	Vesc. fill	46.94	0.07	14.10	n.d.	2.58	n.d.	7.38	1.53	0.41	1.92	74.93
35	210	2-15	827.13	Vesc. fill	47.74	n.d.	14.82	n.d.	2.59	n.d.	6.78	0.89	0.38	2.06	75.26
36	210	2-16	827.13	Vesc. rim	56.55	0.22	18.26	n.d.	3.09	n.d.	6.22	1.55	0.32	2.67	88.88
37	210	2-17	827.13	Vesc. rim	50.70	0.23	16.25	n.d.	2.73	n.d.	6.88	2.01	0.33	2.62	81.75
38	210	2-18	827.13	Vesc. rim	43.09	0.13	13.98	n.d.	2.16	n.d.	5.30	1.16	0.29	2.06	68.17
39	210	2-19	827.13	Vesc. rim	53.06	0.19	17.64	n.d.	2.75	n.d.	6.35	0.95	0.27	2.42	83.63
40	210	2-20	827.13	Vesc. rim	51.86	0.18	17.03	n.d.	2.66	n.d.	6.71	1.83	0.29	2.55	83.11
41	210	3-1	827.13	M.R.P.	49.78	0.39	13.87	n.d.	6.11	n.d.	7.60	0.21	0.30	4.59	82.85
42	210	3-2	827.13	M.R.P.	49.24	0.41	14.36	n.d.	6.10	n.d.	6.77	0.28	0.32	4.58	82.06
43	210	3-3	827.13	M.R.P.	50.14	0.46	14.33	n.d.	6.11	n.d.	6.57	0.74	0.56	4.14	83.05
44	210	3-4	827.13	M.R.P.	51.28	0.42	15.28	0.06	5.34	n.d.	5.91	0.27	0.39	4.06	83.01
45	210	3-5	827.13	M.R.P.	52.98	0.46	15.70	n.d.	6.34	n.d.	6.03	0.22	0.26	4.22	86.21
46	210	3-6	827.13	M.R.P.	50.10	0.47	14.87	n.d.	6.02	n.d.	6.72	0.60	0.33	4.04	83.15
47	210	3-7	827.13	M.R.P.	50.56	0.31	13.50	n.d.	4.88	n.d.	9.93	1.58	0.89	2.67	84.32
48	210	3-8	827.13	M.R.P.	50.64	0.38	14.53	n.d.	5.04	n.d.	9.21	1.16	0.64	3.15	84.75
49	210	3-9	827.13	M.R.P.	53.00	0.42	16.83	n.d.	5.58	n.d.	5.30	1.60	0.88	3.75	87.36
50	210	3-10	827.13	M.R.P.	48.83	0.43	14.49	n.d.	5.72	n.d.	6.85	0.84	0.56	3.60	81.32

Table A.5. *Continued*

Analysis #	Sample #	Batch #	Depth (m)	Comment	SiO_2	TiO_2	Al_2O_3	Cr_2O_3	FeO_{tot}	MnO	MgO	CaO	Na_2O	K_2O	Total
51	210	3-11	827.13	M.R.P.	52.67	0.45	16.50	n.d.	6.09	0.10	5.67	0.37	0.17	4.15	86.17
52	210	3-12	827.13	M.R.P.	49.97	0.40	15.11	0.05	6.15	n.d.	5.71	0.32	0.23	4.22	82.16
53	210	3-13	827.13	M.R.P.	52.66	0.32	17.36	n.d.	3.72	n.d.	5.27	0.54	0.37	3.20	83.44
54	210	3-14	827.13	M.R.P.	39.96	0.09	13.07	n.d.	4.55	n.d.	13.74	0.92	0.21	1.63	74.17
55	210	3-15	827.13	M.R.P.	39.41	0.07	13.55	n.d.	4.39	n.d.	17.60	1.11	0.16	1.22	77.51
56	210	3-16	827.13	M.R.P.	32.77	n.d.	10.03	n.d.	3.71	n.d.	13.96	10.37	0.16	0.88	71.88
57	210	3-17	827.13	M.R.P.	50.74	0.48	14.98	n.d.	5.70	n.d.	6.02	0.62	0.41	3.94	82.89
58	210	3-18	827.13	M.R.P.	49.38	0.43	14.31	n.d.	5.81	n.d.	7.07	0.77	0.26	3.79	81.82
59	210	3-19	827.13	M.R.P.	47.17	0.43	13.33	n.d.	6.00	n.d.	6.80	0.74	0.39	4.11	78.97
60	210	3-20	827.13	M.R.P.	49.83	0.52	14.13	n.d.	7.53	n.d.	6.12	0.47	0.41	5.67	84.68
61	210	4-1	827.13	M.R.P.	59.16	1.53	20.63	n.d.	0.97	n.d.	0.52	4.33	2.15	9.68	98.97
62	210	4-2	827.13	M.R.P.	60.43	0.64	16.60	n.d.	1.19	n.d.	2.11	4.80	0.81	11.85	98.43
63	210	4-3	827.13	M.R.P.	60.00	0.28	20.57	n.d.	0.71	n.d.	0.21	4.05	2.21	9.80	97.83
64	210	4-4	827.13	M.R.P.	60.03	1.08	19.51	n.d.	0.87	n.d.	0.68	3.97	1.56	10.60	98.30
65	210	4-5	827.13	M.R.P.	61.38	0.27	19.96	n.d.	0.71	n.d.	0.49	3.49	1.20	12.03	99.53
66	210	4-6	827.13	M.R.P.	64.29	0.08	17.99	n.d.	0.21	n.d.	0.34	0.70	0.17	15.67	99.45
67	210	4-7	827.13	M.R.P.	60.37	0.55	16.59	n.d.	1.58	n.d.	2.28	4.49	0.30	12.97	99.13
68	210	4-8	827.13	M.R.P.	60.16	1.47	19.15	n.d.	0.69	n.d.	0.53	2.59	1.39	12.29	98.27
69	210	4-9	827.13	M.R.P.	58.82	1.15	20.22	n.d.	1.22	n.d.	0.97	5.37	2.05	8.95	98.75
70	210	4-10	827.13	M.R.P.	57.87	0.56	18.55	n.d.	1.75	n.d.	2.61	7.17	1.87	8.25	98.63
71	210	4-11	827.13	M.R.P.	59.84	0.36	19.26	n.d.	1.15	n.d.	1.39	5.77	1.69	9.62	99.08
72	210	4-12	827.13	M.R.P.	62.79	0.37	18.05	n.d.	0.57	n.d.	0.60	2.01	0.75	13.44	98.58
73	210	4-13	827.13	M.R.P.	61.53	0.43	19.09	n.d.	0.92	n.d.	1.01	4.28	1.58	10.98	99.82
74	210	4-14	827.13	M.R.P.	61.50	0.23	16.03	n.d.	1.34	n.d.	2.13	4.53	0.33	13.16	99.25
75	210	4-15	827.13	M.R.P.	59.47	0.94	20.80	n.d.	1.06	n.d.	0.73	5.70	2.32	8.46	99.48
76	210	4-16	827.13	M.R.P.	60.51	0.54	19.32	n.d.	1.01	n.d.	1.13	4.89	1.56	10.41	99.37
77	210	4-17	827.13	M.R.P.	59.19	0.28	14.23	n.d.	2.44	n.d.	4.13	7.92	0.26	11.03	99.48
78	210	4-18	827.13	M.R.P.	63.86	0.31	18.61	n.d.	0.32	n.d.	0.39	1.33	0.50	14.78	100.10
79	210	4-19	827.13	M.R.P.	62.31	1.01	18.22	n.d.	0.85	n.d.	0.93	2.99	0.98	12.94	100.23
80	210	4-20	827.13	M.R.P.	56.68	2.47	20.53	n.d.	1.48	n.d.	1.38	6.87	2.49	6.54	98.44
81	210	5-1	827.13	Mic	48.18	0.29	15.48	n.d.	4.43	n.d.	5.50	0.42	0.19	3.63	78.12
82	210	5-2	827.13	Mic	47.61	0.36	14.89	n.d.	4.65	n.d.	6.81	0.39	0.26	3.50	78.47
83	210	5-3	827.13	Mic	43.15	0.35	13.85	n.d.	4.49	n.d.	4.98	1.39	0.78	2.87	71.86
84	210	5-4	827.13	Mic	28.71	0.17	7.62	n.d.	2.69	n.d.	6.46	1.32	0.10	1.52	48.59
85	210	5-5	827.13	Mic	49.57	0.31	14.72	n.d.	4.71	n.d.	7.81	0.83	0.26	3.42	81.63
86	210	5-6	827.13	Mic	46.57	0.24	14.33	n.d.	4.27	n.d.	6.20	0.24	0.18	2.85	74.88
87	210	5-7	827.13	Mic	45.36	0.13	11.65	n.d.	3.71	n.d.	11.44	0.51	0.19	1.82	74.81
88	210	5-8	827.13	Mic	35.30	0.31	12.84	n.d.	2.92	n.d.	4.96	3.14	1.76	1.88	63.11
89	210	5-9	827.13	Mic	48.26	0.40	18.18	n.d.	3.79	n.d.	3.81	3.99	1.68	2.35	82.46
90	210	5-10	827.13	Mic	47.86	0.25	16.22	n.d.	3.30	n.d.	9.47	4.51	1.98	1.30	84.89
91	210	5-11	827.13	Mic	44.47	0.32	14.03	n.d.	4.14	n.d.	6.52	0.75	0.23	3.01	73.47
92	210	5-12	827.13	Mic	46.80	0.85	14.24	n.d.	4.03	n.d.	7.58	1.75	0.79	2.37	78.41
93	210	5-13	827.13	Mic	47.20	0.84	13.95	n.d.	4.26	n.d.	8.13	2.05	0.79	2.43	79.65
94	210	5-14	827.13	Mic	50.85	0.39	15.79	n.d.	4.27	n.d.	7.49	1.52	0.47	2.90	83.68
95	210	5-15	827.13	Mic	44.95	0.39	15.78	n.d.	3.00	n.d.	5.01	4.42	1.88	1.73	77.16
96	210	5-16	827.13	Mic	47.85	0.88	15.14	n.d.	3.88	n.d.	7.11	1.60	0.86	2.94	80.26
97	210	5-17	827.13	Mic	49.87	0.84	16.86	n.d.	3.75	n.d.	6.40	2.79	1.53	2.53	84.57
98	210	5-18	827.13	Mic	51.55	0.33	14.73	n.d.	4.65	n.d.	9.82	1.65	0.54	2.83	86.10
99	210	5-19	827.13	Mic	51.05	0.69	17.92	n.d.	3.73	n.d.	5.87	1.92	1.10	3.02	85.30
100	210	5-20	827.13	Mic	40.85	0.35	11.73	n.d.	3.69	n.d.	7.22	5.56	0.68	1.97	72.05

Table A.5. *Continued*

Analysis #	Sample #	Batch #	Depth (m)	Comment	SiO_2	TiO_2	Al_2O_3	Cr_2O_3	FeO_{tot}	MnO	MgO	CaO	Na_2O	K_2O	Total
101	210	6-1	827.13	Vesc. fill	34.60	n.d.	4.42	n.d.	3.12	n.d.	17.88	1.15	0.14	n.d.	61.31
102	210	6-2	827.13	Vesc. fill	39.72	n.d.	5.25	n.d.	3.59	n.d.	19.14	1.61	0.18	0.09	69.58
103	210	6-3	827.13	Vesc. fill	37.59	n.d.	4.67	n.d.	3.52	n.d.	20.41	1.38	0.13	0.10	67.80
104	210	6-4	827.13	Vesc. fill	36.49	n.d.	4.79	n.d.	3.17	n.d.	18.20	1.54	0.17	0.10	64.46
105	210	6-5	827.13	Vesc. fill	36.79	n.d.	4.79	n.d.	3.52	n.d.	19.22	1.24	0.13	0.07	65.76
106	210	6-6	827.13	Vesc. fill	34.42	n.d.	4.43	n.d.	3.06	n.d.	17.52	0.92	0.13	0.06	60.54
107	210	6-7	827.13	Vesc. fill	33.77	n.d.	4.44	n.d.	2.66	n.d.	16.68	1.05	0.12	0.08	58.80
108	210	6-8	827.13	Vesc. fill	27.89	0.05	3.62	n.d.	2.30	n.d.	14.23	1.37	0.12	0.07	49.65
109	210	6-9	827.13	Vesc. fill	29.53	n.d.	3.71	n.d.	2.71	n.d.	13.94	1.30	0.09	0.07	51.35
110	210	6-10	827.13	Vesc. fill	35.62	n.d.	4.68	n.d.	3.24	n.d.	18.28	1.22	0.13	0.06	63.23
111	210	6-11	827.13	Vesc. fill	47.93	0.21	15.00	n.d.	3.47	n.d.	5.28	0.55	0.27	2.88	75.59
112	210	6-12	827.13	Vesc. fill	4.23	0.12	0.94	0.07	1.14	n.d.	16.59	24.54	0.15	0.35	48.13
113	210	6-13	827.13	Vesc. fill	0.28	n.d.	0.08	n.d.	n.d.	n.d.	0.09	0.06	0.02	n.d.	0.53
114	210	6-14	827.13	Vesc. fill	0.26	n.d.	0.08	n.d.	n.d.	n.d.	0.07	n.d.	n.d.	n.d.	0.41
115	210	6-15	827.13	Vesc. fill	52.43	0.16	16.80	n.d.	3.07	n.d.	6.28	0.37	0.26	2.77	82.14
116	210	6-16	827.13	Vesc. fill	51.06	0.20	16.36	n.d.	2.94	n.d.	6.15	0.76	0.43	2.99	80.89
117	210	6-17	827.13	Vesc. fill	0.19	n.d.	0.08	n.d.	n.d.	n.d.	0.08	0.07	n.d.	n.d.	0.42
118	210	6-18	827.13	Vesc. fill	52.52	0.21	16.66	n.d.	3.28	n.d.	6.12	0.25	0.21	2.73	81.98
119	210	6-19	827.13	Vesc. fill	52.42	0.14	16.59	n.d.	3.14	n.d.	6.14	0.38	0.20	2.72	81.73
120	210	6-20	827.13	Vesc. fill	51.56	0.36	15.54	n.d.	4.99	n.d.	6.16	0.25	0.24	4.12	83.22
121	210	7-1	827.13	Vesc. fill	38.46	n.d.	5.23	n.d.	3.18	n.d.	19.86	1.63	0.13	0.07	68.56
122	210	7-2	827.13	Vesc. fill	38.13	n.d.	5.02	n.d.	3.33	n.d.	19.54	1.60	0.17	0.06	67.85
123	210	7-3	827.13	Vesc. fill	38.60	n.d.	5.00	n.d.	3.41	n.d.	20.22	1.28	0.17	0.08	68.76
124	210	7-4	827.13	Vesc. fill	39.32	n.d.	4.95	n.d.	3.27	n.d.	20.38	1.28	0.17	0.05	69.42
125	210	7-5	827.13	Vesc. fill	38.84	n.d.	5.17	n.d.	3.39	n.d.	20.15	1.37	0.14	0.07	69.13
126	210	7-6	827.13	Vesc. fill	52.21	0.35	16.21	n.d.	6.44	n.d.	6.05	0.34	0.22	5.34	87.16
127	210	7-7	827.13	Vesc. fill	51.19	0.46	15.98	n.d.	6.22	n.d.	5.93	0.22	0.26	4.70	84.96
128	210	7-8	827.13	Vesc. fill	48.60	0.32	14.76	n.d.	7.51	n.d.	5.44	0.25	0.14	5.47	82.49
129	210	7-9	827.13	Vesc. fill	52.76	0.32	15.31	n.d.	7.81	n.d.	5.76	0.18	0.25	5.54	87.93
130	210	7-10	827.13	Vesc. fill	52.17	0.39	15.63	n.d.	7.32	n.d.	5.66	0.20	0.19	5.72	87.28
131	210	7-11	827.13	Vesc. fill	35.76	n.d.	4.47	n.d.	3.39	n.d.	18.37	1.48	0.14	0.06	63.67
132	210	7-12	827.13	Vesc. fill	37.95	n.d.	4.94	n.d.	3.45	n.d.	19.59	1.34	0.11	0.08	67.46
133	210	7-13	827.13	Vesc. fill	39.70	n.d.	5.26	n.d.	3.44	n.d.	20.36	1.44	0.13	0.10	70.43
134	210	7-14	827.13	Vesc. fill	37.61	n.d.	4.95	n.d.	3.27	n.d.	20.17	1.41	0.16	0.07	67.64
135	210	7-15	827.13	Vesc. fill	39.53	n.d.	5.17	n.d.	3.52	n.d.	21.30	1.98	0.18	0.14	71.82
136	210	7-16	827.13	Vesc. rim	n.d.	n.d.	n.d.	n.d.	n.d.	n.d.	0.81	53.15	n.d.	n.d.	53.96
137	210	7-17	827.13	Qtz	97.41	n.d.	0.05	n.d.	n.d.	n.d.	n.d.	n.d.	0.03	n.d.	97.49
138	210	7-18	827.13	Vesc. rim	61.72	n.d.	24.06	n.d.	n.d.	n.d.	n.d.	4.62	8.06	1.79	100.25
139	210	7-19	827.13	Qtz	97.03	n.d.	n.d.	n.d.	n.d.	n.d.	n.d.	n.d.	0.04	n.d.	97.07
140	210	7-20	827.13	Vesc. rim	60.77	n.d.	24.19	n.d.	n.d.	n.d.	n.d.	5.00	9.00	0.49	99.45
141	210	8-1	827.13	Cc	0.54	n.d.	0.15	n.d.	0.10	n.d.	0.58	51.42	n.d.	0.20	52.99
142	210	8-2	827.13	Cc	0.11	n.d.	0.06	n.d.	0.16	0.11	0.31	52.11	0.03	0.08	52.97
143	210	8-3	827.13	M.R.P.	22.41	0.13	5.98	0.06	1.95	n.d.	2.27	2.55	0.09	0.80	36.24
144	210	8-4	827.13	M.R.P.	38.91	0.20	11.04	n.d.	3.71	n.d.	4.86	2.75	0.18	1.60	63.25
145	210	8-5	827.13	M.R.P.	47.49	0.29	13.36	n.d.	5.37	n.d.	5.96	1.70	0.64	3.80	78.61
146	210	8-6	827.13	M.R.P.	43.06	0.21	10.99	n.d.	9.02	n.d.	4.72	0.47	0.30	4.61	73.38
147	210	8-7	827.13	M.R.P.	44.98	0.33	12.65	n.d.	6.02	n.d.	6.46	1.98	0.76	4.34	77.52
148	210	8-8	827.13	M.R.P.	23.39	0.13	5.77	n.d.	3.18	n.d.	3.08	0.31	0.22	1.86	37.94
149	210	8-9	827.13	M.R.P.	28.03	0.12	6.40	n.d.	3.95	n.d.	3.59	0.30	0.29	2.38	45.06
150	210	8-10	827.13	M.R.P.	41.50	0.22	9.84	n.d.	8.60	n.d.	5.50	0.34	0.37	4.39	70.76

Table A.5. *Continued*

Analysis #	Sample #	Batch #	Depth (m)	Comment	SiO_2	TiO_2	Al_2O_3	Cr_2O_3	FeO_{tot}	MnO	MgO	CaO	Na_2O	K_2O	Total
151	210	8-11	827.13	M.R.P.	42.65	0.23	10.03	n.d.	6.48	n.d.	5.45	0.34	0.58	3.08	68.84
152	210	8-12	827.13	M.R.P.	43.39	0.21	10.16	n.d.	8.49	n.d.	5.45	0.52	0.43	4.15	72.80
153	210	8-13	827.13	M.R.P.	42.14	0.17	9.52	0.06	7.77	n.d.	5.23	0.45	0.47	3.92	69.73
154	210	8-14	827.13	M.R.P.	43.52	0.25	10.27	n.d.	7.34	n.d.	5.53	0.49	0.48	3.64	71.52
155	210	8-15	827.13	M.R.P.	46.99	0.21	12.07	n.d.	8.54	n.d.	5.07	1.17	0.65	4.42	79.12
156	210	8-16	827.13	M.R.P.	24.62	0.05	6.73	n.d.	1.04	n.d.	1.24	31.72	0.18	4.66	70.24
157	210	8-17	827.13	M.R.P.	48.48	0.05	13.42	n.d.	2.02	n.d.	2.15	7.75	0.34	9.20	83.41
158	210	8-18	827.13	M.R.P.	46.31	0.21	14.58	n.d.	2.83	n.d.	3.35	5.56	1.48	4.53	78.85
159	210	8-19	827.13	M.R.P.	46.00	0.26	13.77	n.d.	3.60	n.d.	4.92	3.22	0.50	2.81	75.08
160	210	8-20	827.13	M.R.P.	46.09	0.25	10.56	n.d.	9.84	n.d.	5.39	0.46	0.23	5.10	77.92
161	774	1-1	827.13	Cc	n.d.	n.d.	n.d.	n.d.	n.d.	n.d.	1.09	59.52	n.d.	n.d.	60.61
162	774	1-2	827.13	Cc	n.d.	n.d.	n.d.	n.d.	n.d.	n.d.	1.03	56.55	n.d.	n.d.	57.58
163	774	1-3	827.13	Cc	n.d.	n.d.	n.d.	n.d.	n.d.	n.d.	1.14	59.66	n.d.	n.d.	60.80
164	774	1-4	827.13	Cc	n.d.	n.d.	n.d.	n.d.	n.d.	n.d.	1.24	55.23	0.03	n.d.	56.50
165	774	1-5	827.13	Cc	0.05	n.d.	n.d.	n.d.	n.d.	n.d.	1.00	59.52	n.d.	n.d.	60.57
166	774	1-6	827.13	Cc	n.d.	n.d.	n.d.	n.d.	n.d.	n.d.	1.54	56.09	n.d.	n.d.	57.63
167	774	1-7	827.13	Cc	n.d.	n.d.	n.d.	n.d.	n.d.	n.d.	0.92	58.58	0.02	n.d.	59.52
168	774	1-8	827.13	Qtz	97.86	n.d.	0.05	n.d.	n.d.	n.d.	n.d.	n.d.	n.d.	n.d.	97.91
169	774	1-9	827.13	Qtz	97.43	n.d.	n.d.	n.d.	n.d.	n.d.	n.d.	n.d.	0.02	n.d.	97.45
170	774	1-10	827.13	M.R.P.	48.99	0.28	12.04	n.d.	9.80	n.d.	5.70	0.25	0.09	5.24	82.39
171	774	1-11	827.13	M.R.P.	49.73	0.24	12.09	n.d.	9.40	n.d.	6.28	0.23	0.12	5.20	83.29
172	774	1-12	827.13	M.R.P.	49.85	0.24	11.91	n.d.	9.59	n.d.	6.40	0.28	0.10	5.40	83.77
173	774	1-13	827.13	M.R.P.	49.67	0.26	11.77	n.d.	10.56	n.d.	5.91	n.d.	0.14	5.37	83.68
174	774	1-14	827.13	M.R.P.	47.87	0.29	11.13	n.d.	10.35	n.d.	5.63	0.16	0.13	5.22	80.78
175	774	1-15	827.13	M.R.P.	43.00	0.16	9.99	n.d.	8.35	n.d.	5.64	0.98	0.10	4.40	72.62
176	774	1-16	827.13	M.R.P.	46.41	1.72	11.34	n.d.	9.69	n.d.	5.48	0.81	0.11	4.98	80.54
177	774	1-17	827.13	M.R.P.	48.77	0.26	11.58	n.d.	9.79	n.d.	5.94	0.20	0.08	4.97	81.59
178	774	1-18	827.13	M.R.P.	43.92	0.22	9.76	n.d.	7.84	n.d.	6.07	0.51	0.29	4.13	72.74
179	774	1-19	827.13	M.R.P.	41.21	0.22	9.87	n.d.	6.84	n.d.	5.65	0.60	0.12	3.46	67.97
180	774	1-20	827.13	M.R.P.	47.19	0.64	11.75	n.d.	7.04	n.d.	7.50	0.70	0.33	3.21	78.36
181	774	2-1	827.13	M.R.P.	50.60	0.30	12.13	n.d.	7.94	n.d.	6.11	0.18	0.13	4.41	81.80
182	774	2-2	827.13	M.R.P.	49.10	0.36	12.02	n.d.	6.83	n.d.	6.87	0.30	0.16	3.39	79.03
183	774	2-3	827.13	M.R.P.	49.61	0.43	12.19	n.d.	8.92	n.d.	5.82	0.87	0.11	4.72	82.67
184	774	2-4	827.13	M.R.P.	45.21	2.38	10.51	n.d.	7.56	n.d.	7.31	0.53	0.22	3.61	77.33
185	774	2-5	827.13	M.R.P.	50.89	0.43	12.75	n.d.	9.44	n.d.	5.96	1.10	0.11	5.31	85.99
186	774	2-6	827.13	M.R.P.	53.27	0.37	12.59	0.05	9.82	n.d.	6.78	0.21	0.20	4.87	88.16
187	774	2-7	827.13	M.R.P.	49.93	0.34	12.15	n.d.	8.64	n.d.	6.58	0.37	0.20	4.29	82.50
188	774	2-8	827.13	M.R.P.	46.57	0.25	10.57	n.d.	9.58	n.d.	6.27	1.52	0.11	5.12	79.99
189	774	2-9	827.13	M.R.P.	50.01	0.26	12.26	n.d.	9.55	n.d.	5.93	0.28	0.14	5.33	83.76
190	774	2-10	827.13	M.R.P.	47.39	0.29	11.55	n.d.	9.45	n.d.	5.78	0.37	0.14	5.13	80.10
191	774	2-11	827.13	M.R.P.	64.01	n.d.	17.53	n.d.	n.d.	n.d.	n.d.	n.d.	0.08	16.35	97.97
192	774	2-12	827.13	M.R.P.	63.54	n.d.	17.54	n.d.	n.d.	n.d.	n.d.	n.d.	0.07	16.15	97.30
193	774	2-13	827.13	M.R.P.	63.61	n.d.	17.82	n.d.	n.d.	n.d.	n.d.	n.d.	0.10	16.32	97.85
194	774	2-14	827.13	M.R.P.	63.62	n.d.	17.97	n.d.	n.d.	n.d.	n.d.	n.d.	0.07	15.96	97.62
195	774	2-15	827.13	M.R.P.	63.66	n.d.	18.66	n.d.	n.d.	n.d.	n.d.	0.61	0.18	15.73	98.84
196	774	2-16	827.13	M.R.P.	63.80	n.d.	18.59	n.d.	0.09	n.d.	n.d.	0.83	0.38	15.07	98.76
197	774	2-17	827.13	M.R.P.	42.24	0.23	9.97	n.d.	7.40	n.d.	5.32	0.44	0.14	4.05	69.79
198	774	2-18	827.13	M.R.P.	41.22	0.13	10.42	n.d.	6.24	n.d.	5.54	0.35	0.12	3.47	67.49
199	774	2-19	827.13	M.R.P.	45.54	0.17	11.44	n.d.	6.84	n.d.	5.04	0.79	0.49	5.04	75.35
200	774	2-20	827.13	Qtz	95.57	0.05	0.75	n.d.	n.d.	n.d.	n.d.	n.d.	0.15	n.d.	96.52

Table A.5. *Continued*

Analysis #	Sample #	Batch #	Depth (m)	Comment	SiO_2	TiO_2	Al_2O_3	Cr_2O_3	FeO_{tot}	MnO	MgO	CaO	Na_2O	K_2O	Total
201	774	3-1	827.13	Qtz	95.91	n.d.	0.65	n.d.	n.d.	n.d.	n.d.	0.09	0.22	0.05	96.92
202	774	3-2	827.13	Qtz	95.73	n.d.	0.72	n.d.	n.d.	n.d.	n.d.	0.06	0.18	n.d.	96.69
203	774	3-3	827.13	Qtz	95.76	n.d.	0.25	n.d.	0.18	n.d.	0.07	0.41	0.04	0.06	96.77
204	774	3-4	827.13	Qtz	96.10	n.d.	0.31	n.d.	0.20	n.d.	0.10	0.16	0.07	0.08	97.02
205	774	3-5	827.13	M.R.P.	64.12	n.d.	17.96	n.d.	0.15	n.d.	n.d.	0.66	0.41	14.97	98.27
206	774	3-6	827.13	M.R.P.	61.42	0.06	19.22	n.d.	0.43	n.d.	0.14	2.98	1.52	11.27	97.04
207	774	3-7	827.13	M.R.P.	62.06	n.d.	19.99	n.d.	0.39	n.d.	0.09	2.61	0.98	13.05	99.17
208	774	3-8	827.13	M.R.P.	65.57	0.08	19.16	n.d.	0.32	n.d.	n.d.	0.62	10.23	0.43	96.41
209	774	3-9	827.13	M.R.P.	66.98	n.d.	19.39	n.d.	0.44	n.d.	0.07	0.41	10.93	0.21	98.43
210	774	3-10	827.13	M.R.P.	65.68	n.d.	19.52	n.d.	0.71	n.d.	0.22	1.26	9.86	0.56	97.81
211	774	3-11	827.13	M.R.P.	64.56	0.05	19.60	n.d.	0.65	n.d.	0.20	2.04	9.28	1.03	97.41
212	774	3-12	827.13	M.R.P.	66.97	n.d.	18.93	n.d.	0.32	n.d.	n.d.	0.50	11.17	0.49	98.38
213	774	3-13	827.13	M.R.P.	66.99	n.d.	19.17	n.d.	0.30	n.d.	n.d.	0.54	11.43	0.36	98.79
214	774	3-14	827.13	M.R.P.	67.14	n.d.	19.10	n.d.	0.16	n.d.	n.d.	0.61	10.89	0.27	98.17
215	774	3-15	827.13	M.R.P.	66.52	n.d.	19.77	n.d.	0.22	n.d.	0.12	1.10	10.34	0.87	98.94
216	774	3-16	827.13	M.R.P.	51.55	1.22	18.68	n.d.	8.90	0.19	0.37	3.89	3.99	5.58	94.37
217	774	3-17	827.13	M.R.P.	54.64	1.61	19.64	n.d.	1.78	n.d.	0.97	5.27	3.18	6.35	93.44
218	774	3-18	827.13	M.R.P.	65.90	n.d.	19.10	n.d.	0.21	n.d.	0.11	0.48	10.43	0.33	96.56
219	774	3-19	827.13	M.R.P.	46.81	1.10	18.25	n.d.	14.82	0.14	0.32	4.64	5.12	2.96	94.16
220	774	3-20	827.13	M.R.P.	45.50	1.01	17.78	0.05	17.48	0.17	0.24	4.77	5.46	1.99	94.45
221	774	4-1	827.13	M.R.P.	65.77	n.d.	19.04	n.d.	0.58	n.d.	0.16	0.99	10.62	0.58	97.74
222	774	4-2	827.13	M.R.P.	49.07	1.58	19.61	n.d.	14.02	0.17	0.45	4.72	5.79	2.10	97.51
223	774	4-3	827.13	M.R.P.	63.21	0.20	19.68	n.d.	1.02	n.d.	0.86	2.58	8.65	1.16	97.36
224	774	4-4	827.13	M.R.P.	57.08	0.79	21.86	n.d.	2.53	n.d.	0.29	5.81	7.11	1.09	96.56
225	774	4-5	827.13	M.R.P.	55.66	0.37	21.65	n.d.	2.38	n.d.	0.43	8.21	6.54	0.94	96.18
226	774	4-6	827.13	M.R.P.	65.01	0.08	19.10	n.d.	0.67	n.d.	0.36	1.73	10.07	0.56	97.58
227	774	4-7	827.13	M.R.P.	48.37	1.53	18.73	n.d.	11.30	0.15	0.15	4.30	4.81	3.60	92.94
228	774	4-8	827.13	M.R.P.	64.13	0.16	19.68	n.d.	1.40	n.d.	0.49	2.41	9.17	0.96	98.40
229	774	4-9	827.13	M.R.P.	50.99	0.56	20.39	n.d.	5.90	n.d.	0.26	5.88	5.30	3.04	92.32
230	774	4-10	827.13	M.R.P.	54.79	0.57	21.85	n.d.	2.07	n.d.	0.31	6.85	6.17	0.73	93.34
231	774	4-11	827.13	M.R.P.	49.13	1.00	21.34	n.d.	11.42	0.10	0.41	6.88	5.06	1.63	96.97
232	774	4-12	827.13	M.R.P.	53.90	0.11	21.37	n.d.	4.23	n.d.	0.14	6.19	5.45	2.47	93.86
233	774	4-13	827.13	M.R.P.	53.37	3.81	17.77	n.d.	1.70	n.d.	0.36	3.69	3.76	7.06	91.52
234	774	4-14	827.13	M.R.P.	67.06	n.d.	19.39	n.d.	n.d.	n.d.	n.d.	0.25	10.81	0.90	98.41
235	774	4-15	827.13	Qtz	97.79	n.d.	n.d.	n.d.	n.d.	n.d.	n.d.	n.d.	0.03	n.d.	97.82
236	774	4-16	827.13	Cc	52.71	0.14	15.06	n.d.	1.09	n.d.	1.65	10.79	0.62	11.23	93.29
237	774	4-17	827.13	Cc	29.75	0.28	8.78	n.d.	0.82	n.d.	1.13	26.79	0.39	5.84	73.78
238	774	4-18	827.13	Cc	37.35	0.14	11.22	n.d.	0.53	n.d.	0.76	19.78	0.65	8.37	78.80
239	774	4-19	827.13	Cc	14.44	0.14	4.24	n.d.	1.46	n.d.	2.43	37.97	0.14	0.86	61.68
240	774	4-20	827.13	Cc	18.16	0.14	4.87	n.d.	1.60	n.d.	3.47	34.77	0.14	0.86	64.01
241	754	1-1	835.18	Qtz	95.67	n.d.	0.65	n.d.	0.20	n.d.	0.09	0.06	0.14	0.09	96.90
242	754	1-2	835.18	Qtz	96.69	0.11	0.23	n.d.	0.70	n.d.	n.d.	n.d.	0.07	0.05	97.85
243	754	1-3	835.18	M.R.P.	52.02	0.39	28.05	n.d.	1.36	n.d.	1.14	8.30	4.81	1.28	97.35
244	754	1-4	835.18	M.R.P.	64.37	0.06	17.68	n.d.	0.11	n.d.	n.d.	n.d.	0.05	16.41	98.68
245	754	1-5	835.18	M.R.P.	56.18	0.15	24.09	n.d.	1.70	n.d.	0.57	6.22	3.31	6.19	98.41
246	754	1-6	835.18	M.R.P.	63.84	n.d.	18.07	n.d.	n.d.	n.d.	n.d.	n.d.	0.08	16.45	98.44
247	754	1-7	835.18	M.R.P.	62.14	0.06	19.62	n.d.	0.16	n.d.	0.06	2.26	0.95	13.42	98.67
248	754	1-9	835.18	M.R.P.	47.61	0.39	12.19	n.d.	7.90	n.d.	6.72	0.24	0.17	4.41	79.63
249	754	1-10	835.18	M.R.P.	44.89	0.45	11.39	n.d.	7.21	n.d.	7.03	0.51	0.25	4.03	75.76
250	754	1-11	835.18	M.R.P.	49.52	0.32	15.35	n.d.	7.41	n.d.	4.75	2.93	0.98	4.13	85.39

Table A.5. *Continued*

Analysis #	Sample #	Batch #	Depth (m)	Comment	SiO_2	TiO_2	Al_2O_3	Cr_2O_3	FeO_{tot}	MnO	MgO	CaO	Na_2O	K_2O	Total
251	754	1-12	835.18	M.R.P.	47.04	0.43	12.06	n.d.	7.88	n.d.	6.05	0.09	0.15	4.82	78.52
252	754	1-13	835.18	M.R.P.	49.28	0.36	12.66	n.d.	7.92	n.d.	6.01	0.38	0.23	4.85	81.69
253	754	1-14	835.18	M.R.P.	46.54	1.54	12.11	n.d.	6.87	n.d.	6.38	0.49	0.23	4.03	78.19
254	754	1-15	835.18	Hole	6.17	n.d.	1.72	n.d.	0.97	n.d.	0.66	0.33	0.11	0.36	10.32
255	754	1-16	835.18	Hole	0.54	n.d.	0.15	n.d.	0.14	n.d.	0.08	0.17	n.d.	n.d.	1.08
256	754	1-17	835.18	Hole	4.51	n.d.	1.30	n.d.	0.45	n.d.	0.40	0.33	0.32	0.46	7.77
257	754	1-18	835.18	Hole	0.52	n.d.	0.14	n.d.	n.d.	n.d.	0.08	n.d.	0.03	n.d.	0.77
258	754	1-19	835.18	M.R.P.	50.41	0.44	12.90	n.d.	8.25	n.d.	6.00	0.43	0.16	4.87	83.46
259	754	1-20	835.18	M.R.P.	40.08	0.40	10.07	n.d.	7.78	n.d.	4.89	0.43	0.09	4.05	67.79
260	754	2-1	835.18	Qtz	96.86	n.d.	0.14	n.d.	n.d.	n.d.	n.d.	n.d.	0.08	n.d.	97.08
261	754	2-2	835.18	Qtz	91.75	n.d.	0.94	n.d.	1.06	n.d.	0.46	0.34	0.19	0.17	94.91
262	754	2-3	835.18	Qtz	93.09	n.d.	0.93	n.d.	0.43	n.d.	0.48	0.27	0.13	0.14	95.47
263	754	2-4	835.18	Qtz	97.17	n.d.	0.10	n.d.	n.d.	n.d.	n.d.	n.d.	0.05	n.d.	97.32
264	754	2-5	835.18	Qtz	96.68	n.d.	0.13	n.d.	n.d.	n.d.	n.d.	0.08	0.09	n.d.	96.98
265	754	2-6	835.18	Qtz	97.08	n.d.	0.16	n.d.	n.d.	n.d.	n.d.	n.d.	0.06	n.d.	97.30
266	754	2-7	835.18	Qtz	97.44	n.d.	0.06	n.d.	n.d.	n.d.	n.d.	n.d.	0.06	n.d.	97.56
267	754	2-8	835.18	Qtz	97.42	n.d.	0.08	n.d.	n.d.	n.d.	n.d.	0.05	0.05	n.d.	97.60
268	754	2-9	835.18	Qtz	97.36	n.d.	0.45	n.d.	0.09	n.d.	0.06	0.10	0.12	0.05	98.23
269	754	2-10	835.18	Qtz	95.75	n.d.	0.92	n.d.	0.10	n.d.	0.10	0.05	0.26	0.31	97.49
270	754	2-11	835.18	M.R.P.	52.24	0.19	16.74	n.d.	4.10	n.d.	3.22	1.76	2.35	6.47	87.07
271	754	2-12	835.18	M.R.P.	50.54	0.08	14.45	n.d.	2.49	n.d.	3.14	1.01	0.57	6.74	79.02
272	754	2-13	835.18	M.R.P.	47.38	0.22	13.01	n.d.	5.41	n.d.	5.96	1.58	3.91	3.14	80.61
273	754	2-14	835.18	M.R.P.	44.02	0.45	11.24	n.d.	14.41	n.d.	7.49	1.42	3.75	1.62	84.40
274	754	2-15	835.18	M.R.P.	41.48	0.37	11.96	n.d.	8.42	n.d.	8.30	3.25	1.52	3.50	78.80
275	754	2-16	835.18	M.R.P.	43.75	0.25	11.54	n.d.	5.62	n.d.	8.13	2.10	0.82	2.86	75.07
276	754	2-17	835.18	M.R.P.	38.73	1.04	9.23	n.d.	4.44	n.d.	7.99	0.43	0.12	1.28	63.26
277	754	2-18	835.18	M.R.P.	51.45	0.27	11.51	n.d.	6.60	n.d.	3.06	0.98	0.24	8.80	82.91
278	754	2-19	835.18	M.R.P.	36.19	0.10	8.64	n.d.	4.49	n.d.	6.57	0.47	0.20	1.45	58.11
279	754	2-20	835.18	M.R.P.	14.42	0.11	3.78	n.d.	1.77	n.d.	1.91	3.01	0.30	1.23	26.53
280	754	3-1	835.18	M.R.P.	15.16	0.15	4.02	n.d.	1.97	n.d.	2.03	3.61	0.27	1.31	28.52
281	754	3-2	835.18	M.R.P.	26.66	0.10	5.05	n.d.	2.99	n.d.	9.03	1.33	0.22	0.69	46.07
282	754	3-3	835.18	M.R.P.	38.45	0.11	8.80	n.d.	4.82	n.d.	7.25	0.40	0.16	1.65	61.64
283	754	3-4	835.18	M.R.P.	42.56	0.69	8.88	n.d.	19.25	n.d.	3.73	0.49	0.24	6.11	81.95
284	754	3-5	835.18	M.R.P.	42.17	0.16	9.70	n.d.	5.01	n.d.	9.03	0.45	0.22	1.50	68.24
285	754	3-6	835.18	M.R.P.	37.59	0.07	7.44	n.d.	4.34	n.d.	11.11	1.02	0.18	0.96	62.71
286	754	3-7	835.18	M.R.P.	28.39	0.13	6.29	n.d.	4.36	n.d.	5.67	0.64	0.14	1.31	46.93
287	754	3-8	835.18	M.R.P.	30.10	0.10	6.97	n.d.	4.16	n.d.	5.32	0.33	0.10	1.38	48.46
288	754	3-9	835.18	Felds	56.28	n.d.	19.70	n.d.	0.25	n.d.	0.09	2.69	6.81	2.99	88.81
289	754	3-10	835.18	Felds	57.55	0.05	17.25	n.d.	0.22	n.d.	n.d.	0.57	6.75	4.79	87.18
290	754	3-11	835.18	Felds	56.02	n.d.	16.32	n.d.	0.10	n.d.	n.d.	0.52	5.98	5.56	84.50
291	754	3-12	835.18	Felds	56.23	n.d.	16.32	n.d.	0.11	n.d.	n.d.	0.56	7.61	3.39	84.22
292	754	3-13	835.18	Felds	61.36	n.d.	18.38	n.d.	0.14	n.d.	n.d.	0.45	8.82	2.84	91.99
293	754	3-14	835.18	Felds	60.49	n.d.	18.02	n.d.	0.11	n.d.	n.d.	0.45	8.10	3.65	90.82
294	754	3-15	835.18	Felds	61.38	n.d.	18.15	n.d.	0.14	n.d.	n.d.	0.39	8.08	3.26	91.40
295	754	3-16	835.18	Felds	59.38	n.d.	17.61	n.d.	0.13	n.d.	n.d.	0.35	6.82	4.94	89.23
296	754	3-17	835.18	Felds	60.58	n.d.	17.89	n.d.	n.d.	n.d.	n.d.	0.30	7.57	4.28	90.62
297	754	3-18	835.18	Felds	60.45	n.d.	18.13	n.d.	n.d.	n.d.	n.d.	0.46	7.98	3.52	90.54
298	754	3-19	835.18	Felds	64.04	n.d.	19.12	n.d.	0.16	n.d.	n.d.	0.32	8.64	3.92	96.20
299	754	3-20	835.18	Felds	63.01	n.d.	18.19	n.d.	0.36	n.d.	0.38	0.14	4.40	9.45	95.93
300	754	4-1	835.18	Felds	67.08	n.d.	19.54	n.d.	0.16	n.d.	n.d.	n.d.	8.55	5.24	100.57

Table A.5. *Continued*

Analysis #	Sample #	Batch #	Depth (m)	Comment	SiO_2	TiO_2	Al_2O_3	Cr_2O_3	FeO_{tot}	MnO	MgO	CaO	Na_2O	K_2O	Total
301	754	4-2	835.18	Felds	66.95	n.d.	19.82	n.d.	0.21	n.d.	n.d.	0.06	9.63	3.33	100.00
302	754	4-3	835.18	Felds	66.26	n.d.	19.01	n.d.	n.d.	n.d.	n.d.	0.07	5.26	9.25	99.85
303	754	4-4	835.18	Felds	64.38	n.d.	19.16	n.d.	0.14	n.d.	n.d.	0.15	6.56	7.28	97.67
304	754	4-5	835.18	Felds	64.78	n.d.	18.93	n.d.	0.17	n.d.	n.d.	0.18	7.35	5.88	97.29
305	754	4-6	835.18	Felds	63.07	n.d.	18.69	n.d.	0.11	n.d.	n.d.	0.24	6.72	6.43	95.26
306	754	4-7	835.18	Felds	63.23	n.d.	18.47	n.d.	n.d.	n.d.	n.d.	0.24	5.82	7.45	95.21
307	754	4-8	835.18	Felds	63.60	n.d.	18.88	n.d.	0.14	n.d.	n.d.	0.31	6.87	5.83	95.63
308	754	4-9	835.18	Felds	64.96	n.d.	18.97	n.d.	0.13	n.d.	n.d.	0.18	5.83	8.07	98.14
309	754	4-10	835.18	Felds	67.07	n.d.	19.59	n.d.	0.14	n.d.	n.d.	0.12	6.37	8.05	101.34
310	754	4-11	835.18	Felds	64.81	0.05	18.88	n.d.	n.d.	n.d.	n.d.	0.15	5.00	9.13	98.02
311	754	4-12	835.18	Felds	65.80	n.d.	18.82	n.d.	0.13	n.d.	n.d.	0.16	5.30	8.97	99.18
312	754	4-13	835.18	Felds	66.82	n.d.	19.49	n.d.	0.27	n.d.	n.d.	0.07	8.70	4.83	100.18
313	754	4-14	835.18	Felds	66.24	n.d.	19.46	n.d.	0.23	n.d.	n.d.	0.19	9.39	3.35	98.86
314	754	4-15	835.18	Felds	66.47	n.d.	19.80	n.d.	0.25	n.d.	n.d.	0.24	10.21	2.52	99.49
315	754	4-16	835.18	Felds	66.77	n.d.	19.79	0.07	0.27	n.d.	n.d.	0.23	9.21	3.49	99.83
316	754	4-17	835.18	Felds	65.16	n.d.	19.20	n.d.	0.25	n.d.	n.d.	0.39	8.93	3.40	97.33
317	754	4-18	835.18	Felds	65.08	n.d.	19.34	n.d.	0.25	n.d.	n.d.	0.51	8.70	4.06	97.94
318	754	4-19	835.18	Felds	66.07	n.d.	19.65	n.d.	0.27	n.d.	n.d.	0.38	6.51	7.37	100.25
319	754	4-20	835.18	Felds	64.14	n.d.	19.44	n.d.	0.28	n.d.	0.05	0.58	7.92	4.09	96.50
320	754	5-1	835.18	Felds	62.13	n.d.	18.88	n.d.	0.29	n.d.	n.d.	0.72	8.65	2.65	93.32
321	754	5-2	835.18	Felds	61.20	n.d.	18.63	n.d.	1.30	n.d.	n.d.	0.65	8.80	2.37	92.95
322	754	5-3	835.18	qtz	96.68	n.d.	0.75	n.d.	0.19	n.d.	n.d.	n.d.	0.24	0.23	98.09
323	754	5-4	835.18	qtz	97.23	n.d.	0.34	n.d.	0.16	n.d.	n.d.	0.06	0.15	n.d.	97.94
324	754	5-5	835.18	qtz	93.52	0.08	0.71	n.d.	2.60	n.d.	n.d.	0.07	0.23	n.d.	97.21
325	754	5-6	835.18	Fe M.R.P.	37.84	0.17	9.49	n.d.	5.29	n.d.	7.98	1.74	0.61	2.33	65.45
326	754	5-7	835.18	Fe M.R.P.	37.35	0.27	9.09	n.d.	6.08	n.d.	10.63	1.39	0.48	1.43	66.72
327	754	5-8	835.18	Fe M.R.P.	22.88	0.78	4.83	n.d.	24.33	n.d.	9.19	0.36	0.23	0.42	63.02
328	754	5-9	835.18	Fe M.R.P.	43.99	0.85	11.44	0.05	6.32	n.d.	7.44	1.11	0.68	3.29	75.17
329	754	5-10	835.18	Fe M.R.P.	39.04	2.30	9.63	n.d.	6.62	n.d.	8.03	1.58	0.27	1.42	68.89
330	754	5-11	835.18	Fe M.R.P.	23.37	0.79	5.36	n.d.	23.81	n.d.	5.74	2.73	0.23	1.58	63.61
331	754	5-12	835.18	Fe M.R.P.	22.12	1.06	5.78	n.d.	35.47	n.d.	3.59	1.59	0.23	2.40	72.24
332	754	5-13	835.18	Fe M.R.P.	7.60	0.92	1.89	n.d.	37.03	n.d.	3.01	0.28	0.10	0.82	51.65
333	754	5-14	835.18	Fe M.R.P.	17.25	1.22	4.54	n.d.	40.03	n.d.	4.98	0.35	0.23	1.38	69.98
334	754	5-15	835.18	Fe M.R.P.	21.66	1.25	5.46	n.d.	34.64	n.d.	6.35	0.34	0.26	0.43	70.39
335	754	5-16	835.18	Fe M.R.P.	19.17	1.21	3.54	n.d.	32.38	n.d.	11.17	0.38	0.31	0.11	68.27
336	754	5-17	835.18	Fe M.R.P.	20.40	0.92	3.33	n.d.	26.42	n.d.	10.33	0.40	0.26	0.08	62.14
337	754	5-18	835.18	Fe M.R.P.	26.58	1.13	6.51	n.d.	27.76	n.d.	7.52	0.33	0.42	0.54	70.79
338	754	5-19	835.18	Fe M.R.P.	10.58	1.71	2.39	n.d.	52.63	n.d.	4.57	0.35	0.16	0.16	72.55
339	754	5-20	835.18	Fe M.R.P.	14.45	1.59	3.36	n.d.	52.25	n.d.	4.81	0.42	0.32	0.27	77.47
340	754	6-1	835.18	Fe M.R.P.	14.16	1.68	3.43	n.d.	49.57	n.d.	6.16	0.35	0.35	0.27	75.97
341	754	6-2	835.18	Fe M.R.P.	23.84	1.07	5.54	n.d.	32.64	n.d.	8.31	0.46	0.38	0.41	72.65
342	754	6-3	835.18	Fe M.R.P.	13.88	1.63	3.39	0.05	50.47	n.d.	5.07	0.66	0.37	0.30	75.82
343	754	6-4	835.18	Fe M.R.P.	10.76	1.70	2.36	n.d.	48.65	n.d.	4.13	0.27	0.30	0.13	68.30
344	754	6-5	835.18	Fe M.R.P.	32.48	0.56	8.55	n.d.	15.22	n.d.	7.88	0.67	0.47	1.00	66.83
345	754	6-6	835.18	Fe M.R.P.	34.16	1.09	8.84	n.d.	13.39	n.d.	6.92	0.64	0.37	1.09	66.50
346	754	6-7	835.18	Fe M.R.P.	38.90	0.33	11.00	n.d.	9.70	n.d.	15.83	1.24	1.09	1.07	79.16
347	754	6-8	835.18	Cc	52.36	1.06	15.28	n.d.	1.05	n.d.	1.14	6.57	4.26	6.48	88.20
348	754	6-9	835.18	Cc	13.01	1.96	2.50	n.d.	1.83	n.d.	2.37	38.64	0.60	0.99	61.90
349	754	6-10	835.18	Cc	20.44	0.42	6.06	n.d.	0.74	n.d.	1.00	34.65	1.61	2.29	67.21
350	754	6-11	835.18	Cc	55.70	0.09	16.40	n.d.	1.24	n.d.	1.35	4.74	5.96	4.47	89.95

Table A.5. *Continued*

Analysis #	Sample #	Batch #	Depth (m)	Comment	SiO_2	TiO_2	Al_2O_3	Cr_2O_3	FeO_{tot}	MnO	MgO	CaO	Na_2O	K_2O	Total
351	754	6-12	835.18	Cc	43.61	0.13	11.93	n.d.	1.04	n.d.	1.77	14.02	3.77	4.90	81.17
352	754	6-13	835.18	Cc	35.72	0.11	10.45	n.d.	1.44	n.d.	1.13	20.69	3.15	4.31	77.00
353	754	6-14	835.18	Cc	41.82	1.06	12.68	n.d.	1.10	n.d.	1.40	14.83	4.51	3.50	80.90
354	754	6-15	835.18	Cc	39.97	0.05	11.68	n.d.	0.47	n.d.	0.81	19.45	4.15	3.27	79.85
355	754	6-16	835.18	Cc	10.59	n.d.	3.00	n.d.	0.24	n.d.	0.76	44.16	1.04	0.90	60.69
356	754	6-17	835.18	Cc	32.34	0.18	8.10	n.d.	2.06	n.d.	4.03	20.79	2.82	1.66	71.98
357	754	6-18	835.18	Cc	56.88	0.06	16.67	n.d.	0.67	n.d.	0.94	3.38	6.34	3.92	88.86
358	754	6-19	835.18	Cc	38.89	0.24	9.65	n.d.	2.10	n.d.	5.34	13.37	2.46	2.25	74.30
359	754	6-20	835.18	Cc	31.46	1.80	8.09	n.d.	1.64	n.d.	4.58	19.30	1.78	2.04	70.69
360	754	7-1	835.18	Qtz	97.38	n.d.	0.22	n.d.	0.17	n.d.	n.d.	n.d.	0.10	n.d.	97.87
361	754	7-2	835.18	Qtz	98.78	n.d.	0.20	n.d.	0.14	n.d.	n.d.	n.d.	0.10	n.d.	99.22
362	754	7-3	835.18	Qtz	98.71	n.d.	0.17	n.d.	0.09	n.d.	n.d.	n.d.	0.05	n.d.	99.02
363	754	7-4	835.18	Qtz	98.49	n.d.	0.08	n.d.	n.d.	n.d.	n.d.	n.d.	0.05	n.d.	98.62
364	754	7-5	835.18	Qtz	98.01	n.d.	0.23	n.d.	0.13	n.d.	n.d.	n.d.	0.04	0.05	98.46
365	754	7-6	835.18	Qtz	97.32	n.d.	0.42	n.d.	0.13	n.d.	n.d.	n.d.	0.13	0.08	98.08
366	754	7-7	835.18	Qtz	97.41	0.06	0.49	n.d.	0.15	n.d.	0.07	n.d.	0.14	0.08	98.40
367	754	7-8	835.18	Qtz	97.94	0.05	0.30	n.d.	0.29	n.d.	n.d.	n.d.	0.12	n.d.	98.70
368	754	7-9	835.18	Hole	15.05	n.d.	2.01	n.d.	1.21	n.d.	6.83	0.41	0.09	n.d.	25.60
369	754	7-10	835.18	Hole	11.60	n.d.	1.63	n.d.	0.95	n.d.	4.95	0.31	0.06	n.d.	19.50
370	754	7-11	835.18	Hole	19.31	n.d.	2.64	n.d.	1.66	n.d.	9.68	0.63	0.09	0.06	34.07
371	754	7-12	835.18	Hole	11.83	n.d.	1.81	n.d.	0.89	n.d.	6.50	0.36	0.06	n.d.	21.45
372	754	7-13	835.18	M.R.P.	46.95	1.26	10.88	n.d.	7.23	n.d.	6.93	0.41	0.28	3.96	77.90
373	754	7-14	835.18	M.R.P.	45.41	0.86	10.90	n.d.	7.61	n.d.	6.98	0.44	0.26	3.97	76.43
374	754	7-15	835.18	M.R.P.	44.51	0.44	10.53	n.d.	12.36	n.d.	7.05	0.40	0.29	3.50	79.08
375	754	7-16	835.18	M.R.P.	41.93	0.21	9.00	n.d.	6.03	n.d.	10.23	0.43	0.19	2.14	70.16
376	754	7-17	835.18	M.R.P.	47.35	0.29	11.18	n.d.	7.63	n.d.	7.79	0.28	0.20	3.35	78.07
377	754	7-18	835.18	M.R.P.	46.25	0.36	11.20	n.d.	7.35	n.d.	7.37	0.40	0.18	3.13	76.24
378	754	7-19	835.18	M.R.P.	45.94	0.33	11.13	n.d.	7.20	n.d.	7.06	0.37	0.22	3.79	76.04
379	754	7-20	835.18	M.R.P.	45.34	0.42	11.15	n.d.	7.43	n.d.	6.90	0.38	0.16	3.70	75.48
380	214	1-1	844.82	Qtz	98.29	n.d.	0.07	n.d.	n.d.	n.d.	n.d.	n.d.	0.09	n.d.	98.45
381	214	1-2	844.82	Qtz	98.41	n.d.	0.26	n.d.	n.d.	n.d.	0.05	n.d.	0.10	n.d.	98.82
382	214	1-3	844.82	Qtz	98.47	n.d.	0.16	n.d.	n.d.	n.d.	n.d.	n.d.	0.07	n.d.	98.70
383	214	1-4	844.82	Qtz	98.45	n.d.	0.15	n.d.	n.d.	n.d.	n.d.	n.d.	0.07	n.d.	98.67
384	214	1-5	844.82	Qtz	97.18	n.d.	0.34	n.d.	0.13	n.d.	n.d.	0.06	0.11	0.05	97.87
385	214	1-6	844.82	Qtz	98.11	n.d.	0.05	n.d.	n.d.	n.d.	n.d.	n.d.	0.04	n.d.	98.20
386	214	1-7	844.82	Qtz	97.67	n.d.	0.27	n.d.	n.d.	n.d.	0.05	n.d.	0.07	n.d.	98.06
387	214	1-8	844.82	Qtz	98.72	n.d.	n.d.	n.d.	n.d.	n.d.	n.d.	n.d.	0.02	n.d.	98.74
388	214	1-9	844.82	Qtz	98.06	n.d.	n.d.	n.d.	n.d.	n.d.	n.d.	n.d.	n.d.	n.d.	98.06
389	214	1-10	844.82	Qtz	97.76	n.d.	0.08	n.d.	n.d.	n.d.	n.d.	n.d.	n.d.	n.d.	97.84
390	214	1-11	844.82	M.R.P.	61.06	0.31	17.11	n.d.	2.03	n.d.	1.88	5.09	3.70	7.45	98.63
391	214	1-12	844.82	M.R.P.	57.87	0.41	22.77	n.d.	1.82	n.d.	0.40	7.06	4.44	4.21	98.98
392	214	1-13	844.82	M.R.P.	56.48	0.41	21.29	n.d.	2.08	n.d.	1.80	8.60	3.80	4.36	98.82
393	214	1-14	844.82	M.R.P.	59.53	0.41	19.62	n.d.	2.33	n.d.	0.84	5.12	3.35	7.10	98.30
394	214	1-15	844.82	M.R.P.	58.36	0.65	19.79	n.d.	1.84	n.d.	1.15	6.64	3.12	6.80	98.35
395	214	1-16	844.82	M.R.P.	60.43	0.45	18.65	n.d.	1.76	n.d.	0.46	4.00	2.63	9.24	97.62
396	214	1-17	844.82	M.R.P.	58.83	0.44	21.62	n.d.	1.47	n.d.	0.29	5.83	4.55	4.96	97.99
397	214	1-18	844.82	M.R.P.	59.72	0.68	19.96	0.06	2.02	n.d.	0.75	5.21	4.76	4.95	98.11
398	214	1-19	844.82	M.R.P.	57.10	0.32	23.95	n.d.	1.69	n.d.	0.44	8.27	4.33	3.57	99.67
399	214	1-20	844.82	M.R.P.	59.83	0.32	20.36	n.d.	1.79	n.d.	0.40	5.13	5.08	4.73	97.64
400	214	2-1	844.82	M.R.P.	57.98	0.40	21.42	n.d.	1.41	n.d.	1.26	7.04	4.86	3.40	97.77

Table A.5. *Continued*

Analysis #	Sample #	Batch #	Depth (m)	Comment	SiO_2	TiO_2	Al_2O_3	Cr_2O_3	FeO_{tot}	MnO	MgO	CaO	Na_2O	K_2O	Total
401	214	2-2	844.82	M.R.P.	59.43	0.51	19.59	n.d.	1.80	n.d.	1.86	6.22	4.99	3.64	98.04
402	214	2-3	844.82	M.R.P.	61.97	0.20	19.09	n.d.	1.23	n.d.	0.63	3.69	5.98	4.93	97.72
403	214	2-4	844.82	M.R.P.	58.32	0.21	22.51	n.d.	1.49	n.d.	0.66	7.00	5.07	2.96	98.22
404	214	2-5	844.82	M.R.P.	56.72	0.19	25.63	n.d.	1.12	n.d.	0.77	7.90	4.91	2.55	99.79
405	214	2-6	844.82	M.R.P.	55.79	n.d.	26.74	n.d.	1.20	n.d.	0.94	7.86	5.28	1.94	99.75
406	214	2-7	844.82	M.R.P.	58.42	0.58	17.82	n.d.	1.83	n.d.	2.43	6.69	5.10	3.23	96.10
407	214	2-8	844.82	M.R.P.	61.82	0.36	19.42	n.d.	1.17	n.d.	1.01	4.30	6.14	4.12	98.34
408	214	2-9	844.82	M.R.P.	54.97	0.95	15.63	n.d.	2.28	n.d.	4.36	5.16	5.18	3.10	91.63
409	214	2-10	844.82	M.R.P.	60.46	0.41	19.19	n.d.	1.74	n.d.	0.61	4.16	6.40	3.45	96.42
410	214	2-11	844.82	M.R.P.	58.78	0.91	17.74	n.d.	2.23	n.d.	2.31	5.14	4.97	3.44	95.52
411	214	2-12	844.82	M.R.P.	62.14	0.40	17.80	n.d.	1.43	n.d.	2.35	3.47	6.39	3.62	97.60
412	214	2-13	844.82	M.R.P.	61.48	0.24	20.09	n.d.	1.69	n.d.	0.68	4.66	6.08	3.63	98.55
413	214	2-14	844.82	M.R.P.	61.27	0.33	20.25	n.d.	1.76	n.d.	1.00	5.06	5.83	3.54	99.04
414	214	2-15	844.82	M.R.P.	59.64	0.84	17.28	n.d.	1.66	n.d.	3.25	3.45	5.54	3.74	95.40
415	214	2-16	844.82	M.R.P.	60.66	0.25	21.14	n.d.	1.71	n.d.	0.67	5.32	5.43	4.13	99.31
416	214	2-17	844.82	M.R.P.	62.76	0.42	18.02	n.d.	1.59	n.d.	1.32	3.43	5.67	5.67	98.88
417	214	2-18	844.82	M.R.P.	61.48	1.19	18.49	0.05	1.55	n.d.	2.22	4.14	6.17	3.77	99.06
418	214	2-19	844.82	M.R.P.	60.93	1.10	20.11	n.d.	1.60	n.d.	1.08	4.70	5.87	4.10	99.49
419	214	2-20	844.82	M.R.P.	61.21	0.97	18.09	n.d.	1.19	n.d.	0.93	2.80	6.03	5.07	96.29
420	214	3-1	844.82	M.R.P.	62.28	0.36	19.12	n.d.	0.96	n.d.	1.06	3.54	5.80	4.92	98.04
421	214	3-2	844.82	M.R.P.	61.55	0.72	20.68	n.d.	1.06	n.d.	0.39	4.34	5.33	5.26	99.33
422	214	3-3	844.82	M.R.P.	63.11	0.58	17.01	n.d.	1.40	n.d.	1.27	2.86	4.72	7.55	98.50
423	214	3-4	844.82	M.R.P.	63.14	0.22	18.56	n.d.	1.13	n.d.	0.51	2.38	5.30	6.72	97.96
424	214	3-5	844.82	M.R.P.	42.52	0.06	7.56	n.d.	8.12	n.d.	12.84	0.90	0.71	2.06	74.77
425	214	3-6	844.82	M.R.P.	39.26	0.05	10.84	n.d.	2.45	n.d.	8.76	2.00	0.79	2.65	66.80
426	214	3-7	844.82	M.R.P.	43.11	0.07	6.89	n.d.	3.93	n.d.	19.05	1.23	0.28	0.33	74.89
427	214	3-8	844.82	M.R.P.	34.05	0.07	5.69	n.d.	3.97	n.d.	15.38	1.95	0.28	0.33	61.72
428	214	3-9	844.82	M.R.P.	19.13	0.45	3.79	n.d.	3.93	n.d.	6.66	0.71	0.17	0.23	35.07
429	214	3-10	844.82	M.R.P.	21.20	0.76	3.90	n.d.	15.85	n.d.	10.99	0.65	0.33	0.24	53.92
430	214	3-11	844.82	M.R.P.	31.15	0.18	6.49	n.d.	5.89	n.d.	11.64	5.18	0.27	0.38	61.18
431	214	3-12	844.82	M.R.P.	41.89	0.13	6.66	n.d.	4.92	n.d.	19.86	1.23	0.68	0.38	75.75
432	214	3-13	844.82	M.R.P.	33.61	0.25	8.30	n.d.	6.20	n.d.	7.14	0.77	0.34	3.37	59.98
433	214	3-14	844.82	M.R.P.	18.97	n.d.	2.73	n.d.	2.51	n.d.	12.66	0.69	0.19	0.09	37.84
434	214	3-15	844.82	M.R.P.	35.21	0.42	5.61	n.d.	6.04	n.d.	18.39	2.79	0.31	0.19	68.96
435	214	3-16	844.82	M.R.P.	34.29	0.17	6.96	n.d.	6.47	n.d.	12.66	3.25	0.37	0.72	64.89
436	214	3-17	844.82	M.R.P.	37.53	1.55	8.80	n.d.	6.03	n.d.	11.75	1.23	0.81	1.91	69.61
437	214	3-18	844.82	M.R.P.	36.86	0.66	9.89	n.d.	5.87	n.d.	11.16	3.95	0.82	1.35	70.56
438	214	3-19	844.82	M.R.P.	40.25	0.22	10.85	n.d.	5.86	n.d.	11.80	1.38	0.82	2.53	73.71
439	214	3-20	844.82	M.R.P.	35.41	1.20	6.38	n.d.	5.50	n.d.	14.87	2.27	0.45	0.40	66.48
440	214	4-1	844.82	M.R.P.	64.78	0.49	18.24	n.d.	1.05	n.d.	0.34	1.04	5.76	7.26	98.96
441	214	4-2	844.82	M.R.P.	64.47	0.43	17.98	n.d.	1.32	n.d.	0.59	1.78	4.94	7.98	99.49
442	214	4-3	844.82	M.R.P.	61.52	0.31	18.04	n.d.	0.91	n.d.	0.99	1.29	5.80	6.61	95.47
443	214	4-4	844.82	M.R.P.	64.67	0.53	17.75	n.d.	1.17	n.d.	0.58	1.24	5.08	8.55	99.57
444	214	4-5	844.82	M.R.P.	64.43	0.61	17.60	n.d.	1.30	n.d.	0.49	1.50	5.53	7.84	99.30
445	214	4-6	844.82	M.R.P.	62.96	0.47	18.48	n.d.	1.41	n.d.	0.83	2.86	5.20	6.93	99.14
446	214	4-7	844.82	M.R.P.	64.26	0.51	17.74	n.d.	1.47	n.d.	0.48	1.44	5.12	8.30	99.32
447	214	4-8	844.82	M.R.P.	62.73	0.35	18.67	n.d.	1.23	n.d.	0.53	2.71	4.09	8.27	98.58
448	214	4-9	844.82	M.R.P.	63.54	0.60	18.28	n.d.	1.19	n.d.	0.44	1.60	5.63	8.17	99.45
449	214	4-10	844.82	M.R.P.	63.54	0.21	18.64	n.d.	1.37	n.d.	0.47	2.99	5.28	7.03	99.53
450	214	4-11	844.82	M.R.P.	63.23	0.49	17.73	n.d.	1.07	n.d.	0.41	1.44	5.56	7.85	97.78

Table A.5. *Continued*

Analysis #	Sample #	Batch #	Depth (m)	Comment	SiO_2	TiO_2	Al_2O_3	Cr_2O_3	FeO_{tot}	MnO	MgO	CaO	Na_2O	K_2O	Total
451	214	4-12	844.82	M.R.P.	64.19	0.40	18.06	n.d.	0.60	n.d.	0.16	0.92	5.60	8.46	98.39
452	214	4-13	844.82	M.R.P.	63.74	0.43	18.13	n.d.	0.99	n.d.	0.44	1.27	5.78	7.55	98.33
453	214	4-14	844.82	M.R.P.	63.68	0.31	18.48	n.d.	0.71	n.d.	0.18	0.95	7.71	4.80	96.82
454	214	4-15	844.82	M.R.P.	62.69	0.21	18.50	n.d.	0.60	n.d.	0.22	1.07	7.21	5.62	96.12
455	214	4-16	844.82	M.R.P.	63.02	0.33	17.97	n.d.	1.76	n.d.	0.67	1.68	7.24	5.22	97.89
456	214	4-17	844.82	M.R.P.	63.96	0.26	18.38	n.d.	1.57	n.d.	0.72	1.75	6.97	5.23	98.84
457	214	4-18	844.82	M.R.P.	64.64	0.34	17.82	n.d.	3.38	n.d.	0.70	2.15	8.45	2.86	100.34
458	214	4-19	844.82	M.R.P.	64.64	0.26	18.32	n.d.	2.19	n.d.	0.52	1.99	7.72	4.38	100.02
459	214	4-20	844.82	M.R.P.	28.98	3.28	5.47	n.d.	19.38	n.d.	14.06	2.24	0.28	0.33	74.02
460	214	5-1	844.82	M.R.P.	64.28	0.48	18.32	n.d.	0.92	n.d.	0.31	1.68	5.52	7.39	98.90
461	214	5-2	844.82	M.R.P.	62.41	0.37	19.68	n.d.	0.73	n.d.	0.22	2.72	5.41	6.76	98.30
462	214	5-3	844.82	M.R.P.	61.61	0.47	17.72	n.d.	1.65	n.d.	1.38	3.29	4.88	6.37	97.37
463	214	5-4	844.82	M.R.P.	62.14	0.35	19.23	n.d.	0.74	n.d.	0.19	2.43	5.44	7.02	97.54
464	214	5-5	844.82	M.R.P.	64.61	0.54	18.29	n.d.	0.53	n.d.	0.13	0.87	5.57	7.78	98.32
465	214	5-6	844.82	M.R.P.	64.25	0.38	18.35	n.d.	0.83	n.d.	0.26	1.43	5.34	7.95	98.79
466	214	5-7	844.82	M.R.P.	63.31	0.50	17.21	n.d.	1.78	n.d.	0.69	2.34	5.69	6.41	97.93
467	214	5-8	844.82	M.R.P.	97.41	n.d.	0.50	n.d.	0.23	n.d.	n.d.	0.05	0.14	0.21	98.54
468	214	5-9	844.82	M.R.P.	62.44	0.50	18.51	n.d.	3.21	n.d.	0.72	3.81	5.67	4.82	99.68
469	214	5-10	844.82	M.R.P.	60.65	0.61	18.06	n.d.	3.49	n.d.	1.04	4.11	5.60	4.47	98.03
470	214	5-11	844.82	M.R.P.	60.36	0.40	20.75	n.d.	2.89	n.d.	0.59	5.73	6.00	3.28	100.00
471	214	5-12	844.82	M.R.P.	61.47	0.54	18.87	n.d.	3.21	n.d.	0.67	4.56	5.61	3.94	98.87
472	214	5-13	844.82	M.R.P.	62.39	0.37	18.13	n.d.	2.18	n.d.	1.12	1.90	5.06	7.38	98.53
473	214	5-14	844.82	M.R.P.	60.65	0.41	17.76	n.d.	2.01	n.d.	1.39	2.90	4.26	8.07	97.45
474	214	5-15	844.82	M.R.P.	62.82	0.47	18.69	n.d.	1.82	n.d.	0.79	3.01	5.45	6.20	99.25
475	214	5-16	844.82	M.R.P.	59.66	0.31	22.51	n.d.	1.70	n.d.	0.50	6.27	5.62	3.15	99.72
476	214	5-17	844.82	M.R.P.	63.66	0.52	17.60	n.d.	1.81	n.d.	0.52	1.77	5.54	6.97	98.39
477	214	5-18	844.82	M.R.P.	65.19	0.60	18.16	0.05	1.13	n.d.	0.36	1.03	5.45	8.32	100.29
478	214	5-19	844.82	M.R.P.	64.67	0.53	18.25	n.d.	1.44	n.d.	0.43	1.69	5.10	8.12	100.23
479	214	5-20	844.82	M.R.P.	62.82	0.51	19.41	n.d.	1.98	n.d.	0.60	3.03	5.52	6.68	100.55
480	763	1-1	846.01	Meso	54.95	0.21	19.76	n.d.	2.92	n.d.	0.20	5.42	4.43	4.56	92.45
481	763	1-2	846.01	Meso	57.08	0.26	21.87	n.d.	1.47	n.d.	0.29	6.75	4.62	3.82	96.16
482	763	1-3	846.01	Meso	54.56	0.43	17.59	n.d.	2.10	n.d.	1.80	7.26	4.03	3.82	91.59
483	763	1-4	846.01	Meso	57.78	0.26	19.51	n.d.	1.34	n.d.	0.37	5.67	4.87	4.66	94.46
484	763	1-5	846.01	Meso	58.90	0.25	18.17	n.d.	2.14	n.d.	0.45	5.39	4.50	4.95	94.75
485	763	1-6	846.01	Meso	56.98	0.34	17.82	n.d.	1.64	n.d.	0.36	4.78	5.71	3.60	91.23
486	763	1-7	846.01	Meso	57.76	0.19	19.85	n.d.	1.50	n.d.	0.36	5.57	4.91	4.15	94.29
487	763	1-8	846.01	Meso	57.39	0.35	18.22	n.d.	1.67	n.d.	0.92	5.43	3.92	5.23	93.13
488	763	1-9	846.01	Meso	58.25	0.28	19.26	n.d.	1.67	n.d.	0.45	5.08	4.31	5.23	94.53
489	763	1-10	846.01	Meso	55.08	0.16	19.48	n.d.	1.38	n.d.	0.21	5.27	4.72	3.67	89.97
490	763	1-11	846.01	Meso	55.23	0.55	17.21	n.d.	1.31	n.d.	1.20	4.10	4.81	3.73	88.14
491	763	1-12	846.01	Meso	56.92	0.21	18.85	n.d.	1.84	n.d.	0.40	5.78	4.94	3.82	92.76
492	763	1-13	846.01	Meso	57.82	0.17	20.75	n.d.	1.41	n.d.	0.79	7.17	4.50	3.58	96.19
493	763	1-14	846.01	Meso	56.86	0.19	20.19	n.d.	1.88	n.d.	0.93	7.28	4.44	3.69	95.46
494	763	1-15	846.01	Meso	57.94	0.24	20.23	n.d.	2.20	n.d.	0.83	6.86	4.20	4.51	97.01
495	763	1-16	846.01	Meso	57.42	0.31	17.95	n.d.	1.78	n.d.	0.74	5.47	5.00	4.33	93.00
496	763	1-17	846.01	Meso	56.32	0.43	17.19	n.d.	1.67	n.d.	0.98	5.79	5.10	3.68	91.16
497	763	1-18	846.01	Meso	54.57	0.39	16.20	n.d.	3.68	n.d.	2.60	7.64	3.86	4.05	92.99
498	763	1-19	846.01	Meso	57.00	0.27	16.42	n.d.	2.47	n.d.	2.06	6.93	3.57	5.03	93.75
499	763	1-20	846.01	Meso	55.92	0.22	19.14	n.d.	2.33	n.d.	1.34	8.30	4.62	2.81	94.68
500	763	2-1	846.01	M.R.P. Tr.	62.95	0.34	17.95	n.d.	1.04	n.d.	0.25	1.63	6.68	5.06	95.90

Table A.5. *Continued*

Analysis #	Sample #	Batch #	Depth (m)	Comment	SiO_2	TiO_2	Al_2O_3	Cr_2O_3	FeO_{tot}	MnO	MgO	CaO	Na_2O	K_2O	Total
501	763	2-1	846.01	M.R.P. Tr.	64.50	0.70	18.42	n.d.	0.91	n.d.	0.27	1.28	4.80	6.56	97.44
502	763	2-2	846.01	M.R.P. Tr.	59.70	0.21	21.34	n.d.	1.55	n.d.	0.32	5.67	5.25	3.68	97.72
503	763	2-2	846.01	M.R.P. Tr.	64.34	0.30	18.12	n.d.	0.67	n.d.	0.21	1.25	4.63	8.13	97.65
504	763	2-3	846.01	M.R.P. Tr.	58.61	0.15	22.96	n.d.	2.02	n.d.	0.39	8.22	5.09	2.35	99.79
505	763	2-3	846.01	M.R.P. Tr.	64.08	0.32	19.15	n.d.	0.67	n.d.	0.19	1.87	4.17	8.23	98.68
506	763	2-4	846.01	M.R.P. Tr.	62.82	0.47	16.99	n.d.	1.12	n.d.	0.29	1.42	6.34	5.10	94.55
507	763	2-4	846.01	M.R.P. Tr.	61.81	1.86	17.39	n.d.	0.69	n.d.	0.19	1.34	4.28	8.06	95.62
508	763	2-5	846.01	M.R.P. Tr.	62.85	0.38	17.61	n.d.	0.72	n.d.	0.24	1.16	5.73	6.29	94.98
509	763	2-5	846.01	M.R.P. Tr.	62.45	0.33	18.61	0.06	0.89	n.d.	0.38	2.62	4.69	6.68	96.71
510	763	2-6	846.01	M.R.P. Tr.	62.99	0.28	17.94	n.d.	0.94	n.d.	0.33	2.23	5.93	5.55	96.19
511	763	2-6	846.01	M.R.P. Tr.	63.59	0.32	17.73	n.d.	0.85	n.d.	0.26	1.17	5.38	6.93	96.23
512	763	2-7	846.01	M.R.P. Tr.	62.10	0.27	17.70	n.d.	1.12	n.d.	0.39	2.75	5.75	5.25	95.33
513	763	2-7	846.01	M.R.P. Tr.	62.65	0.35	18.55	n.d.	1.23	n.d.	0.32	2.80	5.35	5.00	96.25
514	763	2-8	846.01	M.R.P. Tr.	61.87	0.30	16.86	n.d.	1.58	n.d.	1.00	1.83	5.39	5.88	94.71
515	763	2-8	846.01	M.R.P. Tr.	63.91	0.29	17.74	0.05	0.60	n.d.	0.18	1.08	4.71	7.87	96.43
516	763	2-9	846.01	M.R.P. Tr.	62.07	0.39	17.72	n.d.	1.26	n.d.	1.44	4.02	5.12	5.46	97.48
517	763	2-9	846.01	M.R.P. Tr.	63.51	0.33	17.89	n.d.	0.70	n.d.	0.19	1.17	4.74	7.11	95.64
518	763	2-10	846.01	M.R.P. Tr.	59.57	0.90	22.15	n.d.	1.64	n.d.	0.60	6.63	5.17	2.99	99.65
519	763	2-10	846.01	M.R.P. Tr.	57.85	0.38	22.35	n.d.	1.65	n.d.	0.37	7.36	5.07	2.93	97.96
520	763	2-11	846.01	M.R.P. Tr.	59.41	1.12	21.83	n.d.	1.75	n.d.	0.60	6.22	5.03	3.01	98.97
521	763	2-11	846.01	M.R.P. Tr.	63.56	0.94	17.74	n.d.	0.72	n.d.	0.13	0.97	4.02	8.37	96.45
522	763	2-12	846.01	M.R.P. Tr.	64.25	0.32	17.64	n.d.	1.30	n.d.	0.28	1.33	5.10	7.28	97.50
523	763	2-12	846.01	M.R.P. Tr.	59.15	0.16	21.38	n.d.	1.55	n.d.	0.36	5.85	5.14	3.47	97.06
524	763	2-13	846.01	M.R.P. Tr.	63.40	0.31	18.77	n.d.	1.28	n.d.	0.36	2.07	5.45	5.52	97.16
525	763	2-13	846.01	M.R.P. Tr.	63.31	0.28	18.53	n.d.	0.86	n.d.	0.22	2.20	5.17	6.16	96.73
526	763	2-14	846.01	M.R.P. Tr.	61.54	0.53	17.25	n.d.	1.03	n.d.	0.86	1.58	4.81	6.67	94.27
527	763	2-14	846.01	M.R.P. Tr.	59.14	0.34	19.03	n.d.	1.72	n.d.	0.46	4.87	5.41	3.57	94.54
528	763	2-15	846.01	M.R.P. Tr.	57.14	1.78	20.37	n.d.	1.78	n.d.	1.44	6.04	4.99	2.97	96.51
529	763	2-15	846.01	M.R.P. Tr.	60.18	0.30	18.10	n.d.	1.48	n.d.	0.38	3.09	5.21	4.40	93.14
530	763	2-16	846.01	M.R.P. Tr.	46.77	0.26	10.07	n.d.	4.08	n.d.	6.44	5.44	1.68	4.33	79.07
531	763	2-16	846.01	M.R.P. Tr.	58.67	0.87	17.29	n.d.	2.14	0.09	0.78	3.79	5.52	3.70	92.85
532	763	2-17	846.01	M.R.P. Tr.	63.19	0.46	19.08	n.d.	1.00	n.d.	0.25	2.51	5.34	6.37	98.20
533	763	2-17	846.01	M.R.P. Tr.	57.53	0.40	19.04	n.d.	2.24	n.d.	0.61	5.50	5.67	2.46	93.45
534	763	2-18	846.01	M.R.P. Tr.	62.86	0.19	18.43	n.d.	1.30	n.d.	0.88	3.69	4.10	7.27	98.72
535	763	2-18	846.01	M.R.P. Tr.	58.48	0.29	18.93	n.d.	2.64	n.d.	0.65	5.52	6.14	2.14	94.79
536	763	2-19	846.01	M.R.P. Tr.	62.11	0.31	17.78	n.d.	0.94	n.d.	0.25	1.86	5.23	6.20	94.68
537	763	2-19	846.01	M.R.P. Tr.	59.12	0.29	19.66	n.d.	2.60	n.d.	0.69	6.23	5.78	2.23	96.60
538	763	2-20	846.01	M.R.P. Tr.	63.58	0.69	17.77	n.d.	0.77	n.d.	0.27	1.45	5.58	6.46	96.57
539	763	2-20	846.01	M.R.P. Tr.	61.69	0.61	17.92	0.05	2.27	n.d.	0.35	2.63	5.27	5.69	96.48
540	243	1-1	860.4	Br. M.R.P.	56.20	2.73	22.47	n.d.	2.16	n.d.	0.08	6.75	4.09	4.83	99.31
541	243	1-2	860.4	Br. M.R.P.	59.12	1.55	19.57	n.d.	1.63	n.d.	0.08	3.01	2.66	9.32	96.94
542	243	1-3	860.4	Br. M.R.P.	51.97	0.63	16.52	0.07	12.47	n.d.	0.07	0.43	1.15	10.35	93.66
543	243	1-4	860.4	Br. M.R.P.	59.97	2.69	19.18	n.d.	0.99	n.d.	n.d.	2.56	3.19	8.98	97.56
544	243	1-5	860.4	Br. M.R.P.	54.93	1.34	16.81	n.d.	7.97	0.10	n.d.	1.66	1.67	10.77	95.25
545	243	1-6	860.4	Br. M.R.P.	58.86	1.07	20.60	n.d.	1.49	n.d.	n.d.	4.07	2.93	8.59	97.61
546	243	1-7	860.4	Br. M.R.P.	55.45	2.86	22.15	n.d.	2.77	n.d.	0.08	6.32	3.70	5.68	99.01
547	243	1-8	860.4	Br. M.R.P.	59.82	0.96	21.28	n.d.	1.31	n.d.	0.28	4.99	3.03	7.69	99.36
548	243	1-9	860.4	Br. M.R.P.	56.31	2.19	20.59	n.d.	1.60	n.d.	0.23	5.33	3.63	6.19	96.07
549	243	1-10	860.4	Br. M.R.P.	55.10	2.37	23.25	n.d.	2.51	n.d.	0.13	7.71	4.41	3.38	98.86
550	243	1-11	860.4	Br. M.R.P.	98.26	n.d.	0.12	n.d.	0.19	n.d.	0.14	0.22	0.03	n.d.	98.96

Table A.5. *Continued*

Analysis #	Sample #	Batch #	Depth (m)	Comment	SiO_2	TiO_2	Al_2O_3	Cr_2O_3	FeO_{tot}	MnO	MgO	CaO	Na_2O	K_2O	Total
551	243	1-12	860.4	Br. M.R.P.	98.57	n.d.	0.09	n.d.	0.13	n.d.	n.d.	n.d.	n.d.	0.08	98.87
552	243	1-13	860.4	Br. M.R.P.	56.76	1.51	19.81	n.d.	3.55	n.d.	0.42	4.67	3.60	6.71	97.03
553	243	1-14	860.4	Br. M.R.P.	57.05	0.82	24.26	n.d.	1.84	n.d.	0.17	8.00	5.24	2.34	99.72
554	243	1-15	860.4	Br. M.R.P.	56.86	0.18	20.80	n.d.	2.37	n.d.	0.96	7.20	3.29	5.81	97.47
555	243	1-16	860.4	Br. M.R.P.	55.81	0.32	19.68	n.d.	2.55	n.d.	2.35	9.90	3.53	3.65	97.79
556	243	1-17	860.4	Br. M.R.P.	58.18	0.77	21.29	n.d.	2.85	n.d.	0.38	5.53	3.55	6.93	99.48
557	243	1-18	860.4	Br. M.R.P.	59.78	0.58	20.63	n.d.	2.15	n.d.	0.11	4.03	2.56	9.15	98.99
558	243	1-19	860.4	Br. M.R.P.	60.61	0.35	19.48	n.d.	1.00	n.d.	0.08	2.56	2.25	10.02	96.35
559	243	1-20	860.4	Br. M.R.P.	59.26	1.16	16.80	n.d.	1.66	n.d.	0.22	1.18	1.10	12.41	93.79
560	243	2-1	860.4	Qtz	95.63	n.d.	0.21	n.d.	n.d.	n.d.	0.08	0.06	0.07	n.d.	96.05
561	243	2-2	860.4	Qtz	96.74	n.d.	0.17	n.d.	n.d.	n.d.	n.d.	0.05	0.07	n.d.	97.03
562	243	2-3	860.4	Qtz	96.06	0.43	0.13	n.d.	n.d.	n.d.	n.d.	0.06	0.05	n.d.	96.73
563	243	2-4	860.4	M.R.P.	60.25	n.d.	22.88	n.d.	0.31	n.d.	0.17	4.27	5.78	4.63	98.29
564	243	2-5	860.4	M.R.P.	58.54	n.d.	24.52	n.d.	0.24	n.d.	0.13	6.02	4.83	4.77	99.05
565	243	2-6	860.4	M.R.P.	58.25	n.d.	25.83	n.d.	0.31	n.d.	0.05	7.05	6.99	0.97	99.45
566	243	2-7	860.4	M.R.P.	59.06	n.d.	25.60	n.d.	0.21	n.d.	n.d.	7.07	6.80	1.14	99.88
567	243	2-8	860.4	Qtz	95.22	n.d.	0.33	n.d.	0.46	n.d.	0.06	0.06	0.06	0.05	96.24
568	243	2-9	860.4	Qtz	95.82	n.d.	0.49	n.d.	0.30	n.d.	n.d.	0.12	0.11	n.d.	96.84
569	243	2-10	860.4	M.R.P.	61.46	n.d.	23.81	n.d.	0.23	n.d.	0.05	5.41	7.28	1.76	100.00
570	243	2-11	860.4	M.R.P.	59.62	n.d.	22.70	0.05	0.44	n.d.	0.12	4.86	4.19	6.48	98.46
571	243	2-12	860.4	Qtz	96.47	n.d.	0.05	n.d.	n.d.	n.d.	n.d.	n.d.	n.d.	n.d.	96.52
572	243	2-13	860.4	Qtz	97.77	n.d.	n.d.	n.d.	0.15	n.d.	n.d.	n.d.	0.02	n.d.	97.94
573	243	2-14	860.4	Qtz	93.49	1.05	0.46	0.05	0.11	n.d.	n.d.	0.06	0.09	0.05	95.36
574	243	2-15	860.4	Qtz	94.86	0.12	0.38	n.d.	n.d.	n.d.	n.d.	n.d.	0.15	n.d.	95.51
575	243	2-16	860.4	Qtz	96.96	0.08	0.40	n.d.	n.d.	n.d.	n.d.	n.d.	0.08	0.06	97.58
576	243	2-17	860.4	Qtz	95.36	n.d.	0.34	n.d.	0.09	n.d.	n.d.	n.d.	0.11	0.05	95.95
577	243	2-18	860.4	Qtz	93.18	n.d.	0.46	n.d.	n.d.	n.d.	n.d.	n.d.	0.15	0.06	93.85
578	243	2-19	860.4	Qtz	96.36	0.06	0.40	n.d.	n.d.	n.d.	n.d.	n.d.	0.14	n.d.	96.96
579	243	2-20	860.4	Qtz	96.73	n.d.	0.45	0.05	n.d.	n.d.	n.d.	0.07	0.13	n.d.	97.43
580	243	3-1	860.4	Qtz	97.96	n.d.	0.21	n.d.	n.d.	n.d.	n.d.	n.d.	0.08	n.d.	98.25
581	243	3-2	860.4	Qtz	96.41	n.d.	0.44	n.d.	n.d.	n.d.	n.d.	n.d.	0.20	n.d.	97.05
582	243	3-3	860.4	Qtz	96.23	n.d.	n.d.	n.d.	n.d.	n.d.	n.d.	n.d.	0.05	n.d.	96.28
583	243	3-4	860.4	Qtz	97.84	n.d.	n.d.	n.d.	n.d.	n.d.	n.d.	n.d.	0.05	n.d.	97.89
584	243	3-5	860.4	Hole	0.06	n.d.	n.d.	n.d.	n.d.	n.d.	n.d.	n.d.	0.02	n.d.	0.08
585	243	3-6	860.4	Qtz	97.16	n.d.	0.22	0.07	n.d.	n.d.	n.d.	n.d.	0.08	n.d.	97.53
586	243	3-7	860.4	Br. M.R.P.	59.05	0.40	21.60	n.d.	1.22	n.d.	0.07	4.45	3.51	8.00	98.30
587	243	3-8	860.4	Br. M.R.P.	58.35	0.06	22.37	n.d.	1.20	n.d.	0.23	4.84	4.30	6.33	97.68
588	243	3-9	860.4	Br. M.R.P.	59.60	0.29	18.84	n.d.	1.52	n.d.	0.82	3.80	2.95	9.59	97.41
589	243	3-10	860.4	Br. M.R.P.	60.05	0.06	20.42	n.d.	1.17	n.d.	0.12	3.36	2.37	10.17	97.72
590	243	3-11	860.4	Br. M.R.P.	59.14	0.13	21.79	n.d.	1.26	n.d.	0.13	5.00	3.73	7.14	98.32
591	243	3-12	860.4	Br. M.R.P.	58.57	n.d.	22.36	n.d.	1.55	n.d.	0.16	5.22	3.42	7.10	98.38
592	243	3-13	860.4	Br. M.R.P.	56.98	0.12	23.00	n.d.	1.76	n.d.	0.90	7.79	4.06	4.66	99.27
593	243	3-14	860.4	Br. M.R.P.	63.86	0.06	18.11	n.d.	0.49	n.d.	n.d.	n.d.	0.08	16.34	98.94
594	243	3-15	860.4	Br. M.R.P.	55.91	1.14	22.87	n.d.	2.40	n.d.	0.35	7.35	4.03	4.82	98.87
595	243	3-16	860.4	Br. M.R.P.	96.01	0.07	0.52	n.d.	0.26	n.d.	n.d.	0.06	0.16	0.06	97.14
596	243	3-17	860.4	Br. M.R.P.	56.53	1.75	23.21	n.d.	2.22	n.d.	0.15	6.03	3.72	5.58	99.19
597	243	3-18	860.4	Br. M.R.P.	56.06	1.02	22.53	n.d.	1.89	n.d.	0.75	7.43	3.61	4.99	98.28
598	243	3-19	860.4	Br. M.R.P.	58.04	0.58	21.74	n.d.	1.39	n.d.	0.33	5.37	2.71	7.31	97.47
599	243	3-20	860.4	Br. M.R.P.	59.81	0.28	21.07	n.d.	1.23	n.d.	0.08	3.81	3.37	7.63	97.28
600	243	4-1	860.4	Qtz	97.56	n.d.	n.d.	n.d.	n.d.	n.d.	n.d.	0.06	0.04	n.d.	97.66

Table A.5. *Continued*

Analysis #	Sample #	Batch #	Depth (m)	Comment	SiO_2	TiO_2	Al_2O_3	Cr_2O_3	FeO_{tot}	MnO	MgO	CaO	Na_2O	K_2O	Total
601	243	4-2	860.4	Qtz	95.35	0.27	0.39	n.d.	0.12	n.d.	n.d.	n.d.	0.08	0.07	96.28
602	243	4-3	860.4	Qtz	95.36	0.06	0.44	n.d.	n.d.	n.d.	n.d.	0.08	0.12	0.07	96.13
603	243	4-4	860.4	Qtz	97.69	n.d.	n.d.	0.05	n.d.	n.d.	n.d.	n.d.	n.d.	n.d.	97.74
604	243	4-5	860.4	Qtz	97.42	n.d.	n.d.	n.d.	n.d.	n.d.	n.d.	n.d.	0.03	n.d.	97.45
605	243	4-6	860.4	Qtz	98.11	n.d.	0.21	0.05	n.d.	n.d.	n.d.	n.d.	0.06	0.05	98.48
606	243	4-7	860.4	Br. M.R.P.	70.02	0.11	11.60	n.d.	2.03	n.d.	2.45	6.43	1.46	4.68	98.78
607	243	4-8	860.4	Br. M.R.P.	61.09	n.d.	18.94	n.d.	1.47	n.d.	0.14	2.55	11.97	11.26	107.42
608	243	4-9	860.4	Br. M.R.P.	58.09	0.13	20.57	n.d.	1.90	n.d.	1.28	6.28	3.00	7.20	98.45
609	243	4-10	860.4	Br. M.R.P.	56.84	0.15	19.09	n.d.	2.47	n.d.	1.84	7.07	3.30	6.28	97.04
610	243	4-11	860.4	Br. M.R.P.	60.97	n.d.	22.50	n.d.	0.95	n.d.	0.10	4.22	6.63	4.27	99.64
611	243	4-12	860.4	Br. M.R.P.	57.44	0.11	20.47	n.d.	2.61	n.d.	1.88	7.28	3.29	6.14	99.22
612	243	4-13	860.4	Br. M.R.P.	58.24	0.05	23.33	n.d.	1.54	n.d.	0.38	7.16	4.00	5.49	100.19
613	243	4-14	860.4	Br. M.R.P.	57.51	0.06	22.30	n.d.	1.85	n.d.	0.41	6.08	4.13	5.77	98.11
614	243	4-15	860.4	Br. M.R.P.	58.69	0.06	20.77	n.d.	1.69	n.d.	0.42	4.80	3.20	8.15	97.78
615	243	4-16	860.4	Br. M.R.P.	58.92	0.09	19.56	0.08	1.46	n.d.	0.88	4.92	3.09	7.98	96.98
616	243	4-17	860.4	Br. M.R.P.	59.66	0.09	20.35	n.d.	1.37	n.d.	0.27	4.25	3.32	8.78	98.09
617	243	4-18	860.4	Br. M.R.P.	57.13	0.05	22.45	n.d.	1.54	n.d.	0.19	6.31	4.28	5.01	96.96
618	243	4-19	860.4	Br. M.R.P.	57.61	0.22	19.06	n.d.	2.68	n.d.	2.15	7.48	2.75	6.85	98.80
619	243	4-20	860.4	Br. M.R.P.	60.48	0.13	19.64	0.06	1.32	n.d.	0.22	2.82	2.07	10.90	97.64
620	762	1-1	860.4	Qtz	97.89	n.d.	0.07	n.d.	n.d.	n.d.	n.d.	n.d.	0.02	n.d.	97.98
621	762	1-2	860.4	Qtz	97.55	n.d.	0.07	n.d.	n.d.	n.d.	n.d.	0.07	0.02	n.d.	97.71
622	762	1-3	860.4	M.R.P.	55.79	0.09	23.88	n.d.	1.96	n.d.	0.39	8.60	4.83	2.69	98.23
623	762	1-4	860.4	M.R.P.	58.74	0.09	21.00	n.d.	1.40	n.d.	0.11	4.66	3.19	7.38	96.57
624	762	1-5	860.4	M.R.P.	57.24	n.d.	22.08	n.d.	1.40	n.d.	0.27	7.22	3.32	5.91	97.44
625	762	1-6	860.4	M.R.P.	56.27	0.13	17.39	n.d.	2.19	n.d.	2.65	8.28	2.64	6.44	95.99
626	762	1-7	860.4	M.R.P.	57.21	0.05	21.66	n.d.	1.36	n.d.	0.30	6.36	3.36	6.07	96.37
627	762	1-8	860.4	M.R.P.	56.74	0.18	15.79	n.d.	2.77	n.d.	2.69	6.68	1.61	8.88	95.34
628	762	1-9	860.4	M.R.P.	53.28	0.07	24.52	n.d.	1.71	n.d.	0.34	9.57	4.43	1.67	95.59
629	762	1-10	860.4	M.R.P.	58.24	0.08	20.14	n.d.	1.79	n.d.	0.78	5.47	2.31	8.38	97.19
630	762	1-11	860.4	M.R.P.	57.92	2.67	16.79	n.d.	1.82	n.d.	0.92	3.19	1.76	10.64	95.71
631	762	1-12	860.4	M.R.P.	58.57	0.10	20.33	n.d.	1.33	n.d.	0.56	5.44	2.73	7.95	97.01
632	762	1-13	860.4	M.R.P.	54.19	0.09	24.32	n.d.	1.88	n.d.	0.60	10.00	4.19	2.69	97.96
633	762	1-14	860.4	M.R.P.	55.65	0.08	24.28	n.d.	1.56	n.d.	0.17	8.54	3.96	3.78	98.02
634	762	1-15	860.4	M.R.P.	53.92	n.d.	22.95	n.d.	1.70	n.d.	0.35	7.45	4.23	3.93	94.53
635	762	1-16	860.4	M.R.P.	55.86	n.d.	23.17	n.d.	0.18	n.d.	0.13	5.79	5.84	3.33	94.30
636	762	1-17	860.4	M.R.P.	58.70	0.09	23.14	n.d.	0.26	n.d.	0.18	5.55	5.47	3.73	97.12
637	762	1-18	860.4	M.R.P.	57.96	n.d.	23.78	n.d.	0.23	n.d.	0.19	6.34	5.27	3.34	97.11
638	762	1-19	860.4	M.R.P.	59.70	n.d.	24.07	n.d.	0.21	n.d.	0.10	6.17	6.29	2.60	99.14
639	762	1-20	860.4	M.R.P.	58.67	n.d.	24.40	n.d.	0.20	n.d.	0.15	6.43	6.02	2.71	98.58
640	242	1-1	878.09	Hole	0.13	n.d.	n.d.	n.d.	n.d.	n.d.	0.05	0.05	n.d.	n.d.	0.23
641	242	1-2	878.09	Hole	1.49	n.d.	0.36	n.d.	0.21	n.d.	0.18	0.08	n.d.	0.16	2.48
642	242	1-3	878.09	M.R.P.	61.94	n.d.	19.92	n.d.	0.65	n.d.	0.05	2.42	1.89	11.90	98.77
643	242	1-4	878.09	M.R.P.	61.12	n.d.	20.92	n.d.	0.97	n.d.	0.05	3.45	1.95	10.82	99.28
644	242	1-5	878.09	M.R.P.	59.14	0.81	21.31	n.d.	1.73	n.d.	0.11	4.54	2.26	9.08	98.98
645	242	1-6	878.09	M.R.P.	39.27	0.10	6.24	n.d.	4.84	0.11	14.13	3.57	0.13	1.42	69.81
646	242	1-7	878.09	M.R.P.	26.98	0.19	3.66	n.d.	4.03	0.11	5.35	8.18	0.16	1.27	49.93
647	242	1-8	878.09	M.R.P.	27.17	10.97	5.46	n.d.	4.17	n.d.	9.41	0.81	0.06	1.67	59.72
648	242	1-9	878.09	M.R.P.	33.55	6.34	5.86	n.d.	4.64	n.d.	13.43	0.81	0.09	1.25	65.97
649	242	1-10	878.09	M.R.P.	34.16	0.18	5.97	n.d.	5.68	n.d.	9.39	3.76	0.13	2.33	61.60
650	242	1-11	878.09	M.R.P.	46.17	0.28	2.63	n.d.	6.04	0.16	12.24	18.13	0.31	0.78	86.74

Table A.5. *Continued*

Analysis #	Sample #	Batch #	Depth (m)	Comment	SiO_2	TiO_2	Al_2O_3	Cr_2O_3	FeO_{tot}	MnO	MgO	CaO	Na_2O	K_2O	Total
651	242	1-12	878.09	M.R.P.	63.04	n.d.	17.00	n.d.	0.14	n.d.	n.d.	0.15	0.38	15.43	96.14
652	242	1-13	878.09	M.R.P.	61.85	n.d.	19.78	n.d.	0.58	n.d.	n.d.	2.46	1.67	12.29	98.63
653	242	1-14	878.09	M.R.P.	62.54	n.d.	17.60	n.d.	0.64	n.d.	0.68	1.19	0.17	15.24	98.06
654	242	1-15	878.09	M.R.P.	57.70	n.d.	24.94	n.d.	1.71	n.d.	0.12	7.92	3.66	4.28	100.33
655	242	1-16	878.09	M.R.P.	57.30	n.d.	22.93	n.d.	1.65	n.d.	0.23	6.57	3.35	5.87	97.90
656	242	1-17	878.09	M.R.P.	36.53	0.12	8.38	n.d.	4.16	n.d.	7.25	1.54	0.65	4.17	62.80
657	242	1-18	878.09	M.R.P.	53.69	n.d.	24.89	n.d.	2.08	n.d.	0.23	10.14	4.67	0.93	96.63
658	242	1-19	878.09	M.R.P.	53.97	0.11	19.18	n.d.	2.12	n.d.	1.68	6.34	2.18	6.59	92.17
659	242	1-20	878.09	M.R.P.	57.70	n.d.	22.90	n.d.	1.30	n.d.	0.12	6.09	2.90	6.99	98.00
660	242	1-21	878.09	M.R.P.	63.66	n.d.	18.56	n.d.	0.15	n.d.	n.d.	0.36	0.24	16.20	99.17
661	242	1-22	878.09	M.R.P.	60.74	0.07	19.39	n.d.	1.02	n.d.	0.45	3.52	1.63	10.80	97.62
662	242	1-23	878.09	M.R.P.	62.86	n.d.	18.71	n.d.	0.48	n.d.	n.d.	0.99	0.74	14.39	98.17
663	242	1-24	878.09	M.R.P.	40.70	0.33	10.54	n.d.	7.83	n.d.	5.85	0.87	0.08	4.20	70.40
664	242	1-25	878.09	M.R.P.	63.97	n.d.	17.94	n.d.	0.12	n.d.	n.d.	n.d.	0.04	16.65	98.72
665	242	1-26	878.09	M.R.P.	40.94	n.d.	5.69	n.d.	3.73	n.d.	18.73	1.04	0.13	0.29	70.55
666	242	1-27	878.09	M.R.P.	54.69	0.10	25.07	n.d.	1.92	n.d.	0.17	9.61	4.69	2.35	98.60
667	242	1-28	878.09	M.R.P.	47.39	0.17	14.92	n.d.	4.19	n.d.	5.13	11.41	2.33	0.92	86.46
668	242	1-29	878.09	M.R.P.	63.54	n.d.	19.66	n.d.	0.37	n.d.	n.d.	1.46	1.08	13.31	99.42
669	242	1-30	878.09	M.R.P.	57.49	0.09	23.66	n.d.	1.14	n.d.	0.56	5.60	3.46	6.03	98.03
670	242	2-1	878.09	Chck Pl	56.63	0.05	25.57	n.d.	1.36	n.d.	0.29	7.76	4.45	3.44	99.55
671	242	2-2	878.09	Chck Pl	59.70	0.08	22.67	n.d.	1.18	n.d.	0.72	4.28	3.28	7.65	99.56
672	242	2-3	878.09	Chck Pl	59.21	0.15	22.97	n.d.	1.26	n.d.	0.10	5.64	3.29	7.11	99.73
673	242	2-4	878.09	Chck Pl	57.27	0.08	24.67	n.d.	1.42	n.d.	0.26	7.04	4.19	4.75	99.68
674	242	2-5	878.09	Chck Pl	57.02	0.05	25.85	n.d.	1.15	n.d.	0.12	8.24	4.20	3.68	100.31
675	242	2-6	878.09	Chck Pl	57.66	0.06	24.64	n.d.	1.32	n.d.	0.16	7.43	4.02	4.24	99.53
676	242	2-7	878.09	Chck Pl	59.23	0.12	22.98	n.d.	1.22	n.d.	0.22	5.43	3.34	7.17	99.71
677	242	2-8	878.09	Chck Pl	57.79	0.06	25.19	n.d.	1.42	n.d.	0.15	7.48	4.60	3.82	100.51
678	242	2-9	878.09	Chck Pl	56.95	0.09	24.04	n.d.	1.42	n.d.	0.95	5.57	3.71	5.35	98.08
679	242	2-10	878.09	Chck Pl	57.27	n.d.	24.28	n.d.	1.43	n.d.	0.32	7.16	3.78	4.90	99.14
680	242	2-11	878.09	Chck Pl	58.76	0.07	23.32	n.d.	1.18	n.d.	0.13	5.85	3.90	6.13	99.34
681	242	2-12	878.09	Chck Pl	58.22	0.06	24.12	n.d.	1.11	n.d.	0.40	5.35	3.51	6.30	99.07
682	242	2-13	878.09	Chck Pl	58.22	0.05	23.17	n.d.	1.24	n.d.	0.50	4.75	2.95	7.54	98.42
683	242	2-14	878.09	Chck Pl	61.82	0.09	20.66	n.d.	0.81	n.d.	0.15	3.23	1.93	10.65	99.34
684	242	2-15	878.09	Chck Pl	56.23	1.05	24.65	n.d.	1.30	n.d.	0.12	7.67	4.18	3.86	99.06
685	242	2-16	878.09	Chck Pl	57.10	0.13	24.73	n.d.	1.46	n.d.	0.21	7.97	3.97	3.85	99.42
686	242	2-17	878.09	Chck Pl	60.54	2.01	19.70	n.d.	0.60	n.d.	0.10	2.23	1.42	12.12	98.72
687	242	2-18	878.09	Chck Pl	58.38	0.68	23.05	n.d.	1.26	n.d.	0.27	6.19	3.16	6.55	99.54
688	242	2-19	878.09	Chck Pl	55.15	0.10	26.00	n.d.	1.72	n.d.	0.21	9.05	4.89	1.73	98.85
689	242	2-20	878.09	Chck Pl	55.62	n.d.	25.84	n.d.	1.57	n.d.	0.14	8.91	4.60	2.34	99.02
690	242	2-21	878.09	Chck Pl	60.96	0.44	19.24	n.d.	0.76	n.d.	0.26	1.87	1.02	13.10	97.65
691	242	2-22	878.09	Chck Pl	54.63	1.21	24.53	n.d.	1.35	n.d.	0.31	8.12	4.30	3.07	97.52
692	242	2-23	878.09	Chck Pl	53.52	0.18	26.00	n.d.	1.55	n.d.	0.18	10.00	4.89	0.83	97.15
693	242	2-24	878.09	Chck Pl	54.52	0.16	25.23	n.d.	1.59	n.d.	0.22	9.47	4.84	1.40	97.43
694	242	2-25	878.09	Chck Pl	54.12	n.d.	27.26	0.05	1.33	n.d.	0.09	10.56	5.15	0.41	98.97
695	242	2-26	878.09	Chck Pl	55.60	0.10	26.08	n.d.	1.34	n.d.	0.12	9.38	4.89	1.94	99.45
696	242	2-27	878.09	Chck Pl	55.10	0.13	17.30	n.d.	0.69	n.d.	1.52	4.21	1.38	9.20	89.53
697	242	2-28	878.09	Chck Pl	40.11	0.25	11.95	n.d.	5.43	n.d.	4.86	0.70	0.20	3.98	67.48
698	242	2-29	878.09	Chck Pl	51.77	2.99	19.60	0.00	0.00	2.03	0.00	1.50	5.11	3.26	3.70
699	242	2-30	878.09	Chck Pl	51.24	0.00	18.39	0.00	0.00	1.13	0.00	1.40	5.84	2.71	6.04
700	242	3-1	878.09	Pl	55.92	n.d.	25.79	n.d.	0.90	n.d.	0.11	8.56	5.12	1.95	98.35

Table A.5. *Continued*

Analysis #	Sample #	Batch #	Depth (m)	Comment	SiO_2	TiO_2	Al_2O_3	Cr_2O_3	FeO_{tot}	MnO	MgO	CaO	Na_2O	K_2O	Total
701	242	3-2	878.09	Pl	56.70	n.d.	25.93	n.d.	0.67	n.d.	0.12	8.09	5.42	2.32	99.25
702	242	3-3	878.09	Pl	57.08	n.d.	25.41	n.d.	0.71	n.d.	0.12	8.04	5.01	2.91	99.28
703	242	3-4	878.09	Pl	57.47	0.05	25.05	n.d.	0.64	n.d.	0.09	7.76	5.10	2.76	98.92
704	242	3-5	878.09	Pl	58.21	n.d.	24.84	n.d.	0.48	n.d.	0.09	7.39	4.70	3.61	99.32
705	242	3-6	878.09	Pl	58.30	n.d.	25.18	n.d.	0.38	n.d.	0.09	7.45	5.62	2.41	99.43
706	242	3-7	878.09	Pl	58.30	n.d.	25.51	n.d.	0.18	n.d.	0.08	7.61	5.51	2.26	99.45
707	242	3-8	878.09	Pl	57.94	n.d.	25.87	n.d.	0.20	n.d.	0.07	7.69	5.91	1.89	99.57
708	242	3-9	878.09	Pl	59.48	n.d.	25.09	n.d.	0.12	n.d.	n.d.	6.64	5.79	2.75	99.87
709	242	3-10	878.09	Pl	58.24	n.d.	25.17	n.d.	0.11	n.d.	0.06	7.32	5.69	2.13	98.72
710	242	3-11	878.09	Pl	59.32	n.d.	24.90	n.d.	0.17	n.d.	0.09	6.85	5.50	3.09	99.92
711	242	3-12	878.09	Pl	58.50	n.d.	24.06	0.05	0.23	n.d.	0.13	6.56	4.78	3.99	98.30
712	242	3-13	878.09	Pl	57.70	n.d.	24.61	n.d.	0.34	n.d.	0.15	7.52	5.51	2.70	98.53
713	242	3-14	878.09	Pl	57.94	n.d.	24.22	n.d.	0.19	n.d.	0.11	7.38	5.56	2.30	97.70
714	242	3-15	878.09	Pl	59.19	n.d.	25.04	n.d.	0.19	n.d.	0.06	6.95	5.64	3.01	100.08
715	242	3-16	878.09	Pl	58.10	n.d.	24.68	0.06	0.83	n.d.	0.08	7.63	5.35	2.85	99.58
716	242	3-17	878.09	Pl	55.85	0.20	25.00	n.d.	1.61	n.d.	0.25	8.88	5.14	1.84	98.77
717	242	3-18	878.09	Pl	55.10	0.20	23.96	n.d.	1.97	n.d.	0.32	8.23	4.89	2.08	96.75
718	242	3-19	878.09	Pl	55.31	0.05	24.66	n.d.	1.75	n.d.	0.25	8.51	4.78	2.02	97.33
719	242	3-20	878.09	Pl	53.04	0.13	24.63	n.d.	1.90	n.d.	0.85	9.49	4.43	0.89	95.36
720	242	4-1	878.09	Qtz	98.53	n.d.	n.d.	n.d.	n.d.	n.d.	n.d.	n.d.	n.d.	n.d.	98.53
721	242	4-2	878.09	Qtz	98.62	n.d.	n.d.	n.d.	n.d.	n.d.	n.d.	n.d.	n.d.	n.d.	98.62
722	242	4-3	878.09	Qtz	99.47	n.d.	n.d.	n.d.	n.d.	n.d.	n.d.	n.d.	n.d.	n.d.	99.47
723	242	4-4	878.09	Mf. gr.	39.88	n.d.	5.43	n.d.	3.44	n.d.	21.03	0.89	0.10	n.d.	70.77
724	242	4-5	878.09	Mf. gr.	34.57	0.88	5.28	n.d.	22.02	n.d.	19.33	0.83	0.10	0.18	83.19
725	242	4-6	878.09	Mf. gr.	35.49	1.77	5.44	n.d.	9.66	n.d.	18.23	0.97	0.10	0.30	71.96
726	242	4-7	878.09	Mf. gr.	39.57	n.d.	5.19	n.d.	3.42	n.d.	20.46	0.79	0.05	n.d.	69.48
727	242	4-8	878.09	Mf. gr.	46.55	2.17	16.66	n.d.	17.89	0.14	0.39	3.78	1.39	7.78	96.75
728	242	4-9	878.09	Mf. gr.	36.65	4.88	13.85	n.d.	28.56	0.21	0.47	2.71	1.21	6.66	95.20
729	242	4-10	878.09	Mf. gr.	36.13	5.28	12.94	n.d.	30.61	0.11	0.62	1.42	1.23	6.81	95.15
730	242	4-11	878.09	K-felds	60.94	0.62	17.68	n.d.	4.08	n.d.	0.05	0.18	0.15	15.55	99.25
731	242	4-12	878.09	Qtz	95.40	0.81	0.43	n.d.	0.13	n.d.	0.09	0.05	0.13	0.12	97.16
732	242	4-13	878.09	K-felds	63.09	n.d.	18.40	n.d.	n.d.	n.d.	n.d.	n.d.	0.04	16.50	98.03
733	242	4-14	878.09	K-felds	64.29	n.d.	18.35	n.d.	n.d.	n.d.	n.d.	n.d.	0.06	16.66	99.36
734	242	4-15	878.09	K-felds	63.92	n.d.	18.42	n.d.	0.27	n.d.	n.d.	0.57	0.52	15.19	98.89
735	242	4-16	878.09	K-felds	64.02	n.d.	18.14	n.d.	n.d.	n.d.	n.d.	0.07	0.07	16.79	99.09
736	242	4-17	878.09	Ballen Qtz	96.40	0.26	0.52	n.d.	n.d.	n.d.	n.d.	n.d.	0.19	n.d.	97.37
737	242	4-18	878.09	Ballen Qtz	94.28	0.28	0.47	n.d.	0.09	n.d.	n.d.	n.d.	0.13	0.07	95.32
738	242	4-19	878.09	Ballen Qtz	96.55	0.66	0.41	n.d.	n.d.	n.d.	n.d.	0.07	0.12	n.d.	97.81
739	242	4-20	878.09	Ballen Qtz	96.64	0.40	0.53	n.d.	n.d.	n.d.	n.d.	n.d.	0.15	0.05	97.77
740	242	5-10	878.09	M.R.P.	62.19	n.d.	20.24	n.d.	0.64	n.d.	n.d.	2.39	1.33	1.33	88.12
741	242	5-11	878.09	M.R.P.	57.14	0.14	18.75	0.05	2.43	n.d.	2.80	8.05	1.92	1.92	93.20
742	242	5-12	878.09	M.R.P.	60.03	n.d.	22.29	n.d.	1.05	n.d.	0.05	5.22	2.46	2.46	93.56
743	242	5-13	878.09	M.R.P.	63.45	n.d.	19.61	n.d.	0.38	n.d.	n.d.	1.63	0.96	0.96	86.99
744	242	5-14	878.09	M.R.P.	62.11	n.d.	19.23	n.d.	0.99	n.d.	0.71	3.15	1.21	1.21	88.61
745	242	5-15	878.09	M.R.P.	63.42	n.d.	17.48	n.d.	0.73	n.d.	0.76	1.59	0.11	0.11	84.20
746	242	5-16	878.09	M.R.P.	60.15	0.09	19.29	n.d.	1.53	n.d.	1.10	4.83	1.92	1.92	90.83
747	242	5-17	878.09	M.R.P.	64.01	n.d.	18.67	n.d.	0.30	n.d.	0.10	0.84	0.62	0.62	85.16
748	242	5-18	878.09	M.R.P.	61.91	n.d.	16.19	n.d.	1.13	n.d.	1.86	3.50	0.14	0.14	84.87
749	242	5-19	878.09	M.R.P.	57.80	n.d.	23.73	n.d.	1.57	n.d.	0.12	7.32	3.15	3.15	96.84
750	242	5-20	878.09	M.R.P.	63.91	n.d.	18.31	n.d.	n.d.	n.d.	n.d.	0.06	0.02	n.d.	82.30

Table A.5. *Continued*

Analysis #	Sample #	Batch #	Depth (m)	Comment	SiO_2	TiO_2	Al_2O_3	Cr_2O_3	FeO_{tot}	MnO	MgO	CaO	Na_2O	K_2O	Total
751	240	1-1	890.52	Mic	55.93	0.08	26.65	n.d.	1.62	n.d.	0.33	10.12	5.35	0.46	100.54
752	240	1-2	890.52	Mic	54.31	0.07	26.24	n.d.	1.44	n.d.	0.30	10.18	4.89	0.48	97.91
753	240	1-3	890.52	Mic	52.17	0.06	24.34	n.d.	1.96	n.d.	1.57	9.51	5.14	0.50	95.25
754	240	1-4	890.52	Mic	54.23	0.06	26.25	n.d.	1.64	n.d.	0.84	9.60	5.00	0.48	98.10
755	240	1-5	890.52	Mic	53.99	n.d.	26.79	n.d.	1.49	n.d.	0.22	10.57	4.83	0.50	98.39
756	240	1-6	890.52	Mic	54.91	0.08	26.16	n.d.	1.68	n.d.	0.17	9.97	5.69	0.41	99.07
757	240	1-7	890.52	Mic	53.64	n.d.	25.68	n.d.	1.71	n.d.	0.92	10.03	5.01	0.37	97.36
758	240	1-8	890.52	Mic	54.50	0.08	27.11	n.d.	1.52	n.d.	0.22	11.07	4.93	0.37	99.80
759	240	1-9	890.52	Mic	54.93	0.05	26.10	n.d.	1.42	n.d.	0.51	9.71	5.41	0.65	98.78
760	240	1-10	890.52	Mic	55.15	0.06	22.96	n.d.	1.22	n.d.	0.29	5.75	7.05	0.32	92.80
761	240	1-11	890.52	Mic	53.04	0.09	26.60	n.d.	1.56	n.d.	0.31	10.81	4.86	0.52	97.79
762	240	1-12	890.52	Mic	53.44	0.05	25.48	n.d.	1.64	n.d.	0.59	10.18	5.30	0.50	97.18
763	240	1-13	890.52	Mic	54.46	0.10	26.67	n.d.	1.81	n.d.	0.44	10.49	4.87	0.54	99.38
764	240	1-14	890.52	Mic	53.73	0.10	26.20	n.d.	1.77	n.d.	0.17	10.53	5.37	0.42	98.29
765	240	1-15	890.52	Mic	53.90	n.d.	26.58	n.d.	1.37	n.d.	0.51	10.20	4.79	0.67	98.02
766	240	1-16	890.52	Mic	55.19	n.d.	25.60	n.d.	1.34	n.d.	0.64	8.93	5.67	0.43	97.80
767	240	1-17	890.52	Mic	55.14	n.d.	26.63	n.d.	1.73	n.d.	0.23	10.29	5.09	0.50	99.61
768	240	1-18	890.52	Mic	52.67	0.07	25.66	n.d.	2.57	n.d.	0.71	9.97	5.32	0.46	97.43
769	240	1-19	890.52	Mic	53.88	n.d.	25.82	n.d.	1.63	n.d.	0.86	9.60	4.81	0.62	97.22
770	240	1-20	890.52	Mic	53.78	0.05	26.08	n.d.	1.70	n.d.	0.21	10.66	4.89	0.47	97.84
771	240	2-1	890.52	M.R.P.	41.54	0.64	11.12	n.d.	7.69	n.d.	13.45	1.20	0.44	1.82	77.90
772	240	2-2	890.52	M.R.P.	41.72	0.28	10.03	n.d.	6.90	n.d.	9.40	0.36	0.12	2.87	71.68
773	240	2-3	890.52	M.R.P.	44.23	0.20	9.80	n.d.	6.94	n.d.	10.52	0.59	0.11	2.67	75.06
774	240	2-4	890.52	M.R.P.	45.38	n.d.	7.14	n.d.	4.72	n.d.	18.75	1.56	0.11	1.29	78.95
775	240	2-5	890.52	M.R.P.	41.79	0.34	7.72	n.d.	4.63	n.d.	18.59	1.07	0.23	0.83	75.20
776	240	2-6	890.52	M.R.P.	40.43	0.78	12.19	n.d.	12.89	n.d.	5.57	1.83	3.55	2.33	79.57
777	240	2-7	890.52	M.R.P.	42.12	0.11	12.03	n.d.	6.17	n.d.	20.96	0.78	0.44	1.06	83.67
778	240	2-8	890.52	M.R.P.	43.36	0.12	10.78	n.d.	4.83	n.d.	16.78	1.82	0.18	1.78	79.65
779	240	2-9	890.52	M.R.P.	43.91	n.d.	5.86	0.05	4.25	n.d.	23.23	1.05	0.17	n.d.	78.52
780	240	2-10	890.52	M.R.P.	44.26	n.d.	5.96	n.d.	4.29	n.d.	23.90	0.99	0.17	0.06	79.63
781	240	2-11	890.52	M.R.P.	54.18	0.06	24.74	n.d.	2.04	n.d.	2.06	9.10	4.20	0.50	96.88
782	240	2-12	890.52	M.R.P.	43.82	n.d.	6.17	n.d.	4.55	n.d.	20.39	1.03	0.18	0.22	76.36
783	240	2-13	890.52	M.R.P.	43.54	0.38	9.12	n.d.	5.87	n.d.	19.26	1.01	0.18	1.52	80.88
784	240	2-14	890.52	M.R.P.	42.89	0.24	9.23	0.05	6.24	n.d.	11.08	0.50	0.18	2.42	72.83
785	240	2-15	890.52	M.R.P.	43.88	0.45	9.45	n.d.	6.14	n.d.	14.31	1.94	0.48	2.17	78.82
786	240	2-16	890.52	M.R.P.	42.29	n.d.	5.83	n.d.	3.81	n.d.	21.78	1.00	0.39	0.09	75.19
787	240	2-17	890.52	M.R.P.	43.15	n.d.	5.79	n.d.	3.96	n.d.	22.99	0.85	0.18	n.d.	76.92
788	240	2-18	890.52	M.R.P.	44.00	0.15	5.96	n.d.	4.17	n.d.	22.84	0.96	0.21	0.08	78.37
789	240	2-19	890.52	M.R.P.	44.75	n.d.	6.00	n.d.	4.06	n.d.	22.51	0.47	0.43	n.d.	78.22
790	240	2-20	890.52	M.R.P.	45.74	n.d.	6.25	n.d.	3.99	n.d.	23.35	0.59	0.30	0.05	80.27
791	240	3-1	890.52	M.R.P. rim	4.92	1.65	1.58	n.d.	78.64	n.d.	0.21	0.33	0.17	0.19	87.69
792	240	3-2	890.52	M.R.P. rim	5.14	1.67	1.51	n.d.	78.12	n.d.	0.23	0.38	0.19	0.24	87.48
793	240	3-3	890.52	M.R.P. rim	4.96	1.42	1.49	n.d.	79.24	n.d.	0.24	0.38	0.21	0.22	88.16
794	240	3-4	890.52	M.R.P. rim	5.02	1.53	1.52	n.d.	78.83	n.d.	0.18	0.39	0.16	0.21	87.84
795	240	3-5	890.52	M.R.P. rim	4.94	1.45	1.47	n.d.	79.65	n.d.	0.18	0.51	0.12	0.16	88.48
796	240	3-6	890.52	M.R.P. rim	4.96	1.35	1.48	n.d.	77.09	n.d.	0.18	0.46	0.23	0.20	85.95
797	240	3-7	890.52	M.R.P. rim	5.17	1.58	1.55	n.d.	77.05	n.d.	0.24	0.56	0.25	0.26	86.66
798	240	3-8	890.52	M.R.P. rim	5.07	1.48	1.51	n.d.	77.96	n.d.	0.16	0.45	0.17	0.18	86.98
799	240	3-9	890.52	M.R.P. rim	5.04	1.58	1.47	n.d.	75.59	n.d.	0.19	0.49	0.20	0.22	84.78
800	240	3-10	890.52	M.R.P. rim	5.30	1.64	1.64	n.d.	76.38	n.d.	0.28	0.38	0.15	0.25	86.02

Table A.5. *Continued*

Analysis #	Sample #	Batch #	Depth (m)	Comment	SiO_2	TiO_2	Al_2O_3	Cr_2O_3	FeO_{tot}	MnO	MgO	CaO	Na_2O	K_2O	Total
801	240	3-11	890.52	M.R.P.	60.03	n.d.	22.54	n.d.	0.64	n.d.	0.12	6.32	6.00	3.22	98.87
802	240	3-12	890.52	M.R.P.	57.44	n.d.	22.24	n.d.	0.94	n.d.	0.13	5.78	5.31	4.05	95.89
803	240	3-13	890.52	M.R.P.	59.81	n.d.	22.28	n.d.	0.81	n.d.	0.12	5.57	5.19	4.06	97.84
804	240	3-14	890.52	M.R.P.	59.96	0.05	22.38	n.d.	0.77	n.d.	0.07	5.79	5.53	3.79	98.34
805	240	3-15	890.52	M.R.P.	56.78	n.d.	24.82	n.d.	1.17	n.d.	0.17	7.43	5.84	1.86	98.07
806	240	3-16	890.52	M.R.P.	57.46	0.05	22.18	n.d.	1.60	n.d.	0.20	6.31	4.57	4.12	96.49
807	240	3-17	890.52	M.R.P.	59.30	0.09	21.54	n.d.	1.22	n.d.	0.06	4.88	3.78	6.39	97.26
808	240	3-18	890.52	M.R.P.	58.67	0.09	20.39	n.d.	1.45	n.d.	0.59	5.61	3.21	7.24	97.25
809	240	3-19	890.52	M.R.P.	58.96	0.05	21.04	n.d.	1.30	n.d.	0.21	5.37	3.64	6.33	96.90
810	240	3-20	890.52	M.R.P.	59.93	0.08	19.31	n.d.	1.41	n.d.	0.63	4.72	2.37	9.07	97.52
811	240	4-1	890.52	Cc	n.d.	n.d.	n.d.	n.d.	n.d.	0.18	0.06	63.12	0.02	n.d.	63.38
812	240	4-2	890.52	Cc	n.d.	n.d.	n.d.	n.d.	n.d.	0.20	0.06	59.90	n.d.	n.d.	60.16
813	240	4-3	890.52	Cc	n.d.	n.d.	n.d.	n.d.	n.d.	0.26	0.18	62.35	n.d.	n.d.	62.79
814	240	4-4	890.52	Cc	n.d.	n.d.	n.d.	n.d.	0.15	0.17	0.14	59.44	n.d.	n.d.	59.90
815	240	4-5	890.52	Cc	n.d.	n.d.	n.d.	n.d.	n.d.	0.20	0.06	58.50	n.d.	n.d.	58.76
816	240	4-6	890.52	Cc	n.d.	n.d.	n.d.	n.d.	n.d.	0.23	0.09	57.37	n.d.	n.d.	57.69
817	240	4-7	890.52	Cc	n.d.	n.d.	n.d.	n.d.	n.d.	0.37	0.25	62.04	0.06	n.d.	62.72
818	240	4-8	890.52	Cc	0.06	0.90	n.d.	n.d.	0.10	0.33	0.27	56.10	0.02	n.d.	57.78
819	240	4-9	890.52	Cc	62.99	n.d.	19.63	n.d.	n.d.	n.d.	n.d.	1.23	7.25	3.81	94.91
820	240	4-10	890.52	Cc	94.95	0.08	0.45	n.d.	n.d.	n.d.	0.09	0.08	0.16	0.05	95.86
821	240	4-11	890.52	Cc	97.20	n.d.	0.23	n.d.	n.d.	n.d.	n.d.	0.08	0.06	n.d.	97.57
822	240	4-12	890.52	Cc	0.07	n.d.	n.d.	n.d.	n.d.	0.25	0.35	58.07	0.03	n.d.	58.77
823	240	4-13	890.52	Cc	0.31	n.d.	0.05	n.d.	n.d.	0.29	0.29	60.64	0.02	n.d.	61.60
824	240	4-14	890.52	Cc	n.d.	n.d.	n.d.	n.d.	0.13	0.28	0.44	58.62	0.04	n.d.	59.51
825	240	4-15	890.52	Cc	n.d.	n.d.	n.d.	n.d.	n.d.	0.27	0.28	61.61	0.02	n.d.	62.18
826	240	4-16	890.52	Cc	n.d.	n.d.	n.d.	n.d.	n.d.	0.23	0.15	58.64	n.d.	n.d.	59.02
827	240	4-17	890.52	Cc	n.d.	n.d.	n.d.	n.d.	n.d.	0.29	0.07	61.62	n.d.	n.d.	61.98
828	240	4-18	890.52	Cc	n.d.	n.d.	n.d.	n.d.	n.d.	0.43	0.11	59.70	0.04	n.d.	60.28
829	240	4-19	890.52	Cc	0.49	n.d.	0.10	n.d.	n.d.	0.37	0.68	57.30	0.02	n.d.	58.96
830	240	4-20	890.52	Cc	1.06	0.05	0.26	n.d.	0.18	0.28	0.56	56.93	0.03	0.10	59.45
831	240	5-1	890.52	Mf. M.R.P.	39.14	n.d.	5.20	n.d.	3.39	n.d.	20.81	1.16	0.67	0.09	70.46
832	240	5-2	890.52	Mf. M.R.P.	38.21	n.d.	4.93	n.d.	3.46	n.d.	18.95	1.25	0.61	n.d.	67.41
833	240	5-3	890.52	Mf. M.R.P.	33.59	n.d.	4.42	n.d.	2.90	n.d.	16.73	0.66	0.35	n.d.	58.65
834	240	5-4	890.52	Mf. M.R.P.	36.37	0.05	4.76	n.d.	3.38	n.d.	19.23	0.65	0.43	n.d.	64.87
835	240	5-5	890.52	Mf. M.R.P.	32.97	n.d.	4.30	n.d.	3.22	n.d.	16.63	0.61	0.46	0.06	58.25
836	240	5-6	890.52	Mf. M.R.P.	39.67	n.d.	5.33	n.d.	3.66	n.d.	20.50	0.49	1.10	0.08	70.83
837	240	5-7	890.52	Mf. M.R.P.	41.64	n.d.	5.68	n.d.	3.77	n.d.	21.65	0.68	1.33	0.11	74.86
838	240	5-8	890.52	Mf. M.R.P.	38.56	n.d.	5.29	n.d.	3.36	n.d.	19.98	0.53	1.10	0.07	68.89
839	240	5-9	890.52	Mf. M.R.P.	25.68	n.d.	3.60	n.d.	2.38	n.d.	11.76	0.40	0.30	0.05	44.17
840	240	5-10	890.52	Mf. M.R.P.	39.87	n.d.	5.33	n.d.	3.62	n.d.	20.70	1.48	0.67	0.08	71.75
841	240	5-11	890.52	M.R.P.	58.12	0.07	22.96	n.d.	1.48	n.d.	0.14	6.64	4.62	4.26	98.29
842	240	5-12	890.52	M.R.P.	57.67	0.06	22.78	n.d.	1.43	n.d.	0.14	7.32	4.23	4.85	98.48
843	240	5-13	890.52	M.R.P.	59.60	0.09	21.89	n.d.	1.12	n.d.	0.09	5.43	3.44	7.10	98.76
844	240	5-14	890.52	M.R.P.	56.81	0.09	23.13	n.d.	1.73	n.d.	0.18	7.71	4.66	3.86	98.17
845	240	5-15	890.52	M.R.P.	60.31	0.09	18.12	n.d.	0.40	n.d.	0.06	1.48	1.55	12.01	94.02
846	240	5-16	890.52	M.R.P.	62.54	0.15	19.29	n.d.	0.81	n.d.	n.d.	2.76	2.27	11.09	98.91
847	240	5-17	890.52	M.R.P.	59.48	0.09	22.00	n.d.	1.38	n.d.	0.25	5.72	3.46	6.89	99.27
848	240	5-18	890.52	M.R.P.	59.24	n.d.	22.67	n.d.	1.44	n.d.	0.09	6.05	3.85	5.93	99.27
849	240	5-19	890.52	M.R.P.	59.65	n.d.	23.04	n.d.	0.84	n.d.	0.13	5.73	4.56	4.74	98.69
850	240	5-20	890.52	M.R.P.	59.42	0.11	20.53	n.d.	1.37	n.d.	0.32	4.85	3.67	7.54	97.81

Table A.5. *Continued*

Analysis #	Sample #	Batch #	Depth (m)	Comment	SiO_2	TiO_2	Al_2O_3	Cr_2O_3	FeO_{tot}	MnO	MgO	CaO	Na_2O	K_2O	Total
851	240	6-1	890.52	Mic	53.06	0.11	22.13	0.06	2.99	n.d.	1.66	7.56	3.96	1.85	93.38
852	240	6-2	890.52	Mic	54.12	n.d.	27.76	n.d.	1.84	n.d.	0.17	12.12	4.59	0.44	101.04
853	240	6-3	890.52	Mic	53.64	n.d.	26.35	n.d.	1.59	n.d.	0.24	10.28	5.00	0.46	97.56
854	240	6-4	890.52	Mic	62.56	0.05	19.63	n.d.	0.58	n.d.	0.68	2.50	1.38	10.99	98.37
855	240	6-5	890.52	Mic	54.22	1.04	25.47	n.d.	1.92	n.d.	0.93	9.69	4.64	0.82	98.73
856	240	6-6	890.52	Mic	54.88	n.d.	26.60	n.d.	1.89	n.d.	0.38	10.46	4.79	0.64	99.64
857	240	6-7	890.52	Mic	54.60	1.25	24.55	n.d.	1.81	n.d.	1.10	9.18	4.78	0.54	97.81
858	240	6-8	890.52	Mic	55.23	0.09	24.57	n.d.	2.12	n.d.	0.72	9.05	4.85	1.13	97.76
859	240	6-9	890.52	Mic	55.73	n.d.	27.38	n.d.	1.67	n.d.	0.15	10.68	5.16	0.37	101.14
860	240	6-10	890.52	Mic	54.68	0.07	27.48	n.d.	1.64	n.d.	0.15	11.32	5.05	0.36	100.75
861	240	6-11	890.52	Mic	54.49	n.d.	26.70	n.d.	1.75	n.d.	0.16	10.92	4.84	0.43	99.29
862	240	6-12	890.52	Mic	55.33	n.d.	26.10	n.d.	1.49	n.d.	0.33	10.07	5.23	0.46	99.01
863	240	6-13	890.52	Mic	54.91	0.06	25.64	n.d.	1.59	n.d.	0.61	10.09	5.33	0.51	98.74
864	240	6-14	890.52	Mic	54.43	n.d.	26.72	n.d.	1.74	n.d.	0.28	10.91	4.94	0.36	99.38
865	240	6-15	890.52	Mic	55.99	0.12	24.38	n.d.	1.41	n.d.	0.18	8.64	4.97	1.64	97.33
866	240	6-16	890.52	Mic	55.08	0.06	26.39	n.d.	1.48	n.d.	0.15	10.38	5.12	0.50	99.16
867	240	6-17	890.52	Mic	55.05	0.11	24.79	n.d.	2.33	n.d.	0.21	11.37	4.76	0.61	99.23
868	240	6-18	890.52	Mic	58.53	0.08	23.63	n.d.	1.04	n.d.	0.15	6.62	3.50	6.09	99.64
869	240	6-19	890.52	Mic	54.41	0.07	24.22	n.d.	1.84	n.d.	1.84	9.68	5.04	0.52	97.62
870	240	6-20	890.52	Mic	55.54	n.d.	26.57	n.d.	1.52	n.d.	0.08	10.32	5.50	0.52	100.05
871	240	7-1	890.52	Meso	43.45	0.05	7.40	n.d.	3.77	n.d.	18.20	1.73	0.52	1.00	76.12
872	240	7-2	890.52	Meso	40.65	0.41	6.83	0.07	4.91	n.d.	16.55	1.20	0.30	1.27	72.19
873	240	7-3	890.52	Meso	44.34	0.30	8.92	n.d.	7.61	n.d.	11.35	0.87	0.20	3.20	76.79
874	240	7-4	890.52	Meso	37.96	0.15	9.93	n.d.	6.17	n.d.	10.07	0.50	0.14	2.65	67.57
875	240	7-5	890.52	Meso	39.73	0.16	8.11	n.d.	6.63	n.d.	10.16	0.85	0.26	2.40	68.30
876	240	7-6	890.52	Meso	39.28	0.17	7.80	n.d.	5.63	n.d.	13.22	0.74	0.19	1.87	68.90
877	240	7-7	890.52	Meso	43.75	n.d.	5.69	n.d.	3.66	n.d.	21.84	0.99	0.46	0.05	76.44
878	240	7-8	890.52	Meso	39.15	0.16	8.15	n.d.	5.12	n.d.	14.23	1.11	0.31	1.51	69.74
879	240	7-9	890.52	Meso	38.41	0.09	9.14	0.05	5.82	n.d.	14.77	0.62	0.16	1.77	70.83
880	240	7-10	890.52	Meso	40.88	0.28	11.93	n.d.	4.80	n.d.	13.81	1.48	1.69	1.81	76.68
881	240	7-11	890.52	Meso	39.39	0.22	6.95	n.d.	5.00	n.d.	19.25	0.89	0.47	0.93	73.10
882	240	7-12	890.52	Meso	38.92	1.20	9.05	n.d.	5.16	n.d.	14.60	2.26	0.97	1.40	73.56
883	240	7-13	890.52	Meso	42.24	0.10	7.44	n.d.	4.37	n.d.	16.07	1.45	0.41	0.83	72.91
884	240	7-14	890.52	Meso	37.06	0.59	5.35	n.d.	14.46	n.d.	17.22	0.36	0.26	0.67	75.97
885	240	7-15	890.52	Meso	17.42	3.56	4.65	0.07	48.65	n.d.	2.57	0.91	0.85	1.19	79.87
886	240	7-16	890.52	Meso	42.79	2.03	12.47	n.d.	15.51	n.d.	2.21	1.91	4.55	2.59	84.06
887	240	7-17	890.52	Meso	38.78	0.22	7.46	n.d.	6.41	n.d.	12.80	1.10	0.34	1.32	68.43
888	240	7-18	890.52	Meso	45.45	0.76	12.33	n.d.	12.03	n.d.	5.09	1.45	3.12	3.26	83.49
889	240	7-19	890.52	Meso	41.11	0.13	6.72	n.d.	4.37	n.d.	15.73	0.90	0.41	1.05	70.42
890	240	7-20	890.52	Meso	40.39	0.36	7.27	n.d.	6.35	n.d.	14.06	1.45	0.47	1.46	71.81
891	225	1-1	892.55	M.R.P. tr.	52.94	0.22	16.19	0.05	1.18	n.d.	1.56	1.93	4.93	5.21	84.21
892	225	1-2	892.55	M.R.P. tr.	50.64	0.14	14.90	n.d.	1.46	n.d.	3.60	1.56	3.88	5.04	81.22
893	225	1-3	892.55	M.R.P. tr.	49.17	0.21	15.25	n.d.	1.33	n.d.	2.73	2.15	4.24	4.63	79.71
894	225	1-4	892.55	M.R.P. tr.	45.14	0.17	12.90	n.d.	2.32	0.10	4.94	2.01	3.50	4.47	75.55
895	225	1-5	892.55	M.R.P. tr.	55.73	0.28	16.90	n.d.	0.66	n.d.	0.43	1.81	4.28	6.99	87.08
896	225	1-6	892.55	M.R.P. tr.	50.47	0.17	14.93	n.d.	1.05	n.d.	3.05	1.83	3.97	5.00	80.47
897	225	1-7	892.55	M.R.P. tr.	54.74	0.40	16.75	n.d.	1.06	n.d.	1.21	1.93	4.60	6.05	86.74
898	225	1-8	892.55	M.R.P. tr.	56.12	0.41	16.63	n.d.	0.82	n.d.	0.84	1.50	3.45	8.52	88.29
899	225	1-9	892.55	M.R.P. tr.	56.94	0.40	17.24	n.d.	0.84	n.d.	0.22	1.83	3.91	8.01	89.39
900	225	1-10	892.55	M.R.P. tr.	57.84	0.28	17.75	n.d.	0.86	n.d.	0.09	2.28	4.37	6.97	90.44

Table A.5. *Continued*

Analysis #	Sample #	Batch #	Depth (m)	Comment	SiO_2	TiO_2	Al_2O_3	Cr_2O_3	FeO_{tot}	MnO	MgO	CaO	Na_2O	K_2O	Total
901	225	1-11	892.55	M.R.P. tr.	55.09	0.27	16.82	n.d.	0.76	n.d.	0.35	1.76	4.36	7.19	86.60
902	225	1-12	892.55	M.R.P. tr.	54.54	0.22	16.81	n.d.	0.97	n.d.	0.97	2.09	5.07	5.18	85.85
903	225	1-13	892.55	M.R.P. tr.	56.20	0.29	17.47	n.d.	0.72	n.d.	0.27	2.07	4.66	6.60	88.28
904	225	1-14	892.55	M.R.P. tr.	52.61	2.85	16.29	n.d.	0.68	n.d.	0.12	1.94	3.65	7.29	85.43
905	225	1-15	892.55	M.R.P. tr.	56.72	0.30	17.72	n.d.	0.92	n.d.	0.22	2.55	4.57	6.74	89.74
906	225	1-16	892.55	M.R.P. tr.	53.05	0.29	16.16	n.d.	0.89	n.d.	1.18	2.13	6.24	4.20	84.14
907	225	1-17	892.55	M.R.P. tr.	52.23	0.28	15.63	n.d.	0.91	n.d.	0.75	1.96	4.62	5.97	82.35
908	225	1-18	892.55	M.R.P. tr.	57.75	0.50	18.12	n.d.	0.96	n.d.	0.14	2.54	4.45	7.17	91.63
909	225	1-19	892.55	M.R.P. tr.	52.57	0.44	16.24	n.d.	0.76	n.d.	0.23	2.03	3.87	6.87	83.01
910	225	1-20	892.55	M.R.P. tr.	52.38	0.13	16.24	n.d.	0.93	n.d.	0.26	2.28	4.04	6.82	83.08
911	225	2-1	892.55	M.R.P. tr.	54.80	0.27	16.87	n.d.	0.82	n.d.	0.12	2.17	4.22	7.28	86.55
912	225	2-2	892.55	M.R.P. tr.	51.64	0.11	15.52	n.d.	0.48	n.d.	0.14	1.63	3.33	7.92	80.77
913	225	2-3	892.55	M.R.P. tr.	53.82	0.37	16.62	n.d.	0.67	n.d.	0.15	2.13	4.11	7.40	85.27
914	225	2-4	892.55	M.R.P. tr.	56.23	1.31	17.45	0.05	0.94	n.d.	0.14	2.54	4.04	7.74	90.44
915	225	2-5	892.55	M.R.P. tr.	55.35	0.21	17.42	n.d.	0.72	n.d.	0.06	2.12	3.64	8.06	87.58
916	225	2-6	892.55	M.R.P. tr.	59.50	0.17	17.82	n.d.	0.60	n.d.	n.d.	1.48	2.65	10.81	93.03
917	225	2-7	892.55	M.R.P. tr.	50.95	0.09	15.72	n.d.	0.69	n.d.	1.07	3.45	3.65	7.01	82.63
918	225	2-8	892.55	M.R.P. tr.	53.03	0.50	16.67	n.d.	0.99	n.d.	0.16	2.58	4.44	6.12	84.49
919	225	2-9	892.55	M.R.P. tr.	57.08	0.10	18.00	n.d.	0.69	n.d.	n.d.	2.43	3.46	8.94	90.70
920	225	2-10	892.55	M.R.P. tr.	57.33	0.21	19.32	n.d.	1.26	n.d.	0.47	4.09	4.32	6.37	93.37
921	225	2-11	892.55	M.R.P. tr.	54.40	0.64	18.88	n.d.	1.23	n.d.	0.49	3.76	4.08	6.54	90.02
922	225	2-12	892.55	M.R.P. tr.	57.25	0.12	19.06	n.d.	0.97	n.d.	0.11	3.40	3.87	7.68	92.46
923	225	2-13	892.55	M.R.P. tr.	57.18	1.12	18.70	n.d.	1.09	n.d.	0.25	3.26	4.44	6.98	93.02
924	225	2-14	892.55	M.R.P. tr.	59.05	0.18	19.33	n.d.	0.90	n.d.	0.12	2.91	3.89	8.08	94.46
925	225	2-15	892.55	M.R.P. tr.	57.05	0.13	17.80	n.d.	0.99	n.d.	0.84	2.64	4.31	7.00	90.76
926	225	2-16	892.55	M.R.P. tr.	58.14	0.11	18.96	n.d.	1.07	n.d.	0.21	3.08	3.93	7.26	92.76
927	225	2-17	892.55	M.R.P. tr.	54.76	0.18	16.56	n.d.	0.69	n.d.	0.14	2.73	3.10	8.78	86.94
928	225	2-18	892.55	M.R.P. tr.	58.01	0.14	18.60	n.d.	0.94	n.d.	0.10	3.00	4.16	7.36	92.31
929	225	2-19	892.55	M.R.P. tr.	57.48	0.27	18.16	n.d.	0.80	n.d.	0.06	2.53	3.66	8.30	91.26
930	225	2-20	892.55	M.R.P. tr.	54.34	0.14	16.57	n.d.	0.50	n.d.	0.43	2.23	3.69	7.94	85.84
931	225	3-1	892.55	M.R.P. tr.	57.75	0.13	17.10	n.d.	0.58	n.d.	0.08	1.78	3.49	8.84	89.75
932	225	3-2	892.55	M.R.P. tr.	56.07	0.12	17.06	n.d.	0.98	n.d.	0.18	2.26	3.20	8.42	88.29
933	225	3-3	892.55	M.R.P. tr.	55.36	0.15	17.37	n.d.	0.94	n.d.	0.15	2.65	3.90	7.54	88.06
934	225	3-4	892.55	M.R.P. tr.	57.41	0.16	18.48	n.d.	0.97	n.d.	0.12	2.82	4.07	7.70	91.73
935	225	3-5	892.55	M.R.P. tr.	55.71	0.09	17.66	n.d.	0.93	n.d.	0.10	2.30	4.26	7.70	88.75
936	225	3-6	892.55	M.R.P. tr.	55.61	3.79	16.13	n.d.	1.31	n.d.	1.62	2.10	3.61	7.27	91.44
937	225	3-7	892.55	M.R.P. tr.	52.65	0.36	16.08	n.d.	0.70	n.d.	0.18	2.50	3.41	7.99	83.87
938	225	3-8	892.55	M.R.P. tr.	58.24	0.13	19.88	n.d.	0.58	n.d.	0.07	3.50	4.28	7.16	93.84
939	225	3-9	892.55	M.R.P. tr.	58.24	0.10	21.30	n.d.	0.76	n.d.	0.11	4.44	4.86	5.95	95.76
940	225	3-10	892.55	M.R.P. tr.	54.87	0.12	17.19	n.d.	0.74	n.d.	0.10	2.33	3.65	8.02	87.02
941	225	3-11	892.55	M.R.P. tr.	55.57	0.10	17.07	n.d.	0.73	n.d.	0.08	2.19	3.78	8.01	87.53
942	225	3-12	892.55	M.R.P. tr.	53.29	0.07	17.14	n.d.	0.65	n.d.	0.07	1.94	3.55	8.03	84.74
943	225	3-13	892.55	M.R.P. tr.	55.60	0.05	17.35	n.d.	0.63	n.d.	0.07	2.04	3.18	9.00	87.92
944	225	3-14	892.55	M.R.P. tr.	56.99	0.17	17.65	n.d.	0.66	n.d.	0.05	1.80	3.43	9.09	89.84
945	225	3-15	892.55	M.R.P. tr.	56.66	0.09	17.74	0.06	0.62	n.d.	0.06	1.92	3.41	8.71	89.27
946	225	3-16	892.55	M.R.P. tr.	45.43	n.d.	12.67	n.d.	1.57	n.d.	1.10	1.30	1.82	9.35	73.24
947	225	3-17	892.55	M.R.P. tr.	56.01	0.08	17.04	n.d.	0.80	n.d.	0.09	1.46	3.08	9.13	87.69
948	225	3-18	892.55	M.R.P. tr.	56.86	0.17	17.86	n.d.	1.52	n.d.	0.11	2.30	3.98	7.64	90.44
949	225	3-19	892.55	M.R.P. tr.	14.51	3.76	4.44	0.14	56.93	n.d.	2.13	0.42	0.61	2.08	85.02
950	225	3-20	892.55	M.R.P. tr.	54.21	0.78	16.42	n.d.	4.18	n.d.	0.14	1.25	2.39	9.80	89.17

Table A.5. *Continued*

Analysis #	Sample #	Batch #	Depth (m)	Comment	SiO_2	TiO_2	Al_2O_3	Cr_2O_3	FeO_{tot}	MnO	MgO	CaO	Na_2O	K_2O	Total
951	225	4-1	892.55	M.R.P.	56.47	0.07	17.20	n.d.	0.43	n.d.	0.09	1.60	3.17	9.16	88.19
952	225	4-2	892.55	M.R.P.	59.62	0.14	17.12	n.d.	0.31	n.d.	0.05	0.99	1.92	11.90	92.05
953	225	4-3	892.55	M.R.P.	49.97	0.08	15.92	n.d.	0.56	n.d.	0.07	2.21	3.45	7.38	79.64
954	225	4-4	892.55	M.R.P.	48.62	8.30	14.80	n.d.	1.13	n.d.	0.88	2.12	3.03	7.57	86.45
955	225	4-5	892.55	M.R.P.	58.26	0.11	17.78	n.d.	0.40	n.d.	0.17	1.60	2.81	10.19	91.32
956	225	4-6	892.55	M.R.P.	55.11	0.06	17.37	n.d.	0.85	n.d.	0.09	2.57	4.17	7.42	87.64
957	225	4-7	892.55	M.R.P.	55.11	0.06	17.05	n.d.	0.77	n.d.	0.08	2.22	3.55	7.62	86.46
958	225	4-8	892.55	M.R.P.	55.25	0.06	17.06	n.d.	0.69	n.d.	0.05	1.81	3.48	7.92	86.32
959	225	4-9	892.55	M.R.P.	58.25	0.06	17.73	n.d.	0.79	n.d.	0.09	1.84	3.17	9.66	91.59
960	225	4-10	892.55	M.R.P.	55.84	0.07	17.11	n.d.	0.54	n.d.	0.05	1.72	3.23	9.14	87.70
961	225	4-11	892.55	M.R.P.	56.54	0.11	17.03	n.d.	0.50	n.d.	0.06	1.65	2.84	9.48	88.21
962	225	4-12	892.55	Qtz	97.44	n.d.	0.09	n.d.	n.d.	n.d.	n.d.	n.d.	0.05	n.d.	97.58
963	225	4-13	892.55	Qtz	96.67	n.d.	0.07	n.d.	n.d.	n.d.	n.d.	n.d.	0.05	n.d.	96.79
964	225	4-14	892.55	Qtz	95.54	n.d.	0.21	n.d.	n.d.	n.d.	n.d.	0.07	0.12	0.05	95.99
965	225	4-15	892.55	Qtz	96.12	n.d.	0.14	n.d.	n.d.	n.d.	n.d.	n.d.	0.02	0.05	96.33
966	225	4-16	892.55	M.R.P.	54.02	0.11	17.07	n.d.	0.76	n.d.	0.12	2.19	3.42	8.07	85.76
967	225	4-17	892.55	M.R.P.	56.45	0.13	17.70	n.d.	0.67	n.d.	0.05	2.13	3.27	8.63	89.03
968	225	4-18	892.55	M.R.P.	56.89	0.13	17.75	n.d.	0.56	n.d.	n.d.	1.77	2.98	9.44	89.52
969	225	4-19	892.55	M.R.P.	57.37	0.12	18.41	n.d.	0.89	n.d.	0.10	2.68	3.36	8.49	91.42
970	225	4-20	892.55	M.R.P.	57.85	0.10	18.64	n.d.	0.97	n.d.	0.12	2.97	3.61	8.33	92.59
971	225	5-1	892.55	Qtz	95.40	n.d.	0.55	n.d.	n.d.	n.d.	0.05	0.07	0.10	n.d.	96.17
972	225	5-2	892.55	Qtz	95.85	0.05	0.21	n.d.	0.10	n.d.	0.06	0.08	0.11	0.09	96.55
973	225	5-3	892.55	Qtz	96.27	n.d.	0.17	n.d.	n.d.	n.d.	n.d.	0.08	0.08	0.05	96.65
974	225	5-4	892.55	M.R.P.	64.49	0.14	16.15	n.d.	1.49	n.d.	0.10	0.33	2.23	12.75	97.68
975	225	5-5	892.55	Cc Gdm	0.40	n.d.	0.15	0.05	0.10	0.25	4.06	49.81	n.d.	0.07	54.89
976	225	5-6	892.55	Cc Gdm	13.02	n.d.	4.35	n.d.	n.d.	0.25	1.37	41.13	n.d.	3.20	63.32
977	225	5-7	892.55	Cc Gdm	0.39	n.d.	0.13	n.d.	n.d.	0.34	2.16	52.07	0.02	n.d.	55.11
978	225	5-8	892.55	Cc Gdm	0.48	n.d.	0.13	n.d.	0.12	0.30	2.42	50.07	n.d.	0.06	53.58
979	225	5-9	892.55	Cc Gdm	0.28	n.d.	0.12	n.d.	0.43	0.26	5.34	47.35	n.d.	n.d.	53.78
980	225	5-10	892.55	Cc Gdm	0.93	n.d.	0.28	n.d.	0.18	0.35	3.45	48.43	n.d.	0.10	53.72
981	225	5-11	892.55	Cc Gdm	1.78	n.d.	0.52	n.d.	0.30	0.31	1.85	52.28	n.d.	0.05	57.09
982	225	5-12	892.55	Cc Gdm	0.36	n.d.	0.07	n.d.	0.09	0.36	2.92	49.61	n.d.	n.d.	53.41
983	225	5-13	892.55	Cc Gdm	1.10	0.05	0.27	n.d.	n.d.	0.22	2.79	49.90	n.d.	0.19	54.52
984	225	5-14	892.55	Cc Gdm	0.46	n.d.	0.12	n.d.	n.d.	0.24	5.47	47.02	0.06	n.d.	53.37
985	225	5-15	892.55	Cc Gdm	n.d.	n.d.	n.d.	n.d.	n.d.	0.24	0.07	54.75	n.d.	n.d.	55.06
986	225	5-16	892.55	Cc Gdm	0.76	0.06	0.50	n.d.	n.d.	0.12	8.52	43.07	0.04	0.12	53.19
987	225	5-17	892.55	Cc Gdm	0.23	n.d.	0.05	n.d.	0.10	0.29	2.65	51.49	n.d.	n.d.	54.81
988	225	5-18	892.55	Cc Gdm	0.61	0.20	0.19	n.d.	0.85	0.37	1.38	51.09	0.02	0.07	54.78
989	225	5-19	892.55	Cc Gdm	1.09	0.05	0.29	n.d.	0.20	0.30	1.14	53.20	0.08	0.08	56.43
990	225	5-20	892.55	Cc Gdm	0.36	n.d.	0.10	n.d.	n.d.	0.30	1.30	51.45	n.d.	n.d.	53.51
991	225	6-1	892.55	M.R.P.	58.43	0.09	18.76	n.d.	0.78	n.d.	0.17	2.42	2.73	9.68	93.06
992	225	6-2	892.55	M.R.P.	57.38	0.08	19.05	n.d.	0.82	n.d.	0.11	3.10	3.15	8.74	92.43
993	225	6-3	892.55	M.R.P.	60.06	0.10	19.59	0.06	0.54	n.d.	0.07	2.39	2.43	10.86	96.10
994	225	6-4	892.55	M.R.P.	60.57	0.13	19.68	n.d.	0.80	n.d.	0.16	2.49	2.75	10.53	97.11
995	225	6-5	892.55	M.R.P.	61.18	0.05	19.61	n.d.	0.79	n.d.	0.06	2.83	2.92	9.79	97.23
996	225	6-6	892.55	M.R.P.	59.97	0.15	19.70	n.d.	0.80	n.d.	0.08	2.95	3.32	9.01	95.98
997	225	6-7	892.55	M.R.P.	59.10	0.28	19.57	n.d.	0.86	n.d.	0.23	3.15	2.76	8.81	94.76
998	225	6-8	892.55	M.R.P.	59.62	0.09	19.31	n.d.	0.86	n.d.	n.d.	2.90	3.54	9.13	95.45
999	225	6-9	892.55	M.R.P.	57.27	0.09	19.17	n.d.	0.86	n.d.	0.12	3.38	3.10	8.53	92.52
1000	225	6-10	892.55	M.R.P.	50.57	0.14	15.53	n.d.	2.52	n.d.	8.68	2.89	3.22	2.25	85.80

Table A.5. *Continued*

Analysis #	Sample #	Batch #	Depth (m)	Comment	SiO_2	TiO_2	Al_2O_3	Cr_2O_3	FeO_{tot}	MnO	MgO	CaO	Na_2O	K_2O	Total
1001	225	6-11	892.55	M.R.P.	46.00	0.32	13.57	n.d.	2.71	n.d.	13.21	2.98	2.08	0.92	81.79
1002	225	6-12	892.55	M.R.P.	46.90	0.21	13.99	n.d.	2.96	n.d.	14.14	3.58	2.03	0.96	84.77
1003	225	6-13	892.55	M.R.P.	43.29	0.10	13.37	n.d.	2.95	n.d.	11.80	3.91	2.34	0.91	78.67
1004	225	6-14	892.55	M.R.P.	10.89	n.d.	2.34	n.d.	2.17	0.14	2.22	32.97	0.05	1.00	51.78
1005	225	6-15	892.55	M.R.P.	2.05	0.05	0.49	n.d.	0.50	0.14	0.82	47.84	0.17	0.28	52.34
1006	225	6-16	892.55	Qtz	86.83	n.d.	0.11	n.d.	0.10	n.d.	n.d.	0.27	0.06	n.d.	87.37
1007	225	6-17	892.55	Qtz	97.44	n.d.	0.09	n.d.	0.09	n.d.	n.d.	0.17	0.02	n.d.	97.81
1008	225	6-18	892.55	Qtz	97.65	0.06	0.06	n.d.	n.d.	n.d.	n.d.	n.d.	n.d.	n.d.	97.77
1009	225	6-19	892.55	Qtz	97.51	0.07	0.07	n.d.	n.d.	n.d.	n.d.	n.d.	0.02	n.d.	97.67
1010	225	6-20	892.55	Qtz	97.15	n.d.	n.d.	n.d.	n.d.	n.d.	n.d.	n.d.	n.d.	n.d.	97.15
1011	225	7-1	892.55	Qtz	97.44	n.d.	n.d.	n.d.	n.d.	n.d.	n.d.	n.d.	n.d.	n.d.	97.44
1012	225	7-2	892.55	Qtz	97.40	n.d.	0.07	n.d.	n.d.	n.d.	n.d.	n.d.	n.d.	n.d.	97.47
1013	225	7-3	892.55	Qtz	95.61	0.07	0.10	n.d.	n.d.	n.d.	n.d.	n.d.	0.06	0.05	95.89
1014	225	7-4	892.55	Qtz	97.54	0.05	0.05	n.d.	n.d.	n.d.	n.d.	n.d.	0.09	n.d.	97.73
1015	225	7-5	892.55	Qtz	97.00	n.d.	0.06	n.d.	n.d.	n.d.	n.d.	n.d.	n.d.	n.d.	97.06
1016	225	7-6	892.55	Qtz	97.47	n.d.	0.05	n.d.	n.d.	n.d.	n.d.	n.d.	n.d.	n.d.	97.52
1017	225	7-7	892.55	Qtz	97.43	n.d.	0.14	n.d.	n.d.	n.d.	n.d.	n.d.	0.06	n.d.	97.63
1018	225	7-8	892.55	Qtz	97.79	n.d.	0.09	n.d.	n.d.	n.d.	n.d.	n.d.	0.04	n.d.	97.92
1019	225	7-9	892.55	Qtz	97.97	n.d.	0.08	n.d.	n.d.	n.d.	n.d.	n.d.	0.07	n.d.	98.12
1020	225	7-10	892.55	Qtz	98.16	n.d.	0.13	n.d.	n.d.	n.d.	n.d.	0.05	0.06	0.05	98.45
1021	225	7-11	892.55	Qtz	97.75	n.d.	n.d.	n.d.	n.d.	n.d.	n.d.	n.d.	0.04	n.d.	97.79
1022	225	7-12	892.55	Qtz	96.74	n.d.	0.09	n.d.	n.d.	n.d.	n.d.	n.d.	0.05	n.d.	96.88
1023	225	7-13	892.55	Qtz	97.43	0.07	0.08	n.d.	n.d.	n.d.	n.d.	n.d.	0.05	n.d.	97.63
1024	225	7-14	892.55	Qtz	94.62	1.96	0.36	n.d.	0.27	n.d.	0.08	0.24	0.07	0.06	97.66
1025	225	7-15	892.55	Qtz	97.32	0.06	0.23	n.d.	0.09	n.d.	n.d.	0.10	0.06	0.08	97.94
1026	225	7-16	892.55	Qtz	97.73	n.d.	0.10	n.d.	n.d.	n.d.	n.d.	n.d.	0.04	n.d.	97.87
1027	225	7-17	892.55	Qtz	97.56	0.05	0.07	n.d.	0.09	n.d.	n.d.	0.07	0.03	n.d.	97.87
1028	225	7-18	892.55	Qtz	97.33	n.d.	n.d.	n.d.	n.d.	n.d.	n.d.	0.05	n.d.	n.d.	97.38
1029	225	7-19	892.55	Qtz	97.37	n.d.	0.10	n.d.	n.d.	n.d.	0.05	n.d.	0.02	n.d.	97.54
1030	225	7-20	892.55	Qtz	97.86	n.d.	n.d.	0.05	n.d.	n.d.	n.d.	n.d.	0.04	n.d.	97.95
1031	225	8-1	892.55	Qtz	98.00	n.d.	n.d.	n.d.	n.d.	n.d.	n.d.	n.d.	n.d.	n.d.	98.00
1032	225	8-2	892.55	Qtz	98.79	n.d.	n.d.	0.05	n.d.	n.d.	n.d.	n.d.	n.d.	n.d.	98.84
1033	225	8-3	892.55	Qtz	97.37	n.d.	n.d.	n.d.	n.d.	n.d.	n.d.	n.d.	0.02	n.d.	97.39
1034	225	8-4	892.55	Qtz	97.64	n.d.	n.d.	n.d.	n.d.	n.d.	n.d.	n.d.	0.02	n.d.	97.66
1035	225	8-5	892.55	Qtz	97.52	n.d.	n.d.	n.d.	n.d.	n.d.	n.d.	n.d.	n.d.	n.d.	97.52
1036	225	8-6	892.55	Cc Gdm	3.00	0.05	0.84	0.06	0.15	0.22	0.20	50.17	0.02	0.78	55.49
1037	225	8-7	892.55	Cc Gdm	0.53	n.d.	0.10	0.06	0.12	0.22	0.42	54.90	0.02	0.06	56.43
1038	225	8-8	892.55	Cc Gdm	0.82	0.05	0.23	n.d.	0.14	0.24	0.35	52.85	0.03	0.16	54.87
1039	225	8-9	892.55	Cc Gdm	0.22	n.d.	n.d.	n.d.	0.09	0.36	0.57	53.26	n.d.	0.08	54.58
1040	225	8-10	892.55	Cc Gdm	0.29	n.d.	0.05	n.d.	n.d.	0.32	0.69	52.95	n.d.	0.10	54.40
1041	225	8-11	892.55	Cc Gdm	12.33	n.d.	3.99	n.d.	0.09	0.19	0.25	43.52	0.03	3.08	63.48
1042	225	8-12	892.55	Cc Gdm	0.16	n.d.	n.d.	n.d.	n.d.	0.26	0.41	53.70	0.02	n.d.	54.55
1043	225	8-13	892.55	Cc Gdm	1.80	n.d.	0.56	n.d.	n.d.	0.25	0.26	52.67	0.17	0.35	56.06
1044	225	8-14	892.55	Cc Gdm	0.19	n.d.	0.06	n.d.	n.d.	0.27	0.57	53.03	0.03	0.08	54.23
1045	225	8-15	892.55	Cc Gdm	0.11	n.d.	n.d.	n.d.	n.d.	0.31	0.42	54.81	0.02	0.09	55.76
1046	225	8-16	892.55	Cc Gdm	0.22	n.d.	0.05	n.d.	n.d.	0.32	0.57	52.75	n.d.	n.d.	53.91
1047	225	8-17	892.55	Cc Gdm	2.54	n.d.	0.66	n.d.	n.d.	0.38	0.48	52.58	n.d.	0.70	57.34
1048	225	8-18	892.55	Cc Gdm	0.45	n.d.	0.09	n.d.	0.10	0.27	0.53	52.82	n.d.	0.13	54.39
1049	225	8-19	892.55	Cc Gdm	1.07	n.d.	0.23	n.d.	0.12	0.27	0.53	53.91	n.d.	0.30	56.43
1050	225	8-20	892.55	Cc Gdm	0.15	n.d.	n.d.	0.05	n.d.	0.27	0.51	53.09	n.d.	n.d.	54.07

Table A.5. *Continued*

Analysis #	Sample #	Batch #	Depth (m)	Comment	SiO_2	TiO_2	Al_2O_3	Cr_2O_3	FeO_{tot}	MnO	MgO	CaO	Na_2O	K_2O	Total
1051	225	9-1	892.55	Cc Gdm	0.73	n.d.	0.25	n.d.	n.d.	0.40	0.37	58.94	n.d.	n.d.	60.69
1052	225	9-2	892.55	Cc Gdm	42.03	0.68	12.20	n.d.	1.91	0.11	1.53	15.09	1.41	8.25	83.21
1053	225	9-3	892.55	Cc Gdm	0.63	n.d.	0.08	n.d.	0.73	0.41	0.36	58.64	n.d.	0.07	60.92
1054	225	9-4	892.55	Cc Gdm	17.82	1.01	4.12	n.d.	8.89	0.20	5.68	27.88	0.24	1.71	67.55
1055	225	9-5	892.55	Cc Gdm	0.48	n.d.	0.27	n.d.	0.19	0.24	3.62	54.36	0.03	n.d.	59.19
1056	225	9-6	892.55	Cc Gdm	3.09	n.d.	0.95	0.05	0.39	0.33	0.69	53.85	n.d.	0.55	59.90
1057	225	9-7	892.55	Cc Gdm	0.27	0.09	0.05	n.d.	0.47	0.35	2.74	56.33	0.02	0.05	60.37
1058	225	9-8	892.55	Cc Gdm	0.23	n.d.	0.11	n.d.	0.13	0.33	0.80	57.98	0.02	n.d.	59.60
1059	225	9-9	892.55	Cc Gdm	2.74	0.24	0.65	n.d.	3.80	0.25	1.08	50.19	n.d.	0.26	59.21
1060	225	9-10	892.55	Cc Gdm	22.04	n.d.	7.09	n.d.	0.82	0.19	1.59	35.21	1.27	2.37	70.58
1061	225	9-11	892.55	Cc Gdm	n.d.	n.d.	n.d.	n.d.	n.d.	0.42	0.25	61.14	n.d.	n.d.	61.81
1062	225	9-12	892.55	Cc Gdm	n.d.	n.d.	n.d.	n.d.	n.d.	0.36	0.19	57.41	n.d.	n.d.	57.96
1063	225	9-13	892.55	Cc Gdm	0.50	n.d.	0.12	n.d.	0.21	0.32	2.93	57.70	0.03	0.07	61.88
1064	225	9-14	892.55	Cc Gdm	0.34	n.d.	0.07	n.d.	0.38	0.25	5.60	48.84	0.04	0.06	55.58
1065	225	9-15	892.55	Cc Gdm	2.60	n.d.	0.70	n.d.	0.98	0.36	1.60	51.42	0.11	0.20	57.97
1066	225	9-16	892.55	Cc Gdm	0.83	0.05	0.26	0.05	0.37	0.32	0.67	53.16	n.d.	0.07	55.78
1067	225	9-17	892.55	Cc Gdm	23.71	0.26	6.96	n.d.	3.58	0.09	15.80	15.91	0.11	0.95	67.37
1068	225	9-18	892.55	Cc Gdm	0.62	n.d.	0.19	n.d.	0.17	0.30	0.52	54.88	n.d.	0.08	56.76
1069	225	9-19	892.55	Cc Gdm	0.43	n.d.	0.26	n.d.	0.42	0.29	2.81	55.61	n.d.	0.07	59.89
1070	225	9-20	892.55	Cc Gdm	0.49	n.d.	0.14	n.d.	0.31	0.30	2.73	53.89	0.04	0.09	57.99
1071	225	10-1	892.55	M.R.P. Tr.	63.87	0.08	19.20	n.d.	0.17	n.d.	0.07	1.05	1.05	13.46	98.95
1072	225	10-2	892.55	M.R.P. Tr.	63.12	0.16	19.07	n.d.	0.17	n.d.	0.06	1.10	1.23	13.02	97.93
1073	225	10-3	892.55	M.R.P. Tr.	63.23	0.12	19.29	n.d.	0.11	n.d.	0.06	1.02	1.45	13.02	98.30
1074	225	10-4	892.55	M.R.P. Tr.	64.75	n.d.	18.83	n.d.	n.d.	n.d.	0.08	0.41	0.55	15.17	99.79
1075	225	10-5	892.55	M.R.P. Tr.	63.51	0.08	18.35	n.d.	0.35	n.d.	0.17	0.80	0.86	14.00	98.12
1076	225	10-6	892.55	M.R.P. Tr.	62.28	0.05	18.30	n.d.	2.20	n.d.	n.d.	0.70	1.71	12.53	97.77
1077	225	10-7	892.55	M.R.P. Tr.	62.32	n.d.	18.09	n.d.	0.11	n.d.	0.25	0.54	1.02	13.70	96.03
1078	225	10-8	892.55	M.R.P. Tr.	63.51	n.d.	18.96	n.d.	0.20	n.d.	n.d.	1.10	1.66	12.76	98.19
1079	225	10-9	892.55	M.R.P. Tr.	63.32	n.d.	19.38	n.d.	0.48	n.d.	n.d.	1.08	1.48	13.16	98.90
1080	225	10-10	892.55	M.R.P. Tr.	9.26	6.50	5.87	1.09	65.57	0.52	2.21	0.13	0.18	1.69	93.02
1081	225	10-11	892.55	M.R.P. Tr.	44.93	2.47	15.88	0.43	24.61	0.16	0.66	1.17	1.73	8.42	100.46
1082	225	10-12	892.55	M.R.P. Tr.	63.39	0.10	18.89	n.d.	0.89	n.d.	n.d.	0.72	1.02	13.98	98.99
1083	225	10-13	892.55	M.R.P. Tr.	62.83	n.d.	18.78	n.d.	0.34	n.d.	n.d.	0.87	1.14	13.57	97.53
1084	225	10-14	892.55	M.R.P. Tr.	63.45	0.08	18.55	n.d.	0.19	n.d.	n.d.	0.73	1.03	14.08	98.11
1085	225	10-15	892.55	M.R.P. Tr.	62.66	0.13	18.67	n.d.	0.15	n.d.	n.d.	1.04	1.40	13.60	97.65
1086	225	10-16	892.55	M.R.P. Tr.	61.45	0.09	18.27	n.d.	3.10	n.d.	n.d.	0.88	0.95	13.60	98.34
1087	225	10-17	892.55	M.R.P. Tr.	62.19	0.07	18.70	n.d.	0.69	n.d.	0.06	0.80	0.83	14.23	97.57
1088	225	10-18	892.55	M.R.P. Tr.	62.61	n.d.	19.03	n.d.	0.21	n.d.	n.d.	1.02	1.43	13.38	97.68
1089	225	10-19	892.55	M.R.P. Tr.	62.69	0.06	19.27	n.d.	0.42	n.d.	n.d.	1.28	1.41	13.09	98.22
1090	225	10-20	892.55	M.R.P. Tr.	61.61	0.36	18.68	n.d.	1.13	n.d.	0.20	1.23	1.49	12.83	97.53

Appendix A.6.
Major and trace element results (Chapter 3)

Table A.6. Chemical compositions of bulk impact melt, suevite, and country rocks, Yaxcopoil-1, Chicxulub impact structure[a].

Sample #	1	2	3	4	5	6	7	8	9	10	11	12	13	14
Depth	791.7	800.4	800.4	803.4	803.5	805.3	808.3	808.3	809.0	809.7	809.7	810.8	811.6	815.8
Unit[b]	T. lmst.	1	1	1	1	1	1	1	1	1	1	1	1	1
SiO_2	11.34	44.50	45.70	39.54	39.20	39.00	43.10	42.50	38.92	43.10	42.80	44.10	45.85	45.91
TiO_2	0.10	0.58	0.59	0.49	0.50	0.52	0.53	0.53	0.45	0.56	0.53	0.53	0.59	0.55
Al_2O_3	2.64	12.10	12.40	10.82	10.65	10.80	11.60	11.60	10.40	11.70	11.80	11.56	13.01	11.98
FeO_{tot}	0.88	5.57	5.83	4.36	4.42	4.42	4.71	4.67	4.54	4.77	4.41	5.04	5.39	5.54
MnO	0.08	0.02	0.03	0.03	0.04	0.04	0.04	0.05	0.50	0.05	0.05	0.04	0.03	0.04
MgO	3.74	4.60	4.60	3.84	4.34	4.70	3.88	3.96	4.44	4.10	3.94	4.17	4.48	5.05
CaO	42.30	10.00	8.21	14.90	14.98	16.80	12.40	12.80	14.95	12.40	13.30	11.23	9.21	8.45
Na_2O	0.59	2.83	2.29	1.98	2.24	2.10	3.32	1.27	2.53	2.68	2.73	2.59	2.97	2.63
K_2O	0.24	2.26	2.28	2.17	2.13	2.09	2.27	2.25	2.14	2.24	2.36	2.26	2.37	2.27
P_2O_5	0.18	0.01	0.01	0.06	0.03	0.05	0.04	0.04	0.03	0.05	0.02	0.02	0.02	0.03
Cl	0.20	0.40	0.40	0.30	0.30	0.40	0.60	0.60	0.40	0.60	0.30	0.50	0.40	0.40
L.O.I	37.20	17.50	17.40	20.40	21.40	19.00	17.70	17.90	20.90	17.50	17.30	17.30	15.30	16.80
Total	99.56	100.38	99.74	98.88	100.23	99.91	100.20	99.17	100.21	99.75	99.55	99.35	99.62	99.66
Sulfur content (wt. %)														
S_{tot}	0.04	0.02	<0.02	<0.02	0.03	<0.02	<0.02	<0.02	0.06	0.02	0.05	<0.02	0.02	0.03
SO_3	0.10	0.04	<0.02	0.02	0.07	0.02	<0.02	0.02	0.15	0.02	0.12	0.02	0.09	0.07
Trace														
Sc	3.41	13.2	14.6	13.2	15.9	12.7	16.5	31.3	15.7	16.0	18.5	14.8	15.5	18.1
Cr	2.00	84.0	39.7	43.4	51.0	39.0	55.2	107	51.7	80.4	42.5	57.5	43.3	56.0
Co	3.34	6.39	5.91	5.62	8.05	5.51	8.15	14.5	7.86	6.95	10.5	5.39	8.99	8.42
Ni	2	19	15	15	41	10	23	25	8	35	23	9	31	29
Zn	37	64	70	63	63	58	87	95	75	105	60	79	76	83
As	0.32	0.09	0.35	0.03	0.18	0.21	0.60	0.17	0.11	0.28	0.15	0.28	0.42	0.22
Se	0.2	0.1	0.2	0.3	0.4	0.3	0.3	0.8	0.1	0.1	0.5	0.2	0.2	0.5
Br	10.1	12.5	10.8	1.3	13.2	1.5	26.6	<0.5	14.5	13.2	20.8	6.8	19.9	15.4
Rb	16.8	82.3	58.3	54.6	63.6	50.9	69.5	61.9	54.3	48.6	71.2	54.6	66.0	67.0
Sr	390	223	33	215	184	175	344	66	240	52	313	59	348	196
Zr	33	111	80	125	108	125	105	550	64	120	67	130	120	86
Sb	0.16	0.25	0.13	0.17	0.21	0.14	0.24	0.32	0.23	0.06	0.11	0.10	0.19	0.21
Cs	0.95	2.93	2.45	2.42	2.86	2.37	2.44	2.93	2.24	2.22	2.51	2.34	2.48	2.55
Ba	33	42	30	75	81	2	46	240	98	40	104	264	41	98
La	14.7	5.1	10.6	15.3	15.1	15.2	10.6	34.1	12.9	18.3	6.1	11.3	10.7	9.9
Ce	12.8	10.0	27.9	28.5	28.1	29.8	29.5	56.6	29.8	49.0	12.0	25.2	21.7	26.9
Nd	9.5	4.3	10.8	15.5	13.8	14.6	11.3	24.2	12.0	17.0	6.9	13.06	9.6	9.2
Sm	2.47	1.11	1.98	3.17	2.99	2.83	2.02	4.86	2.47	3.01	1.24	2.23	2.21	2.04
Eu	0.67	0.27	0.57	0.92	0.75	0.78	0.56	0.82	0.68	0.9	0.37	0.76	0.62	0.59
Gd	2.4	1.4	2.5	4.0	2.5	3.1	2.0	4.0	2.5	2.8	1.2	2.0	2.7	2.1
Tb	0.34	0.26	0.39	0.52	0.42	0.45	0.38	0.77	0.43	0.40	0.22	0.33	0.49	0.31
Tm	0.17	0.15	0.23	0.26	0.25	0.22	0.22	0.51	0.22	0.24	0.13	0.22	0.25	0.17
Yb	1.10	0.93	1.59	1.82	1.73	1.71	1.46	3.97	1.59	1.70	0.99	1.40	1.60	1.08
Lu	0.15	0.14	0.24	0.27	0.26	0.25	0.22	0.71	0.24	0.25	0.15	0.22	0.23	0.16
Hf	0.60	3.29	2.61	2.63	2.50	2.33	2.98	16.3	2.44	3.77	2.99	3.23	2.51	3.07
Ta	0.13	0.51	0.35	0.35	0.41	0.36	0.45	1.74	0.37	0.56	0.5	0.38	0.55	0.37
W	n/a	n/a	0.62	0.3	0.94	0.9	1.49	3.0	0.4	0.58	0.29	<1.1	1.05	0.5
Ir (ppb)	<0.5	<2	<1	<1.2	<0.5	<0.8	<0.7	<2	<1	<1	<1	<1.3	<1	<1.2
Au (ppb)	0.2	0.6	0.8	1.1	1.6	0.4	0.1	0.6	0.3	0.4	0.4	3.5	0.3	<0.6
Th	1.10	5.96	5.07	4.95	5.46	4.53	5.93	14.6	5.13	6.98	7.12	5.18	5.60	5.93
U	0.37	0.67	0.64	0.53	0.63	0.42	0.69	3.69	0.66	0.64	0.16	0.56	0.67	0.60
CIA	76	70	73	72	71	72	67	77	69	70	70	70	71	71
K/U	4324	30597	25156	33962	26825	39048	29420	3144	25606	28353	134375	35946	31493	32667
Zr/Hf	56.0	33.7	0.730	47.5	43.2	53.7	35.2	1.09	26.2	1.14	22.5	0.77	47.8	28.1
La/Th	13.4	0.857	30.7	3.09	2.77	3.36	1.79	33.7	2.51	35.9	0.86	42.8	1.91	1.66
Th/U	2.97	8.90	7.92	9.34	8.67	10.8	8.59	3.96	7.77	10.6	44.5	10.2	8.36	9.88
LaN/YbN	9.03	3.71	4.50	5.68	5.90	6.01	4.91	5.80	5.48	7.25	4.16	5.48	4.52	6.16
Eu/Eu*	0.84	0.66	0.78	0.79	0.84	0.81	0.85	0.57	0.84	0.95	0.94	1.36	0.78	0.88

[a]Major elements are presented in wt%, trace elements in ppm, except where indicated. $Eu/Eu^* = Eu_N/(Sm_N \times Gd_N)^{0.5}$. Chemical index of alteration (CIA) = $(Al_2O_3/[Al_2O_3 + CaO_{silicate} + Na_2O + K_2O]) \times 100$ (Nesbitt and Young 1982).

[b]Abbreviations are: T. = Tertiary, C. = Cretaceous, Lmst. = Limestone, Br. = Breccia, n/a = not available.

Table A.6. *Continued*

Sample #	15	16	17	18	19	20	21	22	23	24	25	26	27	28
Depth	816.6	818.2	818.30	819.1	821.4	822.9	822.9	824.0	825.4	827.1	835.1	835.2	837.0	844.8
Unit[b]	1	1	1	1	1	2	2	2	2	2	2	2	2	2
SiO_2	49.40	44.20	44.20	40.10	39.40	43.90	44.40	41.60	54.40	37.80	47.20	45.00	28.05	52.80
TiO_2	0.64	0.60	0.60	0.32	0.33	0.52	0.53	0.54	0.79	0.47	0.60	0.54	0.21	0.64
Al_2O_3	13.60	12.40	12.30	10.60	10.42	11.30	11.50	11.20	14.50	10.10	12.60	11.70	7.04	14.50
FeO_{tot}	5.69	5.22	5.32	3.14	3.07	4.75	5.15	4.19	5.91	4.26	5.75	5.07	2.41	5.05
MnO	0.03	0.04	0.03	0.08	0.07	0.05	0.05	0.03	0.03	0.04	0.02	0.03	0.11	0.03
MgO	3.71	4.40	4.30	2.77	3.05	4.70	4.80	3.58	2.98	4.10	5.13	4.10	3.23	5.40
CaO	7.76	9.94	9.89	19.80	19.70	11.24	10.80	15.95	4.17	17.90	8.60	11.80	28.10	6.39
Na_2O	3.02	4.31	2.97	2.98	2.76	2.80	2.31	2.43	4.48	2.63	3.45	3.44	1.34	4.00
K_2O	3.22	2.58	2.57	2.81	2.62	2.99	3.10	3.42	4.33	2.69	3.21	3.49	2.41	3.21
P_2O_5	0.04	0.02	0.02	0.14	0.09	0.03	0.03	0.09	0.03	0.11	0.07	0.11	0.05	0.04
Cl	0.40	0.50	0.50	0.20	0.30	0.50	0.50	0.40	0.30	0.50	0.70	0.50	0.30	0.40
L.O.I	12.70	17.10	17.20	17.40	18.50	17.40	16.50	16.80	8.39	19.70	12.50	14.50	25.70	8.04
Total	100.21	100.31	99.91	100.35	100.30	100.23	99.72	100.23	100.31	100.29	99.84	100.30	98.97	100.51
Sulfur content (wt. %)														
S_{tot}	0.02	<0.02	0.02	<0.02	0.03	<0.02	<0.02	0.05	0.03	0.03	0.02	<0.02	0.02	0.03
SO_3	0.06	0.02	0.02	0.02	0.09	0.02	0.02	0.12	0.08	0.06	0.04	0.02	0.05	0.08
Trace													Trace	
Sc	18.4	19.5	16.9	9.42	14.7	16.1	13.6	15.9	11.1	21.7	17.5	15.0	7.1	18.5
Cr	41.8	43.6	41.8	24.2	31.1	40.0	33.7	45.1	21.0	72.8	57.5	42.0	15.4	61.6
Co	13.7	6.80	5.85	4.48	7.63	8.08	6.34	7.00	7.29	9.36	8.23	6.62	5.45	10.20
Ni	<25	9	18	18	49	27	16	14	30	25	20	21	30	50
Zn	58	70	64	46	63	75	65	54	46	84	48	47	36	58
As	0.30	0.57	0.33	0.29	0.31	0.05	0.41	<1.00	0.15	0.20	0.22	0.36	0.16	0.49
Se	0.4	0.3	0.1	0.3	0.4	0.1	0.2	0.1	0.1	0.7	0.1	0.2	0.1	<0.1
Br	13.9	9.1	13.5	1.3	24.9	21.9	11.1	21.7	14.0	17.6	3.3	15.1	1.1	27.5
Rb	66.8	37.5	59.6	24.5	40.6	57.1	49.5	70.1	37.0	69.3	66.5	58.2	34.3	52.8
Sr	218	218	39	440	320	256	53	574	138	284	350	37	250	390
Zr	84	230	115	160	115	110	65	120	160	82	115	110	92	138
Sb	0.20	0.21	0.13	0.11	0.23	0.20	0.12	0.19	0.13	0.12	0.17	0.15	0.13	0.06
Cs	2.33	0.99	2.34	0.31	1.01	1.57	1.29	1.60	1.29	1.82	2.09	1.35	0.73	1.34
Ba	107	105	45	220	128	58	45	200	409	24	190	80	125	204
La	10.8	14.8	17.6	37.1	25.6	12.8	18.2	14.8	49.1	3.5	14.2	14.9	18.7	15.3
Ce	26.9	37.8	55.2	47.5	36.4	29.5	41.2	28.1	227.0	6.2	25.9	27.2	24.6	31.3
Nd	11.0	16.0	15.8	30.5	22.8	11.0	17.6	13.4	35.2	3.6	14.9	14.3	14.2	11.2
Sm	2.41	2.8	3.16	6.26	4.72	2.39	3.21	3.05	5.28	0.58	3.05	3.11	2.87	1.82
Eu	0.65	1.37	0.84	1.74	1.21	0.67	0.86	0.81	1.68	0.18	0.84	0.85	0.83	0.41
Gd	2.0	3.5	2.9	6.9	4.5	2.3	3.1	3.2	4.9	0.7	3.3	3.3	3.3	2.4
Tb	0.36	0.72	0.47	1.16	0.82	0.41	0.53	0.60	0.74	0.15	0.45	0.51	0.48	0.42
Tm	0.20	0.39	0.26	0.58	0.45	0.29	0.36	0.30	0.37	0.10	0.62	0.27	0.31	0.22
Yb	1.35	2.60	1.62	4.27	2.90	2.29	2.52	1.85	2.42	0.78	1.61	1.72	2.93	1.17
Lu	0.19	0.39	0.21	0.64	0.42	0.35	0.4	0.27	0.33	0.12	0.24	0.25	0.35	0.16
Hf	2.84	4.87	2.79	2.07	2.24	2.56	2.23	2.67	3.36	3.30	3.09	2.75	1.24	2.73
Ta	0.39	0.55	0.37	0.3	0.33	0.57	0.24	0.52	0.39	0.47	0.36	0.35	0.12	0.43
W	1.02	0.57	0.7	0.5	1.11	0.34	1.4	0.42	0.66	1.08	<1	1.14	0.5	n/a
Ir (ppb)	<1.2	<0.9	<0.8	<0.6	<1.3	<0.7	<1	<1	<1	<0.9	<0.8	<1	0.1	<0.8
Au (ppb)	1.0	3.0	0.4	0.5	0.5	0.1	<1	0.6	1.2	0.4	0.2	<1	0.2	0.3
Th	7.13	4.64	6.19	6.75	5.90	5.10	4.63	5.57	3.02	8.23	6.77	5.03	2.41	9.30
U	0.91	0.84	0.63	0.52	0.77	0.56	0.48	0.83	0.46	0.60	0.56	0.72	0.54	0.80
CIA	69	64	69	65	66	66	68	66	62	66	65	63	65	67
K/U	26154	23571	31587	51923	27403	40536	39167	43976	64783	41167	47857	54306	41852	35750
Zr/Hf	29.8	47.2	1.04	77.3	51.3	43.0	1.34	44.9	47.6	25.1	37.2	0.990	74.2	50.5
La/Th	1.51	3.19	41.2	5.50	4.34	2.51	29.1	2.66	16.3	0.42	2.10	40.0	7.76	1.65
Th/U	7.84	5.52	9.83	13.0	7.66	9.11	9.65	6.71	6.57	13.7	12.1	6.99	4.46	11.6
LaN/YbN	5.41	3.85	7.34	5.87	5.97	3.78	4.88	5.41	13.7	3.00	5.96	5.85	4.31	8.84
Eu/Eu*	0.90	1.34	0.85	0.81	0.80	0.88	0.84	0.79	1.01	0.90	0.81	0.82	0.83	0.60

Table A.6. *Continued*

Sample #	29	30	31	32	33	34	35	36	37	38	39	40	41	42
Depth	846.8	851.2	851.2	875.8	882.5	886.8	886.8	888.1	888.9	890.5	892.6	894.1	916.4	916.4
Unit[b]	3	3	3	4	4	5	5	5	5	5	5	5	C. lmt. lithic br.	C. lmst. lithic br.
SiO_2	37.20	51.50	43.27	54.64	52.80	2.22	2.39	20.00	33.60	40.40	32.53	15.50	18.60	8.60
TiO_2	0.48	0.63	0.54	0.41	0.55	<0.1	<0.1	0.17	0.32	0.39	0.29	0.10	0.19	<0.1
Al_2O_3	9.90	14.50	11.69	15.13	15.60	0.45	0.50	5.51	9.08	11.40	8.89	3.42	5.60	2.50
FeO_{tot}	3.42	3.71	2.86	5.37	6.55	0.17	0.26	2.05	3.69	4.26	2.88	0.50	1.61	0.66
MnO	0.07	0.05	0.10	0.03	0.02	0.27	0.39	0.18	0.10	0.08	0.14	0.34	0.15	0.20
MgO	2.93	4.50	4.10	5.81	5.80	11.20	4.90	6.63	7.00	4.96	3.25	3.50	3.51	2.66
CaO	20.90	7.68	15.23	5.43	4.96	40.60	47.90	30.90	19.60	16.50	24.00	39.30	35.60	45.70
Na_2O	3.460	5.17	3.82	3.10	4.63	0.17	0.11	1.42	2.39	2.85	2.36	0.86	1.02	0.76
K_2O	2.55	2.36	2.74	4.50	2.85	0.15	0.06	1.40	2.63	3.07	3.24	1.16	1.03	0.57
P_2O_5	0.20	0.19	0.74	0.07	0.14	<0.01	<0.01	0.08	0.05	0.10	0.10	0.02	0.01	<0.01
Cl	0.40	0.40	0.50	0.40	0.50	0.10	0.10	0.20	0.30	0.20	0.40	0.20	0.30	0.20
L.O.I	18.80	7.86	14.40	4.98	5.82	44.50	42.70	30.80	21.30	15.20	21.90	35.00	31.30	38.20
Total	100.41	98.98	100.04	99.88	100.23	99.88	99.38	99.39	100.06	100.13	100.01	100.02	99.42	100.16
Sulfur content (wt. %)														
S_{tot}	<0.02	<0.02	0.03	0.02	0.02	<0.02	0.02	0.02	<0.02	<0.02	0.02	0.02	0.02	<0.02
SO_3	<0.02	0.02	0.07	0.05	0.05	<0.02	0.04	0.04	0.02	<0.02	0.04	0.02	0.02	<0.02
Trace														
Sc	12.4	12.8	15.1	13.9	16.2	0.5	0.4	5.1	8.9	10.5	9.0	2.2	4.6	2.8
Cr	38.4	62.9	47.5	37.1	41.4	3.2	2.5	22.2	23.6	22.2	26.1	7.9	13.9	6.7
Co	7.23	6.68	5.36	8.90	9.44	1.02	0.66	3.89	8.38	5.51	3.16	1.03	3.35	4.34
Ni	18	15	15	11	5	2	5	12	18	35	11	8	9	16
Zn	43	50	46	50	55	4	6	18	35	31	20	16	8	8
As	0.84	0.42	0.80	0.74	0.95	0.05	0.18	0.21	0.27	0.17	0.30	2.17	2.42	1.20
Se	0.2	0.5	0.3	0.3	0.4	0.1	0.1	0.1	0.2	0.1	0.6	<0.1	0.1	0.2
Br	2.3	2.9	2.6	22.9	3.3	0.5	4.0	0.9	1.6	13.9	2.0	5.3	7.7	7.9
Rb	32.5	25.5	38.7	51.9	32.5	1.8	0.5	16.7	37.6	20.5	28.8	11.6	17.2	8.4
Sr	335	442	430	66	590	200	233	340	350	519	385	307	66	483
Zr	120	145	160	85	90	20	18	60	71	100	271	31	40	23
Sb	0.31	0.17	0.19	0.10	0.17	0.03	0.03	0.11	0.20	0.14	0.15	0.08	0.06	0.12
Cs	0.42	0.64	0.74	0.62	0.74	0.07	0.02	0.26	0.56	0.30	0.20	0.12	0.86	0.45
Ba	240	255	580	99	320	30	10	150	155	120	500	390	145	253
La	25.2	21.5	45.5	16.9	23.8	2.0	1.4	9.7	15.8	24.5	22.5	5.7	6.6	8.2
Ce	49.5	31.7	67.9	51.1	38.6	2.9	2.4	14.1	30.8	48.8	36.5	10.9	13.3	16.7
Nd	22.5	18.1	39.2	14.4	20.0	1.6	1.2	7.4	13.6	19.6	16.2	6.5	6.85	7.7
Sm	4.08	3.58	7.51	2.94	3.3	0.36	0.29	1.47	1.98	3.75	2.95	1.08	1.14	1.54
Eu	1.06	0.94	1.82	0.69	0.82	0.05	0.04	0.36	0.46	0.98	0.62	0.24	0.28	0.36
Gd	4.1	4.1	9.1	2.5	3.0	0.2	0.4	1.7	2.3	3.9	3.0	1.0	1.1	1.2
Tb	0.73	0.61	1.37	0.39	0.45	0.03	0.07	0.23	0.33	0.62	0.46	0.15	0.17	0.23
Tm	0.36	0.28	0.54	0.15	0.26	0.02	0.04	0.12	0.21	0.35	0.22	0.08	0.12	0.15
Yb	2.62	1.77	4.17	0.98	1.72	0.13	0.26	0.89	1.46	2.38	1.42	0.51	0.92	1.10
Lu	0.44	0.26	0.61	0.14	0.26	0.02	0.04	0.15	0.21	0.37	0.22	0.08	0.15	0.17
Hf	2.25	3.18	2.79	2.49	3.21	0.09	0.13	1.11	1.93	1.56	0.69	0.66	0.93	0.46
Ta	0.35	0.48	0.41	0.87	0.47	0.01	0.04	0.13	0.26	0.41	0.71	0.1	0.12	0.13
W	0.3	0.3	0.3	0.4	0.5	0.1	n/a	<0.6	0.8	0.39	22.5	n/a	0.62	n/a
Ir (ppb)	<0.9	<1.2	<1.5	<0.5	<1.5	<0.3	<0.2	<0.8	<0.8	<0.5	<0.9	<0.2	<1.6	<0.7
Au (ppb)	0.2	0.6	<1	0.2	0.5	0.2	0.8	0.2	0.1	0.1	0.6	0.2	<0.6	0.4
Th	4.73	8.93	6.37	11.1	10.9	0.26	0.04	3.78	6.02	6.56	6.52	1.33	2.68	1.31
U	0.96	1.29	0.98	0.26	0.78	1.85	1.74	2.17	1.15	1.00	1.86	3.05	1.06	0.96
CIA	62	66	64	67	68	59	74	66	64	66	61	63	73	65
K/U	23646	16202	25918	180000	28205	865	1724	6037	22522	24100	17043	5049	8019	6042
Zr/Hf	53.3	45.6	57.4	34.1	28.0	230	143	54.1	36.8	64.1	390	48.0	1.42	51.3
La/Th	5.33	2.41	7.14	1.52	2.18	7.73	36.0	2.56	2.62	3.73	3.45	4.31	43.0	6.24
Th/U	4.93	6.92	6.50	42.7	14.0	0.14	0.02	1.74	5.23	6.56	3.51	0.436	2.53	1.36
LaN/YbN	6.50	8.21	7.37	11.7	9.35	10.4	3.74	7.33	7.31	6.96	10.7	7.59	4.82	5.03
Eu/Eu*	0.80	0.75	0.67	0.78	0.80	0.56	0.36	0.71	0.65	0.78	0.63	0.72	0.76	0.81

Table A.6. *Continued*

Sample #	43	44	45	46
Depth	840.3	843.5	860.4	879.0
Unit[b]	Brown melt	Brown melt	Brown melt	Brown melt
SiO_2	51.70	48.70	55.80	52.32
TiO_2	0.65	0.59	0.64	1.10
Al_2O_3	14.60	13.91	17.10	19.30
FeO_{tot}	5.08	4.70	4.66	4.99
MnO	0.07	0.09	0.05	0.03
MgO	3.94	4.12	3.46	3.14
CaO	8.95	11.71	7.71	6.56
Na_2O	3.88	4.12	4.97	4.85
K_2O	3.44	3.14	3.86	2.43
P_2O_5	0.11	0.10	0.12	0.38
Cl	0.30	0.30	0.10	0.40
L.O.I	7.59	9.35	4.97	5.18
Total	100.33	100.84	100.62	100.68
Sulfur content (wt. %)				
S_{tot}	<0.02	0.03	<0.02	0.02
SO_3	0.02	0.08	0.02	0.05
Trace elements (ppm, except where noted)				
Sc	32.9	15.6	20.9	23.1
Cr	19.0	47.0	61.3	23.2
Co	9.44	9.27	8.86	6.95
Ni	30	34	41	22
Zn	153	68	39	140
As	0.31	0.51	0.22	0.97
Se	0.4	<0.1	0.1	<0.1
Br	13.5	22.6	37.5	24.9
Rb	37.3	20.9	23.7	41.2
Sr	69	607	751	555
Zr	218	115	90	150
Sb	0.09	0.18	0.15	0.09
Cs	0.80	0.33	0.54	1.04
Ba	160	251	248	281
La	32.7	16.7	12.4	53.1
Ce	74.4	20.3	19.6	85.5
Nd	25.45	13.3	11.8	44.0
Sm	4.355	2.94	2.16	11.5
Eu	1.245	0.77	0.82	3.42
Gd	3.7	2.9	2.0	10.7
Tb	0.69	0.51	0.29	1.56
Tm	0.42	0.29	0.16	0.76
Yb	2.89	2.08	1.00	5.21
Lu	0.48	0.31	0.14	0.78
Hf	5.96	3.23	3.12	4.35
Ta	0.9	0.43	0.45	0.77
W	0.72	n/a	0.48	n/a
Ir (ppb)	<1.2	<0.6	<1	<2
Au (ppb)	0.5	<0.2	0.2	1.6
Th	9.80	0.81	11.3	9.83
U	1.225	1.08	1.14	1.30
CIA	67	66	68	73
K/U	18867	23981	21316	9615
Zr/Hf	36.7	35.6	28.9	34.5
La/Th	3.34	20.6	1.10	5.40
Th/U	8.02	0.75	9.91	7.56
LaN/YbN	7.66	5.43	8.38	6.89
Eu/Eu*	0.96	0.81	1.21	0.94

Appendix A.7.
Major and trace element results (Chapter 4)

Table A.7. Trace† and selected major element abundances of impactites (suevitic groundmass, bulk suevite, melt particles, and clasts) from the Yaxcopoil-1 borehole, by INAA.

Lithology	Green suevite	Green suevite	Green suevite	Gray melt particle	Light gray melt particle	Green suevite	Green suevite	Green suevite	Finely laminated gneiss	Med. gray ground-mass	Dark gray ground-mass	Gray melt particle	Med. gray ground-mass
Unit	1	1	1	1	1	1	1	1	2	2	2	2	2
ID #	768	768D**	770A	770B	752A	752B	771	772	208B	769A	769B	769C	210B
Depth (m)	805.34	805.34	809.70	809.70	810.84	810.84	815.80	816.62	824.03	825.43	825.43	825.43	827.13
Na_2O	2.10	2.24	2.10	3.26	1.92	3.27	2.09	1.75	4.80	4.46	5.04	3.68	2.09
K_2O	1.90	2.06	1.94	2.40	2.01	2.39	2.25	4.64	2.70	3.30	3.82	4.08	2.99
Sc	11.9	12.1	15.6	16.3	14.7	14.9	13.5	13.7	12.5	5.25	5.82	31.2	13.4
Cr	38.3	39.1	39.8	121.0	39.2	75.8	43.6	38.1	19.5	16.2	19.1	85.4	36.2
FeO_{tot}	3.41	3.49	3.72	5.25	3.43	5.04	4.22	4.05	4.70	1.79	2.01	12.18	4.12
Co	5.91	6.45	7.09	6.80	5.83	4.95	6.28	5.04	8.08	3.42	3.66	10.3	6.26
Ni	14	15	39	30	10	8	14	16	23	10	11	50	73
Zn	81	60	70	140	68	90	72	55	76	31	35	95	50
As	0.61	0.31	0.21	0.34	0.25	0.31	0.16	0.26	0.19	0.37	0.25	1.16	0.15
Se	0.2	0.2	0.1	0.1	0.2	0.2	0.2	0.1	0.1	0.05	0.1	0.2	0.1
Br	10.5	10.2	14.6	11.8	5.1	8.5	18.3	23.2	9.0	4.1	3.7	20.0	22.0
Rb	51.3	53.2	50.4	46.8	52.1	57.0	69.5	73.5	30.5	30.4	31.6	79.5	54.3
Sr	34	27	56	48	75	43	35	48	287	39	49	120	477
Zr	120	120	110	130	120	140	110	120	185	60	55	192	110
Sb	0.15	0.11	0.06	0.06	0.08	0.11	0.21	0.18	0.21	0.06	0.04	0.24	0.24
Cs	2.30	2.63	2.20	2.24	2.32	2.36	2.66	2.02	0.64	2.77	2.64	2.21	1.30
Ba	40	50	20	60	480	48	24	200	229	150	160	890	60
La	20.5	22.1	13.1	23.4	14.6	8.1	14.8	10.9	29.2	14.5	15.8	10.5	17.3
Ce	38.7	42.9	27.8	70.1	29.6	20.7	25.7	25.7	40.2	51.7	54.9	27	31.0
Nd	20.3	24.1	13.2	20.7	16.4	9.7	14.4	12.1	18.6	13.5	13.6	10.8	17.2
Sm	4.64	4.79	2.48	3.54	3.05	1.40	3.05	2.32	3.98	2.14	2.27	2.09	4.13
Eu	1.25	1.35	0.75	1.05	0.81	0.71	0.77	0.54	1.30	0.64	0.68	1.31	1.11
Gd	3.57	3.86	2.47	3.07	3.08	0.92	2.95	2.35	4.80	2.07	1.92	2.46	3.68
Tb	0.68	0.66	0.37	0.42	0.46	0.2	0.37	0.33	0.84	0.31	0.35	0.55	0.65
Tm	0.36	0.37	0.23	0.25	0.25	0.18	0.23	0.20	0.52	0.19	0.25	0.46	0.37
Yb	2.07	2.27	1.67	1.73	1.69	1.11	1.63	1.39	3.61	1.64	1.84	3.52	2.14
Lu	0.28	0.31	0.24	0.26	0.25	0.18	0.24	0.22	0.51	0.22	0.28	0.57	0.32
Hf	2.75	2.72	2.36	5.18	2.31	4.15	2.56	2.62	3.46	1.20	1.42	5.98	2.23
Ta	0.35	0.34	0.32	0.79	0.24	0.52	0.33	0.28	0.40	0.14	0.11	0.39	0.54
W	0.9	1.1	0.6	0.6	<1.0	<1.2	2.4	0.9	0.7	0.6	0.8	1.1	0.7
Ir (ppb)	<1.0	<1.0	<1.0	<1.0	<1.0	<1.6	<1.2	<0.8	<2.0	<1.1	<1.0	<0.5	<0.7
Au (ppb)	1.0	0.4	0.4	0.3	0.8	3.5	0.9	1.0	2.0	0.6	0.4	5.2	0.2
Th	5.20	5.27	4.71	9.24	4.75	5.61	5.27	4.75	4.52	1.31	1.38	3.50	4.66
U	0.64	0.59	0.54	0.74	0.37	0.74	0.64	1.04	0.95	0.25	0.34	0.66	0.67
K/U	24688	28983	29815	26892	45135	26757	29219	37019	23579	109600	93235	51364	37015
Zr/Hf	43.6	44.1	46.6	25.1	51.9	33.7	43.0	45.8	53.5	50.0	38.7	32.1	49.3
La/Th	3.94	4.19	2.78	2.53	3.07	1.44	2.81	2.29	6.46	11.07	11.45	3.00	3.71
Hf/Ta	7.86	8.00	7.38	6.56	9.63	7.98	7.76	9.36	8.65	8.57	12.91	15.33	4.13
Th/U	8.13	8.93	8.72	12.49	12.84	7.58	8.23	4.57	4.76	5.24	4.06	5.30	6.96
La_N/Yb_N	6.69	6.58	5.30	9.14	5.84	4.93	6.14	5.30	5.47	5.97	5.80	2.02	5.46
Gd_N/Yb_N	1.40	1.38	1.20	1.44	1.48	0.67	1.47	1.37	1.08	1.02	0.85	0.57	1.39
Eu/Eu*	0.94	0.96	0.93	0.97	0.81	1.91	0.78	0.71	0.91	0.93	1.00	1.77	0.87

†Trace elements in ppm except where indicated, Na_2O, K_2O, and FeO_{tot} in wt%, $Eu/Eu^* = Eu_N/(Sm_N \times Gd_N)^{0.5}$, **duplicate analysis, n.d. = not detected, N = chondrite normalized (Taylor and McLennan, 1985), ID # are those given by the Universidad Nacional Autónoma de México (UNAM).

Table A.7. *Continued*

Lithology	Green suevite	Green melt particles	Med. gray ground-mass	Dark gray ground-mass	Med. gray ground-mass	Gray melt particle	Gray melt particle	Variegated suevite	Variegated suevite	Variegated suevite	Green suevite	Variegated suevite	Green melt particles
Unit	2	2	2	2	2	2	2	3	3	3	3	3	3
ID #	774	211A	211B	212A	212B	755A	755AD**	763	244A	244B	215A	215B	756
Depth (m)	827.13	835.14	835.14	836.98	836.98	840.30	840.30	846.01	846.80	846.80	851.15	851.15	851.15
Na_2O	1.68	3.26	3.65	3.14	2.19	4.04	3.73	3.12	4.10	3.65	4.21	4.09	5.58
K_2O	2.10	3.65	4.41	3.87	3.70	2.82	2.73	2.72	2.61	2.63	3.75	2.36	3.10
Sc	9.7	17.1	14.3	15.3	10.7	34.2	31.6	10.9	12.6	13.2	15.3	15.4	14.9
Cr	32.5	62.5	43.9	39.1	29.7	20.8	17.1	37.1	42.3	38.9	44.1	46.7	67.3
FeO_{tot}	3.15	4.89	4.72	5.16	3.13	8.83	8.23	3.09	3.65	3.24	2.59	2.64	3.02
Co	4.13	8.89	8.29	9.65	8.36	9.87	9.01	5.02	7.54	7.14	5.42	6.83	7.95
Ni	30	34	42	52	62	20	40	25	30	34	33	30	20
Zn	38	41.6	67	72	60	160	145	30	52	43	49	46	57
As	0.52	0.24	0.34	0.27	0.31	0.27	0.35	0.55	1.51	0.32	0.09	0.27	0.29
Se	0.1	0.2	n.d.	0.2	0.2	0.3	0.4	0.1	0.6	0.1	n.d.	n.d.	0.2
Br	22.6	42.0	27.5	25.0	19.0	13.8	13.1	9.5	28.0	23.0	30.9	31.9	18.5
Rb	39.6	75.3	54.4	65.9	51.6	37.2	37.4	27.5	35.9	31.6	43.3	40.9	32.5
Sr	64	363	447	478	525	76	61	95	383	404	544	425	110
Zr	110	99	93	120	90	245	192	125	140	115	190	148	153
Sb	0.29	0.13	0.2	0.21	0.16	0.15	0.03	0.12	0.53	0.18	0.13	0.12	0.03
Cs	1.32	2.24	1.26	1.61	1.23	0.67	0.93	0.17	0.45	0.36	0.46	0.60	0.58
Ba	41	69	194	121	91	170	150	150	161	183	243	196	1280
La	19.7	11.4	15.0	16.2	29.2	33.7	31.7	30.6	27.8	25.8	41.3	27.8	15.8
Ce	33.9	21.0	31.9	35.1	27.2	75.8	72.9	58.3	47.9	50.9	92.4	59.4	28.1
Nd	19.1	10.2	14.6	19.0	28.8	26.6	24.3	25.1	18.8	19.9	40.4	28.0	14.6
Sm	4.22	2.21	3.11	3.81	5.59	4.49	4.22	4.62	3.78	4.11	9.04	5.84	2.86
Eu	0.97	0.63	0.80	0.93	1.53	1.31	1.18	1.05	0.97	1.11	2.01	1.75	0.71
Gd	3.03	2.05	2.90	3.60	4.70	4.37	3.03	4.59	4.60	3.40	8.20	5.50	2.55
Tb	0.54	0.36	0.47	0.55	0.80	0.76	0.61	0.74	0.79	0.64	1.16	0.82	0.4
Tm	0.32	0.20	0.28	0.28	0.48	0.47	0.37	0.36	0.43	0.38	0.55	0.42	0.2
Yb	2.03	1.29	1.80	1.84	3.37	3.05	2.72	2.64	2.80	2.60	3.51	2.76	1.19
Lu	0.31	0.19	0.26	0.27	0.52	0.5	0.45	0.45	0.42	0.36	0.53	0.39	0.2
Hf	2.16	3.05	3.20	2.51	1.71	5.95	5.96	1.99	2.20	2.22	3.43	2.72	3.69
Ta	0.23	0.83	0.38	0.61	0.44	0.85	0.94	0.26	0.55	0.50	0.42	0.42	0.49
W	2.4	0.3	n.d.	<1.0	0.3	0.7	0.8	0.4	0.4	<4.0	n.d.	n.d.	0.9
Ir (ppb)	<1.0	<1.0	<2.0	<1.0	<1.0	<1.2	<1.2	<1.1	<2.0	<0.9	<0.7	<0.6	<0.5
Au (ppb)	0.6	0.9	2.0	0.3	0.6	0.5	1.0	1.0	0.3	0.2	0.6	0.4	1.0
Th	4.83	7.13	5.57	5.84	3.85	10.00	9.59	4.31	4.89	5.31	6.11	6.14	10.10
U	0.82	0.49	1.27	0.75	6.42	1.17	1.28	1.35	1.30	1.13	1.20	1.14	1.82
K/U	21220	61837	28819	42800	4782	20000	17734	16741	16692	19292	25917	17193	14121
Zr/Hf	50.9	32.5	28.9	47.8	52.6	41.2	32.2	62.8	63.6	51.8	55.4	54.4	41.5
La/Th	4.08	1.60	2.69	2.77	7.58	3.37	3.31	7.10	5.69	4.86	6.76	4.53	1.56
Hf/Ta	9.39	3.67	8.42	4.11	3.89	7.00	6.34	7.65	4.00	4.44	8.17	6.48	7.53
Th/U	5.89	14.55	4.39	7.79	0.60	8.55	7.49	3.19	3.76	4.70	5.09	5.39	5.55
La_N/Yb_N	6.56	5.97	5.63	5.95	5.86	7.47	7.88	7.83	6.71	6.71	7.95	6.81	8.97
Gd_N/Yb_N	1.21	1.29	1.31	1.59	1.13	1.16	0.90	1.41	1.33	1.06	1.89	1.62	1.74
Eu/Eu*	0.83	0.90	0.81	0.77	0.91	0.90	1.01	0.70	0.71	0.91	0.71	0.94	0.80

Table A.7. *Continued*

Lithology	Variegated suevite	Green melt particles	Green melt particles	Dolomite	Variegated suevite	Grano-diorite clast	Med. gray ground-mass	Dark gray ground-mass	Beige melt particle	Green suevite
Unit	3	4	4	5	5	5	5	5	5	5
ID #	762	242	241	218A	218B	775A	775B	225A	225B	759
Depth (m)	860.40	878.09	882.45	888.09	888.09	888.92	888.92	892.55	892.55	894.14
Na_2O	3.31	3.09	5.33	0.10	1.53	3.75	1.68	0.47	3.83	0.22
K_2O	4.51	5.64	2.20	0.23	2.06	4.18	1.63	0.76	6.23	0.65
Sc	14.8	13.9	15.8	1.0	5.3	4.4	6.6	10.1	5.9	2.1
Cr	42.5	37.1	37.3	4.32	17.4	32.9	10.3	14.6	41.9	5.4
FeO_{tot}	3.41	3.89	5.31	0.08	1.94	2.11	1.96	1.38	3.25	0.21
Co	5.37	8.90	10.70	1.26	5.01	4.48	7.08	2.05	3.38	1.04
Ni	23	11	31	9	16	8	13	4	11	13
Zn	36	50	60	3	24	95	29	14	25	3
As	0.48	0.74	0.76	0.80	0.15	0.27	0.31	0.06	0.36	2.02
Se	0.1	0.3	0.3	0.1	0.1	0.1	0.2	0.2	0.7	0.1
Br	19.0	23.0	50.0	3.6	9.9	9.1	15.8	7.7	10.2	3.0
Rb	30.5	51.9	38.2	0.9	18.8	66.5	27.6	7.8	41.0	6.1
Sr	165	66	903	286	335	36	38	294	372	48
Zr	85	85	120	10.6	59.3	135	50	54	129	40
Sb	0.07	0.10	0.19	0.04	0.12	0.10	0.11	0.09	0.21	0.07
Cs	0.29	0.62	0.74	0.05	0.26	0.54	0.49	0.11	0.23	0.21
Ba	453	99	256	38	86.4	970	76	87	600	55
La	13.5	16.9	22.6	2.74	9.5	7.2	13.4	15.0	19.1	5.6
Ce	17.8	51.1	41.4	3.9	14.5	14.2	26.3	24.0	33.5	10.7
Nd	10.9	14.4	18.3	1.5	7.3	8.2	11.6	10.3	13.3	5.3
Sm	1.87	2.94	3.56	0.39	1.39	1.66	1.93	1.81	2.37	1.07
Eu	0.56	0.69	0.85	0.06	0.33	0.49	0.36	0.44	0.58	0.22
Gd	2.01	2.51	2.87	0.4	1.30	1.75	1.82	1.65	1.7	0.70
Tb	0.31	0.39	0.50	0.07	0.23	0.26	0.25	0.34	0.27	0.14
Tm	0.19	0.15	0.29	0.04	0.14	0.18	0.19	0.20	0.15	0.0940
Yb	1.32	0.98	1.94	0.29	0.97	1.21	1.43	1.35	0.90	0.73
Lu	0.20	0.14	0.28	0.04	0.14	0.19	0.23	0.21	0.12	0.120
Hf	2.30	2.49	3.17	0.14	1.12	3.58	1.34	1.19	2.80	0.26
Ta	0.31	0.87	0.63	0.03	0.15	0.31	0.13	0.13	0.46	0.04
W	0.5	0.4	0.2	n.d.	n.d.	1.25	<1.0	0.3	0.8	0.7
Ir (ppb)	<1.3	<0.5	<2.0	<0.2	<1.0	<0.5	<0.5	<0.6	0.4	<0.6
Au (ppb)	0.8	0.2	0.2	0.5	6.9	0.8	0.1	0.5	0.4	0.5
Th	6.63	11.10	12.20	0.07	4.09	2.37	3.79	1.41	14.10	0.82
U	0.49	0.26	0.70	1.31	1.86	0.81	0.77	1.00	2.33	2.47
K/U	76327	180000	26143	1450	9194	42840	17532	6300	22189	2186
Zr/Hf	37.0	34.1	37.9	75.7	52.9	37.7	37.3	45.2	46.1	153.8
La/Th	2.04	1.52	1.85	39.14	2.31	3.02	3.54	10.64	1.35	6.77
Hf/Ta	7.42	2.86	5.03	4.67	7.47	11.55	10.31	9.15	6.09	7.03
Th/U	13.53	42.69	17.43	0.05	2.20	2.93	4.92	1.41	6.05	0.33
La_N/Yb_N	6.91	11.65	7.87	6.38	6.58	4.00	6.33	7.51	14.34	5.14
Gd_N/Yb_N	1.23	2.08	1.20	1.12	1.09	1.17	1.03	0.99	1.53	0.78
Eu/Eu*	0.88	0.78	0.81	0.46	0.75	0.88	0.59	0.78	0.88	0.78

Appendix A.8.
Cretaceous rocks
Major and trace element results (Chapter 4)

Table A.8. Major and trace† element compositions of Cretaceous rock samples from the Yaxcopoil-1 borehole, determined by XRF and INAA, respectively.

Lithology	Anhydrite vein	Dolomitic breccia dike	Dolomitic breccia dike	Dolomitic breccia dike	Dolomite	Dolomitic breccia dike	Dolomitic breccia dike	Dolomitic breccia dike	Dolomitic breccia	Alteration zone	Alteration zone	Dolomitic breccia	Dolomite with oil shale
ID #	233A	233B	223A	223B	227A	227B	235	236	225C	219	226	237	228
Depth (m)	1314.83	1314.83	1315.86	1315.86	1316.06	1316.06	1341.61	1341.82	1342.91	1347.56	1348.32	1348.31	1369.52
SiO_2	8.06							0.97		16.50		1.44	4.80
TiO_2	0.15							n.d.		0.38		0.01	0.06
Al_2O_3	1.97							0.30		7.50		0.60	1.41
FeO_{tot}	0.82	0.80	0.75	0.23	0.51	0.69	0.24	0.16	0.08	2.87	0.62	0.33	0.41
MnO	n.d.							n.d.		0.01		n.d.	n.d.
MgO	0.72							19.80		15.20		16.90	19.20
CaO	38.80							30.90		20.40		33.50	28.20
Na_2O	0.05	0.15	1.05	0.24	0.29	0.81	0.73	0.70	0.47	1.05	0.24	0.19	0.35
K_2O	0.98	1.46	1.00	0.28	0.71	1.34	0.60	0.08	0.07	2.15	0.61	0.13	0.43
P_2O_5	0.02							n.d.		n.d.		n.d.	n.d.
Cl	0.05							0.50		0.50		0.08	0.40
L.O.I	2.23							44.60		33.10		36.30	44.30
Total	100.30							98.04		99.83		100.48	99.60
Sulfur content (wt%)													
S_{tot}	18.60							0.02		0.07		4.40	0.02
SO_3	46.45							0.03		0.17		11.00	0.04
Trace elements (ppm, except where indicated)													
Sc	0.50	2.70	1.80	0.65	1.59	1.68	0.54	0.28	0.24	10.8	1.93	0.90	
Cr	5.47	7.99	10.4	3.52	5.71	8.63	1.50	2.17	2.96	29.6	6.06	3.18	
Co	0.55	2.52	2.95	1.33	1.91	2.49	1.43	0.92	0.84	5.08	1.49	0.98	
Ni	5	8	4	3	13	22	3	5	6	26	5	7	
Zn	5	21	15	6	19	19	4	3	3	23	6	2	
As	0.50	6.52	7.73	2.62	3.14	7.46	1.17	0.67	0.82	4.05	4.93	0.91	
Se	n.d.	n.d.	0.2	0.1	0.9	1.1	n.d.	n.d.	0.2	0.7	0.8	n.d.	
Br	1.9	8.8	60.5	17.9	16.0	51.0	39.0	42.9	27.0	30.9	13.0	4.4	
Rb	6.2	12.7	10.1	3.8	5.0	11.3	4.2	1.5	1.1	112	17.7	8.3	
Sr	1603	177	143	81	89	189	251	264	286	107	88	43	
Zr	6	25	97	35	23	55	26	15	9	91	25	5	
Sb	0.04	0.18	0.20	0.07	0.10	0.51	0.07	0.06	0.07	0.37	0.15	0.06	
Cs	0.28	0.36	0.45	0.17	0.19	0.44	0.09	0.05	0.08	4.06	0.64	0.29	
Ba	16	17	33	13	7	57	29	20	12	20	23	19	
La	1.0	3.1	3.2	1.4	2.0	3.0	1.0	0.6	0.6	7.2	2.0	1.7	
Ce	2.1	6.0	5.9	2.6	4.2	6.4	1.1	1.2	1.1	13.0	4.3	2.9	
Nd	0.8	3.4	3.3	1.8	2.7	3.03	1.4	0.9	1.0	7.0	1.5	1.7	
Sm	0.19	0.74	0.81	0.36	0.54	0.87	0.37	0.26	0.17	1.37	0.38	0.24	
Eu	0.03	0.16	0.15	0.08	0.15	0.16	0.04	0.03	0.04	0.33	0.29	0.05	
Gd	0.13	0.60	0.60	0.22	0.48	0.50	0.30	0.17	0.14	1.40	0.39	0.21	
Tb	0.02	0.10	0.08	0.03	0.07	0.08	0.05	0.02	0.02	0.25	0.06	0.03	
Tm	0.01	0.06	0.04	0.01	0.04	0.05	0.03	0.01	0.01	0.15	0.04	0.02	
Yb	0.07	0.40	0.27	0.07	0.22	0.35	0.18	0.07	0.05	0.99	0.24	0.12	
Lu	0.01	0.06	0.04	0.01	0.03	0.05	0.03	0.01	0.01	0.14	0.03	0.02	
Hf	0.31	0.79	1.60	0.47	0.19	0.65	0.25	0.11	0.06	2.84	0.45	0.23	
Ta	0.04	0.11	0.25	0.09	0.13	0.16	0.02	0.02	0.02	0.43	0.14	0.06	
W	n.d.	n.d.	0.4	1.5	0.3	0.2	n.d.	n.d.	0.1	n.d.	0.1	n.d.	
Ir (ppb)	<0.2	<0.5	<0.6	<0.5	<4	<0.5	<0.1	<0.2	<3	<1	<0.9	<0.5	
Au (ppb)	0.1	0.1	0.7	0.3	0.1	<1	0.4	0.2	0.1	1.0	0.1	0.1	
Th	0.44	0.78	1.02	0.27	0.50	1.25	0.17	0.07	0.09	3.06	0.59	0.31	
U	0.52	2.56	2.93	1.24	1.04	3.64	2.77	1.94	0.20	2.29	0.80	0.53	
K/U	8846	4727	2833	1855	5673	3049	1805	412	3000	8253	6375	2830	
Zr/Hf	19.6	31.1	60.6	74.7	121.1	84.6	105.2	136.4	150.0	31.9	55.6	20.1	
La/Th	2.27	3.95	3.14	5.30	4.08	2.38	6.06	8.86	7.11	2.35	3.42	5.39	
Hf/Ta	7.75	7.18	6.40	5.22	1.46	4.06	12.50	5.50	3.00	6.60	3.21	3.83	
Th/U	0.85	0.30	0.35	0.22	0.48	0.34	0.06	0.04	0.45	1.34	0.74	0.58	
La_N/Yb_N	9.65	5.20	8.01	13.80	6.27	5.75	3.87	5.99	8.65	4.91	5.69	9.40	
Gd_N/Yb_N	1.51	1.22	1.80	2.55	1.77	1.16	1.35	1.97	2.27	1.15	1.32	1.42	
Eu/Eu*	0.58	0.73	0.66	0.87	0.90	0.74	0.37	0.44	0.79	0.73	2.30	0.68	

†Trace elements in ppm except where indicated, *Eu/Eu* = $Eu_N/(Sm_N \times Gd_N)^{0.5}$, n.d. = not detected, N = chondrite normalized (Taylor and McLennan, 1985), ID # are those given by the Universidad Nacional Autónoma de México (UNAM).

Table A.8. *Continued*

Lithology	Beige dolomite	Oil shale	Dolomite with oil shale	Beige dolomite	Oil shale	Argillaceous dolomite	Argillaceous dolomite	Dol. limestone	Oil shale	Dol. breccia dike & oil shale	Argillaceous dolomite	White dol. limestone	Speckled argillaceous limestone	Argillaceous limestone with oil shale
ID #	228A	228B	229	229A	229B	220A + B	220A	220B	230	221	238A	238B	231	224
Depth (m)	1369.52	1369.52	1372.87	1372.87	1372.87	1381.64	1381.64	1381.64	1394.02	1395.19	1397.82	1397.82	1398.25	1399.07
SiO_2			3.06			14.70			33.50				21.90	39.40
TiO_2			0.10			0.53			0.65				0.59	0.88
Al_2O_3			1.14			4.10			9.10				6.20	10.40
FeO_{tot}	0.08	3.72	0.84	0.09	5.04	3.06	8.01	0.36	5.52	0.04	0.55	0.76	5.25	4.89
MnO			n.d.			n.d.			n.d.				0.02	0.01
MgO			19.70			15.30			7.32				0.47	0.42
CaO			28.60			23.60			12.45				35.10	19.50
Na_2O	0.17	0.53	0.79	0.41	1.17	0.45	0.70	0.20	1.36	0.17	0.27	0.17	0.14	0.37
K_2O	0.17	13.73	0.11	0.08	3.00	2.58	0.60	0.22	7.08	0.60	0.10	1.11	4.02	7.94
P_2O_5			0.01			0.10			0.12				0.06	0.07
Cl			0.50			0.20			0.50				0.10	0.20
L.O.I			44.30			34.00			19.87				24.23	6.60
Total			99.26			99.45			99.70				98.56	98.72
Sulfur content (wt%)														
S_{tot}			0.04			0.33			0.89				0.19	3.22
SO_3			0.11			0.83			2.23				0.48	8.04
Trace elements (ppm, except where indicated)														
Sc	1.06	3.19	1.59	9.95		6.69	5.70	3.82	0.88	2.46	9.31	19.3	23.6	
Cr	4.31	65.6	8.1	18.3		59.9	9.0	111	6.4	13.1	3.1	78.9	247	
Co	0.39	4.87	0.53	15.2		25.2	1.53	24.9	3.66	1.88	5.01	16.0	38.3	
Ni	<14	52	<10	91		38	18	78	6	18	3	35	61	
Zn	4	68	<2	31		19	8	79	2	24	8	28	16	
As	0.35	21.3	0.3	22.4		43.9	1.9	32.9	0.1	1.4	0.7	2.1	3.5	
Se	0.1	1.8	0.1	2.2		1.9	0.3	1.7	0.1	n.d.	0.1	n.d.	0.1	
Br	17.0	82	25	87		57	11	90	10	16	16	13	32	
Rb	0.7	0.9	0.9	44.6		54.1	1.3	48.0	1.9	1.3	2.3	19.8	44.0	
Sr	89	131	131	146		41	60	75	61	283	373	268	61	
Zr	8	330	5	125		414	29	240	9	13	14	41	34	
Sb	0.07	0.06	0.06	1.77		1.37	0.11	1.17	0.01	0.10	0.05	0.12	0.06	
Cs	0.07	0.34	0.05	1.02		0.34	0.07	0.22	0.04	0.01	0.06	0.07	0.06	
Ba	<10	5	5	68		200	16	148	11	5	12	20	34	
La	1.3	7.6	0.8	2.2		14.4	1.8	3.7	1.2	1.2	1.7	1.7	0.9	
Ce	2.0	6.7	0.9	4.4		20.5	3.4	9.0	0.3	0.6	1.7	2.8	2.6	
Nd	1.3	7.0	0.8	2.9		17.6	2.4	6.4	0.8	1.5	2.0	2.6	2.1	
Sm	0.30	1.99	0.18	0.98		5.30	0.62	2.57	0.17	0.28	0.59	0.74	0.81	
Eu	0.08	0.17	0.07	0.21		0.72	0.14	0.23	0.03	0.08	0.18	0.25	0.19	
Gd	0.28	1.6	0.2	0.8		2.6	0.8	1.8	0.2	0.3	0.8	1.1	1.0	
Tb	0.05	0.26	0.03	0.15		0.43	0.13	0.25	0.04	0.05	0.15	0.21	0.18	
Tm	0.03	0.14	0.02	0.08		0.20	0.07	0.11	0.02	0.03	0.09	0.13	0.09	
Yb	0.21	0.87	0.15	0.48		1.01	0.47	0.65	0.15	0.20	0.62	0.93	0.62	
Lu	0.03	0.12	0.02	0.07		0.10	0.07	0.09	0.02	0.03	0.09	0.14	0.09	
Hf	0.08	6.96	0.04	1.09		6.34	0.44	2.85	0.04	0.09	0.10	0.50	1.31	
Ta	0.11	1.04	0.02	0.21		0.81	0.07	0.85	0.02	0.03	0.06	0.07	0.19	
W	0.1	0.1	0.1	0.4		n.d.	n.d.	0.2	n.d.	n.d.	n.d.	n.d.	n.d.	
Ir (ppb)	<0.6	<1.0	<1.0	<0.8		<0.2	<0.9	<2.0	<0.2	<0.2	<0.2	<2.0	<0.8	
Au (ppb)	0.1	0.3	0.2	0.2		0.7	0.6	0.3	0.3	0.1	0.2	0.5	0.8	
Th	0.19	7.43	0.05	0.78		6.4	0.33	11.5	0.07	0.07	0.17	0.17	0.1	
U	0.62	14.8	0.10	9.17		23.5	1.39	16.8	0.49	0.46	0.58	0.68	0.85	
K/U	2258	7703	7000	2715		213	1295	3613	10204	1739	15862	53824	76471	
Zr/Hf	100.0	47.4	125	114		65.3	64.8	84.2	222	147	142	81.4	26.1	
La/Th	7.00	1.02	16.2	2.77		2.24	5.58	0.32	17.3	16.86	9.88	10.1	9.40	
Hf/Ta	0.73	6.69	2.00	5.19		7.83	6.29	3.35	2.00	3.00	1.67	7.14	6.89	
Th/U	0.31	0.50	0.50	0.09		0.27	0.24	0.68	0.14	0.15	0.29	0.25	0.12	
La_N/Yb_N	4.28	5.86	3.65	3.04		9.63	2.65	3.79	5.45	3.99	1.83	1.25	1.02	
Gd_N/Yb_N	1.08	1.49	0.86	1.37		2.09	1.29	2.24	1.19	1.22	1.05	0.96	1.31	
Eu/Eu*	0.84	0.29	1.26	0.72		0.59	0.63	0.33	0.47	0.84	0.80	0.85	0.65	

Appendix A.9.
Melt particle LA-ICP-MS results (Chapter 5)

Table A.9. LA-ICP-MS analyses of selected melt particles.

Unit	1	1	1	2	2	2	2	2	2	2	2	2
Analyses #	1	2	3	4	5	6	7	8	9	10	11	12
Sample depth	805.34	805.34	805.34	824.03	824.03	824.03	835.14	835.14	835.14	835.14	835.14	835.14
P	55	57	40	41	1	20	230	307	396	385	1149	272
Sc	0.7	1.2	0.6	1.7	0.3	2.0	1.2	1.2	1.7	1.7	7.0	1.6
Ti	135	569	67	585	76	179	598	698	869	856	4997	996
V	0.8	1.7	0.6	2.2	0.4	2.7	13.5	10.4	17.3	15.1	685	22.3
Cr	1	-	-	-	-	6	18	20	32	28	-	529
Co	0.5	1.0	0.3	0.4	0.1	0.5	1.0	1.2	1.6	1.5	106.3	2.1
Ni	2	2	1	5	1	16	47	34	40	46	1525	64
Rb	30	26	16	28	3	28	19	24	25	31	30	23
Sr	33	29	19	29	4	41	63	60	71	76	195	92
Y	1.2	1.3	0.7	1.3	0.2	0.9	5.8	10.1	11.8	12.6	39.9	8.1
Zr	79	74	44	64	7	51	53	68	74	76	97	63
Nb	0.4	1.2	0.2	1.0	0.1	0.3	1.2	1.1	1.1	1.2	3.9	1.8
Ba	196	170	114	153	15	129	111	144	152	182	154	142
La	1.8	1.3	1.0	1.3	0.2	1.1	4.9	8.7	10.0	10.5	31.0	7.5
Ce	2.8	2.7	1.8	2.7	0.3	2.3	8.6	13.8	18.1	16.8	48.6	13.6
Pr	0.32	0.42	0.20	0.30	0.05	0.19	1.21	2.14	2.54	2.77	7.85	1.98
Nd	1.5	1.0	0.7	1.1	0.2	0.8	5.3	9.6	11.2	11.3	36.4	8.3
Sm	0.20	0.21	0.33	0.21	0.01	0.10	1.21	2.16	2.48	2.48	7.84	1.70
Eu	0.20	0.21	0.13	0.06	0.02	0.13	0.36	0.64	0.69	0.72	2.30	0.53
Gd	0.38	0.26	0.29	0.21	0.03	0.15	1.11	1.79	2.60	2.70	8.16	1.64
Tb	0.04	0.11	0.05	0.03	-	0.03	0.17	0.30	0.36	0.37	1.21	0.25
Dy	0.31	0.38	0.09	0.33	0.04	0.19	1.03	1.65	2.18	2.04	6.96	1.53
Ho	0.10	0.11	0.06	0.07	-	0.04	0.26	0.30	0.43	0.41	1.43	0.30
Er	0.22	0.15	0.15	0.15	0.04	0.13	0.59	0.84	1.02	1.08	3.33	0.75
Tm	0.03	0.03	0.01	0.03	-	0.01	0.08	0.12	0.12	0.14	0.39	0.10
Yb	0.30	0.39	0.09	0.14	0.02	0.08	0.49	0.76	0.85	0.84	2.55	0.67
Lu	0.09	0.07	0.05	0.16	0.01	0.04	0.09	0.09	0.14	0.12	0.36	0.08
Y/Zr	0.02	0.02	0.02	0.02	0.02	0.02	0.11	0.15	0.16	0.16	0.41	0.13
Sc/Zr	0.01	0.02	0.01	0.03	0.05	0.04	0.02	0.02	0.02	0.02	0.07	0.03
Ba/Zr	2.46	2.28	2.59	2.40	2.24	2.54	2.11	2.13	2.06	2.38	1.58	2.26
Ba/Rb	6.45	6.51	6.99	5.57	5.28	4.69	5.96	6.04	6.06	5.82	5.16	6.16
Sr/Rb	1.08	1.12	1.18	1.05	1.31	1.49	3.39	2.50	2.82	2.44	6.53	3.99
Gd/Yb	1.25	0.66	3.20	1.48	1.32	1.84	2.28	2.37	3.05	3.23	3.19	2.44
La/Sm	9.01	6.46	3.04	6.19	22.12	11.49	4.09	4.02	4.03	4.22	3.96	4.40

Table A.9. *Continued*

Unit	2	2	2	2	2	2	3	3	3	3	3	3
Analyses #	13	14	15	16	17	18	19	20	21	22	23	24
Sample depth	843.46	843.46	843.46	843.46	843.46	843.46	846.06	846.06	846.06	846.06	846.06	846.06
P	64	90	54	50	51	59	117	219	136	150	141	209
Sc	1.3	3.8	1.7	2.1	2.5	2.3	3.3	5.4	4.9	6.3	6.0	4.0
Ti	330	1350	237	354	435	340	1211	1939	1765	1763	1761	1347
V	4.3	37.6	3.4	5.7	7.0	4.4	34.1	52.9	44.5	59.1	54.1	26.2
Cr	15	24	8	12	12	13	27	28	27	31	31	26
Co	0.7	1.8	0.6	0.9	1.0	1.3	1.3	2.2	3.6	2.2	2.1	2.8
Ni	6	124	4	8	12	8	70	145	128	155	137	92
Rb	25	25	26	28	28	27	31	34	30	35	37	36
Sr	57	132	58	82	77	79	124	168	147	152	153	102
Y	1.9	4.0	1.8	1.9	2.1	2.1	6.0	8.0	7.5	8.7	8.9	4.1
Zr	64	85	72	68	70	68	92	121	113	120	124	101
Nb	0.8	3.2	0.4	0.5	0.7	0.5	2.4	4.1	3.5	3.6	3.8	3.0
Ba	160	223	181	174	174	178	269	332	291	327	320	245
La	2.5	5.9	2.3	2.5	2.4	2.5	5.7	10.2	9.5	10.9	9.1	5.6
Ce	4.1	9.4	3.6	4.0	4.1	4.3	11.0	20.2	13.9	16.5	13.9	8.9
Pr	0.50	1.01	0.42	0.48	0.44	0.58	0.78	1.16	1.10	1.24	1.15	0.69
Nd	2.0	4.2	1.6	1.8	1.9	2.4	2.9	4.2	3.6	4.7	3.7	2.4
Sm	0.36	0.78	0.25	0.48	0.47	0.61	0.64	0.97	0.77	0.98	0.98	0.54
Eu	0.24	0.40	0.20	0.20	0.21	0.22	0.31	0.39	0.36	0.35	0.33	0.39
Gd	0.33	0.77	0.39	0.42	0.48	0.49	0.75	1.00	0.86	1.05	0.96	0.56
Tb	0.04	0.11	0.04	0.03	0.06	0.08	0.17	0.20	0.20	0.26	0.20	0.12
Dy	0.37	0.80	0.16	0.44	0.36	0.38	1.10	1.38	1.25	1.42	1.50	0.62
Ho	0.08	0.14	0.01	0.05	0.08	0.07	0.26	0.34	0.36	0.36	0.43	0.20
Er	0.24	0.50	0.17	0.32	0.27	0.24	0.98	1.22	1.16	1.29	1.25	0.62
Tm	0.07	0.10	0.03	0.03	0.02	0.03	0.17	0.19	0.19	0.19	0.33	0.12
Yb	0.31	0.69	0.38	0.34	0.45	0.25	1.31	1.61	1.65	1.78	1.71	0.81
Lu	0.03	0.07	0.01	0.01	0.04	0.02	0.25	0.29	0.29	0.29	0.36	0.18
Y/Zr	0.03	0.05	0.03	0.03	0.03	0.03	0.07	0.07	0.07	0.07	0.07	0.04
Sc/Zr	0.02	0.04	0.02	0.03	0.04	0.03	0.04	0.04	0.04	0.05	0.05	0.04
Ba/Zr	2.51	2.60	2.52	2.55	2.47	2.63	2.92	2.75	2.56	2.73	2.59	2.42
Ba/Rb	6.45	8.87	6.94	6.30	6.21	6.56	8.59	9.87	9.74	9.26	8.59	6.77
Sr/Rb	2.28	5.24	2.23	2.96	2.74	2.90	3.96	4.99	4.92	4.31	4.11	2.82
Gd/Yb	1.09	1.12	1.02	1.25	1.06	1.96	0.57	0.62	0.52	0.59	0.56	0.69
La/Sm	6.86	7.54	9.05	5.33	5.08	4.06	8.95	10.48	12.27	11.16	9.21	10.35

Table A.9. *Continued*

Unit	3	3	3	3	3	3	3	3	4	4	4	4
Analyses #	25	26	27	28	29	30	31	32	33	34	35	36
Sample depth	846.06	846.06	846.06	846.06	846.06	846.06	846.06	846.06	878.09	878.09	878.09	878.09
P	61	176	165	248	236	116	256	209	6	47	55	63
Sc	2.0	3.2	1.9	1.3	0.8	0.5	1.2	1.1	1.3	1.8	2.5	3.3
Ti	525	1025	776	519	381	364	326	279	373	176	544	374
V	37.7	22.4	9.9	8.5	6.0	3.2	6.5	5.9	2.6	1.4	4.0	3.9
Cr	9	19	-	-	-	-	-	-	5	-	-	-
Co	0.5	2.2	2.0	1.3	0.8	0.6	0.9	0.9	6.0	1.4	2.2	1.5
Ni	111	19	6	3	5	7	6	5	33	7	28	19
Rb	12	49	41	27	27	28	32	28	36	36	39	39
Sr	56	130	103	83	66	57	88	82	115	116	99	84
Y	3.1	5.9	3.9	5.6	4.0	2.5	5.1	3.9	1.5	1.9	2.3	2.2
Zr	40	94	85	69	69	76	76	64	62	61	91	88
Nb	0.8	1.7	1.7	1.0	0.7	0.6	0.7	0.6	0.4	0.3	1.2	0.9
Ba	102	295	261	204	194	187	224	200	176	167	193	194
La	2.7	5.2	5.0	5.4	4.3	3.2	4.6	4.2	2.1	5.2	2.9	2.5
Ce	4.2	9.6	9.2	10.2	8.4	5.4	9.8	8.1	3.4	17.3	5.3	4.5
Pr	0.38	1.02	0.90	1.27	1.07	0.62	1.14	1.01	0.46	1.02	0.53	0.51
Nd	1.5	4.1	3.6	5.4	4.2	2.7	4.8	4.0	2.1	4.0	2.1	2.0
Sm	0.29	0.98	0.65	1.23	0.96	0.58	0.97	0.76	0.22	0.60	0.32	0.29
Eu	0.10	0.24	0.30	0.35	0.33	0.27	0.35	0.25	0.20	0.23	0.17	0.18
Gd	0.32	0.81	0.69	1.12	0.79	0.46	0.97	0.91	0.39	0.60	0.30	0.35
Tb	0.07	0.14	0.13	0.17	0.17	0.07	0.14	0.15	0.08	0.12	0.07	0.06
Dy	0.50	0.93	0.87	1.05	0.77	0.44	0.94	0.74	0.27	0.52	0.35	0.49
Ho	0.12	0.20	0.21	0.20	0.15	0.10	0.14	0.17	0.11	0.06	0.07	0.09
Er	0.38	0.81	0.46	0.46	0.30	0.24	0.44	0.44	0.30	0.17	0.23	0.31
Tm	0.07	0.10	0.07	0.05	0.06	0.04	0.06	0.06	0.03	0.02	0.03	0.02
Yb	0.71	0.76	0.49	0.28	0.41	0.29	0.36	0.22	0.23	0.16	0.48	0.34
Lu	0.09	0.10	0.12	0.07	0.01	0.05	0.08	0.08	0.06	0.02	0.06	0.08
Y/Zr	0.08	0.06	0.05	0.08	0.06	0.03	0.07	0.06	0.02	0.03	0.03	0.02
Sc/Zr	0.05	0.03	0.02	0.02	0.01	0.01	0.02	0.02	0.02	0.03	0.03	0.04
Ba/Zr	2.56	3.14	3.06	2.98	2.80	2.45	2.93	3.14	2.84	2.74	2.14	2.19
Ba/Rb	8.82	6.03	6.41	7.62	7.22	6.59	7.06	7.05	4.95	4.57	4.98	5.02
Sr/Rb	4.83	2.67	2.53	3.10	2.45	2.00	2.76	2.90	3.24	3.17	2.56	2.18
Gd/Yb	0.44	1.06	1.41	3.98	1.91	1.60	2.70	4.07	1.75	3.71	0.62	1.01
La/Sm	9.31	5.26	7.63	4.36	4.44	5.54	4.78	5.45	9.31	8.75	9.12	8.67

Table A.9. *Continued*

Unit	4	5	5	5	5	5	5	5	5
Analyses #	37	38	39	40	41	42	43	44	45
Sample depth	878.09	892.55	892.55	892.55	892.55	892.55	892.55	892.55	892.55
P	35	82	49	382	103	101	219	93	100
Sc	3.3	0.4	0.8	3.1	0.7	0.5	0.9	0.5	0.6
Ti	742	202	384	1882	409	461	441	311	316
V	5.2	11.8	24.9	140	7.3	8.2	6.2	5.4	6.1
Cr	5	22	28	82	21	8	10	8	8
Co	1.5	0.9	2.2	2.5	1.5	0.4	0.7	0.4	0.8
Ni	28	34	67	568	9	5	4	6	6
Rb	39	19	27	35	33	35	36	35	35
Sr	98	24	35	130	138	131	131	121	119
Y	2.3	1.0	1.7	5.2	2.6	2.9	2.7	2.8	2.6
Zr	85	46	73	121	74	78	78	75	76
Nb	1.9	0.5	0.8	4.8	2	1.5	1.1	1.1	1
Ba	161	117	171	232	241	247	250	245	242
La	2.6	1.6	2.5	9.5	4.5	5.2	5.4	4.9	4.6
Ce	4.7	2.6	4.2	15.1	8.3	9.7	9.4	8	7.9
Pr	0.41	0.28	0.93	1.59	1.09	0.98	0.93	0.86	0.85
Nd	2.0	1.1	2.0	5.6	3.3	3.7	3.5	2.9	4
Sm	0.36	0.17	0.38	1.3	0.62	0.8	0.6	0.64	0.59
Eu	0.17	0.13	0.38	0.33	0.21	0.27	0.22	0.21	0.21
Gd	0.34	0.12	0.36	1.24	0.53	0.53	0.48	0.45	0.55
Tb	0.10	0.04	0.09	0.17	0.11	0.09	0.08	0.1	0.1
Dy	0.42	0.18	0.20	1.09	0.45	0.46	0.46	0.45	0.41
Ho	0.11	0.06	0.08	0.18	0.13	0.12	0.11	0.11	0.12
Er	0.32	0.06	0.20	0.65	0.23	0.2	0.27	0.19	0.2
Tm	0.04	0.02	0.02	0.11	0.04	0.03	0.03	0.03	0.03
Yb	0.48	0.17	0.19	0.62	0.29	0.27	0.35	0.32	0.2
Lu	0.09	-	0.19	0.09	0.03	0.04	0.05	-	0.04
Y/Zr	0.03	0.02	0.02	0.04	0.03	0.04	0.04	0.04	0.03
Sc/Zr	0.04	0.01	0.01	0.03	0.01	0.01	0.01	0.01	0.01
Ba/Zr	1.90	2.52	2.34	1.92	3.25	3.17	3.22	3.26	3.18
Ba/Rb	4.11	6.07	6.25	6.63	7.27	7.13	6.98	6.94	6.96
Sr/Rb	2.52	1.26	1.30	3.72	4.17	3.78	3.65	3.42	3.41
Gd/Yb	0.70	0.72	1.88	2.01	1.83	1.99	1.38	1.42	2.79
La/Sm	7.18	9.21	6.68	7.29	7.21	6.45	8.98	7.54	7.72

Appendix A.10.
Melt particle EMPA results (Chapter 5)

Table A.10. Melt particle EMPA results

Unit	Analyses #	Sample depth	SiO_2	TiO_2	Al_2O_3	Cr_2O_3	FeO_{tot}	MnO	MgO	CaO	Na_2O	K_2O	Total
1	1	805.34	53.58	0.41	14.74	-	6.67	-	5.57	1.24	0.61	3.67	86.49
1	2	805.34	55.54	0.76	16.49	-	4.94	-	6.03	1.38	0.57	3.53	89.24
1	3	805.34	55.10	0.61	16.24	0.06	7.14	-	5.46	0.99	0.54	4.77	90.91
1	4	805.34	53.59	0.66	15.50	-	6.87	-	5.58	1.20	0.39	4.89	88.68
1	5	805.34	47.64	0.56	13.48	0.05	5.87	-	4.45	0.93	0.34	3.86	77.18
1	6	805.34	54.79	0.66	15.65	-	6.53	-	5.52	1.65	0.36	4.99	90.15
1	7	805.34	51.91	0.97	14.55	0.05	7.74	-	5.63	1.51	0.44	5.59	88.39
1	8	805.34	51.65	2.41	14.34	-	7.45	-	4.87	1.25	0.36	5.67	88.00
2	9	824.03	53.15	0.34	11.82	-	9.86	-	7.19	1.10	0.19	5.26	88.91
2	10	824.03	53.82	0.30	11.88	-	10.94	-	6.77	1.15	0.25	6.10	91.21
2	11	824.03	50.04	0.29	10.60	-	9.70	-	6.76	1.24	0.22	4.56	83.41
2	12	824.03	45.38	0.17	8.99	-	7.12	-	8.80	2.40	0.26	3.51	76.63
2	13	824.03	41.46	0.18	8.89	-	7.24	-	6.91	0.68	0.35	3.28	68.99
2	14	824.03	48.70	1.32	10.69	-	11.05	-	6.19	0.83	0.18	5.84	84.80
2	15	824.03	52.80	0.35	11.49	-	9.89	-	8.12	1.51	0.29	4.85	89.30
2	16	824.03	50.45	0.31	10.87	-	9.55	-	7.34	1.11	0.18	4.40	84.21
2	17	824.03	52.13	0.56	11.34	-	11.32	-	6.09	1.37	0.24	6.21	89.26
2	18	824.03	54.49	0.33	12.07	0.05	11.31	-	6.80	1.15	0.19	6.33	92.72
2	19	824.03	56.90	0.41	12.35	-	13.01	-	7.00	1.17	0.22	6.42	97.48
2	20	835.14	50.22	0.44	12.94	0.12	6.67	-	10.63	4.01	1.75	1.50	88.28
2	21	835.14	51.61	0.57	22.68	-	7.87	-	0.27	7.46	5.58	1.49	97.53
2	22	835.14	49.92	0.79	20.62	-	11.82	-	0.42	6.46	4.57	1.02	95.62
2	23	835.14	50.71	0.80	17.96	-	7.08	-	1.39	4.72	4.33	3.20	90.19
2	24	835.14	50.19	0.68	19.20	0.11	10.71	-	0.12	4.09	5.72	1.92	92.74
2	25	835.14	58.46	0.19	19.82	0.25	5.09	-	0.38	3.38	3.60	1.57	92.74
2	26	835.14	51.28	1.38	20.50	0.17	9.51	-	0.57	6.20	4.59	1.30	95.50
2	27	835.14	52.88	0.40	14.20	0.33	6.19	-	5.38	2.12	1.56	3.01	86.07
2	28	835.14	54.55	0.19	23.77	-	1.75	-	0.61	9.14	5.45	1.44	96.90
2	29	835.14	55.93	0.84	22.96	-	2.67	-	1.29	7.76	3.99	1.34	96.78
2	30	835.14	54.02	0.65	17.35	-	5.86	-	2.75	5.35	3.73	3.00	92.71
2	31	835.14	48.56	0.47	17.87	0.05	7.70	-	3.22	8.11	3.53	1.40	90.91
2	32	835.14	55.30	0.37	14.33	-	7.43	-	6.98	2.16	1.26	3.20	91.03
2	33	835.14	48.71	0.23	12.58	-	5.87	-	6.45	2.08	1.72	3.24	80.88
2	34	835.14	56.17	0.25	23.69	-	2.91	-	0.29	8.19	3.92	3.47	98.89
2	35	835.14	51.80	0.19	17.12	0.15	4.73	-	5.26	4.48	2.10	1.95	87.78
2	36	835.14	55.82	0.41	20.90	-	2.31	0.10	1.16	6.53	3.18	1.78	92.19
2	37	835.14	56.69	0.24	24.75	-	1.98	-	0.73	8.83	4.57	1.10	98.89
2	38	835.14	61.46	0.15	21.36	-	0.84	-	0.71	4.98	4.15	2.35	96.00
2	39	835.14	48.36	0.83	17.07	-	5.91	-	3.70	6.60	3.27	1.85	87.59
2	40	835.14	50.14	0.74	17.48	-	5.88	-	3.31	7.88	4.26	2.13	91.82
2	41	835.14	55.05	0.35	22.30	-	3.27	-	1.10	8.13	3.84	1.98	96.02
2	42	835.14	55.81	0.87	24.29	-	2.26	-	0.62	8.75	5.29	0.95	98.84
2	43	835.14	56.51	0.29	16.24	-	2.53	-	3.45	2.35	2.32	2.93	86.62
2	44	835.14	36.43	1.19	11.97	-	28.76	-	3.31	2.82	3.25	1.87	89.60
2	45	835.14	52.69	0.40	20.88	-	4.14	0.11	2.31	8.39	4.44	1.31	94.67
2	46	835.14	52.66	0.61	18.42	0.09	5.44	-	2.79	5.53	3.53	1.92	90.99
2	47	835.14	58.71	0.28	20.64	-	2.84	-	1.81	4.75	3.57	3.16	95.76
2	48	835.14	56.03	0.25	25.29	-	1.65	-	0.80	9.91	5.32	0.76	100.01
2	49	835.14	54.11	0.43	20.19	0.05	3.61	-	2.87	5.73	3.74	2.23	92.96
2	50	835.14	56.30	0.15	20.62	-	3.00	-	1.75	6.16	4.02	2.66	94.66

Table A.10. *Continued*

Unit	Analyses #	Sample depth	SiO_2	TiO_2	Al_2O_3	Cr_2O_3	FeO_{tot}	MnO	MgO	CaO	Na_2O	K_2O	Total
2	51	835.14	54.86	0.34	20.69	-	5.86	-	2.89	6.76	3.58	1.14	96.12
2	52	835.14	56.11	0.26	23.64	0.05	2.72	-	0.78	8.47	4.90	0.90	97.83
2	53	835.14	55.28	2.73	21.43	-	2.78	-	1.98	6.24	4.77	1.60	96.81
2	54	835.14	50.81	2.33	14.46	0.05	4.09	-	5.48	2.84	1.67	2.46	84.19
2	55	835.14	55.51	2.28	21.77	-	1.98	-	1.39	6.59	4.03	2.07	95.62
2	56	843.46	55.64	0.86	24.52	-	3.05	-	0.14	8.22	5.20	2.60	100.23
2	57	843.46	52.56	2.94	20.87	-	7.64	-	0.34	5.47	4.61	3.96	98.39
2	58	843.46	58.29	0.20	20.97	0.05	3.56	-	1.23	7.35	3.46	5.89	101.00
2	59	843.46	56.90	0.05	24.56	-	2.38	-	0.23	8.56	4.88	2.75	100.31
2	60	843.46	60.59	0.08	19.70	-	1.87	-	0.29	3.21	2.51	10.66	98.91
2	61	843.46	57.42	0.08	23.46	-	3.28	-	0.24	7.39	4.48	4.00	100.35
2	62	843.46	60.36	0.08	21.55	-	1.68	-	0.36	4.35	3.06	7.94	99.38
2	63	843.46	54.19	0.09	24.36	-	2.99	-	2.83	8.94	4.33	0.97	98.70
2	64	843.46	59.05	0.18	17.40	-	3.29	-	2.15	5.49	1.57	9.85	98.98
2	65	843.46	60.27	0.10	19.17	-	2.07	-	1.53	4.35	1.91	9.64	99.04
2	66	843.46	58.45	0.07	22.33	-	1.93	-	0.53	5.84	3.57	7.26	99.98
2	67	843.46	57.01	0.26	18.63	-	4.02	-	2.92	9.52	3.00	5.04	100.40
2	68	843.46	56.36	0.20	19.68	-	6.02	-	0.87	4.24	1.96	9.48	98.81
2	69	843.46	58.81	0.22	17.03	-	8.20	-	0.34	0.72	0.28	14.09	99.69
2	70	843.46	57.85	0.08	23.81	-	1.93	-	0.22	7.03	4.03	5.10	100.05
2	71	843.46	57.06	0.10	24.29	-	2.11	-	0.46	9.09	4.92	2.21	100.24
2	72	843.46	57.51	0.16	18.08	-	2.87	-	2.93	8.70	2.29	6.69	99.23
2	73	843.46	56.38	-	22.80	-	2.45	-	1.84	8.14	4.68	2.61	98.90
2	74	843.46	42.85	0.14	8.86	-	3.70	-	13.23	2.06	0.38	1.38	72.60
2	75	843.46	45.92	0.09	6.64	-	5.28	-	21.65	2.82	0.20	0.21	82.81
2	76	843.46	47.22	-	6.26	-	5.18	-	24.93	2.99	0.19	0.11	86.88
2	77	843.46	49.78	0.05	6.62	-	4.91	-	23.66	2.54	0.18	0.15	87.89
2	78	843.46	39.15	1.59	12.41	-	28.78	-	2.64	2.54	2.14	4.26	93.51
2	79	843.46	45.58	0.90	15.58	-	20.36	0.14	3.04	2.84	2.71	4.96	96.11
2	80	843.46	52.85	0.34	19.87	-	3.87	-	3.93	7.03	4.38	1.04	93.31
2	81	843.46	55.26	0.70	16.94	-	3.82	-	2.85	3.33	2.08	8.77	93.75
2	82	843.46	53.46	0.52	17.21	0.07	4.53	-	2.32	3.26	2.10	7.86	91.33
2	83	843.46	53.63	0.29	13.34	-	4.12	0.11	5.68	7.86	0.74	8.53	94.30
2	84	843.46	54.45	0.16	19.45	-	5.09	-	1.67	5.12	3.15	5.56	94.65
2	85	843.46	58.02	0.50	19.20	-	1.67	-	0.64	3.79	2.10	9.67	95.59
3	86	846.06	65.21	0.20	19.61	-	1.27	-	0.25	2.03	3.35	2.92	94.84
3	87	846.06	63.62	0.51	18.12	-	1.39	-	0.10	0.64	4.98	5.78	95.14
3	88	846.06	59.80	0.37	18.82	0.27	3.82	-	0.39	3.09	3.72	2.06	92.34
3	89	846.06	58.77	0.41	19.01	0.41	3.88	-	0.33	3.12	5.12	2.29	93.34
3	90	846.06	60.14	0.42	18.22	0.09	3.34	-	0.32	2.40	4.32	2.73	91.98
3	91	846.06	58.51	0.66	18.02	0.08	4.72	-	0.24	1.40	5.43	3.74	92.80
3	92	846.06	61.98	0.44	18.85	-	2.79	-	0.25	1.89	3.45	3.17	92.82
3	93	846.06	62.63	0.60	17.84	-	3.74	-	0.22	0.75	3.57	5.11	94.46
3	94	846.06	58.32	0.19	18.12	-	2.44	-	0.53	4.35	5.63	2.00	91.58
3	95	846.06	59.07	0.08	22.06	-	2.25	-	0.44	7.33	5.66	1.39	98.28
3	96	846.06	63.71	0.24	19.42	-	1.31	-	0.22	2.15	2.87	3.68	93.60
3	97	846.06	64.63	0.30	18.80	-	0.90	-	0.10	0.70	3.81	4.17	93.41
3	98	846.06	56.03	0.13	17.10	-	2.34	-	2.31	2.77	2.49	6.10	89.27
3	99	846.06	52.01	0.94	12.55	-	8.71	-	5.67	1.94	0.73	3.52	86.07
3	100	846.06	43.78	0.52	12.31	-	9.01	-	2.79	3.23	1.01	6.41	79.06

Table A.10. *Continued*

Unit	Analyses #	Sample depth	SiO_2	TiO_2	Al_2O_3	Cr_2O_3	FeO_{tot}	MnO	MgO	CaO	Na_2O	K_2O	Total
3	101	846.06	59.05	0.81	18.01	-	7.60	-	0.26	1.28	4.47	3.02	94.50
3	102	846.06	57.02	0.90	17.01	-	7.85	0.09	0.35	1.29	3.75	3.85	92.11
3	103	846.06	60.09	0.65	18.41	0.29	5.22	-	0.23	1.87	3.53	3.38	93.67
3	104	846.06	57.93	0.98	17.12	-	7.73	-	0.54	0.98	4.78	4.49	94.55
3	105	846.06	65.36	0.77	19.68	-	5.38	-	0.30	1.65	6.10	3.44	102.68
3	106	846.06	59.22	0.76	17.80	0.22	5.67	-	0.29	1.09	5.38	3.61	94.04
3	107	846.06	59.05	0.81	18.01	-	7.60	-	0.26	1.28	4.47	3.02	94.50
3	108	846.06	61.06	2.62	19.70	-	1.07	-	0.14	2.66	5.12	3.41	95.78
3	109	846.06	60.59	6.30	17.58	0.09	2.41	-	0.27	0.66	5.49	5.83	99.22
3	110	846.06	60.37	2.97	17.33	-	1.15	-	0.13	0.86	4.52	4.56	91.89
3	111	846.06	56.76	0.20	22.55	-	2.49	-	0.37	7.15	5.67	1.38	96.57
3	112	846.06	56.77	0.19	22.80	0.09	2.36	-	0.34	7.75	4.54	1.23	96.07
3	113	846.06	58.77	0.06	16.77	0.40	1.33	-	1.85	1.94	0.61	10.46	92.19
3	114	846.06	60.23	0.05	17.83	0.23	0.40	-	0.17	4.03	0.45	11.53	94.92
3	115	846.06	56.58	0.12	24.35	0.16	1.43	-	0.42	9.14	4.90	1.38	98.48
3	116	846.06	61.81	0.33	20.10	-	2.38	-	0.63	5.11	5.73	2.81	98.90
3	117	846.06	65.68	1.10	19.12	-	1.14	-	0.16	1.47	2.72	4.52	95.91
3	118	846.06	62.40	0.49	18.64	0.09	1.47	-	0.14	2.00	4.16	5.12	94.51
3	119	846.06	64.15	0.36	19.14	-	1.78	-	0.23	2.09	2.75	5.53	96.03
3	120	846.06	61.78	0.54	19.61	-	1.79	-	0.17	2.97	4.23	4.67	95.76
3	121	846.06	65.10	0.50	18.21	-	1.16	-	0.09	0.54	2.70	7.94	96.24
3	122	846.06	62.68	0.33	19.18	0.15	0.92	-	0.05	1.83	3.78	6.78	95.70
3	123	846.06	54.24	-	26.89	0.12	1.28	-	0.27	11.44	5.21	0.55	100.00
3	124	846.06	57.03	0.49	19.56	0.18	3.08	-	0.47	5.68	6.56	2.24	95.29
3	125	846.06	54.52	0.11	23.35	-	2.06	-	0.39	9.48	5.79	0.84	96.54
3	126	846.06	59.64	0.11	19.78	-	1.08	-	0.12	3.41	3.69	7.35	95.18
3	127	846.06	62.15	0.17	19.84	-	1.07	-	0.19	2.73	2.95	7.17	96.27
3	128	846.06	57.17	0.09	23.50	-	1.53	-	0.87	8.55	5.30	1.98	98.99
3	129	846.06	62.96	0.15	17.27	0.34	1.02	-	1.69	2.27	1.01	8.77	95.48
3	130	846.06	53.72	0.05	25.20	0.16	1.62	-	0.65	11.14	4.50	0.70	97.74
3	131	846.06	49.66	0.91	27.10	-	2.45	-	0.70	5.38	5.28	1.35	92.83
3	132	846.06	43.64	0.17	13.76	0.08	2.18	-	1.23	3.20	3.44	3.27	70.97
3	133	846.06	54.12	0.11	24.29	0.12	1.67	-	0.86	10.04	4.77	0.63	96.61
3	134	846.06	52.90	0.05	18.57	0.16	2.43	-	0.76	6.88	5.53	1.31	88.59
3	135	846.06	58.13	0.13	19.82	-	2.29	-	0.55	5.77	4.36	1.05	92.10
3	136	846.06	49.54	0.05	16.69	-	1.13	-	1.79	3.82	3.94	4.48	81.44
3	137	846.06	56.66	-	19.16	-	2.24	-	1.04	6.42	5.31	2.96	93.79
3	138	846.06	57.43	0.05	18.97	-	1.22	-	0.46	3.46	4.46	2.57	88.62
3	139	846.06	53.42	0.87	18.23	0.07	4.75	-	0.27	4.55	4.29	4.08	90.53
3	140	846.06	47.72	0.12	16.70	-	1.03	-	0.64	4.28	4.00	1.98	76.47
3	141	846.06	58.79	0.15	18.91	0.11	1.07	-	0.43	3.16	2.45	7.56	92.63
3	142	846.06	50.65	0.24	16.82	0.13	3.01	-	0.17	3.79	4.35	4.72	83.88
3	143	846.06	63.44	0.14	18.08	-	0.77	-	0.29	0.65	0.99	12.15	96.51
3	144	846.06	55.18	-	16.16	0.08	0.63	-	1.02	1.06	1.05	10.94	86.12
3	145	846.06	65.98	0.51	19.19	0.11	0.69	-	0.14	0.75	3.38	5.72	96.47
3	146	846.06	63.71	0.52	18.62	-	0.78	-	0.22	1.02	4.54	6.63	96.04
3	147	846.06	65.04	0.88	19.20	0.09	0.78	-	0.20	1.51	2.43	4.28	94.41
4	148	878.09	38.82	-	5.29	-	4.13	-	21.67	2.01	0.32	-	72.24
4	149	878.09	46.73	-	6.43	-	4.47	-	24.54	2.42	0.23	-	84.82
4	150	878.09	48.07	-	6.45	-	4.41	-	24.03	2.65	0.21	-	85.82

Table A.10. *Continued*

Unit	Analyses #	Sample depth	SiO_2	TiO_2	Al_2O_3	Cr_2O_3	FeO_{tot}	MnO	MgO	CaO	Na_2O	K_2O	Total
4	151	878.09	47.80	-	6.29	-	4.84	-	24.31	2.68	0.42	0.05	86.39
4	152	878.09	47.48	-	6.16	-	4.50	-	24.21	2.51	0.29	-	85.15
4	153	878.09	45.54	-	5.85	-	4.91	0.10	22.28	2.73	0.36	0.08	81.85
4	154	878.09	39.73	0.39	5.25	-	14.48	-	22.50	2.33	0.55	0.06	85.29
5	155	892.55	33.52	-	4.80	-	3.85	-	18.55	1.15	0.80	0.08	62.75
5	156	892.55	34.42	0.29	5.30	-	6.82	-	15.11	0.87	0.87	0.76	64.44
5	157	892.55	60.95	0.11	19.95	-	2.03	-	0.08	3.19	4.10	8.01	98.42
5	158	892.55	33.24	0.06	4.19	0.05	4.09	0.12	15.86	1.65	0.76	0.15	60.17
5	159	892.55	57.77	0.15	18.18	-	2.86	-	0.07	2.44	2.44	9.70	93.61
5	160	892.55	59.45	0.09	19.31	-	0.92	-	0.15	2.67	3.09	7.68	93.36
5	161	892.55	50.42	0.09	13.47	-	2.02	-	9.14	2.10	2.23	3.78	83.25
5	162	892.55	34.99	0.08	5.45	-	4.06	-	13.99	1.46	0.28	0.55	60.86
5	163	892.55	60.21	0.11	19.84	-	0.97	-	0.15	3.41	3.43	7.57	95.69
5	164	892.55	64.36	0.21	19.50	-	0.65	-	-	2.03	2.49	8.74	97.98
5	165	892.55	59.76	0.30	19.26	-	0.65	-	0.06	2.73	3.88	7.47	94.11
5	166	892.55	62.61	0.11	20.30	-	1.21	-	0.07	3.38	3.21	7.50	98.39
5	167	892.55	96.95	0.14	0.40	-	0.11	-	-	0.16	0.02	0.09	97.87
5	168	892.55	56.52	0.10	17.82	-	0.73	-	0.06	2.35	3.53	7.85	88.96
5	169	892.55	60.97	0.12	19.71	-	0.80	-	-	3.04	3.51	8.68	96.83
5	170	892.55	60.91	0.66	19.20	-	1.00	-	0.09	3.15	3.40	7.83	96.24
5	171	892.55	60.88	0.12	18.77	-	0.91	-	0.07	2.95	3.38	8.75	95.83
5	172	892.55	59.71	0.06	20.35	-	2.01	-	0.24	4.52	4.30	5.49	96.68

Appendix A.11.
Groundmass EMPA results (Chapter 5)

Table A.11. Groundmass EMPA results (Chapter 5)

Unit	Analyses #	Sample depth	SiO_2	TiO_2	Al_2O_3	Cr_2O_3	FeO_{tot}	MnO	MgO	CaO	Na_2O	K_2O	Total
2	1	835.14	30.86	0.06	7.45	-	2.33	0.09	5.01	30.86	0.72	1.47	78.85
2	2	835.14	36.75	0.09	6.65	-	4.48	-	12.73	18.82	0.37	0.50	80.39
2	3	835.14	46.77	0.47	9.55	0.28	13.28	-	11.09	2.90	0.53	0.84	85.71
2	4	835.14	44.90	0.12	8.07	-	6.36	0.09	15.48	7.31	0.63	0.77	83.73
2	5	835.14	43.72	0.23	7.55	-	6.22	0.12	14.53	9.65	0.71	0.62	83.35
2	6	835.14	35.13	0.12	6.49	-	4.66	-	11.49	18.94	0.46	0.52	77.81
2	7	835.14	26.58	-	4.57	-	3.58	-	9.47	25.19	0.74	0.73	70.86
2	8	835.14	44.75	0.08	8.27	-	5.63	-	15.03	7.27	0.58	0.55	82.16
2	9	835.14	46.74	0.12	10.29	0.28	5.61	-	9.38	6.15	0.53	0.10	79.20
2	10	835.14	45.93	0.14	9.31	-	5.25	-	13.35	8.36	0.55	0.69	83.58
2	11	835.14	45.92	0.08	10.00	0.30	5.31	-	12.10	8.75	0.63	0.81	83.90
3	12	mrp1_ 846.06	-	-	-	0.06	-	0.20	0.33	55.97	-	-	56.56
3	13	mrp1_ 846.06	0.10	-	-	-	-	0.28	0.30	66.59	0.05	-	67.32
3	14	mrp1_ 846.06	-	-	-	0.23	0.09	0.29	0.22	58.95	0.02	-	59.80
3	15	mrp1_ 846.06	10.52	-	2.24	-	1.35	0.22	3.10	41.03	0.22	0.34	59.02
3	16	mrp1_ 846.06	14.81	2.50	3.93	0.15	61.99	-	2.36	1.76	0.41	1.45	89.36
3	17	mrp1_ 846.06	1.54	-	0.10	-	0.31	0.29	1.04	60.09	0.03	0.09	63.49
3	18	mrp1_ 846.06	32.66	0.11	11.16	-	5.81	-	6.97	20.60	0.21	0.50	78.02
3	19	mrp1_ 846.06	48.01	0.08	8.85	-	5.58	-	15.95	2.28	0.38	0.67	81.80
3	20	mrp1_ 846.06	44.70	-	7.64	-	6.09	-	15.31	1.95	0.35	0.67	76.71
3	21	mrp1_ 846.06	41.58	0.11	7.32	-	6.18	-	13.67	2.22	0.36	1.16	72.60
3	22	mrp1_ 846.06	45.59	0.12	8.48	0.23	6.27	-	18.89	4.30	0.67	0.74	85.29
3	23	mrp1_ 846.06	44.17	0.07	8.08	-	7.10	-	14.81	1.67	0.26	1.76	77.92
3	24	mrp1_ 846.06	41.93	0.10	7.40	-	6.91	-	13.56	1.66	0.25	1.48	73.29
3	25	mrp1_ 846.06	49.40	0.15	13.46	0.07	4.35	-	4.05	2.25	1.13	6.93	81.79
3	26	mrp1_ 846.06	33.31	0.83	8.45	-	16.61	-	5.91	0.94	1.16	4.57	71.78
3	27	mrp1_ 846.06	37.07	-	9.12	0.21	2.56	-	4.44	0.92	0.37	4.33	59.02
3	28	mrp1_ 846.06	49.31	0.11	10.71	-	6.98	-	10.00	1.31	0.43	2.68	81.53
3	29	mrp2_ 846.06	48.01	0.08	8.85	-	5.58	-	15.95	2.28	0.38	0.67	81.80
3	30	mrp2_ 846.06	44.70	-	7.64	-	6.09	-	15.31	1.95	0.35	0.67	76.71
3	31	mrp2_ 846.06	41.58	0.11	7.32	-	6.18	-	13.67	2.22	0.36	1.16	72.60
3	32	mrp2_ 846.06	45.59	0.12	8.48	0.23	6.27	-	18.89	4.30	0.67	0.74	85.29
3	33	mrp2_ 846.06	44.17	0.07	8.08	-	7.10	-	14.81	1.67	0.26	1.76	77.92
3	34	mrp2_ 846.06	41.93	0.10	7.40	-	6.91	-	13.56	1.66	0.25	1.48	73.29
3	35	mrp2_ 846.06	49.40	0.15	13.46	0.07	4.35	-	4.05	2.25	1.13	6.93	81.79
3	36	mrp2_ 846.06	33.31	0.83	8.45	-	16.61	-	5.91	0.94	1.16	4.57	71.78
3	37	mrp2_ 846.06	37.07	-	9.12	0.21	2.56	-	4.44	0.92	0.37	4.33	59.02
3	38	mrp2_ 846.06	49.31	0.11	10.71	-	6.98	-	10.00	1.31	0.43	2.68	81.53
5	39	892.55	0.19	-	-	-	0.14	0.37	0.37	63.79	0.03	0.06	64.95
5	40	892.55	-	-	-	-	0.10	0.31	6.72	52.86	0.03	0.05	60.07